Natural Resources Canada | Ressources naturelles Canada

Contents

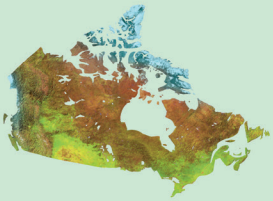

Geological Survey of Canada
Bulletin 616

Targeted Geoscience Initiative 5: contributions to the understanding and exploration of porphyry deposits

Edited by A. Plouffe and E. Schetselaar

2021

Canada

Geological Survey of Canada
Bulletin 616

Targeted Geoscience Initiative 5: contributions to the understanding and exploration of porphyry deposits

Edited by
A. Plouffe and E. Schetselaar

2021

Contents

ISSN 2560-7219
ISBN 978-0-660-39279-0
Catalogue No. M42-616E-PDF
https://doi.org/10.4095/327940

A copy of this publication is also available for reference in depository libraries across Canada through access to the Depository Services Program's Web site at http://dsp-psd.pwgsc.gc.ca.

This publication is available for free download through GEOSCAN (https://geoscan.nrcan.gc.ca).

Cover illustration
(Clockwise from left): New Afton open pit, south-central British Columbia (photograph by E. Schetselaar, NRCan photo 2020-126); haul trucks and excavator at Gibraltar Mine, south-central British Columbia (photograph by A. Plouffe, NRCan photo 2020-124); supergene mineralization of native copper, chalcocite, and hematite at New Afton mine, south-central British Columbia (photograph by E. Schetselaar, NRCan photo 2020-127); chalcopyrite and molybdenite in mine-phase tonalite at Gibraltar Mine, south-central British Columbia (photograph by A. Plouffe, NRCan photo 2020-125).

Editors' address
A. Plouffe (alain.plouffe@nrcan-rncan.gc.ca)
E. Schetselaar (ernst.schetselaar@nrcan-rncan.gc.ca)
Geological Survey of Canada
601 Booth Street
Ottawa, Ontario
K1A 0E8

CONTENTS

SUMMARY

Porphyry deposits are high-volume, low-grade orebodies consisting of disseminated sulfide minerals genetically related to felsic to intermediate intrusions. Previous compilations have shown that they represent the world's largest source of copper, approximately half the source of the world's molybdenum, and contain significant quantities of gold, silver, tungsten, and tin. In Canada, porphyry deposits are dominantly present within the Cordillera of British Columbia and Yukon, and notable porphyry-style deposits occur in the southern Superior Craton and the Appalachian Orogen.

Most porphyry ore systems are intimately associated with magmatic processes at convergent plate margins and are commonly associated with skarn and epithermal deposits. Metal-rich magma and hydrothermal fluids are sourced episodically from metasomatized subcontinental lithospheric mantle or lower crust, which may lead to porphyry mineralization during subduction beneath island arcs or continental margins, as well as during post-collisional thickening and mantle upwelling in response to crustal delamination and extension. Long-lived magmatism and metasomatism within the mantle wedge below the upper plate can be critical for sufficient metal enrichment. Transport of magmatic fluids to shallow crustal levels that form porphyry deposits is believed to preferentially occur during periods of plate reorganization and/or local changes in stress regimes associated with flattening angles of subduction, ridge subduction, slab tear, or roll-back.

Although porphyry deposits and their associated alteration zones may extend over a few square kilometres, their exploration can be challenging due to geological complexity, typically low metal grade, poor exposure, and common post-mineralization sedimentary cover. At a regional scale, the key to exploration success is to identify the exceptional porphyry-bearing belts of intermediate to felsic intrusive rocks that were mobilized from a fertile mantle or lower crustal reservoir and emplaced at a favourable crustal depth to enable their preservation and discovery. At a local scale, vectoring toward a porphyry deposit can be based on detecting geophysical, geochemical, and mineralogical anomalies generated by the ore zone itself but also on detecting anomalous responses from the enveloping alteration, supergene, and/or secondary mineralization zones.

SOMMAIRE

Les gisements porphyriques sont des amas minéralisés à fort volume et à faible teneur constitués de minéraux sulfurés disséminés, qui sont génétiquement associés à des intrusions felsiques à intermédiaires. Des compilations précédentes ont permis d'établir que ces gisements représentent les plus importantes sources de cuivre au monde, constituent environ la moitié des sources mondiales de molybdène, et contiennent des quantités importantes d'or, d'argent, de tungstène et d'étain. Au Canada, ils se trouvent principalement dans la Cordillère de la Colombie-Britannique et du Yukon, mais des gisements importants de style porphyrique sont également présents dans la partie sud du craton du lac Supérieur ainsi que dans l'orogène des Appalaches.

La plupart des systèmes minéralisateurs porphyriques sont intimement associés à des processus magmatiques aux limites de plaques convergentes et sont communément associés à des skarns minéralisés et à des gîtes épithermaux. Le magma riche en métaux et les fluides hydrothermaux proviennent épisodiquement de la croûte inférieure ou du manteau lithosphérique subcontinental métasomatisé, ce qui peut donner lieu à la formation d'une minéralisation porphyrique au cours de la subduction sous les arcs insulaires ou les marges continentales, ou encore lors de l'épaississement crustal et de la remontée mantellique postcollision, qui se produisent en réponse à une délamination et à une distension de la croûte continentale. Un magmatisme et un métasomatisme de longue durée à l'intérieur du prisme mantellique au-dessous de la plaque supérieure peuvent s'avérer indispensables à un enrichissement suffisant en métaux. Il semble que le transport des fluides magmatiques vers les niveaux crustaux peu profonds à l'origine de la formation des gîtes porphyriques se produise de préférence pendant les périodes de réorganisation des plaques ou de changements locaux dans les régimes de contraintes associés à la réduction des angles de subduction, à la subduction de dorsales, ou encore à la déchirure ou au repli de dalles tectoniques.

Bien que les gîtes porphyriques et les zones d'altération qui leur sont associées puissent s'étendre sur quelques kilomètres carrés, leur exploration peut s'avérer difficile en raison de la complexité géologique, de leur teneur en métaux typiquement faible, d'une mauvaise exposition et de la présence commune d'une couverture sédimentaire postérieure à la minéralisation. À l'échelle régionale, la clé d'une exploration réussie consiste à détecter les ceintures exceptionnelles de roches intrusives intermédiaires à felsiques à texture porphyrique, qui ont été mobilisées à partir d'un réservoir fertile situé dans le manteau ou la croûte inférieure et ont été mises en place à une profondeur crustale favorable à leur préservation et à leur découverte. À l'échelle locale, les vecteurs pointant vers des gîtes porphyriques peuvent être fondés sur la détection d'anomalies géophysiques, géochimiques ou minéralogiques générées par la zone minéralisée elle-même, mais également par la détection des réponses anomales provenant des zones d'altération et des zones de minéralisation supergène ou secondaire qui enveloppent la zone minéralisée.

This Geological Survey of Canada (GSC) Bulletin contains 10 papers dedicated to advancing knowledge of the tectono-magmatic settings of porphyry-style mineralization and the development of new methods for their exploration. The research was conducted by the GSC and partner organizations under the auspices of the Government of Canada's Targeted Geoscience Initiative 5 (TGI-5) program, which aimed to develop new geoscience knowledge and techniques to facilitate the discovery of deep mineral deposits.

Spatial and temporal distribution of porphyry deposits

In the first paper, Kellett and coauthors examine the spatial and temporal distribution of porphyry-style mineralization with respect to post-accretionary granitic suites in the Canadian Appalachians. This investigation is supported by an orogen-wide compilation of U-Pb zircon granite crystallization ages, augmented with new age determinations. From the comparison of orogen-wide timing and distribution of post-accretionary granitoid suites with the distribution and timing of shear zone and fault reactivation within the orogen, a picture emerges in which magma transport and emplacement of Middle to Late Devonian granitoids and associated Sn-W-Mo mineralization occurred more or less simultaneously across all terrane boundaries, and in close spatial association with active structures. Together with petrological evidence for an upper mantle origin of magma and metals, these new data lead the authors to postulate that the voluminous orogen-parallel intrusions in the upper crust are the result of lithospheric delamination of the upper mantle, with transport of the hydrous magmas and fluids enriched in Sn, W, and Mn to shallow crustal levels being facilitated syn-kinematically by the reactivated shear zones.

In the second paper, Rogers also focuses on orogen-scale spatial and temporal relationships between porphyry intrusive complexes, terrane boundaries, and regional tectonic structures. In reviewing the tectono-stratigraphic setting of porphyry belts and their supracrustal host rocks, Rogers provides an alternative model to explain the spatial distribution of porphyry belts of the Quesnel terrane in the Canadian Cordillera of British Columbia. Contrary to the widely accepted model of eastward migration of east-dipping subduction, Rogers suggests that Middle Triassic to Middle Jurassic arc magmatism might have been relatively static along the western margin of the Quesnel terrane and explains the present-day configuration of eastward-younging plutonic belts in the southern Quesnel terrane by post-depositional structural re-alignments. Although additional stratigraphic and structural restoration studies would be needed to validate Rogers'

Le présent bulletin de la Commission géologique du Canada (CGC) comprend dix articles consacrés à l'avancement des connaissances sur les cadres tectonomagmatiques des minéralisations de style porphyrique et au développement de nouvelles méthodes visant leur exploration. La CGC a mené ces recherches de concert avec des organisations partenaires dans le cadre de la phase 5 du programme de l'Initiative géoscientifique ciblée (IGC-5) du gouvernement du Canada, qui encourage le développement de nouvelles connaissances et techniques géoscientifiques pour faciliter la découverte de gîtes minéraux en profondeur.

Distribution spatiale et temporelle des gîtes porphyriques

Dans le premier article, Kellett et ses coauteurs examinent la distribution spatiale et temporelle de la minéralisation de style porphyrique par rapport aux suites granitiques postaccrétionnaires des Appalaches canadiennes. Cette recherche est soutenue par une compilation des âges de cristallisation des granites obtenus par datation U-Pb sur zircon à l'échelle de l'orogène, et enrichie par de nouveaux résultats de datation. En comparant la chronologie et la distribution des suites granitoïdes postaccrétionnaires à l'échelle de l'orogène à la chronologie de la réactivation et à la distribution des zones de cisaillement et des failles au sein de l'orogène, on s'aperçoit que le transport du magma et la mise en place des granitoïdes du Dévonien moyen-tardif et de la minéralisation à Sn-W-Mo associée se sont produits plus ou moins simultanément de part et d'autre de toutes les limites des terranes, et en étroite association spatiale avec les structures actives. Ces nouvelles données, ainsi que les preuves pétrologiques qui indiquent que le magma et les métaux proviennent du manteau supérieur, ont amené les auteurs à supposer que les volumineuses intrusions parallèles à l'orogène mises en place dans la croûte supérieure sont le résultat d'une délamination lithosphérique du manteau supérieur et que le transport des magmas hydratés et des fluides enrichis en Sn, W et Mn vers les niveaux crustaux peu profonds a été facilité de façon syncinématique par la réactivation des zones de cisaillement.

Dans le deuxième article, Rogers se concentre également sur les relations spatiales et temporelles à l'échelle de l'orogène entre les complexes intrusifs porphyriques, les limites des terranes et les structures tectoniques régionales. En examinant le cadre tectono-stratigraphique des ceintures d'intrusions porphyriques et de leurs roches hôtes supracrustales, Rogers fournit un modèle différent pour expliquer la distribution spatiale des ceintures d'intrusions porphyriques du terrane de Quesnel de la Cordillère canadienne, en Colombie-Britannique. Rogers suggère que, contrairement au modèle largement accepté de migration vers l'est de la subduction suivant une surface inclinée vers l'est, le magmatisme d'arc survenu du Trias moyen au Jurassique moyen pourrait avoir été relativement statique le long de la marge occidentale du terrane de Quesnel, et il ajoute que la configuration actuelle des ceintures plutoniques, qui rajeunissent vers l'est dans la partie sud du terrane de Quesnel, s'explique par des réalignements structuraux postérieurs au dépôt de séquences sédimentaires. Bien que d'autres études de restauration stratigraphique et structurale soient nécessaires pour valider le modèle de Rogers, celui-ci offre un point de

model, it provides an interesting alternative view with important implications for regional exploration, since regional fault displacement may have resulted in omission and/or duplication of fertile plutonic suites.

Geophysical responses of porphyry deposits

Three papers address the geophysical responses of porphyry deposits located in the Iron Mask batholith, British Columbia. Bellefleur and coauthors present a new method for vertical seismic profiling (VSP) that was tested by imaging the structure of the deeper part of the New Afton porphyry Cu-Au deposit. This survey provides the first distributed acoustic sensing (DAS) VSPs for mineral exploration in Canada. The DAS survey was based on two arrays of fibre-optic cables in two boreholes intersecting the hypogene ore and enveloping alteration zones of the New Afton deposit. The DAS system provided high signal-to-noise ratio data with semi-continuous sensing along a fibre-optic cable. To interpret the DAS data, physical rock property measurements were acquired from wireline logs and drill core samples. These data indicate that seismic impedance contrast between potassic and propylitic alteration zones is sufficient to generate seismic reflections. The 3-D seismic image obtained from processing DAS data shows a number of shallowly dipping seismic reflections that, in addition to faults and fracture zones, are possibly controlled by impedance contrasts at sheared contacts between different Nicola Group metavolcanic rocks.

In the second geophysical paper, Roots and coauthors present 3-D inversions from magnetotelluric (MT) data collected along eight lines over the New Afton deposit. The 3-D inversions show conductive cover explained by high primary porosity of clastic sedimentary rocks underlain by the more resistive metavolcanic rocks of the Nicola Group and intrusive rocks of the Iron Mask batholith. Within these rocks with a low primary porosity, conductive and resistive linear features are spatially associated with northeast-southwest–trending fault zones that structurally control the New Afton and Pothook mineralization. These linear anomalous zones of resistivity are explained by variations in secondary porosity induced by higher order fracture systems associated with the northeast-southwest–striking fault zones. The investigation of Roots and coauthors demonstrates the potential of MT surveys for imaging deep-seated structural controls of porphyry mineralization.

In the third geophysical paper, Thomas revisits the close association of magnetic highs with porphyry Cu-Au mineralization, using proprietary

vue intéressant ayant des retombées importantes pour l'exploration régionale, puisque les déplacements le long des failles régionales pourraient avoir entraîné l'élimination ou la répétition de suites plutoniques fertiles.

Réponses géophysiques des gîtes porphyriques

Trois articles traitent des réponses géophysiques des gîtes porphyriques situés dans le batholite d'Iron Mask, en Colombie-Britannique. Bellefleur et ses coauteurs présentent une nouvelle méthode de profilage sismique vertical (PSV) qui a été mise à l'essai en produisant une image de la structure de la partie plus profonde du gisement porphyrique à Cu-Au de New Afton. Ce levé fournit les premiers PSV acquis au moyen de la détection acoustique répartie (distributed acoustic sensing; DAS) pour l'exploration minérale au Canada. Le levé DAS était basé sur deux ensembles de câbles à fibres optiques placés dans deux trous de forage qui recoupaient la zone de minéralisation hypogène et les enveloppes d'altération du gisement de New Afton. Le système DAS a permis d'obtenir des valeurs élevées du rapport signal/bruit avec détection semi-continue le long d'un câble à fibres optiques. Afin de pouvoir interpréter les données du levé DAS, l'équipe de Bellefleur a acquis des mesures des propriétés physiques des roches à partir de diagraphies par câble et d'échantillons de carottes de forage. Les données indiquent que le contraste d'impédance sismique entre les zones d'altération potassique et propylitique est suffisant pour générer des réflexions sismiques. L'image sismique tridimensionnelle (3D) obtenue par le traitement des données DAS montre un certain nombre de réflexions sismiques faiblement inclinées qui, en plus des failles et des zones de fracture, sont probablement régies par les contrastes d'impédance aux zones de contact cisaillées entre différentes roches métavolcaniques du Groupe de Nicola.

Dans le deuxième article portant sur la géophysique, Roots et ses coauteurs présentent des inversions 3D des données magnétotelluriques (MT) recueillies le long de huit lignes surmontant le gisement de New Afton. Les inversions 3D indiquent la présence d'une couche conductrice supérieure, qui peut être expliquée par la forte porosité primaire de roches sédimentaires détritiques, surmontant des roches plus résistives formées des roches métavolcaniques du Groupe de Nicola et de roches intrusives du batholite d'Iron Mask. Dans ces roches à faible porosité primaire, des entités linéaires conductrices et résistives sont associées sur le plan spatial à des zones de failles d'orientation nord-est–sud-ouest qui exercent un contrôle structural sur la minéralisation des gisements de New Afton et de Pothook. Ces zones linéaires à résistivité anomale s'expliquent par des variations de la porosité secondaire induites par des réseaux de fracture d'ordre supérieur associés aux zones de failles d'orientation nord-est–sud-ouest. L'étude de Roots et de ses coauteurs démontre le potentiel des levés MT pour l'imagerie des contrôles structuraux de la minéralisation en profondeur dans les systèmes porphyriques.

Dans le troisième article portant sur la géophysique, Thomas réexamine l'association étroite entre les crêtes magnétiques et la minéralisation porphyrique à Cu-Au à l'aide de données aéro-

high-resolution aeromagnetic data acquired over the Iron Mask batholith host of the New Afton deposit. Clusters of magnetic highs are close (approximately 500 m) to numerous porphyry Cu-Au occurrences within the batholith. The close association between magnetic highs and porphyry mineralization correlates with high magnetite content of alteration zones and magnetite veins near the mineralization. Given that a porphyry system is typically characterized by multiple hydrothermal events, the close association of magnetic highs with porphyry mineralization holds if the events that have produced magnetite and copper-gold mineralization are genetically linked to the magmatic-hydrothermal fluid pathways of the porphyry ore system. In a mineral exploration scenario, the inferred link between magnetic anomalies and porphyry mineralization can be corroborated using airborne gamma-ray spectrometry data (K, Th, U) because low Th-K ratios are commonly associated with potassic alteration of granitoid intrusive rocks. Used in combination, these airborne geophysical surveys can focus mineral exploration within larger belts of prospective intrusions.

Porphyry mineral chemistry

Three papers present a detailed investigation of the chemical composition of specific minerals associated with porphyry mineralization using laser-ablation inductively coupled plasma mass spectrometry (LA-ICP-MS). Percival and coauthors analyzed the composition of abundant magnetite in the New Afton deposit as a potential vector to mineralization within the Iron Mask Batholith. On a Ti versus Ni-Cr plot, both disseminated and vein magnetite fall within the hydrothermal field. In contrast, on a Ti versus V diagram, most magnetite samples plot within the magmatic field and overlapping magmatic-hydrothermal field of porphyry mineralization. On the same diagram, some samples have V concentrations above the porphyry field. Although this study is inconclusive at providing a magnetite vector to mineralization, Percival and coauthors suggest that magnetite of magmatic and hydrothermal origins at New Afton formed in high-temperature, oxidized crystallization conditions that are characteristic of many porphyry ore systems.

In their study of tourmaline in rocks and detrital sediments at the Casino porphyry copper deposit (Yukon) and the Woodjam porphyry copper prospect (British Columbia), Beckett-Brown and coauthors report that tourmaline grains from porphyry alteration zones display oscillatory and sector zoning and range from schorl (Fe^{2+}-rich) to dravite (Mg-rich) with lesser povondraite (Fe^{3+}-rich). Porphyry tourmaline contains

magnétiques haute résolution acquises au-dessus du batholite d'Iron Mask, hôte du gisement de New Afton. Des groupes de crêtes magnétiques sont situés près (soit à approximativement 500 m) de nombreux indices de Cu-Au de type porphyrique au sein du batholite. L'association étroite entre les crêtes magnétiques et la minéralisation porphyrique est en corrélation avec la forte teneur en magnétite des zones d'altération et des filons de magnétite à proximité de la minéralisation. Comme un système porphyrique est habituellement caractérisé par de nombreux événements hydrothermaux, cette association étroite entre les crêtes magnétiques et la minéralisation porphyrique est valable si les événements à l'origine du dépôt de la magnétite et de la minéralisation cuproaurifère sont génétiquement liés aux voies de migration des fluides magmatiques-hydrothermaux du système minéralisateur porphyrique. Dans un contexte d'exploration minérale, le lien inféré entre les anomalies magnétiques et la minéralisation porphyrique peut être corroboré à l'aide de données de spectrométrie gamma (K, Th, U) de levés aéroportés, car les faibles rapports Th/K sont généralement associés à l'altération potassique des roches intrusives granitoïdes. Lorsqu'on les utilise en combinaison avec d'autres sources de données, ces levés géophysiques aéroportés permettent, lors de campagnes d'exploration minérale, de cibler les zones d'intérêt au sein de grandes ceintures d'intrusions prometteuses.

Chimie des minéraux de systèmes porphyriques

Trois articles présentent une étude détaillée de la composition chimique de minéraux particuliers associés à la minéralisation porphyrique en utilisant la spectrométrie de masse avec plasma à couplage inductif jumelée à l'ablation par laser (LA-ICP-MS). Percival et ses coauteurs ont analysé la composition de l'abondante magnétite présente dans le gisement de New Afton comme vecteur potentiel de la minéralisation à l'intérieur du batholite d'Iron Mask. Dans un diagramme de la concentration de Ti en fonction du rapport Ni/Cr, la magnétite disséminée et la magnétite filonienne se trouvent toutes deux dans le champ hydrothermal. En revanche, dans un diagramme comparant la concentration de Ti à celle de V, la plupart des échantillons de magnétite se situent dans le champ magmatique et chevauchent le champ magmatique-hydrothermal de la minéralisation porphyrique. Dans le même diagramme, certains échantillons ont des concentrations de V supérieures à celles définies par le champ porphyrique. Bien que cette étude ne permette pas de confirmer que la magnétite puisse agir comme un vecteur de la minéralisation, Percival et ses coauteurs suggèrent que la magnétite d'origine magmatique et hydrothermale du gisement de New Afton s'est formée à haute température dans des conditions de cristallisation oxydées qui sont caractéristiques de nombreux systèmes minéralisateurs porphyriques.

Dans leur étude de la présence de tourmaline dans les roches et les sédiments détritiques du gisement de cuivre porphyrique de Casino (Yukon) et du prospect de minéralisation de cuivre porphyrique de Woodjam (Colombie-Britannique), Beckett-Brown et ses coauteurs mentionnent que les grains de tourmaline dans les zones d'altération du système porphyrique affichent une zonation oscillatoire et sectorielle où la composition de la tourmaline s'étend du schorl (riche en Fe^{2+}) à la dravite (riche en Mg) avec une présence

elevated concentrations of Cu and Sr and low levels of Pb and Zn compared to tourmaline from other geological settings. Tourmaline grains recovered from till at Woodjam and from stream sediments at Casino display the same zonation as that observed in porphyry tourmaline, with composition partly overlapping that of the porphyry tourmaline, suggesting mixed provenances.

With the objective of identifying epidote grains in till that have been eroded from porphyry alteration zones, Plouffe and coauthors analyzed epidote from intrusive rocks hosting porphyry mineralization and from regionally metamorphosed rocks of the Nicola Group. These rocks are the two dominant sources of epidote at three porphyry copper study sites in British Columbia: Gibraltar mine, Mount Polley mine, and Woodjam prospect. Epidote in porphyry-mineralized intrusive rocks contains lower concentrations of Hf, Th, Sc, Cr, and Y and higher concentrations of As, Sb, and Cu compared to epidote in Nicola Group rocks. Abundant epidote grains in till display a composition similar to the porphyry-related epidote. This study concludes that analyzing the composition of epidote in till can be used in mineral exploration to detect buried hydrothermal alteration associated with porphyry copper mineralization.

Geochemical and mineralogical footprint of porphyry deposits

The last two papers of the volume present studies of the mineralogical and geochemical footprint of porphyry mineralization in detrital sediments of unglaciated and glaciated landscapes. In their evaluation of stream sediment geochemistry and mineralogy at the Casino porphyry Cu-Au-Mo deposit in the unglaciated landscape of Yukon, McClenaghan and coauthors identified a suite of indicator minerals including gold, chalcopyrite, molybdenite, sphalerite, jarosite, goethite, and pyrite in bulk stream sediments at least 14 km downstream from the main mineralized zones at Casino and in streams draining other nearby porphyry mineral occurrences. Similarly, the stream sediment (<0.177 mm) and streamwater geochemistry display multi-element anomalies identified downstream from porphyry mineralization. McClenaghan and coauthors conclude that indicator minerals provide information that conventional stream-sediment geochemistry alone does not, making them a valuable addition to regional sampling programs for porphyry Cu exploration.

moindre de povondraïte (riche en Fe^{3+}). La tourmaline de système porphyrique renferme des concentrations élevées de Cu et de Sr et de faibles niveaux de Pb et de Zn par rapport à la tourmaline issue d'autres contextes géologiques. Les grains de tourmaline récupérés dans le till au prospect de Woodjam et dans les sédiments de ruisseau au gisement de Casino présentent la même zonation que celle observée dans la tourmaline de système porphyrique, avec une composition qui ne chevauche que partiellement celle de la tourmaline de système porphyrique, suggérant ainsi des provenances diverses.

Dans le but de repérer dans le till des grains d'épidote ayant été érodés des zones d'altération de système porphyrique, Plouffe et ses coauteurs ont analysé l'épidote présente dans des roches intrusives renfermant de la minéralisation porphyrique et dans des roches du Groupe de Nicola métamorphisées à l'échelle régionale. Ces roches sont les deux sources principales d'épidote à trois sites d'étude de la minéralisation de cuivre porphyrique en Colombie-Britannique : la mine Gibraltar, la mine Mount Polley et le prospect de Woodjam. Dans les roches intrusives à minéralisation porphyrique, l'épidote contient des concentrations plus faibles de Hf, Th, Sc, Cr et Y et des concentrations plus élevées de As, Sb et Cu par rapport à l'épidote présente dans les roches du Groupe de Nicola. Les grains d'épidote abondants dans le till affichent une composition semblable à celle de l'épidote de système porphyrique. Cette étude conclut que l'analyse de la composition de l'épidote dans le till peut être utile en exploration minérale pour détecter l'altération hydrothermale associée à des minéralisations de cuivre porphyriques enfouies.

Empreinte géochimique et minéralogique des gîtes porphyriques

Les deux derniers articles du volume présentent des études portant sur l'empreinte minéralogique et géochimique de la minéralisation porphyrique dans les sédiments détritiques des paysages glaciaires et non glaciaires. Dans leur évaluation de la géochimie et de la minéralogie des sédiments de ruisseau au gisement porphyrique à Cu-Au-Mo de Casino, situé dans le paysage non glaciaire du Yukon, McClenaghan et ses coauteurs ont répertorié une suite de minéraux indicateurs, dont l'or, la chalcopyrite, la molybdénite, la sphalérite, la jarosite, la goethite et la pyrite, dans les sédiments de ruisseau en vrac recueillis jusqu'à 14 km au moins en aval des principales zones minéralisées du gisement de Casino et dans les ruisseaux drainant d'autres indices minéralisés de type porphyrique situés à proximité. De même, la géochimie des sédiments de ruisseau (fraction de < 0,177 mm) et des eaux de ruisseau présente des anomalies multiéléments détectées en aval de la minéralisation porphyrique. McClenaghan et ses coauteurs concluent que les minéraux indicateurs fournissent de l'information qu'il est impossible d'obtenir uniquement par la géochimie classique des sédiments de ruisseau, et que ces minéraux indicateurs constituent donc un ajout précieux aux programmes d'échantillonnage régionaux des campagnes d'exploration visant les minéralisations de cuivre porphyriques.

Using an automated mineral identification method that combines a mineral liberation analysis (MLA) database and scanning electron microscopy (SEM), a second paper by Plouffe and coauthors report a greater abundance of chalcopyrite and epidote in the fine-sand heavy mineral concentrates of till close to mineralization compared to till in background regions at four porphyry study sites in British Columbia. One key advantage of the MLA-SEM method is that it requires smaller bulk till samples than those required for optical analysis of the mineralogy of medium-sand heavy mineral concentrates. Smaller samples can lower the costs of sample shipping and processing in a mineral exploration program. Plouffe and coauthors conclude that automated indicator-mineral analysis by MLA-SEM can be used for porphyry copper exploration.

Dans un deuxième article, Plouffe et ses coauteurs constatent que la chalcopyrite et l'épidote sont plus abondantes dans la fraction du sable fin des concentrés de minéraux lourds du till tirés d'échantillons prélevés près de la minéralisation que dans le till des régions de référence à quatre sites d'étude de la minéralisation porphyrique en Colombie-Britannique. Ces résultats ont été obtenus à l'aide d'une méthode automatisée d'identification des minéraux qui combine une base de données d'analyse de libération minérale (ALM) et la microscopie électronique à balayage (MEB). L'un des principaux avantages de la méthode ALM-MEB est qu'elle utilise des échantillons de till en vrac plus petits que ceux requis pour l'analyse optique de la minéralogie de la fraction du sable moyen des concentrés de minéraux lourds. Des échantillons plus petits peuvent réduire les coûts d'expédition et de traitement des échantillons dans le cadre d'un programme d'exploration minérale. Plouffe et ses coauteurs concluent donc que l'analyse automatisée des minéraux indicateurs par ALM-MEB peut servir en exploration visant les minéralisations de cuivre porphyriques.

ACKNOWLEDGMENTS

This publication would not have been possible without reviewers who took the time to evaluate the research and to provide comments that resulted in better scientific papers. In this regard, we acknowledge the thoughtful reviews provided by Ademola Adetunji, Seyed Masoud Ansari, Dennis Arne, Paul Gammon, Lee Groat, Lionel Jackson, Andrew Kerr, Sheida Makvandi, Matthew Polivchuk, André Pugin, Neil Rogers, Alexei Rukhlov, Paul Schiarizza, Gary Thompson, Cees van Staal, Devin Wade, and Alex Zagorevski. Christine Hutton was instrumental in organizing a contract with technical editors to ensure a timely delivery of this publication. Dedication and continuous effort provided by Jessica Tomkins allowed a smooth progression of this publication and clear communication with technical editors. Technical editors at Purple Rock Inc., Nicole Barlow and Moretta Shuert, are acknowledged for their meticulous review of papers to ensure consistency and quality following GSC guidelines.

REMERCIEMENTS

La présente publication n'aurait pas été possible sans l'aide d'examinateurs qui ont pris le temps d'évaluer les recherches et de formuler des commentaires nous permettant de publier des articles scientifiques de qualité. À cet égard, nous remercions Ademola Adetunji, Seyed Masoud Ansari, Dennis Arne, Paul Gammon, Lee Groat, Lionel Jackson, Andrew Kerr, Sheida Makvandi, Matthew Polivchuk, André Pugin, Neil Rogers, Alexei Rukhlov, Paul Schiarizza, Gary Thompson, Cees van Staal, Devin Wade et Alex Zagorevski pour leurs commentaires avisés. Christine Hutton a joué un rôle clé dans l'organisation d'un contrat avec les réviseures techniques pour assurer la livraison de la présente publication dans les délais impartis. Le dévouement et les efforts continus de Jessica Tomkins ont permis le bon déroulement du projet ainsi que des communications claires avec les réviseures techniques. Nous remercions également les réviseures techniques de Purple Rock inc., Nicole Barlow et Moretta Shuert, pour leur révision minutieuse des articles, qui a permis d'en assurer la cohérence et la qualité conformément aux lignes directrices de la CGC.

Spatio-temporal distribution of Devonian post-accretionary granitoids in the Canadian Appalachians: implications for tectonic controls on intrusion-related mineralization

D.A. Kellett[1*], N. Piette-Lauzière[2], N. Mohammadi[3, 6], L. Bickerton[4], D. Kontak[4], N. Rogers[5], and K. Larson[2]

Kellett, D.A., Piette-Lauzière, N., Mohammadi, N., Bickerton, L., Kontak, D., Rogers, N., and Larson, K., 2021. Spatio-temporal distribution of Devonian post-accretionary granitoids in the Canadian Appalachians: implications for tectonic controls on intrusion-related mineralization; in *Targeted Geoscience Initiative 5: contributions to the understanding and exploration of porphyry deposits, (ed.) A. Plouffe and E. Schetselaar; Geological Survey of Canada, Bulletin 616, p. 7–23. https://doi.org/10.4095/327955*

Abstract: Intrusion-related mineralization in the Canadian Appalachian Orogen is widespread and associated with Devonian post-accretionary granitoids. Here we review the spatial and temporal distribution of post-accretionary magmatism across the orogen, and the coeval structural network that may have facilitated magma ascent and emplacement. We demonstrate that magmatism and associated intrusion-related mineralization were particularly widespread during the Late Devonian, occurring within all tectonic zones of the orogen. This, along with published petrological arguments, suggests a deep and orogen-scale source for both magma and metals. Lithospheric delamination following terminal continent–continent collision may be a plausible process to initiate magmatism at such a scale, and if so, may be an important geodynamic process for intrusion-related mineralization. The magmatic belts are spatially associated with shear zones and faults that formed or reactivated during the Late Devonian and likely facilitated magma ascent independent of their kinematics. Further work is required to relate fault kinematics and slip events to magma emplacement.

Résumé : Dans l'orogène des Appalaches au Canada, de la minéralisation apparentée à des intrusions est très répandue et est associée à des granitoïdes post-accrétionnaires du Dévonien. Nous examinons ici la distribution spatiale et temporelle du magmatisme post-accrétionnaire dans l'orogène, ainsi que le réseau structural existant à la même époque qui a pu faciliter la remontée et la mise en place du magma. Nous démontrons que l'activité magmatique et les processus associés de minéralisation apparentée à des intrusions étaient particulièrement étendus au Dévonien tardif, se manifestant dans toutes les zones tectoniques de l'orogène. Ceci, en accord avec les arguments pétrologiques déjà publiés, suggère l'existence d'une source profonde, à l'échelle de l'orogène, tant pour le magma que pour les métaux. Une délamination lithosphérique consécutive à la collision terminale continent-continent pourrait être un processus plausible de déclenchement du magmatisme à une telle échelle et, si tel est le cas, pourrait être un processus géodynamique important pour la minéralisation apparentée à des intrusions. Les ceintures magmatiques sont spatialement associées à des zones de cisaillement et à des failles qui se sont formées ou ont été réactivées au Dévonien tardif et qui ont probablement facilité la remontée du magma, indépendamment de leurs cinématiques. De plus amples travaux sont nécessaires pour relier la cinématique des failles et les épisodes de coulissage à la mise en place du magma.

[1]Geological Survey of Canada, 1 Challenger Dr, P.O. Box 1006, Dartmouth, Nova Scotia B2Y 4A2
[2]The University of British Columbia, Okanagan, 3187 University Way, ASC 413 Kelowna, British Columbia V1V 1V7
[3] University of New Brunswick, P.O. Box 4400, Fredericton, New Brunswick E3B 5A3
[4] Laurentian University, 935 Ramsey Lake Road, Sudbury, Ontario P3E 2C6
[5] Geological Survey of Canada, 601 Booth Street, Ottawa, Ontario K1A 0E8
[6] Carleton University, 1125 Colonel By Drive, Ottawa, Ontario K1S 5B6
*Corresponding author: D.A. Kellett (email: dawn.kellett@canada.ca)

INTRODUCTION

Tin, tungsten, and molybdenum are expected to play a critical role in Canada's future. Global demand for these metals is projected to increase due to their importance in alloys used in the high-tech industry, and because of China's dominance of their global production, access may be affected by evolving geopolitics. There are several major Sn±W±Mo polymetallic intrusion-related deposits in the Canadian Appalachian Orogen, including the Mount Pleasant, Sisson, and Burnt Hill deposits in New Brunswick; the East Kemptville Sn deposit on mainland Nova Scotia; and the Ackley, Grey River, and Granite Lake deposits in Newfoundland. Many other smaller deposits in the region have similar ages and tectonic settings (Fig. 1). The causative intrusions to these deposits are regionally extensive suites of post-accretionary granitoid rocks of which the latest, most-evolved phases tend to be the most highly mineralized (e.g. Lentz and Mohammadi, 2014; Mohammadi et al., 2019). Although crystallization ages, duration of magmatism, potential magma sources, and geodynamic setting have been examined or proposed for several of these suites (e.g. Kerr, 1997; Wilson and Kamo, 2016), they have not yet been comprehensively discussed at the scale of the orogen. Similarly, the potential structural controls on their emplacement have not yet been considered at this scale. Under the Targeted Geoscience Initiative (TGI) program of the Geological Survey of Canada, we aim to address this missing perspective by contributing new geochronological data to refine the spatio-temporal history of post-accretionary magmatism in the Canadian Appalachian Orogen and determining the impact of coeval structures on magma emplacement by characterizing their deformation ages and kinematics. Our progress to date has been presented in several TGI reports of activities, as well as in additional publications (e.g. Kellett et al., 2014, 2016, 2017, 2018; Bickerton et al., 2018, 2019; Moning et al., 2018, 2019; Piette-Lauzière et al., 2018, 2019; van Rooyen et al., 2018; Grant et al., 2019). In this synthesis report, we review the results from previous work and these new investigations, including a compilation of >150 crystallization ages for Devonian plutonic and a few volcanic rocks (Appendix A). We also review published and new evidence for a network of reactivated faults that we hypothesize provided the structural pathways for magma ascent during the Devonian.

TECTONIC HISTORY OF THE CANADIAN APPALACHIANS

The Appalachian Orogen is an accretionary orogen that formed from the latest Precambrian to the mid-Paleozoic along the eastern margin (today's coordinates) of Laurentia and includes much of southeastern Quebec and all of Newfoundland, New Brunswick, P.E.I., and Nova Scotia (Fig. 1). Following the Neoproterozoic breakup of the supercontinent Rodinia, a passive margin developed in the newly formed Iapetus Ocean on Laurentia's eastern flank. Subduction initiated in the late Cambrian to Ordovician, and peri-Laurentian elements (the western Dunnage zone) subsequently accreted to the Laurentian margin in the Taconic Orogeny. The outer region of the Laurentian passive margin and adjacent continental slope was transported to the west, and the well-known ophiolites of western Newfoundland were emplaced. Subduction then moved outboard and peri-Gondwanan arcs, back-arc basins, and microcontinental blocks, collectively known as Ganderia, were progressively accreted to Laurentia during the Silurian, producing the widespread Salinic Orogeny. This was followed by latest Silurian accretion of Gondwanan-derived Avalonia to the now composite Laurentian margin, closing the Iapetus Ocean and forming the Acadian Orogeny. Finally, the Rheic Ocean, lying between Avalonia and Gondwana, started to close and in the process Megumia accreted to Laurentia, recorded by the Middle to Late Devonian Neoacadian Orogeny, ultimately forming the supercontinent Pangaea during Alleghenian terminal closure of the Rheic Ocean (for a full review, *see* van Staal (2007), Hatcher (2010)). Post-accretionary (i.e. occurring in previously accreted terranes) granitoid rocks intruded throughout all tectonic zones of the greater Canadian Appalachian Orogen during the Devonian, extending >500 km across the strike length of the orogen and >1000 km along its length, from close to the Appalachian front to Meguma (Fig. 1, 2). Below we review current knowledge on the type, distribution, and timing of those post-accretionary granitoids.

DURATION AND SPATIAL EXTENT OF DEVONIAN POST-ACCRETIONARY MAGMATISM

Quebec Appalachians

Devonian granitoid rocks occur in two regions of the Quebec Appalachian belt: on the Gaspé Peninsula and in southeasternmost Quebec, straddling the U.S.A. border (Fig. 2–4). The group of plutons on the Gaspé Peninsula, most of which lack published crystallization ages apart from the McGerrigle Mountains plutonic complex, tends to be elongated along the Appalachian structural trend. Those in the south are generally more equant in shape and form the northern extent of a more extensive belt of ca. 390 to 365 Ma granites, termed the New Hampshire plutonic suite (Aleinikoff et al., 2011; Ratcliffe et al., 2011). This pattern fits an interpretation of syn-tectonic emplacement for the northern suite and post-tectonic emplacement for the southern suite, as the Quebec Appalachians were broadly affected by the Neoacadian Orogeny (Tremblay and Pinet, 2016). Positive εNd and $\delta^{18}O$ values from the northern suite suggest a mantle to lower crust magma source (Whalen et al., 1994a).

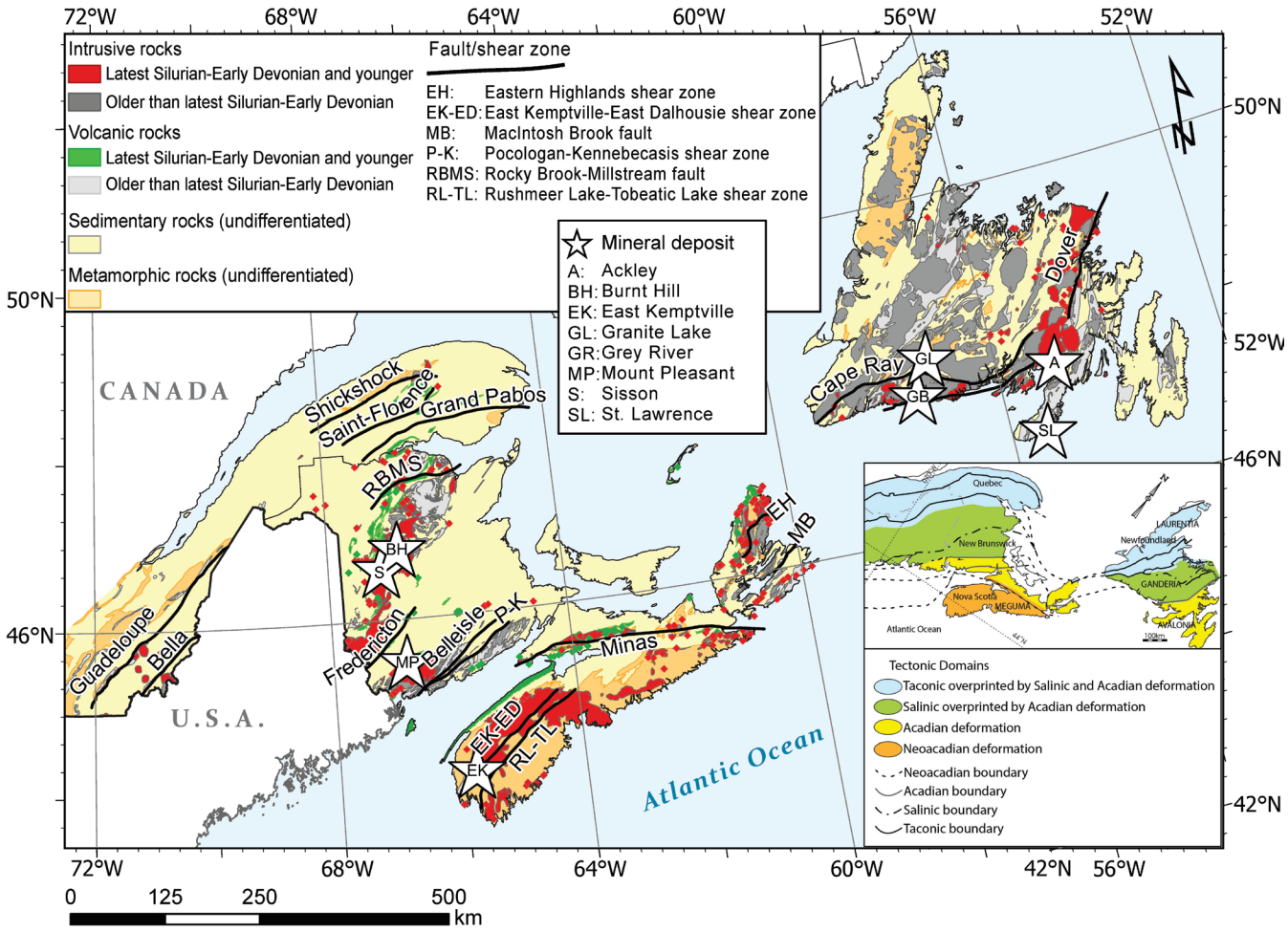

Figure 1. Geological map of the Canadian Appalachian Orogen, showing rock type and distribution of Silurian to early Carboniferous granites and structures (Keppie, 2006 (Nova Scotia); Department of Energy and Mines 2015 (New Brunswick); Thériault and Beauséjour, 2012 (Quebec); Colman-Sadd et al., 2000 (Newfoundland)). Tectonic domains and the extent of deformation of orogenic events for the Appalachian Orogen in Eastern Canada, modified from van Staal et al. (2009), are presented in the inset.

The available published ages for the Quebec Appalachians do not include Early Devonian granitoids. The McGerrigle Mountains plutonic complex is ca. 390 Ma (Whalen et al., 1991), whereas cooling ages for other plutons in the region indicate that they are older than ca.375 Ma (Whalen et al., 1994a). The southern suite ranges in age from ca. 385 to 368 Ma (*see* data and references in Appendices 1 and 2).

New Brunswick

Devonian post-accretionary granitoids and less extensive volcanic rocks occur primarily along two major belts in New Brunswick (Fig. 4). The Central plutonic belt of New Brunswick and coeval extrusive rocks were emplaced into the Miramichi Highlands (Fyffe et al., 1981; Bevier and Whalen, 1990; Whalen, 1993; Whalen et al., 1996). This belt also includes Ordovician and abundant Silurian intrusive rocks (Wilson and Kamo, 2016) that are concurrent with the main phase of the Acadian Orogeny. A few smaller, mineralized Devonian granitoid plutons and dykes also occur between the Central Plutonic Belt and the Gaspé Peninsula (Massawe and Lentz, 2019). The Southern plutonic belt is mostly composed of the late Silurian to Late Devonian Saint George Batholith and exposures are interpreted to represent the upper portions of this complex body (McLeod, 1987; 1990; Mohammadi et al., 2017). Within both belts, granitoid rocks span the entire Devonian period, though they are apparently more voluminous in the Early Devonian, and wane towards the end of the Late Devonian.

A recent study of several Devonian granitoid rocks across New Brunswick has defined three petrogenetic suites. Groups 1 and 2 overlap in distribution and age from Early to Late Devonian, and both are interpreted as I-type granites, but with arc and mantle to lower crustal sources, respectively. Group 3 rocks are Late Devonian or probable Late Devonian where undated, and are also interpreted as I-type, but are highly evolved, and have been interpreted as products of lithospheric delamination (Azadbakht et al., 2019).

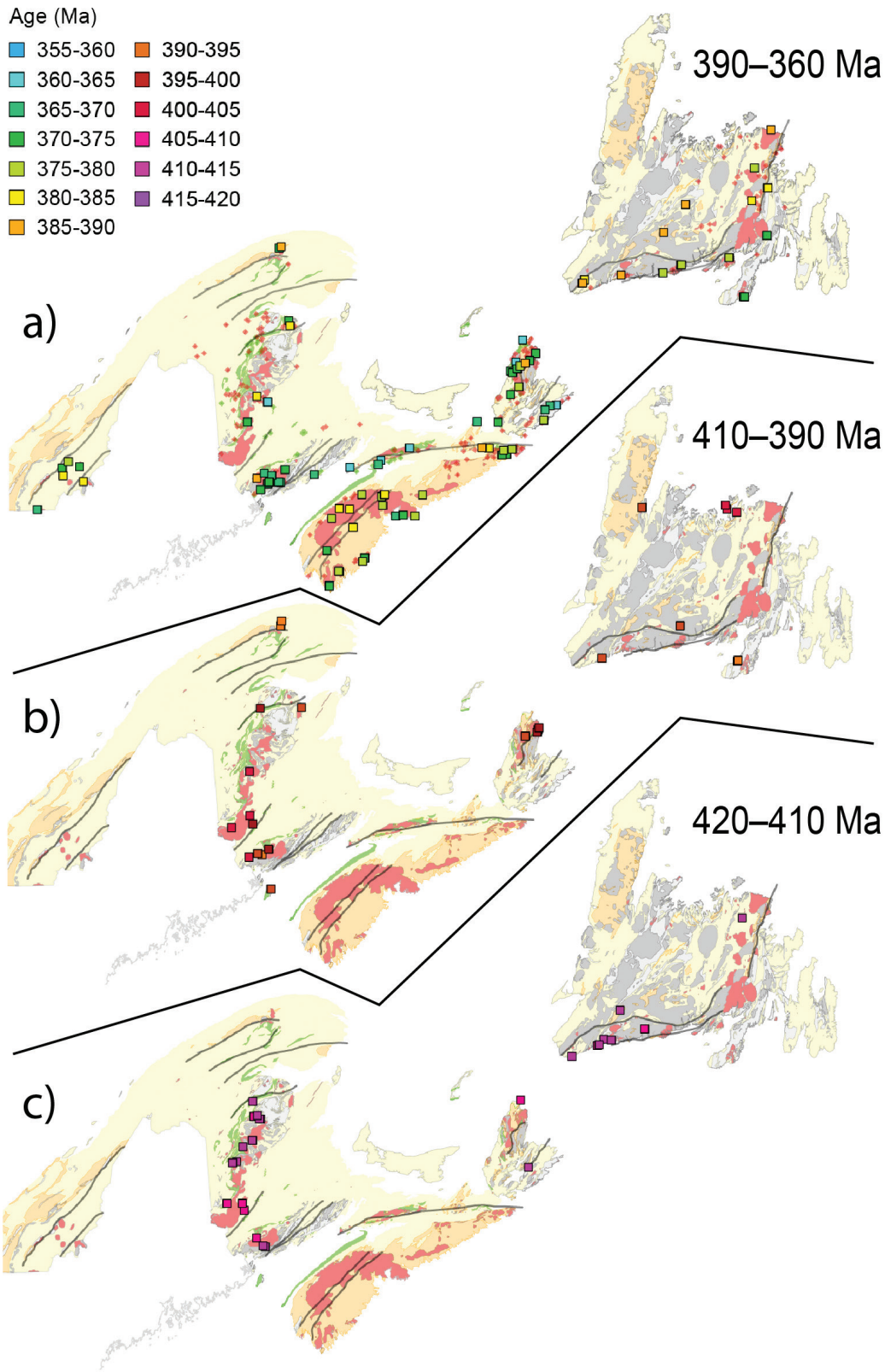

Figure 2. Maps of the Appalachian Orogen showing distribution of U-Pb ages during three-time intervals that span the Devonian period: **a)** 390–360 Ma, **b)** 410–390 Ma, **c)** and 420–410 Ma. *See* Figure 1 for legend. Crystallization ages used are listed in Appendix A.

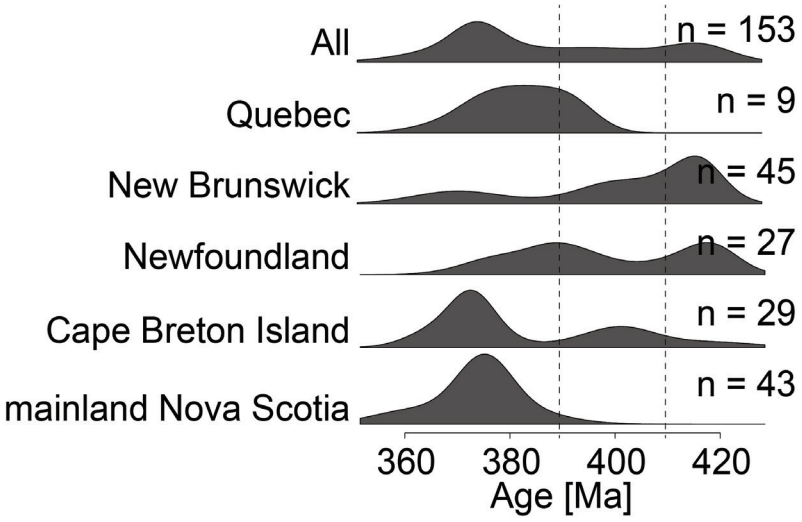

Figure 3. Kernel density estimate plots summarizing Devonian magmatic crystallization ages for the Canadian Appalachians, by region, plotted using IsoplotR (Vermeesch, 2018) such that the y-axis corresponds to density. Dashed lines show age divisions plotted in Fig. 2a–c.

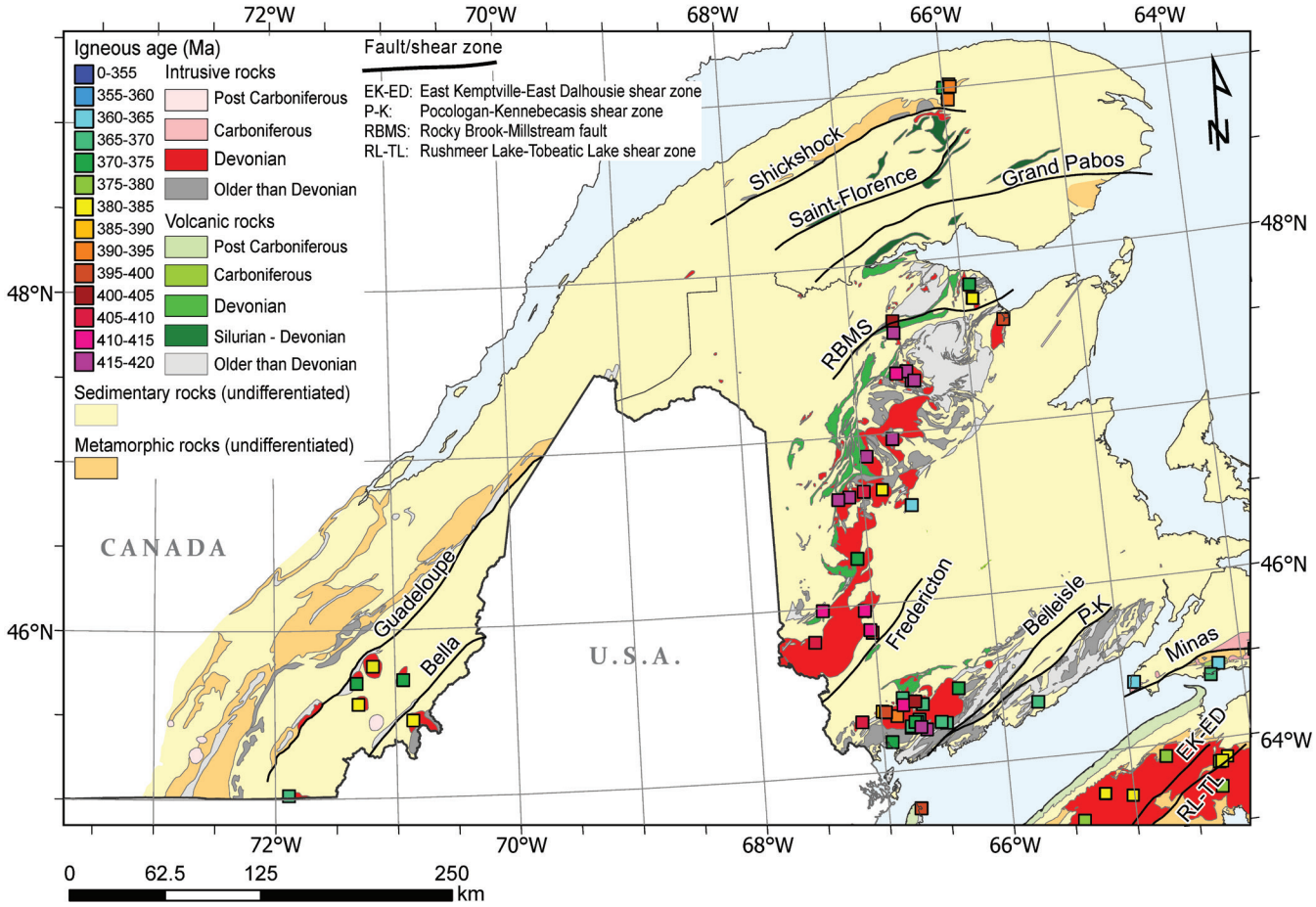

Figure 4. Geological map of Quebec Appalachians and New Brunswick showing rock type and Devonian magmatic crystallization ages (Department of Energy and Mines, 2015 (New Brunswick)); Thériault and Beauséjour, 2012 (Quebec)). Crystallization ages used are listed in Appendix A.

Newfoundland

Devonian granites in Newfoundland occur in a long sinuous belt that broadly follows the orogenic trend, although the granites themselves are generally undeformed (Fig. 5). Magmatism appears to have waned somewhat during the later Early Devonian, and the youngest of the Middle and Late Devonian granites tend to be the most highly evolved and host most of the intrusion-related mineralization (Kerr et al., 2009). Examples include the ca. 377 Ma Ackley Granite Suite, which hosts the Ackley W deposit (Tuach et al., 1987; Kontak, 1995; Kellett et al., 2014), and the ca. 387 Ma Grey River granite, which has been linked to the Grey River W and Moly Brook Mo deposits (Kerr and McNicoll, 2012). These older and younger suites have been denoted as Group A and Group B, respectively, in Kellett et al. (2014). Group A granites are locally deformed and interpreted to be syntectonic with the Acadian Orogeny (Kellett et al., 2014, 2016). Group B granites have a mixed mantle-crust source (Kerr, 1997), which has been interpreted to be the result of lithospheric delamination (Kerr, 1997; Schofield and D'Lemos, 2000), although slab breakoff of the Avalonia slab beneath Ganderia has also been considered (Kellett et al., 2014).

Cape Breton Island

As in New Brunswick and Newfoundland, granitoid magmatism on Cape Breton Island spans the Devonian, from ca. 415 to 365 Ma, and falls broadly into late Silurian to Devonian and Late Devonian suites, with an apparent waning of magmatism during the Middle Devonian (Fig. 2, 3, 6). Both age suites are represented in the Aspy terrane (Ganderia), and form a significant portion of the bedrock in the northern part of the terrane. Only the younger Late Devonian suite is represented in the Mira terrane (Avalonia), and there is a distinct absence of post-accretionary magmatism in the intervening Bras D'Or terrane (Ganderia basement; Barr et al., 2018). This heterogeneous distribution suggests both structural and tectonic controls on Devonian granitoid magma emplacement.

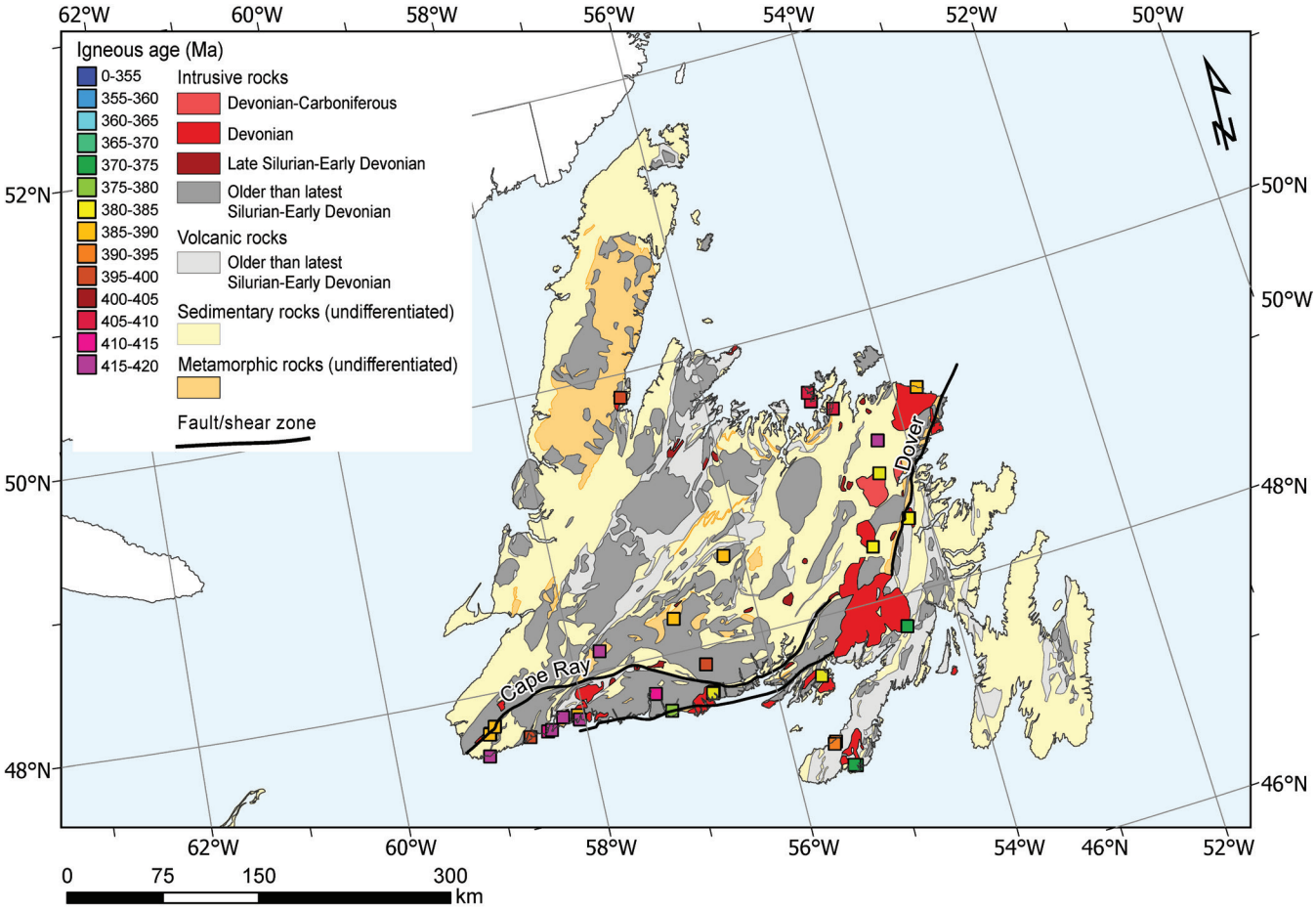

Figure 5. Geological map of Newfoundland showing rock type and Devonian magmatic crystallization ages (Colman-Sadd et al., 2000). Crystallization ages used are listed in Appendix A.

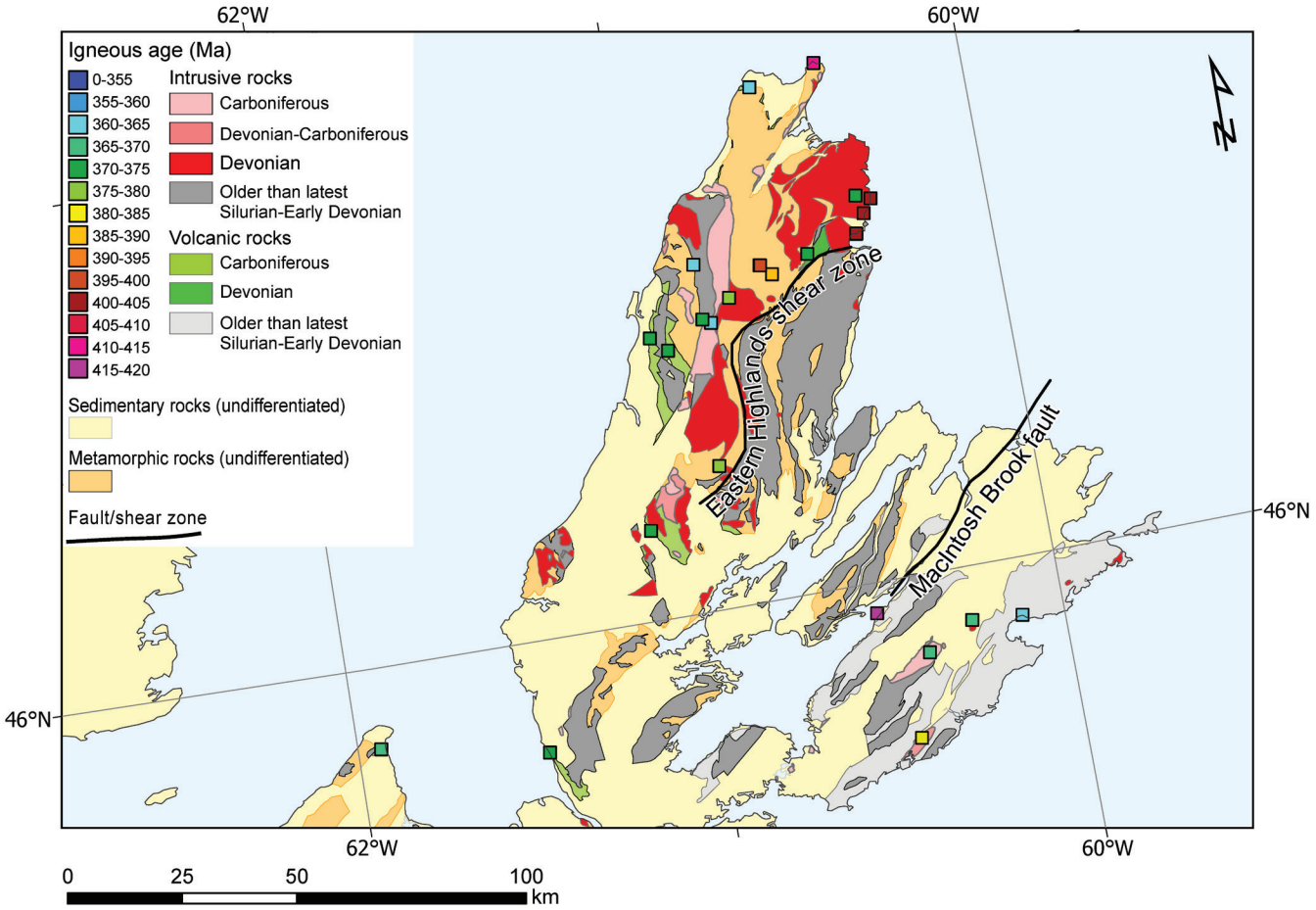

Figure 6. Geological map of Cape Breton Island showing rock type and Devonian magmatic crystallization ages (Keppie, 2006). Crystallization ages used are listed in Appendix A.

Mainland Nova Scotia

Devonian to Carboniferous intrusive rocks on mainland Nova Scotia are dominantly peraluminous felsic granites with lesser tonalite to granodiorite and subordinate (< 5%) bimodal plutonism (e.g. Clarke et al., 1997). The most voluminous of these intrusive rocks are granites, which make up the approximately 7300 km^2 South Mountain Batholith on the southern half of mainland Nova Scotia. The South Mountain Batholith is host to the past-producing East Kemptville Sn deposit (cf. Kontak et al., 2001) and is a meta- to peraluminous composite granite body that was emplaced syn- to post-tectonically (e.g. Clarke and Chatterjee, 1988; Benn et al., 1999; Culshaw and Bhatnagar, 2001; MacDonald, 2001).

The South Mountain Batholith comprises two suites of plutons distinguished by textural and mineralogical characteristics: an early suite dominated by granodiorite to monzogranite, and a later, more evolved suite of monzogranite to leucogranite (MacDonald, 2001). Recent age data from Bickerton et al. (2018, 2019) indicate that the South Mountain Batholith intrusive suite spans a wide range of crystallization ages from ca. 383 to 375 Ma in the less evolved plutons and ca. 379 to 370 Ma in the more evolved plutons (Fig. 2, 3). Peripheral to the South Mountain Batholith are slightly younger mafic intrusions and their hybridized intermediate to felsic equivalents, which range in crystallization age from ca. 368 to 357 Ma (Fig. 7; e.g. Tate and Clarke, 1995; MacLean et al., 2003; Shellnutt and Dostal, 2019).

DEVONIAN STRUCTURAL HISTORY OF THE CANADIAN APPALACHIANS

In this section we discuss some of the better-known faults that were active during the Devonian period. Although we attempt to describe most of the major, crustal-scale faults and shear zones, we cannot cover all of the structures in this complex area, so this should be considered a representative, rather than exhaustive, list.

Quebec Appalachians

Several faults were active in southern Quebec and the Gaspé Peninsula during the Devonian, at which time the entire region was pervasively deformed at low metamorphic

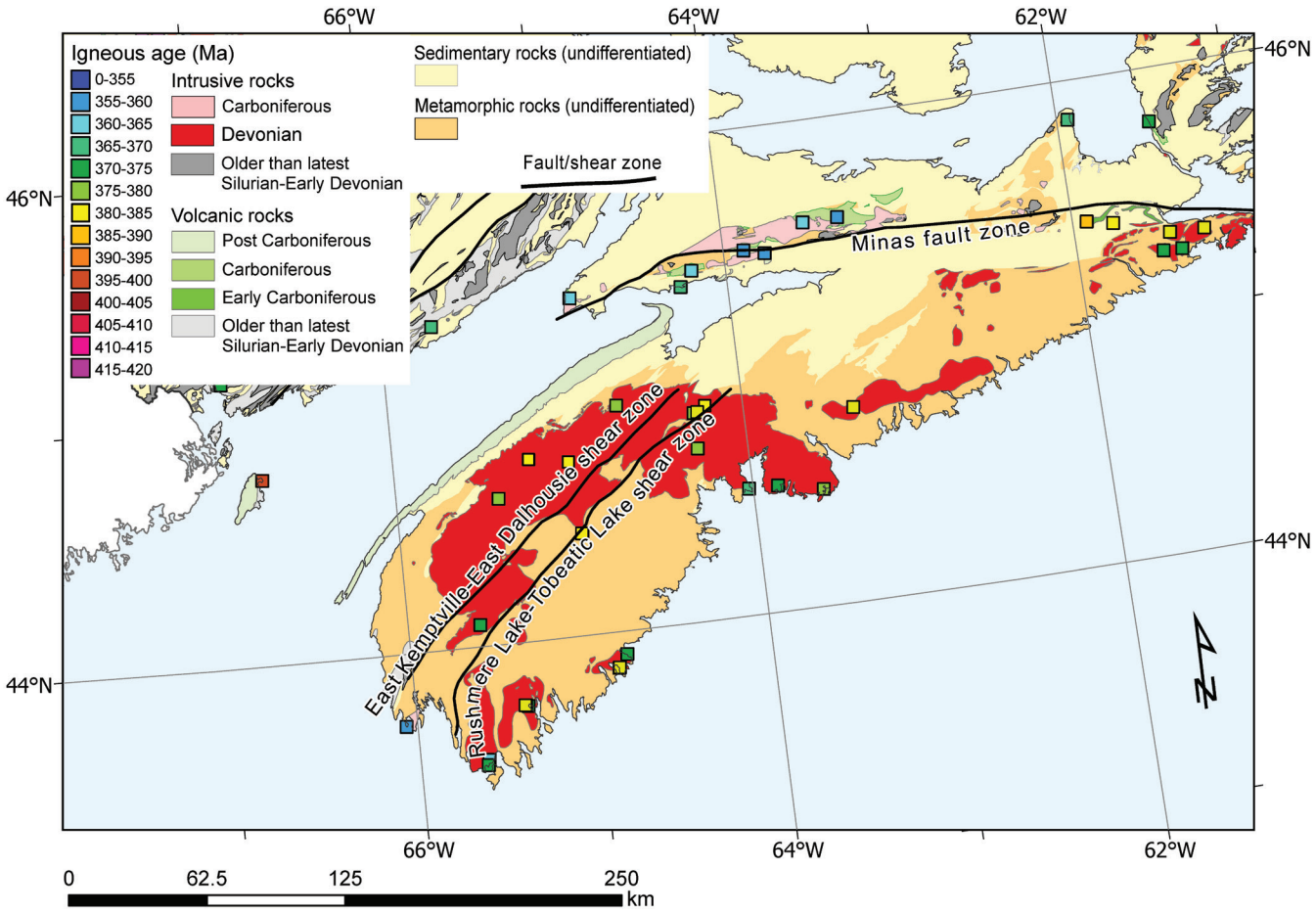

Figure 7. Geological map of mainland Nova Scotia showing rock type and Devonian magmatic crystallization ages (Keppie, 2006). Crystallization ages used are listed in Appendix A.

grade during the Neoacadian Orogeny (Tremblay and Pinet, 2016). Thrusts such as the Guadeloupe and Bella faults dominate in southern Quebec (Fig. 1, 4) Tremblay and Pinet, 1994; Tremblay et al., 2015), whereas dextral strike-slip faults including the Saint-Florence, Grand Pabos, and Shickshock faults occur in the Gaspé Peninsula region (Kirkwood and Malo, 1993; Malo et al., 1992, 1995). Detailed structural analyses demonstrate that shortening and thrusting predate strike-slip faulting (Kirkwood, 1995), although both structural sets were likely active from the Middle to Late Devonian (Tremblay and Pinet, 2016), and the kinematic differences may largely be a function of collision geometry during northwest-directed shortening (Malo et al., 1995).

New Brunswick

Structures that were active during the Devonian in New Brunswick are primarily strike-slip in type, although they may have originated as dip-slip structures (Fig. 1, 5; e.g. Park et al., 1994; Park and Whitehead, 2003). The Fredericton fault lies along the eastern boundary of the Central plutonic belt in New Brunswick, adjacent to the Pokiok Batholith, and cuts the Silurian Fredericton trough (Park and Whitehead, 2003). This fault lies along strike of the Waite strand of the Norumbega fault, which is a major ductile-brittle, dextral strike-slip fault system that extends south into Maine, U.S.A., and is thought to have first initiated at ca. 380 Ma (Wang and Ludman, 2002, 2004). The Rocky Brook–Millstream fault, lying on the northwest margin of the Central plutonic belt, has a dextral transpressional history that may also involve Devonian slip (Fyffe and Fricker, 1987; Tremblay and Dubé, 1991; van Staal and de Roo, 1995).

The Belleisle shear zone and the Pocologan-Kennebecasis shear zone are two structures internal to Ganderia that lie to the east of the Southern plutonic belt (Fig. 1). The Belleisle shear zone separates Neoproterozoic to early Cambrian granites, felsic tuffs, and pyroclastic rocks of the New River terrane to the northwest from Silurian bimodal orthogneiss of the Kingston complex to the southeast (Park et al., 1994; White and Barr, 1996, 2006). The Pocologan-Kennebecasis shear zone separates the Kingston complex from low-pressure, high-temperature gneiss, metasedimentary rocks, and Cambrian

diorite to granodiorite and granite plutons of the Brookville terrane (Park et al., 1994; White and Barr, 1996, 2006). The Belleisle shear zone is characterized by strike-slip sinistral kinematics but was partially reactivated with a dextral sense of motion during deformation along the Pocologan-Kennebecasis shear zone (Doig et al., 1990). Doig et al. (1990) interpreted the orientation of rhyolite dykes in the Kingston complex to record asymmetric opening during sinistral deformation along the Belleisle shear zone; therefore, their crystallization age of 435.5 ± 1.5 Ma (U-Pb on zircon; Doig et al., 1990) is interpreted to represent the timing of the sinistral movement in the shear zone. The dextral shearing along the Pocologan-Kennebecasis shear zone, and associated partial reactivation of the Belleisle shear zone, is interpreted to be synchronous with local metamorphism of the Kingston complex because of the syn-kinematic development of a garnet-staurolite assemblage (White et al., 2006). Amphibole from deformed mafic dykes in the Kingston complex with $^{40}Ar/^{39}Ar$ ages of ca. 416 to 390 Ma are, therefore, interpreted to date metamorphism-related deformation along the Pocologan-Kennebecasis shear zone (Nance and Dallmeyer, 1993). That interpretation is consistent with metamorphic U-Pb monazite ages of ca. 417 and 388 Ma in specimens from the Pocologan metamorphic suite, which forms the high-strain zone of the Pocologan-Kennebecasis shear zone at the southeastern edge of the Kingston complex (Massonne et al., 2018). These ages are interpreted to record monazite growth during syn-kinematic exhumation of the metamorphic suite (Massonne et al., 2018). Similarly, extrusion and related exhumation of the Kingston complex is also interpreted to be related to motion along the Pocologan-Kennebecasis shear zone, reflecting significant transpression across the shear zone (Nance and Dallmeyer, 1993). This transpression-driven exhumation is consistent with the transition from ductile to brittle fabrics (Park et al., 1994) in the shear zone and may have lasted until 342 Ma, the $^{40}Ar/^{39}Ar$ age of muscovite from shear fabrics located close to the high-strain zones of the Pocologan-Kennebecasis shear zone (White and Barr, 2006).

Newfoundland

The Dover-Hermitage fault is the structural boundary separating the Ganderia and Avalonia terranes in Newfoundland. It formed as an approximately 20 km wide, ductile, sinistral strike-slip shear zone during ca. 423 to 395 Ma, was reactivated as a narrow, ductile-brittle, dextral strike-slip fault active at least during ca. 384 Ma, and was stitched by the Ackley Granite Suite by ca. 377 Ma (Holdsworth, 1994; Schofield and D'Lemos, 2000; Kellett et al., 2014, 2016). Although the extension of the Ganderia-Avalonia boundary southwest of the Hermitage Bay fault is generally interpreted to bend southward in offshore regions to pass into Cape Breton Island, the region along the south coast of Newfoundland has many geochronological and lithological similarities to either the Bras d'Or terrane or to Avalonia. This suggests that another terrane-bounding shear zone may intersect in this region, in which case Devonian granites there (e.g. Grey River granite) may also be situated along a reactivated structure (Dunning and O'Brien, 1989, Rogers et al., 2015).

The Cape Ray shear zone is located inboard of Ganderia in Newfoundland. It separates, from the northwest to the southeast, Proterozoic mafic to ultramafic orthogneiss of the Cape Ray igneous complex, Ordovician to Silurian volcano-sedimentary rocks of the Windsor Point Group (which form the high-strain zone of the Cape Ray shear zone), psammite mylonite of the Grand Bay Complex, and Ordovician felsic orthogneiss of the Port aux Basques gneiss (Wilton, 1983; Dubé and Lauzière, 1996; Dubé et al., 1996; Schofield et al., 1998). The Grand Bay Complex records two major ductile deformation events: 1) southeast-side-up sinistral oblique kinematics recorded in amphibolite-grade metamorphic rocks; and 2) reactivation during retrograde metamorphism, with the northeast-trending segment of the Cape Ray shear zone recording southeast-side-up kinematics and the east-northeast segment recording dextral strike-slip kinematics (Dubé and Lauzière, 1996). The maximum age of the first episode of deformation is interpreted to correspond to the crystallization age of the deformed Windowglass Hill Granite in the Windsor Point Group (424 ± 2 Ma; Dubé et al., 1996), whereas the age of the main shear event is approximated to the age of syn-deformation metamorphic monazite and titanite from the Port aux Basques gneiss (415 ± 2 Ma and 412 ± 2 Ma, respectively, U-Pb; Dunning et al., 1990, van Staal et al., 1994). Because the reactivation of the Cape Ray shear zone occurred during retrograde metamorphism, the $^{40}Ar/^{39}Ar$ hornblende and biotite ages of 407 ± 4 and 403 ± 4 Ma, respectively, from the Port aux Basques gneiss may be interpreted as broadly coeval with motion along the Cape Ray shear zone. The minimum age of the fault reactivation is defined by the undeformed, crosscutting Strawberry Hill granite (384 ± 2 Ma, U-Pb on zircon; Dubé et al., 1996).

Cape Breton Island

The northwestern tip of Cape Breton Island is underlain by Precambrian gneiss of the Blair River inlier, interpreted as part of the basement of the Humber zone of the Laurentian margin (Loncarevic et al., 1989). The inlier is separated from Ganderia on its south and southeast margin by the Red River and Wilkie Brook shear zones, respectively. The Wilkie Brook shear zone recorded sinistral strike-slip kinematics. It deformed rhyolite from the Money Point Group (427± 4 Ma, U-Pb zircon); is intruded by the syn-tectonic 414 ± 3 Ma Cape North granite (Keppie et al., 1992), and is stitched by the undeformed Margaree pluton (ca. 365.5 ± 3.3 Ma, U-Pb on zircon; Sombini dos Santos, 2018). This deformation can be correlated with the 423 to 395 Ma Acadian ductile deformation accommodated by the Dover-Hermitage fault (Kellett et al., 2016).

The Ordovician to Silurian volcano-sedimentary rocks and Devonian granitoids of the Aspy terrane and the Precambrian metasedimentary rocks and late Proterozoic dioritic to granitic plutons of the Bras d'Or terrane are both considered part of Ganderia (Barr and Raeside, 1989; Raeside and Barr, 1992; Lin, 1993; Barr et al., 1998). The boundary between these two terranes is the Eastern Highlands shear zone, where Ordovician to Silurian sedimentary rocks of the Bras d'Or terrane are interpreted to have been deposited unconformably on older rocks of the Aspy terrane. These sedimentary rocks have a detrital zircon record spanning the igneous crystallization ages found in the Aspy and Bras d'Or terranes, suggesting a basement-cover relationship (Lin, 1993; Chen et al., 1995). East-over-west dip-slip with minor sinistral strike-slip kinematics were initially recorded on the Eastern Highlands shear zone. The maximum age of this deformation event is constrained by the crystallization age of a rhyolite deformed within the shear zone (424 ± 4 Ma, U-Pb on zircon; Piette-Lauzière et al., 2019). The minimum age of this event has yet to be fully constrained; however, the crystallization age of an undeformed pegmatite dyke (ca. 391 ± 8 Ma; U-Pb on zircon) may provide a lower limit for its activity (Piette-Lauzière et al., 2019). The Eastern Highland and Wilkie Brook shear zones were, therefore, probably both active during the Acadian Orogeny, but only the Eastern Highlands shear zone was later reactivated. Lin (1993) reported oblique west-side-up and dextral reactivation with a maximum age constrained by the crystallization age of a deformed granite dyke dated at ca. 372 ± 4 Ma (U-Pb on zircon; Piette-Lauzière et al., 2019). No crosscutting relationships have been identified to determine the minimum age of reactivation of the Eastern Highlands shear zone and, based on the current data set, this reactivation is attributed to the Neoacadian Orogeny.

Farther southeast, the MacIntosh Brook fault separates the Bras d'Or terrane from the Mira terrane and is generally interpreted to represent the extension of the Dover-Hermitage fault in Nova Scotia (Barr et al., 1998); however, the MacIntosh Brook fault is poorly exposed so the time of motion is unknown.

Mainland Nova Scotia

The granites of the South Mountain Batholith on mainland Nova Scotia are thought to have been emplaced along northeast-trending structures, broadly parallel to the trend of the orogen, during regional northwest-directed transpression. The evidence for these structures comes largely from interpretation of regional gravity surveys and magnetic lineation maps, as well as the orientations of minor faults, primary igneous flow features, joints, dykes, and veins (Horne et al., 1992; Benn et al., 1999; MacDonald, 2001). The South Mountain Batholith and surrounding host rocks are transected by a series of the northeast-trending faults and shear zones in southern Nova Scotia (e.g. East Kemptville–East Dalhousie shear zone and Rushmeer Lake–Tobeatic Lake shear zone); this relationship and $^{40}Ar/^{39}Ar$ muscovite cooling ages indicate protracted displacement along these shear zones, from pre- to syn- to post-emplacement of the South Mountain Batholith (cf. Culshaw and Reynolds, 1997). Dextral transpression along the northeast-trending structures in southern Nova Scotia is indicated from field relationships such as a prominent C-S fabric observed within the East Kemptville shear zone (e.g. Kontak and Cormier, 1991). As a result of the emplacement setting and kinematics of the major faults in the area, several of the South Mountain Batholith plutons are elongated where they are transected by the shear zones, with their long dimensions parallel to the northeast trend of the orogen (e.g. East Dalhousie pluton and Davis Lake pluton; Horne et al., 1992).

The Minas fault zone is a major, dextral, transpressional, terrane-bounding structure that separates Avalonia from Meguma on mainland Nova Scotia (Keppie, 1982). The ca. 375 Ma Kelly Brook pluton is elongated and was deformed within the Minas fault zone (Archibald et al., 2018). Ductile deformation of the pluton was coeval with rapid exhumation of the southern wall of the shear zone, associated with regional exhumation of Meguma to the surface by ca. 359 Ma (Archibald et al., 2018).

DISCUSSION

Several first-order observations can be made from the above review of the spatio-temporal distribution of post-accretionary magmatism in the Canadian Appalachians and the relationships of magmatic suites to major structures active during the same general time period. Magmatism during the Early Devonian was largely confined to Ganderia, including intrusions in the Central and Southern plutonic belts of New Brunswick and those proximal to the Cape Ray shear zone in Newfoundland and Eastern Highlands shear zone on Cape Breton Island (Fig. 1–3). This distribution fits with a tectonic scenario in which Avalonia was advancing toward Laurentia as the lower plate and Meguma remained offshore, so that magmatism within Ganderia was generally subduction related (e.g. van Staal et al., 2009). In contrast, Middle to Late Devonian magmatism spans the orogen, intruding all of its tectonic zones (Humber, Ganderia, Avalonia, and Meguma). Furthermore, the Late Devonian episode of magmatism in particular was responsible for all the major Sn-W-Mo deposits, and for numerous smaller deposits. There is some intrusion-related mineralization associated with Early Devonian suites (e.g. *see* review for New Brunswick in Azadbakht et al. (2019)), but this is of comparatively minor extent. Notably, significant intrusion-related mineralization occurred within all tectonic domains. For example, the Lac Lyster W deposit in Quebec is associated with the ca. 368 Ma Averill pluton within the Humber zone (Perrot et al., 2018); the East Kemptville Sn deposit is hosted within the ca. 373 Ma Davis Lake pluton in Meguma (Bickerton et al., 2018); the Mount Pleasant caldera W-Mo deposit is thought

to be the subvolcanic equivalent of the deeper ca. 368 Ma Sn-W-Mo–bearing Mount Douglas Granite, hosted in Ganderia (Thorne et al, 2013; Mohammadi, 2018, Mohammadi et al., 2020); and the Ackley Sn-W-Mo deposit formed in the ca. 372 Ma Ackley Granite Suite, hosted within Avalonia (Kellett et al., 2014). The broadening in spatial extent of magmatism suggests that the heat source and tectonic processes that generated Middle to Late Devonian magmatism occurred on the scale of the entire orogen. The widespread nature of mineralization further suggests that metal endowment is not tied to any particular tectonic domain. These two points suggest a mantle-derived heat source and potentially a mantle-derived metal source.

Lithospheric delamination is a geodynamic process that can add heat to the base of the crust over an extensive area and may be triggered by terminal continent-continent collision and associated crustal shortening (Kay and Kay, 1993). The manifestation of lithospheric delamination in the overlying crust includes rapid uplift and, in particular, abundant crustal- and mantle-derived magmatism. Many studies of distinct Devonian granitoid belts have invoked lithospheric delamination as a plausible process for producing this bloom of post-accretionary magmatism, including in Gaspé Peninsula (Whalen et al., 1994a; Tremblay and Pinet, 2005), New Brunswick (Whalen et al., 1994a, 1994b, 1996), and Newfoundland (Kerr, 1997; Schofield and D'Lemos, 2000), generally on the basis of petrological and geochemical/isotopic evidence for lower crust and/or mantle-derived melting (e.g. Azadbakht et al., 2019). However, only certain structurally bounded regions of the orogen experienced rapid uplift and exhumation immediately following Late Devonian magma emplacement, including northeastern Meguma (e.g. Archibald et al., 2018), western Ganderia in Newfoundland (e.g. Kellett et al., 2014), and the Aspy terrane in Cape Breton Island (e.g. Kellett et al., 2018). Elsewhere in the orogen, preserved Devonian sedimentary rocks, volcanic rocks, and relatively unmetamorphosed rocks attest to minimal exhumation. Recent geodynamic models of lithospheric delamination for composite orogens composed of terranes with diverse mantle lithosphere strengths and densities illustrate that delamination is likely to be non-uniform and idiosyncratic, in contrast to our previous understanding (Kelly et al., 2020).

Alternative tectonic scenarios proposed for particular regions of the orogen include subduction of a hotspot beneath Meguma (Keppie and Krogh, 1999) and, more commonly, (flat) slab breakoff of the Avalonia and/or Meguma slabs (van Staal et al., 2009; Kellett et al., 2014; Massawe and Lentz, 2019). Although slab breakoff of the Iapetus and Rheic slabs may have occurred, producing localized Devonian magmatism, we propose here that slab breakoff events may not sufficiently explain the orogen-wide extent of Late Devonian magmatism, particularly on both sides of the Avalonia-Meguma plate boundary.

Although intrusive magmatism is widespread during the Late Devonian, it is still largely confined to structural trends aligned with contemporaneous faults and shear zones, such as the Cape Ray and Dover shear zones of Newfoundland; the Eastern Highlands shear zone on Cape Breton Island; the Minas, East Kemptville–East Dalhousie, and Rushmeer Lake–Tobeatic Lake shear zones on mainland Nova Scotia; the Belleisle and Pocologan-Kennebecasis shear zones adjacent to the Southern plutonic belt and the Fredericton and Rocky Brook–Millstream faults adjacent to the Central plutonic belt in New Brunswick; and dextral and strike-slip fault sets in the Quebec Appalachians (Fig. 1, 2). From our compilation, it appears that nearly all fault kinematics (thrust, strike-slip, transpressive) were equally favourable as magma channels; however, new studies have highlighted that the kinematics of ductile shear zones can be more complex than initially interpreted from field observations (e.g. Xypolias et al., 2018; Kruckenberg et al., 2019) and that kinematic flow such as transpressive and triclinic might be more common in the Appalachian Orogen than is currently documented (e.g. Lin et al., 1998). Our understanding of the kinematics of shear zones, their timing of deformation, and magma emplacement may evolve as we develop new microstructural tools to better characterize their kinematics. Nevertheless, it seems plausible that active structures were required to weaken the crust; enhance the local porosity; and allow magma transfer, and as a result, heat through the crust (e.g. D'Lemos et al., 1997). It also seems that larger volume batholiths were emplaced both at the sutures between terranes (e.g. Black Brook granitic suite) and internally (e.g. South Mountain Batholith), which highlights the fact that shear zone surface expression is not necessarily proportional to its crustal extent. The deep crustal expression of these structures requires further study by combining and leveraging the existing geophysical databases.

CONCLUSIONS

Our regional compilation of granitoid and related magmatism crystallization ages across the Canadian Appalachian Orogen and assessment of their spatial links to coeval structures during the Devonian reveals that the dynamic processes responsible for granite generation had an orogen-wide extent, were broadly coeval with terminal continent-continent collision, and were locally immediately followed by rapid exhumation. Petrological studies in most regions point to lower crust and/or mantle magma sources with varying degrees of crustal assimilation. Associated intrusion-related Sn-W-Mo mineralization is not confined to particular compositional groups or tectonic terranes, suggesting a deep, more homogeneous metal source. We propose that the role of lithospheric delamination in the Canadian Appalachian Orogen be investigated further as a plausible mechanism for delivering metals from the mantle to the crust via granitoid melts.

ACKNOWLEDGMENTS

This work was funded by the Targeted Geoscience Initiative program of the Geological Survey of Canada. Leith MacLeod and Ernst Schetselaar are gratefully acknowledged for GIS support and assistance with figure drafting, respectively. Reviews by Cees van Staal and Andrew Kerr improved this paper.

REFERENCES

Aleinikoff, J.N., Ratcliffe, N.M., and Walsh, G.J., 2011. Provisional zircon and monazite uranium-lead geochronology for selected rocks from Vermont; US Geological Survey, Open File Report 2011-1309, 46 p. https://doi.org/10.3133/ofr20111309

Archibald, D.B., Murphy, J.B., Reddy, S.M., Jourdan, F., Gillespie, J., and Glorie, S., 2018. Post-accretionary exhumation of the Meguma terrane relative to the Avalon terrane in the Canadian Appalachians; Tectonophysics, v. 747–748, p. 343–356. https://doi.org/10.1016/j.tecto.2018.10.016

Azadbakht, Z., Rogers, N., Lentz, D.R., and McFarlane, C.R.M., 2019. Petrogenesis and associated mineralization of Acadian related granitoids in New Brunswick; in Targeted Geoscience Initiative: 2018 report of activities, (ed.) N. Rogers; Geological Survey of Canada, Open File 8549, p. 243–278. https://doi.org/10.4095/313658

Barr, S.M., van Rooyen, D., and White, C.E., 2018. Granitoid plutons in peri-Gondwanan terranes of Cape Breton Island, Nova Scotia, Canada: new U-Pb (zircon) age constraints; Atlantic Geology, v. 54, p. 21–80. https://doi.org/10.4138/atlgeol.2018.002

Benn, K., Roest, W.R., Rochette, P., Evans, N.G., and Pignotta, G.S., 1999. Geophysical and structural signatures of syntectonic batholith construction: the South Mountain batholith, Meguma terrane, Nova Scotia; Geophysics Journal International, v. 136, no. 1, p. 144–158. https://doi.org/10.1046/j.1365-246X.1999.00700.x

Bevier, M.L. and Whalen, J.B., 1990. Tectonic significance of Silurian magmatism in the Canadian Appalachians; Geology, v. 18, no. 5, p. 411–414. https://doi.org/10.1130/0091-7613(1990)018%3C0411:TSOSMI%3E2.3.CO;2

Bickerton, L., Kontak, D.J., Samson, I.M., Murphy, J.B., and Kellett, D.A., 2018. U-Pb geochronology of the South Mountain batholith, Nova Scotia; *in* Targeted Geoscience Initiative: 2017 report of activities, volume 1, (ed.) N. Rogers; Geological Survey of Canada, Open File 8358, p. 51–55. http://doi.org/10.4095/306391

Bickerton, L., Kontak, D.J., Samson, I.M., Murphy, J.B., and Kellett, D.A., 2019. SHRIMP U-Pb zircon dating of the South Mountain batholith, Nova Scotia: timing and duration of crystallization and evidence for inheritance; *in* Targeted Geoscience Initiative: 2018 report of activities, (ed.) N. Rogers; Geological Survey of Canada, Open File 8549, p. 307–320. https://doi.org/10.4095/313664

Clarke, D.B. and Chatterjee, A.K., 1988. Physical and chemical processes in the South Mountain Batholith; *in* Recent advances in the geology of granite-related mineral deposits: proceedings of the CIM conference on granite-related mineral deposits, September 1985, (ed.) R.P. Taylor and D.F. Strong; The Canadian Institute of Mining and Metallurgy, Special Volume 39, p. 223–233.

Clarke, D.B., MacDonald, M.A., and Tate, M.C., 1997. Late Devonian mafic-felsic magmatism in the Meguma zone, Nova Scotia; *in* The nature of magmatism in the Appalachian Orogen, (ed.) A.K. Sinha, J.B. Whalen, and J.P. Hogan;Geological Society America Memoir, v. 191, p. 107–127. https://doi.org/10.1130/0-8137-1191-6.107

Colman-Sadd, S.P., Hayes, J.P., and Knight, I., 2000. Geology of the island of Newfoundland; Government of Newfoundland and Labrador, Department of Mines and Energy, Geological Survey Branch, scale 1:1 000 000. <https://geoatlas.gov.nl.ca/Default.htm> [accessed March 4, 2020]

Culshaw, N. and Bhatnagar, P., 2001. The interplay of regional structure and emplacement mechanisms at the contact of the South Mountain batholith, Nova Scotia: floor-down or wall-up?; Canadian Journal of Earth Sciences, v. 38, no. 9, p. 1285–1299. https://doi.org/10.1139/e01-029

Culshaw, N. and Reynolds, P., 1997. 40Ar/39Ar age of shear zones in the southwest Meguma zone between Yarmouth and Meteghan, Nova Scotia; Canadian Journal of Earth Sciences, v. 34, no. 6, p. 848–853. https://doi.org/10.1139/e17-069

Department of Energy and Mines, 2015. Generalized bedrock geology map of New Brunswick; Service New Brunswick, scale 1:500 000. <http://www.snb.ca/geonb1/e/DC/BROCK.asp> [accessed March 4, 2020]

D'Lemos, R.S., Schofield, D.I., Holdsworth, R.E., and King, T.R., 1997. Deep crustal and local rheological controls on the siting and reactivation of fault and shear zones, northeastern Newfoundland; Journal of the Geological Society, v. 154, no. 1, p. 117–121. https://doi.org/10.1144/gsjgs.154.1.0117

Doig, R., Nance, R.D., Murphy, J.B., and Casseday, R.P., 1990. Evidence for Silurian sinistral accretion of Avalon composite terrane in Canada; Journal of the Geological Society, v. 147, no. 6, p. 927–930. https://doi.org/10.1144/gsjgs.147.6.0927

Dubé, B. and Lauzière, K., 1996. Structural evolution of a major fault zone: the Cape Ray fault zone, southwestern Newfoundland, Canada; Canadian Journal of Earth Sciences, v. 33, no. 2, p. 199–215. https://doi.org/10.1139/e96-018

Dubé, B., Dunning, G.R., Lauziere, K., and Roddick, J.C., 1996. New insights into the Appalachian Orogen from geology and geochronology along the Cape Ray fault zone, southwest Newfoundland; Geological Society of America Bulletin, v. 108, no. 1, p. 101–116. https://doi.org/10.1130/0091-7613(1996)108%3C0101:NIITAT%3E2.3.CO;2

Dunning, G.R. and O'Brien, S.J. 1989. Late Proterozoic-early Paleozoic crust in the Hermitage flexure, Newfoundland Appalachians: U/Pb ages and tectonic significance; Geology, v. 17, no. 6, p. 548–551. https://doi.org/10.1130/0091-7613(1989)017%3C0548:LPEPCI%3E2.3.CO;2

Dunning, G.R., Barr, S.M., Raeside, R.P., and Jamieson, R.A., 1990. U-Pb zircon, titanite, and monazite ages in the Bras-Dor and Aspy terranes of Cape Breton Island, Nova Scotia: implications for igneous and metamorphic history; Geological Society of America Bulletin, v. 102, no. 3, p. 322–330. https://doi.org/10.1130/0016-7606(1990)102%3C0322:UPZTAM%3E2.3.CO;2

Fyffe, L.R. and Fricker, A., 1987. Tectonostratigraphic terrane analysis of New Brunswick; Marine Sediments and Atlantic Geology, v. 23, no. 3, p. 113–122. https://doi.org/10.4138/1626

Fyffe, L.R., Pajari, G.E., and Cherry, M.E., 1981. The Acadian plutonic rocks of New Brunswick; Maritime Sediments and Atlantic Geology, v. 17, no 1, p. 23–36. https://doi.org/10.4138/1373

Grant, C., Archibald, D.B, Kellett, D.A., and Cottle, J.M., 2019. The relationship between the Ganderian Aspy and Bras d'Or terranes explored using Devonian plutonic rocks, Cape Breton, Nova Scotia; *in* Targeted Geoscience Initiative: 2018 report of activities, (ed.) N. Rogers; Geological Survey of Canada, Open File 8549, p. 279–286. https://doi.org/10.4095/313659.

Hatcher, R.D., 2010. The Appalachian Orogen: a brief summary; *in* From Rodinia to Pangea: The lithotectonic record of the Appalachian Region, (ed.) R.P. Tollo, M.J. Bartholomew, J.P. Hibbard, and P.M. Karabinos; Geological Society of America, Memoir 206, p. 1–19. https://doi.org/10.1130/2010.1206(01)

Holdsworth, R.E., 1994. Structural evolution of the Gander-Avalon terrane boundary: a reactivated transpression zone in the NE Newfoundland Appalachians; Journal of the Geological Society, v. 151, no. 4, p. 629–646. https://doi.org/10.1144/gsjgs.151.4.0629

Horne, R.J., MacDonald, M.A., Corey, M.C., and Ham, L.J., 1992. Structure and emplacement of the South Mountain batholith, southwestern Nova Scotia; Atlantic Geology, v. 28, p. 29–50.

Kay, R.W. and Kay, S.M., 1993. Delamination and delamination magmatism; Tectonophysics, v. 219, no. 1–3, p. 177–189. https://doi.org/10.1016/0040-1951(93)90295-U

Kellett, D. A., Rogers, N., McNicoll, V., Kerr, A., and van Staal, C., 2014. New age data refine extent and duration of Paleozoic and Neoproterozoic plutonism at Ganderia–Avalonia boundary, Newfoundland; Canadian Journal of Earth Sciences, v. 51, no. 10, p. 943–972. https://doi.org/10.1139/cjes-2014-0090

Kellett, D.A., Warren, C., Larson, K.P., Zwingmann, H., van Staal, C.R., and Rogers, N., 2016. Influence of deformation and fluids on Ar retention in white mica: dating the Dover fault, Newfoundland Appalachians; Lithos, v. 254–255, p. 1–17. https://doi.org/10.1016/j.lithos.2016.03.003

Kellett, D.A., Rogers, N., Barr, S.M., Kontak, D.J., Larson, K., Piette-Lauzière, N., van Rooyen, D., White, C.E., and Wilson, R.A., 2017. Linking characteristics of post-orogenic, polymetallic porphyry-style ores to tectonically-driven temporal and spatial controls across an accretionary orogen; *in* Targeted Geoscience Initiative: 2016 report of activities, (ed) N. Rogers, Geological Survey of Canada, Open File 8199, p. 75–78. https://doi.org/10.4095/299597

Kellett, D.A., Barr, S.M., van Rooyen, D., and White, C.E., 2018. Ar/Ar thermochronology of the Aspy and Bras d'Or terranes, Cape Breton Island, Nova Scotia; *in* Targeted Geoscience Initiative: 2017 report of activities, volume 1, (ed.) N. Rogers; Geological Survey of Canada, Open File 8358, p. 47–49. http://doi.org/10.4095/306415

Kelly, S., Beaumont, C., and Butler, J.P., 2020. Inherited terrane properties explain enigmatic post-collisional Himalayan-Tibetan evolution; Geology, v. 48, no. 1, p. 8–14. https://doi.org/10.1130/G46701.1

Keppie, J.D., 1982. The Minas geofracture; *in* Major structural zones and faults of the northern Appalachians, (ed.) P. St-Julien and J. Beland; Geological Association of Canada, Special Paper 24, p. 263–280.

Keppie, J.D., 2006. Geological map of the province of Nova Scotia, version 2. Nova Scotia Department of Natural Resources, Geoscience and Mines Branch, Map ME2000-1, scale 1:500 000, https://novascotia.ca/natr/meb/download/dp043.asp

Keppie, J.D. and Krogh, T.E., 1999. U-Pb geochronology of Devonian granites in the Meguma terrane of Nova Scotia, Canada: evidence for hotspot melting of a Neoproterozoic source; The Journal of Geology, v. 107, no. 5, p. 555–568. https://doi.org/10.1086/314369

Keppie, J.D., Dallmeyer, R.D., and Krogh, T.E., 1992. U-Pb and $^{40}Ar/^{39}Ar$ mineral ages from Cape North, northern Cape Breton Island: implications for accretion of the Avalon Composite terrane; Canadian Journal of Earth Science, v. 29, no. 2, p. 277–295. https://doi.org/10.1139/e92-025

Kerr, A., 1997. Space-time composition relationships among Appalachian-cycle plutonic suites in Newfoundland; in The nature of magmatism in the Appalachian Orogen, (ed.) A.K. Sinha, J.B. Whalen, and J.P. Hogan; Geological Society of America, Memoir 191, p. 193–220. https://doi.org/10.1130/0-8137-1191-6.193

Kerr, A. and McNicoll, V., 2012. New U–Pb geochronological constraints from mineralized granites in southern Newfoundland; *in* Current Research, Newfoundland and Labrador, Department of Natural Resources, Geological Survey, Report 12-1, p. 21–38.

Kerr, A., van Nostrand, T.S., Dickson, W.L., and Lynch, E.P., 2009. Molybdenum and tungsten in Newfoundland: a geological overview and a summary of recent exploration developments; *in* Current Research, Newfoundland and Labrador Department of Natural Resources, Geological Survey, Report 09-1, p. 43–80.

Kirkwood, D., 1995. Strain partitioning and progressive deformation history in a transpressive belt, northern Appalachians. Tectonophysics, v. 241, no. 1–2, p. 15–34. https://doi.org/10.1016/0040-1951(94)00182-9

Kirkwood, D., and Malo, M., 1993. Across-strike geometry of the Grand Pabos fault zone: evidence for Devonian dextral transpression in the Quebec Appalachians; Canadian Journal of Earth Sciences, v. 30, p. 1363–1373, https://doi.org/10.1139/e93-117

Kontak, D., 1995. A study of feldspar phases in the high-silica, high-level Ackley Granite, southeastern Newfoundland; The Canadian Mineralogist, v. 33, no. 5, p. 985–1010.

Kontak, D.J. and Cormier, R.F., 1991. Geochronological evidence for multiple tectono-thermal overprinting events in the East Kemptville muscovite-topaz leucogranite, Yarmouth County, Nova Scotia, Canada; Canadian Journal of Earth Sciences, v. 28, no. 2, p. 209–224. https://doi.org/10.1139/e91-020

Kontak, D.J., Dostal, J., Ansdell, K., Halter, W., Martin, R.F., and Williams-Jones, A.E., 2001. The nature and origin of pegmatite in a fluorine-rich leucogranite, East Kemptville, Nova Scotia; Royal Society of Edinburgh, Transactions: Earth Sciences, v. 92, no. 2, p. 173–2000. https://doi.org/10.1017/S0263593300000122

Kruckenberg, S.C., Michels, Z.D., and Parsons, M.M., 2019. From intracrystalline distortion to plate motion: unifying structural, kinematic, and textural analysis in heterogeneous shear zones through crystallographic orientation-dispersion methods; Geosphere, v. 15, no. 2, p. 357–381. https://doi.org/10.1130/GES01585.1

Lentz, D.R. and Mohammadi, N., 2014. Petrogenesis and evolution of peraluminous Mount Douglas leucogranites, southwestern New Brunswick, Canada: extreme fractionation linked to Sn-W-Mo-polymetallic mineralization; Acta Geologica Sinica – English Edition, v. 88, no. s2, p. 1518–1520. https://doi.org/10.1111/1755-6724.12383_9

Lin, S., 1993. Relationship between the Aspy and Bras d'Or "terranes" in the northeastern Cape Breton Highlands, Nova Scotia; Canadian Journal of Earth Sciences, v. 30, p. 1773–1781.

Lin, S., Jiang, D., and Williams, P.F., 1998. Transpression (or transtension) zones of triclinic symmetry: natural example and theoretical modelling; Geological Society of London, Special Publication 135, p. 41–57. https://doi.org/10.1144/GSL.SP.1998.135.01.04

MacDonald, M.A., 2001. Geology of the South Mountain batholith, southwestern Nova Scotia; Nova Scotia Department of Natural Resources, Mineral Resources Branch, Open File ME2001-2.

MacLean, N.J., Barr, S.M., White, C.E., and Ketchum, J.W.F., 2003. New U-Pb (zircon) age and geochemistry of the Wedgeport, Meguma terrane, Nova Scotia; Atlantic Geology, v. 39, no. 3, p. 239–253. https://doi.org/10.4138/1184

Malo, M., Kirkwood, D., De Broucker, G., and St-Julien, P., 1992. A re-evaluation of the position of the Baie Verte – Brompton Line in the Quebec Appalachians: the influence of Middle Devonian strike-slip faulting in Gaspé Peninsula; Canadian Journal of Earth Sciences, v. 29, no. 6, p. 1265–1273. https://doi.org/10.1139/e92-101

Malo, M., Tremblay, A., Kirkwood, D., and Cousineau, P., 1995. Along-strike structural variations in the Quebec Appalachians: consequence of a collision along an irregular margin; Tectonics, v. 14, no. 6, p. 1327–1338. https://doi.org/10.1029/95TC01449

Massawe, R.J. and Lentz, D.R., 2019. Petrochemistry and U-Pb (zircon) age of porphyry dykes at the McKenzie Gulch porphyry-skarn Cu-Ag-Au deposit, north-central New Brunswick, Canada: implications for emplacement age, tectonic setting and mineralization potential; Canadian Journal of Earth Sciences, e-First article, p. 1–26. https://doi.org/10.1139/cjes-2018-0313

Massonne, H.-J., Barr, S.M., White, C.E., and Miller, B.V, 2018. The Pocologan metamorphic suite of southern New Brunswick, Canada: new constraints on age and conditions of medium- to high-pressure metamorphism on the Ganderian margin of the Rheic Ocean; Tectonophysics, v. 747–748, p. 177–190. https://doi.org/10.1016/j.tecto.2018.09.006

McLeod, M.J., 1987. Saint George batholith project (east); *in* Twelfth Annual Review of Activities, (ed) S.D. Abbott; New Brunswick Department of Natural Resources and Energy, Mineral and Energy Division, Information Circular 87-2, p. 33–36.

McLeod, M.J., 1990. Geology, geochemistry and related mineral deposits of the Saint George batholith, Charlotte, Queens and Kings counties, New Brunswick; New Brunswick Department of Natural Resources and Energy, Mineral Resources Report 5, 169 p.

Mohammadi, N., 2018. Petrogenesis of tin-tungsten-molybdenum mineralized intragranitic systems within the highly evolved Mount Douglas polyphase intrusive complex, southwestern New Brunswick, Canada; Ph.D. Thesis, University of New Brunswick, Fredericton, New Brunswick, 456 p.

Mohammadi, N., Fyffe, L., McFarlane, C.R.M., Thorne, K.G., Lentz, D.R., Charnley B., Branscombe, L., and Butler, S., 2017. Geological relationships and laser ablation ICP-MS U-Pb geochronology of the Saint George batholith, southwestern New Brunswick, Canada: implications for its tectonomagmatic evolution; Atlantic Geology, v. 53, p. 207–240. https://doi.org/10.4138/atlgeol.2017.008

Mohammadi, N., McFarlane, C.R.M., and Lentz, D.R., 2019. U-Pb geochronology of hydrothermal monazite from uraniferous greisen veins associated with the high heat production Mount Douglas granite, NB, Canada; Geosciences, v. 9, no. 5, p. 244. https://doi.org/10.3390/geosciences9050224

Mohammadi, N., McFarlane, C.R.M., Lentz, D.R., and Thorne K., 2020. Timing of magmatic crystallization and Sn-W-Mo greisen vein formation within the Mount Douglas Granite, NB, Canada; Canadian Journal of Earth Sciences, v. 57, no. 7, p. 814–839. https://doi.org/10.1139/cjes-2019-0043

Moning, A., Barr, S.M., White, C.E., Sombini dos Santos, G., and van Rooyen, D., 2018. Factors controlling intrusion-related mineralization in Cape Breton Island, Nova Scotia: a comparison of Silurian-Devonian plutons in Ganderia and Avalonia; *in* Targeted Geoscience Initiative: 2017 report of activities, volume 1, (ed.) N. Rogers; Geological Survey of Canada, Open File 8358, p. 31–35. http://doi.org/10.4095/306391

Moning, A., Barr, S.M., White, C.E., and van Rooyen, D., 2019. Contrasts in petrological features between Silurian-Devonian plutons in the Mira and Aspy terranes of Cape Breton Island, Nova Scotia: implications for porphyry-style mineralization; *in* Targeted Geoscience Initiative: 2018 report of activities, (ed.) N. Rogers; Geological Survey of Canada, Open File 8549, p. 287–294. https://doi.org/10.4095/313662

Nance, R.D. and Dallmeyer, R.D., 1993. 40Ar/39Ar amphibole ages from the Kingston Complex, New Brunswick: evidence for Silurian-Devonian tectonothermal activity and implications for the accretion of the Avalon composite terrane; The Journal of Geology, v. 101, no. 3, p. 375–388. https://doi.org/10.1086/648230

Park, A.F. and Whitehead, J., 2003. Structural transect through Silurian turbidites of the Fredericton Belt southwest of Fredericton, New Brunswick: the role of the Fredericton fault in late Iapetus convergence; Atlantic Geology, v. 39, no. 3, p. 227–237. https://doi.org/10.4138/1183

Park, A.F., Williams, P.F., Ralser, S., and Leger, A., 1994. Geometry and kinematics of a major crustal shear zone segment in the Appalachians of southern New Brunswick; Canadian Journal of Earth Sciences, v. 31, no. 10, p. 1523–1535. https://doi.org/10.1139/e94-135

Perrot, M., Tremblay, A., Ruffet, G., and David, J., 2018. Detrital U-Pb and 40Ar/39Ar geochronology of the Connecticut Valley-Gaspé trough, southern Quebec and northern Vermont – transitional tectonism from Salinic to Acadian orogenic cycles; Tectonophysics, v. 745, p. 430–452. https://doi.org/10.1016/j.tecto.2018.08.006

Piette-Lauzière, N., Larson, K.P., and Kellett, D.A., 2018. Field mapping of the Eastern Highlands shear zone, Cape Breton Island, Nova Scotia; *in* Targeted Geoscience Initiative: 2017 report of activities, volume 1, (ed.) N. Rogers; Geological Survey of Canada, Open File 8358, p. 23–29. http://doi.org/10.4095/306391

Piette-Lauzière, N., Graziani, R., Larson, K.P., and Kellett, D.A., 2019. Reactivation of the Eastern Highlands shear zone, Cape Breton Island, Appalachian Orogen; *in* Targeted Geoscience Initiative: 2018 report of activities, (ed.) N. Rogers; Geological Survey of Canada, Open File 8549, p. 295–305. https://doi.org/10.4095/313663

Ratcliffe, N.M., Stanley, R.S., Gale, M.H., Thompson, P.J., and Walsh, G.J., 2011. Bedrock geologic map of Vermont, United States Geological Survey, Scientific Investigations Series, Map 3184, 3 sheets, scale 1:100 000.

Rogers, N., Kellett, D.A., McNicoll, V.J, van Staal, C., Ruberti, G., and Kerr, A., 2015. Tectonostratigraphic controls on the Connaigre Peninsula of south-central Newfoundland and their implications for intrusion-related mineral resources; *in* TGI 4 – Intrusion Related Mineralisation Project: new vectors to buried porphyry-style mineralisation, (ed.) N. Rogers; Geological Survey of Canada, Open File 7843, p. 59–78. https://doi.org/10.4095/296466

Schofield, D.I. and D'Lemos, R.S., 2000. Granite petrogenesis in the Gander zone, NE Newfoundland: mixing of melts from multiple sources and the role of lithospheric delamination; Canadian Journal of Earth Sciences, v. 37, no. 4, p. 535–547. https://doi.org/10.1139/e99-116

Schofield, D.I., van Staal, C.R., and Winchester, J.A., 1998. Tectonic setting and regional significance of the 'Port aux Basques Gneiss', SW Newfoundland; Journal of the Geological Society, v. 155, no. 2, p. 323–334. https://doi.org/10.1144/gsjgs.155.2.0323

Sombini dos Santos, G., 2018. Petrology, geochemistry, age, and tectonic setting of the Margaree pluton, Aspy terrane, Cape Breton Island, Nova Scotia; M.Sc. thesis, Acadia University, Wolfville, Nova Scotia, 229 p.

Shellnutt, J.G. and Dostal, J., 2019. Derivation of the Early Carboniferous Wedgeport pluton by crystal fractionation of a mafic parental magma: a rare case of an A-type granite within the Meguma terrane (Nova Scotia, Canada); Geological Magazine, v. 157, no. 2, p. 248–262. https://doi.org/10.1017/S0016756819000694

Tate, M.C. and Clarke, D.B., 1995. Petrogenesis and regional tectonic significance of Late Devonian mafic intrusions in the Meguma zone, Nova Scotia; Canadian Journal of Earth Sciences, v. 32, no. 11, p. 1883–1898. https://doi.org/10.1139/e95-145

Thériault, R. and Beauséjour, S., 2012. Geological map of Québec; Ressources Naturelles Québec, Géologie Québec, DV 2012-07, scale 1:2 000 000. http://gq.mines.gouv.qc.ca/documents/examine/DV201207/

Thorne, K.G., Fyffe, L.R., and Creaser, R.A., 2013. Re-Os geochronological constraints on the mineralizing events within the Mount Pleasant Caldera: implications for the timing of sub-volcanic magmatism; Atlantic Geology, v. 49, p. 131–150. https://doi.org/10.4138/atlgeol.2013.007

Tremblay, A. and Dubé, B., 1991. Structural relationships between some gold occurences and fault zones in the Bathurst area, northern New Brunswick; *in* Current Research, Part D; Geological Survey of Canada. Paper 91-1D, p. 89–100. https://doi.org/10.4095/132590

Tremblay, A. and Pinet, N., 1994. Distribution and characteristics of the Taconian and Acadian deformation, southern Quebec Appalachians; Geological Society of America Bulletin, v. 106, no. 9, p. 1172–1181. https://doi.org/10.1130/0016-7606(1994)106%3C1172:DACOTA%3E2.3.CO;2

Tremblay, A. and Pinet, N., 2005. Diachronous supracrustal extension in an intraplate setting and the origin of the Connecticut Valley–Gaspé and Merrimack troughs, northern Appalachians; Geological Magazine, v. 142, no. 1, p. 7–22. https://doi.org/10.1017/S001675680400038X

Tremblay, A. and Pinet, N., 2016. Late Neoproterozoic to Permian tectonic evolution of the Quebec Appalachians, Canada; Earth Science Reviews, v. 160, p. 131–170. https://doi.org/10.1016/j.earscirev.2016.06.015

Tremblay, A., de Souza, S., Perrot, M., and Thériault, R., 2015. Géologie des Appalaches du Québec: feuillet Sud-Ouest, regions de Montérégie, Cantons de l'Est, Centre-du-Québec et Chaudière-Appalaches; Ministère des Ressources Naturelles, Québec, MB 2015-11, scale 1:300 000

Tuach, J., 1987. The Ackley high-silica magmatic/metallogenic system and associated post-tectonic granites, southeast Newfoundland; Ph.D. thesis, Memorial University, St-John's, Newfoundland, 455 p.

van Rooyen, D., Barr, S.M., and White, C.E., 2018. New U-Pb (zircon and monazite) ages and Sm-Nd isotopic data from granitoid plutons in the Aspy and Bras d'Or terranes of Cape Breton Island, Nova Scotia: implications for tectonic evolution and mineralization potential; *in* Targeted Geoscience Initiative: 2017 report of activities, volume 1, (ed.) N. Rogers; Geological Survey of Canada, Open File 8358, p. 37–45. http://doi.org/10.4095/306391

van Staal, C.R., 2007. Pre-Carboniferous tectonic evolution and metallogeny of the Canadian Appalachians; *in* Mineral deposits of Canada: a synthesis of major deposit-types, district metallogeny, the evolution of geological provinces, and exploration methods, (ed.) W.D. Goodfellow; Geological Association of Canada, Mineral Deposits Division, Special Publication No. 5, p. 793–818.

van Staal, C. R. and de Roo, J.A., 1995. Mid-Paleozoic tectonic evolution of the Appalachian Central Mobile Belt in northern New Brunswick, Canada: collision, extensional collapse and dextral transpression; *in* Current perspectives in the Appalachian-Caledonian Orogen, (ed.) J.P. Hibbard, C.R. van Staal, and P.A. Cawood; Geological Association of Canada, Special Paper 41 or Geological Survey of Canada, Contribution Series 55293, p. 367–389.

van Staal, C., Dunning, G.R., Valverde, P., Burgess, J., and Brown, M., 1994. Arenig and younger evolution of the Gander margin: a comparison of the New Brunswick and Newfoundland segments; *in* New perspectives in the Appalachian-Caledonian Orogen; Geological Association of Canada (NUNA conference, Grand Falls, Newfoundland, August 1994), Program with abstracts, p. 28–29.

van Staal, C.R., Whalen, J.B., Valverde-Vaquero, P., Zagorevski, A., and Rogers, N., 2009. Pre-Carboniferous, episodic accretion-related, orogenesis along the Laurentian margin of the northern Appalachians; *in* Ancient orogens and modern analogues, (ed.) J.B. Murphy, J.D. Keppie, and A.J. Hynes; Geological Society of London, Special Publication No. 327, p. 271–316. https://doi.org/10.1144/SP327.13

Vermeesch, P., 2018. IsoplotR: a free and open toolbox for geochronology; Geoscience Frontiers, v. 9, no. 5, p. 1479–1493. https://doi.org/10.1016/j.gsf.2018.04.001

Wang, C. and Ludman, A., 2002. Evidence for post-Acadian through Alleghanian deformation in eastern Maine: multiple brittle reactivation of the Norumbega fault system; Atlantic Geology, v. 38, no. 1, p. 37–52. https://doi.org/10.4138/1254

Wang, C. and Ludman, A., 2004. Deformation conditions, kinematics, and displacement history of shallow crustal ductile shearing in the Norumbega fault system in the Northern Appalachians, eastern Maine; Tectonophysics, v. 384, no 1–4, p. 129–148. https://doi.org/10.1016/j.tecto.2004.03.013

Whalen, J.B., 1993. Geology, petrography, and geochemistry of Appalachian granites in New Brunswick and Gaspésie, Québec; Geological Survey of Canada, Bulletin 436, 130 p. https://doi.org/10.4095/183907

Whalen, J.B., Mortensen, J.K., and Roddick, J.C., 1991. Implications of U-Pb and K-Ar geochronology for petrogenesis and cooling history of the McGerrigle Mountains plutonic complex, Gaspe, Quebec. Canadian Journal of Earth Sciences, v. 28, no. 5, p. 754–761. https://doi.org/10.1139/e91-065

Whalen, J.B., Jenner, G.A., Hegner, E., Gariépy, C., and Longstaffe, F.J., 1994a. Geochemical and isotopic (Nd, O, and Pb) constraints on granite sources in the Humber and Dunnage zones, Gaspésie, Quebec, and New Brunswick: implications for tectonics and crustal structure; Canadian Journal of Earth Sciences, v. 31, no. 2, p. 323–340. https://doi.org/10.1139/e94-030

Whalen, J.B., Jenner, G.A., Currie, K.L., Barr, S.M., Longstaffe, F.J., and Hegner, E., 1994b. Geochemical and isotopic characteristics of granitoids of the Avalon zone, southern New Brunswick: possible evidence for repeated delamination events; Journal of Geology, v. 102, no. 3, p. 269–282. https://doi.org/10.1086/629670

Whalen, J.B., Jenner, G.A., Longstaffe, F.J., and Hegner, E., 1996. Nature and evolution of the eastern margin of Iapetus: geochemical and isotopic constraints from Siluro-Devonian granitoid plutons in the New Brunswick Appalachians; Canadian Journal of Earth Sciences, v. 33, no. 2, p. 140–155. https://doi.org/10.1139/e96-014

White, C.E. and Barr, S.M., 1996. Geology of the Brookville terrane, southern New Brunswick, Canada; *in* Avalonian and related Peri-Gondwanan terranes of the circum–North Atlantic, (ed.) R.D. Nance, and M.D. Thompson; Geological Society of America, Special Paper 304, p. 133–148. https://doi.org/10.1130/0-8137-2304-3.133

White, C.E. and Barr, S.M., 2006. The Pocologan metamorphic suite: high-pressure metamorphism in a Silurian fore-arc complex, Kingston terrane, southern New Brunswick; The Canadian Mineralogist, v. 44, no. 4, p. 905–927. https://doi.org/10.2113/gscanmin.44.4.905

Wilson, R.A. and Kamo, S.L., 2016. Geochronology and lithogeochemistry of granitoid rocks from the central part of the Central plutonic belt, New Brunswick, Canada: implications for Sn-W-Mo exploration; Atlantic Geology, v. 52, p. 125–167. https://doi.org/10.4138/atlgeol.2016.007

Wilton, H.C., 1983. The geology and structural history of the Cape Ray fault zone in southwestern Newfoundland; Canadian Journal of Earth Sciences, v. 20, no. 7, p. 1119–1133. https://doi.org/10.1139/e83-100

Xypolias, P., Gerogiannis, N., Chatzaras, V., Papapavlou, K., Kruckenberg, S.C., Aravadinou, E., and Michels, Z., 2018. Using incremental elongation and shearing to unravel the kinematics of a complex transpressional zone; Journal of Structural Geology v. 115, p. 64–81. https://doi.org/10.1016/j.jsg.2018.07.004

APPENDIX A

Devonian magmatic crystallization ages, Canadian Appalachians

All published magmatic crystallization ages used in this study are found in file POR-04_Appendix A_Aug 28.xlsx. This Appendix has not been edited to Geological Survey of Canada specifications. The headings follow the format used in the Canadian Geochronology Knowledgebase (Canadian Geochronology Knowledgebase, 2017, Geological Survey of Canada, Earth Science Sector, Natural Resources Canada, https://atlas.gc.ca/geochron/en/). Age technique abbreviations are as follows: TIMS: thermal ionization mass spectrometry; SHRIMP: sensitive, high-resolution ion microprobe; LA-ICP-MS: laser-ablation inductively-coupled plasma mass spectrometry; EMP: electron microprobe. All references related to these ages are included in a separate worksheet.

Spatial and temporal distribution of the Late Triassic to Early Jurassic porphyry-style mineralized plutons of the Quesnel terrane, British Columbia: inferences on tectonic controls and porphyry prospectivity

N. Rogers[1*]

Rogers, N., 2021. Spatial and temporal distribution of the Late Triassic to Early Jurassic porphyry-style mineralized plutons of the Quesnel terrane, British Columbia: inferences on tectonic controls and porphyry prospectivity; in *Targeted Geoscience Initiative 5: contributions to the understanding and exploration of porphyry deposits, (ed.) A. Plouffe and E. Schetselaar; Geological Survey of Canada, Bulletin 616, p. 25–42. https://doi.org/10.4095/327961*

Abstract: Middle Triassic to Middle Jurassic arc-related sequences of the Quesnel terrane, British Columbia, host numerous major porphyry deposits. In south-central Quesnel terrane, temporal and spatial distribution of deposits have been related to eastward-younging, subparallel belts of coeval, compositionally similar associated plutonic suites corresponding to shallowing of Cache Creek subduction beneath the Quesnel terrane.

Changes in alkalinity of arc magmatism is best explained by ingress of hot primitive mantle due to tectonic processes (i.e. slab rollback, tears, or break-off); however, such mechanisms are inconsistent with eastward migration of magmatism within a dominantly submergent (largely marine) arc built above east-dipping subduction. Furthermore, the plutonic belts were defined for the southern Quesnel terrane and are far less apparent farther north. Notably, the plutonic belts are defined on the oldest exposed intrusions, with their distribution correlating to the overall eastward-younging of fault-bounded country-rock panels.

In this paper, it is suggested that the axis of arc magmatism could remain largely static relative to the leading edge of the Quesnel terrane, with the observed distribution of southern Quesnel plutonism explained by post-depositional structural arrangement of fault-bounded blocks. This model raises the possibility of undiscovered early mineralization being buried beneath Rhaetian and younger sequences exposed in central and eastern Quesnel fault panels

Résumé : Dans le terrane de Quesnel, en Colombie-Britannique, des séquences du Trias moyen au Jurassique moyen apparentées à un arc renferment de nombreux gîtes porphyriques d'importance. Dans la partie centre sud du terrane de Quesnel, la distribution temporelle et spatiale des gîtes a été rattachée à des ceintures subparallèles de suites plutoniques d'âges et de compositions semblables montrant un rajeunissement vers l'est, lequel rend compte d'un exhaussement du terrane de Cache Creek subducté sous le terrane de Quesnel.

Les changements dans l'alcalinité du magmatisme d'arc s'expliquent bien par l'infiltration de manteau primitif chaud par le jeu de processus tectoniques (c.-à-d. le repli, la déchirure ou la rupture de dalles). Toutefois, ces mécanismes sont incompatibles avec la migration vers l'est de l'activité magmatique dans un arc principalement submergé (en grande partie en milieu marin), édifié au-dessus d'une zone de subduction inclinée vers l'est. En outre, les ceintures plutoniques qui ont été définies dans la partie sud du terrane de Quesnel sont beaucoup moins apparentes plus au nord. Plus spécialement, les ceintures plutoniques sont définies à partir des intrusions affleurantes les plus anciennes et leur distribution est corrélée à celle des panneaux de roches encaissantes délimités par des failles qui montrent globalement un rajeunissement vers l'est.

Dans cet article, nous suggérons que l'axe du magmatisme d'arc pourrait être demeuré en grande partie statique par rapport à la bordure externe du terrane de Quesnel, où la distribution observée de l'activité plutonique dans la partie sud de celui-ci s'expliquerait par la disposition structurale postsédimentaire des blocs délimités par des failles. Ce modèle laisse entrevoir la possibilité qu'une minéralisation précoce non encore découverte soit enfouie sous les séquences du Rhétien et de temps plus récents qui affleurent dans les panneaux délimités par des failles dans les parties centre et est du terrane de Quesnel.

[1]Geological Survey of Canada, 601 Booth Street, Ottawa, Ontario K1A 0E8
*Corresponding author: N. Rogers (email: neil.rogers@canada.ca)

INTRODUCTION

The Quesnel terrane of British Columbia hosts numerous major porphyry and related mineral deposits, making it one of Canada's most important metallogenic belts (Fig. 1, 2). The terrane consists of Triassic to Jurassic volcanic and sedimentary rocks that are intruded by multiple calc-alkaline to alkaline magmatic pulses (Nelson and Bellefontaine, 1996; Breitsprecher et al., 2007, 2010; Logan and Mihalynuk, 2014; Mihalynuk et al., 2014, 2016; Schiarizza, 2016, 2017, 2019). Several workers have noted that these intrusions define multiple subparallel linear belts of coeval, compositionally similar plutonic suites (e.g. Parrish and Monger, 1992; Breitsprecher et al., 2010; Logan and Mihalynuk, 2014). Although the designations of these belts across the Quesnel terrane are not universally accepted (Breitsprecher et al. (2010) defined four belts, whereas Logan and Mihalynuk (2014) described three belts), the consensus is that they represent an eastward-younging progression of calc-alkaline to alkaline magmatic events, each of which extends over a 4 to 10 Ma period.

This paper examines the tectonic implications of the defined eastward progression of magmatic belts across the southern to central portion of the Quesnel terrane and assesses whether there are potential inferences that could apply to mineral prospectivity. To understand the underlying tectonic controls behind the observed distribution of plutonic suites, this paper reviews previously obtained age determinations for the Quesnel terrane, from the southern border of British Columbia to the Hogem Batholith at approximately 56.5° north (Fig. 2). The location, age, precision, method, interpretation, and source of analyses under consideration are compiled in Appendix A.

TECTONOSTRATIGRAPHIC FRAMEWORK

The Canadian Cordillera is divided into five morphological belts (from west to east: Insular, Coast, Intermontane, Omineca, and Foreland) characterized by differences in land forms, geological units, and structure (Monger et al., 1972; Gabrielse et al., 1991). These belts are composed of one or more terranes, which have been defined as fault-bounded geological entities of regional extent that are characterized by a largely coherent stratigraphy (Coney et al., 1980; Coney, 1989). The Quesnel terrane (Fig. 1, 2), along with the Cache Creek and Stikine terranes, constitute the Intermontane Belt (Coney et al., 1980; Monger et al., 1982; Silberling et al., 1992).

The prevailing tectonic paradigm for the evolution of the Quesnel terrane is that it is a Paleozoic continental block derived from the western margin of Ancestral North America

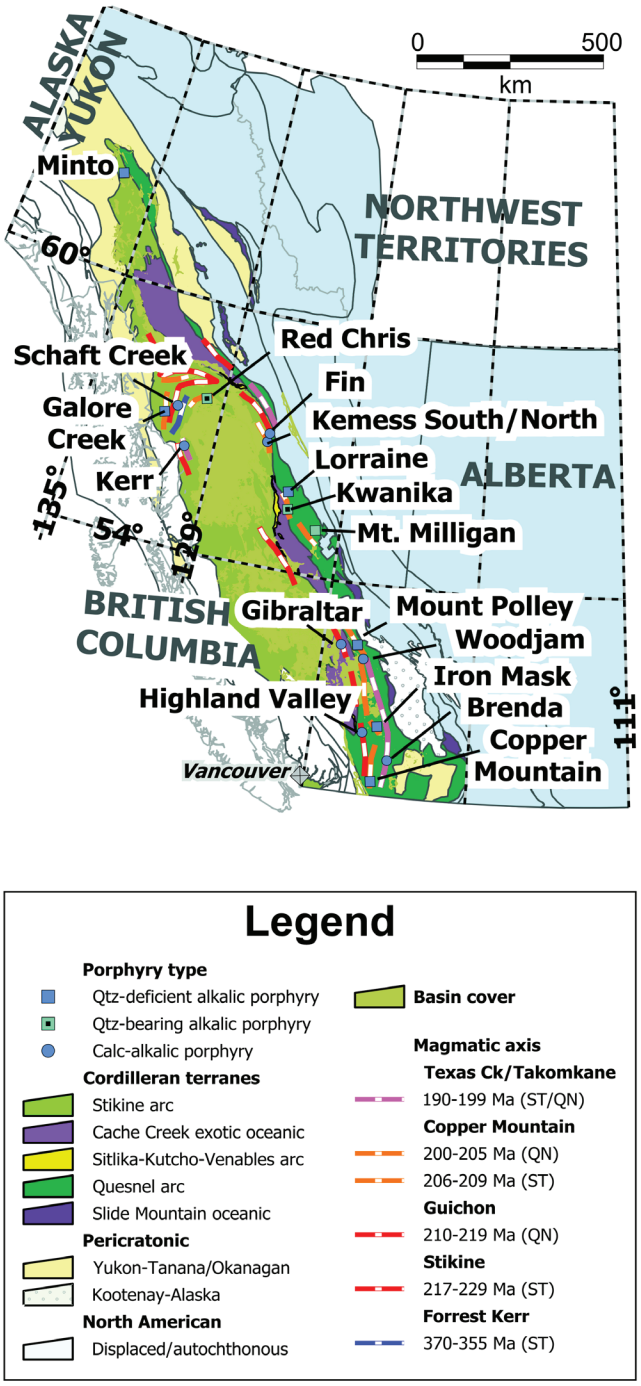

Figure 1. Major porphyry deposits of the Quesnel and Stikine terranes, Canadian Cordillera; *modified from* Logan and Mihalynuk (2014) and Mihalynuk et al. (2016).

on which a west-facing Mesozoic arc formed (Gabrielse et al., 1991). In this model, the Quesnel terrane is separated from Ancestral North America by the remnants of an oceanic tract (Slide Mountain terrane), with it becoming accreted to composite Laurentia by the Middle Jurassic (Monger et al., 1982; Mihalynuk et al., 1994). The Mesozoic arc magmatism

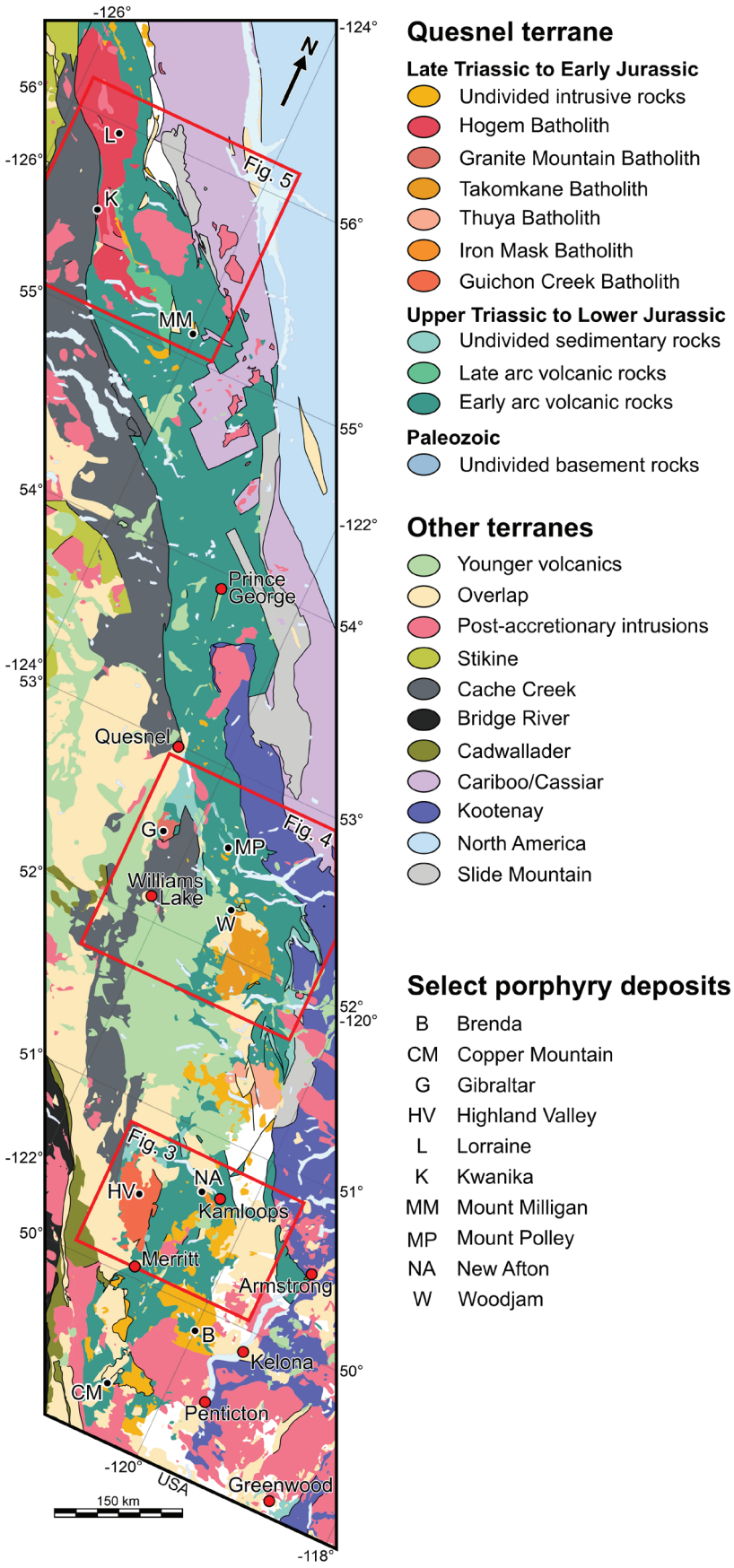

Figure 2. Simplified bedrock geology of the central portion of British Columbia between 49° and 56.5° north. Red boxes indicate the areas of more detailed bedrock geology shown in Figures 3 to 5. *Modified from* British Columbia Geological Survey's MapPlace 2 digital geology (Cui et al., 2017).

developed on the Quesnel terrane is related to the eastward (current orientation) subduction of the oceanic Cache Creek terrane. The Stikine terrane is broadly correlative to Quesnel, but is now positioned to the west of the Cache Creek terrane in British Columbia (Fig. 2). This organization of terranes has been explained by an 'enclosure' model (Nelson and Mihalynuk, 1993; Mihalynuk et al., 1994; Nelson and Colpron, 2007), whereby the Stikine terrane originated as the northern extension of the Quesnel terrane prior to wrapping around the Cache Creek terrane forming an orocline. A consequence of this model is that, through the Late Triassic to Early Jurassic, the oceanic Cache Creek terrane is experiencing concurrent eastward subduction beneath the Quesnel terrane and westward subduction beneath the Stikine terrane (current coordinates).

SUPRACRUSTAL SEQUENCES OF THE QUESNEL TERRANE

In the simplest terms, the Quesnel terrane consists of Middle Triassic to Middle Jurassic arc volcanic and siliciclastic rocks, built on Late Paleozoic sequences (Fig. 3–5). The Quesnel terrane Paleozoic sequences were allocated by Monger et al. (1991) to the Okanagan and Harper Ranch subterranes. The Okanagan subterrane is recognized only in southern British Columbia. It consists predominantly of basalt and chert, along with minor limestone and serpentinized ultramafic rocks, and was likely formed in a marginal basin, potentially related to the Slide Mountain terrane (Monger et al., 1991). In the southern part of the Quesnel terrane, the Harper Ranch subterrane is largely represented by the Late Devonian to Late Permian Harper Ranch Group (Fig. 3; Beatty et al., 2006), which consists of arc-derived volcaniclastic rocks along with limestone, argillite, chert, and clastic sedimentary rocks. Farther north in the Quesnel terrane, the Harper Ranch subterrane is represented by Carboniferous to Permian arc volcanic and sedimentary rocks of the Lay Range assemblage (Fig. 5; Nelson et al., 1993; Ferri, 1997). The composite diorite-gabbro Lounge Lizard Intrusive Complex (Nelson et al., 1993) occurs as a faulted block within Lay Range assemblage rocks. This body is classified as Paleozoic, but it is notable that Nelson et al. (1993) observed the similarity of this complex with components of the Jurassic Boundary phase of the Hogem Batholith. Furthermore, the ca. 186 Ma Polaris Ultramafic Complex occupies a very similar structural position, approximately 75 km to the north-northwest (Nixon et al., 1997).

The Triassic Slocan Group primarily outcrops along the south and central portion of the eastern margin of the Quesnel terrane, adjacent to the Slide Mountain terrane (Fig. 4; Rees, 1987; Panteleyev et al., 1996; Schiarizza et al., 2013; Schiarizza, 2016). This unit that forms a relatively narrow band to the north of Kamloops, whereas farther south it discontinuously occurs over a significantly wider area, consists mostly of dark grey to black slate and phyllite, with minor light to medium grey siltstone (Schiarizza, 2016). Previous studies recognized these sedimentary sequences as distinct (e.g. Campbell and Tipper, 1971), with Schiarizza et al. (2013) mapping them as a separate unit within the primarily arc volcanic Nicola Group. Schiarizza (2016), following Rees (1987), subsequently defined them as the distinct and discretely mappable Slocan Group.

The Nicola Group represents the dominant supracrustal sequence in the south and central portions of the Quesnel terrane (Fig. 3, 4). The equivalent stratigraphic unit in the northern part of the Quesnel terrane, and indeed the related Stikine terrane, is the Takla Group (Fig. 5). The Nicola Group largely consists of submarine volcanic, volcaniclastic, and sedimentary rocks (Preto, 1979; Mortimer, 1987; Mihalynuk et al., 2016) representing more than a dozen individual lithostratigraphic units (Mihalynuk et al., 2016). Recent age determinations indicate that Nicola magmatism occurred in several pulses during the Middle and Upper Triassic (Mihalynuk et al., 2015, 2016).

In the southern portion of the Quesnel terrane, the Nicola Group is divided between three subparallel belts separated along north-trending faults, referred to as the Eastern, Central, and Western belts (Fig. 3; Preto, 1979; Mihalynuk et al., 2016). The Western belt of the Nicola Group contains the 'lower mafic unit' that is dominated by massive, poorly-layered, oxidized to epidotized, dark green, augite-phyric calc-alkalic basaltic lava flows, interlayered with mafic tuff, and the 'upper stratified unit' consisting of variable andesitic to rhyolitic volcanic and volcaniclastic rocks interbedded with feldspathic wacke, conglomerate, siltstone and limestone (Mihalynuk et al., 2016). The Western belt includes Ladinian (ca. 238 Ma) and lower Norian (ca. 224 Ma) magmatism, as well as middle to upper Norian clastic sedimentation (ca. 210 Ma; Appendix A; Mihalynuk et al., 2016). The Central belt also contains a Ladinian magmatic pulse, along with a younger pulse in the latest Triassic/lowermost Jurassic (ca. 201 Ma). There are also Norian zircon-bearing clastic sedimentary rocks that are interpreted as the product of uplift that eroded middle Norian components (Mihalynuk et al., 2016). The Eastern belt consists mostly of well-bedded, clastic sedimentary rocks, along with (mostly) mafic volcanic units that are middle Norian to latest Triassic/lowermost Jurassic (Mihalynuk et al., 2016). This recent dating also demonstrated that the main sedimentary successions of the Eastern belt (or at the very least those exposed toward the west of this belt) are coeval to younger than the last vestiges of Nicola volcanism, and not representative of a thick turbiditic basement to arc magmatism, as previously believed (e.g. Mihalynuk et al., 2015).

Farther north, between Bonaparte Lake and the Quesnel River, the Nicola Group is separated into four lithostratigraphic assemblages (Fig. 4; Schiarizza, 2016, 2017, 2019) that at least in part demonstrate superpositional relationships.

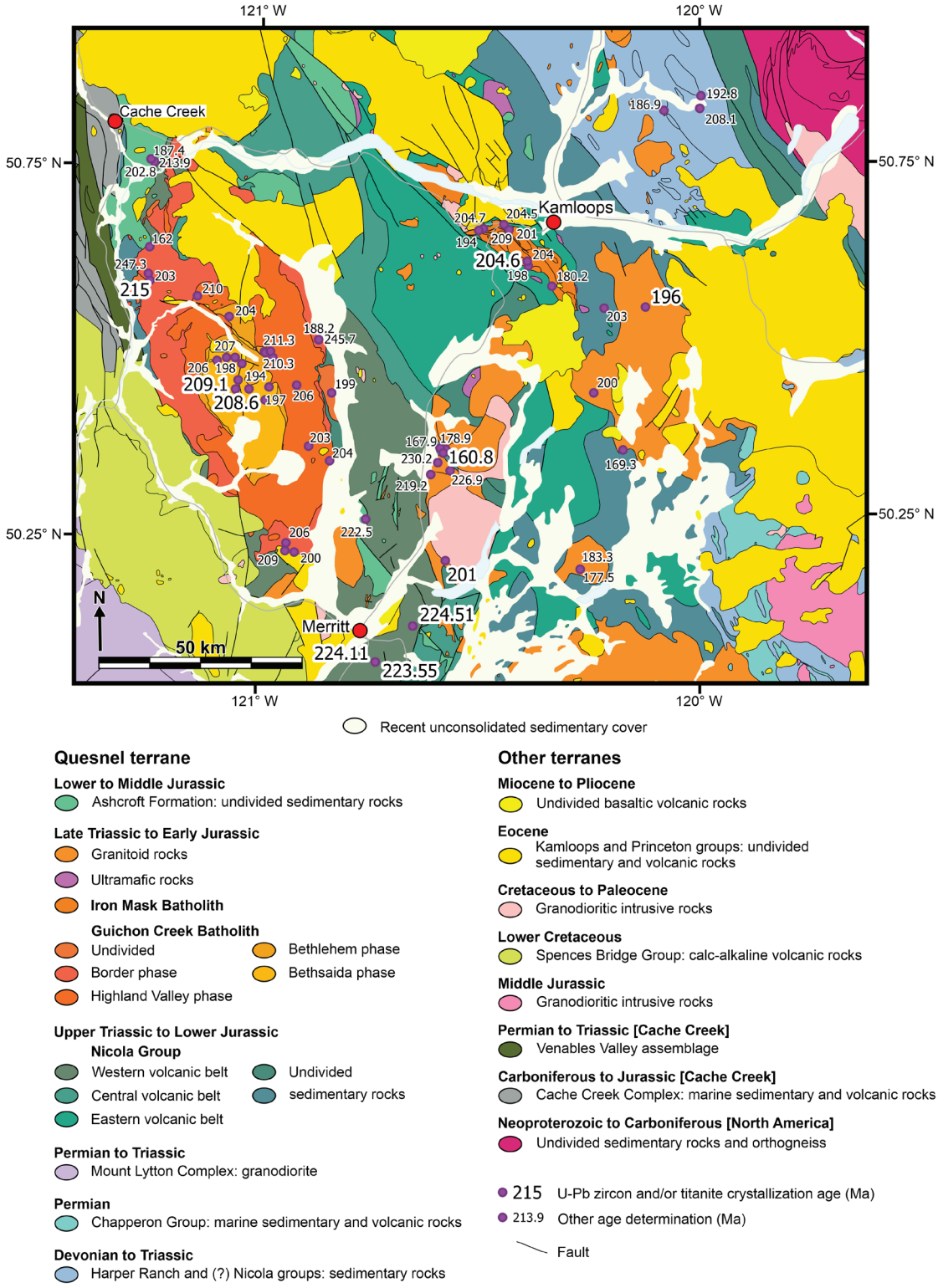

Figure 3. Bedrock geology of the Guichon Creek and Iron Mask batholith area. *Modified from* British Columbia Geological Survey's MapPlace 2 digital geology (Cui et al., 2017), in association with Beatty et al. (2006), Breitsprecher (2010), Friedman et al. (2016), Mihalynuk et al. (2016), and Whalen et al. (2017). Distribution of select Mesozoic Quesnel terrane age determinations are shown (Wanless et al., 1965, 1968; White et al., 1967; Chrismas et al., 1969; Blanchflower, 1971; Jones, 1975; Preto et al., 1979; Hunt and Roddick, 1987; Mortimer et al., 1990; Parrish and Monger, 1992; Mortensen et al., 1995; Moore et al., 2000; Erdmer et al., 2002; Friedman et al., 2002, 2016; Petersen et al., 2004; Breitsprecher et al., 2010; Whalen et al., 2017). Additional age determination data are compiled in Appendix A.

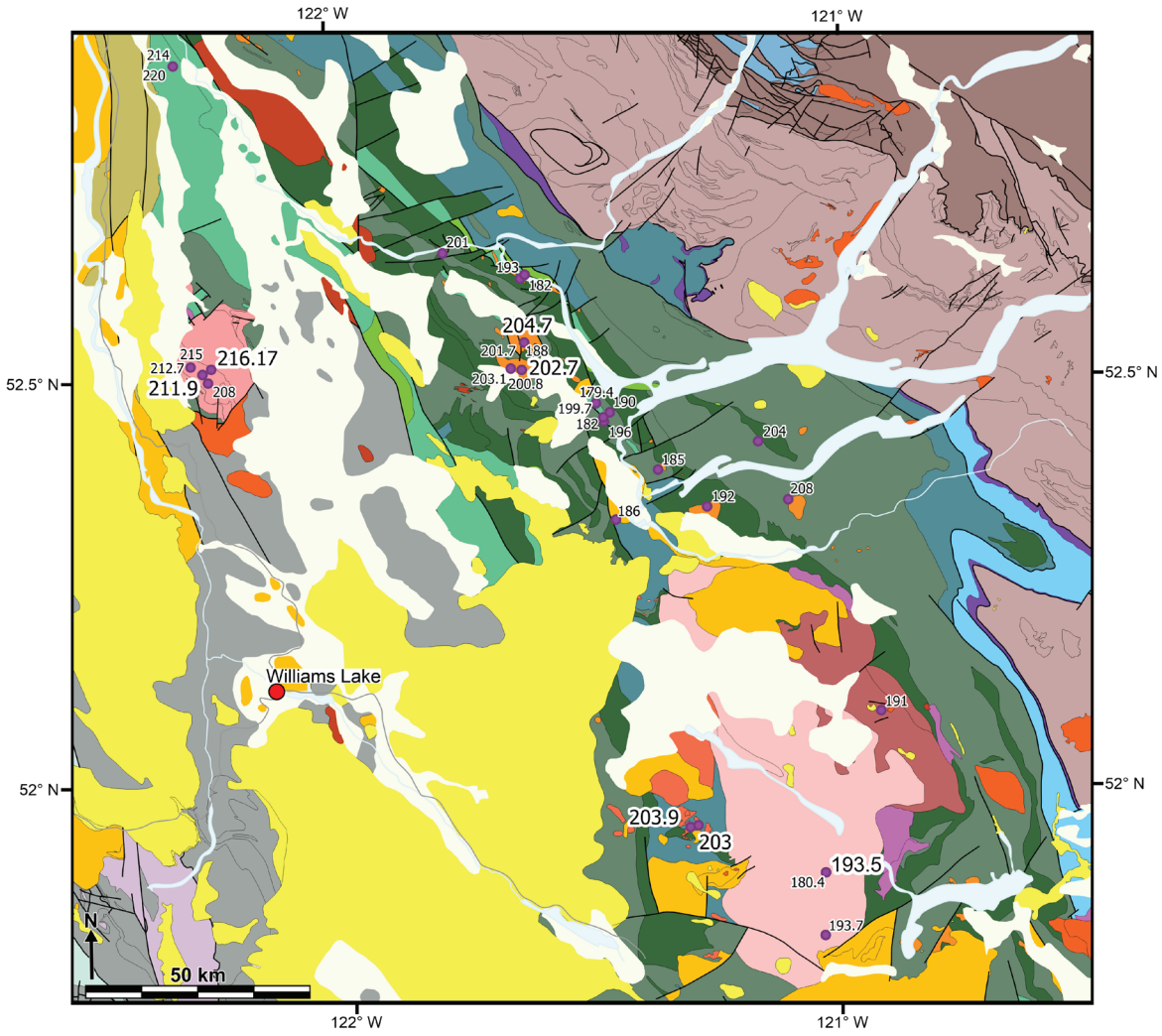

Recent unconsolidated sedimentary cover

Quesnel terrane

Lower to Middle Jurassic
- Undivided Ashcroft Formation and Dragon Mountain succession

Early Jurassic
- Iron Lake suite
- Takomkane Batholith: quartz-feldspar porphyry

Late Triassic to Early Jurassic
- Granodioritic intrusive rocks
- Takomkane Batholith: granodioritic intrusive rocks

Late Triassic
- Copper Mountain plutonic suite
- Granite Mountain Batholith: tonalitic intrusive rocks

Upper Triassic to Lower Jurassic

Nicola Group
- Undivided
- Sedimentary rocks
- Basaltic volcanic rocks

Triassic
- Slocan Group: sedimentary rocks

Post-accretionary units

Miocene to Holocene
- Undivided basaltic volcanic rocks

Oligocene to Pliocene
- Conglomerate, coarse clastic sedimentary rocks

Eocene
- Undivided volcanic and sedimentary rocks

Cretaceous to Paleogene
- Undivided granitoid intrusive rocks
- Undivided sedimentary rocks

Middle to Late Jurassic
- Undivided granitoid intrusive rocks

215 U-Pb zircon and/or titanite crystallization age (Ma)

213.9 Other age determination (Ma)

Fault

Other terranes

Early Jurassic [Cache Creek]
- Fine clastic sedimentary rocks

Upper Permian to Upper Triassic [Cadwallader]
- Undivided coarse clastic sedimentary and bimodal volcanic rocks

Carboniferous to Middle Triassic [Cache Creek]
- Undivided marine sedimentary, volcanic and intrusive rocks

Carboniferous to Permian [Slide Mountain]
- Undivided greenschist metamorphic and serpentinite ultramafic rocks

Neoproterozoic to Carboniferous [Kootenay]
- Undivided metasedimentary rocks and orthogneiss

Neoproterozoic to Paleozoic [North America]
- Fine clastic sedimentary rocks

Neoproterozoic [Cassiar]
- Undivided sedimentary rocks

Figure 4. Bedrock geology of the Granite Mountain and Takomkane batholith area. *Modified from* British Columbia Geological Survey's MapPlace 2 digital geology (Cui et al., 2017), in association with Schiarizza (2014, 2015, 2016) and Mostaghimi (2016). Distribution of select Mesozoic Quesnel terrane age determinations are shown (Leech et al., 1963; Schink, 1974; Drummond et al., 1976; Jung, 1986; Bailey and Archibald, 1990; Mortensen et al., 1995; Panteleyev et al., 1996; Whiteaker et al., 1998; Petersen, 2001; Petersen et al., 2004; Oliver et al., 2009; R.G. Anderson, pers. comm., 2012; Mostaghimi, 2016). Additional age determination data are compiled in Appendix A.

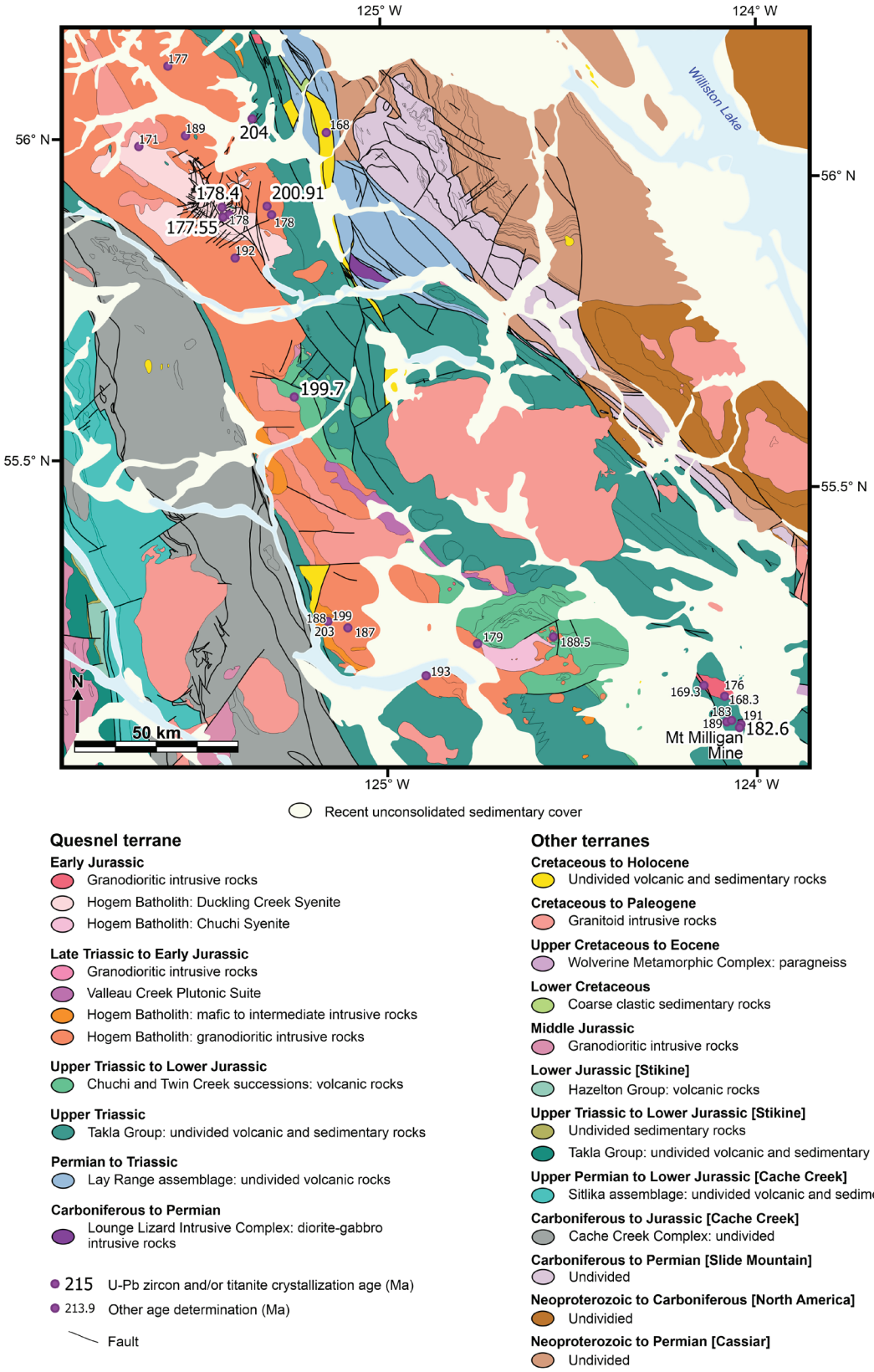

Figure 5. Bedrock geology of the Hogem Batholith area. *Modified from* British Columbia Geological Survey's MapPlace 2 digital geology (Cui et al., 2017), in association with Bath et al. (2014), Devine (2014), and Ootes (2019). Distribution of select Mesozoic Quesnel terrane age determinations are shown (Eadie, 1976; Garnett, 1978; Parrish and Tipper, 1992; Mortensen et al., 1995; Nelson and Bellefontaine, 1996; Bath et al., 2014; Devine et al., 2014). Additional age determination data are compiled in Appendix A.

Assemblage one, which is exposed in a relatively extensive and continuous zone along the east margin of the group, along with a tentatively correlated zone in the interior of the belt, consists of Middle Triassic units composed dominantly of siltstone, argillite, chert, and volcanic sandstone, along with occasional lenses of lithologically distinct pillow basalt that is interpreted as non-arc (Logan and Bath, 2006; Schiarizza, 2019). Assemblage two, which is the most widespread component of the Nicola Group in this area, largely consists of volcanic sandstone and pyroxene-phyric basalt and breccia (Schiarizza, 2019). Sparse fossil collections indicate an early Carnian to early Norian age for this assemblage (Schiarizza, 2016, 2019). Assemblage three is represented by homogeneous pyroxene-phyric basaltic rocks that form two belts defining a regional syncline, and is presumed to be Norian (Schiarizza, 2019). Assemblage four consists of a potentially unconformable set of latest Triassic to Early Jurassic conglomerate, sandstone and volcanic rocks that form the uppermost portion of the Nicola Group (Schiarizza, 2019). Assemblage four rocks are mainly exposed as the core of a regional syncline observed west of the Takomkane Batholith (Fig. 4; Schiarizza, 2016).

The Middle to Upper Triassic Takla Group of the northern Quesnel terrane (Fig. 5; Nelson et al., 1993) is lithologically similar to, and effectively coeval with, Nicola Group rocks. The oldest rocks of the Takla Group are dark grey to black shales and siltstones, with minor epiclastic and pyroclastic deposits. Younger (presumably late Carnian to middle Norian) rocks include augite-xenocrystic, lapilli-bearing volcaniclastic rocks and fine-grained, black siltstone and argillite. These are overlain, at least in part, by a thick sequence of coarse-grained, augite-xenocrystic, pyroclastic basaltic rocks, with lesser flows and minor plagioclase-dominant units and epiclastic sedimentary beds.

The Takla Group in this area is unconformably (to possibly disconformably) overlain by Lower Jurassic rocks of the volcanic Chuchi Lake and Twin Creek sequences and the clastic sedimentary Discovery Creek sequence (Fig. 5; Nelson and Bellefontaine, 1996). These rocks were originally included within the Takla Group and might correspond with the broadly coeval units that postdate the Nicola Group in the south and central portion of the Quesnel terrane (Nelson and Bellefontaine, 1996). Such units include the locally sourced conglomerate, sandstone, siltstone, grey and carbonaceous black shale, and limestone of the Ashcroft Formation (Fig. 3, 4; McMillan, 1974) and interbedded conglomerate and sandstone of the Dragon Mountain succession (Fig. 4; Logan and Moynihan, 2009). Dragon Mountain succession conglomerate is described as notably polymictic, including granitoid and Nicola Group–sourced volcanic detritus (Schiarizza et al., 2002; Logan and Moynihan, 2009; Schiarizza, 2015). It seems reasonable that the Chuchi Lake, Twin Creek, and Discovery Creek sequences are equivalent to the Early to Middle Jurassic Rossland and Ymir groups that are exposed along the southeast margin of the Quesnel terrane (in the area south of Castlegar to Nelson, British Columbia). The Elise Formation volcanic rocks of the Rossland Group overlie Sinemurian sedimentary rocks (Archibald Formation, Rossland Group) and are interpreted as largely marine, calc-alkalic to alkalic, arc volcanic rocks built on attenuated continental crust (Höy and Dunne, 1997).

LATE TRIASSIC TO MIDDLE JURASSIC QUESNEL TERRANE INTRUSIVE ROCKS

The Late Triassic to Middle Jurassic intrusions into the Quesnel terrane are the driver/source of the porphyry-style mineralization that makes this region economically important. Although individual batholiths (i.e. Guichon Creek) typically exhibit distinct pulses of magmatism, over the terrane as a whole age determinations indicate effectively continuous magmatic activity for over 50 Ma (*see* Appendix A for select age determinations). Note, this assertion assumes that Ar-Ar and K-Ar cooling and/or alteration age determinations are broadly representative of magmatic activity (although not necessarily exposed intrusive bodies) given that Middle Triassic and younger rocks of the Quesnel terrane experienced only zeolite to prehnite-pumpellyite metamorphism (Greenwood et al., 1991; Read et al., 1991).

In the southern Quesnel terrane, intrusive magmatism has been split into paired calc-alkalic to alkalic belts that migrated to the east over time in response to east-dipping subduction (Logan and Mihalynuk, 2014). Breitsprecher et al. (2010) defined the magmatic progression as i) Late Triassic (ca. 212–208 Ma) Guichon Creek suite—calc-alkaline porphyry Cu-Mo±Au mineralization; ii) latest Late Triassic (ca. 206–200 Ma) Copper Mountain suite—significant alkaline porphyry Cu-Au±Ag mineralization; iii) Early Jurassic (ca. 197–192 Ma) Wildhorse suite—local calc-alkaline porphyry Cu±Au±Mo mineralization; and iv) latest Early Jurassic (ca. 190–182 Ma) Iron Lake suite—poorly mineralized alkaline mafic to ultramafic units. Logan and Mihalynuk (2014), as well as extending the belts to the Stikine terrane, correlated the early phases of the Hogem Batholith (Mortensen et al., 1995) with the Copper Mountain suite and extended the second pulse of alkalic magmatism to ca. 178 Ma for the northern Quesnel terrane based on the Lorraine deposit ages (Duckling Creek phase of the Hogem Batholith; Bath et al., 2014; Devine et al., 2014).

Guichon Creek Batholith

The Guichon Creek Batholith (Fig. 3) is a concentrically zoned, calc-alkalic body, approximately 65 by 30 km in size, that intrudes Nicola Group rocks (McMillan et al., 2009; Anderson et al., 2012; Bouzari et al., 2016, 2017; Whalen et al., 2017). The batholith contains diorite, quartz diorite,

quartz monzonite, and granodiorite components distributed between the Border, Highland Valley (consisting of the Guichon and Chataway subphases), Bethlehem (consisting of the Bethlehem and Skeena subphases), and Bethsaida phases (Casselman et al., 1995; McMillan et al., 2009). The Highland Valley porphyry Cu-Mo-Ag-Au deposits (Valley, Lornex, Highmont, Alwin, Bethlehem, and JA) are hosted within the Bethlehem and Skeena subphases and Bethsaida phase (McMillan et al., 2009; Logan and Mihalynuk, 2014). Crystallization ages determined with U-Pb zircon range between 215 and 206 Ma, with Ar ages clustering from 202 to 197 Ma and 194 to 188 Ma (Fig. 3; Appendix A).

Granite Mountain Batholith

The Late Triassic Granite Mountain Batholith occurs in a fault-bounded panel of Quesnel terrane rocks, partially enveloped by Cache Creek terrane, southwest of the main belt of Quesnel rocks in south-central British Columbia (Fig. 4; Schiarizza, 2015). The batholith, which hosts the Gibraltar porphyry Cu-Mo mine, is divided into three main units. These are, from southwest to northeast: the Border phase (diorite to quartz diorite), the Mine phase (tonalite) and the Granite Mountain phase (leucocratic tonalite). Kobylinski et al. (2020) noted that intrusive contacts are not apparent between these phases, nor are there wholly distinctive characteristics for each phase. Thus, they proposed a simpler division into copper-bearing and barren phases. In this scheme the copper-bearing tonalite contains visible chalcopyrite, whereas chalcopyrite grains are absent in the barren tonalite. Age determinations are largely between 216 and 208 Ma (Fig. 4; Appendix A), making the Granite Mountain Batholith effectively coeval with the Guichon Creek Batholith approximately 250 km to the south-southeast. Note, Kobylinski et al. (2020), following the suggestion of Ash et al. (1999), include the Burgess Creek stock (Panteleyev, 1978; Schiarizza, 2014, 2015) within the Granite Mountain Batholith, extending the range for barren rocks to ca. 229 Ma.

Iron Mask Batholith

The Iron Mask Batholith (Fig. 3), which hosts the New Afton and Ajax deposits, is a diorite–monzonite complex that outcrops as two bodies separated by a graben of Eocene rocks (Kamloops Group). The batholith is divided into the Pothook diorite, Cherry Creek monzonite, Sugarloaf diorite, and Iron Mask Hybrid phase (Logan et al., 2006, 2007). Age determinations for the Iron Mask Batholith are largely between ca. 205 and 194 Ma, although a distinctly younger ca. 180 Ma Ar determination is assigned to pegmatite associated with late mineralization (Fig. 3; Appendix A).

Takomkane Batholith

The large, Late Triassic to Early Jurassic, composite calc-alkalic Takomkane Batholith (Fig. 4; Schiarizza et al., 2013) is host to at least three mineralizing events spread over several centres (Schiarizza et al., 2009; Bouzari et al., 2016, 2017). Currently, the Woodjam property contains six mineralized zones (Megabuck, Deerhorn, Takom, Three Firs, Southeast, and Megaton). The batholith consists of two major units: the Late Triassic to Early Jurassic Boss Creek unit and the Early Jurassic, megacrystic Schoolhouse Lake unit. The Woodjam Creek unit in the northwestern part of the batholith is texturally distinct, but compositionally similar to the Schoolhouse Lake unit (Schiarizza et al., 2009). Along the northwestern boundary of the batholith, porphyry Cu-Mo-Au mineralization is hosted by the Woodjam Creek unit or small satellite porphyry dykes and adjacent volcanic rocks (Bouzari et al., 2016, 2017).

Hogem Batholith

The large, composite, Early Jurassic to Cretaceous Hogem Batholith occurs in the northern Quesnel terrane, along its western edge (Fig. 5). The north-central part of the batholith, as mapped by Ootes et al. (2019), is separated into four suites. The oldest of these is the Thane Creek suite, which includes diorite, quartz monzodiorite, granodiorite, and tonalite. These rocks are cut by the Duckling Creek suite, which is composed of K-feldspar–rich syenite to monzonite and hosts the Lorraine deposit (Bath et al., 2014; Devine et al., 2014). Elsewhere, the Jurassic to Cretaceous, granitic Mesilinka suite and Cretaceous, mafic-poor, equigranular Osilinka suite also cut the Thane Creek suite. Age determinations for the Thane Creek suite cluster at ca. 204 to 203 Ma and ca. 199 to 188 Ma, whereas the Duckling Creek suite is dated at ca. 181 to 176 Ma (Fig. 5; Appendix A).

DISCUSSION

The temporal changes in alkalinity of the Late Triassic to Middle Jurassic intrusions of the Quesnel terrane in British Columbia have been well established (Breitsprecher et al., 2010; Logan and Mihalynuk, 2014; Schiarizza, 2014). What is less apparent is what the associated spatial distribution means in relation to the underlying tectonic controls. Logan and Mihalynuk (2014) ascribed the spatial distribution to the eastward migration of arc magmatism as the system evolved over two calc-alkalic to alkalic cycles. The transition to alkalic magmatism within an arc is best explained by the ingress of hot primitive mantle from the downgoing slab into the mantle wedge, with resulting radical changes to the

conditions of partial melting (Hole et al., 1991; van de Zedde and Wortel, 2001; Logan and Mihalynuk, 2014). There are several potential mechanisms by which such mantle ingress can be achieved, such as slab rollback, slab window development, slab breakoff, or slab tears (Thorkelson, 1996; Wortel and Spakman, 2000; Niu et al., 2003; Thorkelson and Breitsprecher, 2005). Logan and Mihalynuk (2014) presented the case for slab tears being the underlying mechanism given the speed of magmatic character changes and the perceived temporal continuity of the change along the whole of the Quesnel terrane.

The interpreted spatial distribution of magmatic events was initially identified in the southern Quesnel terrane (Breitsprecher et al., 2010), where the terrane is distinctly broader than it is in north-central British Columbia (Fig. 2). It is apparent, though, that even in the region within which the spatial distribution was defined, the pattern only really reflects the oldest phase of intrusive magmatism in each specific area (Fig. 6). For instance, the Takomkane Batholith and adjacent bodies includes components that correspond to the Copper Mountain, Wildhorse, and Iron Lake suites of Breitsprecher et al. (2010). Consequently, the only sense of an eastward migration of magmatic centres at this latitude (52.0–52.5°N) is dependent on the Norian Granite Mountain Batholith (Fig. 4, 6); however, Schiarizza (2014) determined that the Granite Mountain Batholith is fault bounded, and so whilst it undoubtedly is representative of the Cache Creek–Quesnel terrane boundary region, it is not evident if it has any spatial relationship with the rest of the Quesnel terrane at this latitude. Furthermore, in the northern portion of the Quesnel terrane, in the vicinity of the Hogem Batholith (Fig. 5), sense of a temporal-spatial relationship to the intrusive magmatism is even less evident. The Thane Creek and Duckling Creek phases of the Hogem Batholith do not readily correlate with the time windows demarcated by the temporal-spatial suites that were defined for the southern Quesnel terrane. In addition, the Hogem Batholith contains the Mesilinka and Osilinka phases, which extend Hogem magmatism into the Cretaceous (post-accretionary setting). It is notable that the undated Lounge Lizard Intrusive Complex, which is positioned along the eastern margin of the Quesnel terrane at the same latitude as the Hogem Batholith (Fig. 5), was described by Nelson et al. (1993) as being petrographically similar to the mafic component of the Hogem Batholith (western margin of the Quesnel terrane). Irrespective of whether the Lounge Lizard Intrusive Complex is correlative with the Hogem Batholith, there is Alaskan-type Polaris Ultramafic Complex (Nixon et al., 1997) at the same structural horizon that is coeval with the pre-Middle Jurassic portions of the Hogem Batholith (Cui et al., 2017); hence, the structural position of these units dictates that the magmatic front transects the full width of the terrane at these latitudes.

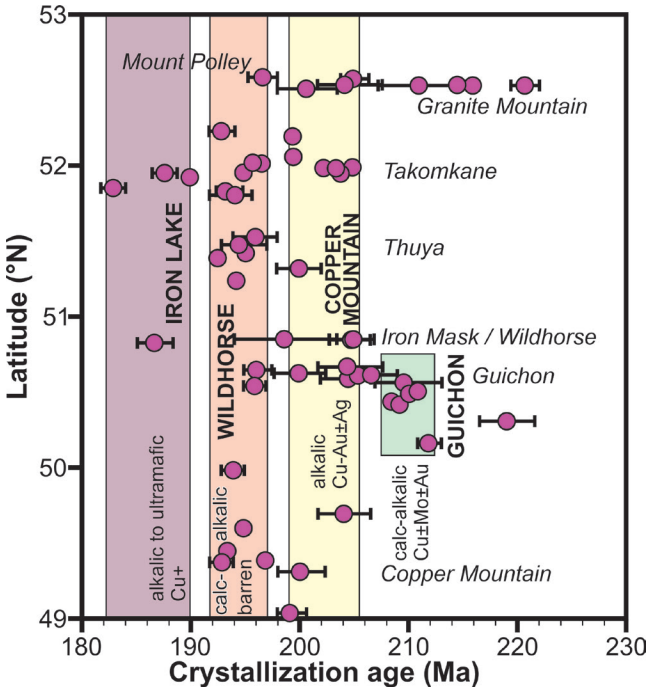

Figure 6. Time-space distribution of age determinations for Late Triassic to Early Jurassic intrusions in the southern to central Quesnel terrane. *Modified from* Breitsprecher et al. (2010) with additional data for the Granite Mountain (Oliver et al., 2009; R.G. Anderson, pers. comm., 2012; Mostaghimi, 2016), Iron Mask (Logan et al., 2007), and Takomkane (del Real et al., 2017) batholiths (*see also* Appendix A).

It is arguable that the northern Quesnel terrane is too narrow to display distinct temporal-spatial suites in the way that is apparent in southern British Columbia where the terrane is much broader (Fig. 2); however, even in this region where there is an across terrane temporal distribution defined, an eastward migration of arc magmatism is counter-intuitive within the overarching tectonic regime. Although occasional (and at least locally appreciable) erosive events are recorded through the Middle Triassic to Middle Jurassic due to local tectonic uplift (*see* Nelson et al., 1993; Höy and Dunne, 1997; Mihalynuk et al., 2014) or potentially surface erosion of a volcanic edifice (England and Molnar, 1990; A. Zagorevski, pers. comm., 2020), the overall paleoenvironment is marine (i.e. a submergent margin setting). For a continental arc to be dominantly submergent throughout its history, the upper plate would have to be in general extensional, or at least in a neutral setting rather than compressional, where the arc overrides the trench. The simplest way to model an extensional arc setting with migration of the magmatic loci would be via slab rollback or the stepping back of the subduction zone. In either case, the migration of arc magmatism would be toward the subducting plate, not away from the margin. Given an east-dipping subduction zone, eastward migration of magmatism would require a shallowing of the slab over time, which would likely cause an Andes-style, emergent upper plate.

Similarly, the enclosure model for the amalgamation of the Intermontane superterrane (Mihalynuk et al., 1994) describes the development of an orocline, which requires the limbs of the orocline to be rotational relative to the apex; consequently, the relative rate of subduction would increase along the limbs away from the oroclinal apex. In terms of the Quesnel terrane, this would suggest that the relative subduction rate is highest at the southern end of the terrane near the British Columbia–Washington State border. The most likely mechanism to explain such an arrangement would be differential slab rollback, but this is antithetical with eastward magmatic migration becoming more prevalent at the terrane's southern end. Theoretically, upper plate motion could be the driver, which would be consistent with eastward migration of magmatism, but the submergent setting and the observed changing width of the terrane are not consistent with such circumstances. Also, there is no obvious mechanism to explain such upper plate–driven motion.

An alternative explanation for the observed eastward progression of intrusive units in the southern Quesnel terrane is provided by the distribution of supracrustal units. In the Princeton - Merritt area, the Eastern, Central, and Western belts of the Nicola Group are distributed between multiple fault panels corresponding to different levels of the Nicola Group. The Western belt is dominated by the lower parts of the Nicola Group (Ladinian–Norian), whereas the Eastern belt is dominated by sequences that are Rhaetian and possibly younger. Evidently it is not possible for supracrustal sequences to be cut by intrusions that are older than they are. Hence, Guichon Creek age rocks, for instance, would be unlikely to be exposed in the Eastern belt as defined for this area. This simple organizational constraint also explains why relatively young magmatic products are present on the western side of the terrane. In the Quesnel terrane of south-central British Columbia, the Lower Jurassic volcanic and sedimentary rocks of the Rossland Group are limited to the eastern margin of the terrane, whereas the presumably equivalent sequences farther north (Chuchi Lake, Twin Creek, and Discovery Creek) do not exhibit such constraints; therefore, the observed distribution of both the Middle Triassic to Middle Jurassic supracrustal and intrusive rocks in the Princeton - Merritt area can be rationalized to the Quesnel terrane having an overall effective homoclinal structure that is at the very least fault-modified, if not primarily fault controlled, with no significant migration of magmatism required during this time period. This is not suggesting that a *sensu stricto* homocline is present, as that would likely require an infeasibly thick supracrustal sequence, but rather that the observed distribution in the southern Quesnel terrane can be achieved through various combinations of faulting and folding without the necessity of substantive eastward migration of magmatism (Fig. 7).

Although the above interpretation does not require the wholesale migration of magmatic centres, the type of magmatism does cycle between calc-alkalic and alkalic systems. Logan and Mihalynuk's (2014) preferred mechanism of slab tears to explain these changes in magmatism is fully compliant with the homoclinal distribution model. Logan and Mihalynuk (2014) further contend that the magmatic types "changed abruptly along the entire length of the arc". Given the oroclinal tectonic paradigm for Intermontane amalgamation that defines a relative rotational motion for the orocline limbs, it would require a remarkably convenient orientation of structures in the downgoing plate to produce margin-parallel impacts to the upper plate (cf. Zagorevski (2015) in regards to the related Cache Creek terrane entrapment). Furthermore, subsequent age determinations indicate that the exact timing of the calc-alkalic to alkalic cycles are actually somewhat transgressive along the length of the terrane (Fig. 2). Variations in the timing of calc-alkalic to alkalic transitions along a rotating arc segment are to be expected, and fit well with slab tears as the fundamental control on the observed chemical transition of magmatism. Low-angle convergence between breaks (e.g. transform faults) on the downgoing plate and the trench can form a slab window should the break open up as a tear and the orientation of slab subduction shift (Thorkelson, 1996; Thorkelson and Breitsprecher, 2005). A segmented break or series of parallel breaks in the downgoing plate could result in the opening of multiple slab windows along the margin that correspond to the temporal and spatial distribution of magmatism both across and along the Quesnel terrane.

CONCLUSION

The Late Triassic to Early Jurassic subduction-related intrusions into the Quesnel terrane, British Columbia, host numerous, major porphyry-style mineral deposits. Detailed mapping and analysis by numerous researchers have established the temporal evolution of magmatism through repeated cycles of calc-alkalic to alkalic plutonism, which have been linked to changes in the subduction dynamics. There have also been attempts to link these compositional changes to spatial patterns that define orogen-long bands of related plutonism. Given that the type and likely commodity of a porphyry deposit is genetically controlled by magma composition (i.e. Cu-Mo±Ag±Au for calc-alkalic systems; Cu-Au for alkalic systems) and there are somewhat subjective indications that the magnitude of deposit corresponds to the age of mineralization (such observations are subjective as it is not possible to consider resources that remain undiscovered, underdeveloped, or have been excised), a reliable distribution model for porphyry mineralization would define prospectivity. As discussed above, the apparent distribution of plutonism derived from the Quesnel terrane of

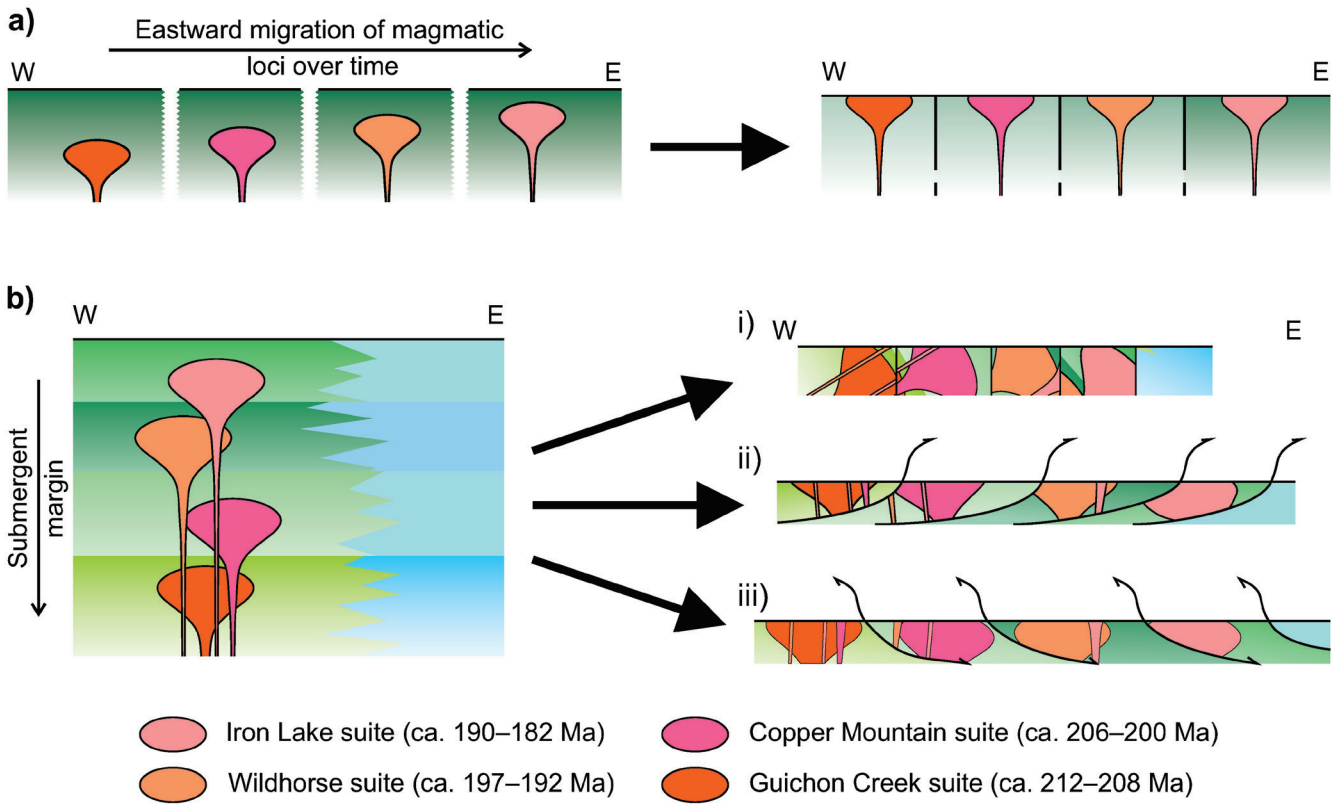

Figure 7. Schematic representation of end-member models to explain the observed distribution of porphyry mineralization within the southern Quesnel terrane. These models follow the division of Late Triassic to Early Jurassic intrusions given in Breitsprecher et al. (2010). These representations are dimensionally non-representative; specifically, there is no correlation between vertical and horizontal dimensions within or between figure panels: **a)** A representation of porphyry mineralization distribution primarily controlled by eastward migration of magmatic centres over time. The left panel represents an original distribution of intrusions that progressively migrated to the east as the Nicola Group evolved. There are indeterminate distances both across and along the arc between the different periods of magmatism. The right panel represents the final distribution with the various intrusions partially excised within a series of fault-bounded blocks. The green shading of the country rocks (e.g. Nicola Group basaltic volcanic rocks) is indicative of younging, but is not intended to have any specific stratigraphic significance. **b)** Representation of magmatic pulses in a progressively submerging basin. Apparent basin depth in the left panel is greatly exaggerated for clarity, with actual magmatism likely to have formed in a basin that attained a maximum depth in the range of 2 to 5 km, with the individual intrusive bodies spread over several tens of kilometres both across and along the eastern margin of the Quesnel terrane. Country rock shading does not have any specific stratigraphic significance, but is intended to indicate temporal evolution of volcanic dominated sequences toward the east of the terrane (e.g. Nicola Group basaltic volcanic rocks) and sedimentary dominated sequences toward the west of the terrane (e.g. Slocan Group). The right panels represent different combinations of structural processes that can produce a similar final surface distribution of units: i) folding followed by dominantly strike-slip faulting; ii) dominantly thrust faulting; and iii) dominantly extensional faulting.

south-central British Columbia, and the associated model for eastward migration of magmatism over time, is not readily applicable farther north.

An alternative explanation for the observed distribution of Late Triassic to Early Jurassic intrusions in south-central British Columbia is given by the southern Quesnel terrane having an overall, effective homoclinal structure. This alternate model does not equate with a *sensu stricto* homocline and it is beyond the scope of this paper to infer what combination of structural controls are present; however, it is clear that surface distribution of the southern Quesnel terrane is at the very least fault modified, if not primarily fault controlled. The broadly homoclinal distribution is supported by the dominantly Ladinian to Norian Western belt of the Nicola Group marking the western margin of the terrane, whereas the Late Jurassic Rossland and Ymir groups occur adjacent to the eastern margin. If this structural control of distribution is correct, then it raises the possibility that porphyry deposits comparable to those hosted by the Norian Guichon Creek and Granite Mountain batholiths (Highland Valley and Gibraltar deposits, respectively) could be repeated at depth within the different fault panels. Given that whole-scale migration of magmatic centres is not required by this model, it follows that it is likely that the location for such buried porphyry deposits would be in the vicinity of subsequent plutonism. That said, given the duration of magmatism, it is virtually inevitable that the downgoing plate consisted of several plates that controlled the temporal

and spatial distribution of magmatic centres. As the deposition of porphyry mineralization is broadly constrained by the depth of intrusion, any younger intrusions within the more deeply excised (i.e. western) fault panels are unlikely to preserve significant, associated mineralization. Younger magmatism in such excised panels could induce thermal overprints and remobilization of ore resources, as is observed in the Guichon Creek, Granite Mountain, Iron Mask, Thuya, and Takomkane batholiths.

ACKNOWLEDGMENTS

I acknowledge all the previous researchers who did the hard work of bedrock mapping and data collection that forms the basis for this paper. In particular, the British Columbia Geological Survey is recognized; without their knowledge and data, this paper would not have been possible. Special thanks are reserved for Alex Zagorevski (Geological Survey of Canada) for sharing his insights into Cordilleran stratigraphy and tectonic models. This paper greatly benefited from detailed reviews by Paul Schiarizza (British Columbia Geological Survey) and Alex Zagorevski.

REFERENCES

Anderson, R.G., Plouffe, A., Ferbey, T., and Dunn, C.E., 2012. The search for surficial expressions of buried Cordilleran porphyry deposits; background and progress in a new Targeted Geoscience Initiative 4 activity in the southern Canadian Cordillera, British Columbia; Geological Survey of Canada, Current Research, 2012–7, 19 p. https://doi.org/10.4095/290295

Ash, C.H., Rydman, M.O., Payne, C.W., and Panteleyev, A., 1999. Geological setting of the Gibraltar mine, south-central British Columbia (93B/8, 9); *in* Exploration and Mining in British Columbia, 1998; British Columbia Ministry of Energy and Mines, p. A1–A15.

Bailey, D.G. and Archibald, D.A., 1990. Age of the Bootjack Stock, Quesnel Terrane, south-central British Columbia (93A); *in* Geological Fieldwork 1989; British Columbia Ministry of Energy, Mines and Petroleum Resources, British Columbia Geological Survey, Paper 1990-1, p. 79–82.

Bath, A.B., Cooke, D.R., Friedman, R.M., Faure, K., Kamenetsky, V.S., Tosdal, R.M, and Berry, R.F., 2014. Mineralization, U-Pb geochronology, and stable isotope geochemistry of the Lower Main zone of the Lorraine deposit, north-central British Columbia: a replacement-style alkalic Cu-Au porphyry; Economic Geology, v. 109, p. 979–1004. https://doi.org/10.2113/econgeo.109.4.979

Beatty, T.W., Orchard, M.J., and Mustard, P.S., 2006. Geology and tectonic history of the Quesnel terrane in the area of Kamloops, British Columbia; *in* Paleozoic evolution and metallogeny of pericratonic terranes at the ancient Pacific margin of North America, Canadian and Alaskan Cordillera, (ed.) M. Colpron and J.L. Nelson; Geological Association of Canada, Special Paper 45, p. 483–504.

Blanchflower, J.D., 1971. Isotopic dating of copper mineralization at Alwin and Valley properties, Highland Valley, southcentral British Columbia; B.Sc. thesis, The University of British Columbia, Vancouver, British Columbia, 83 p.

Bouzari, F., Hart, C.R.J., Bissig, T., and Lesage, G., 2016. Mineralogical and geochemical characteristics of porphyry-fertile plutons: Guichon Creek, Takomkane and Granite Mountain batholiths, south-central British Columbia; *in* Summary of Activities 2015; Geoscience BC, Report 2016-1, p. 17–22.

Bouzari, F., Hart, C.R.J., Bissig, T., and Lesage, G., 2017. Mineralogical and geochemical characteristics of porphyry-fertile plutons: Guichon Creek, Takomkane and Granite Mountain batholiths, south-central British Columbia (NTS 092I, 093A, B); *in* Summary of Activities 2016; Geoscience BC, Report 2017–1, p. 189–200.

Breitsprecher, K., Scoates, J.S., Anderson, R.G., and Weis, D., 2007. Geochemistry of Mesozoic intrusions, Quesnel and Stikine terranes (NTS 082; 092; 093), south-central British Columbia: preliminary characterization of sampled suites; *in* Geological Fieldwork 2006; Ministry of Energy, Mines and Petroleum Resources, British Columbia Geological Survey, Paper 2007-1 and Geoscience BC, Report 2007-1, p. 247–258.

Breitsprecher, K., Weis, D., Scoates, J.S., and Anderson, R.G., 2010. Targeting mineralized Late Triassic to Early Jurassic plutons in the Nicola arc, southern Quesnel terrane, Canadian Cordillera; TGI-3 Workshop: Public Geoscience is Support of Base Metal Exploration, Simon Fraser University, Vancouver, British Columbia, March 22, 2010, p. 49–51 (abstract).

Campbell, R.B. and Tipper, H.W., 1971. Geology of Bonaparte Lake map area, British Columbia; Geological Survey of Canada, Memoir 363, 100 p. https://doi.org/10.4095/102418

Casselman, M.J., McMillan, W.J., and Newman, K.M., 1995. Highland Valley porphyry copper deposits near Kamloops, British Columbia: a review and update with emphasis on the Valley deposit; *in* Porphyry deposits of the northwestern Cordillera of North America, (ed.) T.G. Schroeter; Canadian Institute of Mining and Metallurgy, Special Volume 46, p. 161–191.

Chrismas, L., Baadsgaard, H., Folinsbee, R.E., Fritz, P., Krouse, H.R., and Sasaki, A., 1969. Rb/Sr, S and O isotopic analyses indicating source and date of contact metasomatic copper deposits, Craigmont, British Columbia, Canada; Economic Geology, v. 64, no. 5, p. 479–488. https://doi.org/10.2113/gsecongeo.64.5.479

Coney, P.J., 1989. Structural aspects of suspect terranes and accretionary tectonics in western North America; Journal of Structural Geology, v. 11, no. 1–2, p. 107–125. https://doi.org/10.1016/0191-8141(89)90038-2

Coney, P.J., Jones, D.L., and Monger, J.W.H., 1980. Cordilleran suspect terranes; Nature, v. 288, p. 329–333. https://doi.org/10.1038/288329a0

Cui, Y., Miller, D., Schiarizza, P., and Diakow, L.J., 2017. British Columbia digital geology; British Columbia Ministry of Energy, Mines and Petroleum Resources, British Columbia Geological Survey, Open File 2017-8, data version 2018-04-05, 9 p.

del Real, I., Bouzari, F., Rainbow, A., Bissig, T., Blackwell, J., Sherlock, R., Thompson, J.F.M., and Hart, C.J.R., 2017. Spatially and temporally associated porphyry deposits with distinct Cu/Au/Mo ratios, Woodjam district, central British Columbia; Economic Geology, v. 112, p. 1673–1717. https://doi.org/10.5382/econgeo.2017.4526

Devine, F.A.M., Chamberlain, C.M., Davies, A.G.S., Friedman, R.M., and Baxter, P., 2014. Geology and district-scale setting of tilted alkalic porphyry Cu-Au mineralization at the Lorraine deposit, British Columbia; Economic Geology, v. 109, p. 939–977. https://doi.org/10.2113/econgeo.109.4.939

Drummond, A.D., Sutherland Brown, A., Young, R.J., and Tennant, S.J., 1976. Gibraltar - regional metamorphism, mineralization, hydrothermal alteration and structural development; Porphyry deposits of the Canadian Cordillera, (ed.) A. Sutherland Brown; Canadian Institute of Mining, Special Volume 15, p. 195–205.

Eadie, E.T., 1976. K-Ar and Rb-Sr Geochronology of the Northern Hogem Batholith, B.C.; B.Sc. thesis, The University of British Columbia, Vancouver, British Columbia, 46 p.

England, P. and Molnar, P., 1990. Surface uplift, uplift of rocks, and exhumation of rocks; Geology, v. 18, p. 1173–1177. https://doi.org/10.1130/0091-7613(1990)018%3C1173:SUUORA%3E2.3.CO;2

Erdmer, P., Moore, J.M., Heaman, L., Thompson, R.I., Daughtry, K.L., and Creaser, R.A., 2002. Extending the ancient margin outboard in the Canadian Cordillera: record of Proterozoic crust and Paleocene regional metamorphism in the Nicola horst, southern British Columbia; Canadian Journal of Earth Sciences, v. 39, p. 1605–1623. https://doi.org/10.1139/e02-072

Ferri, F., 1997. Nina Creek Group and Lay Range Assemblage, north-central British Columbia: remnants of late Paleozoic oceanic and arc terranes; Canadian Journal of Earth Sciences, v. 34, p. 854–874. https://doi.org/10.1139/e17-070

Friedman, R.M., Ray, G., and Webster, I., 2002. U-Pb zircon and titanite dating of intrusive rocks in the Heffley Lake area, south-central British Columbia; *in* Geological Fieldwork 2001; British Columbia Ministry of Energy, Mines and Petroleum Resources, British Columbia Geological Survey, Paper 2002-1, p. 109–118.

Friedman, R.M., Mihalynuk, M.G., Diakow, L.J., and Gabites, J.E., 2016. Southern Nicola Arc Project 2015: Geochronologic data constraining Nicola Arc history along a transect near 50°N; British Columbia Ministry of Energy and Mines, British Columbia Geological Survey, GeoFile 2016-3. 1 .zip file.

Gabrielse, H., Monger, J.W.H., Wheeler, J.O., and Yorath, C.J., 1991. Morphogeological belts, tectonic assemblages, and terranes; *in* Chapter 2: Tectonic framework; Geology of the Cordilleran Orogen in Canada, (ed.) H. Gabrielse and C.J. Yorath; Geological Survey of Canada, Geology of Canada Series no. 4, p. 15–28. https://doi.org/10.4095/134073

Garnett, J.A., 1978. Geology and mineral occurrences of the Southern Hogem Batholith; British Columbia Ministry of Mines and Petroleum Resources, Bulletin 70, 75 p.

Greenwood, H.J., Woodsworth, G.J., Read, P.B., Ghent, E.D., and Evenchick, C.A., 1991. Chapter 16: Metamorphism; *in* Geology of the Cordilleran Orogen in Canada, (ed.) H. Gabrielse and C.J. Yorath; Geological Survey of Canada, Geology of Canada Series no. 4, p. 533–570.

Hole, M.J., Rogers, G., Saunders, A.D., and Storey, M., 1991. Relation between alkalic volcanism and slab-window formation; Geology, v. 19, p. 657–660. https://doi.org/10.1130/0091-7613(1991)019%3C0657:RBAVAS%3E2.3.CO;2

Höy, T. and Dunne, K.P.E., 1997. Late Jurassic Rossland Group, southern British Columbia: Part I - Stratigraphy and tectonics; British Columbia Ministry of Energy and Mines; British Columbia Geological Survey, Bulletin 102, 125 p.

Hunt, P.A. and Roddick, J.C., 1987. A compilation of K-Ar ages, report 17; *in* Radiogenic age and isotopic studies: report 1; Geological Survey of Canada, Paper 87-2, p. 1–56. https://doi.org/10.4095/122759

Jones, M.B., 1975. Hydrothermal alteration and mineralization of the Valley Copper deposit, Highland Valley, British Columbia; Ph.D. thesis, Oregon State University, Corvalis, Oregon, 262 p.

Jung, A., 1986. Geochronometry and geochemistry of the Thuya, Takomkane, Raft, and Baldy batholiths, west of the Shuswap metamorphic complex, south-central British Columbia; B.Sc. thesis, The University of British Columbia, Vancouver, British Columbia, 140 p.

Kobylinski, C., Hattori, K., Smith, S., and Plouffe, A., 2020. Protracted magmatism and mineralized hydrothermal activity at the Gibraltar porphyry copper-molybdenum deposit, British Columbia; Economic Geology, 18 p. https://doi.org/10.5382/econgeo.4724

Leech, G.B., Lowdon, J.A., Stockwell, C.H., and Wanless, R.K., 1963. Age determinations by the Geological Survey of Canada (including isotopic ages-report 4); Geological Survey of Canada, Paper 63-17, 146 p. https://doi.org/10.4095/101067

Logan, J.M. and Bath, A.B., 2006. Geochemistry of Nicola Group basalt from the central Quesnel trough at the latitude of Mount Polley (NTS 093A/5, 6, 11, 12); *in* Geological Fieldwork 2005, British Columbia Ministry of Energy, Mines and Petroleum Resources, British Columbia Geological Survey, Paper 2006-1, p. 83–98.

Logan, J.M. and Mihalynuk, M.G., 2014. Tectonic controls on early Mesozoic paired alkaline porphyry deposit belts (Cu-Au ± Ag-Pt-Pd-Mo) within the Canadian Cordillera; Economic Geology, v. 109, p. 827–858. https://doi.org/10.2113/econgeo.109.4.827

Logan, J.M. and Moynihan, D.P., 2009. Geology and mineral occurrences of the Quesnel River map area, central British Columbia (NTS 093B/16); *in* Geological Fieldwork 2008, British Columbia Ministry of Energy, Mines and Petroleum Resources, British Columbia Geological Survey, Paper 2009-1, p. 127–152.

Logan, J.M., Mihalynuk, M.G., Ullrich, T.D., and Friedman, R.M., 2006. Geology of the Iron Mask Batholith, southern British Columbia (NTS 92I/9, 10); British Columbia Ministry of Energy, Mines and Petroleum Resources, British Columbia Geological Survey, Open File 2006-11, scale 1:25 000.

Logan, J.M., Mihalynuk, M.G., Ullrich, T.D., and Friedman, R.M., 2007. U-Pb Ages of intrusive rocks and $^{40}Ar/^{39}Ar$ plateau ages of copper-gold-silver mineralization associated with alkaline intrusive centres at Mount Polley and the Iron Mask Batholith, southern and central British Columbia; *in* Geological Fieldwork 2006, British Columbia Ministry of Energy and Mines, British Columbia Geological Survey, Paper 2007-1, p. 93–116.

McMillan, W.J., 1974. Stratigraphic section from the Jurassic Ashcroft Formation and Triassic Nicola Group contiguous to the Guichon Creek Batholith; *in* Geological Fieldwork 1973, British Columbia Department of Mines and Petroleum Resources, British Columbia Geological Survey, p. 27–34.

McMillan, W.J., Anderson, R.G., Chen, R., and Chen, W., 2009. Geology and mineral occurrences (MINFILE), the Guichon Creek Batholith and Highland Valley porphyry copper district, British Columbia; Geological Survey of Canada, Open File 6079, 2 sheets. https://doi.org/10.4095/248060

Mihalynuk, M.G., Nelson, J.L., and Diakow, L.J., 1994. Cache Creek terrane entrapment: Oroclinal paradox within the Canadian Cordillera; Tectonics, v. 13, no. 3, p. 575–595. https://doi.org/10.1029/93TC03492

Mihalynuk, M.G., Logan, J.M., Diakow, L.J., Friedman, R.M. and Gabities, J., 2014. Southern Nicola Arc Project (SNAP): preliminary results; *in* Geological Fieldwork 2013, British Columbia Ministry of Energy and Mines, British Columbia Geological Survey, Paper 2014-1, p. 29–57.

Mihalynuk, M.G., Diakow, L.J., Logan, J.M., and Friedman, R.M., 2015. Preliminary geology of the Shrimpton Creek area (NTS 092H/15E, 16W) Southern Nicola Arc Project; *in* Geological Fieldwork 2014, British Columbia Ministry of Energy and Mines, British Columbia Geological Survey, Paper 2015-1, p. 129–163.

Mihalynuk, M.G., Diakow, L.J., Friedman, R.M., and Logan, J.M., 2016. Chronology of southern Nicola arc stratigraphy and deformation; *in* Geological Fieldwork 2015, British Columbia Ministry of Energy and Mines, British Columbia Geological Survey, Paper 2016-1, p. 31–63.

Monger, J.W.H., Souther, J.G., and Gabrielse, H., 1972. Evolution of the Canadian Cordillera – a plate tectonic model; American Journal of Science, v. 272, no. 7, p. 557–602. https://doi.org/10.2475/ajs.272.7.577

Monger, J.W.H., Price, R.A., and Tempelman-Kluit, D.J., 1982. Tectonic accretion and the origin of the two major metamorphic and plutonic welts in the Canadian Cordillera; Geology, v. 10, p. 70–75. https://doi.org/10.1130/0091-7613(1982)10%3C70:TAATOO%3E2.0.CO;2

Monger, J.W.H., Wheeler, J.O., Tipper, H.W., Gabrielse, H., Harms, T., Struik, L.C., Campbell, R.B., Dodds, C.J., Gehrels, G.E., and O'Brien, J., 1991. Cordilleran terranes; *in* Chapter 8: Upper Devonian to Middle Jurassic assemblages; Geology of the Cordilleran Orogen in Canada, (ed.) H. Gabrielse and C.J. Yorath. Geological Survey of Canada, Geology of Canada Series no. 4, p. 281–327. https://doi.org/10.4095/134091

Moore, J.M., Gabites, J.E., and Friedman, R.M., 2000. Nicola horst: toward a geochronology and cooling history; Slave-Northern Cordillera Lithospheric Evolution (SNORCLE) Transect and Cordilleran Tectonics Workshop Meeting, University of Calgary, (comp.) F. Cook and P. Erdner; Lithoprobe Report No.72, p. 177–185.

Mortensen, J.K., Ghosh, D.K., and Ferri, F., 1995. U-Pb geochronology of intrusive rocks associated with copper-gold porphyry deposits in the Canadian Cordillera; Porphyry deposits of the Northwestern Cordillera of North America; CIM Special Volume 46, p. 142–158.

Mortimer, N., 1987. The Nicola Group: Late Triassic and Early Jurassic subduction-related volcanism in British Columbia; Canadian Journal of Earth Sciences, v. 24, p. 2521–2536. https://doi.org/10.1139/e87-236

Mortimer, N., van der Heyden, P., Armstrong, R.L., and Harakal, J., 1990. U-Pb and K-Ar dates related to the timing of magmatism and deformation in the Cache Creek terrane and Quesnellia, southern British Columbia; Canadian Journal of Earth Sciences, v. 27, no. 1, p. 117–123. https://doi.org/10.1139/e90-009

Mostaghimi, N., 2016. Structural geology and timing of deformation at the Gibraltar copper-molybdenum porphyry deposit, south-central British Columbia; M.Sc. thesis, The University of British Columbia, Vancouver, British Columbia, 372 p.

Nelson, J.L. and Bellefontaine, K.A., 1996. The geology and mineral deposits of north-central Quesnellia; Tezzeron Lake to Discovery Creek, central British Columbia; British Columbia Ministry of Energy, Mines and Petroleum Resources, British Columbia Geological Survey, Bulletin 99, 112 p.

Nelson, J.L. and Colpron, M., 2007. Tectonics and metallogeny of the British Columbia, Yukon and Alaskan Cordillera, 1.8 Ga to the present; *in* Mineral deposits of Canada: a synthesis of major deposit types, district metallogeny, the evolution of geological provinces, and exploration methods, (ed.) W.D. Goodfellow; Geological Association of Canada, Mineral Deposits Division, Special Publication No. 5, p. 755–791.

Nelson, J.L. and Mihalynuk, M.G., 1993. Cache Creek ocean: Closure or enclosure?; Geology, v. 21, no. 2, p. 173–176. https://doi.org/10.1130/0091-7613(1993)021%3C0173:CCOCOE%3E2.3.CO;2

Nelson, J.L., Bellefontaine, K.A., MacLean, M.E., and Mountjoy, K.J., 1993. Geology of the Klawli Lake, Kwanika Creek and Discovery Creek map areas, northern Quesnel Terrane, British Columbia (93N/7W, 11E, 14E); *in* Geological Fieldwork 1992; British Columbia Geological Survey, Report 1993-1, p. 87–107.

Niu, Y.L., O'Hara, M.J., and Pearce, J.A., 2003. Initiation of subduction zones as a consequence of lateral compositional buoyancy contrast within the lithosphere: A petrological perspective; Journal of Petrology, v. 44, no. 5, p. 851–866. https://doi.org/10.1093/petrology/44.5.851

Nixon, G.T., Hammack, J.L., Ash, C.H., Cabri, L.J., Case, G., Connelly, J.N., Heaman, L.M., Laflamme, J.H.G., Nuttall, C., Paterson, W.P.E., and Wong, R.H., 1997. Geology and platinum-group-element mineralization of Alaskan-type ultramafic-mafic complexes in British Columbia; British Columbia Ministry of Energy, Mines and Petroleum Resources, British Columbia Geological Survey, Bulletin 93, 142 p.

Oliver, J., Crozier, J., Kamionko, M., and Fleming, J., 2009. The Gibraltar Mine, British Columbia. A billion tonne deep copper-molybdenum porphyry system: structural style, patterns of mineralization and rock alteration; Association for Mineral Exploration 2009 Mineral Exploration Roundup, Program with abstracts, p. 35–36.

Ootes, L., Bergen, A., Milidragovic, D., Graham, B., and Simmonds, R., 2019. Preliminary geology of northern Hogem Batholith, Quesnel terrane, north-central British Columbia; *in* Geological Fieldwork 2018, British Columbia Ministry of Energy, Mines, and Petroleum Resources, British Columbia Geological Survey, Paper 2019-1, p. 31–53.

Panteleyev, A., 1978. Granite Mountain project (93B/8); *in* Geological Fieldwork 1977, British Columbia Ministry of Energy, Mines and Petroleum Resources, British Columbia Geological Survey, Paper 1978-1, p. 39–42.

Panteleyev, A., Bailey, D.G., Bloodgood, M.A., and Hancock, K.D., 1996. Geology and mineral deposits of the Quesnel River – Horsefly map area, central Quesnel trough, British Columbia; British Columbia Ministry of Energy, Mines and Petroleum Resources, British Columbia Geological Survey, Bulletin 97, 156 p.

Parrish, R.R. and Monger, J.W.H., 1992. New U-Pb dates from southwestern British Columbia; *in* Radiogenic age and isotopic studies: report 5; Geological Survey of Canada, Paper 91-2, p. 87–108. https://doi.org/10.4095/132915

Parrish, R.R. and Tipper, H.W., 1992. U-Pb zircon age of a clast from the Uslika Formation, north-central British Columbia, and implications for the age of the Uslika Formation; *in* Radiogenic age and isotopic studies: report 5; Geological Survey of Canada, Paper 91-2, p. 163–166. https://doi.org/10.4095/132921

Petersen, N.T., 2001. Provenance of Jurassic sedimentary rocks of Quesnellia: implications for paleogeography; M.Sc. thesis, The University of British Columbia, Vancouver, British Columbia, 153 p.

Petersen, N.T., Smith, P.L., Mortensen, J.K., Creaser, R.A., and Tipper, H.W., 2004. Provenance of Jurassic sedimentary rocks of south-central Quesnellia, British Columbia: implications for paleogeography; Canadian Journal of Earth Sciences, v. 41, p. 103–125. https://doi.org/10.1139/e03-073

Preto, V.A., 1979. Geology of the Nicola Group between Merritt and Princeton; British Columbia Ministry of Energy, Mines and Petroleum Resources, British Columbia Geological Survey, Bulletin 69, 90 p.

Preto, V.A., Osatenko, M.J., McMillan, W.J., and Armstrong, R.L., 1979. Isotopic dates and strontium isotopic ratios for plutonic and volcanic rocks in the Quesnel trough and Nicola belt, south-central British Columbia; Canadian Journal of Earth Sciences, v. 16, p. 1658–1672. https://doi.org/10.1139/e79-155

Read, P.B., Woodsworth, G.J., Greenwood, H.J., Ghent, E.D., and Evenchick, C.A., 1991. Metamorphic map of the Canadian Cordillera; Geological Survey of Canada, Canadian Geoscience 'A' Series Map 1714A, scale 1:2 000 000. https://doi.org/10.4095/134142

Rees, C.J., 1987. The Intermontane – Omineca belt boundary in the Quesnel Lake area, east-central British Columbia: Tectonic implications based on geology, structure and paleomagnetism; Ph.D. thesis, Carlton University, Ottawa, Ontario, 421 p. https://doi.org/10.22215/etd/1987-01330

Schiarizza, P., 2014. Geological setting of the Granite Mountain Batholith, host to the Gibraltar porphyry Cu-Mo deposit, south-central British Columbia; *in* Geological Fieldwork 2013; British Columbia Ministry of Energy and Mines, British Columbia Geological Survey, Paper 2014-1, p. 95–110.

Schiarizza, P., 2015. Geological setting of the Granite Mountain Batholith, south-central British Columbia; *in* Geological Fieldwork 2014; British Columbia Ministry of Energy and Mines, British Columbia Geological Survey, Paper 2015-1, p. 19–39.

Schiarizza, P., 2016. Toward a regional stratigraphic framework for the Nicola Group: Preliminary results from the Bridge Lake – Quesnel River area; *in* Geological Fieldwork 2015; British Columbia Ministry of Energy and Mines, British Columbia Geological Survey, Paper 2016-1, p. 13–30.

Schiarizza, P., 2017. Ongoing stratigraphic studies in the Nicola Group: Stump Lake – Salmon River area, south-central British Columbia; *in* Geological Fieldwork 2016; British Columbia Ministry of Energy and Mines, British Columbia Geological Survey, Paper 2017-1, p. 17–33.

Schiarizza, P., 2019. Geology of the Nicola Group in the Bridge Lake – Quesnel River area, south-central British Columbia; *in* Geological Fieldwork 2018; British Columbia Ministry Of Energy, Mines, and Petroleum Resources, British Columbia Geological Survey, Paper 2019-11, p. 15–30.

Schiarizza, P., Heffernan, S., and Zuber, J., 2002. Geology of Quesnel and Slide Mountain terranes west of Clearwater, south-central British Columbia (92P/9, 10, 15, 16); *in* Geological Fieldwork 2001; British Columbia Ministry of Energy and Mines, British Columbia Geological Survey, Paper 2002-1, p. 83–108.

Schiarizza, P., Bell, K., and Bayliss, S., 2009. Geology and mineral occurrences of the Murphy Lake area, south-central British Columbia (NTS 093A/03); *in* Geological Fieldwork 2008; British Columbia Ministry of Energy and Mines, British Columbia Geological Survey, Paper 2009-1, p. 169–188.

Schiarizza, P., Israel, S., Heffernan, S., Boulton, A., Bligh, J., Bell, K., Bayliss, S., Macauley, J., Bluemel, B., Zuber, J., Friedman, R.M., Orchard, M.J., and Poulton, T.P., 2013. Bedrock geology between Thuya and Woodjam creeks, south-central British Columbia, NTS 92P/7, 8, 9, 10, 14, 15, 16; 93A/2, 3, 6; British Columbia Ministry of Energy, Mines and Natural Gas, British Columbia Geological Survey, Open File 2013-05; 4 sheets, scale 1:100 000.

Schink, E.A., 1974. Geology of the Shiko Lake Stock, near Quesnel Lake, British Columbia; B.Sc. thesis, The University of British Columbia, Vancouver, British Columbia, 64 p.

Silberling, N.J., Jones, D.L., Monger, J.W.H., and Coney, P.J., 1992. Lithotectonic terrane map of the North American Cordillera; U.S. Geological Survey, Miscellaneous Investigations Series, Map 2176, 2 sheets, scale 1:5 000 000.

Thorkelson, D.J., 1996. Subduction of diverging plates and the principles of slab window formation; Tectonophysics, v. 255, no. 1–2, p. 47–63. https://doi.org/10.1016/0040-1951(95)00106-9

Thorkelson, D.J. and Breitsprecher, K., 2005. Partial melting of slab window margins: genesis of adakitic and non-adakitic magmas; Lithos, v. 79, p. 25–41. https://doi.org/10.1016/j.lithos.2004.04.049

van de Zedde, D.M.A. and Wortel, M.J.R., 2001. Shallow slab detachment as a transient source of heat at mid-lithospheric depths; Tectonics, v. 20, p. 868–882. https://doi.org/10.1029/2001TC900018

Wanless, R.K., Stevens, R.D., Lachance, G.R., and Rimsaite, J.Y.H., 1965. Age determinations and geological studies, part 1 - isotopic ages, report 5; Geological Survey of Canada, Paper 64-17, 132 p. https://doi.org/10.4095/101021

Wanless, R.K., Stevens, R.D., Lachance, G.R., and Edmonds, C.M., 1968. Age determinations and geological studies, K-Ar isotopic ages, report 8; Geological Survey of Canada, Paper 67-2A, 141 p. https://doi.org/10.4095/103342

Whalen, J.B., Davis, W.J., and Anderson, R.A., 2017. Temporal and geochemical evolution of the Guichon Creek Batholith and Highland Valley porphyry copper district, British Columbia: implications for generation and tectonic setting of porphyry systems; Geological Survey of Canada, Open File 8334, 45 p. https://doi.org/10.4095/306147

White, W.H., Erickson, G.P., Northcote, K.E., Dirom, G.E., and Harakal, J.E., 1967. Isotopic dating of the Guichon Batholith, B.C.; Canadian Journal of Earth Sciences, v. 4, p. 677–690. https://doi.org/10.1139/e67-045

Whiteaker, R.J., Mortensen, J.K., and Friedman, R.M., 1998. U-Pb geochronology, Pb isotopic signatures and geochemistry of an early Jurassic alkalic porphyry system near Lac La Hache, B.C.; *in* Geological Fieldwork 1997; British Columbia Ministry of Energy, Mines and Petroleum Resources, British Columbia Geological Survey, Paper 1998-1, 14 p.

Wortel, M.J.R. and Spakman, W., 2000. Subduction and slab detachment in the Mediterranean-Carpathian region; Science, v. 290, p. 1910–1917. https://doi.org/10.1126/science.290.5498.1910

Zagorevski, A., 2015. Testing the entrapment of the Cache Creek terrane in British Columbia and Yukon; Geological Society of America, abstracts with programs, v. 47, p. 18.

APPENDIX A

Compilation of Mesozoic age determinations from the Quesnel terrane

Compiled summary data of Mesozoic radiogenic isotope age determinations from the Quesnel terrane between 49° and 56.5° north is available in file POR6_Rogers_TGI5syn_App_A_FINAL.xlsx. Information recorded includes sample number codes, location, interpreted age and 2σ error, epoch, stage, analytical method deployed, rock type, additional notes and original source. For age determinations that are included within British Columbia Geological Survey's MapPlace 2 digital geology (Cui et al., 2017) the BCGS age number is also provided. This Appendix has not been edited to Geological Survey of Canada specifications.

Seismic imaging of porphyry deposits with distributed acoustic sensing of fibre-optic cables: a summary of results at the New Afton Cu-Au mine, British Columbia

G. Bellefleur[1*], E. Schetselaar[1], and D. White[1]

Bellefleur, G., Schetselaar, E., and White, D., 2021. Seismic imaging of porphyry deposits with distributed acoustic sensing of fibre-optic cables: a summary of results at the New Afton Cu-Au mine, British Columbia; in *Targeted Geoscience Initiative 5: contributions to the understanding and exploration of porphyry deposits, (ed.) A. Plouffe and E. Schetselaar; Geological Survey of Canada, Bulletin 616, p. 43–51. https://doi.org/10.4095/327942*

Abstract: We present a summary of physical rock properties and vertical seismic profiling (VSP) results acquired with distributed acoustic sensing (DAS) in boreholes that intersect the main mineralized zone and alteration halo at the New Afton Cu-Au porphyry deposit, British Columbia. We used an advanced DAS system that achieves signal-to-noise ratio of conventional geophones but offers high-density sensing of the entire fibre-optic cable. Straight and helically wound fibre-optic cables specifically engineered for the advanced DAS system were installed in two boreholes and compared with conventional fibre-optic cables with similar configurations connected to a standard DAS interrogator. Comparison of raw field data and processed data of both systems demonstrates a significantly higher signal-to-noise ratio for the new DAS system. Processed VSP data show several reflections with shallow dips that are mostly explained by faults and fractures observed in wireline logs and intersecting the surveyed boreholes.

Résumé : Nous présentons un résumé des propriétés physiques des roches et des résultats de profilage sismique vertical (PSV) acquis au moyen de la détection acoustique répartie (DAS) dans des trous de forage qui recoupent la zone minéralisée principale et le halo d'altération du gisement porphyrique à Cu-Au de New Afton, en Colombie-Britannique. Nous avons utilisé un système DAS perfectionné qui permet d'obtenir un rapport signal/bruit comparable à celui des géophones classiques, mais qui offre une détection à haute densité sur l'ensemble du câble à fibres optiques. Des câbles à fibres optiques droits et à enroulement hélicoïdal spécialement conçus pour ce système ont été installés dans deux trous de forage et comparés à des câbles à fibres optiques classiques de configuration similaire reliés à un interrogateur DAS standard. La comparaison des données brutes de terrain et des données traitées montre un rapport signal/bruit nettement plus élevé pour le nouveau système DAS. Les données PSV traitées montrent plusieurs réflexions faiblement inclinées qui s'expliquent principalement par la présence de failles et de fractures recoupant les trous de forage étudiés et dont les traces peuvent être observées dans les diagraphies par câble.

[1]Geological Survey of Canada, 601 Booth Street, Ottawa, Ontario K1A 0E8
*Corresponding author: G. Bellefleur (email: gilles.bellefleur@canada.ca)

INTRODUCTION

Distributed acoustic sensing (DAS) is a distributed sensing technology that uses the optical scattering response to a laser pulse to measure changes in strain occurring along a fibre-optic cable (Hartog, 2018). Distributed acoustic sensing does not use point receivers but rather simultaneously senses the entire length of a fibre-optic cable for strain changes due to the passage of seismic waves. This ability to measure data over an entire fibre-optic cable at once is particularly advantageous from a data-acquisition perspective and has led to the development of a variety of applications, primarily for the oil and gas industry (Hartog, 2018). Distributed acoustic sensing also offers cost-effective solutions for mineral exploration, particularly for vertical seismic profiling (VSP) surveys, which are sometimes used to provide high-resolution images of the subsurface near known deposits or in prospective areas. Currently, there is a very limited number of published results on the application of DAS for mineral exploration and mining applications. One early example is the imaging of steeply dipping ore at the Kylylahti polymetallic deposit in Finland using DAS-VSP data (Riedel et al., 2018).

Here we present results from one of the first applications of DAS-VSP data for mineral exploration. We acquired DAS-VSP data as part of the Geological Survey of Canada's Targeted Geoscience Initiative (TGI) for the development of an integrated geophysical imaging and 3-D geological modelling research study of the New Afton porphyry deposit, which is part of the Canadian Cordillera and is located in south-central British Columbia. This alkaline Cu-Au porphyry deposit previously supported an open-pit operation and is currently being mined at deeper levels through underground workings, which provide geological constraints extending beyond 1.5 km in depth. At New Afton, we used an advanced DAS system recently developed by Silixa, which achieves signal-to-noise ratio of conventional geophones but offers high-density sensing of the entire fibre-optic cable. Straight and helically wound fibre-optic cables specifically engineered for the advanced DAS system were installed in two boreholes starting in a drill bay located approximately 650 m below the surface. Conventional straight and helically wound fibre-optic cables connected to a standard DAS interrogator were also deployed in the same boreholes for comparison purposes.

The results presented in this paper are a summary of comprehensive TGI work conducted at New Afton and recently published with open access rights in Geophysical Prospecting (Bellefleur et al., 2020). Here we briefly introduce the local geology of the New Afton deposit and present wireline logging results that are used to support the interpretation of DAS-VSP data. Then, we compare field data acquired with both DAS systems with straight fibre-optic cables. DAS-VSP data measured with straight fibre-optic cables were further processed and compared with geological and wireline logs. Reflections observed in processed data obtained with straight fibre-optic cables spatially correlate with fault and fracture zones intersected in the two boreholes used for acquisition.

NEW AFTON CU-AU PORPHYRY DEPOSIT

This summary of the local mine geology is based on drill core logging, 3-D geological modelling, and surface mapping recently conducted by New Gold Inc. (J. Lipske and D. Wade, unpub. rept., 2014). The New Afton Cu-Au porphyry deposit is dominantly hosted by fragmental and crystalline volcanic rocks of the Late Triassic Nicola Group and to a lesser extent by the 204 Ma Cherry Creek monzonite of the Iron Mask batholith; the latter is interpreted as the heat source that caused alteration and mineralization in this alkalic porphyry (Fig. 1). A subvertical southwest-plunging zone of primary hypogene mineralization, largely coincident with the potassic alteration zone, contains disseminated chalcopyrite and bornite. This hypogene ore zone is controlled structurally by two subvertical northeast-southwest-striking fault zones, known as the footwall and hanging-wall faults. The hanging-wall fault juxtaposes volcanic fragmental rocks with a subvertical body of serpentinized picrite. This tectonic contact within the incompetent serpentinized picrite is defined by a high-strain zone of ductile deformation rich in magnetite that locally confines a zone of calcic alteration. The primary hypogene ore zone is cut by numerous moderately to steeply dipping fault zones that controlled secondary hypogene mineralization of tetrahedrite and tennantite. Supergene mineralization of native copper and chalcocite in hematite-rich oxidation zones is more abundant at higher structural levels in the vicinity of the open pit, but native copper extends to 700 m below surface beneath the pit along older, long-lived structures.

Figure 1. a) Plan view of the main lithological units (top) and main alteration zones (bottom) at New Afton. The main hypogene mineralized zone (0.4% Cu equivalent) is outlined in red with no color fill and coincides with the biotite-dominant and feldspar-dominant potassic alteration zone. HW Flt and FW Flt are the hanging wall and footwall faults, respectively. MO indicates monzonite. **b)** N-S sections showing lithologies, alteration, and mineralization. Mt and Hm in the mineralization subfigure refer to zones with magnetite and hematite, respectively; Pl stands for propylitic. Units are in mine grid co-ordinates (*from* J. Lipske and D. Wade, unpub. rept., 2014).

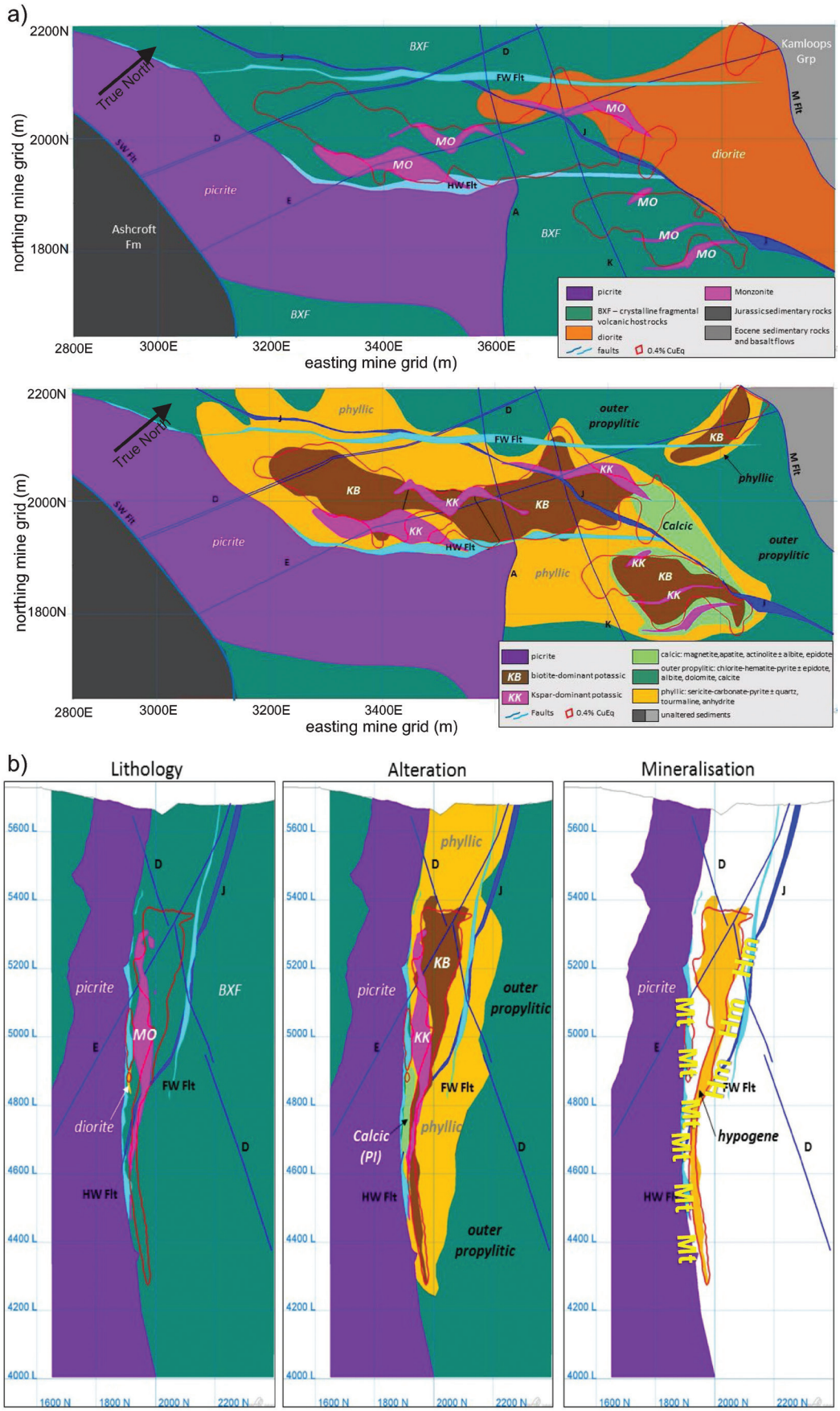
a)
2200N
2000N
1800N
northing mine grid (m)
2800E
3000E
3200E
3400E
3600E
easting mine grid (m)
True North
BXF
Kamloops Grp
FW Flt
M Flt
SW Flt
HW Flt
MO
diorite
picrite
Ashcroft Fm
BXF
picrite
Monzonite
BXF – crystalline fragmental volcanic host rocks
Jurassic sedimentary rocks
diorite
Eocene sedimentary rocks and basalt flows
faults
0.4% CuEq
phyllic
outer propylitic
KB
KK
Calcic
phyllic
biotite-dominant potassic
K-spar-dominant potassic
calcic: magnetite,apatite, actinolite ± albite, epidote
outer propylitic: chlorite-hematite-pyrite ± epidote, albite, dolomite, calcite
phyllic: sericite-carbonate-pyrite ± quartz, tourmaline, anhydrite
unaltered sediments
b)
Lithology
Alteration
Mineralisation
5600 L
5400 L
5200 L
5000 L
4800 L
4600 L
4400 L
4200 L
4000 L
1600 N
1800 N
2000 N
2200 N
Calcic (Pl)
hypogene
Mt
Hm

VERTICAL SEISMIC PROFILING WITH DISTRIBUTED ACOUSTIC SENSING

Figure 2 shows the survey area with locations of shot points and surface projection of the two boreholes and of the main hypogene mineralized zone. The mine site has infrastructure including mills, offices, subsidence zones, and tailings ponds that restricted areas where seismic sources could be deployed. The open pit of the old Afton mine was avoided due to slope stability issues. In addition, the presence of the Trans-Canada Highway, two high-pressure gas pipelines, and numerous power lines, along with concerns raised to protect a vulnerable spadefoot toad species, were addressed during the planning of the survey. The survey included 50 shot locations located in 4 clusters, with most shot points located southwest of the open pit. At each source location, 1 kg of pentolite explosive with two electronic detonators was placed in a 20 m deep shot hole. Each shot hole was tamped with 90 kg of bentonite mixed with water and drilling sand.

We acquired VSP-DAS data in boreholes EA16-171 and EA17-197 (Fig. 2), starting in a drill bay located approximately 650 m below the surface. The two boreholes start from the same drill bay but have different dip and azimuth. Borehole EA17-197 has a length of 701 m and borehole EA16-171 is 870 m long. Both boreholes are uncased and intersect numerous faults that tend to cave in, which complicated the acquisition of the open-hole wireline logs and the deployment of the fibre-optic cables. Straight, standard, single-mode and straight Constellation™

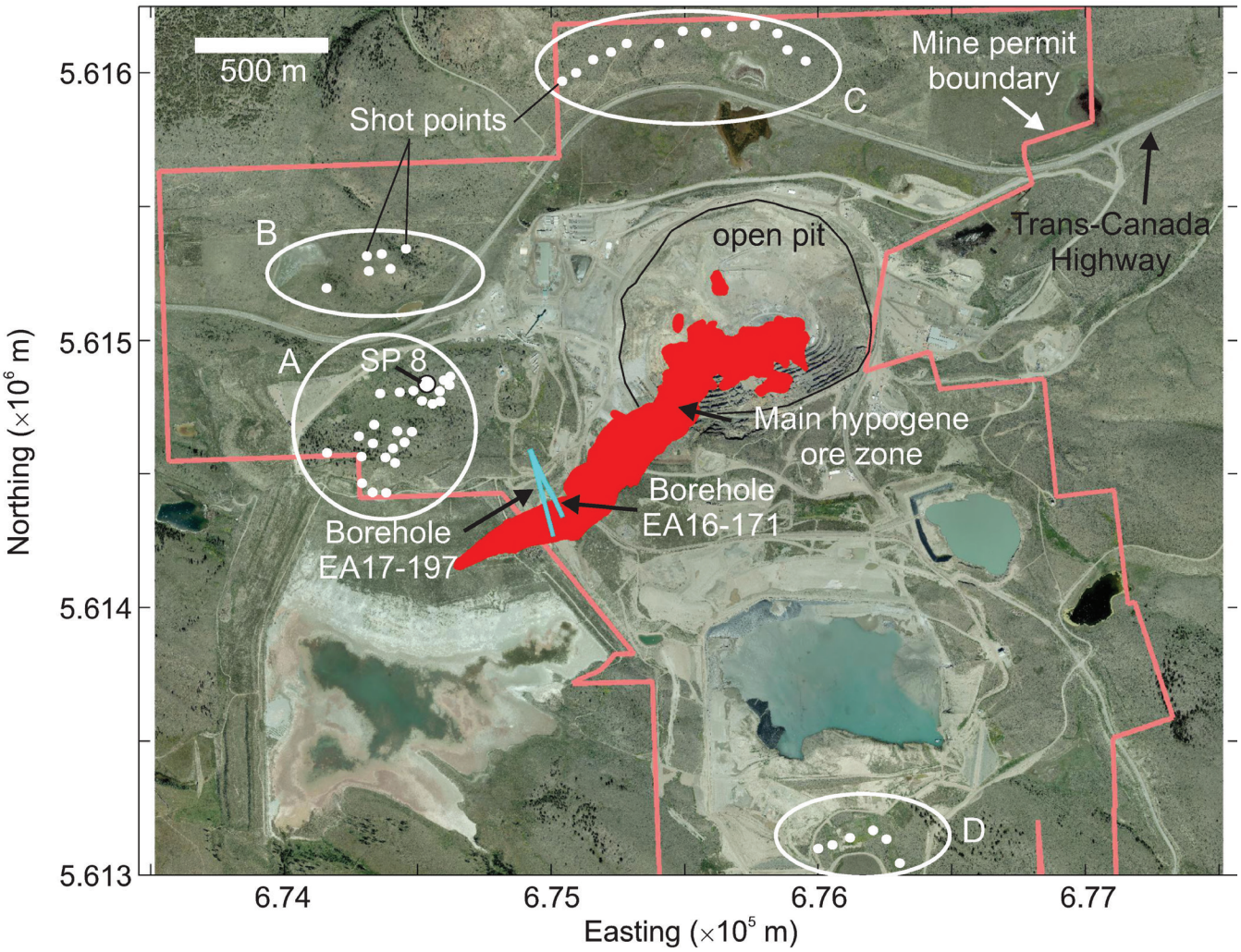

Figure 2. Surface locations of seismic shot points, surface projection of the two surveyed boreholes; and surface projection of the main hypogene mineralized zone. Seismic sources are located in four clusters labelled A, B, C, and D. Borehole EA17-197 and EA16-171 start from the same drill bay, located approximately 650 m below the surface. Borehole EA16-171 dips at approximately 70° and is 870 m long. Borehole EA17-197 dips at approximately 60° and is 701 m long.

single-mode (hereafter referred to as Constellation) fibre-optic cables were installed in the two boreholes. In addition, a helically wound single-mode fibre-optic cable containing both types of fibre was installed in borehole EA16-171. Standard fibre-optic cables placed in the two boreholes were 'daisy-chained' together to form an approximately 5 km long continuous fibre combining the straight and helically wound cables. The Constellation fibre-optic cables were also daisy-chained together. All fibre-optic cables were cemented in the boreholes to provide optimal coupling with rock formations.

Two DAS recording systems were used for the VSP survey: one for the standard fibre-optic cables (hereafter referred to as V2) and one for the Constellation fibre-optic cables (V3 — also known as the Carina® sensing system). The Constellation fibre-optic cables combined with the V3 recording unit provides seismic data with a higher signal-to-noise ratio, whereas the helically wound fibre-optic cable has enhanced transverse sensitivity relative to the straight cable, which is most sensitive to wavefields that exert longitudinal strain on the fibre. Seismic waves generated at each source location were recorded every 0.25 m along the standard fibre-optic cable and every 1 m along the Constellation fibre-optic cable using a sampling rate of 0.5 ms. Synchronization between surface shots and underground DAS recording units was done using GPS time. A high-precision clock synchronized at surface using GPS time was brought underground and used to keep the time of continuous seismic records. At surface, the GPS time stamp was saved at the firing time of each shot point and served as the basis to extract shot gathers from continuous DAS recordings.

Figure 3 shows the field data acquired for the straight fibre-optic cable in borehole EA17-197 at shot point 8 (*see* Fig. 2 for location). Figure 3a compares the field records for the V2 and V3 systems with the same gain display. Both V2 and V3 data show clear down-going waves and some weaker reflections. The signal-to-noise ratio is significantly higher for V3 data. Figure 3b shows the same data after the application of an f-k filter to remove down-going waves and first-break muting. Several reflections are observed on both V2 and V3 data. V3 data show more detail and clearer reflections, again due to a higher signal-to-noise ratio.

WIRELINE LOGGING AND PHYSICAL ROCK PROPERTIES

Wireline logs were acquired prior to the VSP survey from the same boreholes instrumented with fibre-optic cables (EA16-171 and EA17-197). Logging measurements included caliper, density, natural and gamma-ray spectrometry, magnetic susceptibility, resistivity, induced polarization, induction conductivity, and full-waveform sonic logs. Caliper, density, and sonic logs were used to support the interpretation of the DAS-VSP data. Additional physical rock property measurements were taken from core samples. In general, low density and velocity values exhibit a strong correlation with caved-in zones, indicated with large caliper values and corresponding to faults and/or fracture zones (*see* Bellefleur et al., 2020). The significant number of faults intersected in both boreholes further indicates that their response likely dominates the reflected seismic wavefield. Figure 4 shows violin plots of acoustic impedances (product of density and velocity) for the various lithological units and alteration types intersected in the boreholes. The feldspar-dominant potassic zones (Kk in Fig. 4) are characterized by higher acoustic impedances, suggesting that such alteration may be detectable on VSP data when juxtaposed against rocks with lower acoustic impedances.

RESULTS

Figure 5 shows an example of processed data from shot point 8 in borehole EA17-197. Lithological units, alteration, and some geophysical logs are also shown in this figure. Several reflections intersect the borehole and are indicated by arrows. Reflections A, B, and C in the upper part of the borehole coincide with faults determined from low-density values on logs. Low P-wave velocities and low acoustic impedance values are also observed for reflection A. Reflection D is located in an area with no anomalies reported on any of the logs. In addition, no lithological contacts or changes in alteration are observed at the location of this reflection. Thus, reflection D remains unexplained. Reflection E is located at a lithological contact (between Bxf and Bxff in Fig. 5), which is almost coincident with a change in alteration (between Kk and Kb in Fig. 5). Velocity logs do not show significant variations on either side of reflection E. A similar observation is made from the density log; however, the log does not extend significantly below reflection E (i.e. within the Bxff and Kb in Fig. 5). Thus, logging data appears to preclude both lithological and alteration contacts as plausible causes of reflection E. All logs have low values at the location of reflection E, suggesting that a fault explains this reflection. Reflection F does not intersect the fibre-optic cable but originates just below the deepest DAS channel in this borehole. A possible cause for this reflection is the contact between volcanic fragmental rocks with biotite-dominant potassic alteration and picrite. Alternatively, a fault mapped at that contact may also explain reflection F. Note that not all intervals with low density and low velocity values produced reflections (white arrows in Fig. 5). Some of those intervals may be related to caved-in zones that affected only the immediate vicinity of the borehole, or faults may exist at locations that are too thin to be detected with DAS-VSP data. Reflections that do not intersect the borehole are also observed in the DAS-VSP data (yellow arrows in Fig. 5).

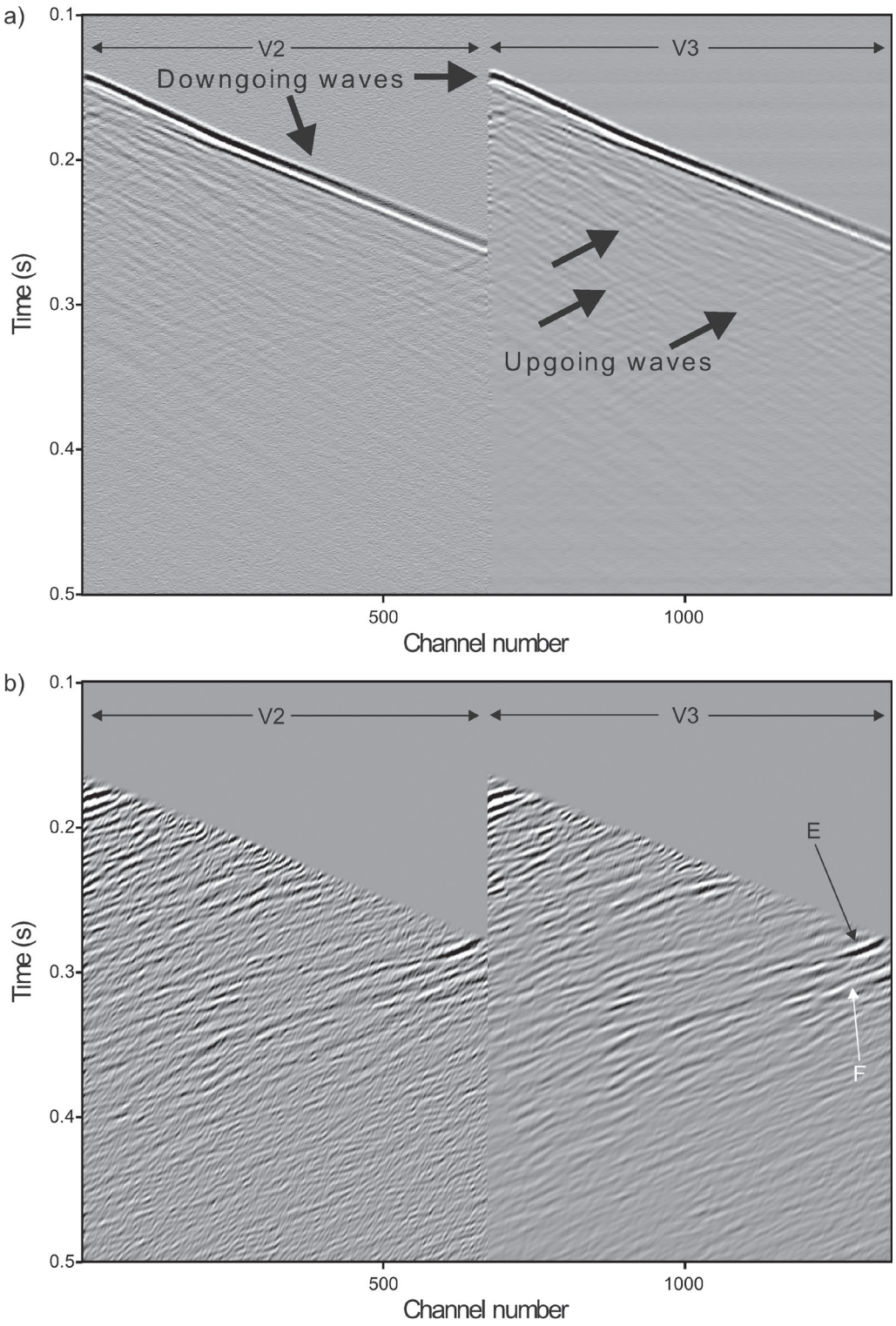

Figure 3. Comparison of standard DAS interrogator combined with a standard fibre-optic cable (V2) and the advanced DAS interrogator combined with the Constellation fibre-optic cable (V3) distributed acoustic sensing data sampled at 1 m intervals (one channel corresponds to 1 m) from EA17-197. The first channel is at 116 m above sea level, approximately 650 m below surface. **a)** Field data without any processing showing strong downgoing waves and some reflections. Both V2 and V3 data have the same gain for display. Signal-to-noise ratio is lower for the standard fibre-optic cable (V2) than for the Constellation fibre-optic cable (V3). **b)** Reflections and other upgoing signals after the application of an f-k filter and muting of first breaks. Arrows E and F point to reflections discussed in Figure 5.

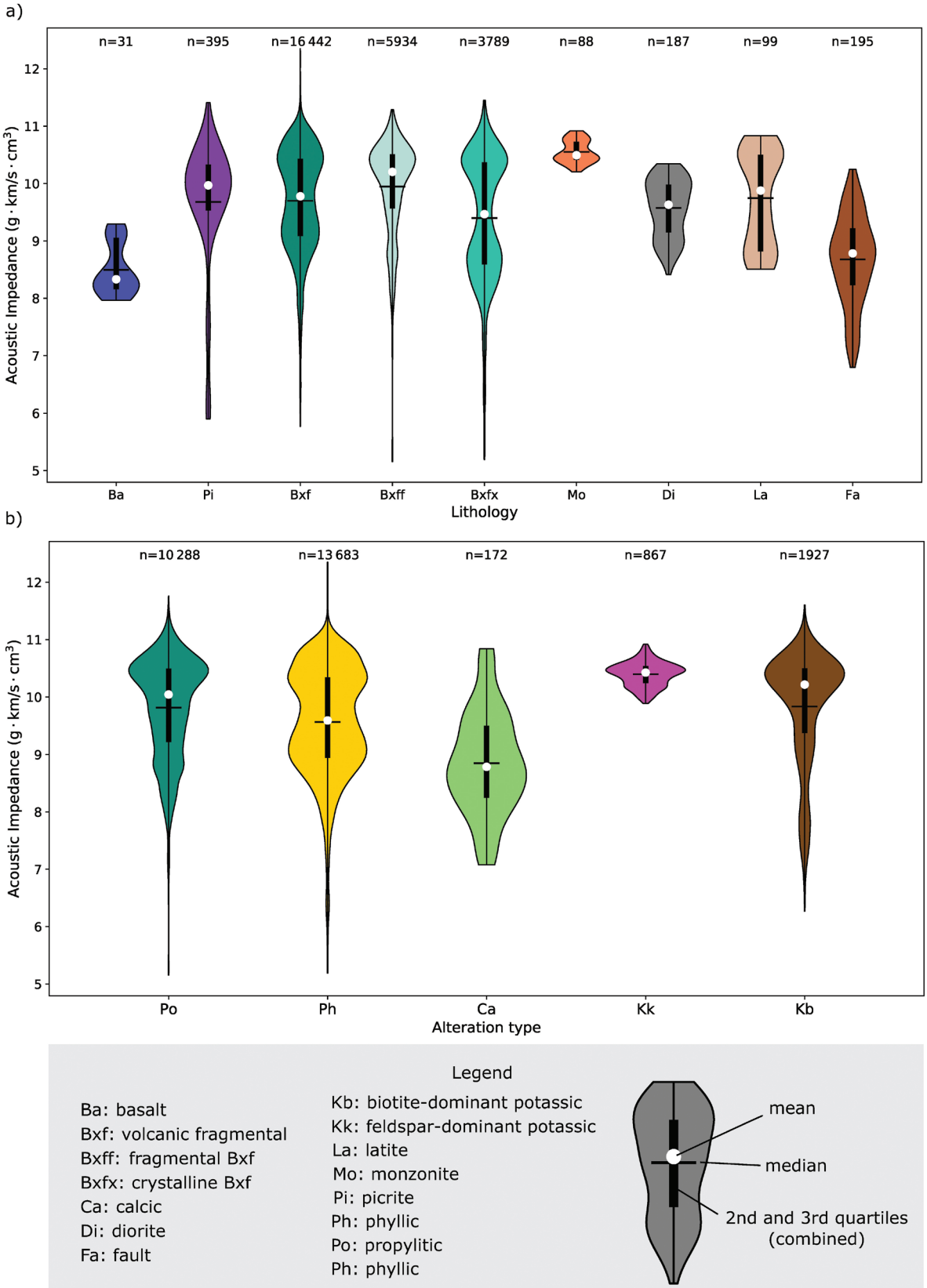

Figure 4. Distribution of acoustic impedance from logs for **a)** lithological units and **b)** alteration types at New Afton. Adjacent lithological units with sufficient acoustic impedance contrast will generate a detectable seismic reflection when juxtaposed.

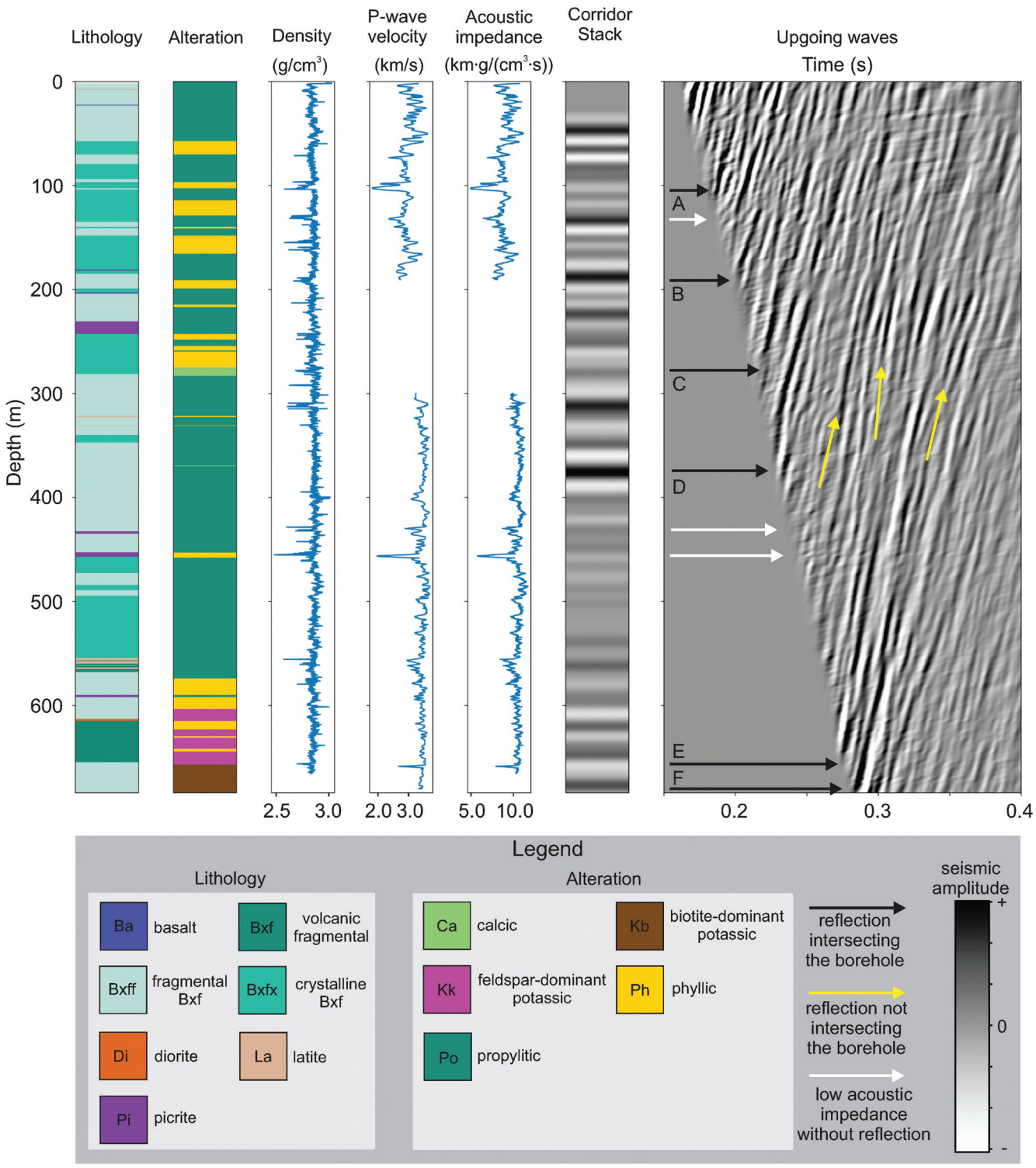

Figure 5. Lithology, alteration, density, P-wave velocity, acoustic impedance, seismic corridor stack (inside corridor stack), and upgoing waves (reflections) from the VSP data from borehole EA17-197. Arrows with labels (A–F) are discussed in the text.

ADVANTAGES OF DAS

Several logistical factors complicated the acquisition of borehole wireline logs and DAS-VSP data at New Afton. One important complication was the instability of the boreholes (i.e. faults and caved-in zones) that required the use of a drill rig for the wireline logging program and for the installation of the fibre-optic cables. Open-hole deployment of any instrument over the entire length of the two boreholes used in this work was simply not possible. The difficult borehole conditions increased the time required to complete the wireline logging program by a factor of three. A VSP survey with a string of conventional geophones would have been subject to the same time-consuming complications. To this end, the use of DAS greatly simplified the logistics and effort required to collect the VSP data. Installation of fibre-optic cables in the two boreholes took approximately 2.5 days, including cementing but excluding reaming of the boreholes. The use of fibre-optic cable also simplified survey logistics by requiring only one dynamite charge per shot location. This reduced the number of shots and the cost of the survey and simplified the permitting process to use explosives at surface on the mine site. By comparison, 12 shots per source location would have been required for a conventional slim-hole geophone system with 12 levels to obtain VSP data with a trace spacing of 5 m in the two boreholes. The difficult borehole conditions at New Afton would have also required the presence of a drill rig for the deployment of geophones during data acquisition. At New Afton, DAS was a cost-effective alternative to down-hole geophones, even when factoring in the cost of fibre-optic cables, which were permanently installed for this survey.

CONCLUSIONS

Wireline logs and DAS-VSP data were acquired from two boreholes intersecting the New Afton Cu-Au porphyry deposit located in south-central British Columbia. Wireline logs, and in particular caliper logs, revealed many faults and caved-in zones indicating generally poor rock conditions in the immediate vicinity of borehole wall. The significant number of faults and caved-in zones on logs suggests that their response may dominate the seismic wavefield. Logs also suggest that reflections between potassic alterations (i.e. between feldspar-dominant and biotite-dominant potassic alteration) and other types of alteration may be possible, depending on local geological context.

The use of DAS greatly simplified the logistics and effort required to collect VSP data at New Afton. This includes the use of only one dynamite charge per shot location to simultaneously collect V2 and V3 data in the two acquisition boreholes, which reduced the cost of survey and simplified the permitting process to use explosives for seismic surveying at the mine site. Comparison of raw field data and processed data of both DAS systems for straight fibre-optic cables demonstrated a significantly higher signal-to-noise ratio for V3 data. Reflections revealed by processingV3 data measured with straight fibre-optic cables show a strong correlation with fault and fracture zones intersected in the two boreholes. Although most of the imaged faults and fractures are significant for geotechnical characterization of the rock mass at the mine, their relationship with the ore zone, alteration, and ore genesis could not be unequivocally determined. Readers are invited to consult Bellefleur et al. (2020) for detailed information about the physical rock properties and VSP-DAS data acquired at the New Afton porphyry deposit.

ACKNOWLEDGMENTS

We thank Atlas Drilling, Clean Harbors, DGI Geoscience, Silixa, and Western Protection Alliance for their diligent work and patience in the planning and execution stages of this project. This work would not have been possible without the outstanding support from New Gold Inc. Sincere thanks to M. Della Libera, S. Davidson, and all New Afton employees who provided support in one form or another and made this project possible.

REFERENCES

Bellefleur, G., Schetselaar, E., Wade, D., White, D., Enkin, R., and Schmitt, D.R., 2020. Vertical seismic profiling using distributed acoustic sensing (DAS) with scatter-enhanced fibre-optic cable at the Cu-Au New Afton porphyry deposit, British Columbia, Canada; Geophysical Prospecting. v. 68, p. 313–333. https://doi.org/10.1111/1365-2478.12828

Hartog, A.H., 2018. An introduction to distributed optical fibre sensors; CRC Press, Boca Raton, 472 p.

Riedel, M., Cosma, C., Enescu, N., Koivisto, E., Komminaho, K., Vaittinen, K., Malinowski, M., 2018. Underground vertical seismic profiling with conventional and fiber-optic systems for exploration in the Kylylahti polymetallic mine, eastern Finland; Minerals, v. 8, no. 11, 538. https://doi.org/10.3390/min8110538

Three-dimensional analysis of magnetotelluric data from the New Afton porphyry deposit, central British Columbia

E. Roots[1, 2*], J.A. Craven[2], E. Schetselaar[2], R. Enkin[3], and D. Wade[4]

Roots, E., Craven, J.A., Schetselaar, E., Enkin, R., and Wade, D., 2021. Three-dimensional analysis of magnetotelluric data from the New Afton porphyry deposit, central British Columbia; in *Targeted Geoscience Initiative 5: contributions to the understanding and exploration of porphyry deposits, (ed.) A. Plouffe and E. Schetselaar; Geological Survey of Canada, Bulletin 616, p. 53–64. https://doi.org/10.4095/327952*

Abstract: Magnetotelluric data were collected along eight lines perpendicular to the mineralized zone and alteration halo of the New Afton Cu-Au porphyry deposit. The data were collected at an interstation spacing of 100 m and a line spacing of 300 m, and with a bandwidth of approximately 0.01 to 10 000 Hz. Phase tensor maps show an approximately east-west delineation of the survey into northern and southern sections. Determinant phase maps show conductivities initially increasing with depth in the north and decreasing in the south, with this trend reversing at depth. Preliminary results from 3-D inversions show conductive cover underlain by more resistive material throughout most of the survey area, with notably lower resistivities to the north. Two linear northeast-southwest features, spatially associated with the New Afton and Pothook mineralization, are imaged crosscutting the primary east-west fault zone, with high resistivities in the north and low resistivities in the south.

Résumé : Des données magnétotelluriques ont été recueillies le long de huit lignes perpendiculaires à la zone minéralisée et à l'auréole d'altération du gisement porphyrique à Cu-Au de New Afton. Les données ont été recueillies suivant un espacement entre les stations de 100 m et un espacement entre les lignes de 300 m, dans une largeur de bande d'environ 0,01 à 10 000 Hz. Les cartes des tenseurs de phase montrent une limite grossièrement est-ouest séparant l'aire du levé en une section nord et une section sud. Les cartes des phases du déterminant montrent d'abord une augmentation de la conductivité en fonction de la profondeur dans le nord, et une diminution dans le sud, avec une inversion de cette tendance en profondeur. Les résultats préliminaires des inversions 3D montrent une couche conductrice reposant sur des matériaux plus résistifs dans la plus grande partie de l'aire du levé, et des résistivités significativement plus faibles au nord. Des données d'imagerie montrent que deux entités linéaires d'orientation nord-est–sud-ouest, associées sur le plan spatial aux minéralisations de New Afton et de Pothook, recoupent la zone de failles principale est-ouest, avec de fortes résistivités au nord et de faibles résistivités au sud.

[1]Mineral Exploration Research Centre, Laurentian University, 935 Ramsey Lake Road, Sudbury, Ontario P3E 2C6
[2]Geological Survey of Canada, 601 Booth Street, Ottawa, Ontario K1A 0E8
[3]Geological Survey of Canada, 9860 West Saanich Road, Sidney, British Columbia V8L 4B2
[4]New Gold Inc., 4050 West Trans Canada Highway, Kamloops, British Columbia V1S 2A3
*Corresponding author: E. Roots (email: eroots@laurentian.ca)

INTRODUCTION

Electromagnetic methods have been widely used for mineral exploration due to their sensitivity and ability to resolve features associated with mineralization. As shallow targets have become increasingly scarce, the ability to image targets at depth as well as the deeper structures controlling mineralization has become increasingly important. The magnetotelluric (MT) method is an electromagnetic technique that can image at great depths compared to many controlled-source prospecting methods. As such, the use of the MT method as an exploration tool is becoming more popular in exploration for uranium (e.g. Heinson et al., 2006, 2018; Farquharson and Craven, 2009), diamonds (e.g. Jones et al., 2009; Türkoğlu et al., 2009), and base and precious metals (e.g. Zhang et al., 1995; Stevens and McNeice, 1998). The use of the MT method was previously restricted to 1-D and 2-D cases, limiting its applicability in complex geological environments; however, 3-D inversion of MT data is now becoming routine due to developments in inversion techniques and computational capabilities during the past few decades (Siripunvaraporn et al., 2005; Egbert and Kelbert, 2012; Miensopust et al., 2013; Newman, 2014).

Presented here are preliminary results of the 3-D inversion of MT data collected at the New Afton porphyry deposit in British Columbia, Canada, as part of the Geological Survey of Canada's Targeted Geoscience Initiative 5. The New Afton deposit is an alkaline Cu-Au porphyry deposit, with mineralization consisting primarily of disseminated sulfides. Because disseminated sulfides are generally resistive due to the lack of interconnectivity between grains, the resistivity contrast between sulfides and their host rock is unlikely to be detectable using the MT data. Because of this, as with previous studies in this area (e.g. Bellefleur et al., 2019), the focus of our investigation is on imaging alteration envelopes and structures controlling the emplacement of mineralization.

GEOLOGICAL SETTING

The New Afton Cu-Au porphyry deposit is hosted by Late Triassic Nicola Formation fragmental and crystalline volcanic rocks (referred to as the BXF hereafter) and, to a lesser extent, by the 204 Ma Cherry Creek monzonite of the Iron Mask batholith (J. Lipske and D. Wade, unpub. rept., 2014; Bergen et al., 2015). The Nicola Formation is unconformably overlain by clastic sedimentary and volcanic rocks of the Eocene Kamloops Group.

The primary hypogene ore zone of the New Afton deposit (Fig. 1) consists of disseminated chalcopyrite and bornite and has a subvertical southwest plunge that is largely coincident with potassic alteration. The hypogene ore zone is structurally controlled by two subvertical southwest-northeast-striking fault zones, known as the Footwall and Hanging Wall faults. The BXF is juxtaposed by the Hanging Wall fault against a subvertical body of a serpentinized picrite unit, whose margin is characterized by a high-strain zone of brittle-ductile deformation. Numerous moderately to steeply dipping fault zones controlling late hypogene mineralization cut the primary ore. Supergene mineralization, consisting of native copper and chalcocite within hematite-rich oxidation zones, is more abundant at higher structural levels near the open pit, but native copper also extends to 700 m below the surface, beneath the pit and along older, long-lived structures.

The Pothook Cu-Au mineralization, located 1 km southeast of the New Afton deposit (Fig. 1) is characterized by a network of supergene and chalcopyrite-bornite-bearing veins hosted in dominantly Pothook diorite and lesser Nicola Formation volcanic rocks adjacent to younger, causative intrusions (Stanley, 1994). The centre of the historical pit, seen in drill core, contained a large body of hydrothermal breccia consisting of Pothook diorite, Nicola BXF, Cherry Creek monzonite, and Sugarloaf diorite that graded outward from a rotational to crackle breccia. Distribution of mineralization coincides with both potassic alteration associated with Cherry Creek monzonite and with albite alteration associated with the emplacement of the younger Sugarloaf diorite. Dykes, alteration, and mineralization are structurally controlled. The west side of the orebody is bounded by a sharp northwest-southeast contact represented by the locally faulted rheological picrite–Pothook diorite–BXF contact. Within the deposit and surrounding host rocks, the causative Cherry Creek monzonite and Sugarloaf diorite dykes also have a dominant northwest-southeast strike. Mapped supergene and chalcopyrite-bornite-bearing veins tend to be less regular, however, and have a dominant east-west-striking trend (Stanley, 1994).

DRILL CORE RESISTIVITY AND POROSITY MEASUREMENTS

Physical properties were measured in the GSC Pacific Paleomagnetism and Petrophysical Laboratory, following the methods outlined in GSC Open File 7227 (Enkin et al., 2012). Cylindrical subsamples, 2.5 cm in diameter and 2.2 cm long, were taken from 254 approximately 10 cm long pieces of split diamond-drill core selected to span the rock types and alterations present in the New Afton deposit. Porosity was measured by combining measurements of the dry, water-saturated, and water-immersed weights. Electrical resistivities are dependent on the resistivity of the pore water in the samples, which is approximated by allowing deionized water to dissolve pore-space solutes for 24 hours prior to measurement. The water was introduced under vacuum, and the beakers were shaken for 2 minutes, still under vacuum, to help the water infiltrate fine permeability pathways within the samples. The samples were placed between copper–copper sulfate electrodes, and the complex electric impedance

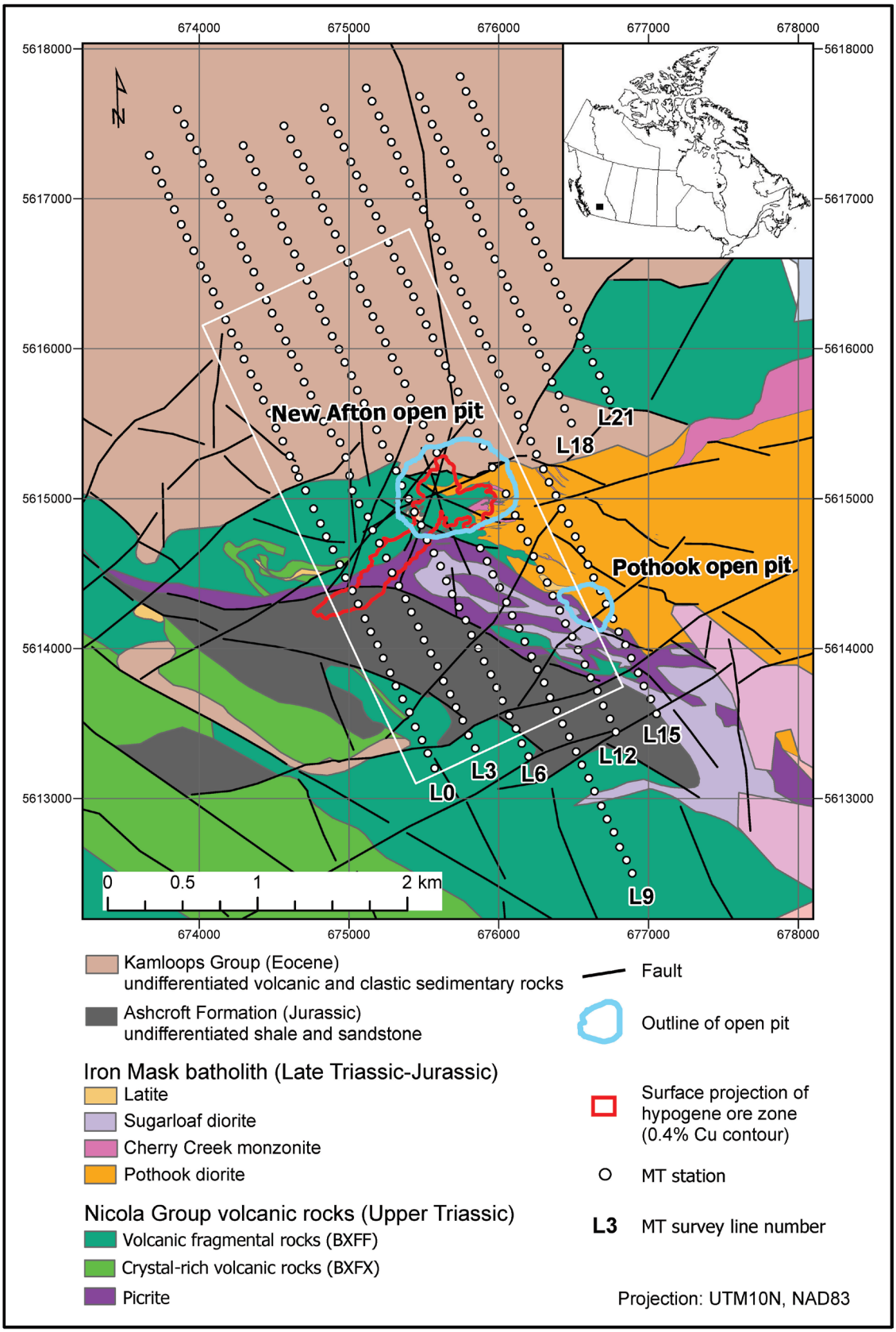

Figure 1. Map showing magnetotelluric (MT) stations and geology of the New Afton deposit. The white line indicates the subset of stations used in the presented focused inversion.

spectrum was measured using a Solartron 1260 impedance/gain-phase analyzer, at five frequencies per decade from 1 MHz down to 0.025 Hz. The resistivity at 0.1 Hz was measured after curve fitting and removing the very low frequency sample holder impedance. The resistivity is nearly inversely proportional to the porosity (Fig. 2). Excluding outliers, the best-fitting exponent is –1.2, with the implication that porosity is the major control on the resistivity in this data set.

MAGNETOTELLURIC DATA SET

Fieldwork was performed by Quantec Geoscience Ltd. in 2008 and 2009, with 332 audio-magnetotelluric (AMT) stations sampled (E. Gowan, T. Eadie, and R. Sharpe, unpub. rept., 2008). The stations were distributed across eight northwest-southeast-oriented lines, with a nominal interline spacing of 300 m and interstation spacing of 100 m (Fig. 1). Horizontal electric and magnetic fields were recorded and processed, resulting in MT impedance tensor measurements at frequencies between approximately 0.01 and 10 000 Hz. The data are generally of good quality between approximately 0.1 and 10 000 Hz with some degradation at lower frequencies. Mine infrastructure had an effect on the data quality in some locations; stations under major power lines or pipelines and near the highway have considerably higher errors at frequencies above 10 Hz, and those in areas with variable topography have slightly higher errors at frequencies below 0.5 Hz (E. Gowan, T. Eadie, and R. Sharpe, unpub. rept., 2008).

Analysis of the MT data was carried out using the phase tensor method (Caldwell et al., 2004). The phase tensor, Φ, is a 2 × 2 tensor that can be derived at each period of the MT impedance tensor and has the property of being independent of local site-dependent distortions created by small-scale (i.e. beneath the resolving power of the MT method) variations in near-surface geology. The phase tensor and its derived parameters can be visualized as ellipses (e.g. Fig. 3), which can be used to determine undistorted first-order characteristics of the MT data and therefore the geo-electric structure of the survey area. In 1-D environments, Φ is diagonal with equal components, and the corresponding ellipse reduces to a circle. In 2-D, Φ is symmetric, and can be made diagonal by multiplying it with a rotation matrix, where angle α represents the geo-electric strike direction with a 90° ambiguity. In the 3-D case, Φ is rotated again by a skew

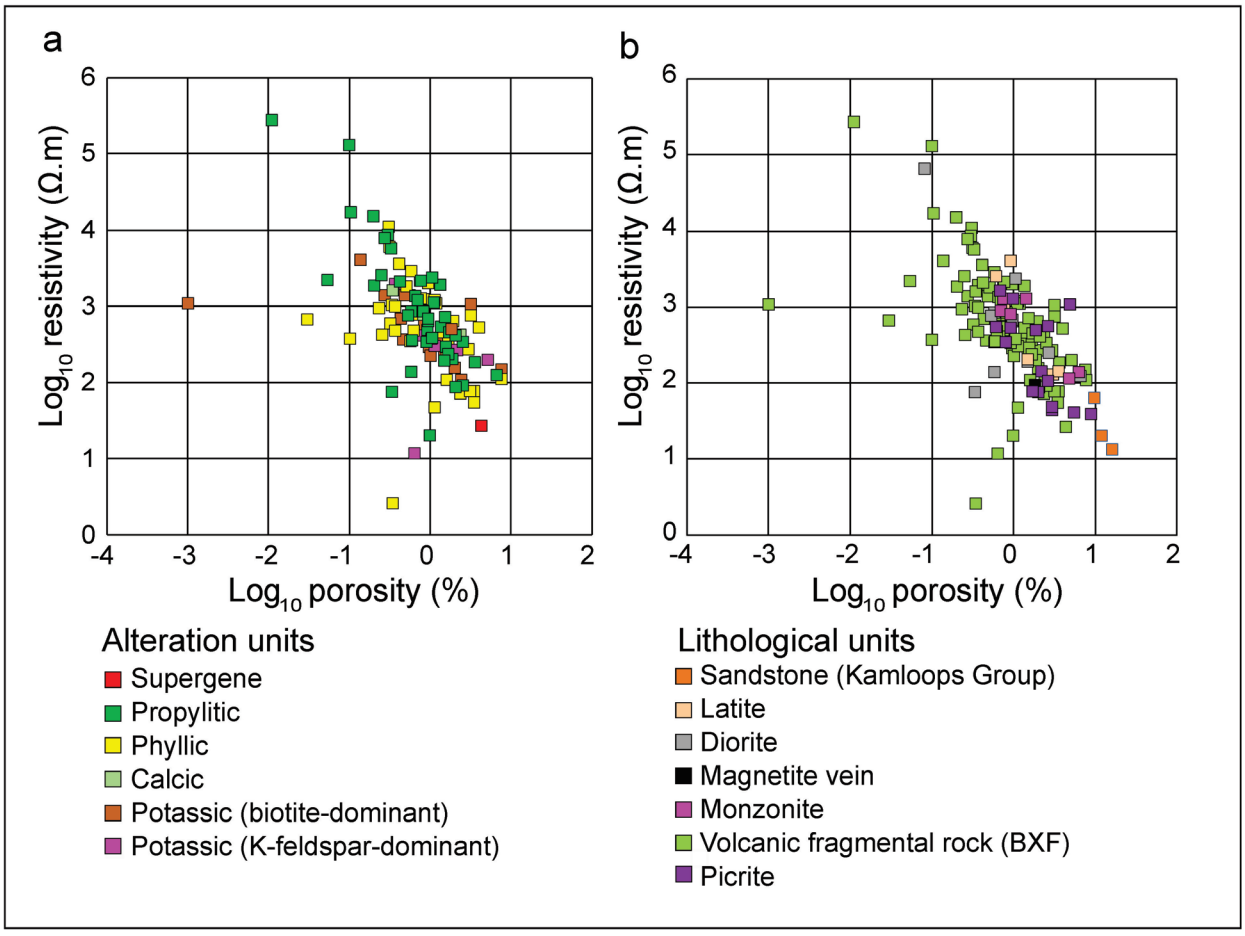

Figure 2. Resistivity-porosity scatterplots (log-scale) grouped according to **a)** lithological units and **b)** alteration units.

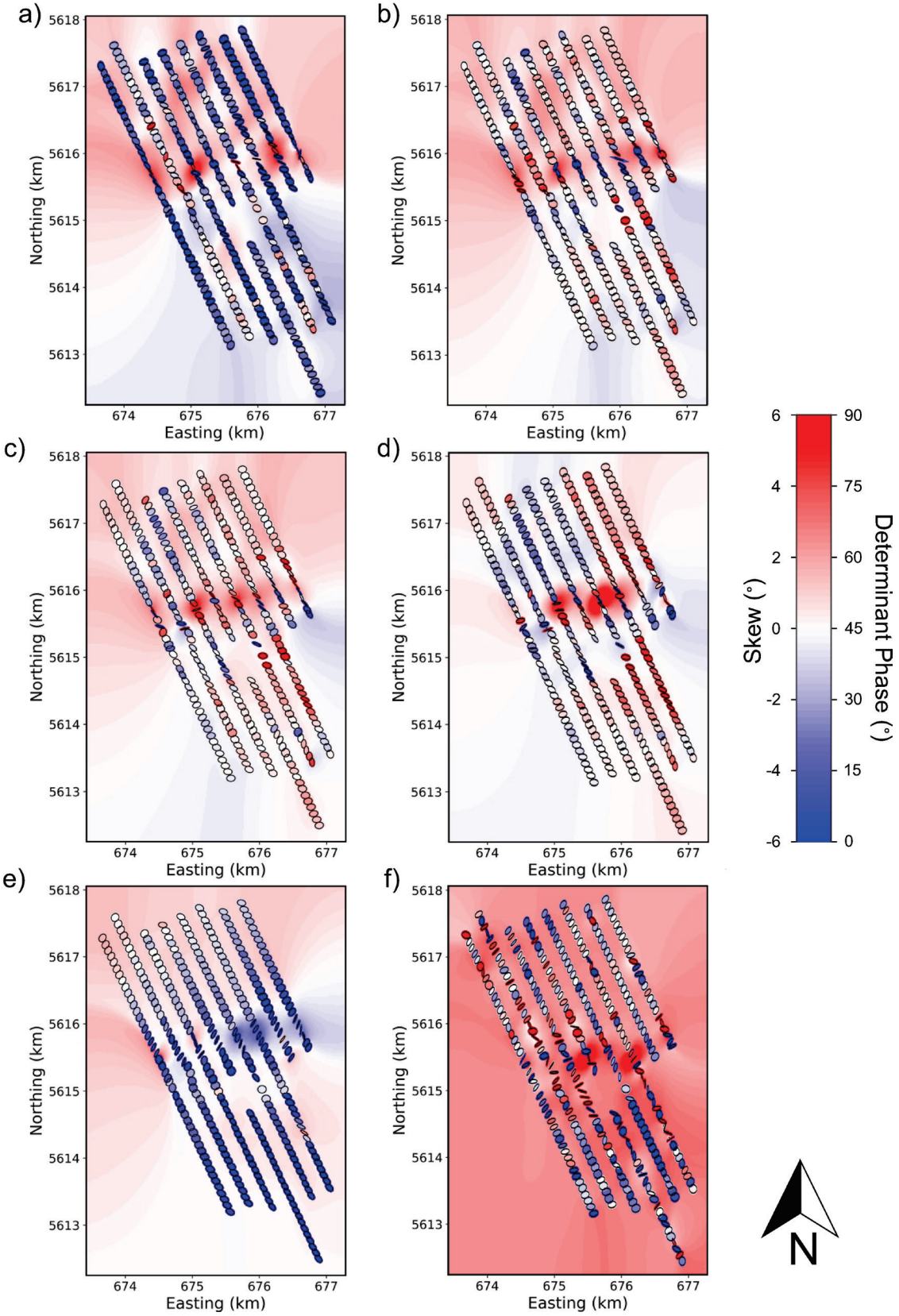

Figure 3. Plan view phase tensor maps of the magnetotelluric (MT) stations at various frequencies: **a)** 1500 Hz, **b)** 469 Hz, **c)** 143 Hz, **d)** 49.2 Hz, **e)** 2.46 Hz, and **f)** 0.111 Hz; background is coloured according to determinant phase; phase tensor ellipses are coloured by skew angle.

angle, β, representing a rotation of the phase tensor from an equivalent symmetric (i.e. 2-D) tensor. As such, analysis of the skew and azimuth values across a survey can be used to justify a 2-D or 3-D approach. Generally, for a 2-D approach to be valid, the strike directions must be consistent as a function of both space and frequency, and the skew values should be low (|β|<3; Caldwell et al., 2004; Booker, 2014). Furthermore, the determinant of the phase tensor, det|Φ|, with increasing period provides an estimate of increasing (det|Φ| increasing) or decreasing (det|Φ| decreasing) conductivity with increasing depth.

Determinant phase and skew angles across the survey area are shown in Figure 3. Between 1400 and 142.9 Hz, the area is separated into northern and southern sections by a sharp transition in phase, with generally high values (>60°) in the north and lower values (<45°) to the south. The relatively high phase in the north is consistent with the Kamloops sediments, which are generally porous and variably water saturated. At 49.2 Hz, the phase in the north drops to below 45°, possibly representing the base of the Kamloops Formation. At shorter frequencies (or equivalently, at greater depths), phases increase across most of the survey area to >45°, and exceed 70° at frequencies lower than 1 Hz, suggesting an underlying unit with relatively high conductivity. The phase tensor skew values are also frequency dependent, with generally low values (|β|<3) at frequencies between approximately 10 and 1000 Hz, and higher values outside of this range. Despite the relatively low skew values, the orientation of the phase tensor ellipses is highly variable. From north to south, the ellipses rotate clockwise until reaching a northing of approximately 5615 km, and then rotate back counterclockwise. A similar clockwise rotation goes from west to east, for example, at 2.4 Hz. These inconsistent azimuths combined with high skew values at the shorter frequencies suggest significant 3-D structure, necessitating the use of 3-D inversion for this data set.

THREE-DIMENSIONAL INVERSION

The 3-D inversion software ModEM (Kelbert et al., 2014) was used to produce 3-D resistivity models of the survey area. ModEM uses the standard Occam approach (Constable et al., 1987; de Groot-Hedlin and Constable, 1990), inverting the data to produce a model that minimizes the RMS misfit between the data and model response, as well as the gradient of the model conductivity. This produces spatially smooth models. Due to the large computational requirements of 3-D inversions, not all data could be inverted simultaneously; therefore, models were calculated at two scales: a regional scale that included every third station from all eight lines, and a focused scale using every station from a select area surrounding the ore zone (inside the solid white line in Fig. 1).

More than thirty inversions were performed to ensure the robustness of the produced models to changes in input parameters (e.g. mesh, rotation angle, starting model, inverted data points). In general, models at both scales agree where they overlap. Furthermore, the additional anomalies seen in the regional models tend to lie at the outer edge of the survey area and are not well constrained, so a preferred focused-scale model is presented in this paper. This inversion used a starting model with a half-space resistivity of 100 Ω-m and a mesh with 200 × 89 × 57 cells in the east-west, north-south, and vertical directions, respectively. A 165 × 50 cell inner mesh (Fig. 4) with 30 × 40 m cells was used directly around the stations, with exterior padding cell sizes increasing by a factor of 1.2. Although a uniform mesh is desirable, slightly elongated cells were required to stay within the limits of the available computational resources. To further optimize the mesh, the data were rotated by –25°, and a 25° rotation was applied to the station locations (or equivalently, a –25° rotation of the mesh) to ensure the inversion and measurement axes were aligned. The full impedance tensor was inverted using 19 logarithmically spaced frequencies between approximately 0.1 and 2400 Hz. Error floors were set to 5 and 10% for the off-diagonal and diagonal impedance components, respectively, with increased errors assigned to outliers. The inversion converged to an overall RMS of 1.7. Most stations have misfits of 1 to 2, but stations near the power lines north of the open pit have significantly reduced data quality and, therefore, have higher misfits of 3 to 6 (Fig. 4).

Plan view slices through the model are shown in Figure 5. Given the lateral cell sizes used, it is likely that the resistivity distributions at depths between 0 and 200 m are largely noise introduced by the inversions to accommodate static shifts and other local site distortion in the data. The trends seen in the phase tensor maps (Fig. 3) become evident in the model at depths of approximately 205 m, with the northern end of the survey having resistivities between approximately 1 and 30 Ω-m, whereas those in the south are between 100 and 1000 Ω-m with the exception of a few isolated regions, largely within the southeast corner. A linear resistive feature (R1) is seen between depths of 205 and 562 m with resistivities of approximately 300 to 500 Ω-m, trending parallel to southwest-northeast-trending secondary faults within the BXF unit. Toward the southeast, a smaller conductive zone (C1) runs parallel to the resistor. This conductor is partly associated with hypogene ore and the supergene alteration zone of the New Afton deposit. The larger R1 resistor cuts across most of the inverted stations, terminating just before the easternmost line (L12). At depth, R1 spreads into a broader region of high resistivity, at least partially as a result of the reduced resolving power of the MT method at depth. Approximately 2 km to the southeast, a second linear resistor-conductor pair (R2/C2) can be seen on the 316 and 562 m depth slices (Fig. 5b, c). The C2 conductor is also spatially associated with porphyry mineralization known as the Pothook deposit (Stanley, 1994), suggesting that economic mineralization in the surveyed area is structurally controlled in a consistent orientation. Another feature,

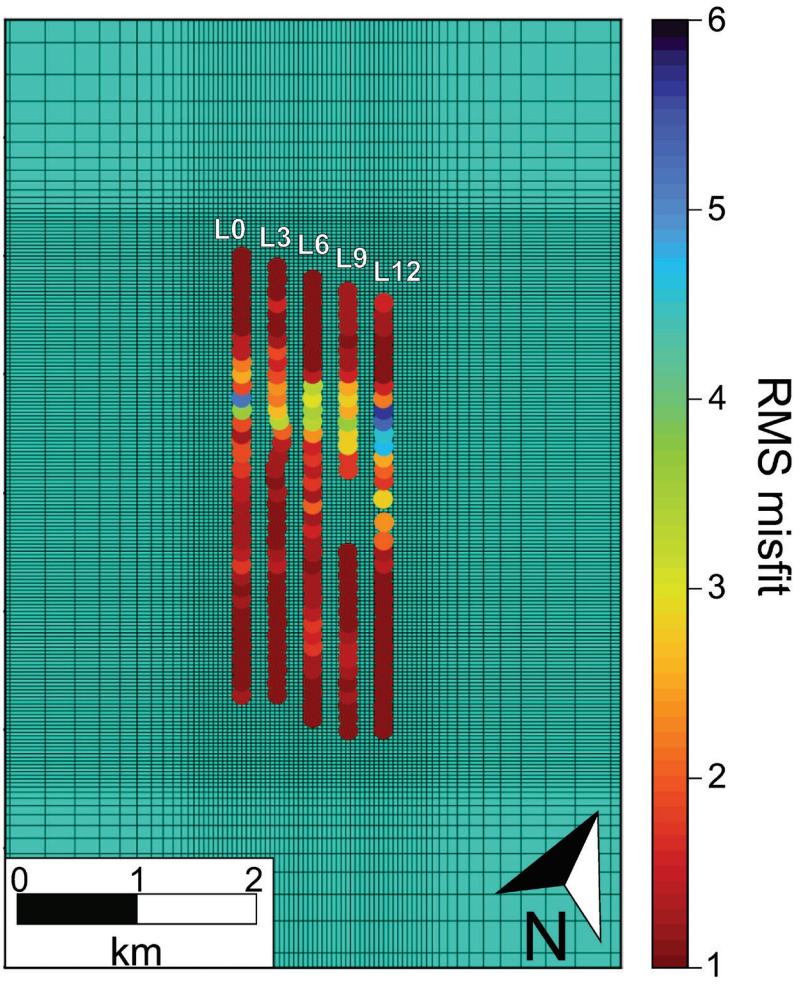

Figure 4. Interior mesh used in inversion and station layout (circles). Stations are coloured according to their respective RMS misfits from the preferred focused model.

C3, with resistivities between 1 and 10 Ω-m and oriented approximately east-west, is seen at similar depths and just to the north of R1. As with R1, C3 becomes more diffuse at depths below 500 m.

The geometry and extent of R1/C1 can be seen in depth slices through the model (Fig. 6), with R1/C1 moving progressively further north in each slice. It seems that R1 has a greater depth extent in comparison to C1, whereas C2 seems to have a greater depth extent in comparison to its resistive counterpart, R2 (Fig. 6). A west-southwest-east-northeast-striking conductor, C3, is visible to depths of approximately 500 m in the slices corresponding to L6, L9, and L12. The shallow depth and discordant strike direction suggest that C3 is associated with volcanic and sedimentary rocks of the Eocene Kamloops Group, unconformably overlying the volcanic rocks (mainly volcanic fragmentals of the Nicola Group) that host the porphyry deposits. Stratigraphically equivalent volcanic and sedimentary rocks elsewhere in Quesnellia have a similar conductive response (Spratt and Craven, 2011). A perspective view of the 3-D MT inversion model shows that the hypogene ore zone of the New Afton deposit is not associated with a conductive feature (Fig. 7).

DISCUSSION

The spatial association between the resistor-conductor pairs (C1/R1 and C2/R2) and their consistent southwest-northeast strike, parallel to fault zones established by drilling, strongly suggests that the mineralization is structurally controlled. Nevertheless, the geological significance of these features remains ambiguous, even for C1/R1, where information on the lithology, alteration, and ore mineral assemblages are available from the dense drillhole distribution of the New Afton mine workings. The discordant orientation in strike of C1/R1 and C2/R2 with respect to the dominant east-west strike of the lithological units and the lack of distinct lithology and alteration clusters in the log resistivity–porosity scatterplots (Fig. 2) indicate that variations in host rock mineralogical composition and associated primary porosity are most likely not the dominant factors controlling the resistivity contrasts between these features. Also, the hypogene ore zone with disseminated sulfide mineralization cannot explain C1 because only the extreme northern part of the ore zone coincides with the conductive zone. The largest part of the hypogene ore zone, toward the south, actually corresponds to resistor R1 (Fig. 7) and appears to be more

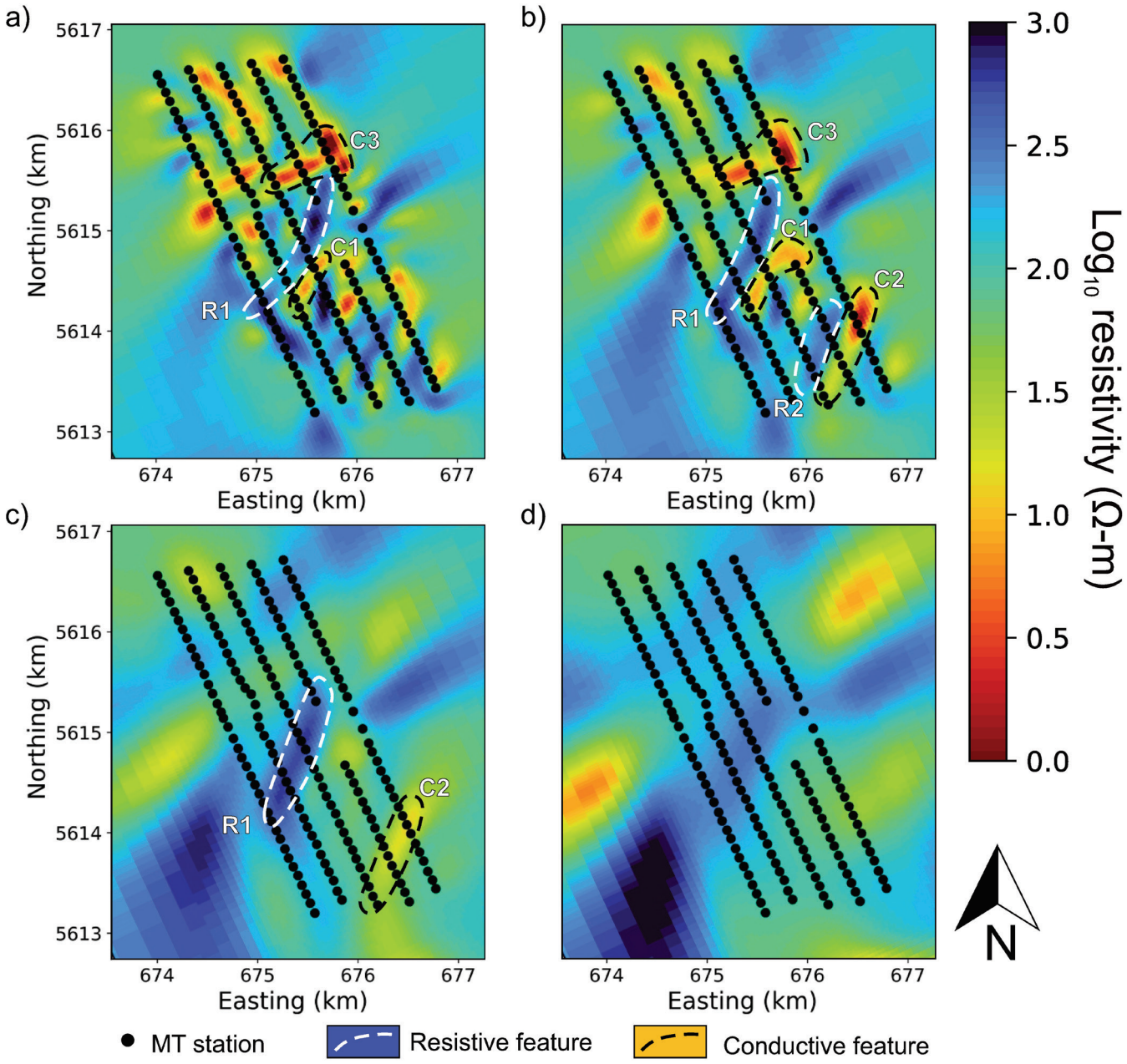

Figure 5. Plan view sections through the preferred model at various depths showing anomalous regions discussed in the text: **a)** 205 m, **b)** 316 m, **c)** 562 m, and **d)** 1000 m. The model and stations have been rotated back to geographic coordinates.

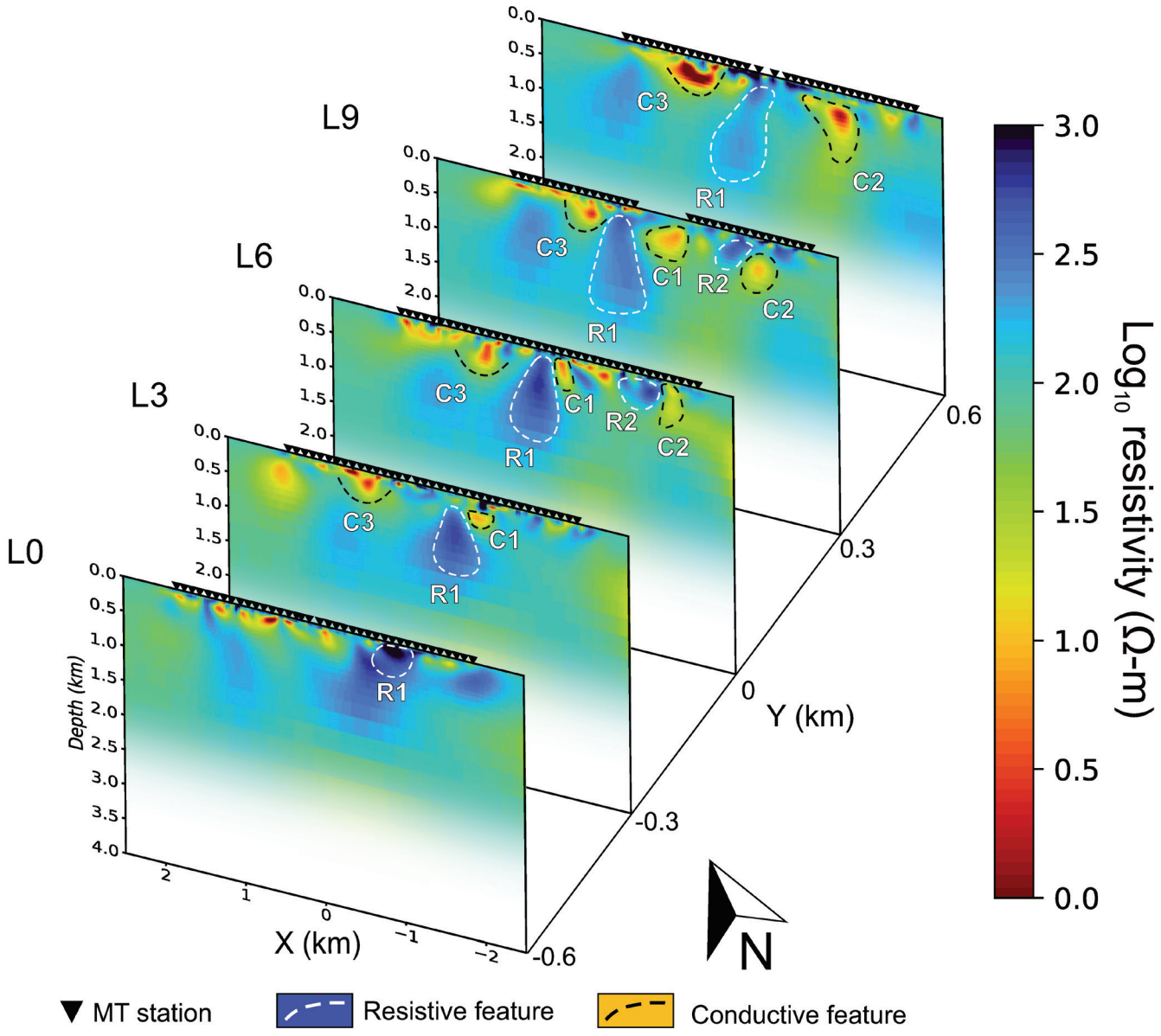

Figure 6. Depth slices through the focused model, coincident with the magnetotelluric (MT) lines, showing features discussed in the text.

resistive compared to the picrite unit; consequently, given the lack of evident relationships with primary lithological composition, hypogene mineralization, and alteration, we prefer an interpretation where secondary porosity, genetically associated with displacement along the previously mentioned southwest-northeast-trending fault zones, was favourable for generating resistivity contrasts. In addition, hydrothermal brecciation in combination with the fracture-controlled sulfide mineralization of the Pothook mineralization (in contrast to the disseminated sulfide mineralization of the New Afton) could provide an explanation for the more prominent conductor C2.

Patterns of alternating high- and low-resistivity linear features (e.g. C1/R1, C2/R2) have been identified as an artefact of isotropic inversions attempting to fit anisotropic data (e.g. Wannamaker, 2005; Miensopust and Jones, 2011). Although the possibility of anisotropy is impossible to fully dismiss without vertical magnetic field data, the phase of the data is generally well behaved at the relevant stations (e.g. smoothly varying and between 0–90°).

Contrary to the samples of the host rocks of the mineralization, the three samples of sandstone of the Kamloops Group in Figure 2a lend some support to interpreting the low resistivity of C3 as being due to primary porosity. The three samples plot on the low-resistivity high extreme of the

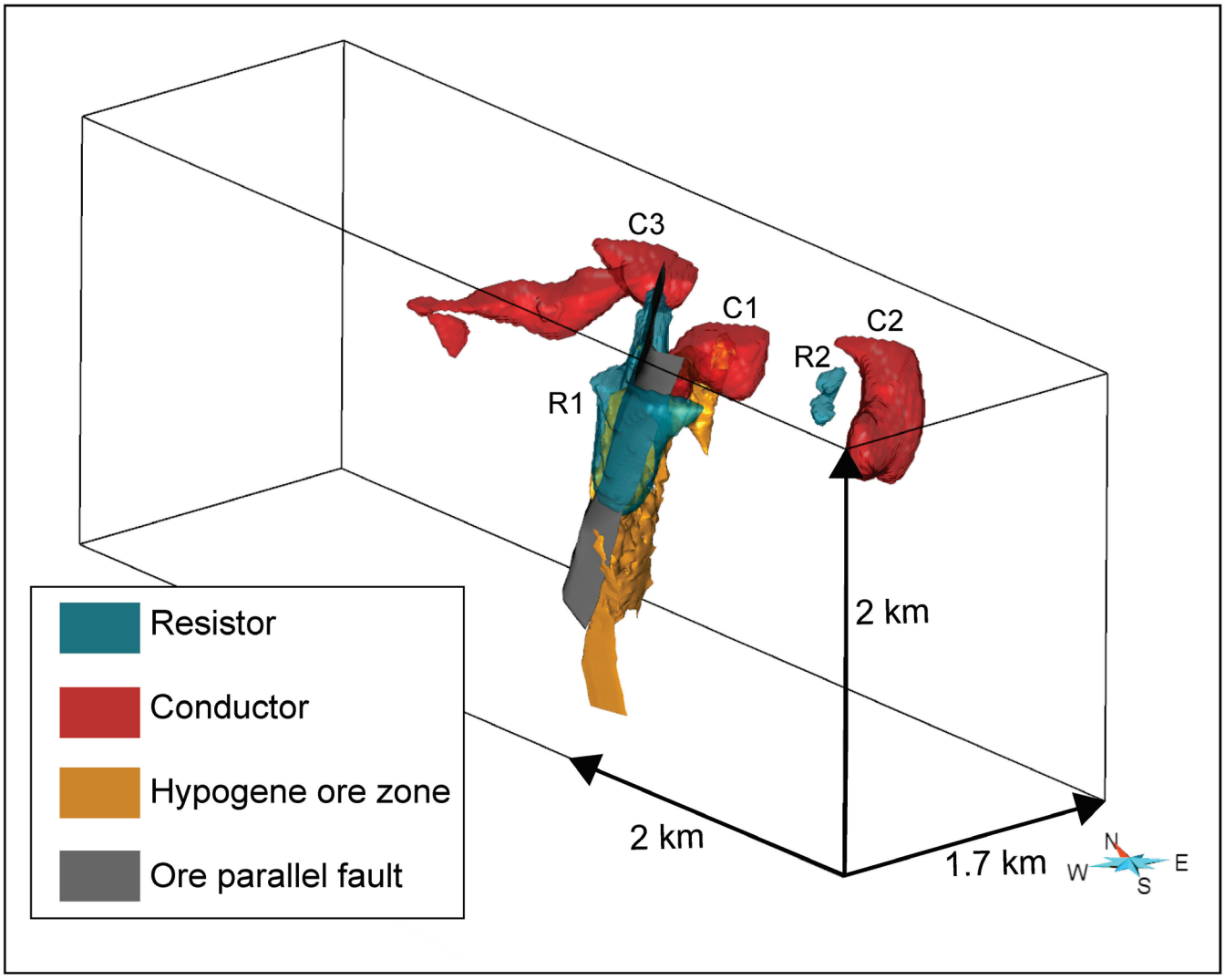

Figure 7. A 3-D view of resistive and conductive features in relation to models of the hypogene ore and northwest-southeast-striking fault zone discussed in the text. Resistive features were defined using a Log10 resistivity threshold of >2.5 (316 Ω-m). Conductive features were defined using a Log10 resistivity threshold of <1.5 (32 Ω-m).

scatterplot with more than 10% porosity. A notable increase in resistivity is seen at approximately 562 m deep, which may mark the base of the sediments. This interpretation is consistent with interpretation of 2-D MT inversions acquired in the Nechako Basin, where stratigraphically equivalent, shallowly dipping Eocene volcanic and sedimentary rocks are prominently marked by low resistivity in contrast with the underlying basement (Spratt and Craven, 2011). It is, however, worth noting that the location of C3 is coincident with power lines north of the open pit (and therefore with the stations with high noise and misfit), so the possibility that C3 is related to cultural noise rather than to geology cannot be ruled out. A feature test on C3 was carried out, whereby the conductive region was replaced with the original background resistivity (100 Ω-m). The resulting model response has an RMS misfit of 2.55, representing a 50% increase from the original inversion result. This suggests that, although the exact geometries and resistivity values are not resolvable due to the high degree of noise in the area, the data do require a conductive body in the vicinity of C3.

CONCLUSIONS

A high-density AMT survey was conducted over the New Afton Cu-Au porphyry deposit, British Columbia, Canada. Analysis of the MT data revealed generally low resistivities and 2-D geo-electric characteristics within a frequency band of 10 to 1000 Hz. At frequencies lower than 10 Hz, and therefore at greater depths, 3-D effects are evident. To image the structural controls on mineralization below the conductive cover, 3-D inversions were performed. Focused inversions in the area around the mineralized zone revealed low resistivities to the north, possibly related to a porous and

interconnected network of fluid within the Kamloops Group sedimentary rocks. Two high- and low-resistivity anomalies that are roughly coincident with the known economic mineralization in the area were imaged with a dominant southwest-northeast strike. Because the primary orientation of the lithological units is east-west and drill core resistivity is independent from the sampled lithological units, we determined that these anomalies are likely related to variations in secondary porosity genetically associated with the southwest-northeast-trending fault zones. In contrast to the poor association between the low resistivity feature at New Afton and its hypogene ore zone, the more prominent low resistivity feature at the Pothook deposit does coincide with its hypogene sulfide mineralization. This is explained by differences in the style of mineralization between the two deposits. The hypogene ore zone at New Afton consists of disseminated mineralization, whereas the Pothook mineralization is controlled by hydrothermal brecciation and tectonic fracturing, which both enhanced secondary porosity and the connectivity of sulfide mineralization in the volcanic and intrusive host rocks.

Due to the high density of MT stations and generally low resistivities of the survey area, it was not possible to model the entire data set with the available computational resources. In the future, a 3-D inversion of the entire data set may become feasible, which would allow high-resolution imaging of the New Afton deposit at greater depths and might provide additional control on its extent and geometry. It was determined that anisotropy is not likely to have had an impact on the isotropic inversion results, but it is also possible to investigate this further by performing 2-D anisotropic inversions. Future forward modelling and/or inversion studies would also benefit from inclusion of constraints derived from other geological or geophysical data sets.

ACKNOWLEDGMENTS

We gratefully acknowledge the support of New Gold Ltd., who provided access to their drillhole and MT data (collected by Quantec Geoscience Ltd.) and shared their expertise on the New Afton Cu-Au deposit. This manuscript benefited from reviews by Ademola Adetunji and Seyed Masoud Ansari.

REFERENCES

Bellefleur, G., Schetselaar, E., Wade, D., White, D., Enkin, R., and Schmitt, D. R., 2019. Vertical seismic profiling using distributed acoustic sensing with scatter-enhanced fibre-optic cable at the Cu–Au New Afton porphyry deposit, British Columbia, Canada; Geophysical Prospecting, v. 68, no. 1, p. 1–21. https://doi.org/10.1111/1365-2478.12828

Bergen, D., Krutzelmann, H., and Rennie, D.W., 2015. Technical report on the New Afton mine, British Columbia, Canada, NI 43-101 report; Roscoe Postle Associates Inc., Project #2400.

Booker, J.R., 2014. The magnetotelluric phase tensor: a critical review; Surveys in Geophysics, v. 35, no. 1, p. 7–40. https://doi.org/10.1007/s10712-013-9234-2

Caldwell, T.G., Bibby, H.M., and Brown, C., 2004. The magnetotelluric phase tensor; Geophysical Journal International, v. 158, no. 2, p. 457–469. https://doi.org/10.1111/j.1365-246X.2004.02281.x

Constable, S.C., Parker, R.L., and Constable, C.G., 1987. Occam's inversion: a practical algorithm for generating smooth models from electromagnetic sounding data; Geophysics, v. 52, no. 3, p. 289–300. https://doi.org/10.1190/1.1442303

de Groot-Hedlin, C. and Constable, S., 1990. Occam's inversion to generate smooth, two-dimensional models from magnetotelluric data; Geophysics, v. 55, no. 12, p. 1613–1624. https://doi.org/10.1190/1.1442813

Egbert, G.D. and Kelbert, A., 2012. Computational recipes for electromagnetic inverse problems; Geophysical Journal International, v. 189, no. 1, p. 51–267. https://doi.org/10.1111/j.1365-246X.2011.05347.x

Enkin, R.J., Cowan, D., Tigner J., Severide, A., Gilmour, D., Tkachyk, A., Kilduff, M., Vidal, B. and Baker, J., 2012. Physical property measurements at the GSC Paleomagnetism and Petrophysics Laboratory, including electric impedance spectrum methodology and analysis; Geological Survey of Canada, Open File 7227, 42 p. https://doi.org/10.4095/291564

Farquharson, C.G. and Craven, J.A., 2009. Three-dimensional inversion of magnetotelluric data for mineral exploration: An example from the McArthur River uranium deposit, Saskatchewan, Canada; Journal of Applied Geophysics, v. 68, no. 4, p. 450–458. https://doi.org/10.1016/j.jappgeo.2008.02.002

Heinson, G., Didana, Y., Soeffky, P., Thiel, S., and Wise, T., 2018. The crustal geophysical signature of a world-class magmatic mineral system; Scientific Reports, v. 8, 10608, p. 1–6. https://doi.org/10.1038/s41598-018-29016-2

Heinson, G.S., Direen, N.G., and Gill, R.M., 2006. Magnetotelluric evidence for a deep-crustal mineralizing system beneath the Olympic Dam iron oxide copper-gold deposit, southern Australia; Geology, v. 34, no. 7, p. 573–576. https://doi.org/10.1130/G22222.1

Jones, A.G., Evans, R.L., Muller, M.R., Hamilton, M.P., Miensopust, M.P., Garcia, X., Cole, P., Ngwisanyi, T., Hutchins, D., Fourie, C.J.S., Jelsma, H., Evans, S., Aravanis, T., Pettit, W., Webb, S., Wasborg, J., and The SAMTEX Team, 2009. Area selection for diamonds using magnetotellurics: examples from southern Africa; Lithos, Proceedings of the 9th International Kimberlite Conference, v. 112, suppl 1, p. 83–92. https://doi.org/10.1016/j.lithos.2009.06.011

Kelbert, A., Meqbel, N., Egbert, G.D., and Tandon, K., 2014. ModEM: a modular system for inversion of electromagnetic geophysical data; Computers and Geosciences, v. 66, p. 40–53. https://doi.org/10.1016/j.cageo.2014.01.010

Miensopust, M.P. and Jones, A.G., 2011. Artefacts of isotropic inversion applied to magnetotelluric data from an anisotropic Earth; Geophysical Journal International, v. 187, no. 2, p. 677–689. https://doi.org/10.1111/j.1365-246X.2011.05157.x

Miensopust, M.P., Queralt, P., Jones, A.G., and the 3D MT modellers, 2013. Magnetotelluric 3-D inversion—a review of two successful workshops on forward and inversion code testing and comparison; Geophysical Journal International, v. 193, no. 3, p. 1216–1238. https://doi.org/10.1093/gji/ggt066

Newman, G.A., 2014. A review of high-performance computational strategies for modeling and imaging of electromagnetic induction data; Surveys in Geophysics, v. 35, no. 1, p. 85–100. https://doi.org/10.1007/s10712-013-9260-0

Siripunvaraporn, W., Egbert, G., Lenbury, Y., and Uyeshima, M., 2005. Three-dimensional magnetotelluric inversion: data-space method; Physics of the Earth and Planetary Interiors, v. 150, p. 3–14. https://doi.org/10.1016/j.pepi.2004.08.023

Spratt, J. and Craven, J., 2011. Near-surface and crustal-scale images of the Nechako basin, British Columbia, Canada, from magnetotelluric investigations; Canadian Journal of Earth Sciences, v. 48, no. 6, p. 987–999. https://doi.org/10.1139/e10-098

Stanley, C. R., 1994. Geology of the Pothook alkalic copper-gold porphyry deposit, New Afton mining camp, British Columbia (92I/ 9 10); British Columbia Geological Fieldwork 1993, British Columbia Ministry of Energy, Mines and Petroleum Resources, Paper 1994-1, p. 275–284.

Stevens, K.M. and McNeice, G., 1998. On the detection of Ni-Cu Ore hosting structures in the Sudbury Igneous Complex using the magnetotelluric method; *in* SEG Technical Program Expanded Abstracts; Society of Exploration Geophysicists, p. 751–755. https://doi.org/10.1190/1.1820581

Türkoğlu, E., Unsworth, M., and Pana, D., 2009. Deep electrical structure of northern Alberta (Canada): implications for diamond exploration; Canadian Journal of Earth Sciences, v. 46, no. 2, p. 139–154. https://doi.org/10.1139/E09-009

Wannamaker, P. E., 2005. Anisotropy versus heterogeneity in continental solid earth electromagnetic studies: fundamental response characteristics and implications for physicochemical state; Surveys in Geophysics, v. 26, no. 6, p. 733–765. https://doi.org/10.1007/s10712-005-1832-1

Zhang, P., Chouteau, M., Mareschal, M., Kurtz, R., and Hubert, C., 1995. High-frequency magnetotelluric investigation of crustal structure in north-central Abitibi, Quebec, Canada; Geophysical Journal International, v. 120, no. 2, p. 406–418. https://doi.org/10.1111/j.1365-246X.1995.tb01828.x

Spatial relationship between porphyritic Cu-Au mineral occurrences and magnetic signatures within the Iron Mask batholith, south-central Cordillera, British Columbia

M.D. Thomas[1*]

Thomas, M.D., 2021. Spatial relationship between porphyritic Cu-Au mineral occurrences and magnetic signatures within the Iron Mask batholith, south-central Cordillera, British Columbia; in *Targeted Geoscience Initiative 5: contributions to the understanding and exploration of porphyry deposits, (ed.) A. Plouffe and E. Schetselaar; Geological Survey of Canada, Bulletin 616, p. 65–90. https://doi.org/10.4095/327943*

Abstract: Gold-rich porphyry copper deposits are commonly associated with magnetic highs related to high magnetite content—up to 10% volume—within potassium silicate alteration zones. This association promoted magnetic highs as exploration targets. The Iron Mask batholith (comprising Iron Mask and Cherry Creek plutons) contains more than 50 porphyry Cu-Au mineral occurrences, including the New Afton deposit. The batholith's strong positive magnetic signatures permit examining magnetic high correlations with porphyry-type mineralization and evaluating the significance of magnetic signatures for mineral exploration.

Groups of prominent magnetic peaks were delineated, with six and two groups present in the Iron Mask pluton and Cherry Creek pluton, respectively. Mineral occurrences occur within the borders of two groups, but are peripheral to other groups, with the nearest occurrence an average of 500 m from the centre of a group. These close spatial relationships support magnetic exploration for porphyry-copper deposits that significantly narrows the search area. Magnetic exploration is also supported by the observation that porphyry (Cu±Mo±Au) and magnetite-apatite mineralization in the Iron Mask batholith are related to a single intrusive event, a characteristic shared by iron-oxide copper gold deposits, where magnetite-apatite mineralization is located laterally or deeper. The New Afton deposit is situated laterally to the Magnet magnetite-apatite deposit near the end of a linear magnetic high passing through the latter.

Résumé : Les gîtes de cuivre porphyriques riches en or sont généralement associés à des crêtes magnétiques liées à une forte teneur en magnétite — jusqu'à 10 % en volume — dans les zones d'altération à silicates potassiques. Cette association a fait des crêtes magnétiques des cibles d'exploration de choix. Le batholite d'Iron Mask (qui comprend les plutons d'Iron Mask et de Cherry Creek) contient plus de 50 indices de minéralisations porphyriques à Cu-Au, dont le gisement de New Afton. Les fortes signatures magnétiques positives du batholite permettent d'examiner la corrélation entre les crêtes magnétiques et les minéralisations de type porphyrique et d'évaluer l'importance des signatures magnétiques pour l'exploration minérale.

Des groupes de pics magnétiques prononcés ont été délimités, dont six dans le pluton d'Iron Mask et deux dans celui de Cherry Creek. Pour deux d'entre eux, les indices minéralisés se trouvent à l'intérieur des limites du groupe, alors que pour les autres groupes, les indices se situent en périphérie, où l'indice le plus proche se trouve en moyenne à 500 m du centre du groupe. Ces relations spatiales étroites appuient l'utilisation de méthodes magnétiques dans l'exploration des gîtes de cuivre porphyriques en permettant de réduire considérablement l'étendue de la zone de recherche. L'exploration par des méthodes magnétiques est également soutenue par le fait qu'on a constaté que, dans le batholite d'Iron Mask, la minéralisation porphyrique (Cu±Mo±Au) et la minéralisation de magnétite-apatite sont liées à un seul événement intrusif, une caractéristique partagée par les gîtes d'oxydes de fer–cuivre-or, où la minéralisation de magnétite-apatite est située dans une position latérale ou plus en profondeur. Le gisement de New Afton est situé latéralement par rapport au gisement de magnétite-apatite de Magnet, près de l'extrémité d'une crête magnétique linéaire traversant le gisement de Magnet.

[1]Geological Survey of Canada, 601 Booth Street, Ottawa, Ontario K1A 0E8
*Corresponding author: M.D. Thomas (email: mike.thomas@canada.ca)

INTRODUCTION

The Geological Survey of Canada's Targeted Geoscience Initiative program includes the study of several mineral systems, including porphyry-related mineral systems. A particular subproject is investigating Cordilleran Cu±Mo±Au porphyry mineralization in space and time, with one objective being to create an integrated 3-D model of magmatic-hydrothermal evolution within the Triassic alkalic Iron Mask batholith (Fig. 1; British Columbia Geological Survey, 2018a) near the producing New Afton mine (Schetselaar et al., 2017). The batholith hosts numerous mineralized occurrences classified by the British Columbia Geological Survey as showings, prospects, developed prospects, producers, or past producers (British Columbia Geological Survey, 2018b). In addition to hosting porphyry Cu-Au-Ag deposits such as New Afton, Crescent, Pothook, Ajax West, and Ajax East, the batholith contains structurally controlled Cu-magnetite veins (Iron Mask, Makaoo/Python, Grey Mask; Logan and Mihalynuk, 2005) with associated copper mineralization noted in the form of chalcopyrite, malachite, azurite, bornite, and cuprite (British Columbia Geological Survey, 2018c, d). The distribution of these and other occurrences are shown in Figure 2 *after* Logan et al. (2006).

The significant potential for porphyry-type mineralization within the batholith and its association with strong magnetic signatures has prompted a wider examination of the batholith from the perspective of determining the significance of the signatures for mineral exploration. An association of magnetic highs with porphyry deposits had been recognized by Sillitoe (1979), who noted that gold in gold-rich porphyry copper deposits worldwide is normally present in potassium silicate alteration commonly associated with an unusually high magnetite content that could form 3 to 10% of the volume.

The association prompted Sillitoe (1979) to propose that ground or even airborne magnetic surveys could be effective in locating such deposits. If the gold-bearing character of a porphyry prospect could be established, it was suggested that drilling could be focused in the location displaying the highest magnetic response. The observations by Sillitoe (1979) leading to a simplistic correlation between gold-rich porphyry copper deposits and magnetic highs merit attention and make a compelling case for the inclusion of magnetic surveys in exploration for porphyry deposits.

Mineralization and associated alteration and hydrothermal processes can be complex, however, and repeated episodes spanning a protracted period of time can complicate interpretation of the significance of magnetic signatures. Furthermore, spatially and temporally different magmatic events could use the same plumbing/conduit system. Clark (2014) reviewed the magnetic effects of hydrothermal alteration in porphyry copper and iron oxide copper gold (IOCG) systems, noting a requirement to understand the magmatic, metamorphic and hydrothermal processes that create, alter and destroy magnetic minerals to achieve meaningful interpretation of mineralized systems. Arancibia and Clark (1996), in investigating the Island Copper porphyry copper-gold-molybdenum deposit on Vancouver Island, British Columbia, proposed that magnetite-rich vein systems within and around some calc-alkaline porphyry deposits are often pre-mineralization and distinct from magnetite-biotite potassic alteration associated with sulfides and Cu-Au mineralization. The early alteration associated with the Island Copper deposit was generated through moderate to intense Fe metasomatism, whereas the principal Island Copper deposit is associated with a later main-stage phase of potassic alteration that is superimposed on the more extensive early alteration mineralized zone. Gold, although correlating overall with copper and potassic alteration, was probably extensively introduced in the early stage of alteration.

The Island Copper deposit illustrates the kind of complexity that might relate to understanding the significance of a magnetic signature related to a porphyry intrusion. Other complicating factors are rock composition, structure, hydrothermal overprinting, porosity-related fracture systems, oxygen fugacity, and iron and sulfide budgets. Despite the large number of variables, magnetite is commonly a conspicuous mineral within porphyry systems with significant potential to contribute to understanding mineralization-forming processes and exploration; therefore, this paper examines relationships between magnetic signatures, geology, and mineral occurrences within the Iron Mask batholith.

GEOLOGICAL SETTING

The northwest-trending alkalic Iron Mask batholith in the south-central part of the Cordilleran Quesnel terrane (Fig. 1) is a Late Triassic to Early Jurassic magmatic-arc complex (Logan and Mihalynuk, 2005). The batholith includes two principal bodies separated by a broad unit of Eocene alkaline volcanic rocks belonging to the Kamloops Group (British Columbia Geological Survey, 2018a). The latter were inferred to be deposited within a graben structure created by renewed fault movement along the margins of the plutons during Paleocene or Early Eocene time (Kwong, 1987). Logan and Mihalynuk (2005) referred to both the entire alkalic intrusive complex and its larger southeastern portion as the Iron Mask batholith, and the smaller northwestern body as the Cherry Creek pluton. To avoid confusion, the bodies are herein named the Iron Mask and Cherry Creek plutons, respectively (Fig. 1), following usage by Kwong (1987) and more recently in a MINFILE report on the Ajax East past producer (British Columbia Geological Survey, 2018e); Iron Mask batholith will be used when both plutons are the subject of discussion. The batholith is viewed as a subvolcanic, multiple intrusion that is comagmatic and coeval with Upper Triassic volcanic and sedimentary rocks of the Nicola Group, which flank the batholith to the southwest and much of its northeastern margin (Fig. 1; British Columbia Geological Survey, 2018e) and with which the batholith is in intrusive contact (Logan and Mihalynuk, 2005). Middle

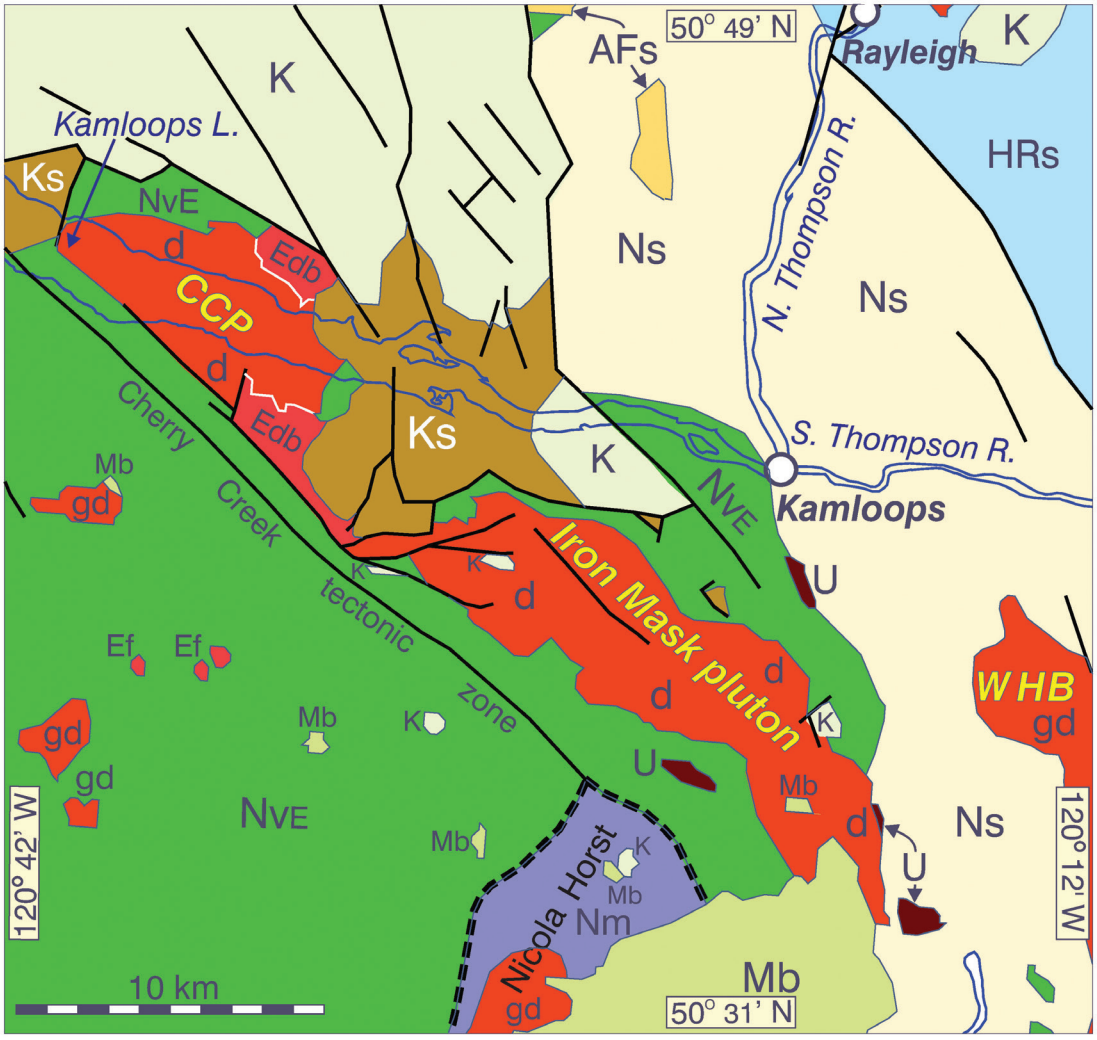

Miocene
- Mb — Basaltic volcanic rocks

Eocene
- K — Kamloops Group, undivided volcanic rocks
- Ks — Kamloops Group, sedimentary rocks

Lower Jurassic–Middle Jurassic
- AFs — Ashcroft Formation, sedimentary rocks

Upper Triassic
- NvE — Nicola Group (Eastern facies), basaltic volc. rocks
- Ns — Nicola Group, fine-grained sedimentary rocks
- Nm — Nicola Group, metamorphic rocks

Devonian–Permian
- HRs — Harper Ranch Group, mudstone, siltstone, shale, fine clastic sedimentary rocks

Intrusive igneous rocks

Eocene
- Ef — Felspar porphyritic intrusive rocks
- Edb — Battle Bluff Complex, diabase, intrusive basaltic rocks

Late Triassic–Early Jurassic
- U — Ultramafic rocks
- d — Dioritic intrusive rocks
- gd — Granodioritic intrusive rocks
- CCP — Cherry Creek pluton
- WHB — Wild Horse batholith
- Fault

Note: Unit abbreviations designated by the author, and are not those used on the MapPlace web site.

Figure 1: Geological map of region including and surrounding Iron Mask batholith that comprises the Iron Mask pluton and Cherry Creek pluton. *Modified from* British Columbia Geological Survey (2018a).

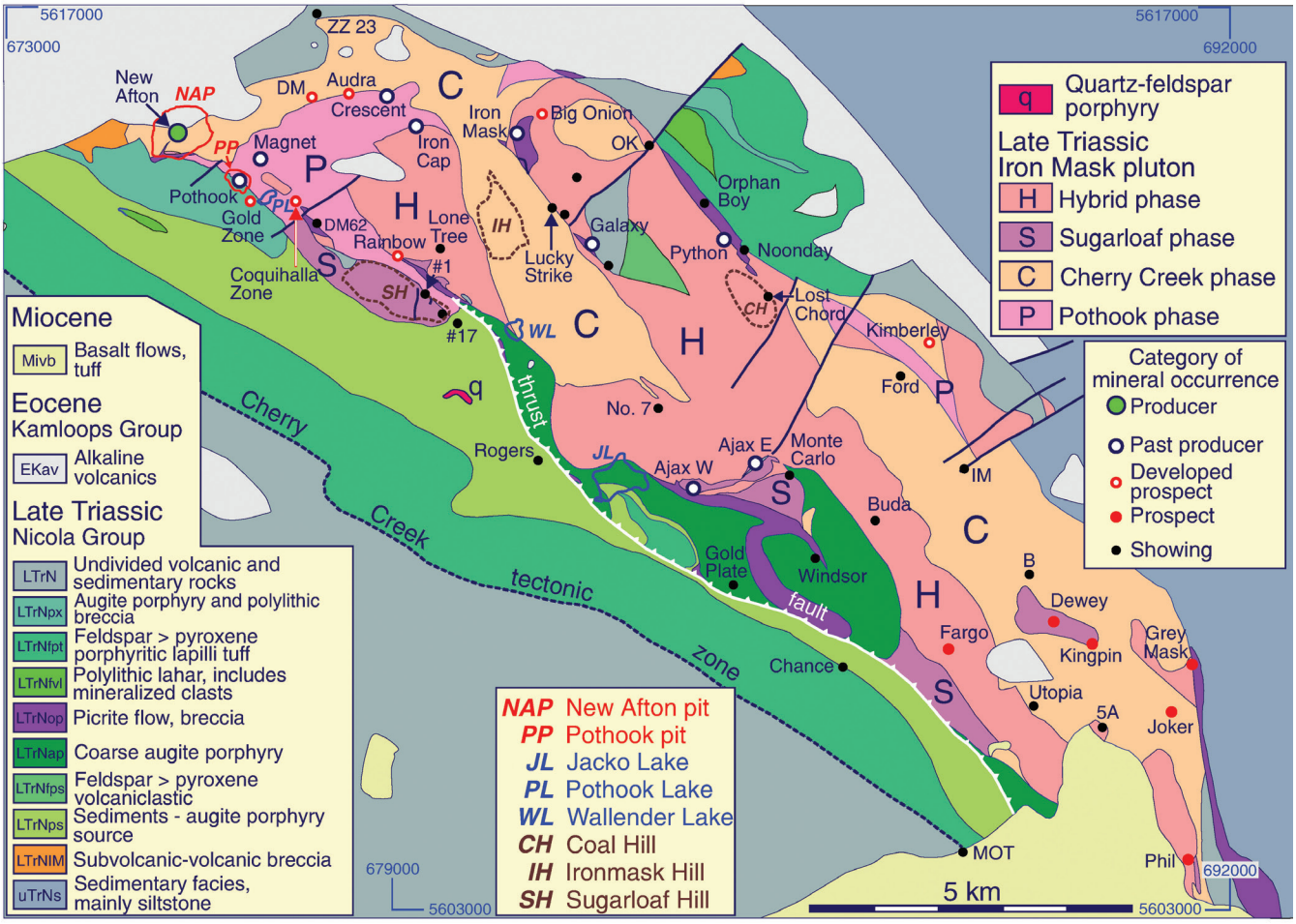

Figure 2: Geological map of Iron Mask pluton *modified from* Logan et al. (2006). Mineralized occurrences as classified by the British Columbia Geological Survey are plotted; some modifications to the category as shown by Logan et al. (2006) are based on more recent information (British Columbia Geological Survey, 2018b). Abbreviations in coloured rectangles of geological legend for Miocene, Eocene, and Late Triassic Nicola Group are those used by Logan et al. (2006). Abbreviations for the phases of the Iron Mask pluton are designated by the author. The age of the quartz-feldspar porphyry unit (q) is not provided.

Eocene volcanic and sedimentary rocks of the Kamloops Group and Miocene alkaline flood basalt unconformably overlie Nicola Group and Iron Mask pluton rocks (Fig. 2). Logan et al. (2006) presented a geological map of the Iron Mask pluton at a scale of 1:25 000 (simplified in Fig. 2) and Logan and Mihalynuk (2005) described the geological units forming the Iron Mask pluton, its porphyry Cu-Au deposits, and marginal Triassic and Eocene units.

Iron Mask pluton

The Iron Mask pluton (Fig. 1, 2) includes three principal intrusions, or phases. In order of decreasing age these are: the Pothook diorite, the Cherry Creek monzonite, and the Sugarloaf diorite (Snyder and Russell, 1993; Logan and Mihalynuk, 2005). A fourth igneous unit, the Iron Mask Hybrid phase, is derived mainly from Pothook diorite and assimilated Nicola Group volcanic rocks. It is a xenolith-rich, heterogeneous unit forming approximately 45% of the batholith. Hybrid rocks mark the contact zones between the three intrusions within the pluton, and between the pluton and volcanic country rock. The xenolith-rich Sugarloaf diorite can also form a hybrid unit. Uranium-lead ages for samples of the Pothook, Hybrid, and Cherry Creek phases are 204 ± 3 Ma, or Upper Triassic (Mortensen et al., 1995). The Sugarloaf diorite is the youngest phase but had not been dated.

Snyder (1994) suggested that magmatic contamination was important in the development of the Iron Mask pluton. The magmatic history is believed to have started with the intrusion of Pothook diorite magma and its interaction with rocks of the Nicola Group that produced the Hybrid unit. Intrusion of the Cherry Creek phase followed closely, possibly partially coeval

with hybridization, and finally Sugarloaf diorite was intruded along pre-existing structures both within the batholith and the Nicola Group country rocks.

The Iron Mask pluton is dominated by the Hybrid and Cherry Creek phases, which cover areas of approximately similar size (Fig. 2). The Hybrid phase is distributed in a Y-shaped belt running parallel to the length of the pluton and occupying much of the southwestern margin and central part of the intrusion. A large belt of Cherry Creek phase flanks the Hybrid phase to the northeast in the southeastern portion of the pluton. A north-northwest-trending unit of Cherry Creek phase lying between the two forks of the Y swings west-southwestward around a belt of Pothook diorite at the top of the western fork and continues to the New Afton pit. A very narrow branch of this Pothook diorite unit extends southeast between the western fork and a short belt of the Sugarloaf phase along the southwestern margin of the pluton. Small units of Pothook, Sugarloaf, and Hybrid phases lie within the unit of Cherry Creek phase in the southeastern part of the pluton. Stanley et al. (1994) reported magnetite concentrations ranging from 10 to 15% in various phases of the pluton. Descriptions of phases of the pluton based on the paper by Logan and Mihalynuk (2005) follow.

Pothook phase

The Pothook diorite is present mainly near the northwestern margin of the pluton, with emplacement apparently controlled by northwest- and northeast-trending faults. The diorite exhibits gradational contacts with the Hybrid unit, faulted contacts masked by strong potassic alteration with the Cherry Creek phase, and reportedly intrusive contacts with the Sugarloaf phase at the Pothook deposit (Stanley, 1994). The Pothook diorite is an equigranular, medium- to coarse-grained diorite containing 40 to 60% plagioclase; 10 to 25% clinopyroxene; 5 to 10% magnetite; 5 to 7% biotite; and up to several per cent K-feldspar, apatite, and lesser accessory minerals. Alteration minerals, including K-feldspar, sericite, epidote, and chlorite, are widespread.

Hybrid phase

The Hybrid phase is a xenolith-rich, heterogeneous igneous component occurring mainly as the extensive Y-shaped belt that traverses most of the Iron Mask pluton. Hybrid rocks delineate contact zones between phases of the pluton, and between the margin of the pluton and volcanic country rocks. Logan and Mihalynuk (2005) noted that Snyder (1994) redefined the Hybrid phase as a facies equivalent of the Pothook diorite, considered to represent outer margins of the Pothook phase that interacted with and incorporated country rock of the Nicola Group. They further noted that the matrix of Hybrid rocks is not necessarily always Pothook diorite, that locally xenolith-rich marginal phases of the Cherry Creek and Sugarloaf phases are hybrid zones and that Snyder and Russell (1995) had subdivided the Hybrid phase into three main types based on texture and clast abundance. From the perspective of studying magnetic signatures of the Iron Mask pluton, the Hybrid phase contains abundant coarse interstitial grains of magnetite in a Pothook dioritic matrix, yielding magnetic susceptibilities typically an order of magnitude higher than most other rock types (Logan and Mihalynuk, 2005). All rock types in the Hybrid unit, which forms approximately 40% of the surface area of the pluton, are described as often containing more than 10% magnetite by volume (British Columbia Geological Survey, 2018f).

Cherry Creek phase

The Cherry Creek phase rivals the Hybrid phase in coverage, forming extensive pluton-parallel belts in both the northwestern and southeastern halves of the pluton (Fig. 2). Historically, there was difficulty distinguishing between Cherry Creek and Pothook phases because of pervasive potassium metasomatism commonly developed adjacent to their contacts (Logan and Mihalynuk, 2005). Textures within the Cherry Creek phase vary from plutonic to hypabyssal and locally volcanic. In the core of the pluton, near Ironmask Hill (Fig. 2), and in the northern part of the southeastern belt, the rocks are leucocratic, fine- to medium-grained, equigranular biotite monzonite. Near the margins of the pluton, rocks are characteristically microporphyries, ranging in composition from monzodiorite to monzonite. Magnetite is disseminated throughout the groundmass in amounts up to 10%.

Sugarloaf phase

The Sugarloaf phase is represented by hornblende porphyritic, trachytic rocks of dioritic composition that crop out mainly along the western margin of the pluton as lenticular bodies or metre-wide dykes in adjacent Nicola Group volcanic rocks. Distribution of the phase was apparently controlled by northwest-trending structures. Dykes of the Sugarloaf phase are oriented radially around Sugarloaf Hill (Fig. 2), interpreted by Snyder and Russell (1993) as a volcanic neck and intrusive centre. The holocrystalline trachytic porphyries of the phase exhibit significant variation in texture, ranging from fine to medium grained. The rocks of the phase are characterized by 1 to 1.5 mm hornblende and plagioclase phenocrysts in a fine-grained groundmass of plagioclase, clinopyroxene, magnetite, and K-feldspar.

Cherry Creek pluton

Kwong (1987) reported that the Cherry Creek pluton consisted entirely of the Cherry Creek unit (i.e. the Cherry Creek phase). As noted in the description of the Iron Mask pluton above, the Cherry Creek phase includes biotite monzonite and microporphyries ranging in composition from monzodiorite to monzonite (Logan and Mihalynuk, 2005).

LARGE-SCALE STRUCTURE OF THE CHERRY CREEK AND IRON MASK PLUTONS

The 3-D geometries of the two component plutons have been investigated by 2-D gravity and magnetic modelling (Thomas, 2019) along lines crossing the central portions of each pluton. Modelling shows the Iron Mask pluton extending from surface to a depth of approximately 5700 m, and laterally for several kilometres on both flanks at a shallow depth below Nicola Group volcanic rocks. The Cherry Creek pluton was determined to be significantly thinner, approximately 2850 m. Magnetic modelling indicates that both plutons are characterized by very steep, relatively narrow magnetic units, and adjacent units may have a significant difference in magnetic susceptibility. The apparent differences in magnetite content are possibly accompanied by petrogenetic differences. Gravity modelling suggests that the densities of diorites in the Cherry Creek pluton are relatively low compared to those in the Iron Mask pluton, hinting that higher density gabbroic varieties may be more prevalent at depth in the latter intrusion.

DISTRIBUTION OF MAGNETIC HIGHS AND PEAK VALUES IN THE IRON MASK AND CHERRY CREEK PLUTONS

The abundance of mineral occurrences (Fig. 2) and strong magnetic signatures within the Iron Mask pluton (Fig. 3), and Sillitoe's (1979) observation of the association of voluminous magnetite with gold-rich porphyry deposits, prompted the examination of magnetic signatures within the pluton from this perspective. Sillitoe (1979) had suggested that if the gold-bearing character of a porphyry prospect could be established, then exploration drilling should be focused in the location displaying the highest magnetic response.

Aeromagnetic coverage of the Iron Mask and Cherry Creek plutons is provided by an airborne magnetic-radiometric survey (Kamloops survey), flown in 2008 over an area centred approximately on Kamloops as a contribution to the Geological Survey of Canada's Mountain Pine Beetle Program (Thomas, 2010). It was flown at 400 m line-spacing and 125 m mean terrain clearance. A higher resolution combined helicopter-borne magnetic-electromagnetic-radiometric survey (Fugro survey) with nominal terrain clearances for the respective instruments of 35 m, 35 m, and 60 m was flown over the northwestern two-thirds of the Iron Mask batholith in 2011 by Fugro Airborne Surveys for New Gold Inc. Flight-lines were oriented northeast and spaced 100 m apart. The potential relationship between magnetic highs and porphyry deposits is examined using magnetic data collected by the higher resolution Fugro survey. These data were kindly made available for analysis by New Gold Inc. with the proviso that magnetic maps produced from the data are not displayed in this report.

Iron Mask pluton

A map of the residual total magnetic field (RTF) over the Iron Mask pluton produced from the Kamloops survey data is presented in Figure 3. The strongest, most positive areas of the magnetic field coincide mainly with most of the Hybrid phase. The magnetic field associated with units of the Pothook and Sugarloaf phases in the northwest of the pluton is also strongly positive, whereas that over the Cherry Creek phase is generally weak throughout the pluton (Fig. 3).

The areas of magnetic highs as displayed in a more detailed image produced from higher resolution Fugro survey data exhibit an apparent roughness, seemingly related to superposed short wavelength magnetic highs. Although the detailed image clearly displays the distribution of the main areas of relatively positive and negative magnetic anomalies, the blending of the various shades of red defining the positive anomalies makes it difficult to clearly identify individual smaller wavelength magnetic highs and the degree to which the magnitude of the field changes over short distances. This problem is alleviated by applying a process to define individual peaks in the grid of values defining the magnetic field. The algorithm compares the value of each grid cell with the values of the surrounding eight grid cells (along the row, column, and both diagonals). A grid cell is defined as a peak when the values of all eight surrounding grid cells are lower. A series of ranges of grid peak sizes is then defined and peaks within these ranges can be colour-coded to help recognize their magnitude. Peak locations and magnitudes are displayed in Figure 4, superposed on the map of the Iron Mask pluton *after* Logan et al. (2006). Concentrations of peaks having noticeably stronger magnitudes have been partitioned into six groups, numbered 1 through 6 (Fig. 5).

Relationship of groups of magnetic peaks to locations of mineral occurrences

A belt of eight strong magnetic peaks (Group 1) runs approximately 1500 m east-southeast from the edge of the producing New Afton pit. Values range from approximately 1625 to 12 240 nT, including four values greater than 3500 nT, with the strongest one positioned on the Magnet past producer. The background level of the magnetic field is locally generally less than 500 nT, dipping down into negative values. The New Afton deposit is hosted in the Cherry Creek phase of the pluton and the Magnet past producer is in the Pothook phase. Curiously, this linear belt of peaks crosses the mutual boundary of the phases at practically right angles, which probably indicates structural control.

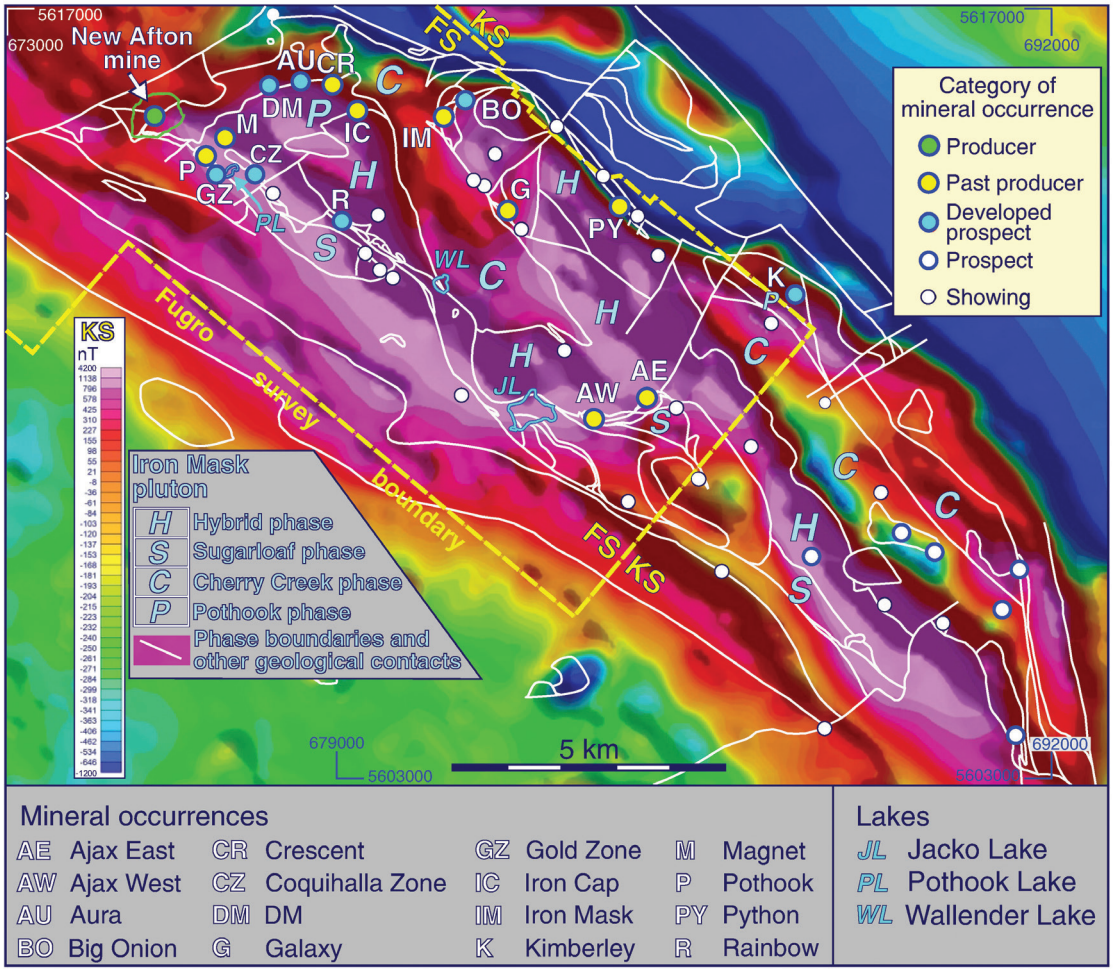

Figure 3: Residual total magnetic field over the Iron Mask pluton defined by the Kamloops survey. The area of higher resolution magnetic data defined by the Fugro survey used to define magnetic peaks is outlined. Geological contacts from a map by Logan et al. (2006) and mineral occurrences (Logan et al., 2006; British Columbia Geological Survey, 2018b) are plotted. FS, Fugro survey; KS, Kamloops survey.

Another conspicuous group of peaks (Group 2), somewhat loosely clustered, is centred approximately 640 m south-southwest of the past-producing Crescent deposit, 650 m west-southwest of the past-producing Iron Cap deposit, and a more distant 1130 m southeast of the DM developed prospect. The Crescent and DM occurrences are hosted by the Pothook and Cherry Creek phases, respectively, and the Iron Cap deposit is located at the boundary between the Cherry Creek and Hybrid phases. The Group 2 peaks range from approximately 2000 to greater than 4900 nT, with most being greater than 3000 nT. Local background values are variable, ranging from approximately 1500 nT to negative values.

Four prominent peaks forming a short curvilinear group (Group 3) trend northwest for approximately 650 m along Coal Hill, passing by the Lost Chord showing just 320 m to the northeast. Peak values range from 2660 to 4525 nT relative to local background levels, which are generally less than 1000 nT but can be up to approximately 1350 nT.

Just north of the Ajax West and Ajax East past producers, a branch of the Hybrid unit extends westward for approximately 2.5 km from the main northwest-trending belt of the unit. Its southern margin lies adjacent to the mineral occurrences and a narrow unit of the Sugarloaf phase. Most peak values within the eastern half of the Hybrid branch are in the range of 2000 to 3000 nT, but lower values between 1000 and 2000 nT dominate the western half with several peaks less than 1000 nT (Fig. 4). In comparison, several peaks in the range of 3000 to 4000 nT are observed in the area marginal to the Ajax West deposit. Near the east end of the Hybrid branch a group of peaks having a similar range extends toward the northwest within the main belt of the Hybrid unit from a point just northeast of Ajax East. The groups near the Ajax East and Ajax West deposits are identified as Group 4 and Group 5, respectively (Fig. 5).

A group of eight relatively high values (Group 6) with limited proximity to mineral occurrences trends northwest from Jacko Lake for approximately 1500 m. It traverses mainly the

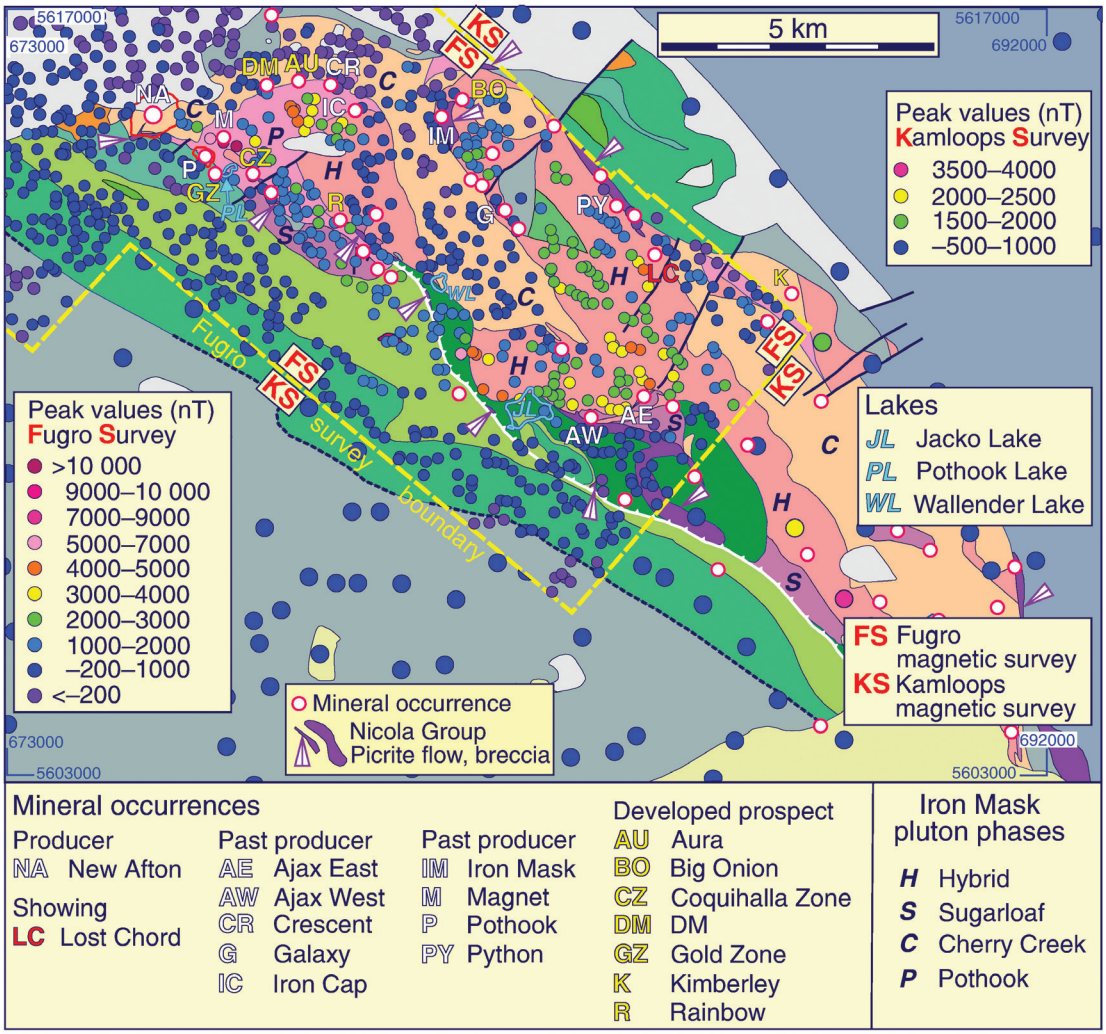

Figure 4: Geological map of the Iron Mask pluton as shown in Figure 2 with locations of mineral occurrences (Logan et al., 2006; British Columbia Geological Survey, 2018b) and magnetic peaks. FS, Fugro survey; KS, Kamloops survey.

Hybrid unit before entering a bordering unit of Nicola Group augite porphyry to the west near its north end. Apart from a relatively weak peak value of 2260 nT at the north end, other values range from 3100 to 5350 nT. With the exception of the highest value, all of the latter peaks (four of which have values greater than 4500 nT) are in the Hybrid unit. The highest peak of 5350 nT is located within the unit of Nicola Group volcanic rocks. The only mineral occurrence close to this group of peaks is the Rogers showing, located 270 m and 210 m southwest of the group and of the boundary between the Hybrid unit and Nicola Group, respectively. The Rogers showing lies within a Nicola Group unit described as sedimentary rocks derived from an augite porphyry source (Logan et al., 2006), though a British Columbia Geological Survey (2018g) MINFILE report identifies the host rocks to be andesitic volcanic rocks. The Rogers showing includes polymetallic veins (Ag-Pb-Zn±Au) and alkalic porphyry Cu-Au mineralization.

Of potential interest for mineral exploration in the area of Group 6 is the presence of a small lens-shaped Nicola Group unit of picrite flow and breccia near the south end of the group at the boundary between the Nicola Group unit hosting the Rogers showing and a Nicola Group unit of augite porphyry (Fig. 2, 4, 5). Such lenses occur intermittently between this occurrence and an occurrence near the New Afton pit and New Afton deposit, forming a discontinuous curvilinear belt falling close to the southwestern margin of the Iron Mask pluton (Fig. 4). Kwong (1987) noted that the picrite unit is one of the geological phenomena associated with hypogene mineralization in the New Afton deposit, further noting that considering wall rocks act as proton sinks during hydrothermal alteration, the presence of picrite is important in the mineralization process, particularly if fractured to enhance the reacting surface area. Kwong (1987)

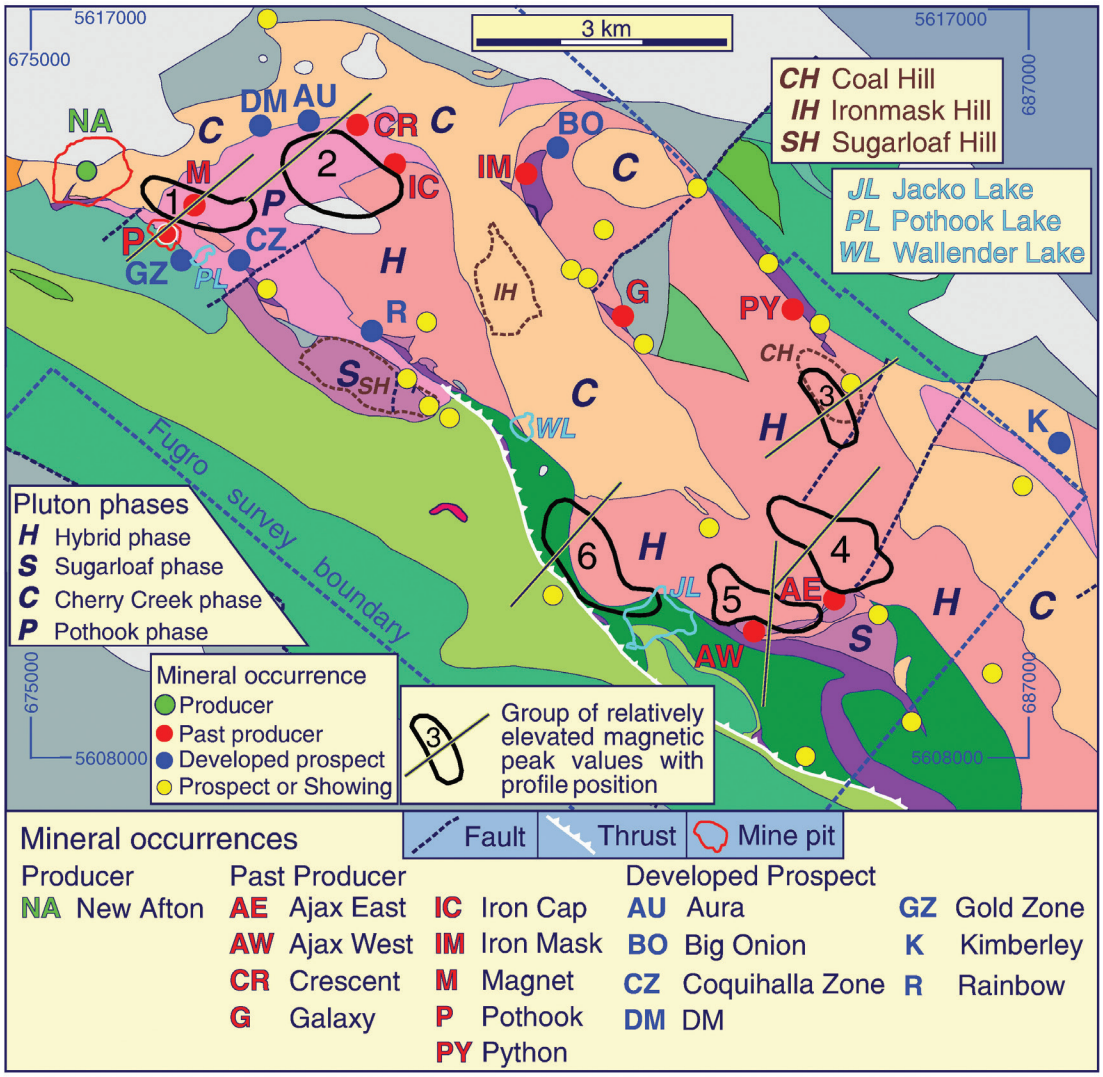

Figure 5: Geological map of the Iron Mask pluton (Logan et al., 2006) displaying locations of mineral occurrences and groups of relatively elevated magnetic peak values. Profile lines for magnetic profiles displayed in Figure 8 are plotted. Complete geological legend is shown in Figure 2.

also drew attention to the fact that picrite bodies, although not well exposed, are generally present within 300 m of most prospects in the district (Carr and Reed, 1976).

Cherry Creek pluton

The Cherry Creek pluton forms the northwest portion of the Iron Mask batholith and is associated with two belts of magnetic highs (Fig. 6): one along its southern margin and the other along the northern margin. Like positive magnetic belts in the Iron Mask pluton, the images of the magnetic field produced from the Fugro survey data exhibit a roughness related to superposed short wavelength magnetic highs. Both plutons are characterized by strong magnetic fields containing magnetic highs having amplitudes greater than 3000 nT. In the Cherry Creek pluton, the eastern part of Kamloops Lake lies between the two belts of magnetic highs, correlating with a relatively smooth magnetic low that is more intense along the southern margin of the lake. In contrast, near the west end of the pluton the lake coincides with part of the northern marginal magnetic high.

Relationship of groups of magnetic peaks to locations of mineral occurrences

Compared to the Iron Mask pluton, the Cherry Creek pluton is relatively poor in mineral occurrences, having just four, although two are past producers. A conspicuous northwest-oriented group (Group 1) of strong magnetic peak values lies between Kamloops Lake and the southwestern margin of the pluton. It extends roughly between

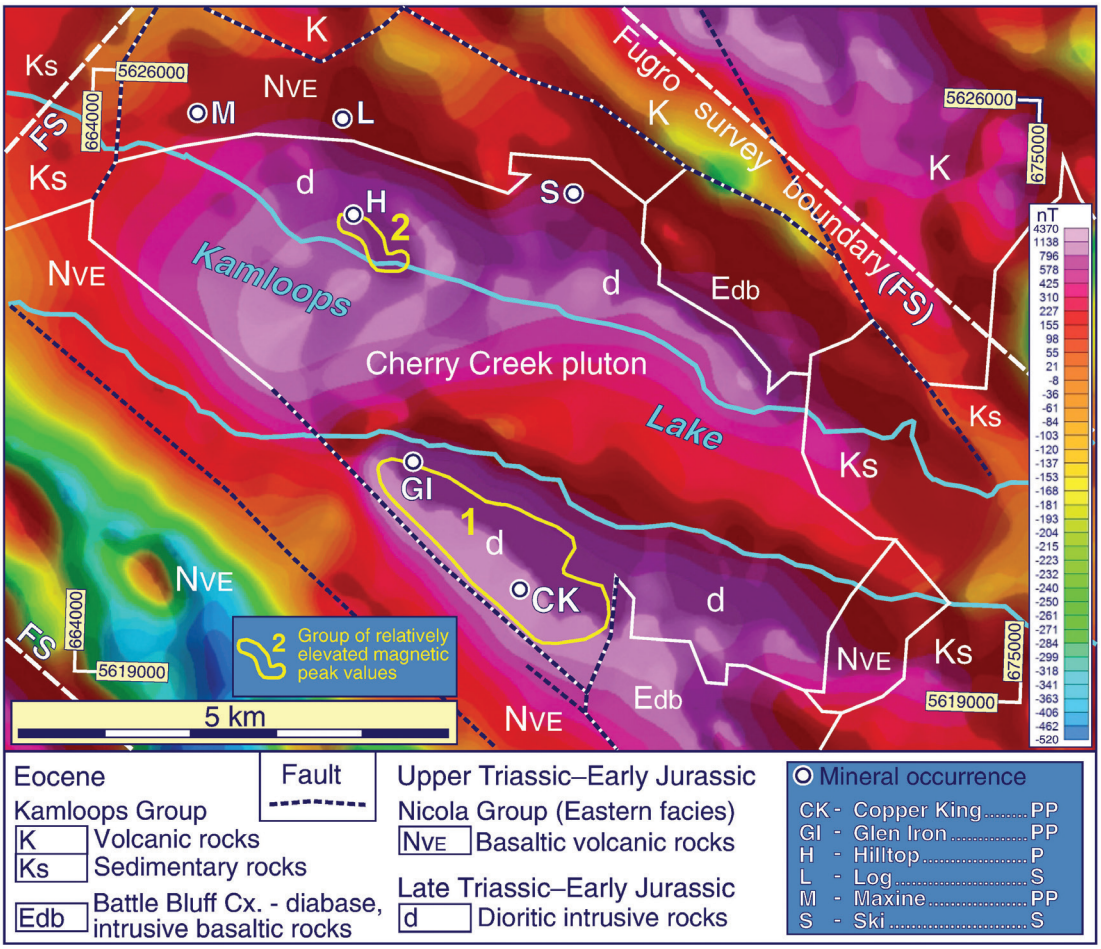

Figure 6: Residual total magnetic field map of Cherry Creek pluton based on the Kamloops aeromagnetic data; the area covered by the Fugro survey is outlined. Geological boundaries and mineral occurrences based on British Columbia Geological Survey (2018a) are plotted. Groups of elevated magnetic peak values (Fig. 7) are outlined. Mineral occurrences are depicted with the same symbol; letters following names indicate the category: PP, Past Producer; P, Prospect; S, Showing.

the past-producing Glen Iron (magnetite, iron) and Copper King (copper, gold, silver, uranium) deposits (Fig. 7). Most peak values fall within the ranges 2000 to 3000 nT or 3000 to 4000 nT and many surround the Copper King deposit. These compare with bordering peak values within the pluton, which are generally in the range of 1000 to 2000 nT or less than 1000 nT, and values within Nicola Group volcanic rocks along the southwest margin of the pluton, which are typically less than 1000 nT. Two small clusters of peaks within Group 1 near the Glen Iron deposit have much stronger values. A cluster southeast of the deposit has values ranging from approximately 5000 to 6250 nT, and the other cluster, immediately southwest of the deposit, has values ranging from 11 000 to approximately 11 680 nT. These very high values close to the Glen Iron deposit are not surprising, given that the deposit comprises magnetite veins varying from less than 30 cm to nearly 10.6 m in width, some of which have been traced for almost 200 m (British Columbia Geological Survey, 2018h). Although magnetite from veins was the main product, Glen Iron is classified as an alkalic porphyry Cu-Au deposit. The Copper King deposit is identified as a polymetallic (Ag-Pb-Zn±Au) vein-hosted deposit within a northwest-trending shear zone (155 × 62 × 55 m) transecting diorite and monzonite of the Cherry Creek pluton and containing chalcopyrite, bornite, pyrite, and magnetite as disseminations and veins (British Columbia Geological Survey, 2018i).

On the north shore of Kamloops Lake, the Hilltop prospect, classified as an alkali porphyry Cu-Au deposit, consists of sparse disseminations of chalcopyrite, bornite, chalcocite, and pyrite in fine- to medium-grained diorites, syenites, and

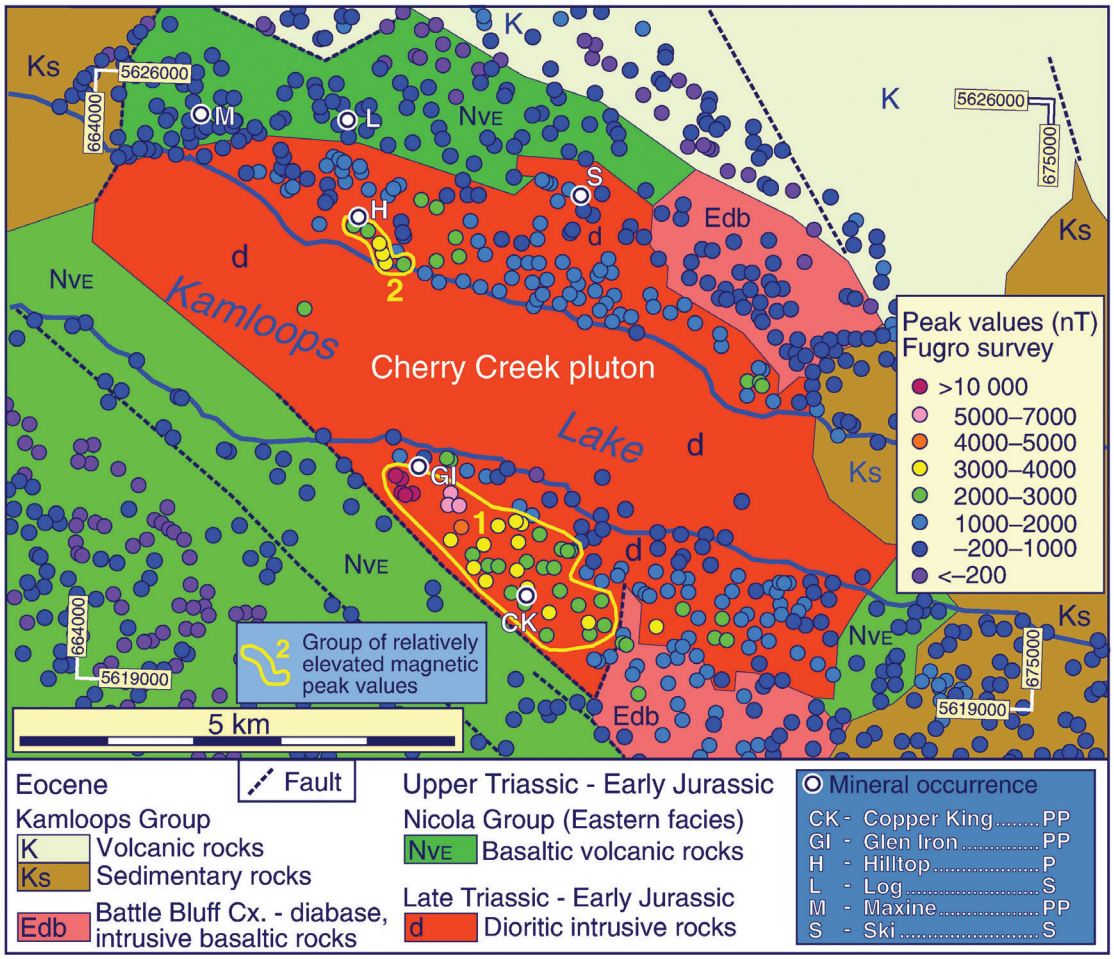

Figure 7: Geological map of the Cherry Creek pluton (British Columbia Geological Survey, 2018a) and magnetic peaks for Fugro magnetic survey data. Mineral occurrences are depicted with the same symbol; letters following names indicate the category: PP, Past Producer; P, Prospect; S, Showing.

monzonites (British Columbia Geological Survey, 2018j). It is located on the northern margin of the only other group of strong peak values (Group 2), which are distributed along a path striking southeast from the deposit (Fig. 7). Three values are greater than 3000 nT and the others are 2320 and 2810 nT; all are significantly larger than proximal peak values, of which roughly half are less than 2000 nT and half are less than 1000 nT. Farther east, the Ski alkalic porphyry Cu-Au showing (British Columbia Geological Survey, 2018k) is not associated with a noticeable magnetic peak. North of the pluton, within marginal volcanic rocks of the Nicola Group, the Maxine past producer (British Columbia Geological Survey, 2018l) and Log showing (British Columbia Geological Survey, 2018m), both classified as alkali porphyry Cu-Au mineralization, occur at or near contacts with rocks of the Cherry Creek pluton. No conspicuous magnetic peaks accompany either mineral occurrence.

SUMMARY OF RELATIONSHIPS BETWEEN MAGNETIC ANOMALIES AND MINERAL OCCURRENCES

The relatively high resolution Fugro survey magnetic data (100 m line-spacing) gridded at a 25 m cell size has defined magnetic signatures at a resolution conducive to relating those signatures to relatively spatially small mineral occurrences within the Iron Mask and Cherry Creek plutons. Both plutons are characterized by strong, expansive positive magnetic signatures, distributed in linear or slightly curvilinear belts running parallel/subparallel to the length of the plutons (Fig. 3, 6).

In the case of the Iron Mask pluton, the generally northwest orientation is doubtless related to its structural setting, which is dominated by north- to northwest-trending high- and moderate-angle faults that likely controlled intrusion of various phases (Logan and Mihalynuk, 2005). Within

the pluton, the signatures are typically associated with the extensive Hybrid phase, though some correlate with smaller areas of the Pothook and Sugar Loaf phases in the northwestern portion of the pluton (Fig. 3). In sharp contrast, the Cherry Creek phase is conspicuous due to its generally muted magnetic signature.

The areas of positive magnetic expression have been examined in detail by defining individual magnetic peaks to estimate the magnitude of shorter wavelength magnetic highs and define their precise locations. This examination enables a greater understanding of the lateral changes in magnetization. Images of the first vertical derivative and tilt angle of the RTF that define short wavelength components of the magnetic field, many having a linear aspect with peaks distributed along them, were also consulted. The spatial relationship of prominent peaks with respect to mineral occurrences has been described, and a close spatial association has been observed in several cases (Fig. 5, 7). Groups of such peaks, indicating relatively high concentrations of magnetite, have been outlined for the Iron Mask pluton (Fig. 5) and the Cherry Creek pluton (Fig. 7).

In the Iron Mask pluton, the locations of Groups 1 and 2 close to many past producers and developed prospects, and to the currently producing New Afton mine (Fig. 5), provide the most persuasive evidence of a genetic connection between the development of magnetite and porphyry-type Cu-Au mineralization. Likewise, the past-producing Ajax East and Ajax West deposits fall on the margins of Groups 4 and 5, respectively. Groups 3 and 6, though they include strong peak values, do not have a close spatial relationship with any mineral occurrences of note. The Lost Chord showing is at the periphery of Group 3, whereas the closest occurrence to Group 6 is the Rogers showing, located 270 m from the group margin within a sedimentary unit of the Nicola Group (Logan et al., 2006) but hosted by andesitic volcanic rocks (British Columbia Geological Survey, 2018g). Despite the lack of mineral occurrences associated with Groups 3 and 6, it is proposed that the areas may hold potential for discovery. The same potential applies to those portions of Groups 2, 4, and 5 that are devoid of occurrences.

In the Cherry Creek pluton, the close relationship between magnetic highs and mineral occurrences is epitomized by Group 1, extending approximately 3 km toward the southeast from the Glen Iron deposit and completely enclosing the Copper King deposit near its southeast end (Fig. 6, 7). Group 2, which is significantly smaller in area, is associated with the Hilltop prospect, one of only two mineral occurrences within the pluton north of Kamloops Lake.

Whereas an unequivocal spatial link between concentrations of magnetite and porphyry-hosted mineral occurrences is apparent, how to best use this relationship to pinpoint the location of mineralization remains a question. The answer is not as simple as Sillitoe (1979) inferred, when he suggested that if the gold-rich character of a porphyry prospect is established, drilling could be focused within portions associated with the strongest magnetic response. Sillitoe noted that high gold values are present mainly in feldspar-stable alteration, commonly of the potassium silicate type. Biotite and K-feldspar (typically in subordinate amounts) are the characteristic alteration minerals. This proposal has merit if the mineralization, alteration, and magnetite-producing phases are co-spatial and coeval. Also, it might require that the various parameters influencing the mineralizing system were essentially uniform throughout, and during the life of the system, which could ensure coproduction of gold and magnetite in much the same relative quantities throughout an eventual deposit. Variation in parameters could possibly result in strong development of magnetite in one part of the system, but weak development of gold. In this situation, using a prominent magnetic signature as a vector for mineralization would be ineffective. As noted by Clark (2014) following a review of magnetic effects of hydrothermal alteration in porphyry copper and IOCG systems, it is necessary to understand the magmatic, metamorphic, and hydrothermal processes that create, alter, and destroy magnetic minerals to achieve meaningful interpretation of mineralized systems.

The fact that porphyry systems may have experienced a series of hydrothermal events is a principal obstacle in evaluating the exploration significance of magnetic signatures. For example, magnetite-rich vein systems associated with some calc-alkaline porphyry deposits may often be pre-mineralization and distinct from magnetite-biotite potassic alteration associated with sulfides and Cu-Au mineralization (Arancibia and Clark, 1996). In their study of the Island Copper porphyry copper-gold-molybdenum deposit, Vancouver Island, moderate to intense Fe metasomatism was believed to have generated early alteration, whereas a later main-stage phase of potassic alteration superimposed on the more extensive early-alteration mineralized zone is associated with the principal Island Copper deposit. Gold, which correlates overall with Cu and potassic alteration, was probably extensively introduced in the early stage of alteration. Arancibia and Clark (1996) also argued that the bulk of magnetite emplacement preceded K metasomatism and the introduction of copper sulfide.

The bulk of copper and molybdenum mineralization in the Island Copper deposit is hosted by flows and pyroclastic rocks of the Bonanza Volcanics and hydrothermal breccias surrounding a major felsic porphyry dyke containing at least 0.1% Cu, but largely sub-ore grade. Despite various episodes of hydrothermal activity, it is perhaps significant that products of the activities exhibit a general spatial coincidence, thus, magnetite as one product of alteration provides a powerful vector toward mineralization via its magnetic signature. Arancibia and Clark (1996) related alteration to a coherent, continuously evolving hydrothermal system associated with subvolcanic intrusive activity centred on the principal porphyry dyke, with superposition of alteration assemblages as a common feature.

The Iron Mask batholith has also experienced several episodes of hydrothermal activity. According to Logan and Mihalynuk (2005), three chemically distinctive hydrothermal events accompanied intrusion and fractionation of its three main phases, the Pothook, Cherry Creek, and Sugarloaf. Copper and gold mineralization are associated with at least two of these phases: the potassic alteration associated with the Cherry Creek monzonite, and the sodic alteration associated with the Sugarloaf diorite. Such alteration may be distributed along extensive belts. The New Afton deposit, for example, lies at the intersection of a corridor of potassic alteration, brittle shearing, hydrothermal breccias, and copper mineralization extending more than 5 km eastward that includes the DM, Audra, Crescent and Big Onion mineral occurrences (Fig. 2), and a corridor of albitic alteration, brittle shearing, and copper-mineralized hydrothermal breccias that includes the Pothook, Rainbow, Ajax West and Ajax East mineral occurrences extending more than 10 km southeastward.

Within these corridors the histories of alteration at several mineral occurrences have been documented in detail. Mineralization is hosted in all phases of the pluton and consists primarily of fracture-controlled chalcopyrite and bornite associated with magnetite, with pyrite, or pyrrhotite occurring peripherally (Logan and Mihalynuk, 2005). Fractures and veins are intimately associated with alteration and mineralization, and various sequences of hydrothermal veins have been documented at different occurrences. At Crescent, within the corridor of potassic alteration, Lang (1994) describes six vein types with crosscutting relationships that allow establishment of a paragenetic sequence. The ore-grade mineralization is associated with chlorite veining. Lang and Stanley (1995) reported that the DM occurrence, within the same corridor, has near-identical characteristics to those of Crescent, with precipitation of copper-gold ore during fracture-controlled potassic alteration, most strongly developed in chlorite-sulfide veins and their alteration envelopes. A series of different vein types is again a characteristic at Pothook, where Stanley (1994) concluded that gold and copper mineralization, hosted in hydrothermal breccia and iron oxide–Cu sulfide (chlorite-epidote) veins, took place after a pervasive albitic alteration, and also at Ajax East and Ajax West deposits (Ross et al., 1995).

SOURCE OF ANOMALIES HAVING ELEVATED PEAKS

Groups of elevated peak values constitute unique signatures within the Iron Mask batholith. Apart from some general correlations with specific lithological units, a link with more specific aspects of the geology is not discerned, with two exceptions: the Magnet past producer (British Columbia Geological Survey, 2018n) in the Iron Mask pluton (Fig. 5), and the Copper King past producer (British Columbia Geological Survey, 2018i) in the Cherry Creek pluton (Fig. 7) are located within the borders of groups. A series of magnetic profiles crossing peak groups in the Iron Mask pluton is displayed in Figure 8. Their paths are plotted in Figure 5. They are derived from the magnetic grid produced from the high-resolution Fugro airborne survey. All profiles are dominated by a central magnetic high, though the high of the profile across Group 6 apparently reflects the coalescence of two separate highs related to two closely adjacent sources. The estimated width at the base of this presumed composite high is much wider (1175 m) than

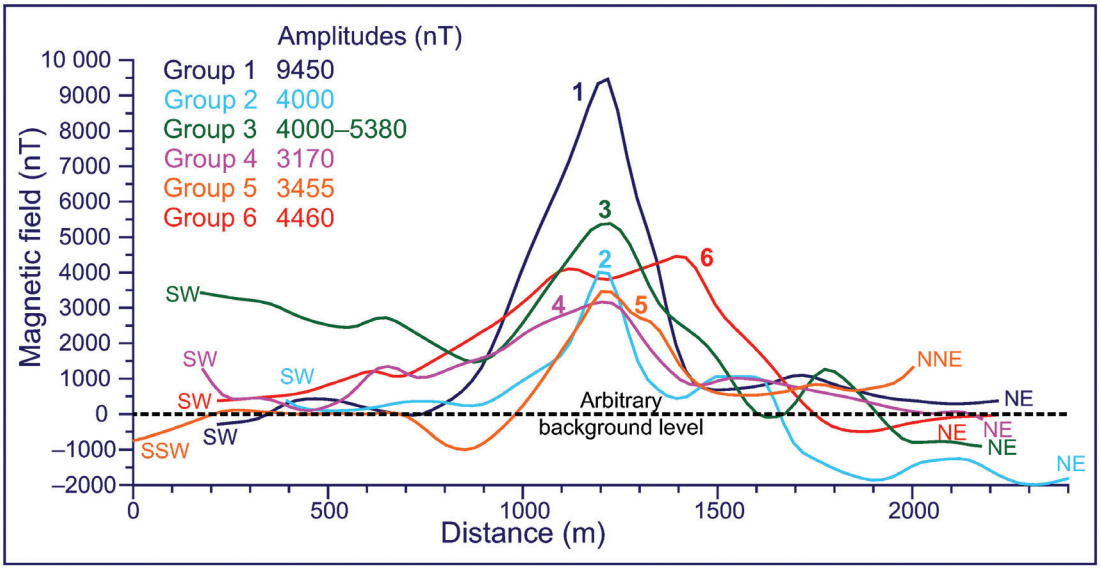

Figure 8: Series of magnetic profiles crossing the various peak groups displayed in Figure 5. Comparison of profiles is enhanced by lining up the central peaks in the profiles. SW, southwest; NE, northeast; SSW, south-southwest; NNE, north-northeast.

those of the other central highs, which are similar and range from approximately 500 to 730 m, even though the range of amplitudes of the central peaks is large: 3170 to 9450 nT.

An opportunity to investigate the potential source of one of these groups is afforded by the presence of the Magnet past producer within the area of Group 1. The investigation is enhanced by access to data collected during a detailed ground magnetic survey (Walcott, 2016, unpub. rept.) that covers most of the area of Group 1.

Model for ground magnetic data within the area of Group 1

A detailed ground magnetic and gravity survey was completed for New Gold Inc. in a small area immediately east-southeast of the New Afton pit, mainly north and northeast of the Pothook pit, with some coverage east and southeast of the Pothook pit (Walcott, 2016, unpub. rept.). The survey covers most of the area of Group 1 peak values (Fig. 5) and is located largely on a unit of Pothook diorite as mapped by New Gold Inc. (Fig. 9a, b). The northeast-trending survey lines have a nominal spacing of between 25 and 50 m, and a total length of approximately 50.5 km. Magnetic readings were taken at 1 s intervals along line, providing a high-resolution grid with a cell size of 5 m.

A total magnetic field image produced from the survey data (Fig. 9a) displays an approximately 1 km long belt of strong positive anomaly trending approximately west-northwest and passing immediately north of the Pothook pit. It trends directly toward the New Afton pit, but terminates within 200 m of the pit at the western limit of the survey. The Fugro and Kamloops survey data indicate this belt continues to just within the easternmost edge of the pit (Fig. 3). Carr and Read (1976) had noted that the Afton deposit (now the New Afton deposit) was located at the west-northwestern end of a conspicuous, 1000 m long, positive aeromagnetic anomaly reflecting a 300 m wide zone of abundant hydrothermal disseminated and vein magnetite, trending northwest from the Magnet deposit to the New Afton orebody. The anomaly terminates in the orebody due to supergene destruction of magnetite.

The belt of strong positive magnetic anomalies, which has a maximum width of approximately 500 m, can be divided into a larger southern element and much smaller northern element near its western end, separated by a narrow, slightly curvilinear magnetic low (Fig. 9a). The low is more pronounced in the east than in the west, where it trends east-west and west-northwest, respectively. Ludwig (2016a, unpub. rept.) proposed that the low might signify the presence of a major structural corridor. The southern magnetic element corresponds with the Group 1 series of peaks defined by the Fugro aeromagnetic survey (Fig. 5), with peaks defined by the ground data displayed in Figure 10a.

The northern element is represented by a single relatively narrow, slightly curvilinear belt of magnetic highs trending west to west-northwest. Its intensity is noticeably lower than the intensities of highs forming a series of narrow, subparallel and intermittently discontinuous linear magnetic highs within the broader southern magnetic element. The trends and definition of all the highs are enhanced in images of the first vertical derivative (Fig. 10b) and tilt (Fig. 10c) of the magnetic field. The highs south of the curvilinear magnetic low generally trend west-northwest in harmony with the trend of the overall composite magnetic high. These highs are transected by faults interpreted from the magnetic data. Some cut across the highs, trending north-northeast to east-northeast, some run subparallel to the essentially west-northwest trend of the highs, and a few trend approximately north-northwest. Faults with various orientations are interpreted north and south of the central belt of positive anomaly.

North and south of the principal belt of magnetic highs the magnetic field is relatively subdued and smooth, though perturbed by some low-amplitude highs. The general background level (areas of green shades, Fig. 9a) is very approximately 56 500 ± 500 nT, with values falling to less than approximately 55 000 nT within some sporadic magnetic lows. In the core area of the positive belt, peak values range generally from 60 000 nT upward; many are between 75 000 and 90 000 nT, with one peak greater than 90 000 nT (Fig. 10a). In terms of amplitude relative to the background field, several peaks have amplitudes of approximately 30 000 nT.

The past-producing Magnet deposit is located on the northern margin of the principal belt of magnetic highs (Fig. 9a) and is the only mineral occurrence associated with the belt. Young and Uglow (1926) described magnetite veins at the Magnet deposit, reporting that the magnetite is generally revealed in shallow trenches and strippings, there being few outcrops. Eight narrow magnetite veins trending mainly east-southeast, an east-trending vein, and an east-northeast-trending vein were interpreted. Widths are variable, ranging from 0.3 to 9.1 m along the length of the veins. Lengths range from a single outcrop a couple of metres long to 427 m. All veins were described to be nearly vertical.

Figure 9: a) Total magnetic field map based on ground survey by New Gold Inc. White circles with black borders indicate mineral occurrences, a legend for which is indicated in b)**.** A-B, line of magnetic model in Figure 11. North-south line labelled 677025 (UTM easting) is line along which inversion of magnetic data was completed by Ludwig (2016b, unpub. rept.). Dashed yellow line labelled F is fault interpreted by Ludwig (2016a, unpub. rept.) to separate a shallow to outcropping magnetite swarm (SOMS) to the west from a buried magnetite swarm (BMS) to the east, linked to the respective magnetic highs in those areas. HMSZ, extent of high magnetic susceptibility (> 300 × 10^{-3} SI) zone at surface defined by Ludwig's (2016b, unpub. rept.) inversion of magnetic data. **b)** Geological map of ground magnetic survey area based on maps by New Gold Inc. and Logan et al. (2006).

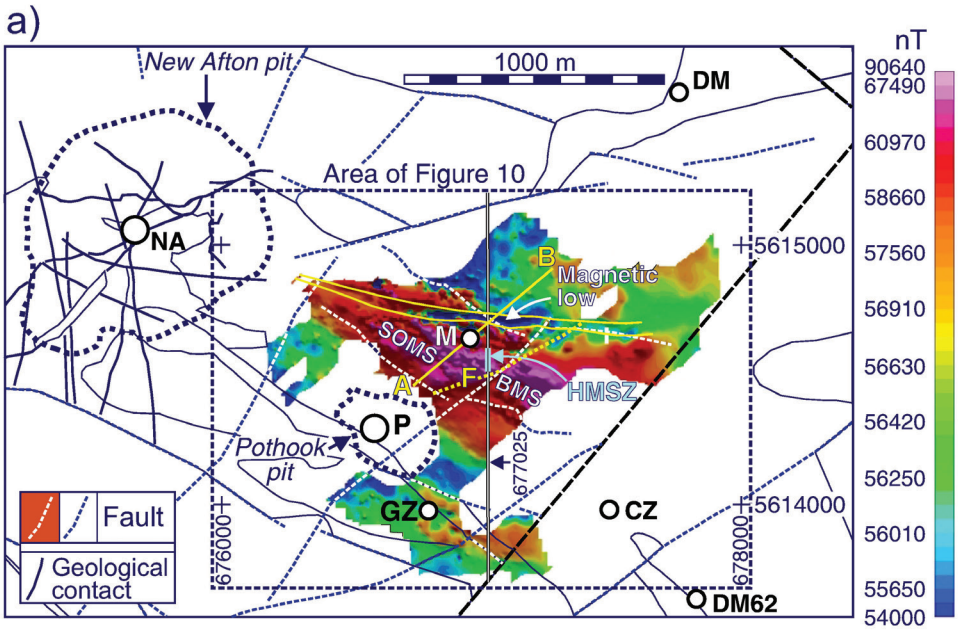

b)

New Gold Inc. legend

Eocene
Kamloops Group
Sedimentary rocks
Jurassic (?)
Conglomerate
Upper Triassic
Nicola Group
Polylithic volcanic breccia
Crystalline volcanic rocks
Picrite
Upper Triassic
Iron Mask pluton
Sugarloaf diorite
Cherry Creek monzonite
Pothook diorite

Logan et al. (2006) legend

Eocene
Kamloops Group
Undivided alkaline rocks
Late Triassic
Nicola Group
Augite porphyry, polylithic breccia
Picrite flow, breccia
Late Triassic
Iron Mask pluton
Hybrid phase
Sugarloaf phase
Cherry Creek phase
Pothook phase

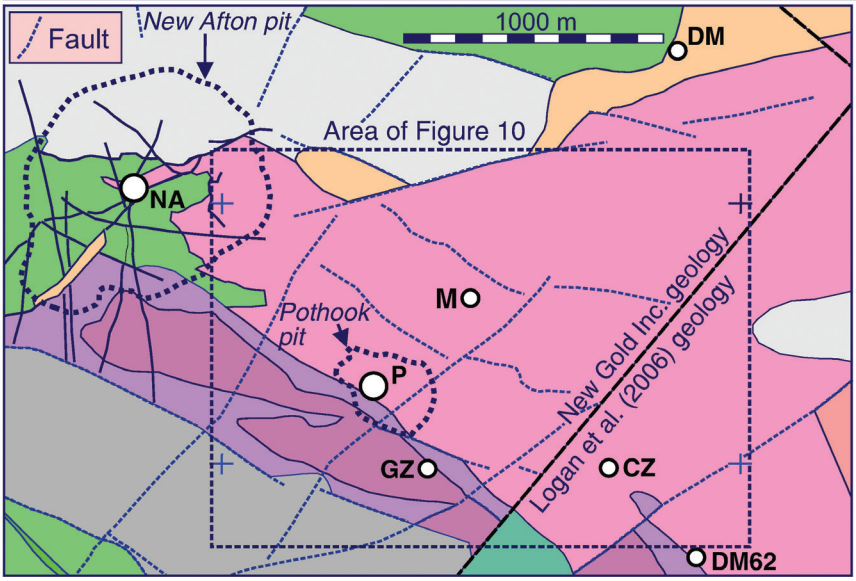

Mineral occurrences

CZ: Coquihalla Zone *(DP)*
GZ: Gold Zone *(DP)*
DM: DM *(DP)*
DM62: DM62 *(S)*
M: Magnet *(PP)*
NA: New Afton *(P)*
P: Pothook *(PP)*

P: Producer
PP: Past producer
DP: Developed prospect
S: Showing

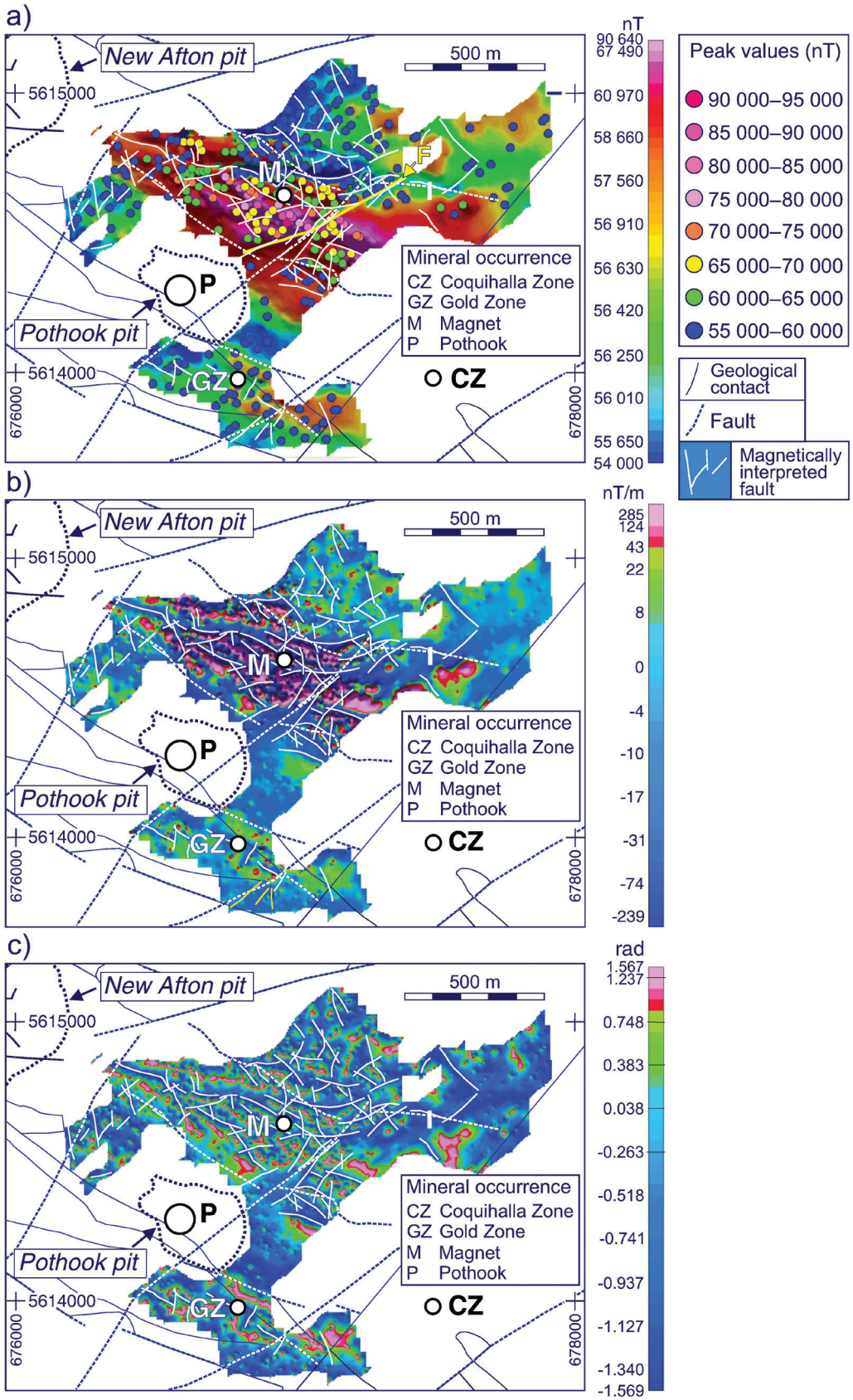

Figure 10: a) Total magnetic field with peak positions for area outlined in Figure 9. F, fault interpreted by Ludwig (2016a, unpub. rept.); **b)** 1st vertical derivative of the total magnetic field; **c)** tilt angle of the total magnetic field.

Young and Uglow (1926) observed that apatite, sometimes in considerable amounts, was commonly associated with the magnetite veins.

Cann (1979) noted that magnetite-apatite lodes (i.e. dykes) in the batholith are tabular bodies up to 200 m long and 6 m wide, containing 50 to 90% magnetite, 10 to 40% apatite, and variable amounts of amphibole. Most are steeply dipping with sharp walls. Their close association with alkaline porphyry-type copper mineralization inspired a proposal that magnetite-apatite lodes could be used as a general exploration guide. Cann (1979) concluded that magnetite-apatite and copper mineralization at the New Afton deposit are genetically linked, but not coeval, because copper mineralization and emplacement of Cherry Creek breccia are younger than magnetite-apatite lodes, with minor younger hypogene copper sulfides present within the lodes. It was believed that the same magma phase was parent to both magnetite and copper mineralization. This conclusion fosters a need to better understand the significance of magnetic signatures, such as those defined by groups of strong magnetic peaks similar to that enclosing the Magnet deposit.

The high-resolution ground magnetic data are used to derive a relatively detailed geological model from the magnetic field. A magnetic profile running southwest-northeast (Fig. 11a) was derived along line A-B passing through the location of the Magnet deposit (Fig. 9a). The geological unit present across the entire profile is the Pothook diorite. Three principal magnetic highs (*a*, *b*, *c*) are present along the southwestern half of the profile, diminishing gradually in amplitude toward the northeast, with the Magnet deposit more or less centred on anomaly *b*. Amplitudes relative to the nadir of the adjacent low to the northeast are 11 600, 10 500, and 6100 nT. The northeastern half of the profile is relatively flat and provides the background level for modelling. In this same area, the Pothook diorite has been assigned a magnetic susceptibility of 20×10^{-3} SI. This value is based on almost 24 000 measurements of drill core samples from the vicinity of the New Afton deposit (mean = 22.6×10^{-3} SI), and 467 measurements of samples of Pothook and Sugarloaf diorites (mean = 19.5×10^{-3} SI). The rounded off value 20×10^{-3} SI represents the non-anomalous background susceptibility.

The magnetic profile is modelled in terms of a series of contiguous, near-vertical, sheet-like units that explain the principal magnetic highs (Fig. 11c). It is assumed that each unit includes magnetite veins similar to those mapped at the Magnet deposit. The different susceptibilities of the sheets, considered as bulk susceptibilities, could thus reflect the variation in size and concentration of veins within the sheets. The sheets range from 12 to 36 m wide and descend essentially from ground surface, at a mean elevation of roughly 740 m above sea level, to a uniform depth of 2000 m below sea level. Upper surfaces of the units actually lie between 5 and 10 m below the ground surface, to simulate the effect of a thin veneer of overburden. The root mean square error (RMSE) of the fit between the observed and modelled profiles is 258.8 nT, which is a good match. A problem with models involving narrow, steep, sheet-like units is that the portions, below a certain critical depth, make a negligible contribution to the magnetic signature of the sheet. Decreasing the depth of the bases of the illustrated sheets from 2000 m below sea level to sea level at intervals of 1000 m produces virtually the same modelled profile, with the RMSE error varying by less than 12 nT (258.8 nT to 246.8 nT). The susceptibility of each sheet remains the same. Raising the bases by another 250 m to lie above sea level does create a noticeable change in RMSE error, which is then 356.5 nT.

It is apparent that a vertical sheet model such as that displayed in Figure 11c, for the indicated susceptibilities, would have a minimum depth to the bottom of the sheets at approximately sea level, roughly equivalent to a depth of approximately 750 m below surface. Ludwig (2016b, unpub. rept.) applied Geosoft's VOXI inversion technique to airborne magnetic data procured for New Gold Inc. in 2005 along lines spaced 100 m apart and oriented north 50° west to south 50° east; flight elevation was quoted to be 'helicopter flying heights'. The data were inverted along UTM easting 677025 passing just east of the Magnet deposit (Fig. 9a) to produce a section of susceptibility values displaying a relatively narrow zone of strong susceptibilities extending from surface to a depth of approximately 1500 m and dipping approximately 75° north. The zone is approximately 250 m wide at surface and increases in width downward to between approximately 700 and 800 m in its lower half, forming an elongate oval that widens toward one end. Characteristic of many inverted models, values increase from the core area outward to the margins, presenting an onion skin pattern. In this model susceptibility values attain a maxima of approximately 630×10^{-3} and 550×10^{-3} SI within the core at depths of approximately 100 and 500 m, respectively.

The model derived from the ground magnetic data (Fig. 11c) presents a similar picture, apart from the distribution pattern of susceptibility values. Instead of the progressive decrease in values outward from the core of the high-susceptibility zone, the ground model has values that constantly vary across the width of the high-susceptibility zone, which has the same 250 m width as the inverted model. Susceptibility values within the individual near-vertical sheets range from 50×10^{-3} to 680×10^{-3} SI, though most values are greater than 210×10^{-3} SI. The 680×10^{-3} SI value is for a near-vertical sheet located within the span of the largest of the three prominent magnetic highs (*a*). Other high susceptibility values for sheets associated with the magnetic highs are 610×10^{-3}, 500×10^{-3}, 385×10^{-3}, and 370×10^{-3} SI, which are consistent with susceptibilities in the inverted model (Ludwig, 2016b, unpub. rept.). The Magnet deposit is located at the southern edge of a 35 m wide sheet with a susceptibility of 610×10^{-3} SI (magnetite content = 19.4%) that is mainly responsible for producing the magnetic high *b* (Fig. 11a). The magnetite dykes defining the deposit (maximum width 9.1 m; Young and Uglow, 1926), do not produce visible individual signatures in this ground magnetic survey, presumably because of their narrow widths.

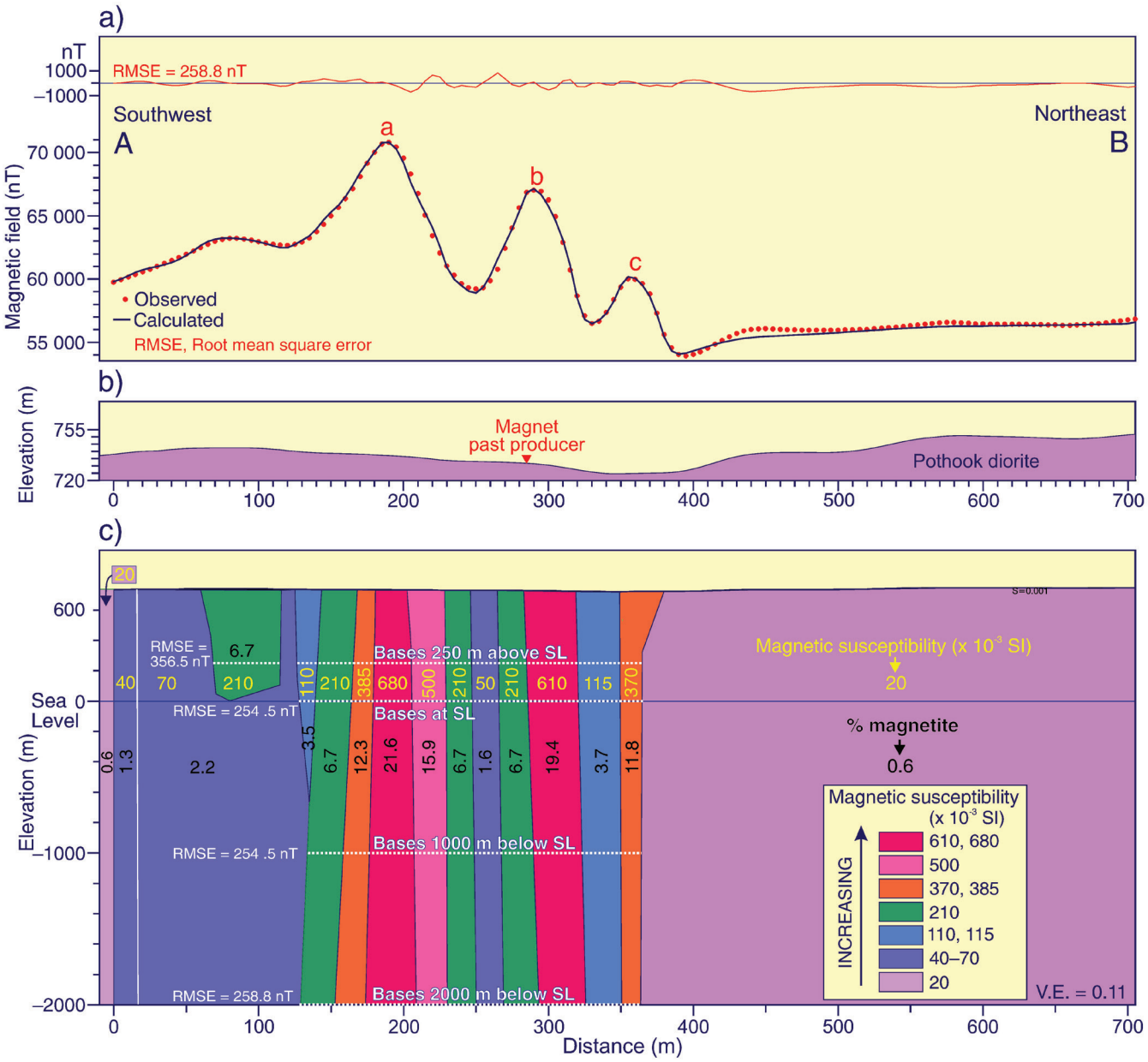

Figure 11: a) Modelled magnetic profile along Line A-B of Figure 9a. **b)** Near-surface geological section. **c)** Magnetic model; the root mean square error (RMSE) for different depths to the bottoms of modelled units is indicated, along with the corresponding positions of the bottoms. V.E., vertical exaggeration.

Transformation of Ludwig's (2016b, unpub. rept.) susceptibility model into percentages of magnetite produces values of approximately 20 and 17% magnetite within the two zones corresponding to the susceptibility maxima, with values decreasing gradually toward the margins of the high-susceptibility zone. Magnetite percentages for the current model were calculated using a formula originally derived by Balsley and Buddington (1958) and modified by McCafferty et al. (2004). Model units co-located with the three prominent magnetic peaks (*a*, *b*, *c*; Fig. 11) have magnetite percentages ranging from 11.8 to 21.6%, and include values similar to those of Ludwig's (2016b, unpub. rept.) model. The current sheet-like model has a different geological significance from that of Ludwig's (2016b, unpub. rept.) onion skin model, that essentially represents a single body within which the susceptibility decreases from the core to the margins. The current model predicts separate contiguous sheets, each of which is believed to include distributed individual magnetite veins. The susceptibility of a sheet represents the weighted mean susceptibility of susceptibilities of veins and relatively non-magnetic host rock. In an earlier qualitative interpretation of the ground magnetic data, Ludwig (2016a, unpub. rept.) defined a northeast-trending fault seemingly sinistrally offsetting the broad

southern portion of the principal belt of magnetic highs (Fig. 9a). West of the fault, Ludwig (2016a, unpub. rept.) noted that linear trends of magnetic highs produced a well-defined, west-northwest-trending grain, attributed to a shallow to outcropping magnetite 'swarm' (SOMS; Fig. 9a). This description is compatible with the near-vertical, sheet-like units of the model in Figure 11c. East of the fault, there are fewer magnetic highs across the width of the belt, though some are very strong, and the magnetic field was related to a buried magnetite swarm (BMS, Fig. 9a). Values of magnetic peaks differ little from west to east across the fault (Fig. 10a), suggesting that magnetite burial on the eastern side of the fault may also be reasonably shallow.

The magnetic model for the Group 1 peaks considered in the context of an essentially co-spatial magnetite vein system provides a geologically reasonable explanation for the magnetic highs within Group 1. It is proposed that the similarity in width of the principal magnetic high in the airborne profile across Group 1 to highs in profiles across other groups (Fig. 8) provides a rationale for considering veins and/or thin dykes of magnetite as the source for all the groups. Though the amplitude of the airborne high associated with Group 1 is exceptionally large (more than two or three times that of the other group highs) it does not rule out a presence of smaller magnetite vein systems. This possibility was investigated by modelling one of the airborne profiles, that across Group 2, to determine the nature of bodies and their susceptibilities that could reproduce the central high.

Model for Group 2 airborne peak profile near past producer Crescent

A 2000 m long magnetic profile crossing the Group 2 peaks (*see* Fig. 5 for location) is displayed in Figure 12a, and the derived model is in Figure 12b. Approximately two-thirds of the southwest-northeast profile crosses the Pothook dioritic phase before traversing the monzonitic to monzodioritic Cherry Creek phase at the northeast end. A prominent high, amplitude roughly 4000 nT relative to the background magnetic field to the southwest, lies near the centre of the

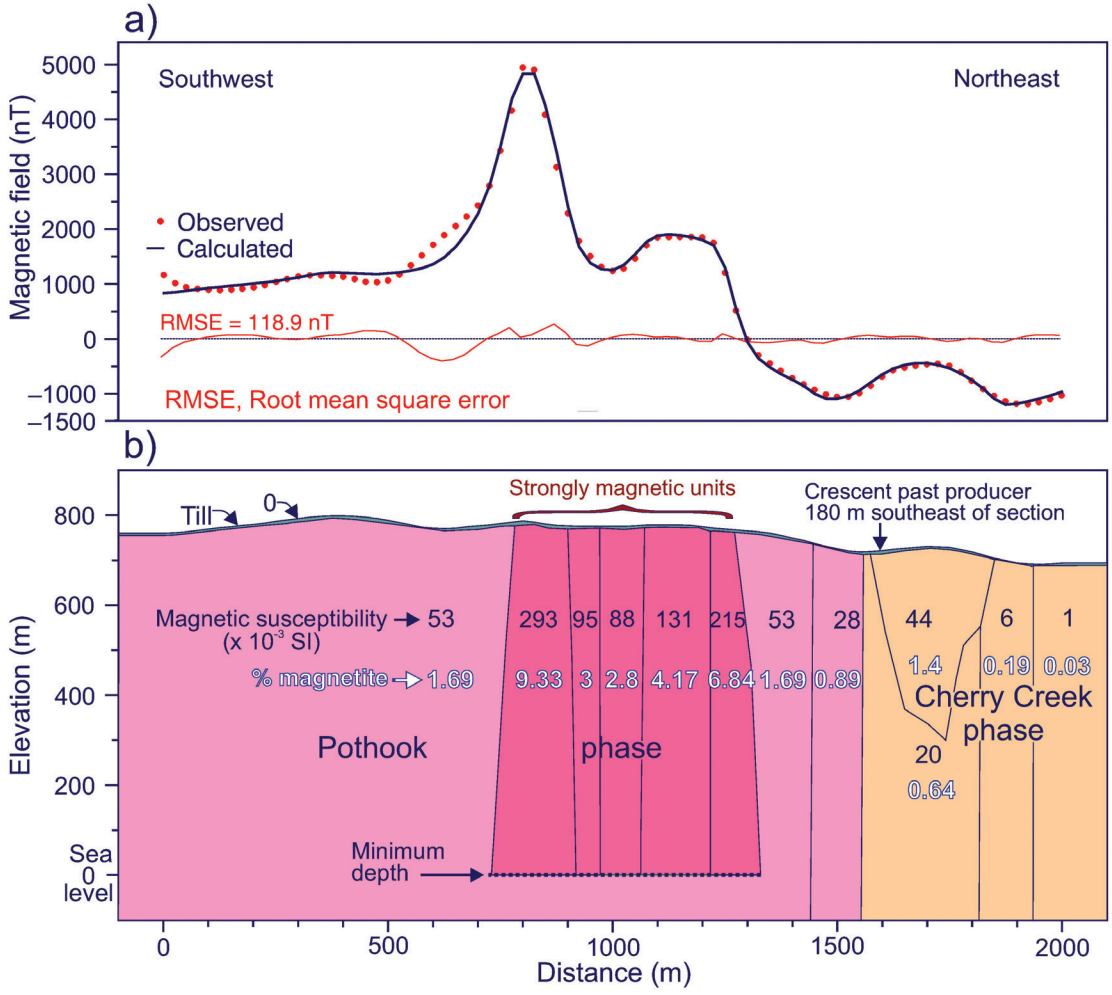

Figure 12: a) Modelled magnetic profile crossing peaks Group 2 (Fig. 5). **b)** Model derived from profile in a). The Pothook and Cherry Creek phases extend to a depth of 5000 m below sea level.

Pothook phase. It is flanked to the northeast, within the Pothook phase, by a conspicuous high with a much lower amplitude of almost 1000 nT relative to the same background. The magnetic field decreases significantly over the northeastern margin of the Pothook phase and the adjoining Cherry Creek phase, within which, with the exception of a broad low-amplitude high, it lies approximately 2000 nT lower than over the southwestern half of the Pothook phase.

The change in level is modelled essentially in terms of a large difference in the magnetic susceptibilities of the two plutonic phases. An arbitrary susceptibility of 20×10^{-3} SI and depth below surface of 5700 m was assigned to the Cherry Creek phase. The depth is similar to that modelled for a profile crossing the Iron Mask pluton farther to the southeast (Thomas, 2019). The base of the Pothook phase was set at the same level, and its susceptibility (53×10^{-3} SI) was determined during the modelling process, which sought as one objective to explain the generally higher magnetic field over this phase (Fig. 12b). The central magnetic high is explained by a narrow (average width $\approx$ 1700 m) vertical block with a strong magnetic susceptibility of 293×10^{-3} SI that descends from near surface to a depth of almost 780 m. An approximately 5 to 10 m thick surficial bed of non-magnetic overburden has been arbitrarily introduced into the model to simulate glacial till in the area. Several other vertical blocks are modelled within the Pothook phase to explain the magnetic high that is flanking the central magnetic high to the northeast, descending to the same depth as that explaining the central high. These have susceptibilities ranging from 88 to 215×10^{-3} SI. The modelled depth of the bottoms of these vertical blocks is considered the critical depth below which deepening of the blocks would not significantly change the magnetic response; hence, it is considered a minimum depth. During the modelling process, the original susceptibility of 20×10^{-3} SI assigned to the Cherry Creek phase was lowered to 6×10^{-3} and 1×10^{-3} SI in the northeastern margin of the phase.

Using the formula by McCafferty et al. (2004) the two largest susceptibilities, 215×10^{-3} SI and 293×10^{-3} SI, indicate magnetite contents of 6.8 and 9.3%, respectively, the latter being within the unit associated with the central magnetic high. These are much lower than the values ranging from 15.9 to 21.6% corresponding to the three highest susceptibilities modelled for the ground magnetic profile crossing Group 1. Nevertheless, they point to possible higher magnetite percentages within magnetic veins and/or dykes, as observed at the Magnet deposit. Considering the similarity in widths and amplitudes of principal magnetic highs along profiles crossing other peak groups (Fig. 8), concentrations of magnetic veins as a source of the observed magnetic highs are a reasonable geological explanation. If such dykes exist in proximal locations to Cu-Au mineral showings, what is their significance for mineral exploration?

SIGNIFICANCE OF MAGNETITE DYKES FOR CU-AU EXPLORATION

Despite the relatively intricate hydrothermal histories of mineral occurrences in the Iron Mask batholith, the association of magnetite with mineralization is spatially and apparently temporally close. Thus, magnetic surveys have a critical role in exploration of porphyry deposits. A challenge is how to derive the best information from the magnetic perspective.

A reasonably close spatial association between groups of strong magnetic peaks and mineral occurrences within the Iron Mask batholith has been noted (Fig. 4–7); however, with the exception of the Copper King (Cu, Au, Ag, U) and Magnet (mainly magnetite) past producers, the mineral occurrences are peripheral to the areas covered by the groups. The argument that they probably relate to concentrations of magnetite dykes has been presented. If this is true, what, if any, is the significance of these strong magnetic signatures for exploration of porphyry deposits?

Cann (1979) noted that magnetite-apatite lodes (dykes) in the batholith occur in close association with alkaline porphyry-type copper mineralization, disseminated magnetite-rich diorite, and late syenite, prompting a proposal that they could be used as a general exploration guide. Lode and disseminated magnetites were studied using atomic absorption spectrophotometry to examine several elements with a view to establishing a genetic model; several samples were also analyzed for minor and major oxides using an electron microprobe. Minor element data indicate that the lodes formed by magmatic injection subsequent to concentration of magnetite by immiscibility between magnetite-apatite and an alkalic magma. Cann (1979) proposed that the Pothook diorite developed by settling of plagioclase and pyroxene crystals within an early magma, leading to enrichment of iron and alkalis in a residual magma; the early magma also differentiated towards the experimentally determined magnetite-apatite eutectic composition. Following crystallization of the Pothook diorite, magnetite and apatite separated from the silicate magma, together forming an immiscible melt and settling on the floor of the magma chamber. This melt was subsequently injected into fractures, forming lodes after the adjacent younger Cherry Creek magma had largely crystallized (Cann, 1979).

Explosively emplaced breccia within the Cherry Creek phase and associated copper mineralization are attributed to a vapour bubble formed during the final stages of crystallization (Cann, 1979). Mineralization at the New Afton deposit is hosted in shattered rocks centred on such an intrusive breccia, and the deposit is contained within a 300 m wide zone of abundant magnetite that extends southeast to the Magnet mineral occurrence. Magnetite-apatite and copper mineralization at the New Afton deposit are believed to be genetically related, but not coeval, because copper mineralization and breccia emplacement are younger than the

magnetite-apatite lodes (Cann, 1979). The same magma phase was believed to be parent to both magnetite and copper mineralization.

Logan and Mihalynuk (2005) are in general agreement with Cann's (1979) temporal sequence of mineralization, noting that magnetite veins in the New Afton pit predate and accompany copper mineralization, and may be part of the same event that produced dilational veins at the Magnet mine; however, they do not favour magmatic injection as the process involved in creation of magnetite lodes, preferring a hydrothermal origin. Magnetite-apatite-actinolite-epidote veins at the New Afton pit and the Magnet occurrence are described as hydrothermal, and no significant amount of copper or gold was introduced during this early hydrothermal event. At the Pothook deposit, copper-gold mineralization postdates development of magnetite-apatite-actinolite veins (Stanley, 1994).

Based on these examples of mineral paragenesis in the Iron Mask batholith, it is reasonable to assume Cu-Au mineralization and magnetite-apatite mineralization may be linked to the same episode of magmatic-hydrothermal activity, with magnetite mineralization preceding Cu-Au mineralization. Richards et al. (2016) noted that Cu±Mo±Au (porphyry) and IOCG deposits share several key characteristics, particularly enrichments in Cu, Au, and Fe. The principal difference is in their respective predominant form of iron, with Fe sulfides predominating in porphyry deposits and Fe oxides (magnetite and hematite) in IOCG deposits. Because magnetite-apatite deposits are perhaps more commonly associated with IOCG deposits than with porphyry deposits, the relationship between magnetite-apatite dykes and Cu-Au mineralization associated with IOCG deposits may provide insight into the significance of magnetite-apatite dykes for exploration of porphyry Cu-Au deposits. Some examples of IOCG magnetite-apatite deposits (IOA) are now examined (Knipping et al., 2015a; Edfelt, 2007).

Some characteristics of magnetite-apatite mineralization associated with iron oxide-copper-gold deposits

Knipping et al. (2015a) investigated the formation and evolution of the Los Colorados IOA deposits in northern Chile through the geochemistry of magnetite with research that included targeting certain trace elements. Results are consistent with a magmatic-hydrothermal model for formation of IOA deposits proposed by Knipping et al. (2015b), involving crystallization of magnetite microlites from a silicate melt, nucleation of aqueous fluid bubbles on magnetite surfaces, and formation and ascent of buoyant fluid bubble-magnetite aggregates. The aggregates ascended through hydraulic fractures along the Atacama fault system, producing dyke-shaped Fe deposits. The magnetite dykes and an adjacent brecciated dioritic intrusion have similar radiometric ages, implying a possible genetic association. Magnetite from the diorite indicates lower temperature hydrothermal processes characteristic of IOCG deposits that are often observed in close relationship with IOA deposits. Knipping et al. (2015a) concluded that an IOCG deposit located laterally to, or stratigraphically above, an IOA system is a possibility, and that an underlying intrusion could provide sufficient Fe for both types of deposit.

In Sweden, Edfelt's (2007) study of the Tjårrojåkka apatite-iron and copper (-gold) deposits revealed similarities in stable isotope and fluid composition, temperature of ore deposition, and ages and assemblages of alterations and mineralization, indicating a genetic link between at least some of these deposit types. Mineralization is ascribed to two stages, with an earlier magnetite ore stage (I) and subsequent, overlapping, copper (chalcopyrite) ore stage (II); there are also two post-ore stages (III and IV). The δD_{H2O} values of fluids from the two deposits overlap, implying the same origin for the fluids involved in their formation. The trend of $\delta^{34}S$ values becomes increasingly larger from stage I to stage III of the paragenesis, suggesting that all mineralization was related to a single evolving system.

Arguments for a single system have been made also by Sillitoe (2003). He considered that the close association between magnetite-dominated IOCG and massive magnetite-(apatite) veins containing minor copper in several districts may signify that the two deposit types are transitional and that copper contents of IOCG veins may decrease downward with the development of massive magnetite veins. The district- and deposit-scale geological evidence, especially the intimate association between IOCG and massive magnetite deposits in parts of the Coastal Cordillera, does not support radically different fluid sources for the two deposit types.

The examples of Cu-Au and magnetite-apatite mineralization within the porphyry-type Iron Mask batholith and within areas of IOCG-type mineralization consistently suggest development of both types of mineralization being related to a single intrusive event, whether mineralization is magmatic, hydrothermal, or magmatic-hydrothermal. Depending on the many physical and chemical factors that influence development of a particular mineral(s) in intrusive systems, this provides encouragement that where one type of mineralization is present, the other type may also be present; however, a consistent pattern in the spatial distribution of the two types of mineralization is apparently not recognized, other than IOA deposits seemingly being generated at lower levels than IOCG deposits. Knipping et al. (2015a) pointed to experimental data supporting the scavenging of significant quantities of metals, for example, Cu and Au from a silicate melt by a saline magmatic-hydrothermal ore fluid. When combined with solubility data for Fe, Cu, and Au, it was considered reasonable that ore fluid continuing to rise from the IOA depositional environment can retain sufficient concentrations of these metals to form IOCG deposits at lateral and/or stratigraphically higher levels in the crust. As previously noted, Sillitoe (2003) also concluded that IOA

deposits developed at a lower crustal level than associated IOCG deposits. The scenarios of Knipping et al. (2015a) and Sillitoe (2003), if also applicable to porphyry deposits, are not entirely encouraging for exploration using magnetite-apatite mineralization as a guide because the presence of such mineralization near or at surface could mean that higher level Cu-Au mineralization has been eroded.

On a more positive note, Knipping et al. (2015a) concluded that an IOCG deposit located laterally to an IOA system is a possibility. In this regard, in the Iron Mask batholith, the New Afton deposit is located laterally to the Magnet magnetite-apatite deposit, near the end of the linear magnetic high passing through the Magnet deposit. Several other mineral occurrences in the Iron Mask batholith are also positioned laterally to groups of prominent magnetic highs (Fig. 5, 7). Modelling of a ground magnetic profile crossing Group 1 and of an airborne magnetic profile crossing Group 2 in the Iron Mask pluton presents reasonably strong evidence that the groups may relate to concentrations of magnetite veins or small dykes that could represent IOA-type mineralization. If this is the case, and the peak groups signal proximity to porphyry deposits, detailed multidisciplinary ground investigations are required in such presumed favourable areas. A method having good potential for such follow-up exploration is afforded by radiometric surveys, examined briefly below.

RADIOMETRIC SIGNATURES

The association of potassic alteration with some of the mineral occurrences in the Iron Mask pluton provides another avenue for exploration, namely via radiometric surveys that measure potassium (K), equivalent thorium (eTh), and equivalent uranium (eU). Shives et al. (1997) reported that many alkaline and calc-alkaline porphyry Au-Cu (±Mo) deposits are associated with extensive potassic hydrothermal alteration halos. Elevated potassium values do not necessarily signify related alteration but could relate to intrinsic lithological variations. This ambiguity can often be resolved by examining Th-K ratios because thorium is relatively stable during hydrothermal alteration and Th-K ratios are likely to decrease in localities subjected to potassic alteration (i.e. addition of potassium). Concentrations of low ratios (Th-K lows) could, therefore, correlate with areas of alteration and related mineralization. It is cautioned that radiometric signatures related to surficial glacial deposits may be displaced from any actual bedrock source for materials within the deposits producing the signatures. The map by Ferbey et al. (2013) shows ice-flow directions in the area of the batholith as being directed between approximately south-southeast and east-southeast.

Shives et al. (1995) reported on radiometric data measured at a mean terrain clearance of 120 m in a multiparameter survey (500 m line-spacing) of the batholith flown in 1993 (Shives and Carson, 1995). They noted that strong correlations between Th-K lows and flanking positive magnetic anomalies were associated with alteration related to mineralization in the areas of the New Afton, Ajax East, and Ajax West deposits, further stating that virtually every known deposit has this signature and that new targets were evident in several areas. The Kamloops survey provided slightly better resolution, having 400 m line-spacing, though flight elevation was practically the same (125 m).

A map of the Th-K ratio is shown in Figure 13. Distinct areas of low Th-K ratio are defined essentially by ratios less than the contour value of 2, displayed as dark blue areas, which cover approximately half of the Iron Mask pluton. The lows do not display any close correlation with the various phases of the pluton, falling equally within the intermediate Pothook, Sugarloaf, and Hybrid phases (typically dioritic) and the somewhat more acidic Cherry Creek phase (typically monzonitic), and frequently crossing contacts between phases at high angles. Remarkably, 40 of the 50 mineral occurrences displayed in this figure fall within, or are right at the edge of, these Th-K lows. Of the 16 past producers or developed prospects, only Iron Mask and Big Onion are not associated with a Th-K low. Although Shives et al. (1995) reported that alteration related to mineralization was associated with strong correlations between Th-K lows and flanking positive magnetic anomalies, it seems that, more specifically, the more intense magnetic highs are essentially co-located with Th-K lows. With the exception of Group 2, all groups of magnetic peaks in the Iron Mask pluton fall within Th-K lows.

A corridor of potassium alteration trending eastward from the New Afton deposit and encompassing the DM, Audra, Crescent, and Big Onion mineral occurrences (Logan and Mihalynuk, 2005) is partially reflected in the Th-K image as a distinct low trending northeast from the Pothook occurrence for approximately 3 km and ending at the Crescent occurrence. The low does not continue eastward to the Big Onion occurrence, approximately 2.5 km away, which falls on a Th-K high. A similar pattern is observed in an image of K values. Curiously, the New Afton deposit, reported to fall at the intersection of the K corridor with a northwest-trending corridor of albitic alteration (Logan and Mihalynuk, 2005), coincides with a local Th-K high (Fig. 13) and a K high. A belt of two Th-K lows extending southeast from the vicinity of the Rainbow developed prospect encompasses three nearby showings west-northwest of Wallender Lake and continues to Jacko Lake, where it swings east to include the Ajax West and Ajax East past producers. From Ajax East the belt broadens significantly as it extends both east-northeast and north-northeast to occupy much of the marginal area of the Iron Mask pluton along its eastern boundary. Notable mineral occurrences within this area of Th-K lows are the Python past producer and Kimberley developed prospect.

The pattern of Th-K variations is noticeably similar to the pattern over the mainly mafic Nicola Group volcanic rocks southwest of the Iron Mask pluton; however, because of the volcanic nature of the terrain in this area, the

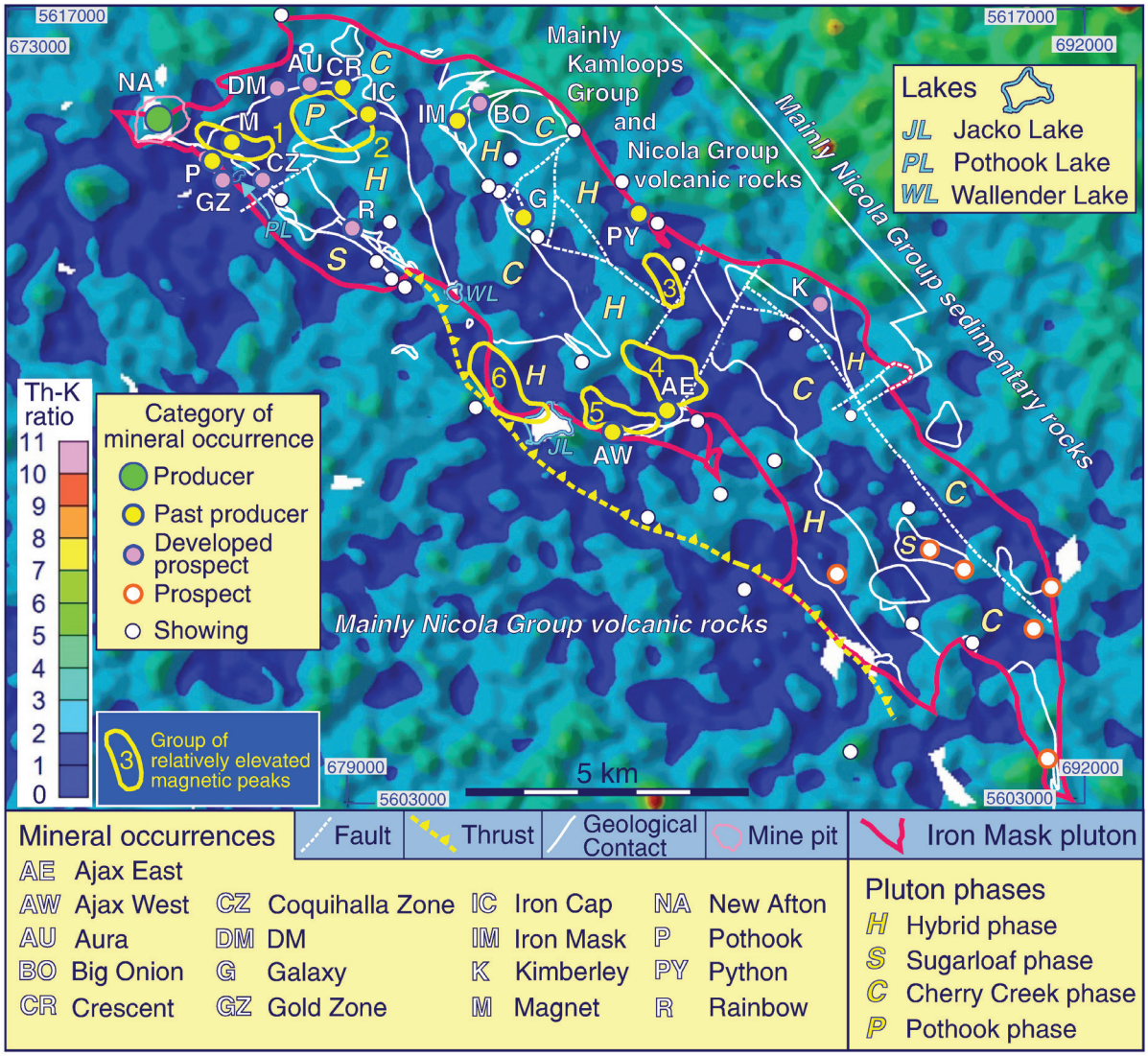

Figure 13: Map of Th-K ratio for the Iron Mask pluton displaying locations of mineral occurrences, areas of relatively elevated magnetic peak values, geological contacts and faults within the pluton; phases of the pluton are identified

significance of the Th-K lows is probably different from that of the lows within the pluton. Killeen's (1979) table of values for radio-element concentrations in different rock type categories indicates that intermediate intrusive rocks have noticeably higher values of K (2.1%) and Th (12.2 ppm), than intermediate extrusive rocks, which have 1.1% and 2.4 ppm, respectively; hence, even without the addition of hydrothermal potassium, the extrusive varieties would theoretically produce a lower Th-K ratio (2.18) than their intrusive counterparts (5.81). The Th-K ratio for basic extrusive rocks (K 0.7%, Th 2.2 ppm) is 3.14. It is difficult, therefore, to attach significance to the patterns of Th-K ratio over the Nicola Group intermediate-basic volcanic rocks, other than to conjecture that they reflect heterogeneity within the volcanic sequences and perhaps a variable presence of sedimentary rocks.

The production of potassium and magnetite related to hydrothermal alteration associated with porphyry-related mineralization, and the described spatial relationships of peak magnetic highs, potassium, and Th-K ratios within the Iron Mask batholith make a compelling case for the inclusion of magnetic and radiometric surveys in exploration strategies for porphyry deposits.

DISCUSSION AND CONCLUSIONS

Despite the relatively intricate hydrothermal histories of mineral occurrences in the Iron Mask batholith, the association of magnetite with porphyry-type mineralization is spatially and possibly temporally close. Lang (1994), for example, noted early K metasomatism at the Crescent

deposit being "closely followed in sequence" by a variety of vein types including magnetite and Cu ore-bearing chlorite-sulfide veins. Magnetic surveys have a critical role in exploration of porphyry deposits, a strategy seemingly founded on Sillitoe's (1979) observation of the common association of significant quantities of magnetite with potassium silicate alteration in gold-rich porphyry copper deposits. More specifically, Sillitoe (1979) suggested that airborne magnetic surveys could be effective in locating deposits, and that if the gold-bearing character of a prospect could be established, drilling could be focused in the vicinity of the highest magnetic response. This strategy may apply to instances of 'well-behaved' porphyry mineralization within stock-like intrusions having symmetrical, concentric alteration-mineralization zones as envisaged in the ovoid porphyry model of Lowell and Guilbert (1970); however, in reality, porphyritic intrusions do not always conform to this type model and may be complex in terms of structure, composition, and the number of phases of intrusion and hydrothermal activity, all of which, individually or in concert, can disrupt initially simple mineralogical or geochemical patterns. The Iron Mask pluton does not conform to the typical concentric model of Lowell and Guilbert (1970), but rather is an elongate intrusion composed in large part of subparallel, belt-like intrusive phases. Despite this difference, magnetite in significant quantities is present.

Notwithstanding potential complications related to nonconformity of an intrusion with a type intrusion, the documented association of magnetite and gold-rich porphyry copper deposits, and of magnetite-apatite deposits (IOA) with porphyry and IOCG deposits, dictates that targeting magnetite via distinct magnetic anomalies in the search for porphyry deposits is a critical element in exploration. The study of relationships between prominent magnetic highs and porphyry Cu-Au mineral occurrences in the alkalic Iron Mask batholith supports this approach. A substantial number of occurrences are positioned peripherally to clusters of prominent magnetic peaks with the nearest located an average of approximately 500 m from the centre of a cluster. These spatial relationships are encouraging from the viewpoint of magnetic exploration, dramatically reducing the size of an area for follow-up exploration.

The alkalic Iron Mask batholith is radically different from the concentric, alteration-mineralization, stock-like porphyry intrusion model of Lowell and Guilbert (1970). It is an elongate intrusion with a length-to-width ratio of approximately 7:1, is composed mainly of dioritic rocks rather than the typical quartz monzonite of the model, and more than 50 mineral occurrences are scattered throughout, in contrast to the apparently singular orebodies associated with the Lowell and Guilbert (1970) model. The common trait of both types of Cu-Au host is the close spatial and genetic association of Cu-Au mineralization with magnetite (plus apatite) mineralization. Thus, magnetic surveys offer a critical approach in exploration strategies directed toward the discovery of porphyry-type deposits, regardless of the nature of the hosting intrusion. The presence of hydrothermal potassium in alteration zones associated with such deposits provides another avenue for exploration through delineation of Th-K lows, yielding information complementing the magnetic signatures. Both types of data can be rapidly collected in a single combined magnetic-radiometric airborne survey.

ACKNOWLEDGMENTS

I thank my colleague, Ernst Schetselaar, for his insightful review of the manuscript, and related comments and suggestions. I also thank Devin Wade at New Gold Inc., Kamloops, British Columbia, for providing information on rock properties and a high-resolution magnetic data set covering much of the Iron Mask batholith, and ground gravity and magnetic data near the New Afton pit. My thanks to Chris Ludwig, consulting geophysicist, Denver, Colorado, consultant to New Gold Inc., for his insight into interpretation of the ground data sets.

REFERENCES

Arancibia, O.N. and Clark, A.H., 1996. Early magnetite-amphibole-plagioclase alteration-mineralization in the Island Copper porphyry copper-gold-molybdenum deposit, British Columbia; Economic Geology, v. 91, no. 2, p. 402–438. https://doi.org/10.2113/gsecongeo.91.2.402

Balsley, J.R. and Buddington, A.F., 1958. Iron-titanium oxide minerals, rocks, and aeromagnetic anomalies of the Adirondack area, New York; Economic Geology, v. 53, no. 7, p. 777–805. https://doi.org/10.2113/gsecongeo.53.7.777

British Columbia Geological Survey, 2018a. MapPlace GIS internet mapping system; British Columbia Ministry of Energy, Mines and Petroleum Resources, British Columbia Geological Survey. <http://www.MapPlace.ca> [accessed February 14, 2019]

British Columbia Geological Survey, 2018b. Mineral inventory; British Columbia Ministry of Energy, Mines and Petroleum Resources, British Columbia Geological Survey. <https://www2.gov.bc.ca/gov/content/industry/mineral-exploration-mining/british-columbia-geological-survey/mineralinventory> [accessed February 14, 2019]

British Columbia Geological Survey, 2018c. MINFILE 092INE010 record summary, MINFILE BC mineral deposits database; British Columbia Ministry of Energy, Mines and Petroleum Resources, British Columbia Geological Survey. <https://minfile.gov.bc.ca/Summary.aspx?minfilno=092INE010> [accessed February13, 2020]

British Columbia Geological Survey, 2018d. MINFILE 092INE002 record summary, MINFILE BC mineral deposits database; British Columbia Ministry of Energy, Mines and Petroleum Resources, British Columbia Geological Survey. <https://minfile.gov.bc.ca/Summary.aspx?minfilno=092INE002> [accessed February 14, 2020]

British Columbia Geological Survey, 2018e. MINFILE 092INE013 record summary, MINFILE BC mineral deposits database; British Columbia Ministry of Energy, Mines and Petroleum Resources, British Columbia Geological Survey. <https://minfile.gov.bc.ca/Summary.aspx?minfilno=092INE013> [accessed February 14, 2020]

British Columbia Geological Survey, 2018f. MINFILE 092INE023 record summary, MINFILE BC mineral deposits database, British Columbia Ministry of Energy, Mines, and Petroleum Resources, British Columbia Geological Survey. <https://minfile.gov.bc.ca/Summary.aspx?minfilno=092INE023> [accessed February 13, 2020]

British Columbia Geological Survey, 2018g. MINFILE 092INE098 record summary, MINFILE BC mineral deposits database; British Columbia Ministry of Energy, Mines and Petroleum Resources, British Columbia Geological Survey. <https://minfile.gov.bc.ca/Summary.aspx?minfilno=092INE098> [accessed February 15, 2020]

British Columbia Geological Survey, 2018h. MINFILE 092INE025 record summary, MINFILE BC mineral deposits database; British Columbia Ministry of Energy, Mines and Petroleum Resources, British Columbia Geological Survey. <https://minfile.gov.bc.ca/Summary.aspx?minfilno=092INE025> [accessed February 15, 2020]

British Columbia Geological Survey, 2018i. MINFILE 092INE024 record summary, MINFILE BC mineral deposits database; British Columbia Ministry of Energy, Mines and Petroleum Resources, British Columbia Geological Survey. <https://minfile.gov.bc.ca/Summary.aspx?minfilno=092INE024> [accessed February 15, 2020]

British Columbia Geological Survey, 2018j. MINFILE 092INE031 record summary, MINFILE BC mineral deposits database; British Columbia Ministry of Energy, Mines and Petroleum Resources, British Columbia Geological Survey. <https://minfile.gov.bc.ca/Summary.aspx?minfilno=092INE031> [accessed February 15, 2020]

British Columbia Geological Survey, 2018k. MINFILE 092INE055 record summary, MINFILE BC mineral deposits database; British Columbia Ministry of Energy, Mines and Petroleum Resources, British Columbia Geological Survey. <https://minfile.gov.bc.ca/Summary.aspx?minfilno=092INE055> [accessed February 15, 2020]

British Columbia Geological Survey, 2018l. MINFILE 092INE032 record summary, MINFILE BC mineral deposits database; British Columbia Ministry of Energy, Mines and Petroleum Resources, British Columbia Geological Survey. <https://minfile.gov.bc.ca/Summary.aspx?minfilno=092INE032> [accessed February 15, 2020]

British Columbia Geological Survey, 2018m. MINFILE 092INE029 record summary, MINFILE BC mineral deposits database; British Columbia Ministry of Energy, Mines and Petroleum Resources, British Columbia Geological Survey. <https://minfile.gov.bc.ca/Summary.aspx?minfilno=092INE029> [accessed February 15, 2020]

British Columbia Geological Survey, 2018n. MINFILE 092INE022 record summary, MINFILE BC mineral deposits database; British Columbia Ministry of Energy, Mines and Petroleum Resources, British Columbia Geological Survey. <https://minfile.gov.bc.ca/Summary.aspx?minfilno=092INE022> [accessed February 15, 2020]

Cann, R.M., 1979. Geochemistry of magnetite and the genesis of magnetite-apatite lodes in the Iron Mask batholith, British Columbia; M.Sc. thesis, The University of British Columbia, Vancouver, British Columbia.

Carr, J.M. and Reed, A.J., 1976. Afton: A supergene copper deposit; *in* Porphyry deposits of the Canadian Cordillera, (ed.) A. Sutherland Brown; Canadian Institute of Mining and Metallurgy, Special Volume 15, p. 376–387.

Clark, D.A., 2014. Magnetic effects of hydrothermal alteration in porphyry copper and iron-oxide copper–gold systems: A review; Tectonophysics, v. 624–625, p. 46–65. https://doi.org/10.1016/j.tecto.2013.12.011

Edfelt, Å., 2007. The Tjårrojåkka apatite-iron and Cu (-Au) deposits, northern Sweden. Ph.D. thesis, Luleå University of Technology, Luleå, Sweden.

Ferbey, T., Arnold, H., and Hickin, A.S., 2013. Ice-flow indicator compilation, British Columbia; British Columbia Geological Survey, Open File 2013-06, Sheet 1 of 2, scale 1:1 650 000.

Killeen, P.G., 1979. Gamma ray spectrometric methods in uranium exploration – application and interpretation; *in* Geophysics and geochemistry in the search for metallic ores, Proceedings of Exploration 77; Geological Survey of Canada, Economic Geology Report 31, p. 163–229. https://doi.org/10.4095/106049

Knipping, J.L., Bilenker, L.D., Simon, A.C., Reich, M., Barra, F., Deditius, A.P., Wälle, M., Heinrich, C.A., Holtz, F., and Munizaga, R., 2015a. Trace elements in magnetite from massive iron oxide-apatite deposits indicate a combined formation by igneous and magmatic-hydrothermal processes; Geochimica et Cosmochimica Acta, v. 171, p. 15–38. https://doi.org/10.1016/j.gca.2015.08.010

Knipping, J.L., Bilenker, L.D., Simon, A.C., Reich, M., Barra, F., Deditius, A.P., Lundstrom, C., Bindeman, I., and Munizaga, R., 2015b. Giant Kiruna-type deposits form by efficient flotation of magmatic magnetite suspensions; Geology, v. 43, no. 7, p. 591–594, https://doi.org/10.1130/G36650.1

Kwong, Y.T.J., 1987. Evolution of the Iron Mask batholith and its associated copper mineralization; British Columbia Ministry of Energy, Mines and Petroleum Resources, Mineral Resources Division, British Columbia Geological Survey, Bulletin 77, 55 p., 1 map, scale 1:50 000.

Lang, J.R., 1994. Geology of the Crescent alkalic porphyry copper-gold deposit, Afton mining camp, British Columbia (92I/9); *in* Geological Fieldwork 1993, a summary of field activities and current research, (ed.) B. Grant and J.M. Newell; British Columbia Ministry of Energy, Mines and Petroleum Resources, British Columbia Geological Survey, Paper 1994-1, p. 285–296.

Lang, J.R. and Stanley, C.R., 1995. Contrasting styles of alkalic porphyry copper-gold deposits in the northern part of the Iron Mask batholith, Kamloops, British Columbia; *in* Porphyry deposits of the northwestern Cordillera of North America, (ed.) T.G. Schroeter; Canadian Institute of Mining, Metallurgy and Petroleum, Special Volume 46, p. 581–592.

Logan, J.M. and Mihalynuk, M.G., 2005. Porphyry Cu-Au deposits of the Iron Mask batholith, southeastern British Columbia; *in* Geological Fieldwork 2004, British Columbia Ministry of Energy, Mines and Petroleum Resources, British Columbia Geological Survey, Paper 2005-1, p. 271–290.

Logan, J.M., Mihalynuk, M.G., Ullrich, T.D., and Friedman, R., 2006. Geology of the Iron Mask batholith; British Columbia Ministry of Energy, Mines and Petroleum Resources, British Columbia Geological Survey, Open File Map 2006-11, scale 1:25 000.

Lowell, J.D. and Guilbert, J.M., 1970. Lateral and vertical alteration-mineralization zoning in porphyry ore deposits; Economic Geology, v. 65, no. 4, p. 373–408. https://doi.org/10.2113/gsecongeo.65.4.373

McCafferty, A.E., Van Gosen, B.S., Smith, B.D., and Sole, T.C., 2004. Geophysical characterization of geologic features with environmental implications from airborne magnetic and apparent resistivity data; Chapter D2 of Integrated investigations of environmental effects of historical mining in the Basin and Boulder mining districts, Boulder River Watershed, Jefferson County, Montana, (ed.) D.A. Nimick, S.E. Church, and S.E. Finger; U.S. Geological Survey, Professional Paper 1652-D2, p. 90–125.

Mortensen, J.K., Ghosh, D.K., and Ferri, F., 1995. U-Pb geochronology of intrusive rocks associated with copper-gold porphyry deposits in the Canadian Cordillera; *in* Porphyry deposits of the northwestern Cordillera of North America, (ed.) T.G. Schroeter; Canadian Institute of Mining, Metallurgy and Petroleum, Special Volume 46, p. 142–158.

Richards, J.P., López, G.P., Zhu, J.-j., and Mumin, A.H., 2016. Links between porphyry and IOCG deposits, Paper 5292, Session T18.1, Ore-forming processes associated with hypabyssal magmatic and related volcanic systems; 35th International Geological Congress, 22nd August – 2nd September 2016, Cape Town, South Africa (abstract). https://www.americangeosciences.org/information/igc/

Ross, K.V., Godwin, C.I., Bond, L., and Dawson, K.M., 1995. Geology, alteration and mineralization of the Ajax East and Ajax West copper-gold alkali porphyry deposits, southern Iron Mask batholith, Kamloops, British Columbia; *in* Porphyry deposits of the northwestern Cordillera of North America, (ed.) T.G. Schroeter, Canadian Institute of Mining, Metallurgy and Petroleum, Special Volume 46, p. 565–580.

Schetselaar, E.M., Bellefleur, G., Craven, J.A., White, D., Thomas, M.D., Tschirhart, V.L., Pilkington, M., Enkin, R.J., Percival, J.A., and Percival, J.B., 2017. Integrated 3D model of magmatic-hydrothermal evolution of the Iron Mask batholith complex near the New Afton Mine; in Targeted Geoscience Initiative: 2016 report of activities, (ed.) N. Rogers; Geological Survey of Canada, Open File 8199, p. 69–73. https//doi.org/10.4095/299573

Shives, R.B.K. and Carson, J.M., 1995. Airborne geophysical survey, Ironmask batholith, British Columbia, NTS 92I/8, 9, 10, 15; Geological Survey of Canada, Open File 2817, 63 p., scale 1:150 000. https://doi.org/10.4095/203472

Shives, R.B.K., Ford, K.L., and Charbonneau, B.W., 1995. Geological Survey of Canada workshop manual: applications of gamma ray spectrometric/magnetic/VLF-EM surveys; Geological Survey of Canada, Open File 3061, 85 p. https://doi.org/10.4095/203485

Shives, R.B.K., Charbonneau, B.W., and Ford, K.L., 1997. The detection of potassic alteration by gamma-ray spectrometry - recognition of alteration related to mineralization; *in* Geophysics and geochemistry at the millenium: proceedings of Exploration 97, the fourth decennial international conference on mineral exploration, (ed.) A.G. Gubins; Prospectors and Developers Association of Canada, Toronto, Ontario, p. 741–752.

Sillitoe, R.H., 1979. Some thoughts on gold-rich porphyry copper deposits; Mineralium Deposita, v. 14, no. 2, p. 161–174. https://doi.org/10.1007/BF00202933

Sillitoe R.H., 2003. Iron oxide–copper–gold deposits: an Andean view; Mineralium Deposita, v. 38, no. 7, p. 787–812. https://doi.org/10.1007/s00126-003-0379-7

Snyder, L.D., 1994. Petrological studies within the Iron Mask batholith, south central British Columbia; M.Sc. thesis, The University of British Columbia, Vancouver, British Columbia, 192 p.

Snyder, L.D. and Russell, J.K., 1993. Field constraints on diverse igneous processes in the Iron Mask Batholith (92I9/10); *in* Geological Fieldwork 1992, (ed.) B. Grant and J.M. Newell; British Columbia Ministry of Energy, Mines and Petroleum Resources, British Columbia Geological Survey, Paper 1993-1, p. 281–286.

Snyder, L.D. and Russell, J.K., 1995. Petrogenetic relationships and assimilation processes in the alkali Iron Mask batholith, south-central British Columbia; *in* Porphyry deposits of the northwestern Cordillera of North America, (ed.) T.G. Schroeter; Canadian Institute of Mining, Metallurgy and Petroleum, Special Volume 46, p. 593–608.

Stanley, C.R., 1994. Geology of the Pothook alkalic copper-gold porphyry deposit, Afton Mining Camp, British Columbia (92I/9,10); *in* Geological Fieldwork 1993, (ed.) B. Grant and J.M. Newell; British Columbia Ministry of Energy, Mines and Petroleum Resources, British Columbia Geological Survey, Paper 1994-1, p. 275–284.

Stanley, C.R., Lang, J.R., and Snyder, L.D., 1994. Geology and mineralization in the northern part of the Iron Mask batholith, Kamloops, British Columbia (92I/9, 10); *in* Geological Fieldwork 1993, (ed.) B. Grant and J.M. Newell; British Columbia Ministry of Energy, Mines and Petroleum Resources, British Columbia Geological Survey, Paper 1994-1, p. 269–274.

Thomas, M.D., 2010. Geological significance of new aeromagnetic data from the Kamloops survey area (Portions of NTS 92I (Ashcroft) and 82L (Vernon)), central British Columbia: a Mountain Pine Beetle Program contribution; Geological Survey of Canada, Open File 6659, 55 p. https://doi.org/10.4095/286265

Thomas, M.D., 2019. Gravity and magnetic models of the Iron Mask batholith, south-central Canadian Cordillera, British Columbia; Geological Survey of Canada, Current Research 2019-1, 24 p. https://doi.org/10.4095/314517

Young, G.A. and Uglow, W.L., 1926. The iron ores of Canada, volume 1, British Columbia and Yukon; Geological Survey, Canada Department of Mines, Ottawa, Economic Geology Series 3, 253 p. https://doi.org/10.4095/103992

Reconnaissance investigation of magnetite trace-element compositions from the New Afton Cu-Au deposit, British Columbia

J.A. Percival[1]*, E. Schetselaar[1], D.C. Petts[1], S.E. Jackson[1], and D. Wade[2]

Percival, J.A., Schetselaar, E., Petts, D.C., Jackson, S.E., and Wade, D., 2020. Reconnaissance investigation of magnetite trace-element compositions from the New Afton Cu-Au deposit, British Columbia; in *Targeted Geoscience Initiative 5: contributions to the understanding and exploration of porphyry deposits, (ed.) A. Plouffe and E. Schetselaar; Geological Survey of Canada, Bulletin 616, p. 91–108. https://doi.org/10.4095/327990*

Abstract: Abundant magnetite occurs sporadically in variable textural settings within the New Afton Cu-Au porphyry deposit. A study to test the utility of magnetic anomalies as an exploration vector was conducted by analyzing magnetite in drill core samples from a variety of rock types and alteration facies. Magnetite samples from various settings (i.e. disseminated, isolated, vein, breccia grains) were analyzed by a laser-ablation inductively coupled plasma-mass spectrometer for iron and trace elements. New Afton magnetite compositions were compared to previously defined compositional fingerprints of porphyry, iron oxide copper gold, skarn, polymetallic vein, and layered intrusion deposit types. On multi-element plots using bulk continental crust as the normalizing factor, most New Afton magnetite analyses plot within the high-temperature hydrothermal magnetite field, although most samples have elevated V and 6 of 19 samples have notably higher W than other deposit types. A hydrothermal origin is supported by a Ti versus Ni-Cr plot, which discriminates hydrothermal from magmatic magnetite; however, a Ti versus V plot suggests mainly magmatic compositions. Copper is generally depleted relative to bulk crust; gold and platinum values are near their detection limits. Veins, one of the main magnetite habits, define brittle fracture patterns, and trace-element characteristics support formation by pulses of oxidized, high-temperature hydrothermal fluid. The texture and composition of the samples suggest that magnetite crystallized from late magmatic fluids that drove porphyry mineralization.

Résumé : Dans le gisement porphyrique à Cu-Au de New Afton, on trouve de grandes quantités de magnétite distribuées sporadiquement dans des contextes texturaux variés. Afin de vérifier si les anomalies magnétiques pouvaient servir de vecteur d'exploration, nous avons analysé la magnétite présente dans des échantillons de carottes de forage recoupant divers types de roches et de faciès d'altération. Nous avons utilisé un spectromètre de masse avec plasma à couplage inductif jumelé à l'ablation par laser pour doser le contenu en fer et en éléments en traces de la magnétite présente dans divers contextes texturaux (c.-à-d. grains disséminés, isolés, dans des filons ou dans des brèches). La composition des grains de magnétite du gisement de New Afton a été comparée aux caractéristiques compositionnelles déterminées antérieurement pour d'autres types de gîtes minéraux : gîtes porphyriques, gîtes d'oxydes de fer–cuivre-or, skarns, gîtes filoniens à minéralisation polymétallique et gîtes associés à des intrusions stratifiées. Dans des diagrammes multiéléments où les valeurs mesurées sont normalisées à la composition globale de la croûte continentale, la majeure partie des résultats d'analyse de la magnétite du gisement de New Afton se situent dans le champ de la magnétite hydrothermale de haute température, bien que la plupart des échantillons contiennent des teneurs élevées en V et que 6 échantillons sur 19 ont des teneurs nettement plus élevées en W que celles relevées dans d'autres types de gîtes. Une origine hydrothermale est appuyée par le diagramme de Ti en fonction du rapport Ni/Cr qui permet de distinguer la magnétite d'origine hydrothermale de celle d'origine magmatique. Toutefois, le diagramme de Ti en fonction de V suggère des compositions surtout magmatiques. Le cuivre est généralement appauvri par rapport à la composition globale de la croûte, et les concentrations d'or et de platine sont près de leur seuil de détection. Les filons, l'un des principaux modes d'occurrence de la magnétite, définissent des configurations de fracturation fragile, tandis que les caractéristiques des éléments en traces appuient une formation de ceux-ci par des impulsions de fluides hydrothermaux oxydés de haute température. La texture et la composition des échantillons suggèrent que la magnétite a cristallisé à partir de fluides magmatiques de phase tardive qui ont produit la minéralisation porphyrique.

[1]Geological Survey of Canada, 601 Booth Street, Ottawa, Ontario K1A 0E8
[2]New Gold Inc., 4050 West Trans-Canada Highway, Kamloops, British Columbia V1S 2A3
*Corresponding author: J.A. Percival (email: john.percival@canada.ca)

INTRODUCTION

Porphyry deposits are generated by granitoid magmatism, but a specific series of processes, from magma generation through fractionation and emplacement, needs to align to concentrate metals into ore deposits. It is well established that oxidizing conditions are required during melting to mobilize metals from mantle reservoirs (e.g. Mungall, 2002; Sillitoe, 2002, 2010; Richards, 2009, 2011a, b; Cooke et al., 2014), and that subsequent fractionation and metal behaviour are determined by magma oxidation state and volatile content.

Magnetite is one of the most obvious indicators of a highly oxidized magma; however, magnetite is uncommon in many porphyry districts and as a result, indirect indicators of oxidation state, such as rare-earth–element distribution in zircon (Ballard et al., 2002; Zhong et al., 2019), have been used to evaluate the prospectivity of plutonic complexes. In this paper, we explore the relationship of widespread magnetite in the New Afton porphyry Cu-Au deposit to magmatic and alteration processes, with a view to defining its utility as an exploration vector within the host Iron Mask batholith.

GEOLOGICAL SETTING

Situated in the Quesnel terrane of south-central British Columbia, the New Afton deposit is one of ten known porphyry deposits associated with the Iron Mask batholith (Sinclair, 2007; Logan and Mihalynuk, 2014). The Late Triassic (ca. 204 Ma; Mortensen et al., 1995), silica-saturated, alkalic, diorite-monzonite complex intrudes volcanic and associated sedimentary rocks of the Nicola Group. Copper-gold mineralization in the New Afton deposit is hosted by fragmental volcanic rocks of the Nicola Group and locally by the Cherry Creek monzonite phase of the Iron Mask batholith (J. Lipske and D. Wade, unpub. rept., 2014). The deposit is bounded partly by a thick picritic unit of the Nicola Group, and partly by north-northwest– and northeast-striking faults. It is also cut by faults of variable orientation, some of which may have channelled mineralizing fluids.

Several alteration facies are recognized with broadly concentric distribution in the New Afton deposit. Central zones of potassic (mainly biotite-dominant, with some K-feldspar–dominant patches) and calcic (magnetite-actinolite-apatite; epidote) alteration are surrounded by outer propylitic alteration. Late, structurally controlled phyllic alteration overprints the potassic and outer propylitic alteration along high-angle fault zones (Bergen et al., 2015; Tolman and Lipske, 2016). In general, protoliths can be identified in spite of the pervasive alteration.

SAMPLING STRATEGY

To explore the role of magnetite in the New Afton porphyry system, magnetite-bearing samples were collected from drill core through different facies of the deposit (Fig. 1, 2). Rock types included fragmental volcanic rocks, Cherry Creek monzonite, and Pothook diorite with variable alteration facies (Table 1). Two main magnetite textural settings were recognized in the field and confirmed petrographically (Fig. 3): finely disseminated and vein (including brecciated veins).

METHODS

Thick polished sections were cut from drill core, photographed, and imaged by a scanning electron microscope in back-scattered electron (BSE) mode. Images were used to select spots for analysis for iron and 36 trace elements by laser-ablation inductively coupled plasma-mass spectrometry (LA-ICP-MS). Beam sizes between 40 and 65 µm were used to ablate nominally inclusion-free material from representative grains of each textural type. A total of 106 analyses were obtained from 19 samples.

Analyses were calibrated using primary standard USGS GSD-1G (Jochum et al., 2007) analyzed with a 50 µm beam. A secondary standard, USGS BCR-2G (Jochum et al., 2007), was analyzed repeatedly during the analytical sessions for quality control purposes. The LA-ICP-MS data were processed using GLITTER (Griffin et al., 2008), using 'GeoReM preferred values' (Jochum, et al., 2005) for elemental contents in GSD-1G and the stoichiometric Fe content of magnetite (approximately 723 600 ppm) for internal standardization. The detection limit varies by element and several elements are consistently near or below detection (5–10 ppb): Pd, Ag, Re, Pt, and Au. Precision and accuracy, assessed via repeated analysis of BCR-2G, are estimated at better than 5% for most elements.

Data were plotted on plots designed to distinguish magnetite in various mineralized environments. Dare et al. (2014) presented comparative data from a number of mineral deposit types, whereas other authors have developed discriminative methods relevant to porphyry deposits (Nadoll et al., 2014, 2015).

RESULTS AND DISCUSSION

Magnetite from New Afton contains low contents of Cu and Au (Appendix A), contributing little to the ore metal budget. The content of Mg, Al, Si, Ca, Ti, V, Cr, and W ranged from 0.01 ppm to more than 1000 ppm, with median values of 870, 2660, 1695, 236, 4120, 3250, 21, and 0.6 ppm, respectively. Maximum P, Mn, Co, Ni, and Zn values fall in the range of 100 to 1000 ppm (median values of 3, 434, 48, 89, and 195 ppm, respectively). The highest values

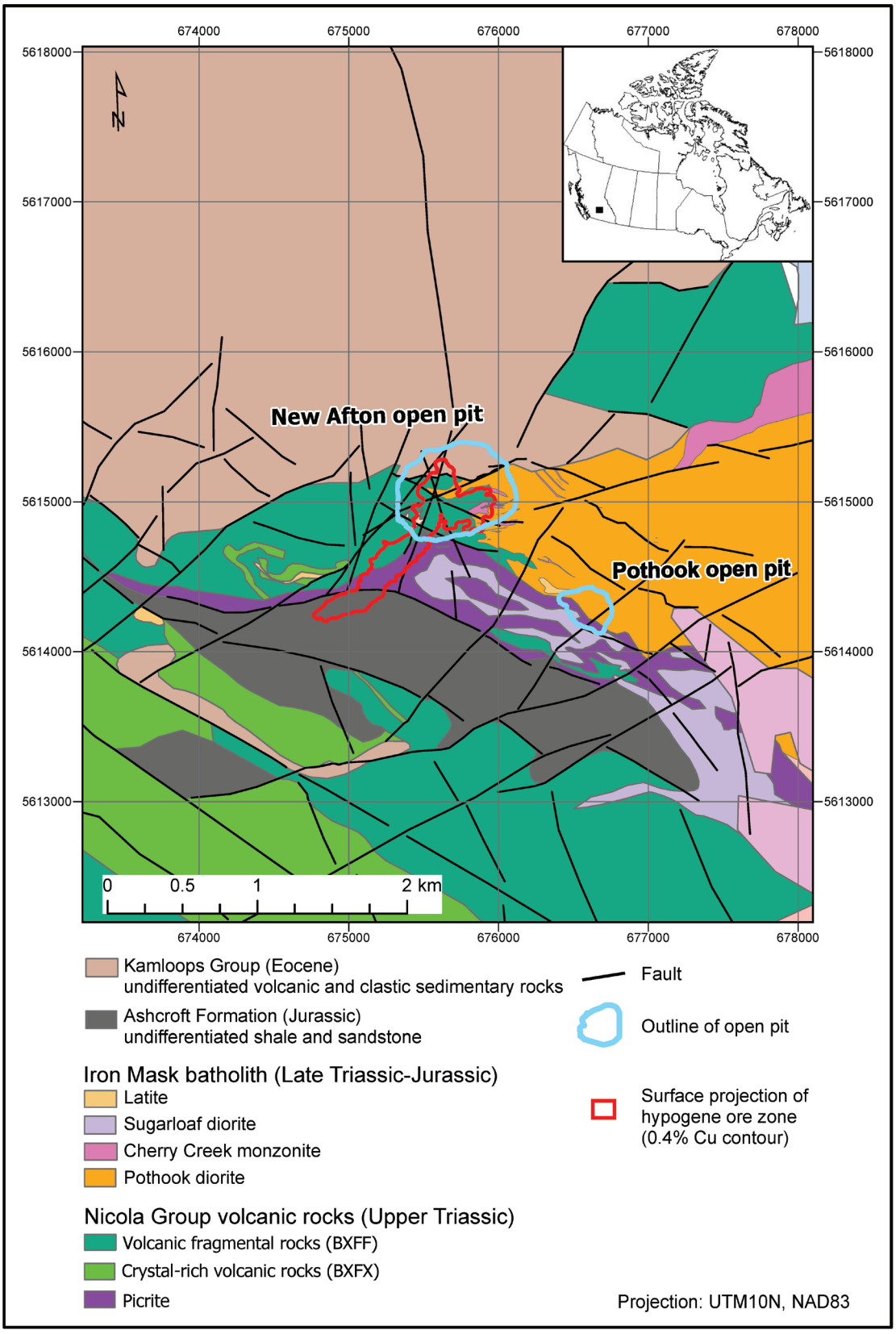

Figure 1. Geological setting of the New Afton deposit (Bergen et al., 2015; Logan et al., 2006).

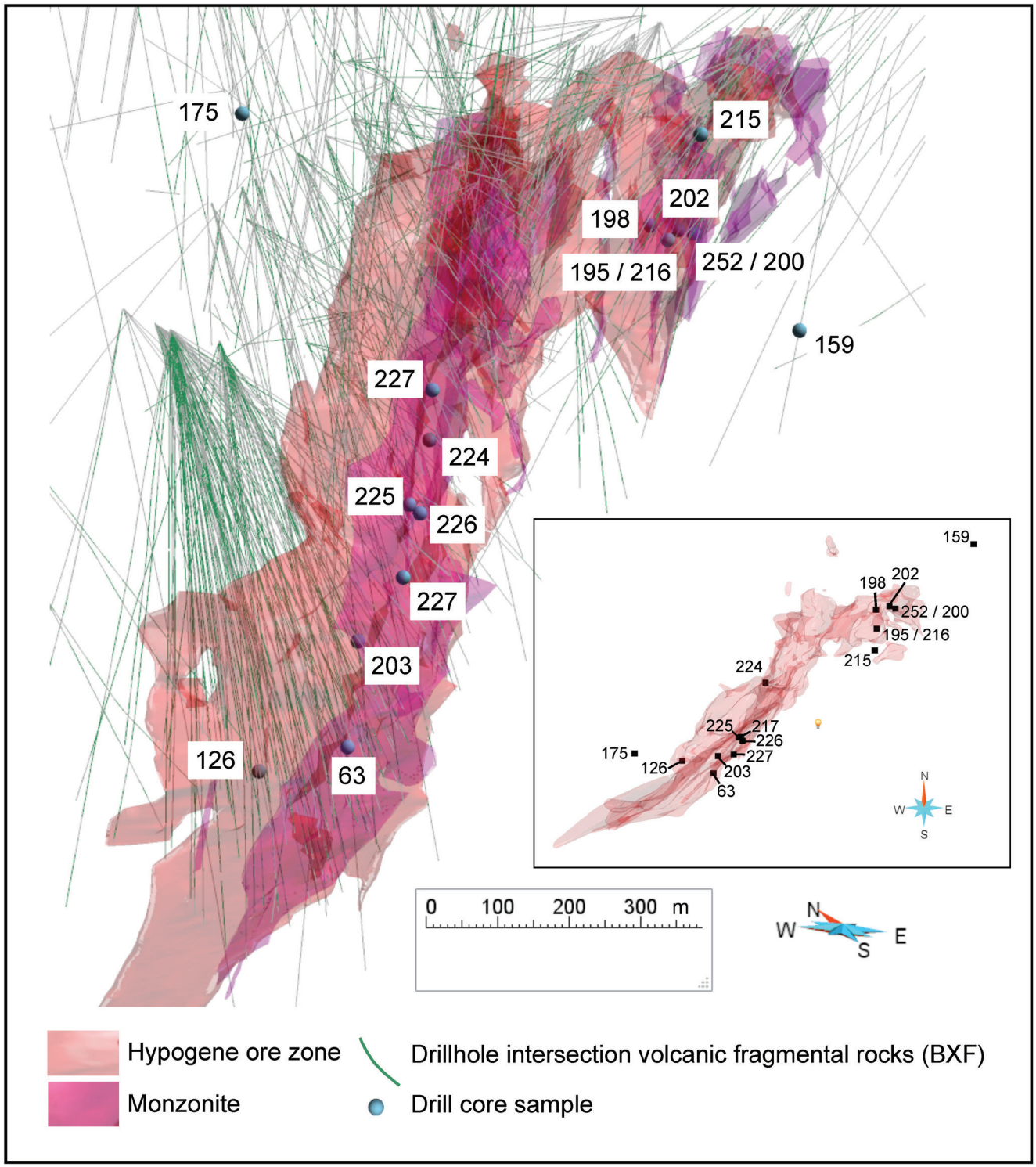

Figure 2. Three-dimensional projection of the spatial distribution of samples from the New Afton ore zone and surrounding area analyzed in this study. Inset map shows plan view of drill core sample locations and hypogene ore zone.

Table 1. Locations and petrographic descriptions of magnetite-bearing samples from the New Afton copper-gold porphyry deposit.

Sample number	Hole identifier	Depth (m)	Rock type	Alteration type	Magnetite habits
63	EA14-133	671.50	Monzonite	Potassic (K-feldspar)	Thick, vein-brecciated, fibrous
126	EA17-187	484.84	Volcanic fragmental	Potassic (K-feldspar)	Magnetite-apatite veins cut by younger quartz veins
159	AF06-94	744.95	Volcanic fragmental mafic volcanic	Potassic (K-feldspar)	Thick magnetite-apatite vein and disseminated in host rock
175	AF03-83	272.97	Diorite	Phyllic	Thick magnetite-apatite vein and disseminated in host rock
195	EA13-058	299.36	Monzonite (trachytic)	Potassic (K-feldspar)	Disseminated fine magnetite
198	ES13-059	339.82	Volcanic fragmental crystal-lithic volcanic	Biotite (potassic) and propylitic	Thin veins and disseminated magnetite
200	ES13-060	332.04	Volcanic fragmental crystal-rich	Biotite (potassic) and propylitic	Thin veins and peripheral disseminated
202	ES13-069	329.98	Volcanic fragmental crystal-rich	Biotite (potassic) and propylitic	Brecciated magnetite veins; hypogene mineralization
203	EA14-125	454.96	Highly altered monzonite?	Potassic (K-feldspar)	Brecciated thin magnetite veins
215	AF08-146	356.90	Monzonite, plagioclase porphyritic	Potassic (K-feldspar)	Disseminated
216	AF08-146	357.70	Monzonite, plagioclase porphyritic	none	Disseminated
217	UA05-44	384.68	Monzonite, coarse grained	Potassic (K-feldspar), propylitic	Disseminated
224	EA13-42	177.00	Monzonite, monzonite dykes	none	Magnetite-apatite vein
225	EA12-008	445.40	Monzonite	Phyllic	Veins, breccia. Late hematite
226	EA12-008	465.30	Monzonite, diorite xenolith	Potassic (K-feldspar)	Disseminated, sigmoidal vein
227	EA14-138	412.06	Monzonite	Potassic (K-feldpar)	Brecciated vein, peripheral disseminated
252	WC17-002	304.61	Fresh diorite	none	Magnetite-epidote vein; disseminated
253	WC17-002	225.55	Fresh diorite, medium grained	none	Disseminated
254	WC17-002	128.70	Monzonite dyke	none	Thin, discontinuous magnetite veins

for Cu, Ga, Y, Zr, Mo, Sn, Sb, Ba, and Pb are between 10 and 100 ppm (median values of 0.9, 24, 0.8, 1.7, 0.3, 1.4, 0.3, 3, and 1.8 ppm, respectively). Maximum Ge, Se, Nb, and Hf contents are between 1 and 10 ppm (median 1.2, 0.3, 0.3, and 0.1 ppm, respectively). The median Ta content is 20 ppb, and Pd, Ag, Te, Re, Pt, and Au occur near the limit of detection during the analytical session. Local anomalous Mg, Si, Al, Ca, and P likely reflect inclusions of amphibole, quartz, feldspar, and apatite in the analyzed magnetite; these analyses, identified in Appendix A, are particularly common in the generally fine, disseminated magnetite grains.

To evaluate compositional variability within and among samples, bivariate element plots were produced. The Ti versus Ni-Cr plot in Dare et al. (Fig. 4a; 2014) is designed to discriminate magmatic from hydrothermal compositions. In this plot, both the disseminated and vein magnetite New Afton samples occur within the hydrothermal field; however, on a Ti versus V plot (Fig. 4b), New Afton magnetite samples with both habits fall within the magmatic field for porphyry deposits as defined by Nadoll et al. (2015), although a substantive subset of disseminated magnetite analyses occur within the overlapping portion of the hydrothermal magnetite field.

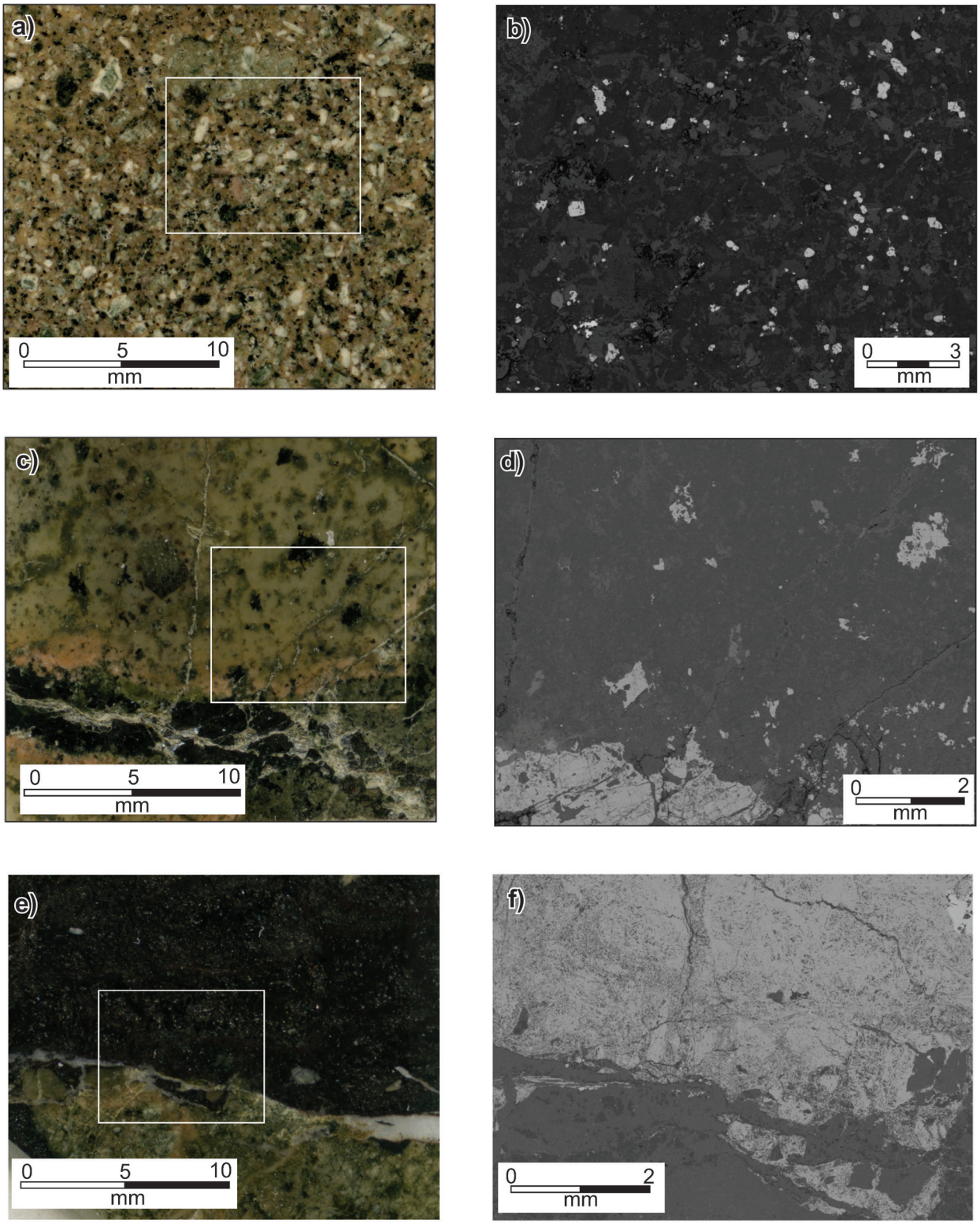

Figure 3. Polished surface and corresponding back-scattered electron (BSE) images of representative magnetite textures in the New Afton ore zone: **a)** polished surface of plagioclase porphyritic monzonite sample 216; **b)** BSE image of the white-outlined area in a) showing disseminated magnetite (light grey) in a well-preserved igneous matrix; **c)** polished surface of altered (biotite potassic, propylitic) fragmental volcanic sample 198 hosting vein and disseminated magnetite; **d)** BSE image of the white-outlined area in c) showing vein magnetite (lower left) and disseminated grains; **e)** polished surface of phyllic-altered diorite sample 175 with a thick magnetite-apatite vein; **f)** BSE image of the white-outlined area in e) showing a coarse magnetite (light grey) vein.

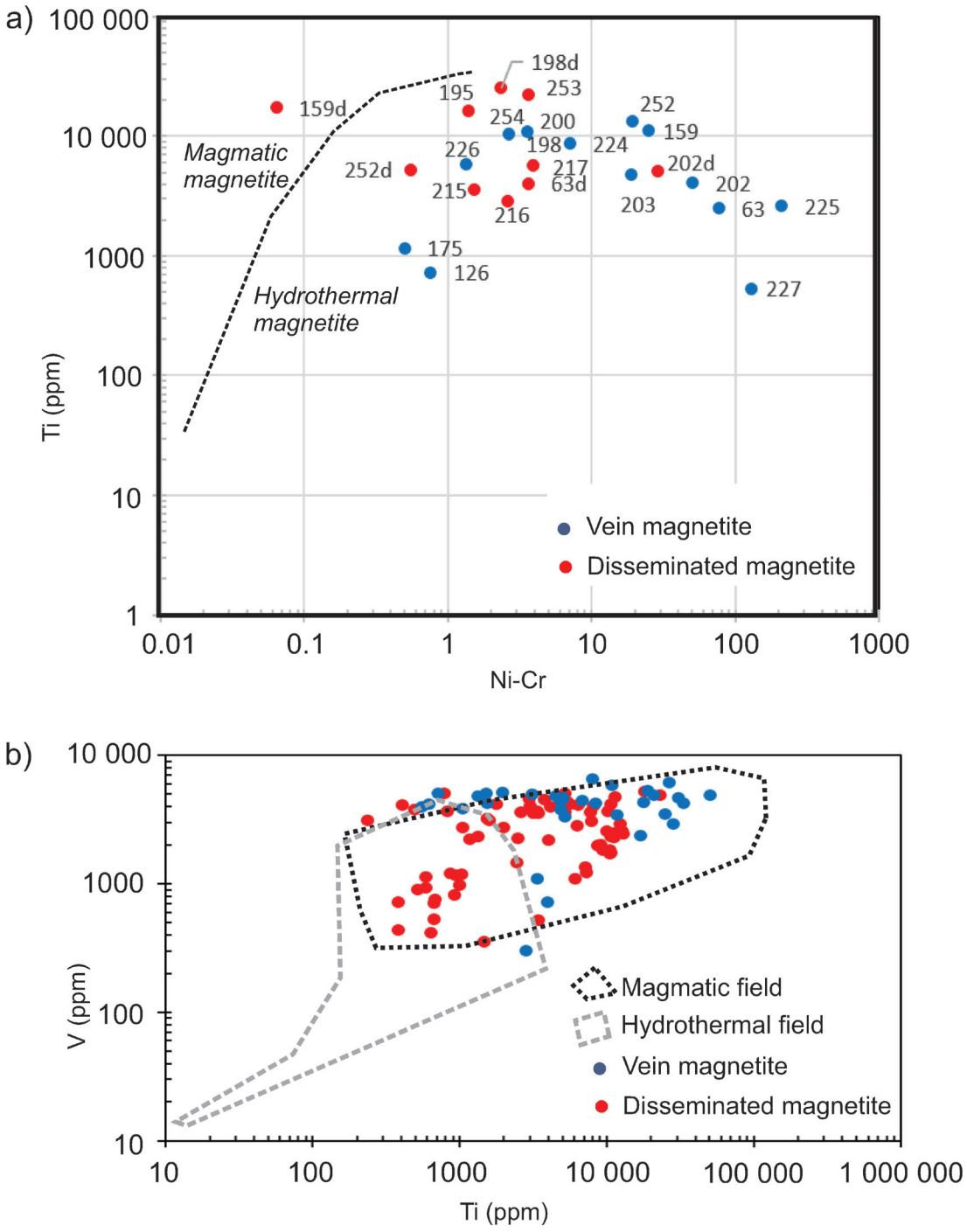

Figure 4. Discrimination plots showing trace-element content of New Afton disseminated and vein magnetite: **a)** Ti content versus Ni-Cr ratio of representative disseminated and vein samples. Fields defining magmatic and hydrothermal magnetite are after Dare et al. (2014); **b)** Ti content versus V content for all magnetite analyses. Fields defining magmatic and hydrothermal magnetite are based on a global compilation of porphyry deposits (*after* Nadoll et al., 2015).

Multi-element plots (Fig. 5, Appendix B) were constructed using the method of Dare et al. (2014), by normalizing analyses to average continental crustal values (Rudnick and Gao, 2003). Both disseminated (Fig. 5a) and vein (Fig. 5b) magnetite compositions from New Afton generally overlap the hydrothermal field, although V content systematically exceeds or falls within the upper reaches of the field for both textural types, matching the high V content of andesites reported by Dare et al. (2014). Niobium and copper values fall near the bottom or below the hydrothermal field limit and, in a few vein samples, magnetite is enriched in W by two orders of magnitude beyond the hydrothermal envelope.

Based on a global compilation, Huang et al. (2019) recognized significant variation in magnetite composition among different types of porphyry deposits based on multivariate statistical analysis of electron microprobe and LA-ICP-MS trace-element data. A combination of variables including origin (magmatic versus hydrothermal), magma composition, fluid composition, oxygen, and sulfur fugacity controls magnetite trace-element signatures. Huang et al.

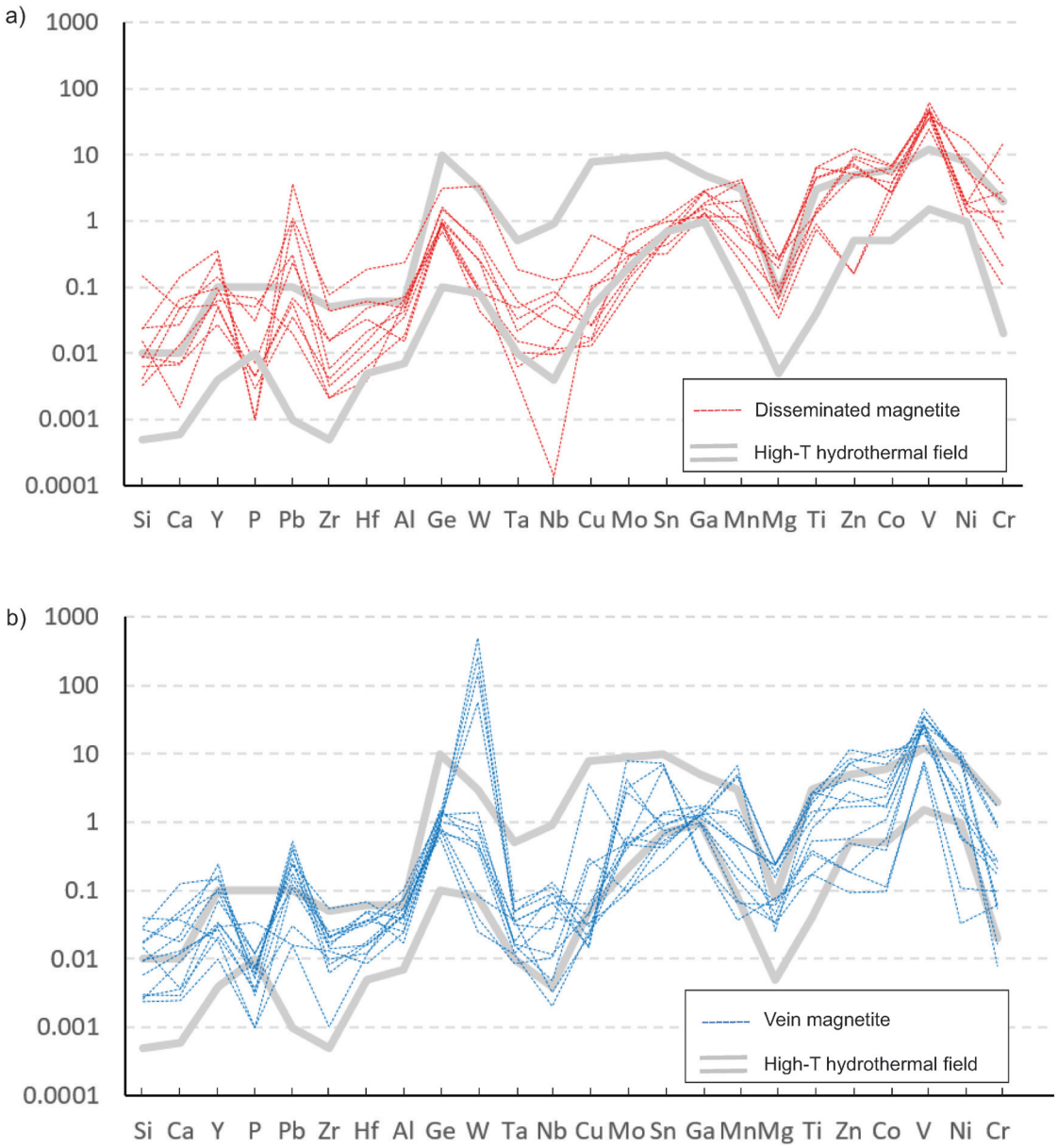

Figure 5. Multi-element (spider) plots showing New Afton magnetite analyses and the reference field for high-temperature hydrothermal magnetite compositions, *after* Dare et al. (2014): **a)** average analyses for disseminated magnetite; **b)** average analyses for vein magnetite.

(2019) found that, in general, magnetite of magmatic origin contains relatively high levels of P, Ti, V, Mn, Zr, Nb, Hf, and Ta, accompanied by generally low Mg, Si, Co, Ni, Ge, Sb, W, and Pb, owing to magnetite-magma partition coefficients. Both disseminated and vein magnetite from New Afton match some of these characteristics — high Ti and V with low Mg, Si, Co, and Ni — but they differ significantly in others — low Zr, Hf, Nb, and Ta, and high W and Pb. Tungsten, which appears to be an effective general magmatic versus hydrothermal discriminator (Dare et al., 2014; Huang et al., 2019), has similar values for disseminated and vein magnetite in New Afton, where both are present in the same sample (Appendix B). The study of Huang et al. (2019) also showed that hydrothermal magnetite in porphyry systems related to alkaline magmas is characterized by high Mg, Mn, Co, Mo, Sn, and high-field-strength elements. Again, New Afton magnetite exhibits similar content for these elements in disseminated and vein textural types where both are present in the same sample (Appendix B).

Based on geochemical characteristics, the first-order textural distinction of New Afton magnetite into disseminated and vein types does not appear to reflect fundamentally different origins. High values of Ti and V, typical of magmatic magnetite, occur in New Afton vein-type magnetite, which is inferred to be hydrothermal in origin. Conversely, most disseminated grains exhibit many hydrothermal trace-element characteristics, and generally have compositions similar to (or the same as) the compositions of magnetite in veins. These observations suggest similar sources for the two textures, but do not suggest a clear magmatic or hydrothermal origin.

CONCLUSIONS

A reconnaissance study of magnetite trace-element compositions from the New Afton porphyry Cu-Au deposit was conducted by LA-ICP-MS on a variety of mineralized and unmineralized samples with diverse alteration characteristics. Two textures of magnetite were recognized and analyzed: disseminated, and massive or brecciated veins. Some analyses show anomalously high values of Mg, Al, Si, Ca, and/or P, which are attributed to inclusions of amphibole, quartz, feldspar, or apatite in the sampled magnetite.

Discrimination plots purported to distinguish magmatic and hydrothermal magnetite in porphyry deposits based on statistical treatment of multi-element analyses (Dare et al., 2014; Nadoll et al., 2015; Canil et al., 2016; Huang et al., 2019) were examined; however, the results were contradictory and inconclusive. Multi-element plots indicated traits related to both magmatic and hydrothermal origins. Where both disseminated and vein magnetite are present in samples, the two textures show similar multi-element patterns, suggesting a common origin.

Veins of magnetite define brittle fracture networks, indicating that they crystallized late in the petrogenetic history. The trace-element characteristics of both disseminated and vein magnetite generally conform to those of hydrothermal magnetite in porphyry deposits, but have systematically higher V content, more akin to magmatic magnetite in andesite. These characteristics may reflect relatively high-temperature, oxidized crystallization conditions (Canil et al., 2016). Together, the texture and composition suggest that magnetite crystallized from late magmatic fluids during porphyry mineralization.

ACKNOWLEDGMENTS

We thank New Gold Inc. for access to drill core and background information. We greatly appreciate critical reviews by N. Rogers and S. Makvandi, which improved the paper.

REFERENCES

Ballard, J.R., Palin, M.J., and Campbell, I.H., 2002. Relative oxidation states of magmas inferred from Ce(IV)/Ce(III) in zircon: application to porphyry copper deposits of northern Chile; Contributions to Mineralogy and Petrology, v. 144, p. 347–364. https://doi.org/10.1007/s00410-002-0402-5

Bergen, D., Krutzelmann, H., and Rennie, D.W., 2015. Technical report on the New Afton mine, British Columbia, Canada; Roscoe Postle Associates Inc. for New Gold Inc., NI 43-101 report, Project #2400, 256 p.

Canil, D., Grondahl, C., Lacourse, T., and Pisiak, L.K., 2016. Trace elements in magnetite from porphyry Cu-Mo-Au deposits in British Columbia, Canada; Ore Geology Reviews, v. 72, p. 1116–1128. https://doi.org/10.1016/j.oregeorev.2015.10.007

Cooke, D.R., Hollings, P., Wilkinson, J.J., and Tosdal, R.M., 2014. Geochemistry of porphyry deposits. Chapter 14 *in* Volume 13: Geochemistry of mineral deposits; Treatise on geochemistry, 2nd edition, (ed.) S.D. Scott; Elsevier, Oxford, U.K., p. 357–381. https://doi.org/10.1016/B978-0-08-095975-7.01116-5

Dare, S.A.S., Barnes, S.-J., Beaudoin, G., Méric, J., Boutroy, E., and Potvin-Doucet, C., 2014. Trace elements in magnetite as petrogenetic indicators; Mineralium Deposita, v. 49, p. 785–796. https://doi.org/10.1007/s00126-014-0529-0

Griffin, W.L., Powell, W.J., Pearson, N.J., and O'Reilly, S.Y., 2008. GLITTER: data reduction software for laser ablation ICP–MS; *in* Laser ablation-ICP-mass spectrometry in the earth sciences: current practices and outstanding issues, (ed.) P. Sylvester, Mineralogical Association of Canada , Short Course Series, v. 40, p. 308–311.

Huang, X.-W., Sappin, A.-A., Boutroy, E., Beaudoin, G., and Makvandi, S., 2019. Trace element composition of igneous and hydrothermal magnetite from porphyry deposits: relationship to deposit subtypes and magmatic affinity; Economic Geology, v. 114, no. 5, p. 917–952. https://doi.org/10.5382/econgeo.4648

Jochum, K.P., Nohl, U., Herwig, K., Lammel, E., Stoll, B., and Hofmann, A.W., 2005. GeoReM: A new geochemical database for reference materials and isotopic standards; Geostandards and Geoanalytical Research, v. 29, no. 3, p. 333–338. https://doi.org/10.1111/j.1751-908X.2005.tb00904.x

Jochum, K.P., Willbold, M., Raczek, I., Stoll, B., and Herwig, K., 2007. Chemical characterisation of the USGS reference glasses GSA-1G, GSC-1G, GSD-1G, GSE-1G, BCR-2G, BHVO-2G and BIR-1G using EPMA, ID-TIMS, ID-ICP-MS and LA-ICP-MS; Geostandards and Geoanalytical Research, v. 29, p. 285–302. https://doi.org/10.1111/j.1751-908X.2005.tb00901.x

Logan, J.M. and Mihalynuk, M.G., 2014. Tectonic controls on Early Mesozoic paired alkaline porphyry deposit belts (Cu-Au±Ag-Pt-Pd-Mo) within the Canadian Cordillera; Economic Geology, v. 109, no. 4, p. 827–858. https://doi.org/10.2113/econgeo.109.4.827

Logan, J.M., Mihalynuk, M.G., Ullrich, T.D., and Friedman, R., 2006. Geology of the Iron Mask batholith; British Columbia Geological Survey, Open File Map 2006-11, scale 1:25 000.

Mungall, J.E., 2002. Roasting the mantle: slab melting and the genesis of major Au and Au-rich Cu deposits; Geology, v. 30, no. 10, p. 915–918. https://doi.org/10.1130/0091-7613(2002)030%3C0915:RTMSMA%3E2.0.CO;2

Nadoll, P., Angerer, T., Mauk, J.L., French, D., and Walshe, J., 2014. The chemistry of hydrothermal magnetite: a review; Ore Geology Reviews, v. 61, p. 1–32. https://doi.org/10.1016/j.oregeorev.2013.12.013

Nadoll, P., Mauk, J.L., Leveille, R.A., and Koenig, A.E., 2015. Geochemistry of magnetite from porphyry Cu and skarn deposits in the southwestern United States; Mineralium Deposita, v. 50, no. 4, p. 493–515. https://doi.org/10.1007/s00126-014-0539-y

Richards, J.P., 2009. Post-subduction porphyry Cu–Au and epithermal Au deposits: products of remelting of subduction-modified lithosphere; Geology, v. 37, no. 3, p. 247–250. https://doi.org/10.1130/G25451A.1

Richards, J.P., 2011a. Magmatic to hydrothermal metal fluxes in convergent and collided margins; Ore Geology Reviews, v. 40, no 1, p. 1–26. https://doi.org/10.1016/j.oregeorev.2011.05.006

Richards, J.P., 2011b. High Sr/Y arc magmas and porphyry Cu-Mo-Au deposits; Economic Geology, v. 106, no. 7, p. 1075–1081. https://doi.org/10.2113/econgeo.106.7.1075

Rudnick, R.L. and Gao, S., 2003. Composition of the continental crust, Chapter 1 *in* Volume 3: The crust; Treatise on geochemistry, 1st edition, (ed.) R.L. Rudnick; Elsevier-Pergamon, Oxford, U.K., p. 1–64. https://doi.org/10.1016/B0-08-043751-6/03016-4

Sillitoe, R.H., 2002. Some metallogenic features of gold and copper deposits related to alkaline rocks and consequences for exploration; Mineralium Deposita, v. 37, p. 4–13. https://doi.org/10.1007/s00126-001-0227-6

Sillitoe, R.H., 2010. Porphyry-copper systems; Economic Geology, v. 105, no. 1, p. 3–41. https://doi.org/10.2113/gsecongeo.105.1.3

Sinclair, W.D., 2007. Porphyry deposits; *in* Mineral deposits of Canada: a synthesis of major deposit types, district metallogeny, the evolution of geological provinces, and exploration methods, (ed.) W.D. Goodfellow; Geological Association of Canada, Mineral Deposits Division, Special Publication No. 5, p. 223–243.

Tolman, J. and Lipske, J., 2016. Geology and mineralization of the new Afton porphyry Cu-Au deposit and C-zone project update: New Gold presentation to Toronto Geological Discussion Group, <https://s2.q4cdn.com/351510513/files/doc_downloads/New_afton/NewAfton-C-Zone-Presentation_TGDG-Feb16.pdf> [accessed March 26, 2021]

Zhong, S., Seltmann, R., Qu, H., and Song, Y., 2019. Characterization of the zircon Ce anomaly for estimation of oxidation state of magmas: a revised Ce/Ce* method; Contributions to Mineralogy and Petrology, v. 113, p. 755–763. https://doi.org/10.1007/s00710-019-00682-y

APPENDIX A

Analyses of trace element concentrations in magnetite in 19 specimens, in various textural settings

This appendix can be found in the file POR-10_Appendix A.xlsx. Values are in parts per million (ppm), as determined by laser-ablation inductively coupled plasma-mass spectrometry. See text for details. This Appendix has not been edited to Geological Survey of Canada specifications.

APPENDIX B

Multi-element (spider) plots showing New Afton magnetite analyses and the reference field for high-temperature hydrothermal, felsic plutonic, and andesite magnetite compositions, *after* Dare et al. (2014). Sample numbers from Table 1.

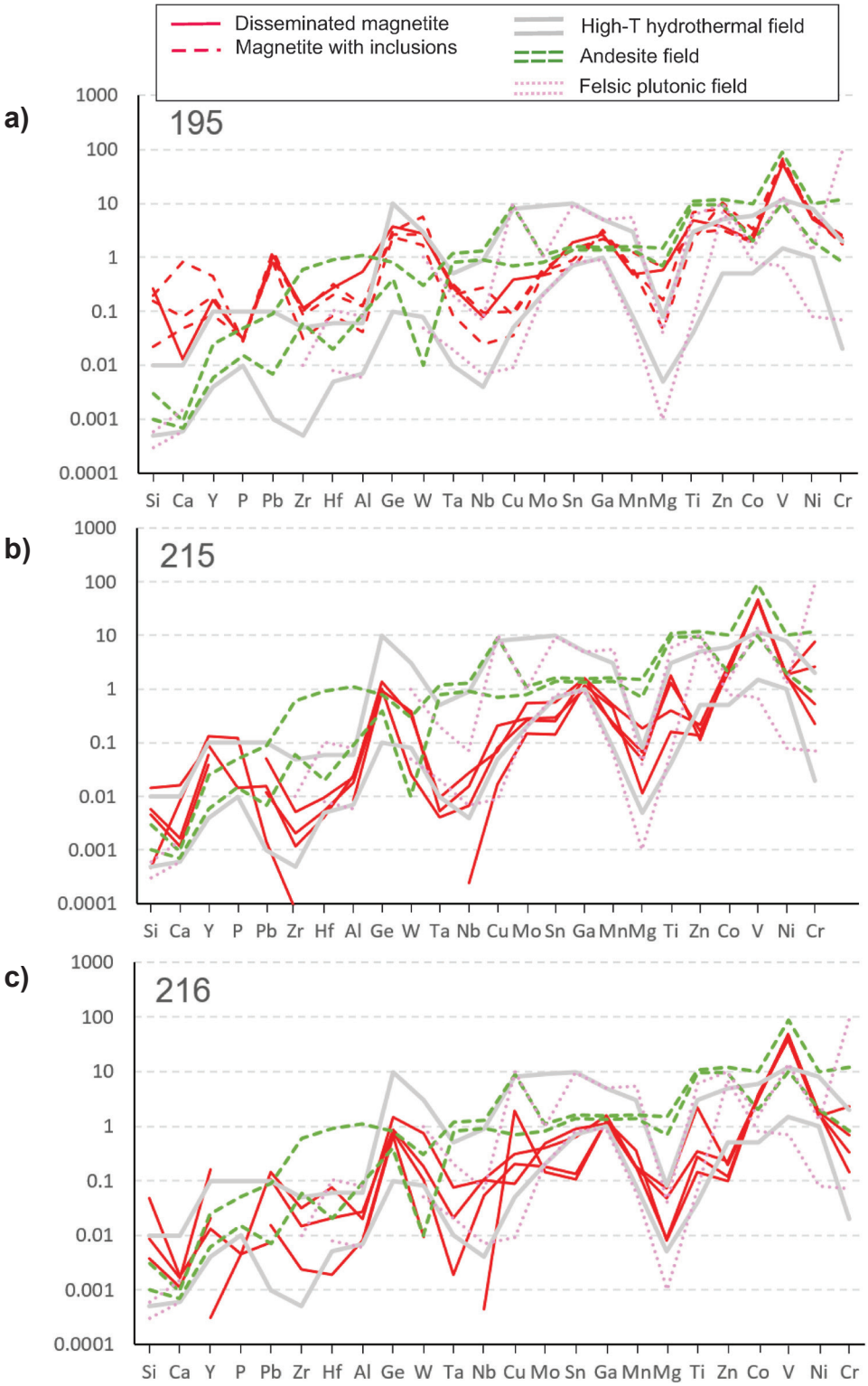

Figure B1. Samples with only disseminated magnetite: **a)** sample 195, **b)** sample 215, **c)** sample 216.

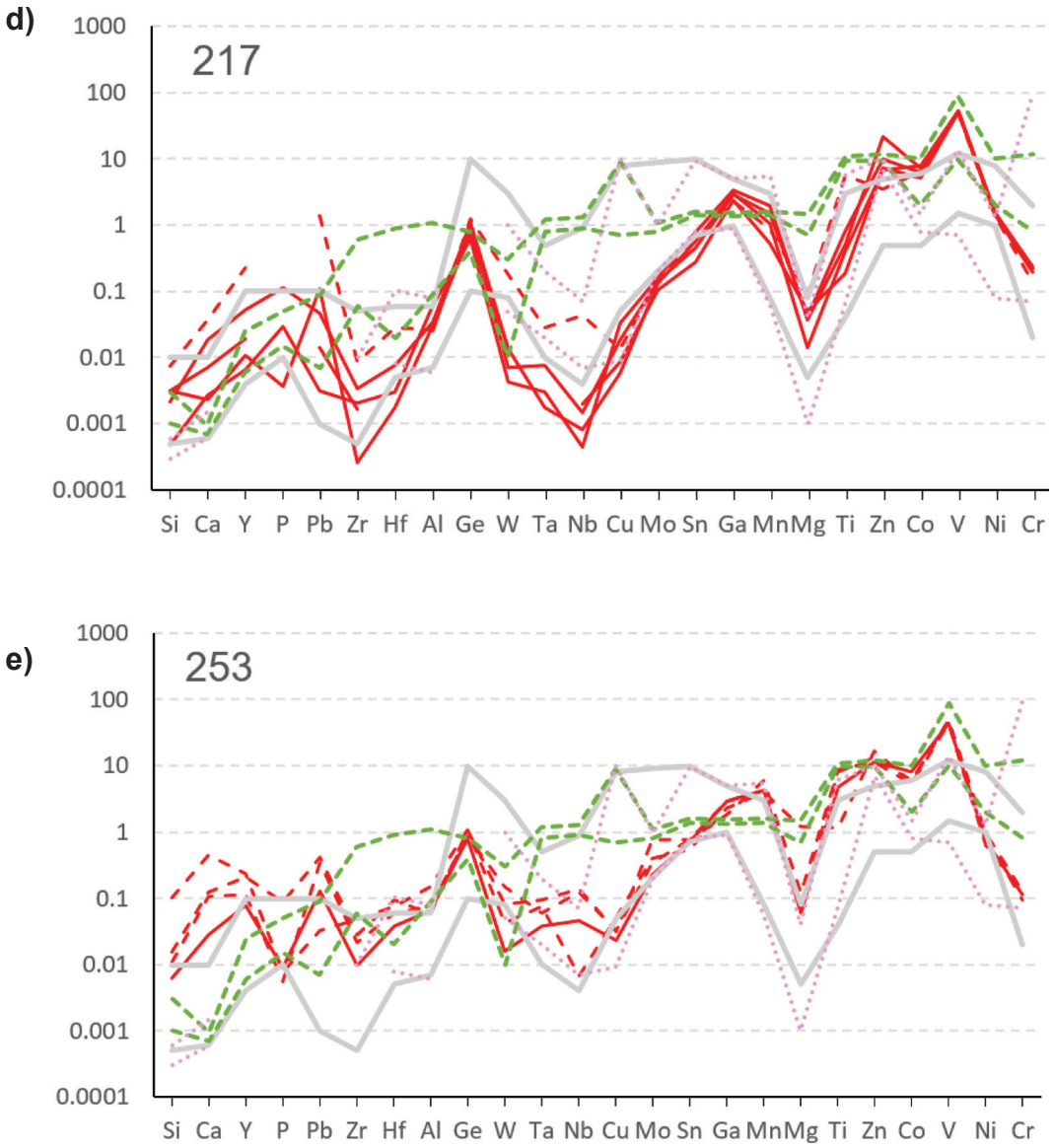

Figure B1. (con't) Samples with only disseminated magnetite: **d)** sample 217, **e)** sample 253.

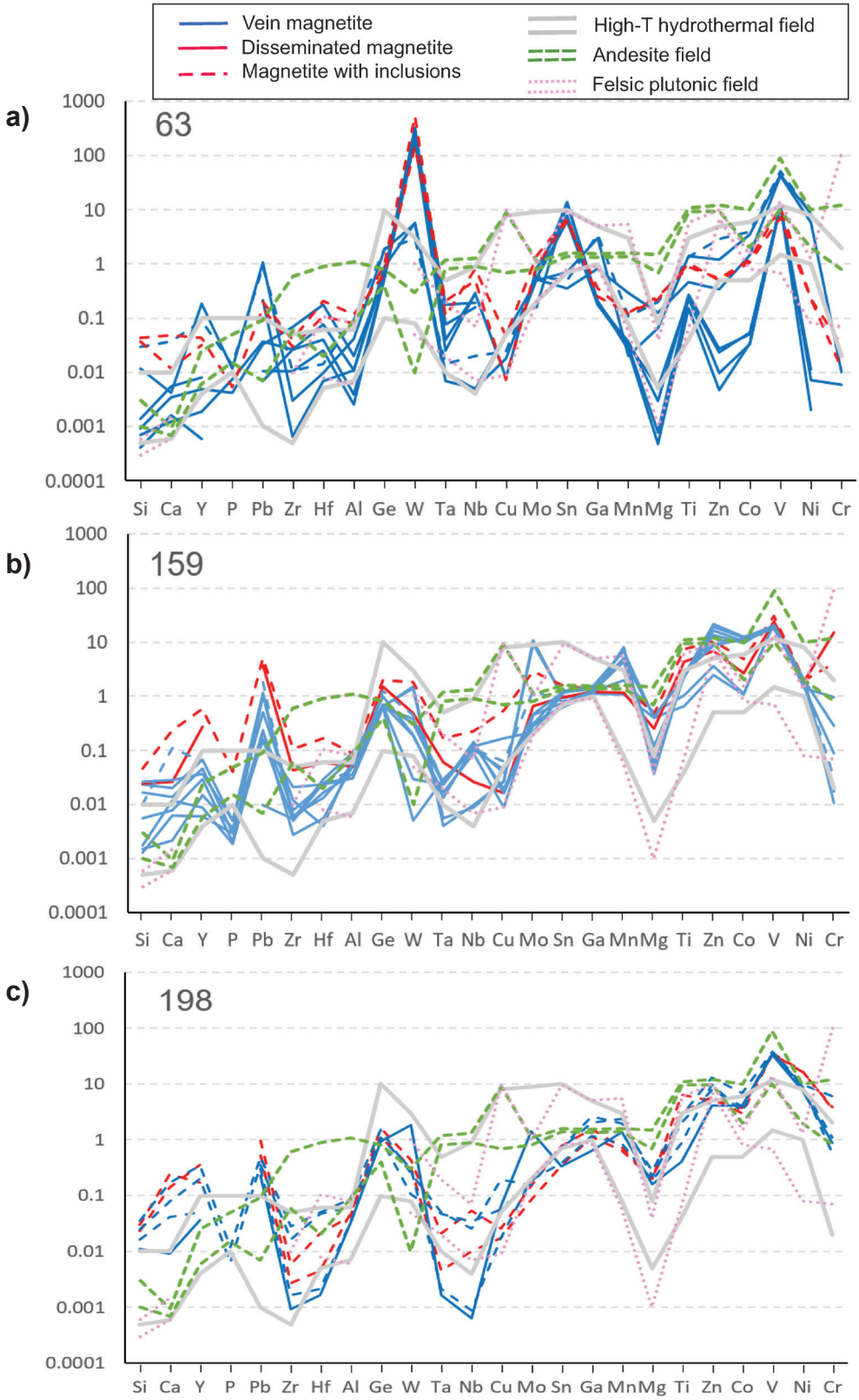

Figure B2. Samples with disseminated and vein magnetite: **a)** sample 63, **b)** sample 159, **c)** sample 198.

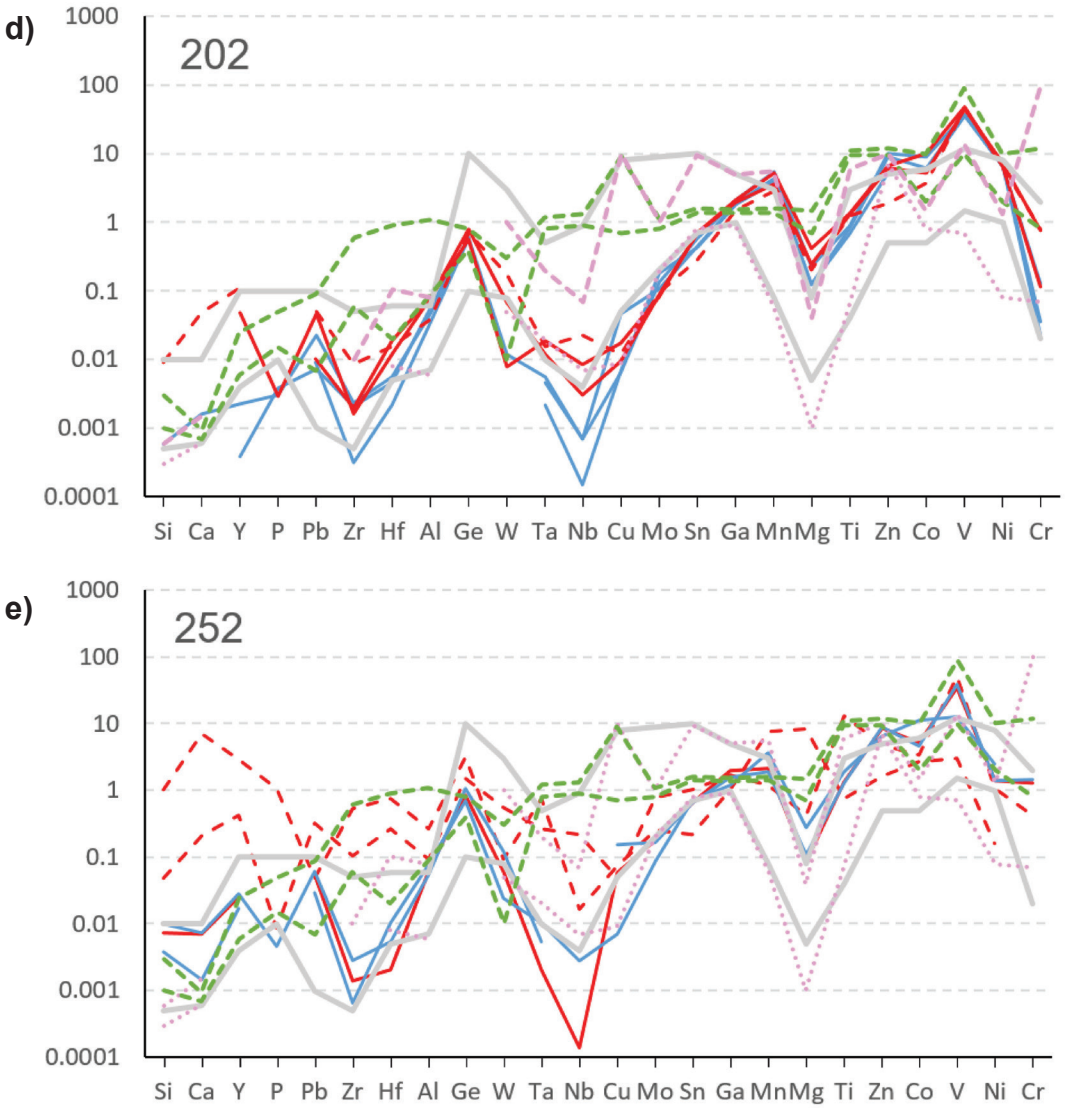

Figure B2. (con't) Samples with disseminated and vein magnetite: **d)** sample 202, **e)** sample 252.

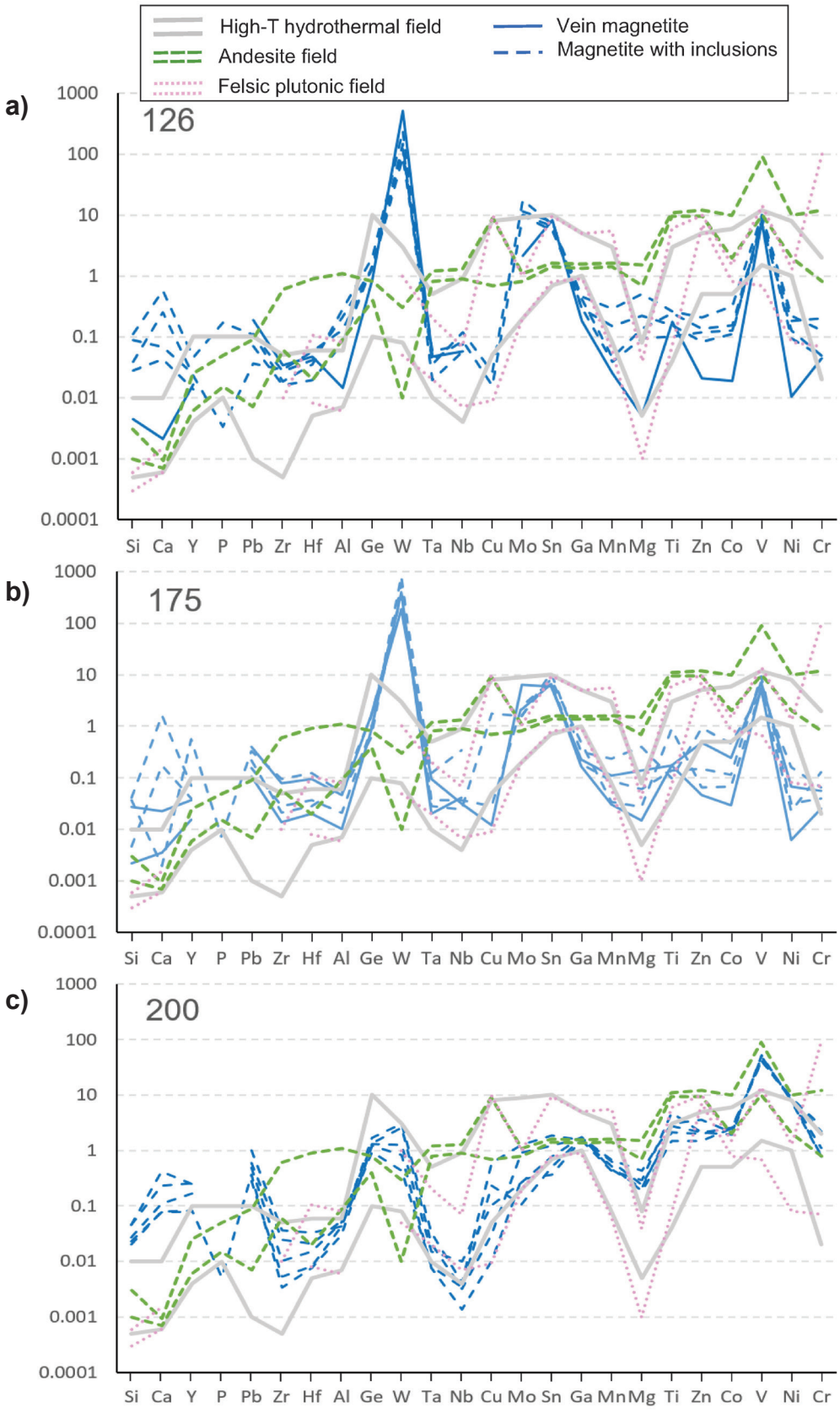

Figure B3. Samples with only vein magnetite: **a)** sample 126, **b)** sample 175, **c)** sample 200.

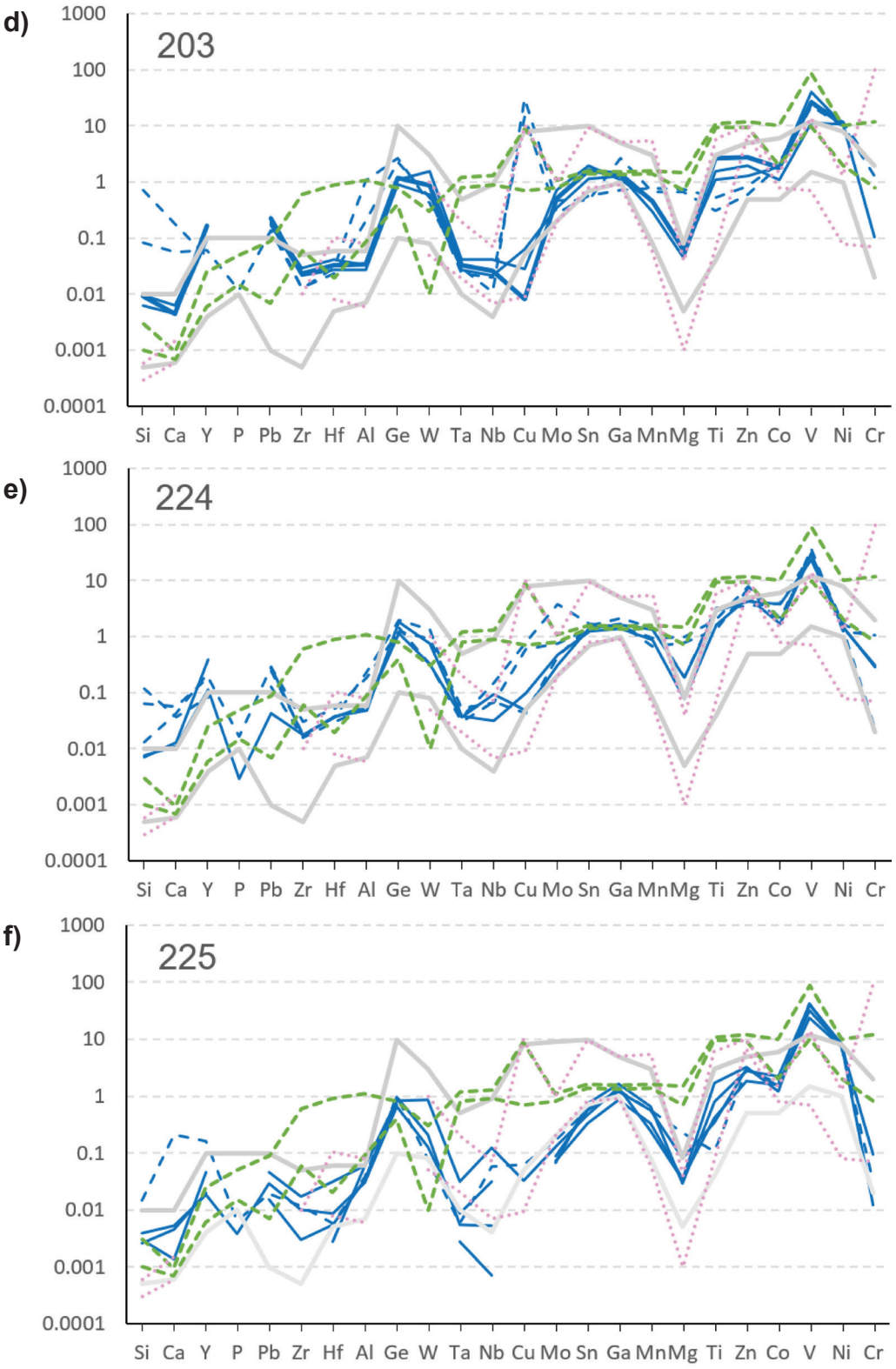

Figure B3. (con't) Samples with only vein magnetite: **d)** sample 203, **e)** sample 224, **f)** sample 225.

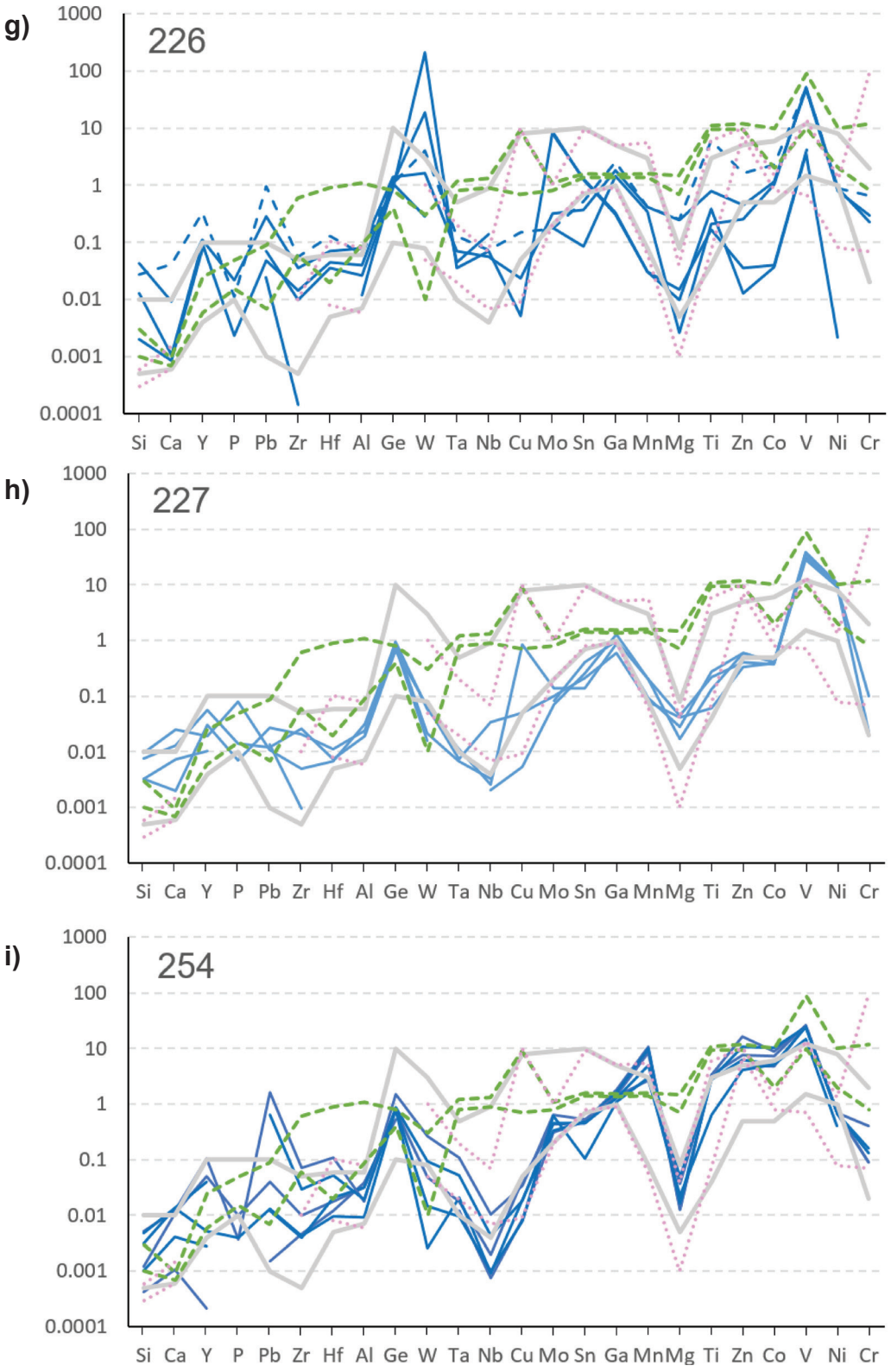

Figure B3. (con't) Samples with only vein magnetite: **g)** sample 226, **h)** sample 227, **i)** sample 254.

Investigation of tourmaline characteristics in bedrock and surficial sediment samples from two Canadian porphyry copper systems

C.E. Beckett-Brown[1]*, A.M. McDonald[1], M.B. McClenaghan[2], A. Plouffe[2], and T. Ferbey[3]

Beckett-Brown, C.E., McDonald, A.M., McClenaghan, M.B., Plouffe, A., and Ferbey, T., 2021. Investigation of tourmaline characteristics in *bedrock and surficial sediment samples from two Canadian porphyry copper systems;* in *Targeted Geoscience Initiative 5: contributions to the understanding and exploration of porphyry deposits, (ed.) E. Schetselaar and A. Plouffe; Geological Survey of Canada, Bulletin 616, p. 109–135. https://doi.org/10.4095/327989*

Abstract: Colour, texture, and chemistry were used to determine the source of tourmaline grains in local surficial (detrital) sediments from two Canadian porphyry systems (Woodjam and Casino). Tourmaline from porphyry bedrock is generally dark brown to black. Crystals frequently exhibit oscillatory and sector zoning, with overgrowth, irregular, and patchy patterns. Major-element analyses show ranges from schorl (Fe^{2+}-rich; 0.04–3.07 *apfu*, av. 0.76) to dravite (Mg-rich, av. 2.00 *apfu*), with a minor povondraite (Fe^{3+}) component. The alkali- and alkaline-earth element concentrations are relatively constant, with Na>Ca>□ and $OH^{-}>O^{2-}$ dominant. Tourmaline in porphyry systems is characterized by high Cu (tens of parts per million) and Sr (hundreds of parts per million), and low Pb (<10 parts per million) and Zn (tens of parts per million). Detrital tourmaline occurs as euhedral grains and contains similar Fe and Mg concentrations and textural zonation patterns to porphyry tourmaline. Its trace-element content shows similarities but with larger ranges of values, likely related to the presence of non-porphyry detrital tourmaline. Overall, a combination of physical and chemical characteristics (oxy-dravite–povondraite trend, high Sr, low Zn and Pb) of tourmaline grains are useful in discriminating between porphyry- versus non-porphyry–derived (or related) tourmaline in both bedrock and surficial sediments.

Résumé : Nous avons utilisé les caractéristiques de couleur, de texture et de chimie pour déterminer la source des grains de tourmaline présents dans les sédiments superficiels (détritiques) locaux de deux systèmes porphyriques (Woodjam et Casino) au Canada. La tourmaline présente dans le substratum rocheux porphyrique exhibe une couleur qui varie généralement du brun foncé au noir. Les cristaux présentent fréquemment une zonation oscillatoire et sectorielle, avec des motifs d'accroissement secondaire, irréguliers et inégaux. Les analyses des éléments majeurs révèlent des plages de composition s'étendant du schorl (riche en Fe^{2+}; de 0,04 à 3,07 atomes par unité de formule, moy. de 0,76) à la dravite (riche en Mg, moy. de 2,00 atomes par unité de formule), avec une composante mineure de povondraïte (Fe^{3+}). Les concentrations d'éléments alcalins et alcalino-terreux sont relativement constantes, avec une dominance de Na>Ca>□ et de $OH^{-}>O^{2-}$. La tourmaline dans les systèmes porphyriques est caractérisée par une teneur élevée en Cu (dizaines de parties par million) et en Sr (centaines de parties par million), et une faible teneur en Pb (<10 parties par million) et en Zn (dizaines de parties par million). La tourmaline détritique se présente sous forme de grains euédriques et affiche des concentrations de Fe et de Mg et des motifs texturaux de zonation semblables à ceux de la tourmaline des systèmes porphyriques. Sa teneur en éléments en traces présente des similitudes, mais avec des fourchettes de valeurs plus larges, ce qui reflète probablement la présence de tourmaline détritique ne provenant pas de systèmes porphyriques. Dans l'ensemble, une combinaison de caractéristiques physiques et chimiques (tendance oxy-dravite–povondraïte, teneur élevée en Sr, faible teneur en Zn et Pb) des grains de tourmaline est utile pour distinguer la tourmaline de systèmes porphyriques de celle qui n'en provient pas (ou qui n'y est pas apparentée) dans le substratum rocheux et les sédiments superficiels.

[1]Harquail School of Earth Sciences, Laurentian University, Willet Green Miller Centre, 935 Ramsey Lake Road, Sudbury, Ontario P3E 2C6
[2]Geological Survey of Canada, 601 Booth Street, Ottawa, Ontario K1A 0E8
[3]British Columbia Geological Survey, P.O. Box 9333, Stn Prov Gov't, Victoria, British Columbia V8W 9N3
*Corresponding author: C.E. Beckett-Brown (email: ce_beckettbrown@laurentian.ca)

INTRODUCTION

Exploration for new mineral deposits is becoming increasingly challenging as discovery rates decrease, expenditures increase, and exploration switches from surface-based methods to those that can detect buried deposits. Indicator mineral identification is one such technique that can detect mineral deposits buried beneath thick glacial sediment cover.

Recent studies have identified two groups of porphyry copper indicator minerals (Plouffe and Ferbey, 2017). Group 1 includes minerals that can be directly linked to porphyry copper mineralization based on their spatial distribution and abundance in surficial sediments (e.g. chalcopyrite, pyrite, gold, jarosite; Averill, 2011; Kelley et al., 2011; Hashmi et al., 2015; Plouffe et al., 2016; Plouffe and Ferbey, 2017). Group 2 includes minerals that are common in many geological environments but have specific chemical characteristics tied directly to mineralized porphyry systems, such as zircon (Lu et al., 2016), epidote (Cooke et al., 2014, 2017), apatite (Bouzari et al., 2016; Mao et al., 2016), titanite (Xu et al., 2015), and magnetite (Dare et al., 2014; Canil et al., 2017; Pisiak et al., 2017). Studies of indicator minerals typically focus either on those present in the bedrock environment (e.g. Cooke et al., 2014, 2017) or those found in surficial sediment such as till (Plouffe and Ferbey, 2017). This study combines multidimensional analyses of a specific supergroup of indicator minerals, tourmaline, derived from both bedrock and surficial (till and stream) sediments.

Several mineral groups have been evaluated as indicator minerals for mineralized porphyry systems (e.g. apatite, epidote, and chlorite group minerals; Wilkinson et al., 2017), but to date, the tourmaline supergroup has been overlooked. Tourmaline is a common constituent of many felsic rocks, notably pegmatites, but it is also common in the calc-alkaline to alkaline environments that characterize porphyry systems. Because of its colour, habit, and specific gravity, tourmaline can often be overlooked or mistaken for similar minerals (e.g. epidote, amphibole). Its hardness and resistance to chemical and physical weathering allow tourmaline to potentially serve as an effective indicator mineral. Tourmaline has proven extremely useful in other geological applications, including as a successful petrogenetic indicator mineral of its host rocks (Henry and Guidotti, 1985). The characteristics of tourmaline that make it an ideal long-term recorder of petrogenetic conditions include 1) the ability to accommodate a wide range of elements, 2) high hardness (7 on Mohs scale) and a lack of cleavage, and 3) insolubility under most terrestrial conditions. The overall long-term stability of tourmaline in the surficial environment also allows it to potentially record fluid evolution (including magmatic, magmatic-hydrothermal, and hydrothermal ore-forming fluids) during its crystallization history (Henry and Dutrow, 1996; Dutrow and Henry, 2011; Marschall and Jiang, 2011; van Hinsberg et al., 2011). In this sense, the growth history of a tourmaline crystal has the potential to record not only major features, but also subtle ones (e.g. trace-element variations). Tourmaline should, therefore, closely reflect the chemical zonation that develops within a mineralized porphyry system.

Tourmaline is a common accessory mineral in hydrothermal deposits worldwide (Slack, 1996) and has been used to understand the development and evolution of select ore systems, including volcanogenic massive sulfide (VMS), orogenic gold, Sn-W, porphyry deposits and even emerald mineralization (Slack and Coad, 1989; Slack et al., 1993; Griffin et al., 1996; Frikken et al., 2005; Galbraith et al., 2009; Baksheev et al., 2010, 2011, 2012; Slack and Trumbull, 2011; Chapman et al., 2015; Codeço et al., 2017, 2019; Kalliomäki et al., 2017; Manéglia et al., 2018).

The purpose of this study is to investigate and evaluate the applicability and usefulness of tourmaline as an indicator of mineralized porphyry copper systems. We focused on two sites, Woodjam in British Columbia and Casino in Yukon, examining tourmaline in the mineralized porphyry system (bedrock) as well as in local surficial sediments (stream sediments or till). This paper provides detailed documentation and comparisons of several key elements in tourmaline, including 1) chemical zonation and textural features, 2) major- and minor-element chemistry, and 3) trace-element chemistry. The comparison of tourmaline derived from the different media (i.e. surficial and bedrock) is crucial to the evaluation of the effectiveness of tourmaline as an indicator for porphyry deposits.

GEOLOGICAL BACKGROUND

Bedrock samples

The Casino deposit is a mineralized porphyry Cu-Mo-Au deposit located 300 km northwest of Whitehorse, Yukon. It is hosted in Late Cretaceous calc-alkalic quartz monzonite of the Casino suite (Casselman and Brown, 2017). Tourmaline is found throughout the deposit, including in breccias and veins, and as disseminations. Samples of all three textures of tourmaline were used in this study.

The Woodjam cluster is located in the Cariboo district, 50 km east of Williams Lake, British Columbia. Several types of mineralized porphyry systems hosted in Early Jurassic calc-alkaline intrusions (del Real et al., 2017) have been identified in the cluster: Megabuck and Deerhorn (Au-Cu), Southeast Zone (Cu-Mo), and Three Firs and Takom (Au-Cu). The tourmaline samples used in our study are from the Deerhorn and Takom deposits, where tourmaline occurs as an early alteration of the host rock, as disseminations, in breccias, and veins. The tourmaline investigated formed in a variety of alteration types, including 1) potassic, 2) phyllic, and 3) propylitic.

For comparison, we also analyzed tourmaline-bearing samples from other mineralized porphyry systems, including 1) Highland Valley Copper, British Columbia; 2) Schaft

Creek, British Columbia; 3) New Afton, British Columbia; and 4) Soledad, Peru. A suite of background tourmaline (i.e. non-porphyry) samples was also examined to provide a frame of reference for comparing tourmaline associated with mineralized porphyry systems to tourmaline not associated with mineralization. A complete listing of bedrock samples is presented in Table 2 of Beckett-Brown et al (2019).

Surficial samples

The Casino deposit is a deeply weathered porphyry that is largely intact due to minimal to no glacial erosion of the region during the past 2 million years (Godwin, 1976; Bond and Lipovsky, 2011). Bulk (10–15 kg) stream-sediment samples containing tourmaline were collected in 2017 from local first- and second-order streams (e.g. Casino Creek) located in narrow V-shaped valleys (Fig. 1b). Sampling details are reported in McCurdy et al. (2019) and McClenaghan et al. (this volume).

The Woodjam area is a glaciated landscape that was most recently affected by two phases of ice flow during the Late Wisconsinan (Fraser glaciation; Clague and Ward, 2011): an older flow to the southwest and a younger flow to the northwest (Plouffe and Ferbey, 2016). As part of the TGI-4 program, the Geological Survey of Canada (GSC) and the British Columbia Geological Survey collected bulk (10–15 kg) till samples around the Woodjam cluster (during 2011–2013). Raw indicator mineral count data for the till samples, including those for tourmaline, were reported in Plouffe and Ferbey (2016). The samples were processed by Overburden Drilling Management (ODM) to produce mid-density (2.8–3.2 specific gravity (SG)) and heavy (>3.2 SG) mineral concentrates for counting indicator minerals in the 0.25 to 0.5 mm size fraction. Tourmaline abundance was reported as i) a percentage of the total heavy minerals in the greater than 3.2 SG fraction, ii) a percentage of the total minerals in the 2.8 to 3.2 SG fraction, and iii) a total number of grains in the 2.8 to 3.2 and greater than 3.2 SG fractions. Maps showing the distribution of tourmaline in till at Woodjam were presented by Chapman et al. (2015), and Plouffe and Ferbey (2017) plotted the number of grains in the 2.8 to 3.2 SG fraction normalized to 10 kg sample mass. In 2015, 50 tourmaline grains were removed from the 2.8 to 3.5 SG fraction of four of the till samples for mineral chemistry, the results of which are reported in Chapman et al. (2015).

The archived 2.8 to 3.2 SG and greater than 3.2 SG Woodjam concentrates were re-examined in 2016 by ODM as part of our current study. The original (2011–2013) tourmaline count data (Plouffe and Ferbey, 2016), the number of grains removed in 2015 for mineral chemistry, and the 2016 tourmaline recount data are summarized in Appendix A. There are important differences between the counts made in 2013 and 2016, specifically for the 2.8 to 3.2 SG fraction. The 2016 tourmaline grain count is more than 50% higher in 75 of 91 samples. It is difficult to visually identify tourmaline in heavy mineral concentrates (HMC) based on its optical and physical properties; the differences in abundance show that the visual identification method can be highly subjective. Given that the 2016 recounts were specifically targeted at the identification of tourmaline and were completed by a senior mineralogist, we assert that the 2016 counts are more accurate. A new tourmaline abundance map for the 2.8 to 3.2 SG fraction of till based on the 2016 data is presented in Figure 1a.

METHODS

Sample processing

Surficial sediment samples (till and stream sediment) were collected by the GSC and processed by ODM to produce nonferromagnetic HMCs. Processing followed protocols outlined by Plouffe and Ferbey (2016) and McClenaghan et al. (2020). Tourmaline grains were primarily recovered in the sand-sized (0.25–2.0 mm), mid-density (2.8–3.2 SG) fraction of the surficial sediment samples, with minor amounts (approximately 1%) also recovered from the heavy (>3.2 SG) fraction. Tourmaline grains were visually identified by their dark brown colour, prismatic crystal habit, parallel striations on crystal faces, and conchoidal fracture (Fig. 2a). Selected grains were mounted in 2.5 cm epoxy pucks for imaging and chemical analysis. Grains were mounted perpendicular and parallel to the c-axis (elongation direction) to provide favourable orientations to examine any variations in chemical zonation with respect to the c-axis. Polished thin sections (PTS) of tourmaline-bearing bedrock samples were also prepared.

Major- and minor-element chemistry

Chemical analyses of major and minor elements in tourmaline grains in PTS and epoxy grain mounts were conducted by scanning electron microscopy–energy-dispersive spectroscopy (SEM-EDS) at Laurentian University on a JEOL 6400 SEM, with an accelerating voltage of 20 kV, a beam current of 1.0 nA, and 15 s counting times. Data were processed using INCA software. The primary standards were well characterized materials, including diopside (Mg*K*α, Ca*K*α, Si*K*α), albite (Al*K*α, Na*K*α), chalcopyrite (Fe*K*α), and syn $CaTiO_3$ (Ti*K*α). Representative chemical analyses are presented in Table 1. The chemical data were reduced to atoms per formula unit (*apfu*) based on 31 anions and this calculation was completed using WinTcac (Yavuz et al., 2011). Tourmaline ubiquitously exhibits zonation, typically about the c-axis, thus individual chemical zones were analyzed.

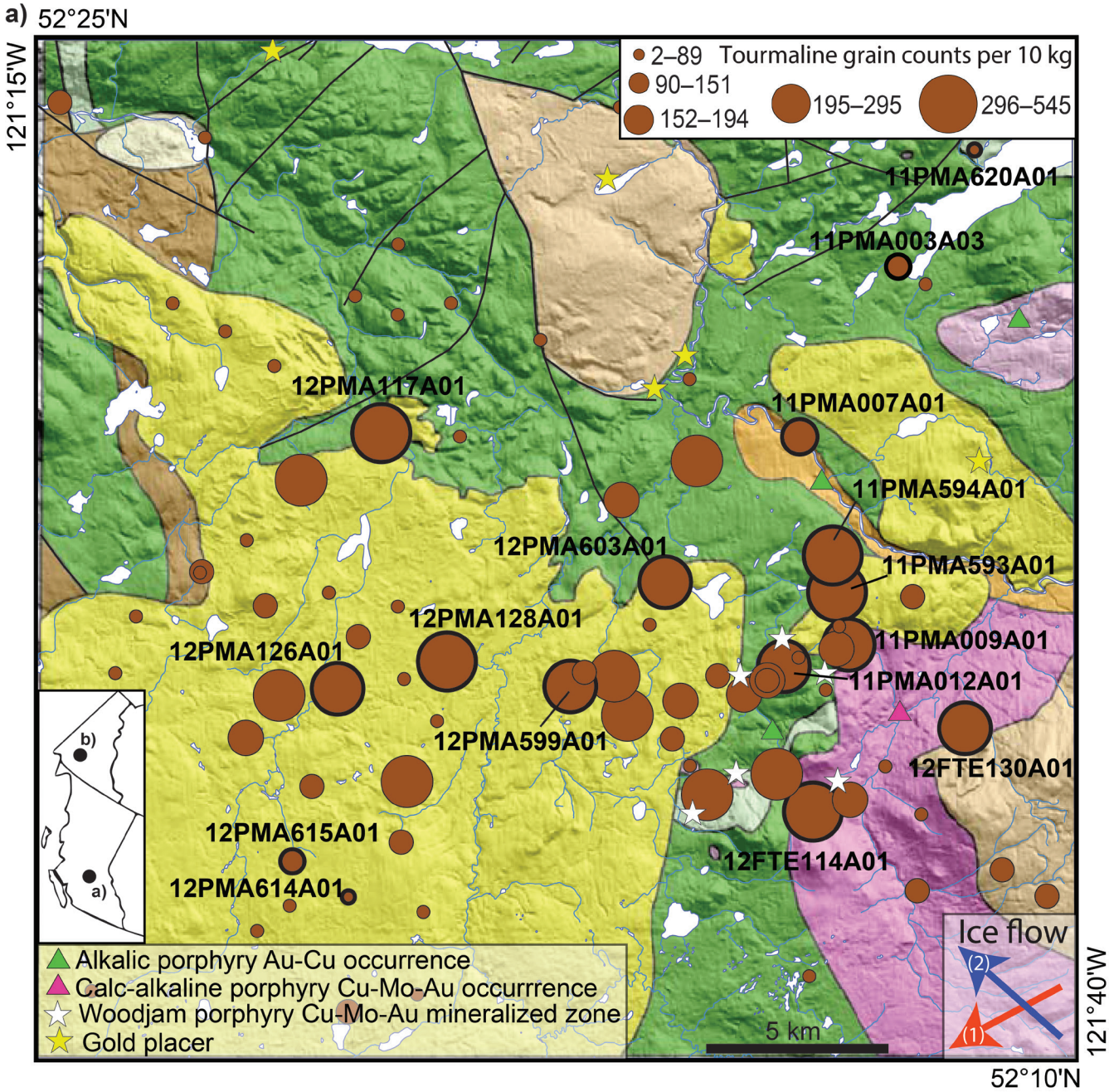

Figure 1. Location of surficial sediment samples from which tourmaline grains were recovered and examined in this study; inset map shows the location of **a)** the Woodjam deposit in British Columbia and **b)** the Casino deposit in Yukon: a) Proportional dot map of tourmaline abundance (grain counts, normalized to 10 kg) in the mid-density (2.8–3.2 SG) 0.25 to 0.5 mm fraction of till samples collected down ice of the Woodjam deposit cluster, British Columbia (unpublished Geological Survey of Canada data). *See* Plouffe and Ferbey (2017) for bedrock geology. Dots with the black outline indicate till samples from which tourmaline grains were investigated;

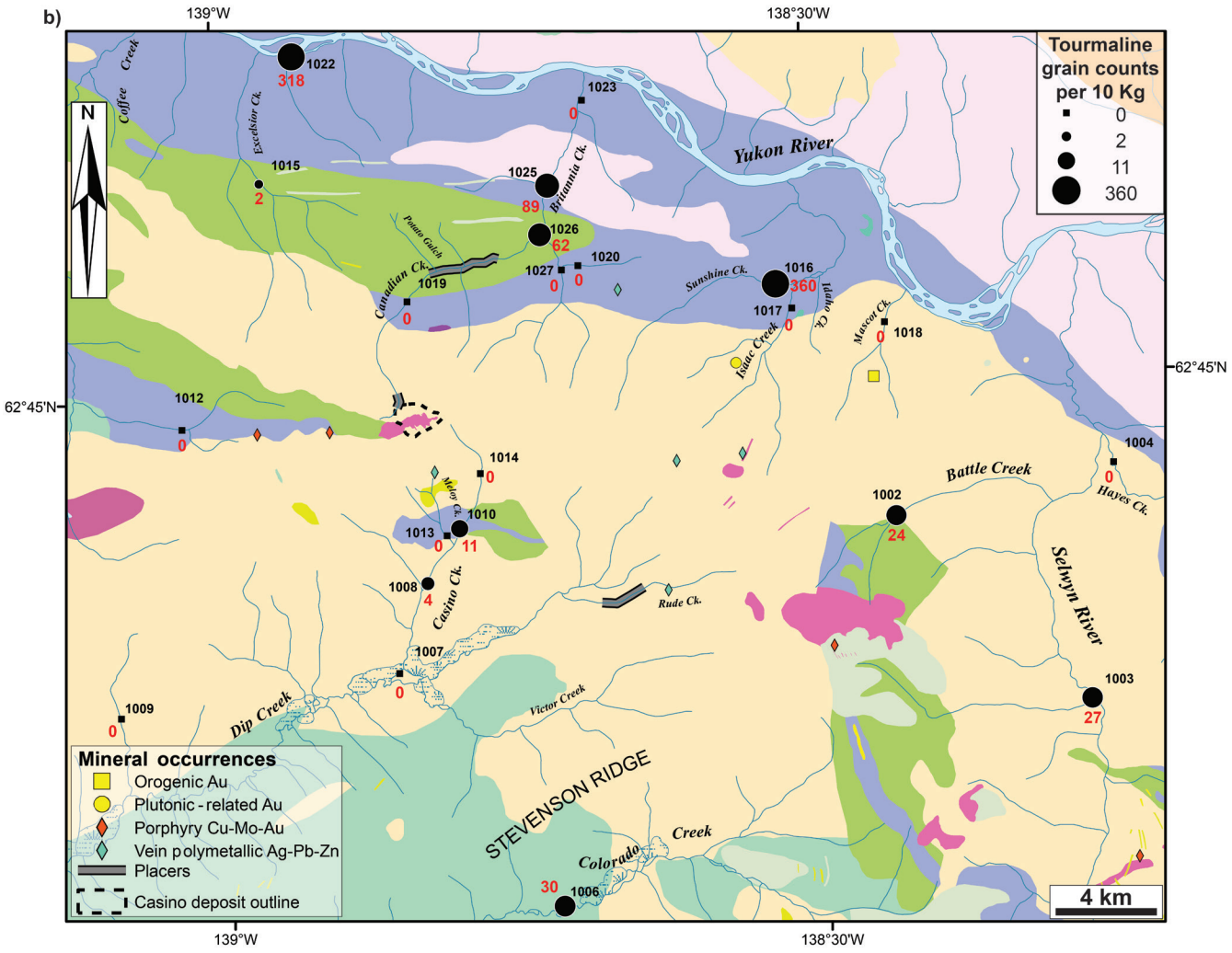

Figure 1. (cont.) b) the location of stream-sediment sample sites (black sample numbers) around the Casino deposit, Yukon, and abundance of tourmaline (grain counts, normalized to 10 kg, in red) in the 2.8 to 3.2 SG, 0.25 to 0.5 mm fraction. *See* McClenaghan et al. (this volume) for Casino bedrock geology.

Trace-element chemistry

In-situ trace-element analyses of tourmaline were carried out using laser-ablation inductively coupled plasma mass spectrometry (LA-ICP-MS) at Laurentian University. Samples were ablated using a Resonetics RESOlution M-50 laser ablation system coupled to a Thermo Fisher XSeries 2 quadrupole ICP-MS. The Resonetics laser uses a 193 nm argon fluoride excimer laser operated at a rate of 8 Hz for line scans with a 30 µm beam and a scan speed between 10 and 15 µm/s with a measured fluence of approximately 3 J/cm^2. External reference materials included NIST 610 (Jochum et al., 2011), NIST 612 (Jochum et al., 2011), and BHVO2G (Raczek et al., 2001). The NIST 610 standard was used as the primary reference material with Si as the internal standard (values collected from SEM-EDS were used for Si). Drift and data reproducibility were assessed using NIST 612, BHVO2G, and an in-house tourmaline standard. Standards were ablated before and after each 10 to 15 tourmaline sample analysis. Drift correction was applied using the baseline reduction scheme in iolite (Paton et al., 2011). Samples were analyzed for major and trace elements, including ^{7}Li, ^{9}Be, ^{11}B, ^{28}Si, ^{31}P, ^{33}S, ^{39}K, ^{45}Sc, ^{47}Ti, ^{51}V, ^{52}Cr, ^{55}Mn, ^{59}Co, ^{60}Ni, ^{65}Cu, ^{66}Zn, ^{71}Ga, ^{72}Ge, ^{75}As, ^{85}Rb, ^{88}Sr, ^{89}Y, ^{90}Zr, ^{93}Nb, ^{95}Mo, ^{107}Ag, ^{115}In, ^{118}Sn, ^{121}Sb, ^{133}Cs, ^{137}Ba, ^{139}La, ^{140}Ce, ^{141}Pr, ^{146}Nd, ^{147}Sm, ^{153}Eu, ^{157}Gd, ^{159}Tb, ^{163}Dy, ^{165}Ho, ^{166}Er, ^{169}Tm, ^{172}Yb, ^{175}Lu, ^{178}Hf, ^{208}Pb, ^{232}Th, and ^{238}U. A summary of the trace-element data is presented in Table 2 for bedrock samples and Table 3 for surficial sediment samples. Data on a large number of elements were collected to create a baseline for future comparison.

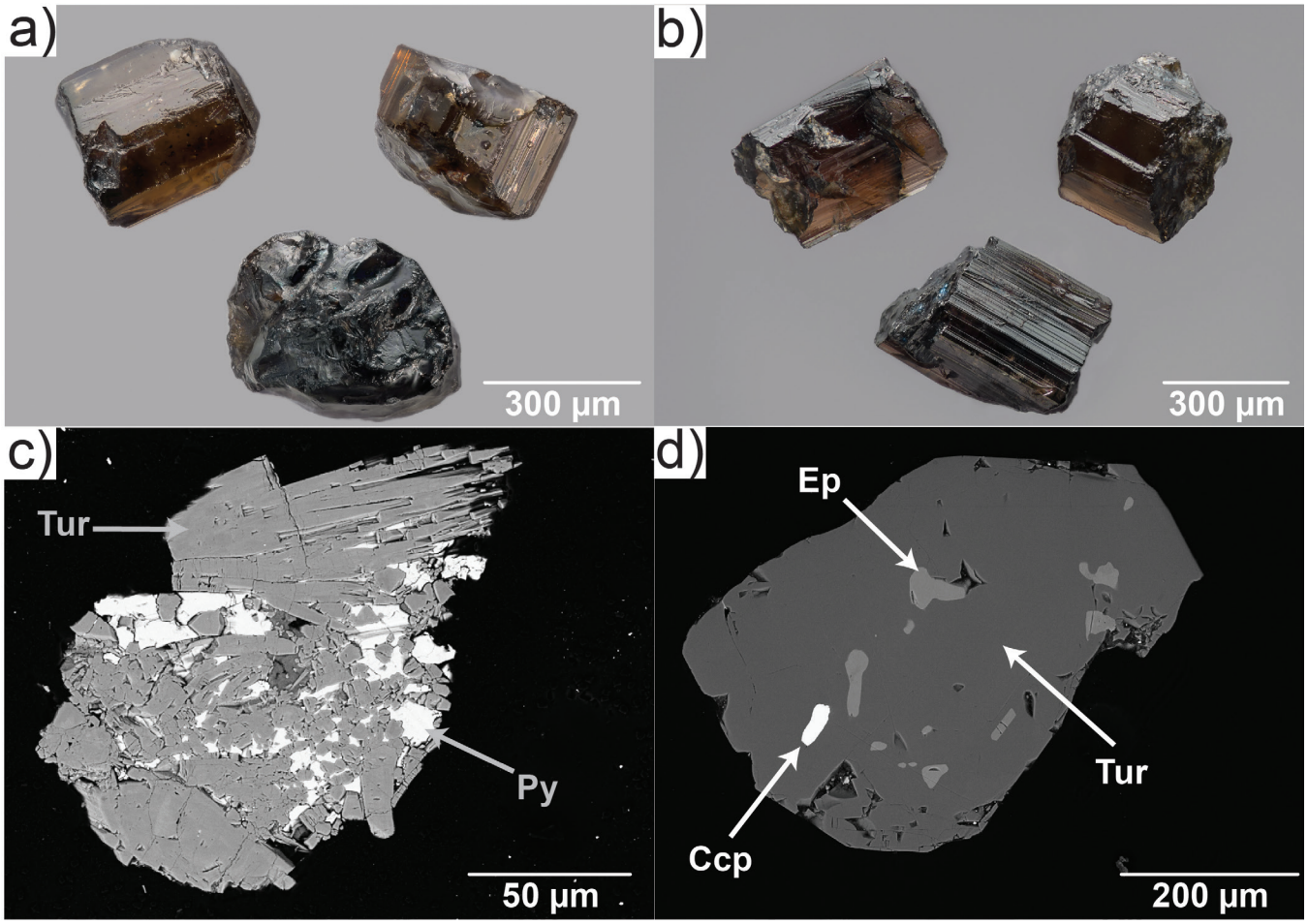

Figure 2. Brown tourmaline grains from the mid-density (2.8–3.2 SG) fraction of: **a)** Geological Survey of Canada (GSC) till sample 11-PMA-009A01, collected less than 1 km northwest (up-ice) of a Woodjam cluster mineralized zone (photograph by Michael J. Bainbridge Photography); **b)** GSC stream-sediment sample 1003, collected downstream of the Cockfield porphyry occurrence, 30 km east of the Casino deposit (photograph by Michael J. Bainbridge Photography); **c)** backscattered electron image of a tourmaline (Tur) grain (from Woodjam till sample 11PMA012A01) infilled by pyrite (Py); and **d)** backscattered electron image of a tourmaline grain (from Casino stream-sediment sample 1025) containing inclusions of chalcopyrite (Ccp) and epidote (Ep).

RESULTS

Tourmaline textures

Bedrock samples

Three distinct styles of bedrock tourmaline have been recognized in samples from Casino and Woodjam: breccia, vein, and disseminated (Fig. 3). One important characteristic is that all three styles of tourmaline can be associated with sulfide mineralization. Sulfides, including chalcopyrite and pyrite, were observed overgrowing prismatic to acicular, subhedral to euhedral tourmaline crystals. Alteration minerals (quartz and albite) are also observed overgrowing euhedral tourmaline crystals; therefore, tourmaline is interpreted to be one of the earliest forming hydrothermal phases (Fig. 4). In hand sample, tourmaline ranges in colour from usually dark-coloured or black to occasionally colourless and is generally massive in form. Examination of tourmaline in PTS using backscattered-electron (BSE) imaging reveals evidence of complex chemical zonation, dissolution, overgrowths and various mineral inclusions (rutile, ilmenite, quartz, and apatite), although inclusions are generally rare. Although typically black in hand sample, in thin section under cross-polarized light tourmaline can range from brown, pale green to green, blue, or nearly colourless. Pleochroism is generally weak in comparison to that observed in tourmaline from other geological settings; porphyry tourmaline pleochroism is colourless to blue-green in most cases.

Table 1. Representative major element compositions of tourmaline from bedrock, till, and stream-sediment samples collected at the Woodjam and Casino deposits. Values are in *apfu*.

	13CDB-WJ09 C2 6-2	13CDB-WJ05 C2 4-1	CEBB-031 C32-3	CEBB-005 C2 4-1	CEBB-7 SOI1-4 2	11PMA-009-01	12PMA-126A-01	Casino-1010-A6	Casino-1026-B1
Deposit	Woodjam	Woodjam	Casino	Casino	Casino	Woodjam	Woodjam	Casino	Casino
Sample type	Bedrock	Bedrock	Bedrock	Bedrock	Bedrock	Till	Till	Stream sediment	Stream sediment
SiO_2	35.88	34.27	37.76	38.76	36.33	37.18	36.50	36.30	36.13
TiO_2	0.33	0.93	0.38		0.22	0.48	0.68	0.80	0.68
Al_2O_3	30.70	20.46	33.03	36.41	34.97	32.65	32.57	34.39	29.61
FeO	9.17	18.96	7.55	2.12	0.45	6.02	5.47	3.98	8.21
MgO	7.03	7.79	6.83	9.55	10.58	7.03	8.11	7.49	8.41
CaO	1.46	3.04				0.15	0.46	0.94	1.74
Na_2O	1.78	1.43	2.63	2.24	2.70	2.36	2.40	1.77	2.21
Si(T)	5.949	5.938	6.059	5.952	5.806	6.093	5.947	5.912	5.960
Al(T)	0.051	0.004	0.000	0.048	0.194	0.000	0.053	0.088	0.040
B(T)	0.000	0.058	0.000	0.000	0.000	0.000	0.000	0.000	0.000
Al(Z)	5.949	4.175	0.247	6.000	6.000	6.000	6.000	6.000	5.716
Mg(Z)	0.051	1.825	0.000	0.000	0.000	0.000	0.000	0.000	0.284
Al(Y)	0.000	0.000	0.247	0.541	0.393	0.305	0.202	0.511	0.000
Ti(Y)	0.042	0.122	0.046	0.000	0.026	0.060	0.084	0.098	0.085
Mg(Y)	1.686	0.188	1.634	2.186	2.520	1.717	1.969	1.819	1.783
Fet(Y)	1.272	2.748	1.013	0.273	0.060	0.825	0.745	0.541	1.132
Ca(X)	0.259	0.564	0.000	0.000	0.000	0.027	0.081	0.164	0.307
Na(X)	0.572	0.480	0.818	0.666	0.835	0.749	0.758	0.558	0.707
Vac	0.169	0.000	0.182	0.334	0.165	0.224	0.161	0.279	0.000

Note: *apfu* (atoms per formula unit) calculated based on 31 anions; Vac: vacancy.

Tourmaline breccias

Tourmaline breccias are the most widely recognized style of tourmaline in porphyry deposits (Sillitoe, 2010); this is consistent with our observations in this study. The tourmaline develops as a matrix material, cementing the breccia (Fig. 3a). Although the matrix can be greater than 90% tourmaline, quartz and sulfides (chalcopyrite and pyrite) that postdate the tourmaline may also be present as matrix cement. The tourmaline grains in the breccia typically develop as radial aggregates of prismatic to acicular crystals that average approximately 50 µm but range from sub-micron up to millimetres in diameter in rare cases. We observed grains to be colour zoned in cross section and along their length.

Tourmaline in veins

The crystals in tourmaline in veins (Fig. 3b) are the smallest among the three tourmaline mineralization styles, typically approximately 20 µm in diameter and only rarely up to 100 µm in length. This tourmaline commonly develops in veins (millimetres to centimetres in vein thickness) associated with paragenetically later quartz and sulfide. The veins are variable in width and commonly have bleached white selvages, mainly of feldspar and quartz (Fig. 3b). Tourmaline grains are randomly oriented with respect to vein margins and tend to occur in densely packed aggregates, the interstices of which are predominantly occupied by quartz and, to a lesser extent, sulfides.

Disseminated tourmaline

Of the three styles observed in the porphyry system, disseminated tourmaline (Fig. 3c) forms the largest crystals, with grains up to several centimetres in length. Texturally, disseminated tourmaline closely resembles tourmaline breccia (i.e. acicular to prismatic radiating masses, commonly infilled by quartz), but the tourmaline develops in discrete anhedral clots instead of the radiating interlocking masses observed in breccias. Some of the clots appear to represent the dissolution of pre-existing phases (feldspar?), based on the shape of the cavities they infill. Disseminated tourmaline can also be found in association with paragenetically later sulfides (pyrite and chalcopyrite).

Table 2. Summary of trace-element analyses in tourmaline from bedrock samples collected from the Casino and Woodjam deposits.

Abundance (ppm)							
Element	**Samples above LOD**	**Av. LOD (ppm)**	**Minimum**	**Maximum**	**Mean**	**Median**	**Standard deviation**
^{39}K	145	20	73	6900	600	240	915
^{45}Sc	145	1	7	250	56	46	40
^{47}Ti	145	5	111	5150	1688	1521	932
^{51}V	145	2	85	1175	439	389	217
^{52}Cr	143	0.1	< LOD	347	50.5	39.1	52.4
^{55}Mn	145	3	21	1300	152	79	186
^{59}Co	145	0.1	0.6	260	14.2	5.4	25.6
^{60}Ni	145	0.1	0.2	31.7	12.8	10.9	8.4
^{65}Cu	140	0.1	< LOD	510	37.8	19.0	68.1
^{66}Zn	145	0.1	5.7	151	34.0	20.1	28.1
^{69}Ga	145	0.1	21.5	103	47.7	47.1	12.3
^{72}Ge	145	0.1	0.8	13.9	5.4	5.2	2.5
^{75}As	143	1	< LOD	322	37.7	21.8	48.7
^{85}Rb	134	0.2	< LOD	25.8	2.4	0.8	4.4
^{88}Sr	145	0.2	34.8	623	209.6	164	143.2
^{89}Y	143	0.03	< LOD	73	6.6	2.9	11.5
^{90}Zr	145	0.1	0.6	45.0	5.3	2.2	7.8
^{93}Nb	143	0.2	< LOD	2.9	0.7	0.6	0.6
^{95}Mo	143	0.1	< LOD	51	4.6	1.3	6.6
^{115}In	140	0.01	< LOD	1.4	0.3	0.2	0.2
^{118}Sn	145	0.5	1.3	57.0	17.1	16.5	10.9
^{121}Sb	143	0.2	< LOD	41.5	2.4	0.9	5.3
^{137}Ba	143	0.2	< LOD	300	17.4	5.4	35.6
^{139}La	143	0.03	< LOD	15.20	3.02	2.01	3.31
^{140}Ce	145	0.03	0.05	29.4	5.14	2.80	5.63
^{141}Pr	143	0.03	< LOD	3.7	0.47	0.25	0.56
^{146}Nd	142	0.01	< LOD	13.80	1.59	0.72	2.00
^{147}Sm	104	0.01	< LOD	4.20	0.31	0.17	0.52
^{153}Eu	136	0.03	< LOD	0.34	0.09	0.08	0.06
^{157}Gd	114	0.01	< LOD	9.8	0.49	0.18	1.13
^{159}Tb	119	0.03	< LOD	1.91	0.10	0.04	0.23
^{163}Dy	132	0.01	< LOD	13.8	0.88	0.35	1.83
^{165}Ho	133	0.03	< LOD	2.69	0.24	0.11	0.42
^{166}Er	142	0.01	< LOD	7.98	0.90	0.49	1.33
^{169}Tm	140	0.03	< LOD	1.30	0.16	0.10	0.20
^{172}Yb	143	0.01	< LOD	10.8	1.49	1.04	1.54
^{175}Lu	141	0.03	< LOD	1.63	0.28	0.21	0.25
^{178}Hf	131	0.04	< LOD	2.53	0.31	0.12	0.48
^{208}Pb	143	0.04	< LOD	11.50	2.55	1.37	2.70
^{232}Th	143	0.04	< LOD	18.00	1.26	0.59	1.82
^{238}U	135	0.04	< LOD	1.59	0.37	0.28	0.31
LOD: limit of detection							

Table 3. Summary of trace-element analyses in tourmaline grains from surficial sediment samples collected surrounding the Casino and Woodjam deposits.

Abundance (ppm)							
Element	**Samples above LOD**	**Av. LOD (ppm)**	**Minimum**	**Maximum**	**Mean**	**Median**	**Standard deviation**
^{39}K	1373	20	< LOD	2900	315	252	265
^{45}Sc	1565	1	< LOD	993	27	11	56
^{47}Ti	1585	5	108	70000	4645	4540	2791
^{51}V	1583	2	< LOD	18900	404	227	921
^{52}Cr	1575	0.1	< LOD	7200	333	243	466
^{55}Mn	1584	3	< LOD	12900	164	76	434
^{59}Co	1572	0.1	< LOD	114	23.5	19.4	16.1
^{60}Ni	1542	0.1	< LOD	672	69.3	45.4	70.4
^{65}Cu	1377	0.1	< LOD	2100	27.1	7.9	107.9
^{66}Zn	1585	0.1	10.3	3020	201	169	178
^{69}Ga	1582	0.1	< LOD	187	37.2	32.4	18.8
^{72}Ge	1200	0.1	< LOD	25	2.5	1.6	2.8
^{75}As	1325	1	< LOD	670	7	3	26
^{85}Rb	1140	0.2	< LOD	31.0	1.5	0.6	3.1
^{88}Sr	1584	0.2	< LOD	2740	300	229	261
^{89}Y	1277	0.03	< LOD	378	1.22	0.11	12.20
^{90}Zr	1516	0.1	< LOD	6200	13.1	0.6	196
^{93}Nb	1415	0.2	< LOD	340	0.8	0.1	9.2
^{95}Mo	1369	0.1	< LOD	150	21.4	0.6	4.4
^{115}In	1108	0.01	< LOD	4.80	0.14	0.04	0.36
^{118}Sn	1544	0.5	< LOD	497	6.6	1.7	23.1
^{121}Sb	1362	0.2	< LOD	360	1.1	0.3	9.9
^{137}Ba	1309	0.2	< LOD	460	6.1	0.9	23.2
^{139}La	1543	0.03	< LOD	21.80	1.90	1.00	2.60
^{140}Ce	1555	0.03	< LOD	77.00	3.23	1.60	4.90
^{141}Pr	1381	0.03	< LOD	4.30	0.33	0.17	0.47
^{146}Nd	1283	0.01	< LOD	11.60	1.15	0.59	1.61
^{147}Sm	541	0.01	< LOD	4.40	0.27	0.13	0.42
^{153}Eu	1362	0.03	< LOD	2.48	0.39	0.30	0.36
^{157}Gd	427	0.01	< LOD	5.50	0.24	0.10	0.48
^{159}Tb	345	0.03	< LOD	1.50	0.04	0.04	0.48
^{163}Dy	332	0.01	< LOD	18.00	0.39	0.06	1.49
^{165}Ho	291	0.03	< LOD	11.60	0.15	0.04	0.78
^{166}Er	266	0.01	< LOD	70.00	0.86	0.06	1.74
^{169}Tm	211	0.03	< LOD	16.20	0.25	0.04	1.24
^{172}Yb	268	0.01	< LOD	158	1.89	0.10	10.91
^{175}Lu	274	0.03	< LOD	31.70	0.41	0.04	2.30
^{178}Hf	320	0.04	< LOD	140	1.51	0.15	10.25
^{208}Pb	1585	0.04	0.27	260	18.73	15.50	15.12
^{232}Th	625	0.04	< LOD	12.70	0.41	0.06	1.02
^{238}U	596	0.04	< LOD	13.00	0.21	0.05	0.78
LOD: limit of detection							

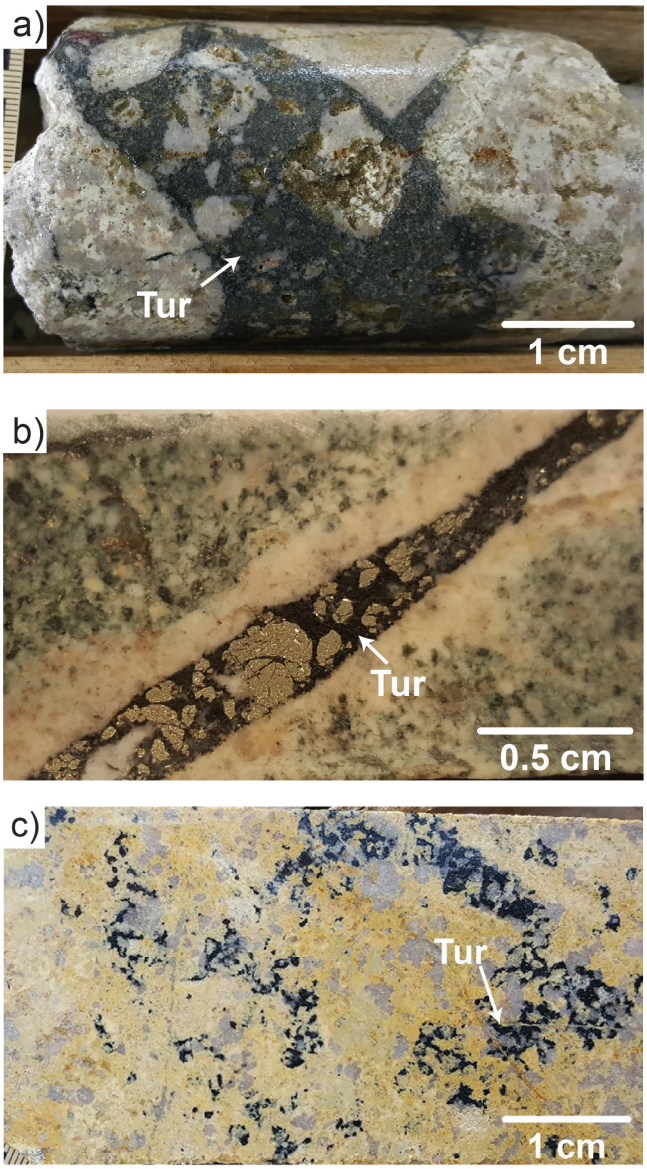

Figure 3. Hand samples of core showing the variable textural styles of tourmaline (Tur) in bedrock: **a)** tourmaline cemented breccia from the Casino deposit (Photograph by C.E. Beckett Brown; NRCan photo 2020-128); **b)** tourmaline from the Woodjam deposit cluster forming as monomineralic veins (Photograph by C.E. Beckett-Brown; NRCan photo 2020-129); **c)** tourmaline from the Casino deposit forming as isolated disseminated clots (Photograph by C.E. Beckett-Brown; NRCan photo 2020-130).

Surficial sediment samples

Tourmaline recovered from surficial sediment samples is predominantly subhedral and brown to black in colour, or rarely yellow, green, or blue (Fig. 2a, b). In general, tourmaline occurs in sediments as individual grains and only rarely as agglomerations (Fig. 2c). The types of mineral inclusions identified in detrital tourmaline grains are summarized in Table 4 for the Woodjam deposit and Table 5 for the Casino deposit. Of the 1545 tourmaline grains examined, 60%

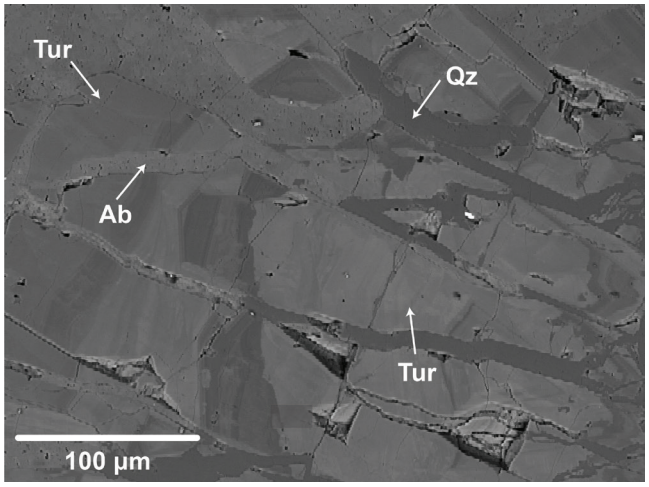

Figure 4. Backscattered-electron image showing the paragenetic position of tourmaline. Tur: tourmaline; Ab: albite; Qz: quartz.

contained mineral inclusions; most are (listed in decreasing abundance) zircon, quartz, rutile, ilmenite, epidote, and chalcopyrite (e.g. Fig. 2d). There are differences in the type and abundance of inclusions at the two study areas. At Woodjam, approximately 50% of the grains contain inclusions (Table 4) and at Casino, approximately 75% of detrital grains contain inclusions (Table 5). Ilmenite inclusions are twice as common in Woodjam tourmaline grains than in Casino tourmaline grains, but pyrite is more abundant in the Casino tourmaline. Detrital tourmaline grains also contain inclusions or attached grains of pyrite (Fig. 2c), chalcopyrite, galena, sphalerite, jarosite, or barite.

Mineral chemistry

Backscattered electron imaging

Tourmaline in bedrock

Minerals in the tourmaline supergroup are able to accommodate a wide range of elements during their crystallization histories (van Hinsberg et al., 2011). The tourmaline from Casino and Woodjam bedrock samples examined in this study exhibits, in general, a high degree of chemical heterogeneity and zonation. These grain-scale features are best observed with BSE imaging, which highlights differences in average atomic number in a given sample. Based on BSE imaging, four types of compositional growth textures are observed in the bedrock samples (Fig. 5). These textures are further subdivided by whether they are likely to be primary (developed at the time of crystallization) or secondary (developed post-crystallization) in origin, as suggested by Slack and Trumbull (2011). Primary features are oscillatory/concentric growth zoning, interpreted to reflect changes in local fluid composition, displaying sharp chemical boundaries or zones developed parallel to [001] (Fig. 5a); and sector/polar zoning that reflects selective partitioning of elements in distinct

Table 4. Mineral inclusions identified in detrital tourmaline grains collected from till at the Woodjam deposit.

Sample number		Total grains	Grains with inclusions	Zircon	Quartz	Rutile	Ilmenite	Biotite	Apatite	Alanite	Epidote	Muscovite	Fe-oxide	Albite	Chlorite	Apatite-REE	Pyrite	K-feldspar	Dumortierite	Titanite	Pentlandite	Ferrosilite	Galena	Calcite	Barite
All samples	# grains	1122	597	251	231	96	65	40	39	38	30	25	17	14	14	14	13	6	6	3	1	1	1	1	1
	%	–	53.2	22.4	20.6	8.6	5.8	3.6	3.5	3.4	2.7	2.2	1.5	1.3	1.3	1.3	1.2	0.5	0.5	0.3	<0.1	<0.1	<0.1	<0.1	<0.1
11PMA003A03	# grains	40	22	9	9	4	1	1	1	–	–	–	–	–	–	1	–	1	–	–	–	–	–	–	–
	%	–	55	22.5	22.5	10.0	2.5	2.5	2.5	–	–	–	–	–	–	2.5	–	2.5	–	–	–	–	–	–	–
11PMA007A01	# grains	70	34	13	11	4	3	2	1	4	1	–	–	1	1	1	–	2	–	–	–	–	–	–	–
	%	–	48.6	18.6	15.7	5.7	4.3	2.9	1.4	5.7	1.4	–	–	1.4	1.4	1.4	–	2.9	–	–	–	–	–	–	–
11PMA009A01	# grains	71	40	14	15	8	3	2	3	1	3	–	1	1	2	–	–	–	–	1	1	–	–	–	–
	%	–	56.3	19.7	21.1	11.3	4.2	2.8	4.2	1.4	4.2	–	1.4	1.4	2.8	–	–	–	–	1.4	1.4	–	–	–	–
11PMA012A01	# grains	28	13	3	4	2	1	–	1	1	1	–	5	1	–	–	–	–	–	–	–	–	–	–	–
	%	–	46.4	10.7	14.3	7.1	3.6	–	3.6	3.6	3.6	–	17.9	3.6	–	–	–	–	–	–	–	–	–	–	–
12PMA117A01	# grains	67	42	21	12	9	5	3	3	1	–	–	–	–	–	1	1	1	1	–	–	–	–	–	–
	%	–	62.7	31.3	17.9	13.4	7.5	4.5	4.5	1.5	–	–	–	–	–	1.5	1.5	1.5	1.5	–	–	–	–	–	–
12PMA126A01	# grains	93	40	15	17	7	3	3	3	3	2	5	1	–	1	–	–	–	2	–	–	1	–	–	–
	%	–	43	16.1	18.3	7.5	3.2	3.2	3.2	3.2	2.2	5.4	1.1	–	1.1	–	–	–	2.2	–	–	1.1	–	–	–
12PMA593A01	# grains	67	37	12	16	5	3	1	1	3	1	1	–	–	1	3	1	–	1	–	–	–	–	–	–
	%	–	55.2	17.9	23.9	7.5	4.5	1.5	1.5	4.5	1.5	1.5	–	–	1.5	4.5	1.5	–	1.5	–	–	–	–	–	–
12PMA128A01	# grains	92	53	26	19	8	4	3	2	–	5	2	5	2	3	1	2	–	1	–	–	–	–	–	–
	%	–	57.6	28.3	20.7	8.7	4.3	3.2	2.2	–	5.4	2.2	5.4	2.2	3.2	1.1	2.2	–	1.1	–	–	–	–	–	–
12PMA594A01	# grains	99	44	14	19	6	5	3	3	–	5	1	1	2	–	–	1	–	–	–	–	–	–	–	–
	%	–	44.4	14.1	19.2	6.1	5.1	3.0	3.0	–	5.1	1.0	1.0	2.0	–	–	1.0	–	–	–	–	–	–	–	–
12PMA599A01	# grains	95	47	18	21	6	7	4	4	7	1	6	–	1	–	3	3	–	–	1	–	–	1	–	–
	%	–	49.5	18.9	22.1	6.3	7.4	4.2	4.2	7.4	1.1	6.3	–	1.1	–	3.2	3.2	–	–	1.1	–	–	1.1	–	–
12PMA603A01	# grains	99	50	23	19	8	4	1	1	3	2	1	–	1	1	–	1	–	–	–	–	–	–	–	–
	%	–	50.5	23.2	19.2	8.1	4.0	1.0	1.0	3.0	2.0	1.0	–	1.0	1.0	–	1.0	–	–	–	–	–	–	–	–
12PMA614A01	# grains	42	22	9	8	4	3	1	3	–	–	–	–	–	2	2	–	–	–	–	–	–	–	–	–
	%	–	52.4	21.4	19.0	9.5	7.1	2.4	7.1	–	–	–	–	–	4.8	4.8	–	–	–	–	–	–	–	–	–
12PMA615A01	# grains	48	25	10	11	3	1	2	–	1	–	2	2	2	–	–	2	1	–	–	–	–	–	–	–
	%	–	52.1	20.8	22.9	6.3	2.1	4.2	–	2.1	–	4.2	4.2	4.2	–	–	4.2	2.1	–	–	–	–	–	–	–
12PMA620A01	# grains	40	27	13	12	8	4	3	1	3	–	1	–	–	–	–	–	–	–	1	–	–	–	–	–
	%	–	67.5	32.5	30.0	20.0	10.0	7.5	2.5	7.5	–	2.5	–	–	–	–	–	–	–	2.5	–	–	–	–	–
12TFE114A01	# grains	85	52	26	18	8	6	5	5	6	4	5	1	2	1	1	–	–	1	–	–	–	–	1	–
	%		61.2	30.6	21.2	9.4	7.1	5.9	5.9	7.1	4.7	5.9	1.2	2.4	1.2	1.2	–	–	1.2	–	–	–	–	1.2	
12TFE130A01	# grains	86	50	25	20	6	12	6	6	5	5	1	1	1	2	1	2	1	–	–	–	–	–	–	1
	%		58.1	29.1	23.3	7.0	14.0	7.0	7.0	5.8	5.8	1.2	1.2	1.2	2.3	1.2	2.3	1.2	–	–	–	–	–	–	1.2

Abbreviations: REE: rare-earth elements

Table 5. Mineral inclusions identified in detrital tourmaline grains collected from stream sediments at the Casino deposit.

Sample number		Total grains	Grains with inclusions	Zircon	Rutile	Quartz	Epidote	Fe-oxide	Apatite	Biotite	Muscovite	Pyrite	Apatite-REE	Alanite	Ilmenite	K-feldspar	Barite	Titanite	Albite	Chlorite	Calcopyrite	Jarosite	Galena	Sphalerite	Dumortierite	Zn-staurolite	Molybdenite	Calcite	Dioside
All samples	# grains	423	331	129	112	74	48	37	34	33	33	33	27	26	22	17	15	12	8	6	5	4	3	3	3	2	1	1	1
	%	–	78.3	30.5	26.5	17.5	11.3	8.7	8.0	7.8	7.8	7.8	6.4	6.1	5.2	4.0	3.5	2.8	1.9	1.4	1.2	0.9	0.7	0.7	0.7	0.5	0.2	0.2	0.2
1002	# grains	16	10	1	2	2	–	1	2	–	–	–	–	1	1	2	–	–	–	–	–	–	–	–	–	–	–	–	–
	%	–	62.5	6.3	12.5	12.5	–	6.3	12.5	–	–	–	–	6.3	6.3	12.5	–	–	–	–	–	–	–	–	–	–	–	–	–
1003	# grains	19	12	2	1	3	–	–	2	1	–	–	1	–	1	2	–	1	–	–	–	–	1	–	–	–	–	–	–
	%	–	63.2	11.1	5.6	16.7	–	–	11.1	5.6	–	–	5.6	–	5.6	11.1	–	5.6	–	–	–	–	5.6	–	–	–	–	–	–
1006	# grains	18	16	4	3	8	2	3	–	–	–	1	1	7	2	3	–	1	–	–	–	–	–	–	1	–	–	–	–
	%	–	88.9	22.2	16.7	44.4	11.1	16.7	–	–	–	5.6	5.6	–	11.1	16.7	–	5.6	–	–	–	–	–	–	5.6	–	–	–	–
1008	# grains	4	4	1	2	3	1	1	–	1	–	–	1	1	–	–	1	–	–	–	–	–	–	–	–	–	–	–	–
	%	–	100.0	25.0	50.0	75.0	25.0	25.0	–	25.0	–	–	25.0	25.0	–	–	25.0	–	–	–	–	–	–	–	–	–	–	–	–
1010	# grains	11	10	5	6	3	1	2	3	3	–	–	–	2	3	–	–	–	–	–	–	–	–	–	–	–	–	–	–
	%	–	90.9	45.5	54.5	27.3	9.1	18.2	27.3	27.3	–	–	–	18.2	27.3	–	–	–	–	–	–	–	–	–	–	–	–	–	–
1015	# grains	3	3	–	1	2	2	–	1	–	–	–	–	3	–	–	–	–	–	–	–	–	–	–	–	–	–	–	–
	%	–	100.0		33.3	66.6	66.6	–	33.3	–	–	–	–	100.0	–	–	–	–	–	–	–	–	–	–	–	–	–	–	–
1016	# grains	92	78	40	28	13	4	8	9	10	10	8	8	5	6	5	4	1	2	1	1	1	1	2	–	–	–	1	–
	%	–	84.8	43.5	30.4	14.1	4.3	8.7	9.8	10.9	10.9	8.7	8.7	5.4	6.5	5.4	4.3	1.1	2.2	1.1	1.1	1.1	1.1	2.2	–	–	–	1.1	–
1022	# grains	150	121	63	46	24	18	10	12	11	16	19	14	5	8	3	5	8	5	3	–	1	–	–	2	2	1	–	1
	%	–	80.7	42.0	30.7	16.0	12.0	6.7	8.0	7.3	10.7	12.7	9.3	3.3	5.3	2.0	3.3	5.3	3.3	2.0	–	0.7	–	–	1.3	1.3	0.7	–	0.7
1025	# grains	52	40	7	14	8	6	7	3	5	3	2	1	–	1	2	3	–	–	1	3	–	–	–	–	–	–	–	–
	%	–	76.9	13.5	26.9	15.4	11.5	13.5	5.7	9.6	5.7	3.8	1.9	–	1.9	3.8	5.7	–	–	1.9	5.7	–	–	–	–	–	–	–	–
1026	# grains	58	37	6	9	8	14	5	2	2	4	3	1	2	–	–	2	1	1	1	1	2	1	1	–	–	–	–	–
	%	–	71.2	10.3	15.5	13.8	24.1	8.6	3.4	3.4	6.9	5.2	1.7	3.4	–	–	3.4	1.7	1.7	1.7	1.7	3.4	1.7	1.7	–	–	–	–	–

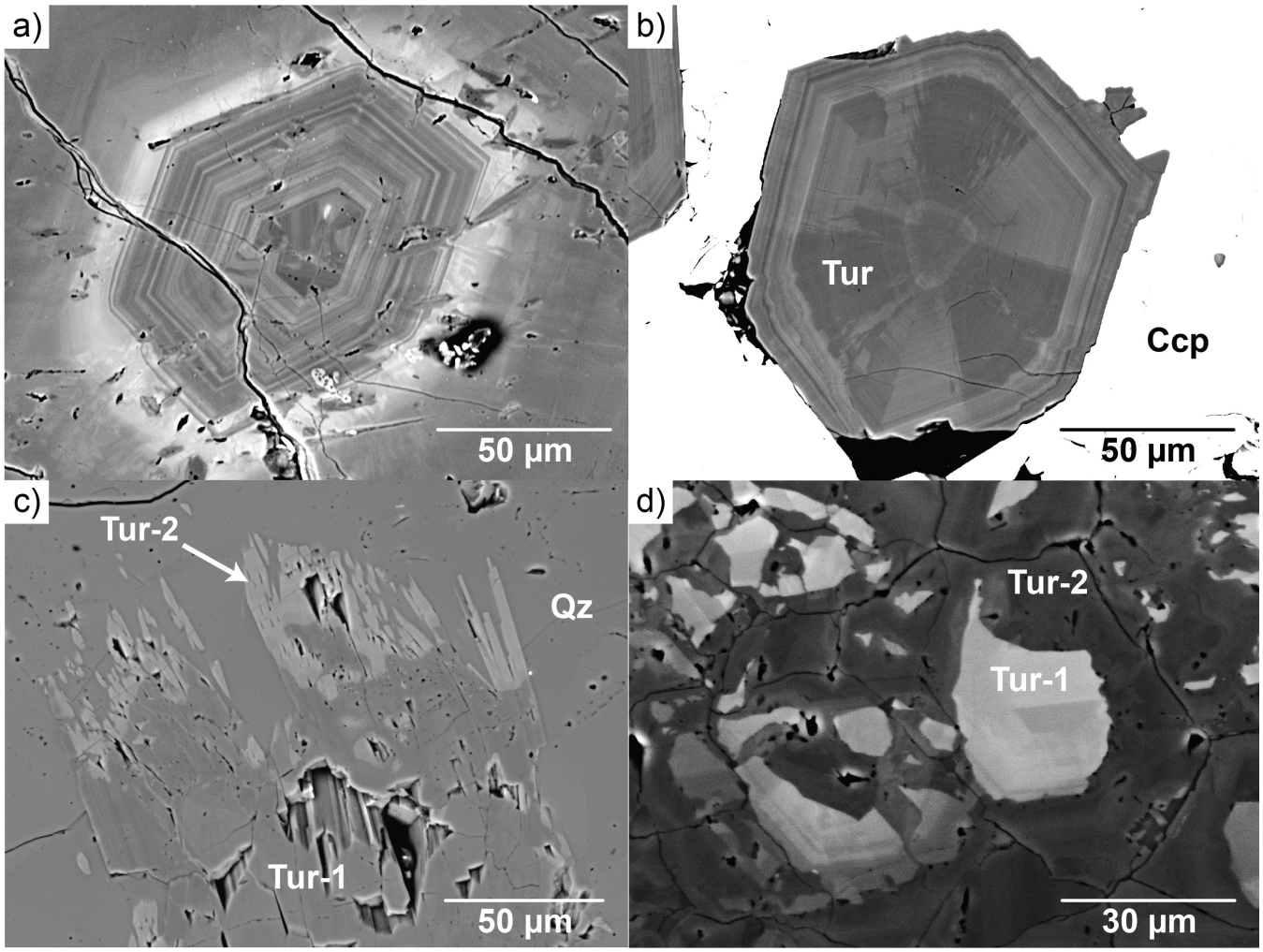

Figure 5. Backscattered-electron images showing the internal textures of tourmaline grains from bedrock samples: **a)** oscillatory zonation; **b)** sector zonation; **c)** overgrowth (Tur-1 is dark, Tur-2 is lighter); **d)** irregular/patchy zonation resulting from recrystallization of pre-existing Tur-1, of which some primary fragments still remain, to Tur-2. The primary chemical difference between Tur-1 and Tur-2 is that Tur-2 contains more Mg than Fe.

sectors (Fig. 5b). Secondary textures are patchy/irregular growth features (Fig. 5c), commonly observed in recrystallized tourmaline, with diffuse grain boundaries, developed perpendicular to [001], and overgrowth or replacement features (Fig. 5d). Coupled dissolution-reprecipitation textures (similar to those developed in minerals such as plagioclase) are not currently included in the classification but could be grouped with the patchy/irregular growth features that result from recrystallization. These dissolution-reprecipitation textures correlate with the change from primary Fe-rich (schorl) compositions to more Mg-rich (dravite) ones. Diffusion-like textures are also occasionally observed (Fig. 6a, b).

Tourmaline in surficial sediments

Tourmaline from surficial samples exhibits a high degree of chemical heterogeneity and zonation at the individual grain scale. All four types of compositional growth textures observed in bedrock are also observed in grains from the surficial samples, with more than 50% of surficial grains exhibiting some type of chemical zonation. Diffusion-like textures similar to those observed in some of the bedrock tourmaline grains from Woodjam were also observed in surficial grains from samples surrounding the deposit cluster (Fig. 6c).

Major- and minor-element chemistry (SEM-EDS)

Tourmaline in bedrock

Tourmaline from the Casino and Woodjam bedrock samples primarily plot within the compositional space of schorl, dravite, and povondraite, regardless of the deposit or tourmaline textural style. The dominant substitution can be summarized by: $R^2 + Na^+ \leftrightarrow Al^{3+} + \square$ ($R^2 = 0.90$) and $Fe^{2+} + (OH)^- \leftrightarrow Al^{3+} + O^{2-}$ ($R^2 = 0.90$). The average (range)

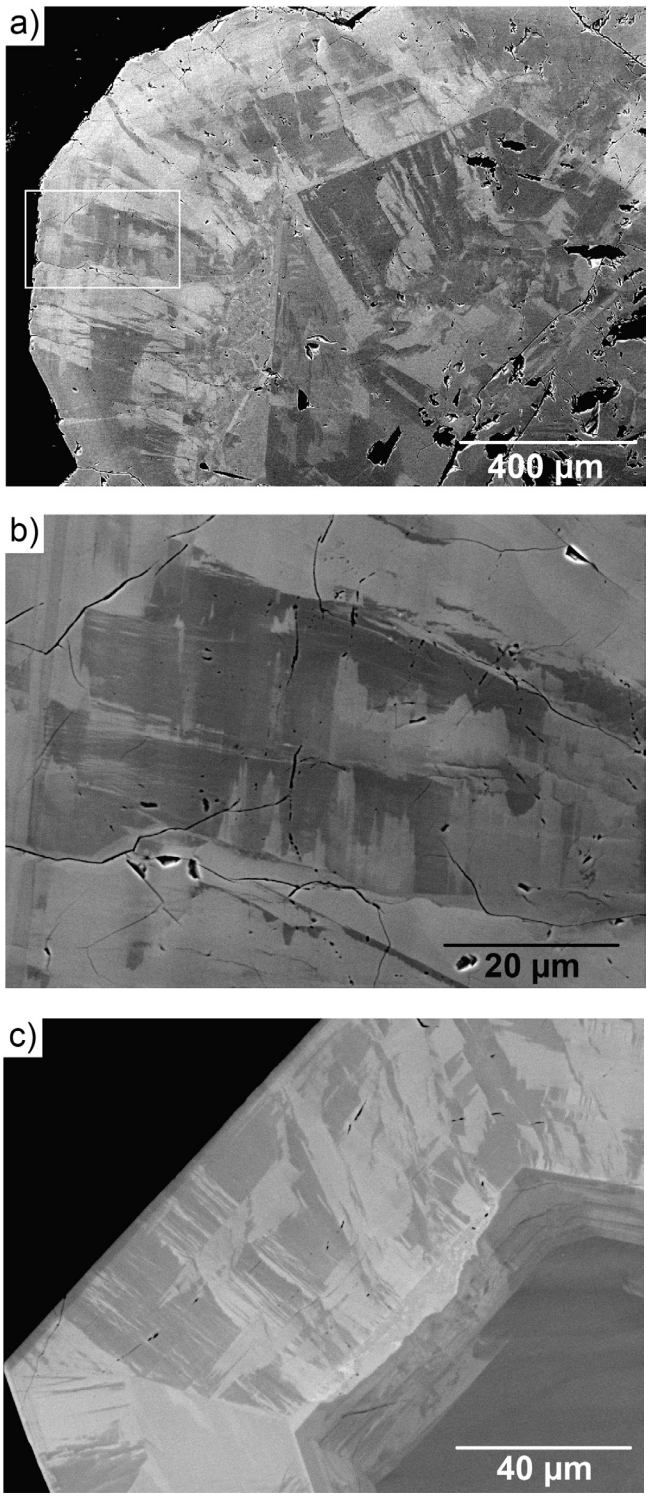

Figure 6. Backscattered-electron images of bedrock and till samples collected at the Woodjam deposit showing tourmaline internal textures in: **a)** a tourmaline grain in a Woodjam bedrock sample showing a combination of oscillatory and sector zoning features as well as some patchy zonation; **b)** magnified view of the white box in a) showing patchy zonation; **c)** a tourmaline grain from a till sample near the Woodjam deposit cluster showing similar zonation textures to those observed in the Woodjam bedrock sample in a).

proportions of major elements, expressed in weight per cent, are Na = 1.75 (0.64–2.36), Ca = 0.49 (< LOD–2.64), Ti = 0.27 (< LOD–1.95), Mg = 4.85 (1.60–6.65), Fe = 4.27 (0.20–16.44), Al = 17.19 (10.78–19.90), and Si = 17.20 (15.52–18.68). The average (range) proportions expressed in *apfu* are Na = 0.75 (0.28–1.00), Ca = 0.10 (< LOD–0.70), Ti = 0.03 (< LOD–0.40), Mg = 1.95 (0.69–2.65), Fe = 0.76 (0.04–3.07), Al = 6.24 (4.18–7.14), and Si = 6.01 (5.60–6.55). In general, broad chemical variations conform to the oxy-dravite–povondraite trend, superimposed on a weaker schorl–dravite trend; the oxy-dravite–povondraite trend within this series reflects the increase in Fe^{3+} (and decrease in Al^{3+}) that may reflect conditions of increasing oxidation (i.e. fO_2; Fig. 7a, b). The predominance of the oxy-dravite–povondraite trend has been previously reported for tourmaline from mineralized porphyry systems in Russia (Baksheev et al., 2012).

Tourmaline in surficial sediments

The chemistry and range in composition determined for detrital tourmaline is similar to that of the tourmaline in bedrock. In terms of end members, most tourmaline grains plot as schorl, dravite, and povondraite, with some grains plotting as uvite-feruvite. The average (range) of major elements, expressed in weight per cent, are Na = 1.58 (0.74–2.58), Ca = 0.72 (<LOD–3.17), Ti = 0.43 (<LOD–2.20), Mg = 4.55 (0.13–7.66), Fe = 4.91 (0.21–15.31), Al = 17.43 (12.06–22.92), and Si = 17.19 (15.54–18.88). The average (range) proportions expressed in *apfu* are Na = 0.69 (0.30–1.00), Ca = 0.17 (< LOD–0.75), Ti = 0.08 (< LOD–0.47), Mg = 1.82 (0.05–3.00), Fe = 0.85 (0.04–2.71), Al = 6.27 (4.49–7.71), and Si = 5.95 (5.51–6.21). This shows that there is no clear difference in major- or minor-element chemistry between tourmaline in bedrock and tourmaline in surficial sediments.

Trace-element chemistry

Tourmaline in bedrock

Trace-element analyses (LA-ICP-MS) for 51 elements were completed on 145 tourmaline grains from 15 samples (Table 2). Concentrations of many elements, including Li, Be, Rb, Nb, Mo, Ag, In, Sb, Cs, Ba, Hf, and rare-earth elements (REE), are at or below the lower detection limit. Many, including Co, Ni, Ge, Y, Zr, Sn Pb, Th, and U, are present in very low concentrations (1–20 ppm), and the remainder, including K, Sc, Ti, V, Cr, Mn, Cu, Zn, Ga, As, and Sr, occur at higher concentrations (hundreds to thousands of parts per million). Significant effort was made to identify relationships between the elements, but very few strong correlations were found. Noteworthy ones include positive correlations between Mn and Zn ($R^2 = 0.61$) and Mn and Sr ($R^2 = 0.48$). It was also found that the trace-element concentration variations in a single, zoned tourmaline grain can be profound,

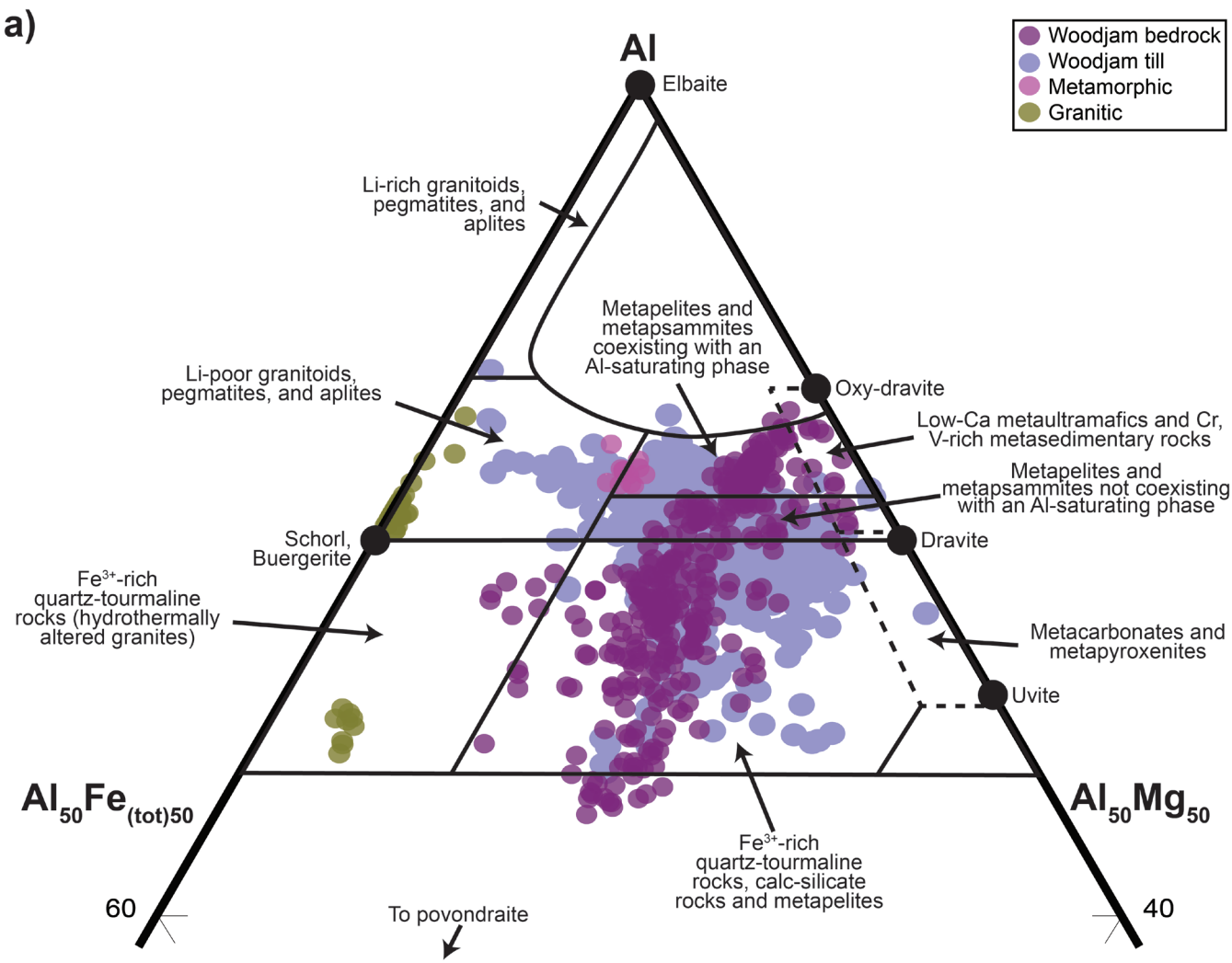

Figure 7. Tourmaline major-element chemistry Al-Mg-Fe for grains from **a)** Woodjam deposit and **b)** Casino deposit bedrock and surficial sediment samples analyzed in this study, plotted using the ternary diagram of Henry and Guidotti (1985). Background unmineralized bedrock is represented by grains classified as metamorphic, from a gneiss from Vandor Falls, Ontario, and grains classified as granitic, from the Seagull batholith, Yukon.

with variations of several magnitudes possible. For example, concentrations of Ti, V, and Mn can vary over an order of magnitude, from hundreds to thousands of parts per million, between zones within a grain.

Given the high degree of variation in trace-element concentration from point to point, attempts were made to discern general trends in tourmaline grains through the use of LA-ICP-MS maps, an example of which is shown in Figure 8. The tourmaline grain shown is from the Woodjam deposit and exhibits oscillatory zonation (zones with sharp boundaries developed parallel to [001]) and complex patchy zonation (areas with diffuse boundaries, developed perpendicular to [001]) that in some places crosses oscillatory zone boundaries. Examination of the maps produced for Sc and Mn indicates that elemental distribution is, in part, linked to oscillatory zonation (Fig. 8). In contrast, high concentrations of other elements, such as Ti, Sr, and Zr, appear to positively correlate with the complex patchy zonation. Closer inspection of Ti and Sr show differences in their zonation patterns, including high concentrations of Ti in the core and intermediate regions but is absent in the rim. Strontium concentrations, in contrast, accentuate the complex zonation throughout the grain and in the rim. In summary, patterns in trace elements are very complex and may or may not correlate with the observed zonation type in all cases.

Tourmaline in surficial sediments

A total of 1585 tourmaline grains were analysed from 26 surficial sediment samples from Casino and Woodjam (Table 3). Some of the elements analyzed occur at or below

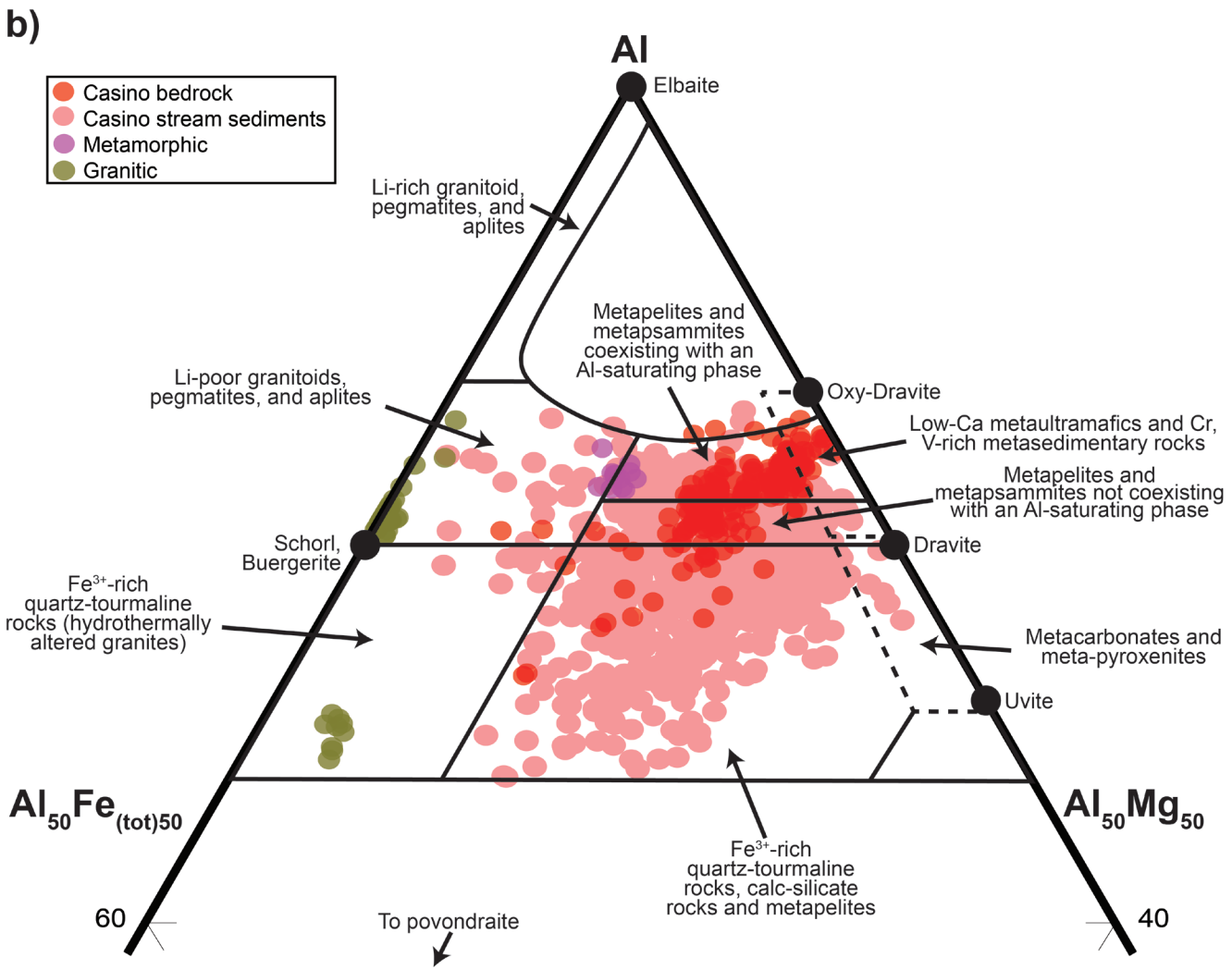

Figure 7. (cont.)

the lower detection limit, including Li, Be, Rb, Nb, Mo, Ag, In, Sb, Cs, Ba, Hf, and REE. The average concentration range of Co, Cu, Ge, As, Y, Zr, Sn, Pb, Th, and U is 1 to 20 ppm, whereas K, Sc, Ti, V, Cr, Mn, Ni, Zn, Ga, and Sr occur in much higher concentrations (hundreds to thousands of parts per million). The positive correlations between Mn and Zn and Mn and Sr observed in tourmaline from bedrock samples were not found in tourmaline grains from surficial sediments; however, a correlation between Co and Ni ($R^2 = 0.74$), not noted in the bedrock material, was observed.

DISCUSSION

Using tourmaline as an indicator for mineralized porphyry systems necessarily involves identification of key features in the mineralized bedrock samples, examination of grains from the surficial sediments to search for these same features, and comparison of these features in tourmaline from a variety of geological settings (i.e. pegmatites; granites; and VMS, orogenic Au, and Sn-W deposits). Observations made as part of this study and a compilation of material from the published literature is provided.

Tourmaline is commonly black in most rock types, except in pegmatites, in which it can be green, blue, pink, and yellow. The tourmaline from mineralized porphyry systems in this study was predominantly black and, less often, was pale brown or colourless. The grain size of tourmaline in bedrock from all geological environments is highly variable and is not a distinctive feature, but the largest tourmaline grains form in pegmatite and granitic settings. Fibrous tourmaline is a morphology not observed in porphyry deposits; it is most typically associated with felsic pegmatites (Dutrow and Henry, 2017). The colour of tourmaline grains under plain polarized light (PPL) can range from browns to greens, blues, and yellows to colourless. A comprehensive analysis of inclusions found within tourmaline does not exist. Zircon appears to be a ubiquitous inclusion in tourmaline from all geological settings, as is quartz. The morphology of quartz

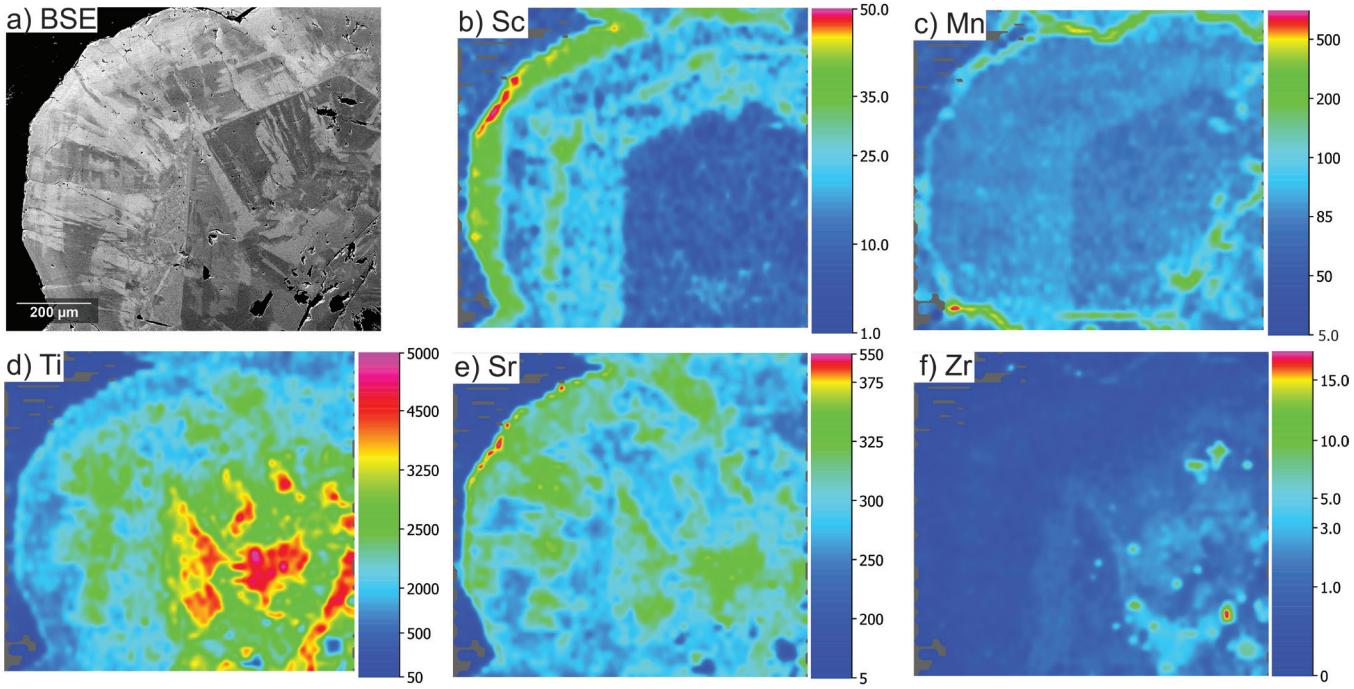

Figure 8: Single Woodjam bedrock-sourced tourmaline grain: **a)** backscatter electron image; **b)** to f) laser-ablation inductively coupled plasma mass spectrometry maps of trace-element content showing b) Sc, **c)** Mn, **d)** Ti, **e)** Sr, and **f)** Zr. Element scales are semi-quantitative (parts per million) and indicate relative changes in element concentrations.

inclusions is variable; however, anhedral, well rounded quartz grains often occur in tourmaline derived from metamorphic terranes, and subhedral to euhedral quartz grains are found in tourmaline from most other geological environments. Tourmaline from porphyry deposits does not contain rounded inclusions of quartz.

Tourmaline grains can also be classified using internal growth textures. The presence of complex growth features, such as those observed in the tourmaline crystals analyzed in this study, can be useful for graphically documenting the variations in pressure-temperature-time (P-T-X) experienced by an evolving crystal (Slack and Trumbull, 2011). Oscillatory and sector zonation is widely observed in tourmaline from a range of geological settings, but the presence of patchy/irregular to even 'chaotic' growth features is not common, based on our observations during this study and analyses of the existing literature, and appears to be unique to mineralized systems. All tourmaline grains from mineralized porphyry systems examined in this study exhibited zonation of one type or another, including both oscillatory and sector zonation; patchy or irregular zonation within oscillatory or sector zones was also observed (Fig. 6, 8a). The patchy zonation is particularly unusual; it does not destroy the primary oscillatory or sector zonation, which suggests it is unlikely to be a product of recrystallization. It is possible that patchy zonation (Fig. 6) is produced through chemical diffusion; however, this idea appears to be at odds with the commonly accepted view that diffusion is negligible (Palmer et al., 1992; Henry and Dutrow, 1996). Still, degrees of chemical diffusion involving major and some trace elements have been noted in tourmaline that has undergone deformation under moderate to high-grade conditions (e.g. mylonite metamorphosed to the amphibolite faces; Büttner and Kasemann, 2007). Tourmaline has also exhibited greater diffusion along the c-axis (Desbois and Ingrin, 2007). For bedrock samples in this study, the effect of deformation can be ignored because the rocks are undeformed. Diffusion features, if present, align well with the orientation perpendicular to [001] of the grains from this study (Fig. 6, 8). The orientation of these diffusion features could also be related to the weak cleavage present in tourmaline [10-10], which has been reported by Hawthorne and Dirlam (2011).

There is only one comprehensive study of the major-element chemistry of tourmaline from porphyry systems: Baksheev et al. (2012) showed that for the most part, the tourmaline that is present belongs to the schorl–dravite series (Fe^{2+}-Mg substitution), with a strong oxy-dravite–povondraite trend overprint. Both trends are observed in our study. As identified by our research, the alkali/alkaline-earth site can be used to help identify non-porphyry tourmaline because porphyry-related tourmaline almost exclusively contains greater than 0.5 *apfu* Na; however, major elements alone cannot definitively distinguish porphyry copper–related tourmaline from tourmaline that has formed in other geological settings.

In general, the application of LA-ICP-MS in the characterization of tourmaline is in its infancy and important issues still need to be resolved, including the complex nature and

wide chemical variation of tourmaline, paired with the difficulty of developing appropriate reference materials and internal element standards. This study has demonstrated that high-quality tourmaline trace-element data can be obtained by LA-ICP-MS. Data from the existing literature show that there are wide variations in the trace-element composition of tourmaline found in differing geological environments (Slack et al., 1999; Novak et al., 2011; Marschall et al., 2013; Hazarika et al., 2015; Kalliomäki et al., 2017). A detailed understanding of what trace elements are present, the ranges in their concentrations, and their internal relationships to other trace elements and textures are all key to understanding the provenance of tourmaline in the surficial environment. Before interpreting tourmaline trace-element data, the intrinsic and extrinsic controls on tourmaline crystal chemistry must be understood and considered. Intrinsic, or crystal-chemical, controls include ideal site size, ionic radius, and valence; extrinsic controls relate to the roles that the geological environment of formation play in affecting elemental incorporation. A summary of trace-element generalizations for tourmaline from a variety of environments is listed in Table 6. Trace elements, including Li, transition metals, reduction-oxidation (redox)–sensitive elements (Mn, As, Sn, Sb?), high field-strength elements, large-ion lithophile elements, and REEs, can be useful for characterizing tourmaline from specific environments and distinguishing it from others. Tourmaline from the Casino and Woodjam porphyry systems, as well as others examined in this study—Schaft Creek (British Columbia), Highland Valley Copper (British Columbia), Soledad (Peru), and Red Spring (British Columbia—generally contain low concentrations of Li (<20 ppm), high concentrations of redox-sensitive elements such as Mn (av. 194 ppm) and As (av. 31.8 ppm), enrichments of Sr (av. 280 ppm), and low concentrations of Pb (<10 ppm), and have light REE–enriched patterns despite having low REE concentrations (<10 ppm ΣREE).

To explore and better explain the trace-element concentrations observed in our study, data from the literature and our data are compiled and presented as box-and-whisker plots (Fig. 9). Figure 9 shows that tourmaline from mineralized geological settings (i.e. orogenic Au, Sn-W, and porphyry deposits) contains relatively high concentrations of Cr, Co, and Ni (tens to hundreds of parts per million) and lower concentrations of Mn, Zn, and Ga relative to tourmaline forming in unmineralized environments. Specifically, tourmaline from porphyry deposits is characterized by high V (hundreds of parts per million), Cu (tens of parts per million), and Sr (hundreds of parts per million) and low Zn (tens of parts per million) and Pb (<10 ppm). Figure 10 shows the contrast of Pb-Zn composition between surficial and bedrock samples in this study and highlights the predominance of non-porphyry tourmaline in the surficial environment. Low concentrations of Pb and Zn also appear to be characteristic of tourmaline derived from surficial sediments. Although Figure 10 only shows data for Casino and Woodjam samples, the other porphyry deposit samples plot in the same Pb-Zn compositional space.

Table 6: Generalizations of trace-element composition for tourmaline from different geological settings

Deposit type	Key trace-element signatures	References
Granite	Low Sr (<25 ppm) High Ga (hundreds of parts per million) Sn (tens of parts per million)	This study – Seagull batholith
Pegmatite	Enriched in REEs, primarily LREEs High Sn (>50 ppm), high Zn (hundreds of parts per million) Commonly contain Li and Be above LOD	Novak et al. (2011); Marks et al. (2013); Hazarika et al. (2017)
Orogenic	Variable Li (tens to hundreds of parts per million) Sr (thousands of parts per million) Transition metals (twenties to hundreds of Cr, Co, Ni)	Kalliomäki et al. (2017)
Volcanogenic massive sulfide	Low Ni (<5 ppm) Variable Zn (hundreds to thousands of parts per million) Enriched in Pb (>10 ppm)	Slack et al. (1999)
Porphyry	< LOD light elements (Li and Be) Redox-sensitive elements (>50 ppm Mn) Low Zn (tens of parts per million) Sr concentrations ~hundreds of parts per million LREE enriched but low total REE to < LOD concentrations	This study
W-Sn	Low Sr (tens of parts per million) High Zn (hundreds of parts per million) High Sn (10 ppm)	Launay et al. (2018)

LOD: Limit of detection; LREE: light rare-earth elements; REE: rare-earth elements

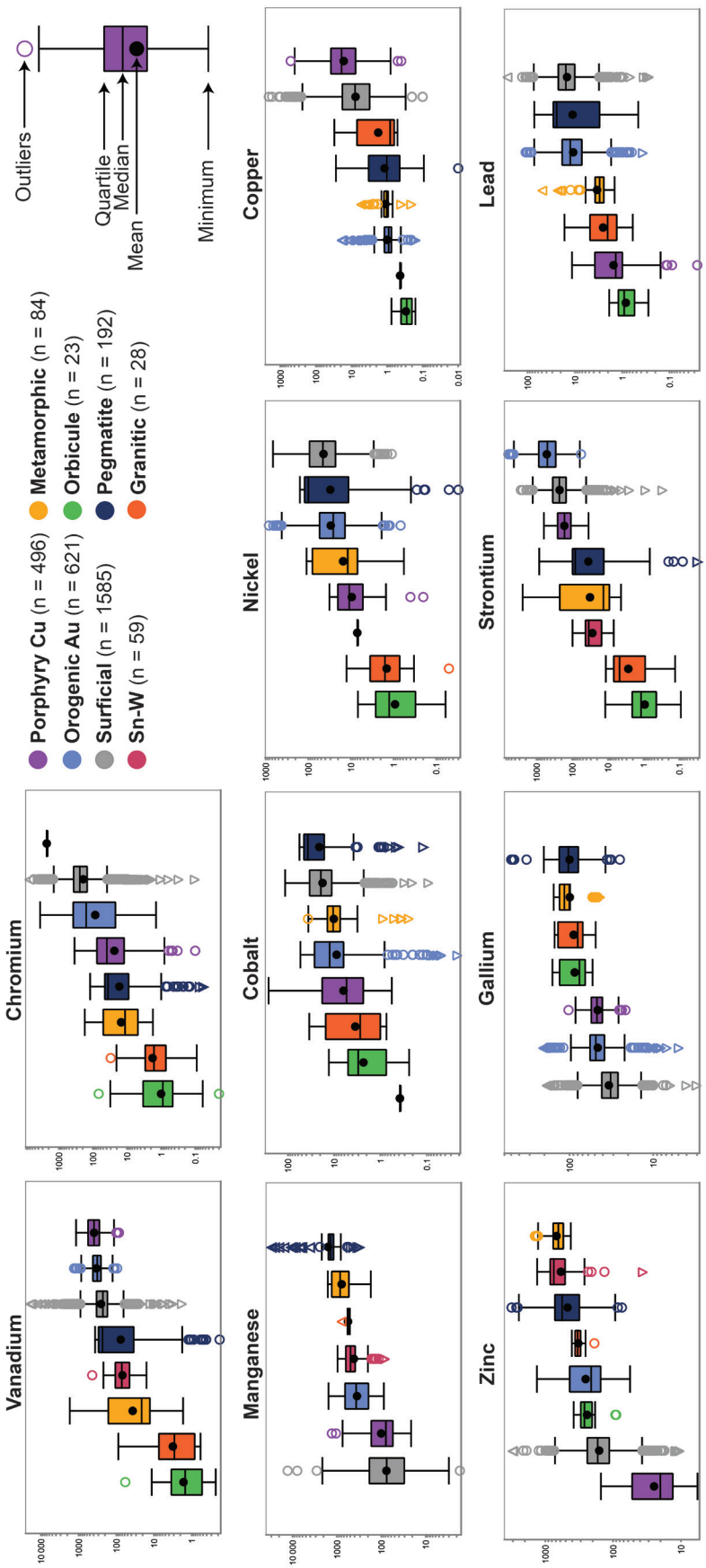

Figure 9. Tourmaline trace-element composition determined by laser-ablation inductively coupled plasma mass spectrometry for bedrock samples from the Casino and Woodjam deposits plotted as box and whisker plots and compared to data from other geological settings (Čopjaková et al., 2015; Kalliomäki et al., 2017; Launay et al., 2018; Trumbull et al., 2019; Zhao et al., 2019). The term 'orbicule' refers to orbicular tourmaline granites (e.g. Sinclair and Richardson, 1992); grains classified as orogenic gold, from Finland (Kalliomäki et al., 2017); grains classified as Sn-W, from the Panasqueira deposit, Portugal (Launay et al., 2018); grains classified as 'metamorphic', from a gneiss from Vandor Falls, Ontario and represent background unmineralized bedrock (this study); and grains classified as granitic are from the Seagull batholith, Yukon and represent background unmineralized bedrock (this study). Due to the lack of published data, not all groups are plotted for all elements (e.g. Mn, Ga, and Pb).

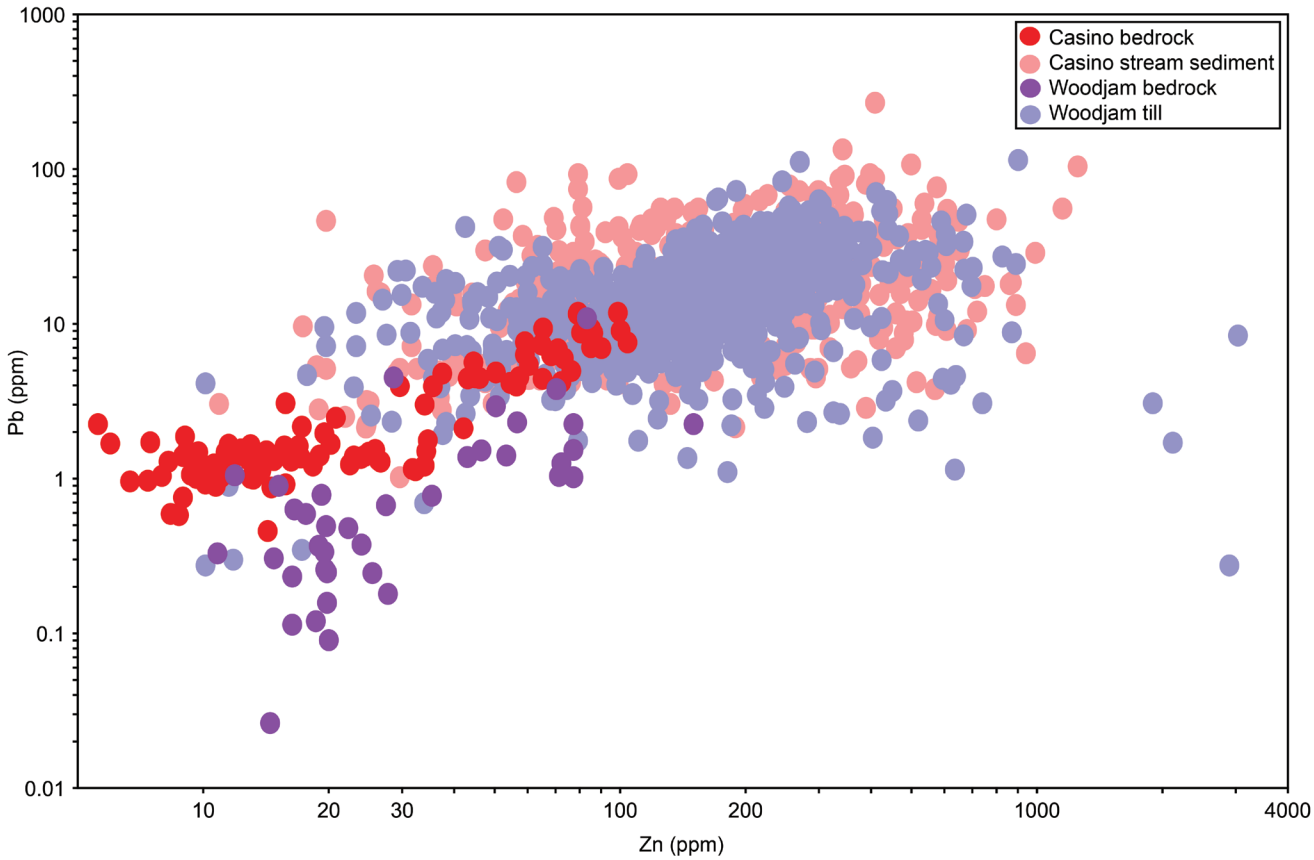

Figure 10. A Pb-Zn correlation diagram highlighting the variability of the composition of detrital tourmaline samples compared to the bedrock tourmaline from the Casino and Woodjam deposits; n = 1930.

The recovery of tourmaline grains from the surficial sediments around the Woodjam and Casino deposits provide an opportunity to apply our understanding of bedrock tourmaline to tourmaline of unknown origin. We classified tourmaline grains from surficial sediment samples using the physical and chemical criteria presented here. Some of the tourmaline grains in surficial sediment samples have trace-element chemical compositions consistent with those formed in porphyry deposits (Fig. 9). Based on the observed trace-element patterns and inclusion populations, greater than 90% of the tourmaline grains in the surficial sediments were likely not derived from nearby porphyry deposits. The bulk of the surficial grains, especially in till samples around the Woodjam deposit, are likely of metamorphic origin based on their physical (colour and inclusion populations) and trace-element (low Sr (tens of parts per million), hundreds of parts per million Zn, and >5000 ppm Ti) characteristics. Only 10%, likely less, of the grains in the surficial samples exhibit characteristics of tourmaline from the Woodjam cluster (Fig. 11a). The small proportion of tourmaline grains that have a composition similar to porphyry-derived grains may be due to tourmaline occurring at low concentrations in porphyry systems. For example, till samples from Woodjam typically collected from above the underlying deposit contain less than 5% porphyry-derived tourmaline, except for two samples: one sample from the immediate deposit contains 43% porphyry-derived tourmaline and a second one, collected 11 km west-southwest (down-ice) from Takom South, the nearest known mineralized zone, contains 7% porphyry-derived tourmaline. At the Casino deposit the results are less clear (Fig. 11b). A large number of tourmaline grains from samples collected downstream of the deposit in Canadian Creek, which drains the north side of the deposit, have been classified as porphyry-derived tourmaline. In contrast, tourmaline grains from Casino Creek, on the south side of the deposit, did not display the porphyry chemical signature.

There are other factors to consider, including the colour and size of the analyzed tourmaline grains. Grain size is a challenge because much of the tourmaline observed in porphyry deposits is less than 0.25 mm or contains fractures. Despite having high hardness, tourmaline lacks distinct cleavage and is relatively brittle. This means that what is recovered from surficial sediments will undoubtedly be fragments of larger grains. As transportation distance away from the bedrock source increases, tourmaline grain size will decrease due to breakage along fractures. In some of the bedrock samples, tourmaline is acicular, with some grains

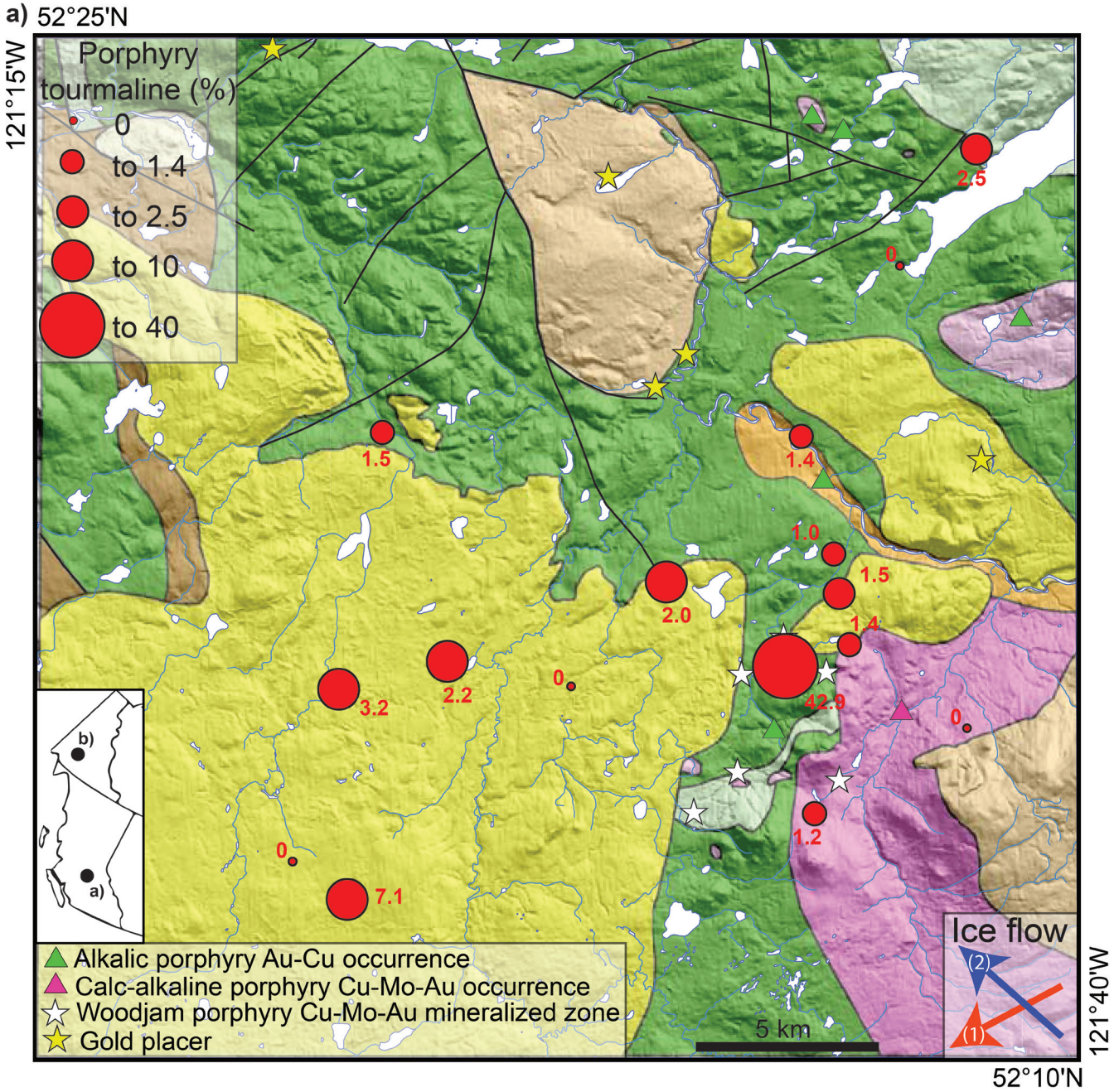

Figure 11. Percentage of tourmaline grains in each till sample identified as being derived from mineralized porphyry bedrock using criteria established in this study (lack of inclusions, high Sr concentration, and low Zn and Pb concentrations); red numbers are individual sample values. Inset map shows the location of a) the Woodjam deposit in British Columbia and b) the Casino deposit in Yukon. **a)** Woodjam deposit, *see* Plouffe and Ferbey (2017) for bedrock geology.

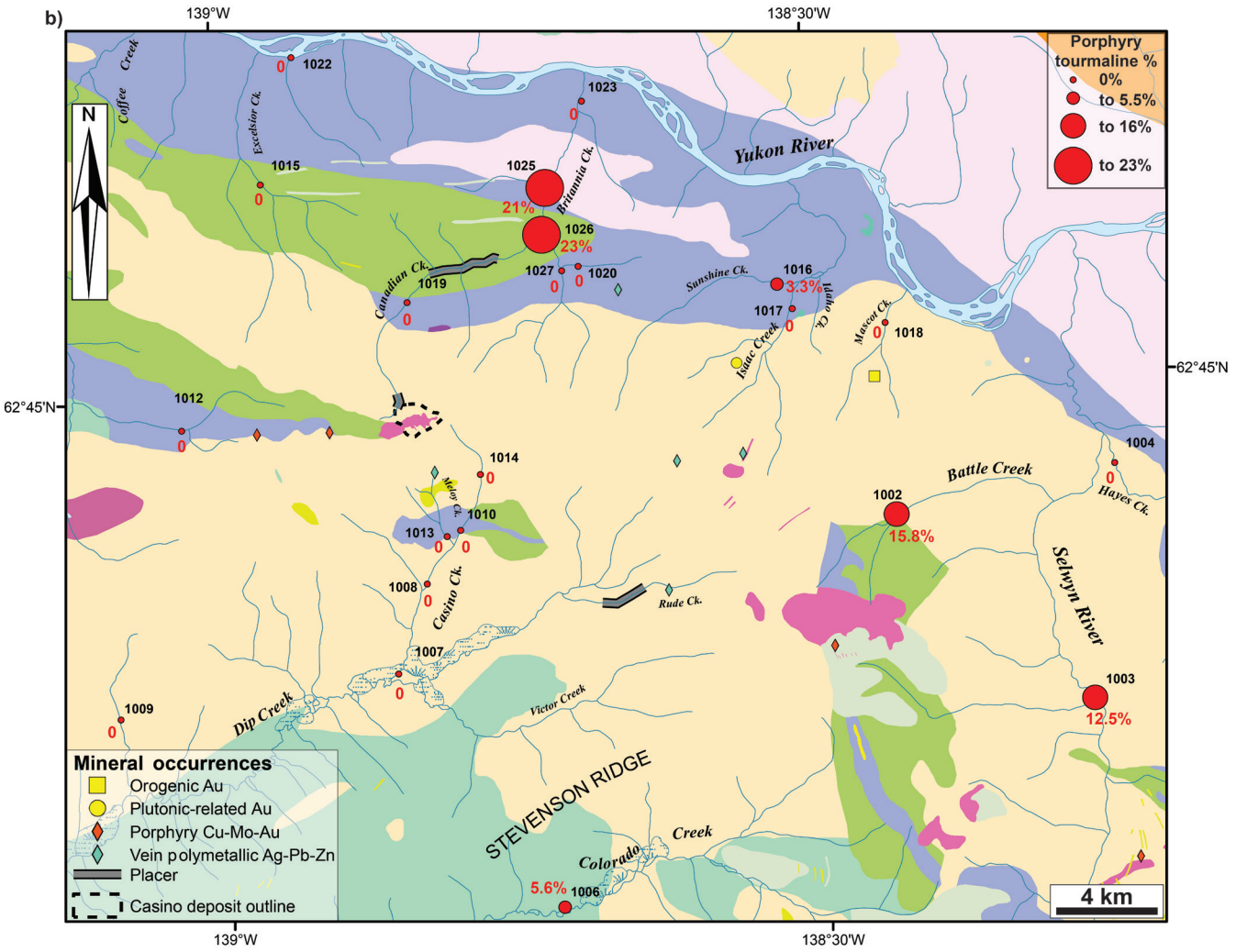

Figure 11. (cont.) b) Casino deposit, *see* McClenaghan et al. (2020, this volume) for bedrock geology.

being approximately 1 µm in diameter. This very small tourmaline would not be recovered in the greater than 0.25 mm fraction of sediment samples.

Colour is also a challenge. Nearly all of the tourmaline grains picked from sediment samples were black to dark brown. The lighter coloured to clear tourmaline found in the porphyry bedrock samples at Casino and Woodjam was not identified in any of the stream-sediment samples. These lighter coloured tourmaline grains may not be recovered during routine visual examinations of the greater than 0.25 mm mid-density or heavy mineral fractions of the sediment samples, possibly due to being mistaken for similarly coloured minerals, such as amphibole or epidote.

CONCLUSIONS

The physical characteristics of tourmaline (e.g. colour, grain size, morphology, colour in PPL) can assist in the classification of environment of formation. One physical characteristic that has proven useful is identifying inclusion populations (type and texture), specifically within the tourmaline grains recovered in the surficial environment.

Internal chemical zonation textures can provide information about variations in P-T-X conditions during growth. Several types of chemical zonation have been observed in tourmaline from mineralized porphyry systems and are divided between primary and secondary origins. Most important for identifying tourmaline formed in hydrothermal deposits, including tourmaline from mineralized porphyry systems, is the presence of patchy/irregular zonation,

which can reflect recrystallization, dissolution reprecipitation, and even diffusion, all features commonly observed in ore-related settings.

Although tourmaline major-element chemistry is commonly reported, it has not been demonstrated to be a definitive tool for discriminating between tourmaline from mineralized and unmineralized settings. Some generalizations about porphyry copper–related tourmaline can be made: it generally plots in the schorl–dravite classification; it follows the oxy-dravite–povondraite trend, and in general, it does not contain large quantities of Li and the X-site is always Na>Ca>K>□.

There is a general paucity of trace-element data for tourmaline in the literature and even more so for tourmaline from porphyry systems. In this study, we have generated a comprehensive database of trace-element data, principally focused on tourmaline from porphyry deposits, but also including data for tourmaline from other mineralized and barren geological environments. These data will be published in a subsequent paper. We have demonstrated that the presence of a combination of V, Cu, Sr, Pb, and Zn and their relative proportions can be useful in recognizing tourmaline from porphyry deposits.

Results from this study also show that recognizing tourmaline grains in sediment samples that are from a mineralized porphyry system can be challenging, even if the sediments are proximal to a deposit. For example, at the Woodjam deposit, porphyry-related tourmaline in the surficial environment accounts for less than 5% of the total tourmaline content, except for one sample located near mineralization (47% porphyry tourmaline) and a second sample located 11 km down-ice from mineralization (7% porphyry tourmaline). Up to 23% porphyry tourmaline was identified in stream sediments in the Casino area, but only in samples from the northern drainage system. The bulk of the brown to black tourmaline recovered from the sediment samples at both study sites appears to be of metamorphic origin. The small size (<0.25 mm) and fractured nature of the tourmaline associated with porphyry mineralization could be limiting factors for its recovery in detrital sediments.

FUTURE WORK

This research is part of a larger TGI-5 project to assess the indicator mineral potential of tourmaline. Samples of tourmaline from porphyry deposits around the world are being examined to create a baseline data set for porphyry-related tourmaline compositions.

Mineral liberation analyses are planned for the 0.25 to 0.5 mm size fraction of the surficial sediment mineral concentrate samples to determine if colour bias during visual grain picking is a factor in the low percentage of porphyry tourmaline grains in the samples.

Statistical analyses of chemical and physical observations will be used to investigate whether any unique populations exist. Such data analyses will be of further aid in distinguishing porphyry-related tourmaline from other environments.

A tourmaline trace-element chemistry discrimination plot will be developed to identify grains from mineralized porphyry systems versus other mineralized or unmineralized rocks. This plot will be tested using bedrock samples and surficial sediment grains.

To investigate fluid sources of the tourmaline examined in bedrock, B, Pb, and Sr isotope analyses will be carried out to increase understanding of the relationship between tourmaline and the porphyry system.

ACKNOWLEDGMENTS

This study was funded by the Geological Survey of Canada's Targeted Geoscience Initiative (2016–2020) program and the Government of Canada's Research Affiliate Program. We are grateful for the support of Western Copper and Gold Corporation and the Casino Mining Corporation. The following companies provided sample material to this study: Chakana Copper Corp., Teck Resources Limited, New Gold Inc., Jaxton Mining Inc., Gold Fields Limited (now owned by Consolidated Woodjam Copper Corp.), Triumph Gold Corp., and Kenorland Minerals. We thank Scott Casselman (Yukon Geological Survey) for providing geological information, advice, and access to samples from deposits in Yukon and John Chapman, Martin McCurdy, and Dave Sinclair (Geological Survey of Canada) for their contributions. The manuscript was greatly improved by the reviews of L. Groat and D. Wade.

REFERENCES

Averill, S.A., 2011. Viable indicator minerals in surficial sediments for two major base metal deposit types: Ni-Cu-PGE and porphyry Cu; Geochemistry: Exploration, Environment, Analysis, v. 11, no. 4, p. 279–291. https://doi.org/10.1144/1467-7873/10-IM-022

Baksheev, I.A., Chitalin, A.F., Yapaskurt, V.O., Vigasina, M.F., Bryzgalov, I.A., and Ustinov, V.I., 2010. Tourmaline in the Vetka porphyry copper-molybdenum deposit of the Chukchi Peninsula of Russia; Moscow University Geology Bulletin, v. 65, p. 27–38. https://doi.org/10.3103/S0145875210010035

Baksheev, I.A., Prokof'ev, V.Y., Yapaskurt, V.O., Vigasina, M.F., Zorina, L.D., and Solov'ev, V.N., 2011. Ferric-iron-rich tourmaline from the Darasun gold deposit, Transbaikalia, Russia; The Canadian Mineralogist, v. 49, no. 1, p. 263–276. https://doi.org/10.3749/canmin.49.1.263

Contents

Baksheev, I.A., Prokof'ev, V.Y., Zaraisky, G.P., Chitalin, A.F., Yapaskurt, V.O., Nikolaev, Y.N., Tikhomirov, P.L., Nagornaya, E.V., Rogacheva, L.I., Gorelikova, N.V., and Kononov, O.V., 2012. Tourmaline as a prospecting guide for the porphyry-style deposits; European Journal of Mineralogy, v. 24, no. 6, p. 957–979. https://doi.org/10.1127/0935-1221/2012/0024-2241

Beckett-Brown, C.E., McDonald, A.M., and McClenaghan, M.B., 2019. Unravelling tourmaline in mineralized porphyry systems: assessment as a valid indicator mineral; *in* Targeted Geoscience Initiative: 2018 report of activities, (ed.) N. Rogers; Geological Survey of Canada, Open File 8549, p. 345–351. https://doi.org/10.4095/313669

Bond, J.D. and Lipovsky, P.S., 2011. Surficial geology, soils and permafrost of the northern Dawson Range; *in* Yukon Exploration and Geology 2010, (ed.) K.E. MacFarlane, L.H. Weston, and C. Relf; Yukon Geological Survey, p. 19–32.

Bouzari, F., Hart, C.J.R., Bissig, T., and Barker, S., 2016. Hydrothermal alteration revealed by apatite luminescence and chemistry: a potential indicator mineral for exploring covered porphyry copper deposits; Economic Geology, v. 111, no. 6, p. 1397–1410. https://doi.org/10.2113/econgeo.111.6.1397

Büttner, S.H. and Kasemann, S.A., 2007. Deformation-controlled cation diffusion in tourmaline: a microanalytical study on trace elements and boron isotopes; American Mineralogist, v. 92, no. 11–12, p. 1862–1874. https://doi.org/10.2138/am.2007.2567

Canil, D., Pisiak, L., Lacourse, T., Plouffe, A., Ferbey, T., and Grondahl, C., 2017. Magnetite as an indicator mineral in porphyry Cu±Au±Mo deposits of British Columbia, Canada; *in* Indicator minerals in till and stream sediments of the Canadian Cordillera, (ed.) T. Ferbey, A. Plouffe, and A.S. Hickin; Geological Association of Canada, Special Paper, v. 50 and Mineralogical Association of Canada, Topics in Mineral Sciences v. 47, p. 161–174.

Casselman, S.C. and Brown, H., 2017. Casino porphyry copper-gold-molybdenum deposit, central Yukon (Yukon MINFILE 115J028); *in* Yukon Exploration and Geology Overview 2016, (ed.) K.W. MacFarlane; Yukon Geological Survey, p. 61–74, plus digital appendices.

Chapman, J.B., Plouffe, A., and Ferbey, T., 2015. Tourmaline: the universal indicator?; *in* Application of indicator mineral methods to exploration; Association of Applied Geochemists, 27th International Applied Geochemistry Symposium, Short Course No. 2, p. 25–31.

Clague, J.J., and Ward, B.W., 2011. Pleistocene glaciation of British Columbia; Chapter 44 *in* Quaternary glaciations – extent and chronology – a closer look, (ed.) J. Ehlers, P.L. Gibbard, and P.D. Hughes; Developments in Quaternary Sciences, v. 15, p. 563–573. https://doi.org/10.1016/B978-0-444-53447-7.00044-1

Codeço, M.S., Weis, P., Trumbull, R.B., Pinto, F., Lecumberri-Sanchez, P., and Wilke, F.D.H., 2017. Chemical and boron isotopic composition of hydrothermal tourmaline from the Panasqueira W-Sn-Cu deposit, Portugal; Chemical Geology, v. 468, p. 1–16. https://doi.org/10.1016/j.chemgeo.2017.07.011

Codeço, M.S., Weis, P., Trumbull, R.B., Glodny, J., Wiedenbeck, M., and Romer, R.L., 2019. Boron isotope muscovite-tourmaline geothermometry indicates fluid cooling during magmatic-hydrothermal W-Sn ore formation; Economic Geology, v. 114, no. 1, p. 153–163. https://doi.org/10.5382/econgeo.2019.4625

Cooke, D.R., Baker, M., Hollings, P., Sweet, G., Chang, Z., Danyushevsky, L.D., Gilbert, S., Zhou, T., White, N.C., Gemmell, J.B., and Inglis, S.I., 2014. New advances in detecting the distal geochemical footprints of porphyry systems – epidote mineral chemistry as a tool for vectoring and fertility assessments; Paper 7 *in* Building exploration capability for the 21st century, (ed.) K.D. Kelley and H.C. Golden; Society of Economic Geologists Special Publication 18, p. 127–152.

Cooke, D.R., Agnew, P., Hollings, P., Baker, M., Chang, Z., Wilkinson, J.J., White, N.C., Zhang, L., Thompson, J., Gemmell, J.B., Fox, N., Chen, H., and Wilkinson, C.C., 2017. Porphyry indicator minerals (PIMS) and porphyry vectoring and fertility tools (PVFTS) – indicators of mineralization styles and recorders of hypogene geochemical dispersion haloes; *in* Proceedings of Exploration '17: Sixth Decennial International Conference on Mineral Exploration, (ed.) V. Tschirhart and M.D. Thomas; p. 457–470.

Čopjaková, R., Škoda, R., Galiová, M.V., Novák, M., and Cempírek, J., 2015. Sc- and REE-rich tourmaline replaced by Sc-rich REE-bearing epidote-group mineral from the mixed (NYF+LCT) Kracovice pegmatite (Moldanubian Zone, Czech Republic); American Mineralogist, v. 100, no. 7, p. 1434–1451. https://doi.org/10.2138/am-2015-4863

Dare, S.A.S., Barnes, S.J., Beaudoin, G., Méric, J., Botroy, E., and Potvin-Doucet, C., 2014. Trace elements in magnetite as petrogenetic indicators; Mineralium Deposita, v. 49, no. 7, p. 785–796. https://doi.org/10.1007/s00126-014-0529-0

del Real, I., Bouzari, F., Rainbow, A., Bissig, T., Blackwell, J., Sherlock, R., Thompson, J.F.H., and Hart, C.R.J., 2017. Spatially and temporally associated porphyry deposits with distinct Cu/Au/Mo ratios, Woodjam district, Central British Columbia; Economic Geology, v. 112, no. 7, p. 1673–1717. https://doi.org/10.5382/econgeo.2017.4526

Desbois, G. and Ingrin, J., 2007. Anisotropy of hydrogen diffusion in tourmaline; Geochimica et Cosmochimica Acta, v. 71, no. 21, p. 5233–5243. https://doi.org/10.1016/j.gca.2007.08.027

Dutrow, B.L. and Henry, D.J., 2011. Tourmaline: a geologic DVD; Elements, v. 7, no. 5, p. 301–306.

Dutrow, B.L. and Henry, D.J., 2017. Fibrous tourmaline: a sensitive probe of fluid compositions and petrologic environments; The Canadian Mineralogist, v. 54, no. 1, p. 311–335. https://doi.org/10.3749/canmin.1600019

Frikken, P.H., Cooke, D.R., Walshe, J.L., Archibald, D., Skarmeta, J., Serrano, L., and Vargas, R., 2005. Mineralogical and isotopic zonation in the Sur-Sur tourmaline breccia, Rio Blanco–Los Bronces Cu-Mo deposit, Chile: implications for ore genesis; Economic Geology, v. 100, no. 5, p. 935–961. https://doi.org/10.2113/100.5.935

Galbraith, C.G., Clarke, D.B., Trumbull, R.B., and Wiedenbeck, M., 2009. Assessment of tourmaline compositions as an indicator of emerald mineralization at the Tsa da Glisza Prospect, Yukon Territory, Canada; Economic Geology, v. 104, no. 5, p. 713–731. https://doi.org/10.2113/gsecongeo.104.5.713

Godwin, C.I., 1976. Casino; *in* Porphyry deposits of the Canadian Cordillera, (ed.) A. Sutherland Brown; Canadian Institute of Mining and Metallurgy, Special Volume 15, p. 344–358.

Griffin, W.L., Slack, J.F., Ramsden, A.R., Win, T.T., and Ryan, C.G., 1996. Trace elements in tourmalines from massive sulfide deposits and tourmalinites; geochemical controls and exploration application; Economic Geology, v. 91, no. 4, p. 657–675. https://doi.org/10.2113/gsecongeo.91.4.657

Hazarika, P., Mishra, B., and Kamal Lochan, P., 2015. Diverse tourmaline compositions from orogenic gold deposits in the Hutti-Maski greenstone belt, India: implications for sources of ore-forming fluids; Economic Geology, v. 110, no. 2, p. 337–353. https://doi.org/10.2113/econgeo.110.2.337

Hashmi, S., Ward, B.C., Plouffe, A., Leybourne, M.I., and Ferbey, T., 2015. Geochemical and mineralogical dispersal in till from the Mount Polley Cu-Au porphyry deposit, central British Columbia, Canada; Geochemistry: Exploration, Environment, Analysis, v. 15, no. 2, p. 234–249. https://doi.org/10.1144/geochem2014-310

Hawthorne, F.C. and Dirlam, D.M., 2011. Tourmaline the indicator mineral: from atomic arrangement to Viking navigation; Elements, v. 7, no. 5, p. 307–312.

Henry, D.J. and Dutrow, B.L., 1996. Metamorphic tourmaline and its petrogenetic applications; *in* Boron: mineralogy, petrology and geochemistry, (ed.) E.S. Grew and L.M. Anovitz; Reviews in Mineralogy, v. 33, p. 503–557.

Henry, D.J. and Guidotti, C.V., 1985. Tourmaline as a petrogenetic indicator mineral an example from the staurolite-grade metapelites of NW Maine; American Mineralogist, v. 70, no. 1–2, p. 1–15.

Jochum, K.P., Weis, U., Stoll, B., Kuzmin, D., Yang, Q., Raczek, I., Jacob, D.E., Stracke, A., Birbaum, K., Frick, D.A., Günther, D., and Enzweiler, J., 2011. Determination of reference values for NIST SRM 610–617 glasses following ISO guidelines; Geostandards and Geoanalytical Research, v. 35, no. 4, p. 397–429. https://doi.org/10.1111/j.1751-908X.2011.00120.x

Kalliomäki, H., Wagner, T., Fusswinkel, T., and Sakellaris, G., 2017. Major and trace element geochemistry of tourmalines from Archean orogenic gold deposits: proxies for the origin of gold mineralizing fluids?; Ore Geology Reviews, v. 91, p. 906–927. https://doi.org/10.1016/j.oregeorev.2017.08.014

Kelley, K.D., Eppinger, R.G., Lang, J., Smith, S.M., and Fey, D.L., 2011. Porphyry Cu indicator minerals in till as an exploration tool: example from the giant Pebble porphyry Cu-Au-Mo deposit, Alaska, USA; Geochemistry: Exploration, Environment, Analysis; v. 11, no. 4, p. 321–334. https://doi.org/10.1144/1467-7873/10-IM-041

Launay, G., Sizaret, S., Guillou-Frottier, L., Gloaguen, E., and Pinto, F., 2018. Deciphering fluid flow at the magmatic-hydrothermal transition: a case study from the world-class Panasqueira W-Sn-(Cu) ore deposit (Portugal); Earth and Planetary Science Letters, v. 499, p. 1–12. https://doi.org/10.1016/j.epsl.2018.07.012

Lu, Y.-J., Loucks, R.R., Fiorentini, M., McCuaig, T.C., Evans, N.J., Yang, Z.-M., Hou, Z.-Q., Kirkland, C.L., Parra-Avila, L.A., and Kobussen, A., 2016. Zircon compositions as a pathfinder for porphyry Cu±Mo±Au deposits; in Tectonics and metallogeny of the Tethyan orogenic belt, (ed.) J.P. Richards; Society of Economic Geologists, Special Publication 19, p. 329–347.

Manéglia, N., Beaudoin, G., and Simard, M., 2018. Indicator minerals of the Meliadine orogenic gold deposits, Nunavut (Canada), and application to till surveys; Geochemistry: Exploration, Environment, Analysis, v. 18, no. 3, p. 241–251. https://doi.org/10.1144/geochem2017-036

Mao, M., Rukhlov, A.S., Rowins, S.M., Spence, J., and Coogan, L.A., 2016. Apatite trace element compositions: a robust new tool for mineral exploration; Economic Geology, v. 111, no. 5, p. 1187–1222. https://doi.org/10.2113/econgeo.111.5.1187

Marks, M.A.W., Marschall, H.R., Schuhle, P., Guth, A., Wenzel, T., Jacob, D.E., Barth, M., and Markl, G., 2013. Trace element systematics of tourmaline in pegmatitic and hydrothermal systems from the Variscan Schwarzwald (Germany): the importance of major element composition, sector zoning, and fluid or melt composition; Chemical Geology, v. 344, p. 73–90. https://doi.org/10.1016/j.chemgeo.2013.02.025

Marschall, H.R. and Jiang, S.Y., 2011. Tourmaline isotopes: no element left behind; Elements, v. 7, no. 5, p. 313–319.

McClenaghan, M.B., McCurdy, M.W., Beckett-Brown, C.E., and Casselman, S.C., 2020. Indicator mineral signatures of the Casino porphyry Cu-Au-Mo deposit, Yukon. Geological Survey of Canada, Open File 8711, 42 p. https://doi.org/10.4095/322191

McCurdy, M.W., McClenaghan, M.B., Garrett, R.G., and Pelchat, P., 2019. The stream sediment geochemical signature of the Casino porphyry Cu-Au-Mo deposit, Yukon Territory: a case study; Geological Survey of Canada, Open File 8632, 39 p. https://doi.org/10.4095/321381

Novak, M., Skoda, R., Filip, J., Macek, I., and Vaculovic, T., 2011. Compositional trends in tourmaline from intragranitic NYF pegmatites of the Trebic pluton, Czech Republic: an electron microprobe, Mossbauer and LA-ICP-MS study; The Canadian Mineralogist, v. 49, no. 1, p. 359–380. https://doi.org/10.3749/canmin.49.1.359

Palmer, M.R., London, D., Morgan, G.B., and Babb, H.A., 1992. Experimental-determination of fractionation of B-11/B-10 between tourmaline and aqueous vapor - a temperature-dependent and pressure-dependent isotopic system; Chemical Geology, v. 101, no. 1–2, p. 123–129. https://doi.org/10.1016/0009-2541(92)90209-N

Paton, C., Hellstrom, J., Paul, B., Woodhead, J., and Hergt, J., 2011. Iolite: freeware for the visualisation and processing of mass spectrometric data; Journal of Analytical Atomic Spectrometry, v. 26, no. 12, p. 2508–2518. https://doi.org/10.1039/C1JA10172B

Pisiak, L., Canil, D., Lacourse, T., Plouffe, A., and Ferbey, T., 2017. Magnetite as an indicator mineral in the exploration of porphyry deposits: a case study in till near the Mount Polley Cu-Au deposit, British Columbia, Canada; Economic Geology, v. 112, no. 4, p. 919–940. https://doi.org/10.2113/econgeo.112.4.919

Plouffe, A. and Ferbey, T., 2016. Till geochemistry, mineralogy and textural data near four Cu porphyry deposits in British Columbia; Geological Survey of Canada, Open File 8038, 44 p. and British Columbia Ministry of Energy and Mines, British Columbia Geological Survey, Geofile 2016-10, 1 .zip file. https://doi.org/10.4095/298805

Plouffe, A. and Ferbey, T., 2017. Porphyry Cu indicator minerals in till: a method to discover buried mineralization; *in* Indicator minerals in till and stream sediments of the Canadian Cordillera, (ed.) T. Ferbey, A. Plouffe, and A. Hicken; Geological Association of Canada, Special Paper, v. 50, and Mineralogical Association of Canada, Topics in Mineral Sciences, v. 47, p. 129–159.

Plouffe, A., Ferbey, T., Hashmi, S., and Ward, B.C., 2016. Till geochemistry and mineralogy: vectoring towards Cu porphyry deposits in British Columbia, Canada; Geochemistry: Exploration, Environment, Analysis, v. 16, no. 3–4, p. 213–232. https://doi.org/10.1144/geochem2015-398

Raczek, I., Stoll, B., Hofmann, A.W., and Jochum, K.P., 2001. High-precision trace element data for the USGS reference materials BCR-1, BCR-2, BHVO-1, BHVO-2, AGV-1, AGV-2, DTS-1, DTS-2, GSP-1 and GSP-2 by ID-TIMS and MIC-SSMS; Geostandards and Geoanalytical Research, v. 25, no. 1, p. 77–86. https://doi.org/10.1111/j.1751-908X.2001.tb00789.x

Sillitoe, R.H., 2010. Porphyry copper systems; Economic Geology, v. 105, no. 1, p. 3–41. https://doi.org/10.2113/gsecongeo.105.1.3

Sinclair, W.D. and Richarson, J.M., 1992. Quartz-tourmaline orbicules in the Seagull Batholith, Yukon Territory; The Canadian Mineralogist, v. 30, no. 3, p. 923–935.

Slack, J.F., 1996. Tourmaline associations with hydrothermal ore deposits. Chapter 11 *in*: Boron: mineralogy, petrology and geochemistry, (ed.) E.S. Grew and L.M. Anovitz; Reviews in Mineralogy, v. 33, p. 559–643.

Slack, J.F. and Coad, P.R., 1989. Multiple hydrothermal and metamorphic events in the Kidd Creek volcanogenic massive sulphide deposit, Timmins, Ontario: evidence from tourmalines and chlorites; Canadian Journal of Earth Sciences, v. 26, no. 4, p. 694–715. https://doi.org/10.1139/e89-059

Slack, J.F. and Trumbull, R.B., 2011. Tourmaline as a recorder of ore-forming processes; Elements, v. 7, no. 5, p. 321–326.

Slack, J.F., Palmer, M.R., Stevens, B.P.J., and Barnes, R.G., 1993. Origin and significance of tourmaline-rich rocks in the Broken Hill district, Australia; Economic Geology, v. 88, no. 3, p. 505–541. https://doi.org/10.2113/gsecongeo.88.3.505

Slack, J.F., Ramsden, A.R., Griffin, W.L., Win, T.T., French, D.H., and Ryan, C.G., 1999. Trace elements in tourmaline from the Kidd Creek massive sulfide deposit and vicinity, Timmins, Ontario: a proton microprobe study; *in* The giant Kidd Creek volcanogenic massive sulfide deposit, western Abitibi Subprovince, Canada, (ed.) M.D. Hannington and C.T. Barrie; Economic Geology Monograph, v. 10, p. 415–430.

Testa, F., Villanueva, C., Cooke, D., and Zhang, L., 2018. Lithological and hydrothermal alteration mapping of epithermal, porphyry and tourmaline breccia districts in the Argentine Andes using ASTER imagery; Remote Sensing, v. 10, no. 2, p. 203. https://doi.org/10.3390/rs10020203

Trumbull, R.B., Garda, G.M., Xavier, R.P., Cavalcanti, J.A.D., and Codeço, M.S., 2019. Tourmaline in the Passagem de Mariana gold deposit (Brazil) revisited: major-element, trace-element and B-isotope constraints on metallogenesis; Mineralium Deposita, v. 54, no. 3, p. 395–414. https://doi.org/10.1007/s00126-018-0819-z

van Hinsberg, V.J., Henry, D.J., and Marschall, H.R., 2011. Tourmaline: an ideal indicator of its host environment; The Canadian Mineralogist, v. 49, no. 1, p. 1–16. https://doi.org/10.3749/canmin.49.1.1

Wilkinson, J.J., Cooke, D.R., Baker, M.J., Chang, Z., Wilkinson, C.C., Chen, H., Fox, N., Hollings, P., White, N.C., Gemmell, J.B., Loader, M.A., Pacey, A., Sievwright, R.H., Hart, L.A., and Brugge, E.R., 2017. Porphyry indicator minerals and their mineral chemistry as vectoring and fertility tools; *in* Application of indicator mineral methods to bedrock and sediments, (ed.) M.B. McClenaghan and D. Layton-Matthews; Geological Survey of Canada, Open File 8345, p. 67–77. https://doi.org/10.4095/306317

Xu, L., Bi, X., Hu, R., Tang, Y., Wang, X., and Xu, Y., 2015. LA-ICP-MS mineral chemistry of titanite and the geological implications for exploration of porphyry Cu deposits in the Jinshajiang – Red River alkaline igneous belt, SW China; Mineralogy and Petrology, v. 109, no. 2, p. 181–200. https://doi.org/10.1007/s00710-014-0359-x

Yavuz, F., Karakaya, N., Yıldırım, D. K., Karakaya, M.Ç., and Kumral, M., 2014. A Windows program for calculation and classification of tourmaline-supergroup (IMA-2011); Computers & Geosciences, v. 63, p. 70–87. https://doi.org/10.1016/j.cageo.2013.10.012

Zhao, H.-D., Zhao, K.-D., Palmer, M.R., and Jiang, S.-Y., 2019. In-situ elemental and boron isotopic variations of tourmaline from the Sanfang granite, South China: insights into magmatic-hydrothermal evolution; Chemical Geology, v. 504, p. 190–204. https://doi.org/10.1016/j.chemgeo.2018.11.013

APPENDIX A

Detrital tourmaline recount data

The table containing tourmaline grain recounts from heavy mineral concentrates of till samples collected surrounding the Woodjam deposit, British Colombia is found in the file POR-09_Appendix A.xlsx. This Appendix has not been edited to Geological Survey of Canada specifications. The data are listed by sample numbers. The location of the samples can be found in Plouffe and Ferbey (2016).

Detrital epidote chemistry: detecting the alteration footprint of porphyry copper mineralization in the Quesnel terrane of the Canadian Cordillera, British Columbia

A. Plouffe[1*], P. Acosta-Góngora[1], I.M. Kjarsgaard[2], D. Petts[1], T. Ferbey[3], and K.E. Venance[1]

Plouffe, A., Acosta-Góngora, P., Kjarsgaard, I.M., Petts, D., Ferbey, T., and Venance, K.E., 2021. Detrital epidote chemistry: detecting the alteration footprint of porphyry copper mineralization in the Quesnel terrane of the Canadian Cordillera, British Columbia; in *Targeted Geoscience Initiative 5: contributions to the understanding and exploration of porphyry deposits, (ed.) A. Plouffe and E. Schetselaar; Geological Survey of Canada, Bulletin 616, p. 137–157. https://doi.org/10.4095/327988*

Abstract: Epidote from detrital sediments derived from propylitic alteration associated with porphyry copper mineralization could be used as a vector for mineral exploration in drift-covered areas; however, differentiating porphyry-related epidote from other sources is crucial. We analyzed the composition of epidote from granitoids associated with porphyry copper mineralization, Nicola Group rocks and grains from till at three sites (Gibraltar, Mount Polley, and Woodjam) within British Columbia's Quesnel terrane, where two main sources of epidote in till are propylitic-altered rocks associated with porphyry mineralization and metamorphosed Nicola Group mafic volcanic and sedimentary rocks. Although principal component analysis was insufficient to distinguish between intrusive- and metamorphic-related epidote, patterns in the abundance of sets of elements indicate provenance. Epidote from granitoids typically has less Hf+Th (<6 ppm) and Sc+Cr+Y (<100 ppm) compared to epidote from Nicola Group rocks; abundances of As and Sb (>>4 ppm As and >>0.6 ppm Sb) in epidote derived from hydrothermal alteration zones associated with porphyry copper mineralization exceed levels measured in metamorphic epidote; and elevated Cu (approximately >30 ppm) in epidote can indicate copper mineralization. These trends in the chemical composition of till-derived epidote can be used in mineral exploration to detect buried hydrothermal alteration associated with porphyry copper mineralization.

Résumé: Dans les régions couvertes de sédiments glaciaires, l'épidote contenue dans des sédiments détritiques qui a été produite par une altération propylitique associée à une minéralisation porphyrique de cuivre pourrait servir de vecteur en exploration minérale. Il est toutefois essentiel de différencier l'épidote des systèmes porphyriques de celle provenant d'autres sources. Nous avons analysé la composition de l'épidote contenue dans des granitoïdes associés à une minéralisation porphyrique de cuivre, des roches du Groupe de Nicola et des grains provenant du till à trois emplacements (Gibraltar, Mount Polley et Woodjam) du terrane de Quesnel, en Colombie-Britannique, où les deux principales sources d'épidote dans le till sont les roches altérées par une altération propylitique associée à une minéralisation porphyrique ainsi que les roches sédimentaires et les roches volcaniques mafiques métamorphisées du Groupe de Nicola. Bien que l'analyse en composantes principales n'ait pas permis de distinguer l'épidote intrusive de l'épidote métamorphique, les profils d'abondance d'ensembles d'éléments révèlent l'origine de l'épidote. L'épidote provenant de granitoïdes contient habituellement moins de Hf+Th (<6 ppm) et de Sc+Cr+Y (<100 ppm) que l'épidote présente dans des roches du Groupe de Nicola; les quantités d'arsenic et d'antimoine (>>4 ppm pour As et >>0,6 ppm pour Sb) dans l'épidote provenant de zones d'altération hydrothermale associée à une minéralisation porphyrique de cuivre dépassent les concentrations mesurées dans de l'épidote métamorphique; et une concentration élevée de Cu (environ >30 ppm) dans l'épidote peut indiquer une minéralisation de cuivre. Ces tendances dans la composition chimique de l'épidote extraite du till peuvent servir en exploration minérale à détecter une altération hydrothermale associée à une minéralisation porphyrique de cuivre enfouie.

[1]Geological Survey of Canada, 601 Booth Street, Ottawa, Ontario K1A 0E8
[2]Mineralogical Consultant, 15 Scotia Place, Ottawa, Ontario K1S 0W2
[3]British Columbia Geological Survey, British Columbia Ministry of Energy, Mines and Petroleum Resources, 1810 Blanshard Street, Victoria, British Columbia V8T 4J1
*Corresponding author: A. Plouffe (email: alain.plouffe@canada.ca)

INTRODUCTION

The Canadian Cordillera has long been known to be rich in porphyry copper mineralization (Sutherland Brown, 1976; Schroeter, 1995; Sinclair, 2007; Logan and Schroeter, 2013; Logan and Mihalynuk, 2014). Both the Quesnel and Stikine terranes, two island arcs accreted to the North American Craton, host a wealth of porphyry copper resources. Porphyry copper deposits are also found in the Wrangell terrane to the west. In British Columbia, copper accounts for 25% of the value of mineral production (Clarke et al., 2018) and in Canada, 40% of the copper production comes from porphyry deposits (Sinclair, 2007). In their assessment of porphyry copper deposits of the Canadian Cordillera, Mihalasky et al. (2011) estimate that approximately 49 000 000 t of Cu remains to be discovered in porphyry deposits. The challenge is that prospective geology of the Stikine and Quesnel terranes is poorly exposed in places; the area is covered to a large extent by glacial sediments.

The challenge of poor exposure can be tackled in part by investigating the geochemistry and mineralogy of till. At four porphyry copper study sites in south-central British Columbia — the Gibraltar, Mount Polley, and Highland Valley Copper mines and the Woodjam prospect — Hashmi et al. (2015), Plouffe and Ferbey (2015b, 2016, 2017), Ferbey et al. (2016), and Plouffe et al. (2016) have demonstrated that till composition can be used as an indicator of the presence of mineralization in the underlying bedrock. In each of these case studies, mineralization was directly exposed to glacial erosion, resulting in glacial dispersal defined by geochemical and mineralogical anomalies in till, schematically shown in Figure 1a. Detecting the presence of porphyry mineralization at a site where the main ore zone remains below the bedrock surface and has not been directly exposed to glacial erosion (Fig. 1b) is a greater challenge. In such a scenario, ore metals (e.g. copper, molybdenum, gold) or associated minerals (e.g. chalcopyrite, gold grains) from the main ore zone would not be present in detrital sediments. Identifying minerals in till that are representative of the alteration zones that surround porphyry mineralization could be key to detecting deeply buried mineralization. One advantage of looking for porphyry alteration mineralogy in detrital sediments is that the alteration halos can extend up to a few kilometres outside the ore zone; consequently, it could result in extensive alteration mineralogy halos (Fig. 1; cf. Averill, 2011). In the context of mineral exploration, this translates into large exploration targets and increases discovery potential.

Epidote is abundant and common in propylitic alteration associated with porphyry copper mineralization (Sinclair, 2007; Sillitoe, 2010) and is dispersed in till near known porphyry copper deposits (Hashmi et al., 2015; Plouffe et al., 2016; Plouffe and Ferbey, 2017). Anomalously high epidote in till might indicate buried porphyry copper mineralization, but in the absence of ore metals or minerals in the sediments (Fig. 1b), the relationship between epidote abundance and porphyry mineralization needs to be demonstrated using epidote chemistry to identify its source. The objective of our study was to use epidote chemistry to develop a porphyry copper mineral exploration method based on alteration mineralogy. The challenge of using epidote chemistry as an indicator of porphyry hydrothermal alteration in the Quesnel terrane of central British Columbia is the need to discriminate between epidote derived from porphyry hydrothermal alteration zones in intrusive rocks and epidote derived from 'background' or unmineralized sources. The dominant source of background epidote in the Quesnel terrane is the Upper Triassic Nicola Group, which includes weakly metamorphosed volcanic and volcaniclastic rocks known to contain metamorphic epidote (Greenwood et al., 1991; Panteleyev et al., 1996; Schiarizza, 2016). Nicola Group rocks located within the alteration zone of porphyry copper mineralization could also contain hydrothermal epidote. We analyzed epidote from mineralized intrusive rocks hosting porphyry copper mineralization at the Gibraltar and Mount Polley mines and at the Woodjam prospect, and epidote from the barren, Nicola Group regional host rocks using laser-ablation inductively coupled plasma mass spectrometry (LA-ICP-MS). In addition, we analyzed epidote grains in till collected within epidote dispersal trains (down-ice) and also up-ice and distal of porphyry mineralization at each study site. We demonstrate that the chemistry of epidote recovered from till at the study sites provides an indication of its provenance from hydrothermal alteration associated with porphyry copper mineralization.

GEOLOGICAL SETTING OF PORPHYRY COPPER MINERALIZATION

Most porphyry copper deposits in the Stikine and Quesnel terranes formed during two episodes. During the earlier and most prolific event, from the Late Triassic to Middle Jurassic, porphyry mineralization formed in an island arc setting prior to accretion to North America (McMillan and Panteleyev, 1995; McMillan et al., 1995, 1996; Logan, 2013). The 208 to 202 Ma time window was a particularly prolific period, during which 90% of the known porphyry copper deposits in British Columbia formed (Logan and Mihalynuk, 2014). The second episode of porphyry formation took place in a continental arc setting after accretion to North America and extended from the Late Cretaceous to the Eocene.

We conducted a geochemical study of epidote using samples from three porphyry copper study sites: 1) the Mount Polley mine, an alkalic Cu-Au-Ag deposit; 2) the Woodjam Cu-Au prospect, which has calc-alkaline affinities; and 3) the Gibraltar mine, a calc-alkaline Cu-Mo deposit (Fig. 2). All three sites are hosted in Late Triassic to Early Jurassic felsic to intermediate intrusive rocks that intrude the Nicola Group, an Upper Triassic succession of volcanic and sedimentary rocks of the Quesnel terrane. The intrusions hosting

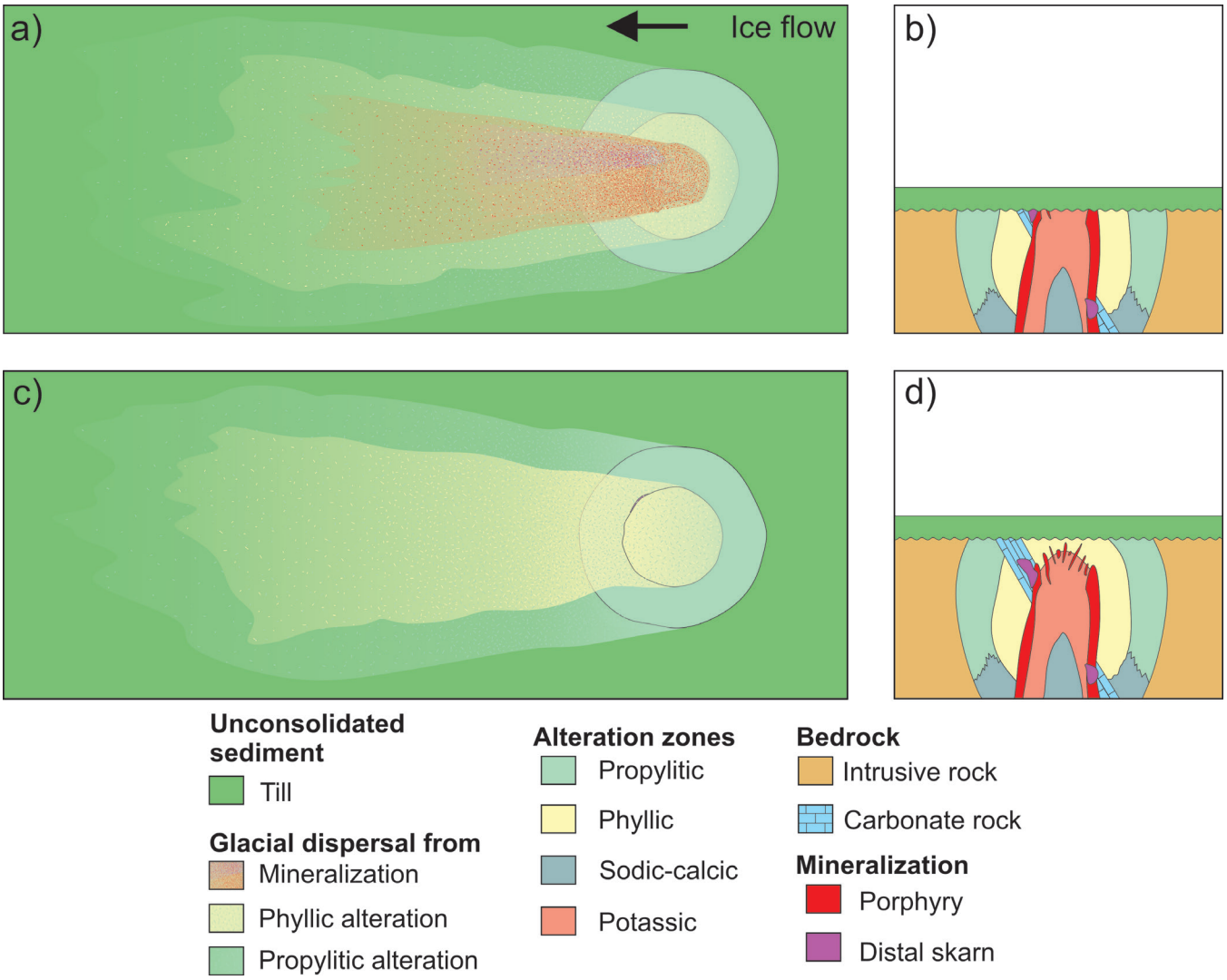

Figure 1. Schematic representation of glacial dispersal from an idealized porphyry copper deposit and associated alteration zones in a scenario with a single phase of ice movement: **a)** plan view and **b)** cross section with all alteration zones and distal skarn mineralization exposed to glacial erosion; **c)** plan view and **d)** cross section in which only the alteration zones are exposed to glacial erosion. The schematic representation of the copper deposit and alteration zones is *modified from* Lowell and Guilbert (1970) and Sillitoe (2010). The representation of the dispersal pattern is *modified from* Hickin and Plouffe (2017).

mineralization include the Mount Polley Intrusive Complex at Mount Polley (Fig. 3a), the Takomkane batholith and associated satellite intrusions at Woodjam (Fig. 3b), and the Granite Mountain batholith at Gibraltar (Fig. 3c). These deposits vary in size, with 150 000 000 t of ore grading 0.2 to 0.3% Cu and 0.2 to 0.3 g/t Au at Mount Polley (Rees, 2013), 221 000 000 t of ore grading 0.2 to 0.3% Cu and 0.3 to 0.5 g/t Au at Woodjam (Sherlock et al., 2013; Sherlock and Trueman, 2013), and 1 220 000 000 t of ore grading 0.3% Cu and 0.01% Mo at Gibraltar (van Straaten et al., 2013; Taseko Mines Ltd., 2020). Hydrothermal alteration zones with disseminated pistachio green epidote and epidote veining extend a few kilometres outward from the ore zone at each site (Drummond et al., 1976; del Real et al., 2013; Rees, 2013; Sherlock and Trueman, 2013; Kobylinski et al., 2017). A unique characteristic at Gibraltar is the presence of syn- and post-mineralization deformation, which does not occur at Mount Polley or Woodjam.

In addition to its presence in the porphyry hydrothermal alteration zones of granitoid rocks, epidote occurs in the Nicola Group rocks of the central Quesnel terrane as a result of burial metamorphism (Greenwood et al., 1991; Panteleyev et al., 1996; Ash et al., 1999). The Nicola Group rocks are dominantly composed of mafic volcanic and associated sedimentary rocks (Schiarizza, 2016). Post-mineralization regional metamorphism reached the zeolite facies at Mount Polley and Woodjam and the greenschist facies at Gibraltar (Greenwood et al., 1991; Bysouth et al., 1995; Panteleyev et al., 1996; Ash et al., 1999; Rees, 2013; van Straaten et al., 2013). The Nicola Group rocks

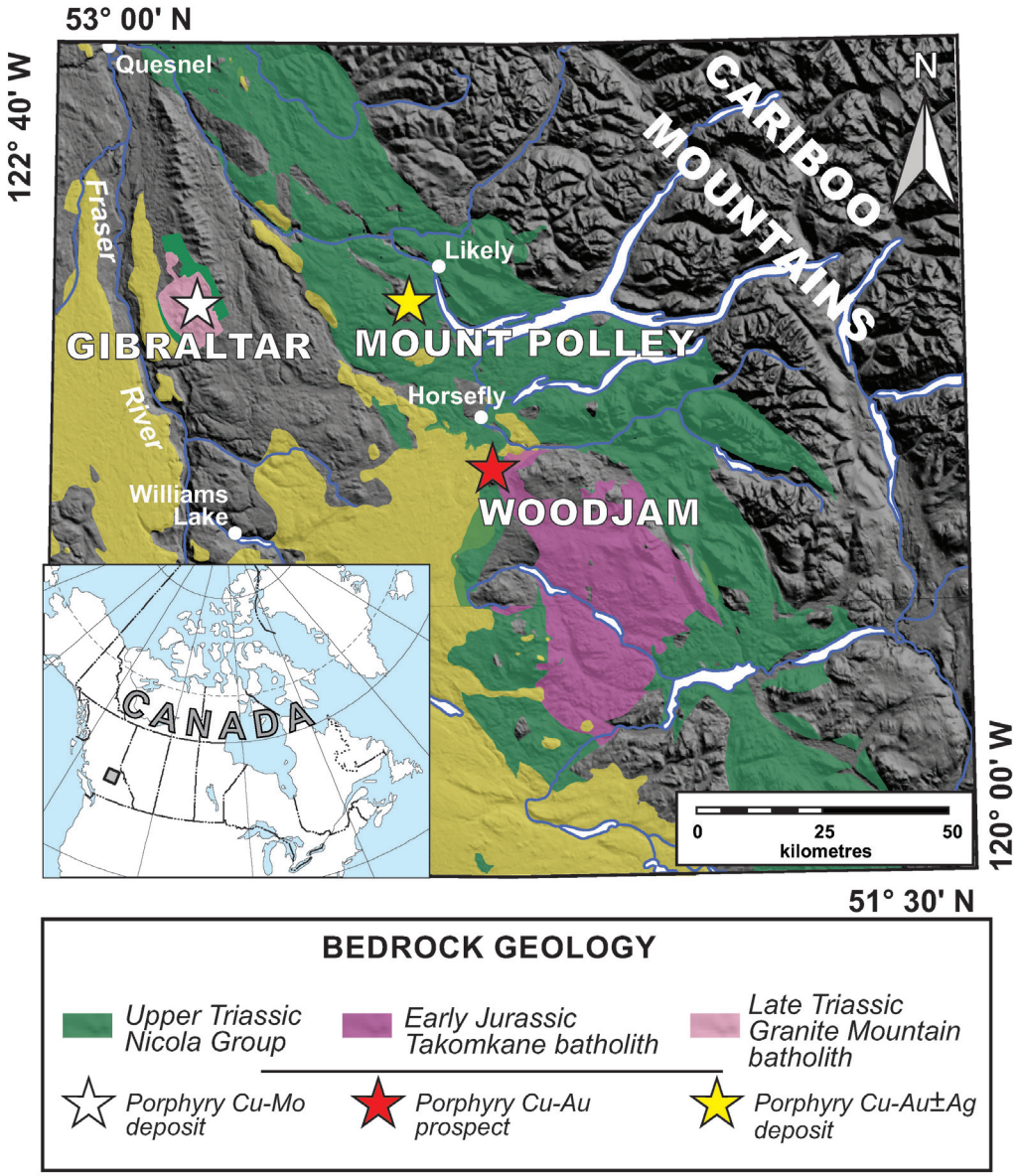

Figure 2. Location of the Gibraltar porphyry Cu-Mo deposit, the Mount Polley porphyry Cu-Au±Ag deposit and the Woodjam porphyry Cu-Au-Mo prospect in south-central British Columbia. Simplified bedrock geology *after* Massey et al. (2005), Logan et al. (2010), and Schiarizza (2019).

(Fig. 2) are the main component of the Quesnel terrane and are the dominant source of detrital epidote derived from unmineralized rocks. We sampled epidote from the Nicola Group rocks in proximity (<1 km) of and distal (>9 km) to porphyry mineralization to establish the geochemical composition of epidote derived from unmineralized rocks.

The Cordilleran Ice Sheet completely covered the three study sites during the Late Wisconsin glaciation. At Gibraltar, three phases of ice movement occurred during this glacial event: a first movement, to the southeast, related to the first glaciers that formed in a small mountain ridge with cirques and arêtes north of the mine site (Plouffe and Ferbey, 2015a); a second movement, to the southwest, derived from glaciers of the Cariboo Mountains; and a third movement, to the northwest, derived from an ice divide that formed around latitude 52°N (Plouffe et al., 2011; Plouffe and Ferbey, 2016). Only the second (southwest) and third (northwest) ice movements occurred at Mount Polley and Woodjam (Fig. 3a, b).

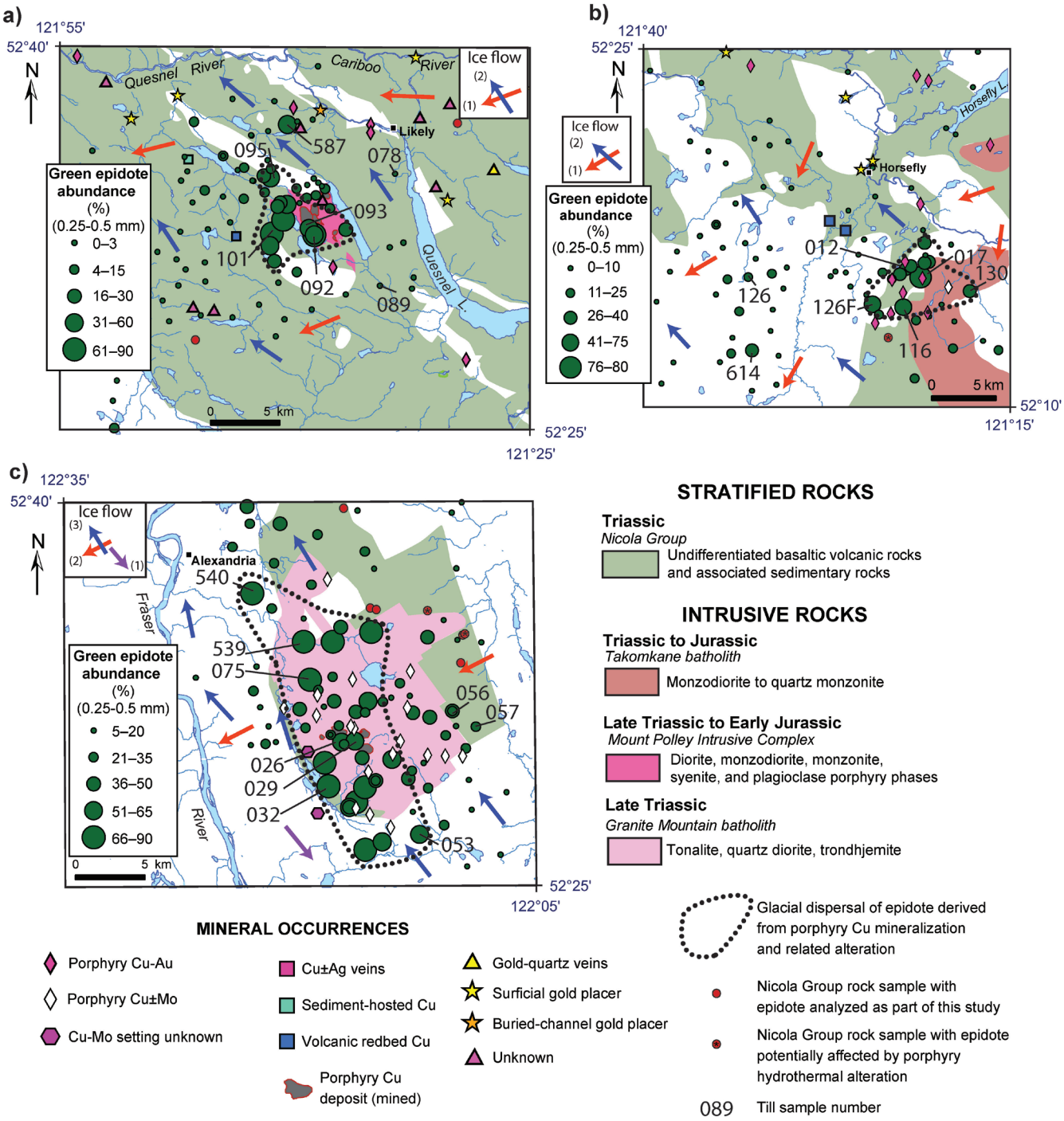

Figure 3. Abundance of green epidote in the 0.25 to 0.5 mm, greater than 3.2 SG, 0.8 to 1.0 A fraction of till samples from the **a)** Mount Polley, **b)** Woodjam, and **c)** Gibraltar occurrences in the Quesnel terrane, south-central British Columbia. The limit of glacial dispersal of epidote interpreted to be derived from porphyry copper mineralization is *modified from* Plouffe and Ferbey (2017). Ice-flow directions are *after* Plouffe and Ferbey (2016).

EPIDOTE: BACKGROUND INFORMATION AND PREVIOUS STUDIES

Minerals of the epidote supergroup are sorosilicates with the general formula $A_2M_3[T_2O_7][TO_4](O,F)(OH,O)$. Homovalent substitutions of di- and trivalent cations (e.g. Ca^{2+}, Mn^{2+}, Sr^{2+}, Pb^{2+}, or rare-earth elements $[REE]^{3+}$) can take place at the A site and trivalent cations (e.g. Al^{3+}, Fe3+, REE^{3+}) substitute in the M site, and the T site is most commonly Si (Armbruster et al., 2006). According to the classifications by Armbruster et al. (2006) and Mills et al. (2009), the epidote supergroup includes three groups: epidote, allanite (REE rich), and dollaseite (the Mg equivalent of allanite). Epidote $[Ca_2Al_2Fe^{3+}[Si_2O_7][SiO_4]O(OH)]$ and clinozoisite $[Ca_2Al_3[Si_2O_7][SiO_4]O(OH)]$ are part of the epidote group and represent the Fe- and Al-rich endmembers, respectively, of a solid solution.

Epidote is common in the propylitic alteration zone associated with porphyry systems as either a replacement product (e.g. after plagioclase) or a direct precipitate of hydrothermal fluids (e.g. in veins; Lowell and Guilbert, 1970; Sillitoe, 2010). It is also common in various metamorphic rocks from upper zeolite facies to intermediate amphibolite facies (Grapes and Hoskin, 2004), but particularly in greenschist facies. It is a mineral resistant to weathering with a hardness of 6 to 7 (Berry et al., 1983) that can withstand glacial erosion and dispersion from its bedrock source. Epidote is more abundant in till near porphyry mineralization compared to surrounding background regions, which results from glacial erosion and dispersal from epidote-bearing porphyry alteration zones (Fig. 2, 3; Hashmi et al., 2015; Plouffe et al., 2016; Plouffe and Ferbey, 2017).

METHODS

In this study, we analyzed the composition of epidote from 27 hydrothermally altered intrusive rock samples from the three porphyry deposits (Gibraltar, Mount Polley, and Woodjam) and 12 rocks from the Nicola Group (Table 1). Intrusive and Nicola Group rock sample locations are shown in Figure 3 and listed in Appendix A. Two Nicola Group rock sample locations fall outside the extent of the maps in Figure 3. Volcanic and volcaniclastic rock samples from the Nicola Group were collected distal (>9 km) to porphyry mineralization, except for one sample collected near Woodjam (<1 km from mineralization; Fig. 3). Thick (75 µm) polished thin sections were prepared from the rock samples. Epidote grains were picked from heavy mineral separates (0.25–0.5 mm, >3.2 SG, and 0.8–1.0 A) of 25 subglacial till samples collected at locations within the epidote dispersal trains (down-ice) and up-ice from or distal to the alteration zones at each site (Fig. 3). Grains were mounted in epoxy and polished to expose their core.

Polished thin sections and grain mounts were examined with a TESCAN Mira3 field emission scanning electron microscope (SEM) at the Geological Survey of Canada (Ottawa, Ontario). Backscattered electron images were captured using a working distance of 15 mm, accelerating voltage of 20 kV, and probe current of 0.4 to 1 nA. Epidote composition analyses (Fe and Al) were performed using the Oxford Instruments energy dispersive spectrometry (EDS) system, which includes an X-MAX 80 silicon drift detector and Aztec 4.1 microanalysis software. Analyses were performed using an acquisition time of 3 s. The standard deviation of EDS analyses is 0.1 weight per cent oxides.

Epidote was analyzed for 58 elements by LA-ICP-MS at the Geological Survey of Canada (Ottawa, Ontario). The LA-ICP-MS analyses were done using a Photon Machines Analyte G2 (193 nm laser, equipped with a dual-volume cell) connected to an Agilent 7700x ICP-MS. Laser conditions included a laser fluence of 5 J/cm2, spot size of 30 to 65 µm (dependent on the size of the epidote), and repetition of 10 Hz. Helium gas (approximately 1 L/min) carried the ablated aerosol to the ICP-MS. A SQUID signal smoothing device was used on the carrier gas line. Signals were acquired on the ICP-MS using a total mass cycle time of 456 ms and dwell times of 2 to 4 ms for major elements, 4 to 8 ms for most trace elements, and 12 to 16 ms for specific trace elements of interest (i.e. As, Ag). Total analytical time was 100 s including 40 s of background measurement (laser off) and 60 s of signal analysis (laser on). The United States Geological Survey GSE-1G was used as the primary calibration standard and was analyzed twice every hour to correct for instrument drift. Once per hour, secondary standards NIST 612, GSD-1G, BCR-2G, and Po689 were analyzed to assess accuracy, with most elements falling within 5 to 10% of their reference values. Reference values for GSD-1G (Guillong et al., 2005), BCR-2G and GSE-1G (Jochum et al., 2005b), and NIST-612 (Kane, 1998) are based on preferred values from GeoReM (Jochum et al., 2005a). Reference values for Po689 (*see* Sylvester et al. (2005) for information about the Po series) were provided by Louis Cabri – CANMET (L. Cabri, pers. comm., 2020) and have been cross-referenced against other S-, As-, Ag-, and Au-bearing reference materials in the laboratory.

Analytical spectra were manually processed in GLITTER (Griffin et al., 2008), keeping only a ‘clean’ (i.e. inclusion-free) portion of each spectrum for data processing. Other mineral phases present as inclusions that were ablated during the analysis, such as Ti, P, or S peaks related to the potential presence of titanite, phosphate, or sulfide, respectively, were identified and excluded from the signals during processing. Trace-element concentrations were calibrated using Ca as an internal standard, determined on a JEOL8230 electron microprobe equipped with five wavelength spectrometers at the University of Ottawa. Operating conditions were 20 kV accelerating voltage, 20 nA beam current, and 5 µm spot size. Count times were 10 s on peak and 5 s on the

Table 1. Number of valid laser-ablation inductively coupled plasma mass spectrometry analyses of epidote in samples collected from porphyry mineralization and one regional rock type at study sites in the Quesnel terrane, British Columbia

Rock type	Site	Number of rock samples	Number of epidote analyses from rock samples	Number of till samples	Number of epidote grain analyses from till samples
Takomkane Batholith	Woodjam	7	69	7	60
Mount Polley Intrusive Complex	Mount Polley	10	81	9	81
Granite Mountain Batholith	Gibraltar	10	38	9	80
Nicola Group	Regional rock type	12	62	N/A	N/A

background to either side of the peak. Calibration standards were a mix of natural and synthetic minerals. Raw data were processed with the CITZAF program (Armstrong, 1988).

Further filtering of LA-ICP-MS analytical results to remove mineral phases other than epidote was based on major-element chemistry. Using the same classification scheme as Plouffe et al. (2019), analyses with greater than 42 weight per cent SiO2, greater than 0.5 weight per cent TiO_2, less than 15 weight per cent Al_2O_3, greater than 16 weight per cent Fe_2O_3, greater than 0.5 weight per cent MgO, greater than 24 weight per cent CaO, greater than 0.5 weight per cent Na_2O, greater than 0.25 weight per cent K_2O, and greater than 0.5 weight per cent P_2O_5 were classified as non-epidote and rejected from the interpreted data set. The result was 250 valid analyses of epidote in rock samples and 221 analyses of epidote grains from till with a rejection percentage of 25% (Table 1; Appendix A). In comparison, Pacey et al. (2020) report 41% rejection of their LA-ICP-MS epidote analyses. Analyses of P, Se, Te, and Pt were deemed to be semi-quantitative due to the absence of certified values in GSE-1G and/or the secondary standards (so that in house values were used for quantification), and although these elements are reported in Appendix A (indicated by '*' and italicized), the data have only been used in the principal component analysis (PCA) to assess relative interelement relationships.

Mean detection limits for LA-ICP-MS analyses are provided in Appendix A and represent the average of all values in the filtered data that fell below the minimum detection limit (i.e. all values with '<' symbols). Table 2 presents the minimum detection limits for the elements reported in this study.

A suite of 57 elements (i.e. variables), as determined by LA-ICP-MS, was used for PCA using the 'rgr' package (Garrett, 2013) within the R statistical software environment (R Core Team, 2018). To avoid the 'closure problem' inherent to compositional data, and prior to performing PCA, the data were transformed using the centred-log ratio transformation (Aitchison, 1986; Thió-Henestrosa and Martín-Fernández, 2005).

RESULTS

Plouffe et al. (2019) recognize three general forms of epidote in the rock samples:

- Euhedral and poikilitic epidote that replaces feldspar or overprinting chlorite is typical of the metamorphosed Nicola Group rocks (Fig. 4a). Some of this epidote is less than 0.25 mm; therefore, it would not be recovered in the 0.25 to 0.5 mm size fraction of till samples.
- Epidote that replaces chlorite pseudomorphs after biotite with a layered and, in places, deformed wavy texture and titanite inclusions is interpreted to be hydrothermal in origin. It is also found in close association with undeformed epidote (Fig. 4b).
- The dark to pale pistachio-green epidote that occurs in veins or in association with chlorite, quartz, and sulfides is interpreted as hydrothermal in origin. This form of epidote has a pitted texture due to abundant mineral inclusions common in hydrothermal minerals. In backscattered electron images, this epidote shows complex crystal growth patterns (Fig. 4c).

The SEM study of epidote revealed variable textures. Backscattered electron images showed mottled to zoned textures attributed to variation in Fe and Al content. For example, based on EDS analyses and assuming total Fe oxides are Fe_2O_3, the darker shades of grey in the epidote samples presented in Figure 4 contain 10.4 to 14.7 weight per cent Fe_2O_3 and 23.1 to 26.6 weight per cent Al_2O_3, and the lighter shades of grey are areas that contain 14.3 to 16 weight per cent Fe_2O_3 and 22.0 to 23.3 weight per cent Al_2O_3. Similar zonation and associated variable Fe and Al content was reported by Cooke et al. (2014) in epidote resulting from hydrothermal alteration in porphyry copper mineralization. With a laser spot size of 30 to 65 µm, we could not avoid the Fe-Al zoning in epidote. Complex crystal growth patterns, as those observed in epidote veins, appear to be a unique characteristic of hydrothermal epidote (Fig. 4c). The same texture was observed in some epidote grains recovered from till (Fig. 4d). In addition to these textures, we observed

Table 2. Mean minimum detection limits (MDL) for reported elements

Element	Mean MDL (ppm)
Sc	0.69
Cr	3.33
Cu	0.13
As	0.09
Y	0.01
Sb	0.38
La	0.01
Ce	0.05
Pr	0.01
Nd	0.07
Sm	1.16
Eu	0.03
Gd	0.56
Tb	0.01
Dy	0.18
Ho	0.02
Er	0.33
Tm	0.08
Yb	0.4
Lu	0.48
Hf	0.59
Th	0.08

a number of mineral inclusions, including titanite, rutile, hematite, and apatite, under the SEM in epidote samples from all rock types. Chalcopyrite inclusions were observed in epidote and allanite in some samples from Gibraltar (see also Kobylinski et al., 2017).

Laser-ablation inductively coupled plasma mass spectrometry analyses of epidote from the various rock types show important differences in the average concentrations of certain elements (Table 3); these geochemical differences have the potential to indicate the source of detrital epidote. The average As and Sb concentrations in epidote vary among the rock types, with no apparent consistent pattern between intrusive and Nicola Group rocks. On the other hand, Y, total REE (ΣREE), Sc, Th, Hf, and Cr occur, on average, in higher concentrations in Nicola Group epidote compared to epidote from intrusive rocks. Using these elements, we present three correlation graphs that could serve to differentiate the source of detrital epidote based on its composition: As versus Sb (Fig. 5), ΣREE versus Y (Fig. 6), and Sc+Cr+Y versus Th+Hf (Fig. 7).

In the As versus Sb correlation graph (Fig. 5), epidote from the Mount Polley Intrusive Complex and the Takomkane batholith (Woodjam) generally plots with higher As (approximately >10 ppm) and Sb (approximately >4 ppm) concentrations than epidote from the Nicola Group rocks (Fig. 5a, b). The notable exceptions are a number of Nicola Group epidotes with greater than 10 ppm As or greater than 4 ppm Sb, shown in a darker green in Figure 5. All of these epidotes are from rock samples located near (<1 km) porphyry mineralization or intrusive rocks hosting the mineralization (see their locations in Fig. 3). The compositions of epidote grains from till at Mount Polley and Woodjam overlap in large part with epidotes from intrusive rocks. No distinction exists between the composition of epidote grains in till in down-ice versus up-ice or distal samples (Fig. 5a, b). Epidote from the Granite Mountain batholith (Gibraltar) generally contains As and Sb in concentrations similar to Nicola Group epidote (Fig. 5c); however, a few epidotes from the Granite Mountain batholith do contain greater than 4 ppm Sb. For comparison, the metamorphic (M) and porphyry (P) epidote fields defined by Wilkinson et al. (2017b) are shown in Figure 5 and discussed below.

Two additional simple correlation graphs accentuate the chemical differences between epidote from Nicola Group rocks and epidote from intrusive rocks. Plots of Y versus ΣREE, corresponding to the total of La to Lu (Appendix A) show that, for the same ΣREE concentration, Y concentrations are generally lower in epidote from the Mount Polley Intrusive Complex compared to Nicola Group epidote (Fig. 6a). At Woodjam, most epidote from the Takomkane batholith contains less than 19 ppm Y and between 10 and 100 ppm ΣREE in contrast to Nicola Group epidote, which generally contains greater than 19 ppm Y and 10 to 6900 ppm ΣREE (Fig. 6b). At Gibraltar, epidote in the Granite Mountain batholith generally has lower Y and ΣREE concentrations than in Nicola Group epidote, but there is a strong overlap between populations (Fig. 6c). At all sites, there is a strong overlap between the composition of epidote in till and epidote from intrusive rocks, irrespective of whether the till samples were collected within the epidote dispersal train (down-ice) or outside of it (distal and up-ice) (Fig. 3, 6).

A plot of Sc+Cr+Y versus Th+Hf provides additional support to discriminate between intrusive and Nicola Group epidotes (Fig. 7). These elements were grouped based on their general concentration ranges: 0.01 to 10 ppm for Th and Hf, and 10 to 1000 ppm for Sc, Cr, and Y. Most of the epidote in intrusive rocks at the three sites contains 0.01 to 6 ppm Hf+Th and 5 to 100 ppm Sc+Cr+Y, as opposed to Nicola Group epidote, which generally contains 0.1 to 10 ppm Hf+Th and 35 to 1600 ppm Sc+Cr+Y. As with the ΣREE versus Y correlation, there is an overlap between the epidote from intrusive and Nicola Group rocks, and most of the epidote in till mimics the composition of epidote from intrusive rocks, with no distinction between the down-ice and up-ice or distal samples (Fig. 7).

Principal component analysis was performed to differentiate the two main populations of epidote based on the entire LA-ICP-MS geochemical data set. The first four principal components (PC1, PC2, PC3, and PC4) correspond to the

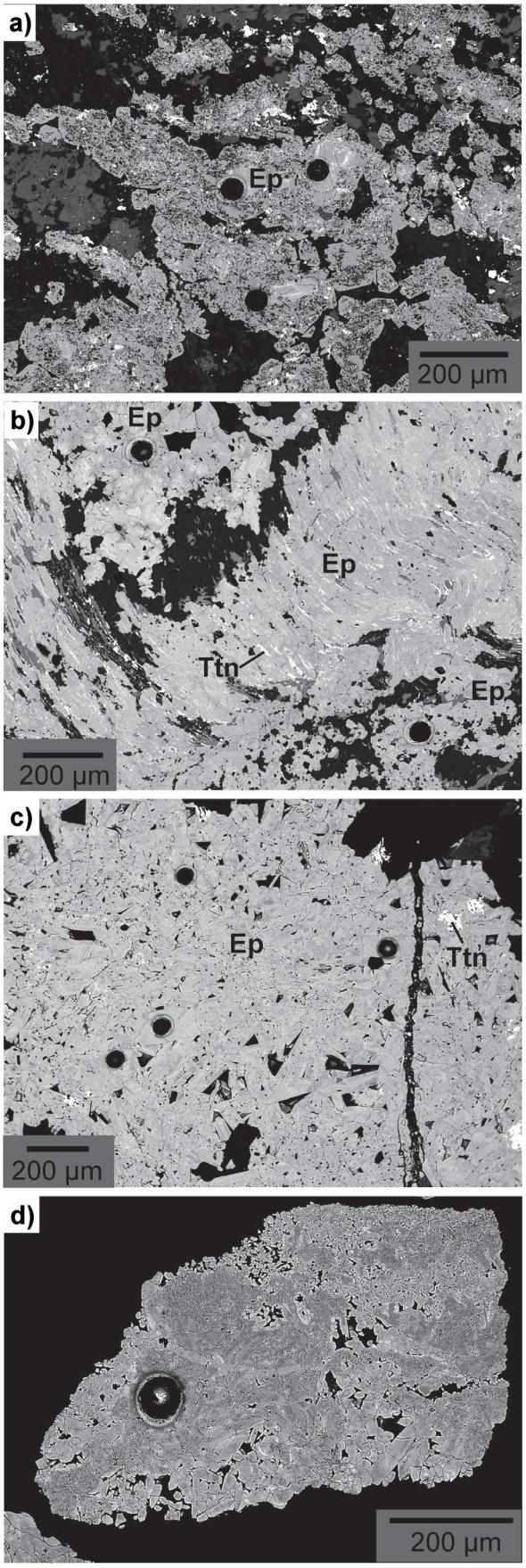

Figure 4. Backscattered electron images of epidote (Ep): **a)** non-homogeneous poikilitic metamorphic epidote with abundant iron-titanium oxide (white specks) in a sample (14PSC357) of Nicola Group rock; **b)** hydrothermal epidote replacing chlorite pseudomorph after biotite with a wavy texture and titanite (Ttn) inclusions, in close association with undeformed epidote (top left), in a sample (73Q202) of the Granite Mountain batholith; **c)** hydrothermal epidote with complex crystal growth patterns in an intrusive rock sample (13CDBWJ05) from the Woodjam prospect; **d)** complex crystal growth patterns in an epidote grain recovered from till (sample 11PMA012) at the Woodjam prospect. Note the 50 µm circular laser ablation pits visible in all images.

Table 3. Average concentration (ppm) of selected elements in epidote in samples collected from porphyry mineralization and one regional rock type at study sites in the Quesnel terrane, British Columbia

Rock type	Site	As	Sb	Y	ΣREE	Sc	Th	Hf	Cr
Takomkane batholith	Woodjam	55	93	13	58	10	0.5	0.6	3*
Mount Polley Intrusive Complex	Mount Polley	38	7	35	416	7	0.4	0.4*	1*
Granite Mountain batholith	Gibraltar	3	6	28	99	57	0.6	0.3*	6
Nicola Group	Regional rock type	25	17	82	552	172	5	1	57
* – below the mean detection limit									

linear combinations of selected elements that account for most of the data variability (55%). For simplicity, the data set variance is displayed in terms of PC1 (24%) and PC2 (16%), which are plotted in Figure 8. Rare-earth elements yield high positive PC1; PC2 is negative for light REE (La, Ce, Pr, Nd, Sm, Eu, Gd), and positive for heavy REE (Tb, Dy, Ho, Er, Tm, Y, Lu). High positive PC2 is observed for Na, Mn, Mg, K, Rb, Cr, and Sc, and Co, Ni, and Zn have overall negative PC1 and PC2 loadings (Fig. 8). Other elements, such as Ga, Fe, and Sr, yield high negative PC2 loadings. Epidotes in intrusive rocks from the Mount Polley, Gibraltar, and Woodjam deposits are roughly distinguished in terms of their PC2 scores (Woodjam>Gibraltar>Mount Polley). Epidote of the Mount Polley Intrusive Complex yields the lowest PC2 scores given its high concentrations of Ga, Ge, Fe, and Sr (Fig. 8a). With high Na, K, Mn, Cr, Th, and Sc concentrations, epidote from the Takomkane batholith at Woodjam yields the highest PC2 scores (Fig. 8b). Epidote in Nicola Group rocks is generally characterized by positive PC1 and PC2 scores, with some exceptions. Nicola Group epidotes with high As or Sb concentrations (identified in Fig. 5), are shown by dark green triangle in Figure 8 and are mostly characterized by a high PC1 score related to high ΣREE content. At Woodjam and Gibraltar, the composition of epidote from intrusive rocks, Nicola Group rocks, and till largely overlap in PC space (Fig. 8b, c). Conversely, at Mount Polley, the till and Nicola Group epidotes are strongly decoupled from epidote in intrusive rocks with respect to their PC2 scores (Fig. 8a).

DISCUSSION

Interpretation of epidote chemistry as a means for detecting hydrothermal alteration associated with porphyry copper mineralization must account for: 1) factors that control epidote composition and 2) the variability of epidote composition in porphyry systems as reported in other studies. Epidote composition is controlled by the primary mineral it replaced, the host rock, hydrothermal fluid composition, temperature, and, to a lesser extent, pressure (Bird and Helgeson, 1980; Arnason et al., 1993; Bird and Spieler, 2004; Pacey et al., 2020). Also, co-forming minerals such as sulfides do affect the composition of epidote in a porphyry system. For instance, within the pyrite-rich phyllic alteration halo of the Black Mountain and Nugget Hill porphyry copper deposits in the Philippines, epidote is depleted in As, Sb, and Pb because these elements are dominantly incorporated by pyrite (Cooke et al., 2014). Outside the pyrite halo and within the propylitic alteration zone, these same elements substitute into epidote (Cooke et al., 2014).

In addition to Cooke et al. (2014), other studies have illustrated the variability in the composition of epidote within a single porphyry copper deposit. At the Bingham deposit in Utah, U.S.A., the MnO content of vein epidote increases from 0.08 weight per cent in the centre of the deposit to 0.73 weight per cent 1.1 km from mineralization (Bowman et al., 1987). At the Tintic deposit, 70 km south of the Bingham deposit, Mn in epidote decreases over a distance of approximately 1 km, from a maximum of 1.18 weight per cent MnO in the actinolite subzone to 0.15 weight per cent MnO in the outer chlorite subzone (Norman et al., 1991). At the Mount Milligan deposit in central British Columbia, along three transects, the Fe content of epidote, expressed as the pistachite ratio (PS = Fe^{3+} / Fe^{3+} + Al^{3+}), decreases over 200 to

Figure 5. Correlation plots of As versus Sb concentrations in epidote from Nicola Group rocks, intrusive rocks, and grains recovered from till from the **a)** Mount Polley, **b)** Woodjam, and **c)** Gibraltar occurrences in south-central British Columbia. Up-ice and distal sample (dark blue crosses) numbers are indicated in the legends and their locations are shown in Figure 3. Note that the same Nicola Group epidote data are presented in all three graphs. Grey dashed and dotted lines define the range of As and Sb concentrations in metamorphic (M) and porphyry (P) epidote determined by Wilkinson et al. (2017b). Horizontal and vertical dashed lines represent the mean minimum detection limit (MDL) for each element. Concentrations below the detection limit are plotted using data not filtered for MDL.

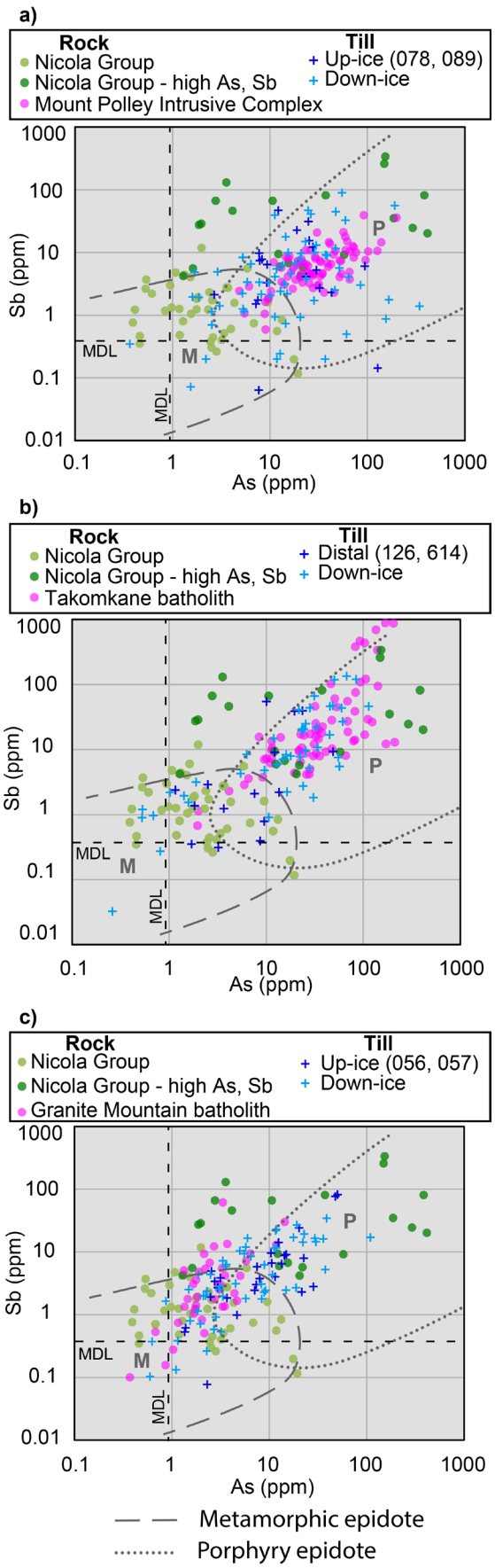

400 m distances, from median values of PS30 and PS36 near the potassic zone to PS25 and PS26 in the outer propylitic zone (Jago et al., 2014). At this same site and in parallel to these trends, epidote trace-element chemistry shows a lateral increase in V, Mn, Sb, Zr, and As, and a lateral decrease in Pb, Cu, Au, and Mo, with increased distance from the potassic zone (Jago et al., 2014). At the El Teniente deposit in Chile, epidote composition follows a pattern similar to that observed by Cook et al. (2014) in the Philippines, having a broad proximal zone of low As in epidote and reaching higher values approximately 3 km from the edge of the ore shell (Wilkinson et al., 2017a). Using gridded values, Wilkinson et al. (2017a) show high concentrations of La, Zr, Zn, Yb, and Y in epidote defining a broad halo around the El Teniente deposit. At the E48 and E26 porphyry Cu-Au deposits in Australia, Pacey et al. (2020) report on the composition of epidote which shows a lateral increase in Ti, As, Sb, and V, and a lateral decrease in Ba towards the deposits. These studies illustrate a wide range of elemental substitutions that can take place in epidote and the variability in epidote composition within a single porphyry system.

Despite this variability in epidote composition within a single porphyry system, Wilkinson et al. (2017b) suggest that porphyry-related epidote is enriched in elements carried by porphyry hydrothermal fluids such as As and Sb, which, in contrast, are at low concentrations in metamorphic epidote. Wilkinson et al. (2017b) reached this conclusion following the analysis of epidote from three porphyry Cu-Au and Cu-Mo systems (Resolution (United States), El Teniente (Chile), Baguio (Philippines)) that contained greater than 4 ppm As and greater than 0.2 ppm Sb, in contrast with epidote from metamorphic rocks of the Dalradian and Moine supergroups in Scotland, which generally yielded less than 20 ppm As and less than 6 ppm Sb (Fig. 5; Wilkinson et al., 2017b, Fig. 3). Wilkinson et al. (2017b) compared metamorphic and porphyry-related epidote from widely separated geological environments. Despite this limitation, the As versus Sb correlation graph of Wilkinson et al. (2017b) provides good indications of the source (metamorphic or porphyry related) of the epidote. The greater abundance of As and Sb in porphyry-related epidote compared to metamorphic epidote is certainly not encountered in all geological environments because the reverse relationship was observed by Pacey et al. (2020). Because of this variability in epidote chemistry, we tested the utility of As and Sb as discriminators of porphyry-related and metamorphic epidote.

The concentrations of As and Sb in epidote from Nicola Group rocks generally fall within the metamorphic field of Wilkinson et al. (2017b), with notable exceptions having greater than 10 ppm As or greater than 4 ppm Sb (dark green in Fig. 5). As indicated above, these epidotes are from one rock sample located less than 1 km from one of the mineralized zones at Woodjam and three rock samples located greater than 9 km from Gibraltar ore but near (less than 1 km) the Granite Mountain batholith, which hosts the mineralization (see Nicola Group samples marked with an asterisk in Fig. 3). Some of these epidotes with high As or

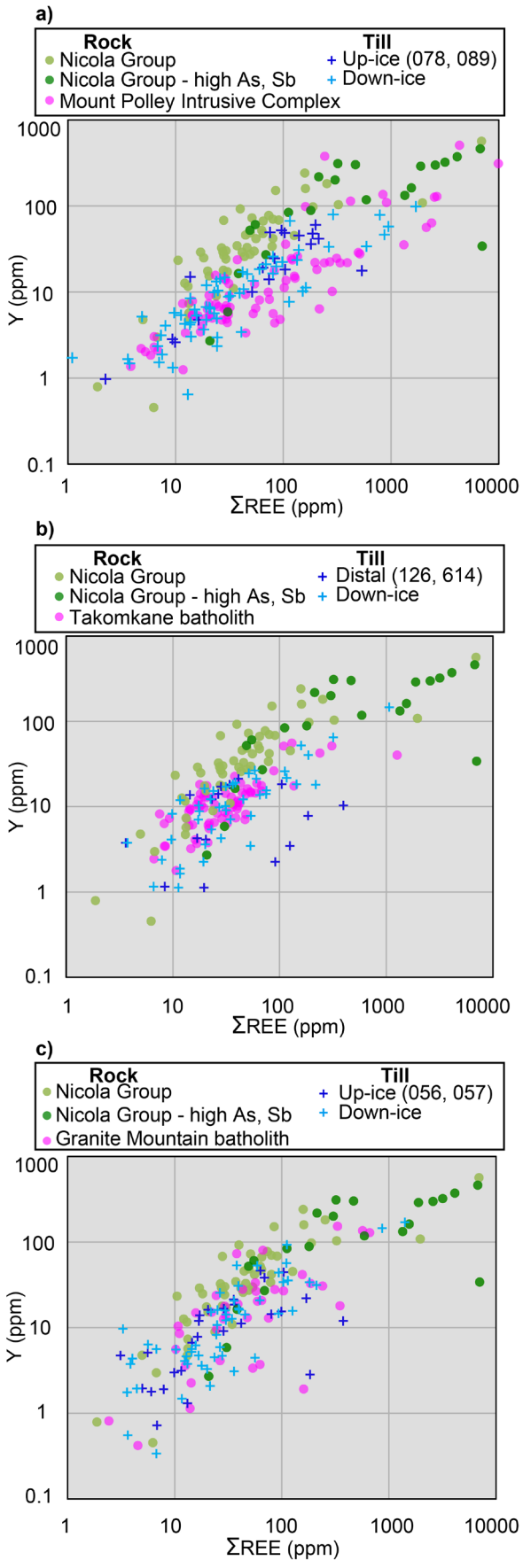

Figure 6. Correlation plots of total rare-earth element (ΣREE) versus Y concentrations in epidote from Nicola Group rocks, intrusive rocks, and grains recovered from till from the **a)** Mount Polley, **b)** Woodjam, and **c)** Gibraltar occurrences in south-central British Columbia. Up-ice and distal sample (dark blue crosses) numbers are indicated in the legends and their locations are shown in Figure 3. Note that the same Nicola Group epidote data are presented in all three graphs.

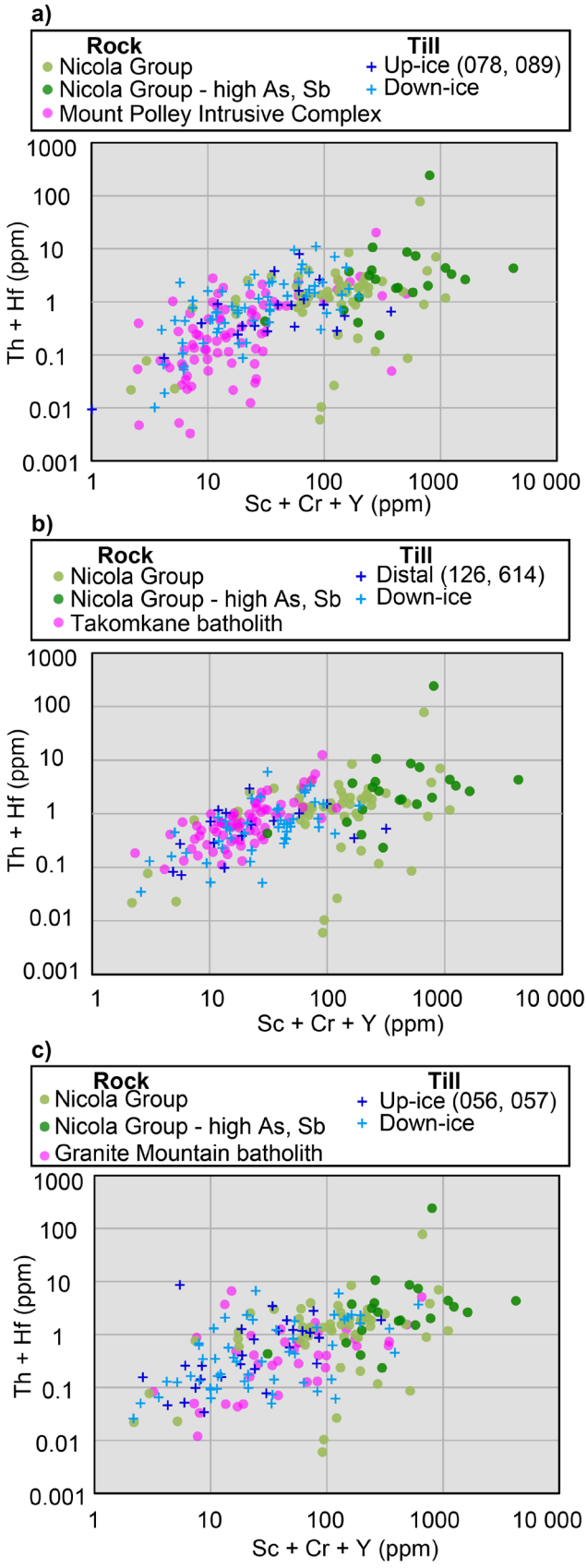

Figure 7. Correlation plots of Sc+Cr+Y versus Th+Hf concentrations in epidote from Nicola Group rocks, intrusive rocks, and grains recovered from till from the **a**) Mount Polley, **b)** Woodjam and, **c)** Gibraltar occurrences in south-central British Columbia. Up-ice and distal sample (dark blue crosses) numbers are indicated in the legends and their locations are shown in Figure 3. Note that the same Nicola Group epidote data are presented in all three graphs.

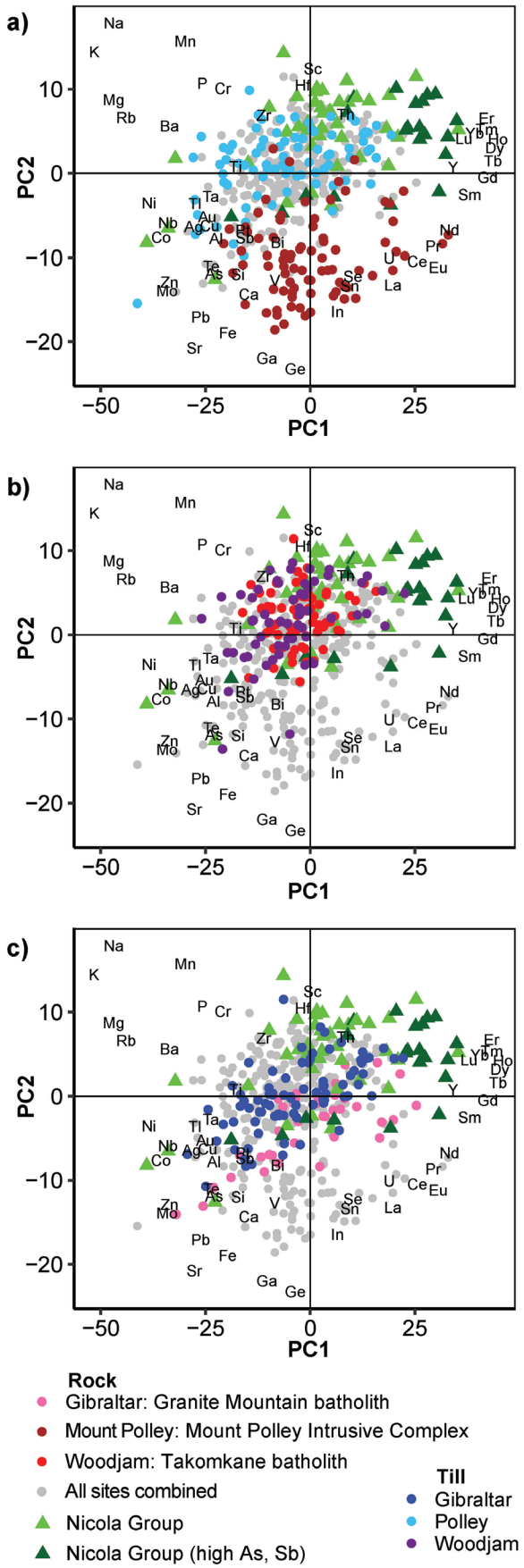

Figure 8. Principal component analysis PC1–PC2 score biplots showing the chemical variation of epidote from mineralized intrusions, Nicola Group volcanic rocks (metamorphic), and till samples collected at the **a)** Mount Polley, **b)** Woodjam, and **c)** Gibraltar occurrences in south-central British Columbia.

Sb levels occur in veins. Building on the observations of Wilkinson et al. (2017b), we interpret epidote occurring in veins within Nicola Group rocks and having greater than 10 ppm As or greater than 4 ppm Sb to be hydrothermal in origin and related to the porphyry mineralization.

Epidote in the intrusive rocks at Mount Polley and Woodjam dominantly fall within the porphyry field, defined by Wilkinson et al. (2017b) as having much greater than 4 ppm As and much greater than 0.6 ppm Sb, suggesting an hydrothermal origin (Fig. 5a, b). In contrast, epidotes at Gibraltar contain concentrations of As and Sb that dominantly fall within the metamorphic field (Wilkinson et al., 2017b) (Fig. 5c). A few epidotes at Gibraltar have greater than 8 ppm Sb and fall outside of both fields (Fig. 5c). It appears that syn- and post-mineralization deformation and associated greenschist metamorphism at Gibraltar (which is a higher metamorphic grade than the two other sites; Greenwood et al., 1991; Read et al., 1991; Panteleyev et al., 1996) has affected the As and Sb content of hydrothermal epidote, or has produced metamorphic epidote with lower As levels; consequently, in a porphyry copper system metamorphosed to greenschist facies, the As and Sb concentrations in epidote might not be a reliable identifier of a hydrothermal versus metamorphic origin.

On the As versus Sb correlation graph (Fig. 5), epidote grains from till at Mount Polley and Woodjam dominantly fall in the porphyry field, with fewer grains within the metamorphic field (Fig. 5a, b), suggesting a predominance of porphyry-related epidote in till (>>4 ppm As and >>0.6 ppm Sb) with only a minor proportion derived from the metamorphosed Nicola Group volcanic rocks. At Gibraltar, epidote grains from till fall within the metamorphic and porphyry fields (Fig. 5c).

Our results indicate that no clear distinction exists between epidote in till collected down-ice, up-ice, or distally from mineralization at each study site (Fig. 5). The presence of porphyry-related epidote with much greater than 4 ppm As and much greater than 0.6 ppm Sb in till samples collected up-ice from the main epidote dispersal train at Gibraltar and Mount Polley might be due to one or a combination of two factors: 1) hydrothermal alteration directly related to these deposits might be more extensive than previously thought and might extend into the up-ice region and/or 2) an unknown source of porphyry mineralization with associated alteration might be present in the up-ice region. At Woodjam, five porphyry-related epidote grains from two till samples (sites 126 and 614; Fig. 3b, 5b) were obtained down-ice and outside of the epidote dispersal train, where the local bedrock (Neogene Chilcotin basalt) is not a source of epidote (Plouffe et al., 2016). We interpret this to represent either 1) glacial transport of porphyry-derived epidote grains 10 km from their source or 2), again, hydrothermal alteration associated with an undiscovered source of porphyry mineralization and alteration in subcropping rock units of this region.

The correlation plots of ΣREE versus Y and Sc+Cr+Y versus Hf+Th do not discriminate between porphyry related (high As and Sb) and metamorphic Nicola Group epidotes (Fig. 6, 7); rather, they discriminate between epidotes from granitoids versus mafic Nicola Group volcanic rock sources. The ΣREE and Y content of granitoids varies from site to site (Fig. 6); however, values of less than 100 ppm Sc+Cr+Y and less than 6 ppm Hf+Th typically reflect a granitoid provenance (Fig. 7). We suspect that the controlling factor of this suite of elements in epidote is in part that the primary mineral composition replaced by epidote is different in felsic (granitoids) and mafic (Nicola Group) rocks. The significant overlap between epidote grains derived from till and epidotes from intrusive rock at the three study sites is observed on these correlation graphs (Fig. 6, 7), and suggests that most of the epidote in till is derived from granitoids.

We interpret the PCA to indicate that epidote composition is the result of multiple geological factors and processes (primary mineral it replaced, the host rock, hydrothermal fluid composition, temperature, and pressure), so that the first four principal components only account for 55% of the total variance. The application of PCA to differentiate the source of epidote in our study is probably further complicated by the fact that magma and fluid sources of the Nicola Group volcanic rocks and the coeval porphyry plutons are similar because both are part of the same magmatic arc; consequently, using the full suite of elements potentially introduces variability into the interpretation of epidote composition that obscures the two-group distinction of epidote attempted here. As a result, PCA alone is insufficient to accurately distinguish between intrusive- and metamorphic-related geochemical subgroups of epidote. Further application of unsupervised machine-learning techniques (e.g. cluster and linear discriminant analysis), potentially using a smaller suite of elements, combined with detailed petrographic studies may provide better results.

It might also be possible to assess porphyry fertility based on epidote composition (Cooke et al., 2014). In their summary of epidote composition of the Baguio porphyry district in the Philippines, Cooke et al. (2014) show that epidote within the pyrite halo of a fertile porphyry system have elevated median concentrations of Cu (11–28 ppm), which they suggest is a potential fertility indicator (Cooke et al., 2014, Fig. 15). At Mount Milligan, 325 km north of Gibraltar, the highest Cu concentration in epidote near porphyry mineralization is 45 ppm (Jago et al., 2014). In contrast, Pacey et al. (2020) detected Cu in only 9% of their LA-ICP-MS epidote analyses, with a maximum concentration of 5 ppm. In our study, some epidotes from the intrusive rocks and till at Gibraltar and Mount Polley have Cu concentrations that exceed the highest median values of ore zone epidote at the Baguio district (Cooke et al., 2014) and Mount Milligan (Fig. 9). In comparison, the mean Cu concentration in epidote from Nicola Group rocks (5 ppm) is lower than at the Granite Mountain batholith (37 ppm) and the Mount Polley Intrusive Complex (207 ppm; Fig. 9). Three of the highest Cu concentrations in epidote (26, 30, and 42 ppm) occur

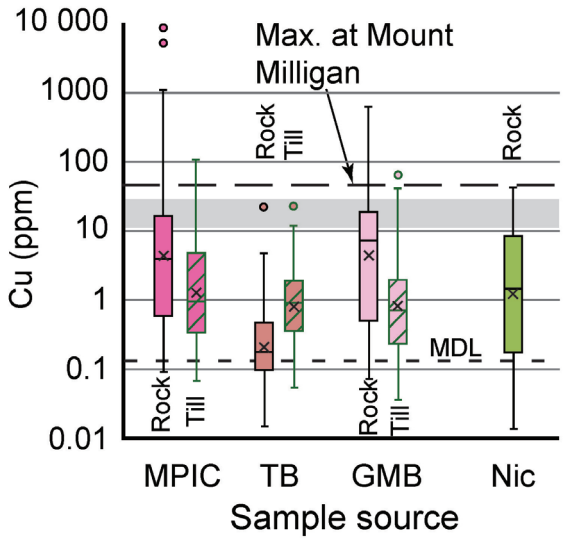

Figure 9. Box and whisker plot showing quartile distribution of Cu concentrations in epidote from rocks and till at the Gibraltar (Granite Mountain batholith (GMB)), Mount Polley (Mount Polley Intrusive Complex (MPIC)), and Woodjam (Takomkane batholith (TB)) occurrences in south-central British Columbia. Concentrations of Cu in epidote in Nicola Group rocks (Nic) are also shown for comparison. The × denotes mean concentration. The grey zone represents the highest Cu median concentrations observed in epidote in rocks collected less than 1 km from porphyry mineralization in the central Baguio district, Philippines (11–28 ppm Cu; Cooke et al., 2014). The upper dashed line shows the maximum concentration observed in epidote at Mount Milligan, British Columbia (Jago et al., 2014). The lower dashed line is the minimum detection limit (MDL); concentrations below the detection limit are plotted using data not filtered for MDL.

in a sample from the Nicola Group rocks with elevated As and Sb values, located less than 1 km northeast of the Granite Mountain batholith, further suggesting that this epidote could be of hydrothermal origin and related to the porphyry copper mineralization. The absence of epidote with high Cu concentration at Woodjam could be related to the position of the shallow hydrothermal alteration zone sampled in our study relative to the main zone of mineralization; the shallow hydrothermal alteration at Woodjam might be in a zone where epidote has low Cu concentrations. Based on the Cu concentrations measured in our samples and those reported by Cooke et al. (2014) and Jago et al. (2014), we suggest that concentrations of greater than 30 ppm Cu in epidote can provide an indication of fertility and are significant from a mineral exploration point of view; moreover, we recognize that more tests on epidote from barren and mineralized intrusions are necessary to assess the robustness of using Cu content in epidote as a fertility indicator. Finally, the form of copper in epidote is still unknown; it could substitute in the epidote crystal lattice or occur as nanoparticles (cf. Cooke et al., 2014).

Results from this study have important implications for mineral exploration. In a favourable geological setting for porphyry mineralization, such as in regions underlain by Late Triassic to Early Jurassic felsic to intermediate intrusions of the Quesnel terrane, greater abundance of epidote in heavy mineral concentrates (HMC) of till compared to regions underlain by Nicola Group rocks can provide a first indication of a porphyry hydrothermal system associated with an intrusion, even in the absence of sought metals (e.g. copper, molybdenum, gold) and indicator minerals (e.g. chalcopyrite, gold grains; Fig. 1b, 3). The texture of epidote grains recovered from detrital sediments with complex crystal growth forms is an apparent indicator of hydrothermal origin (Fig. 4c, d). The chemical composition of detrital epidote grains can provide an indication of their source: granitoids epidote typically contain less than 6 ppm Hf+Th and less than 100 ppm Sc+Cr+Y (Fig. 7), and porphyry-related epidotes much greater than 4 ppm As and much greater than 0.6 ppm Sb (Fig. 5). Lastly, the copper content of epidote (approximately >30 ppm Cu) might provide an indication of copper fertility (Fig. 9); however, given the overlap in epidote data from granitoid rocks versus mafic volcanic rocks (Fig. 6, 7) and from hydrothermal versus metamorphic settings (Fig. 5), and the presence of a Cu fertility signal in only a few detrital grains, we do not recommend a grain-by-grain characterization as was applied, for example, by Mao et al. (2017) to apatite recovered from till in British Columbia. Instead, we suggest that detrital epidote provenance should be established from compositional data using a large population of detrital epidote grains. In our study, LA-ICP-MS analyses of 60 to 81 epidote grains from seven to nine till samples at each study site (Table 1) was sufficient to identify porphyry-related epidote within regional dispersal trains (Fig. 3).

Determining the abundance of epidote in till (Fig. 3), along with its chemical composition, could become a routine exploration method in the search for porphyry copper mineralization buried under glacial sediments in the Canadian Cordillera. Given the size of the studied epidote anomalies in till which reach approximately 19 km^2 at Woodjam, 21 km^2 at Polley, and 135 km^2 at Gibraltar (Fig. 3), a till sample spacing of 2 km (one sample per 4 km^2) would be sufficient to detect an epidote anomaly. This method could be efficient in a scenario where mineralization with metal enrichment is at depth and only the propylitic alteration zone is exposed to glacial erosion.

In addition to epidote, other porphyry copper indicator minerals could be identified in till or other detrital sediments (Plouffe and Ferbey, 2017; Beckett-Brown et al., 2019, this volume; McClenaghan et al., this volume). Of course, the identification of ore minerals (e.g. chalcopyrite) in till represents additional evidence of porphyry copper mineralization in the source region of glaciers. Focusing on the objective of our research — the detection of buried porphyry systems

with no mineralization exposed to glacial erosion — the REE composition of zircon in till (e.g. Ce/Nd) can provide complementary information about the potential of an intrusion to host porphyry mineralization (Ballard et al., 2002; Liang et al., 2006; Dilles et al., 2015; Shen et al., 2015). For instance, in a study at Gibraltar, out of 45 zircon grains recovered from five till samples, only one sample, located close (<1 km) to mineralization, contained zircon with a Ce/Nd ratio greater than 20, which is indicative of oxidizing magmatic conditions favourable for porphyry mineralization (Plouffe et al., 2018, 2019).

CONCLUSION

Our study shows that hydrothermally derived epidote recovered from till can be used for porphyry copper mineral exploration. Its greater abundance in till heavy mineral concentrates near porphyry mineralization along with its composition can be indicative of a porphyry copper source. Epidotes with less than 6 ppm Hf+Th and less than 100 ppm Sc+Cr+Y are typically derived from granitoid rocks. Epidotes with much greater than 4 ppm As and much greater than 0.6 ppm Sb are representative of a hydrothermal alteration zone associated with porphyry mineralization. Concentrations greater than 30 ppm Cu in epidote recovered from till can provide an estimate of the fertility potential of the bedrock source. Epidote as an indicator mineral of porphyry copper mineralization is likely to be widely applicable because it is common in propylitic alteration of porphyry systems.

We have used epidote chemistry to differentiate two broad geological sources of epidote in till within a specific geological setting prospective for porphyry copper mineralization: the Quesnel terrane of south-central British Columbia. The application of epidote as an indicator mineral in mineralizing environments other than porphyry systems remains unexplored. The epidote method tested here for till should be applicable to stream sediment settings, given the resistant nature of this mineral; however, its applicability to epidote obtained from streams or other detrital sediments in unglaciated landscapes with thick regolith requires further testing. Future work should also explore the application of unsupervised machine-learning techniques to characterize epidote genesis and provenance.

ACKNOWLEDGMENTS

This research would not have been possible without the contribution of rock samples by a number of individuals, who took time to retrieve samples from their collection or, in some cases revisit field sites. These include J.B. Chapman, C.H. Kobylinski, C. Rees, and P. Schiarizza. C. Bjerklund, C. Hutton, G. Marquis, N. Rogers, and J. Tomkins from the TGI management team provided support to enable this activity. The manuscript benefited from review by N. Rogers and A. Rukhlov.

REFERENCES

Aitchison, J., 1986. The statistical analysis of compositional data; Monographs on statistics and applied probability; Chapman and Hall, London, 416 p.

Armbruster, T., Bonazzi, P., Akasaka, M., Bermanec, V., Chopin, C., Gieré, R., Heuss-Assbichler, S., Liebscher, A., Menchetti, S., Pan, Y., and Pasero, M., 2006. Recommended nomenclature of epidote-group minerals; European Journal of Mineralogy, v. 18, no. 5, p. 551–567. https://doi.org/10.1127/0935-1221/2006/0018-0551

Armstrong, J.T., 1988. Quantitative analysis of silicates and oxide minerals: comparison of Monte-Carlo, ZAF and Phi-Rho-Z procedures; *in* Microbeam Analysis, (ed.) D.E. Newbury; San Francisco Press, San Francisco, p. 239–246.

Arnason, J.G., Bird, D.K., and Lion, J.G., 1993. Variables controlling epidote composition in hydrothermal and low-pressure regional metamorphic rocks; 125 years Knappenwand –proceedings of a symposium, Salzburg, Austria, p. 17–25.

Ash, C.H., Rydman, M.O., Payne, C.W., and Panteleyev, A., 1999. Geological setting of the Gibraltar mine south central British Columbia (93B/8, 9); *in* Exploration and mining in British Columbia 1998, British Columbia Ministry of Energy and Mines, p. A1–A15.

Averill, S.A., 2011. Viable indicator minerals in surficial sediments for two major base metal deposit types: Ni-Cu-PGE and porphyry Cu; Geochemistry: Exploration, Environment, Analysis, v. 11, p. 279–291. https://doi.org/10.1144/1467-7873/10-IM-022

Ballard, J.R., Palin, J.M., and Campbell, I.H., 2002. Relative oxidation states of magmas inferred from Ce(IV)/Ce(III) in zircon: application to porphyry copper deposits of northern Chile; Contributions to Mineralogy and Petrology, v. 144, p. 347–364. https://doi.org/10.1007/s00410-002-0402-5

Beckett-Brown, C.E., McDonald, A.M., and McClenaghan, M.B., 2019. Unravelling tourmaline in mineralized porphyry systems: assessment as a valid indicator mineral; *in* Targeted Geoscience Initiative: 2018 report of activities, (ed.) N. Rogers; Geological Survey of Canada, Open File 8549, p. 345–351. https://doi.org/10.4095/313669

Berry, L.G., Mason, B., and Dietrich, R.V., 1983. Mineralogy; W.H. Freeman and Company, San Francisco, 561 p.

Bird, D.K. and Helgeson, H.C., 1980. Chemical interaction of aqueous solutions with epidote-feldspar mineral assemblages in geologic systems: 1. Thermodynamic analysis of phase relations in the system CaO-FeO-Fe_2O_3-Al_2O_3-SiO_2-H_2O-CO_2; American Journal of Science, v. 280, no. 9, p. 907–941. https://doi.org/10.2475/ajs.280.9.907

Bird, D.K. and Spieler, A.R., 2004. Epidote in geothermal systems; Reviews in Mineralogy and Geochemistry, v. 56, p. 235–300. https://doi.org/10.2138/gsrmg.56.1.235

Bowman, J.R., Parry, W.T., Kropp, W.P., and Kruer, S.A., 1987. Chemical and isotopic evolution of hydrothermal solutions at Bingham, Utah; Economic Geology, v. 82, no. 2, p. 395–428. https://doi.org/10.2113/gsecongeo.82.2.395

Bysouth, G.D., Campbell, K.V., Barker, G.E., and Gagnier, G.K., 1995. Tonalite-trondhjemite fractionation of peraluminous magma and the formation of syntectonic porphyry copper mineralization, Gibraltar mine, central British Columbia; *in* Porphyry deposits of the northwestern Cordillera of North America, (ed.) T.G. Schroeter; Canadian Institute of Mining, Metallurgy and Petroleum, Special Volume 46, p. 201–213.

Clarke, G., Northcote, B., Katay, F., and DeGrace, J.R., 2018. Exploration and mining in British Columbia, 2018: a summary; *in* Provincial overview of exploration and mining in British Columbia, 2018; British Columbia Ministry of Energy, Mines and Petroleum Resources, British Columbia Geological Survey, Information Circular 2019-01, p. 1–37.

Cooke, D.R., Baker, M., Hollings, P., Sweet, G., Zhaoshan, C., Danyushevsky, L., Gilbert, S., Zhou, T., White, N., Gemmell, J.B., and Inglis, S., 2014. New advances in detecting the distal geochemical footprints of porphyry systems – epidote mineral chemistry as a tool for vectoring and fertility assessments; *in* Building exploration capability for the 21st century, (ed.) K.D. Kelley and H.C. Golden; Society of Economic Geologists, Special Publication No. 18, p. 127–152.

del Real, I., Hart, C.J.R., Bouzari, F., Blackwell, J.L., Rainbow, A., Sherlock, R., and Skinner, T., 2013. Paragenesis and alteration of the Southeast Zone and Deerhorn porphyry deposits, Woodjam property, central British Columbia (Parts of 093A); *in* Geoscience BC Summary of Activities 2012, Geoscience BC, Report 2013-1, p. 79–90.

Dilles, J.H., Kent, A.J.R., Wooden, J.L., Tosdal, R.M., Koleszar, A., Lee, R.G., and Farmer, L.P., 2015. Zircon compositional evidence for sulphur-degassing from ore-forming arc magmas; Economic Geology, v. 110, no. 1, p. 241–251. https://doi.org/10.2113/econgeo.110.1.241

Drummond, A.D., Sutherland Brown, A., Young, R.J., and Tennant, S.J., 1976. Gibraltar – regional metamorphism, mineralization, hydrothermal alteration and structural development; *in* Porphyry deposits of the Canadian Cordillera, (ed.) A. Sutherland Brown; Canadian Institute of Mining and Metallurgy, Special Volume 15, p. 195–205.

Ferbey, T., Plouffe, A., and Bustard, A.L., 2016. Geochemical, mineralogical, and textural data from tills in the Highland Valley Copper mine area, south-central British Columbia; British Columbia Ministry of Energy and Mines, British Columbia Geological Survey, GeoFile 2016–11, 1 .zip file and Geological Survey of Canada, Open File 8119, 1 .zip file. https://doi.org/10.4095/299242

Garrett, R.G., 2013. The 'rgr' package for the R Open Source statistical computing and graphics environment - a tool to support geochemical data interpretation; Geochemistry: Exploration, Environment, Analysis, v. 13, p. 355–378. https://doi.org/10.1144/geochem2011-106

Grapes, R.H. and Hoskin, P.W.O., 2004. Epidote group minerals in low-medium pressure metamorphic terranes; Reviews in Mineralogy and Geochemistry, v. 56, no. 1, p. 301–345. https://doi.org/10.2138/gsrmg.56.1.301

Greenwood, H.J., Woodsworth, G.J., Read, P.B., Ghent, E.D., and Evenchick, C.A., 1991. Metamorphism; *in* Geology of the Cordilleran Orogen in Canada, (ed.) H. Gabrielse and C.J. Yorath; Geological Survey of Canada, Geology of Canada Series no. 4, p. 535–570. https://doi.org/10.4095/134107

Griffin, W.L., Powell, W.J., Pearson, N.J., and O'Reilly, S.Y., 2008. GLITTER: Data reduction software for laser ablation ICP–MS; *in* Laser ablation-ICP-mass spectrometry in the earth sciences: current practices and outstanding issues, (ed.) P. Sylvester; Mineralogical Association of Canada, Short Course Series, v. 40, p. 308–311.

Guillong, M., Hametner, K., Reusser, E., Wilson, S. A., and Günther, D., 2005. Preliminary characterisation of new glass reference materials (GSA-1G, GSC-1G, GSD-1G and GSE-1G) by laser ablation-inductively coupled plasma-mass spectrometry using 193 nm, 213 nm and 266 nm wavelengths; Geostandards and Geoanalytical Research, v. 29, n. 3, p. 315–331. https://doi.org/10.1111/j.1751-908X.2005.tb00903.x

Hashmi, S., Ward, B.C., Plouffe, A., Leybourne, M.I., and Ferbey, T., 2015. Geochemical and mineralogical dispersal in till from the Mount Polley Cu-Au porphyry deposit, central British Columbia, Canada; Geochemistry: Exploration, Environment, Analysis, v. 15, no. 2, p. 234–249. https://doi.org/10.1144/geochem2014-310

Hickin, A.S. and Plouffe, A., 2017. Sampling and interpreting stream, lake, and glacial sediments for mineral exploration in the Canadian Cordillera, a review; *in* Indicator minerals in till and stream sediments of the Canadian Cordillera, (ed.) T. Ferbey, A. Plouffe, and A.S. Hickin; Geological Association of Canada, Special Paper, v. 50 and Mineral Association of Canada, Topics in Mineral Sciences v. 47, p. 27–51.

Jago, C.P., Tosdal, R.M., Cooke, D.R., and Harris, A.C., 2014. Vertical and lateral variation of mineralogy and chemistry in the Early Jurassic Mt. Milligan alkalic porphyry Au-Cu deposit, British Columbia, Canada; Economic Geology, v. 109, no. 4, p. 1005–1033. https://doi.org/10.2113/econgeo.109.4.1005

Jochum, K.P., Nohl, U., Herwig, K., Lammel, E., Stoll, B., and Hofmann, A.W., 2005a. GeoReM : A new geochemical database for reference materials and isotopic standards. Geostandards and Geoanalytical Research, v. 29, p. 333–338. https://doi.org/10.1111/j.1751-908X.2005.tb00904.x

Jochum, K.P., Willbold, M., Raczek, I., Stoll, B., and Herwig, K., 2005b. Chemical characterisation of the USGS reference glasses GSA-1G, GSC-1G, GSD-1G, GSE-1G, BCR-2G, BHVO-2G and BIR-1G using EPMA, ID-TIMS, ID-ICP-MS and LA-ICP-MS; Geostandards and Geoanalytical Research, v. 29, p. 285–302. https://doi.org/10.1111/j.1751-908X.2005.tb00901.x

Kane, J.S., 1998. A history of the development and certification of NIST glass SRMs 610-617; Geostandards Newsletter, v. 22, p. 7–13. https://doi.org/10.1111/j.1751-908X.1998.tb00542.x

Kobylinski, C., Hattori, K., Plouffe, A., and Smith, S., 2017. Epidote associated with the porphyry Cu-Mo mineralization at the Gibraltar deposit, south central British Columbia; Geological Survey of Canada, Open File 8279, 19 p. https://doi.org/10.4095/305912

Liang, H.-Y., Campbell, I.H., Allen, C., Sun, W.-D., Liu, C.-Q., Yu, H.-X., Xie, Y.-W., and Zhang, Y.-Q., 2006. Zircon Ce4+/Ce3+ ratios and ages for Yulong ore-bearing porphyries in eastern Tibet; Mineralium Deposita, v. 41, 152. https://doi.org/10.1007/s00126-005-0047-1

Logan, J.M., 2013. Porphyry systems of central and southern BC: Overview and field trip road log; in Porphyry systems of central and southern British Columbia: tour of central British Columbia porphyry deposits from Prince George to Princeton, (ed.) J.M. Logan and T.G. Schroeter; Society of Economic Geologists, Field Trip Guidebook, Series 44, p. 1–45.

Logan, J.M. and Mihalynuk, M.G., 2014. Tectonic controls on Early Mesozoic paired alkaline porphyry deposit belts (Cu-Au±Ag-Pt-Pd-Mo) within the Canadian Cordillera; Economic Geology, v. 109, p. 827–858. https://doi.org/10.2113/econgeo.109.4.827

Logan, J.M. and Schroeter, T.G. (ed.), 2013. Porphyry systems of central and southern British Columbia: tour of central British Columbia porphyry deposits from Prince George to Princeton; Society of Economic Geologists, Field Trip Guidebook, Series 44, 143 p.

Logan, J.M., Schiarizza, P., Struik, L.C., Barnett, C., Nelson, J.L., Kowalczyk, P., Ferri, F., Mihalynuk, M.G., Thomas, M.D., Gammon, P., Lett, R., Jackaman, W., and Ferbey, T., (comp.), 2010. Bedrock geology of the QUEST map area, central British Columbia; Geoscience BC Report 2010-5, British Columbia Geological Survey Geoscience Map 2010-1 and Geological Survey of Canada Open File 6476, 1 sheet, scale 1:500 000. https://doi.org/10.4095/261517

Lowell, J.D. and Guilbert, J.M., 1970. Lateral and vertical alteration-mineralization zoning in porphyry ore deposits; Economic Geology, v. 65, no. 4, p. 373–408. https://doi.org/10.2113/gsecongeo.65.4.373

Mao, M., Rukhlov, A.S., Rowins, S.M., Hickin, A.S., Ferbey, T., Bustard, A.L., Spence, J., and Coogan, L.A., 2017. A novel approach using detrital apatite and till geochemistry to identify covered mineralization in the TREK area of the Nechako Plateau, British Columbia; *in* Indicator minerals in till and stream sediments of the Canadian Cordillera, (ed.) T. Ferbey, A. Plouffe, and A.S. Hickin; Geological Association of Canada, Special Paper, v. 50 and Mineral Association of Canada, Topics in Mineral Sciences, v. 47, p. 191–243.

Massey, N.W.D., MacIntyre, D.G., Desjardins, P.J., and Cooney, R.T., 2005. Geology of British Columbia; British Columbia Ministry of Energy, Mines and Petroleum Resources, British Columbia Geological Survey, Geoscience map 2005-3, scale 1:1 000 000.

McMillan, W.J. and Panteleyev, A., 1995. Porphyry copper deposits of the Canadian Cordillera; *in* Porphyry copper deposits of the American Cordillera, (ed.) F.W. Pierce and J.G. Bolm; Arizona Geological Society, Digest 20, p. 203–218.

McMillan, W.J., Thompson, J.F.H., Hart, C.J.R., and Johnston, S.T., 1995. Regional geological and tectonic setting of porphyry deposits in British Columbia and Yukon Territory; *in* Porphyry deposits of the northwestern Cordillera of North America, (ed.) T.G. Schroeter; Canadian Institute of Mining, Metallurgy and Petroleum, Special Volume 46, p. 40–57.

McMillan, W.J., Thompson, J.F.H., Hart, C.J.R., and Johnston, S.T., 1996. Porphyry deposits of the Canadian Cordillera; Geoscience Canada, v. 23, no. 3, p. 125–134.

Mihalasky, M.J., Bookstrom, A.A., Frost, T.P., and Ludington, S., with contributions from Logan, J.M., Panteleyev, A., and Abbott G., 2011. Porphyry copper assessment of British Columbia and Yukon Territory, Canada; United States Geological Survey, Scientific Investigations Report 2010-5090-C, 128 p.

Mills, S.J., Hatert, F., Nickel, E.H., and Ferraris, G., 2009. The standardisation of mineral group hierarchies: application to recent nomenclature proposals; European Journal of Mineralogy, v. 21, no. 5, p. 1073–1080. https://doi.org/10.1127/0935-1221/2009/0021-1994

Norman, D.K., Parry, W.T., and Bowman, J.R., 1991. Petrology and geochemistry of propylitic alteration at southwest Tintic, Utah; Economic Geology, v. 86, no. 1, p. 13–28. https://doi.org/10.2113/gsecongeo.86.1.13

Pacey, A., Wilkinson, J.J., and Cooke, D.R., 2020. Chlorite and epidote mineral chemistry in porphyry ore systems: a case study of the Northparkes District, NSW, Australia; Economic Geology, v. 115, no. 4, p. 701–727. https://doi.org/10.5382/econgeo.4700

Panteleyev, A., Bailey, D.G., Bloodgood, M.A., and Hancock, K.D., 1996. Geology and mineral deposits of the Quesnel River-Horsefly map area, central Quesnel Trough, British Columbia; British Columbia Ministry of Employment and Investment, British Columbia Geological Survey, Bulletin 97, 156 p.

Plouffe, A. and Ferbey, T., 2015a. Surficial geology, Granite Mountain area, British Columbia, parts of NTS 93-B/8 and 93-B/9; Geological Survey of Canada, Canadian Geoscience Map 223 (preliminary edition) and British Columbia Geological Survey, Geoscience Map 2015-4, scale 1:50 000. https://doi.org/10.4095/296793

Plouffe, A. and Ferbey, T., 2015b. Till composition near Cu-porphyry deposits in British Columbia: highlights for mineral exploration; *in* TGI 4 – Intrusion related mineralisation project: new vectors to buried porphyry-style mineralisation, (ed.) N. Rogers; Geological Survey of Canada, Open File 7843, p. 15–37. https://doi.org/10.4095/296464

Plouffe, A. and Ferbey, T., 2016. Till geochemistry, mineralogy and textural data near four Cu porphyry deposits in British Columbia; Geological Survey of Canada, Open File 8038 and British Columbia Geological Survey, Geofile 2016-10, 44 p. https://doi.org/10.4095/298805

Plouffe, A. and Ferbey, T., 2017. Porphyry Cu indicator minerals in till: A method to discover buried mineralisation; *in* Indicator minerals in till and stream sediments of the Canadian Cordillera, (ed.) T. Ferbey, A. Plouffe, and A. Hickin; Geological Association of Canada, Special Paper v. 50 and Mineral Association of Canada, Topics in Mineral Sciences, v. 47), p. 129–159.

Plouffe, A., Bednarski, J.M., Huscroft, C.A., Anderson, R.G., and McCuaig, S.J., 2011. Late Wisconsinan glacial history in the Bonaparte Lake map area, south central British Columbia: implications for glacial transport and mineral exploration; Canadian Journal of Earth Sciences, v. 48, no. 6, p. 1091–1111. https://doi.org/10.1139/e10-100

Plouffe, A., Ferbey, T., Hashmi, S., and Ward, B.C., 2016. Till geochemistry and mineralogy: vectoring towards Cu porphyry deposits in British Columbia, Canada; Geochemistry: Exploration, Environment, Analysis, v. 16, no. 3–4, p. 213–232. https://doi.org/10.1144/geochem2015-398

Plouffe, A., Kobylinski, C.H., Hattori, K., Wolfe, L., and Ferbey, T., 2018. Mineral markers of porphyry copper mineralisation: work in progress at the Gibraltar deposit, British Columbia; *in* Targeted Geoscience Initiative: 2017 report of activities, volume 1, (ed.) N. Rogers; Geological Survey of Canada, Open File 8358, p. 57–67. https://doi.org/10.4095/306423

Plouffe, A., Kjarsgaard, I.M., Kobylinski, C., Hattori, K., Petts, D.C., Venance, K.E., and Ferbey, T., 2019. Discovering the next generation of copper porphyry deposits using mineral markers; *in* Targeted Geoscience Initiative: 2018 report of activities, (ed.) N. Rogers; Geological Survey of Canada, Open File 8549, p. 321–331. https://doi.org/10.4095/313666

R Core Team, 2018. R. A language and environment for statistical computer; R Foundation for Statistical Computer, Vienna, Austria. http//www.r-project.org [accessed March 25, 2020]

Read, P.B., Woodsworth, G.J., Greenwood, H.J., Ghent, E.D., and Evenchick, C.A., 1991. Metamorphic map of the Canadian Cordillera; Geological Survey of Canada, Map 1714A, scale 1:2 000 000. https://doi.org/10.4095/134142

Rees, C., 2013. The Mount Polley Cu-Au deposit, south-central British Columbia, Canada; *in* Porphyry systems of central and southern British Columbia: tour of central British Columbia porphyry deposits from Prince George to Princeton, (ed.) J.M. Logan and T.G. Schroeter; Society of Economic Geologists, Field Trip Guidebook, Series 44, p. 67–98.

Schiarizza, P., 2016. Toward a regional stratigraphic framework for the Nicola Group: preliminary results from the Bridge Lake – Quesnel River area; *in* Geological Fieldwork 2015, British Columbia Ministry of Energy, Mines and Petroleum Resources, British Columbia Geological Survey, Paper 2016-1, p. 13–30.

Schiarizza, P., 2019. Geology of the Nicola Group in the Bridge Lake-Quesnel River area, south-central British Columbia; *in* Geological Fieldwork 2018, British Columbia Ministry of Energy, Mines and Petroleum Resources, British Columbia Geological Survey, Paper 2019-01, p. 15–30.

Schroeter, T.G., (ed.), 1995. Porphyry deposits of the northwestern Cordillera of North America; Canadian Institute of Mining, Metallurgy and Petroleum, Special Volume 46, 888 p.

Shen, P., Hattori, K., Pan, H., Jackson, S., and Seitmuratova, E., 2015. Oxidation condition and metal fertility of granitic magmas: zircon trace-element data from porphyry Cu deposits in the central Asian orogenic belt; Economic Geology, v. 110, no. 7, p. 1861–1878. https://doi.org/10.2113/econgeo.110.7.1861

Sherlock, R. and Trueman, A., 2013. NI 43-101 technical report for 2012 activities on the Woodjam South property; Gold Fields Horsefly Exploration Group and Consolidated Woodjam Copper Corporation, Cariboo Mining Division, British Columbia, 158 p.

Sherlock, R., Blackwell, J., and Skinner, T., 2013. NI 43-101 technical report for 2012 activities on the Woodjam North property; Gold Fields Horsefly Exploration Group, Consolidated Woodjam Copper Corporation, Cariboo Mining Division, British Columbia, 275 p.

Sillitoe, R.H., 2010. Porphyry copper systems; Economic Geology, v. 105, no. 1, p. 3–41. https://doi.org/10.2113/gsecongeo.105.1.3

Sinclair, W.D., 2007. Porphyry deposits; *in* Mineral deposits of Canada: a synthesis of major deposit types, district metallogeny, the evolution of geological provinces, and exploration methods, (ed.) W.D. Goodfellow; Geological Association of Canada, Mineral Deposit Division, Special Publication No. 5, p. 223–243.

Sutherland Brown, A.E., (ed.), 1976. Porphyry deposits of the Canadian Cordillera; Canadian Institute of Mining and Metallurgy, Special Volume 15, 510 p.

Sylvester, P.J., Cabri, L.J., Tubrett, M.N., Peregoedova, A., McMahon, G., and Laflamme, J.H.G., 2005. Synthesis and evaluation of a fused pyrrhotite standard reference material for platinum group element and gold analysis by laser ablation–ICPMS; *in* Platinum-group elements from genesis to beneficiation and environmental impact, (ed.) T.O. Törmänen and T.T. Alapieti; Geological Survey of Finland, 10th International Platinum Symposium, Oulu, Finland, p. 16–20, extended abstracts.

Taseko Mines Ltd., 2020. Taseko Mines Limited. <www.tasekomines.com> [accessed March 2020]

Thió-Henestrosa, S. and Martín-Fernández, J., 2005. Dealing with compositional data: the freeware CoDaPack; Mathematical Geosciences, v. 37, p. 773–793. https://doi.org/10.1007/s11004-005-7379-3

van Straaten, B.I., Oliver, J., Crozier, J., and Goodhue, L., 2013. A summary of the Gibraltar porphyry copper-molybdenum deposit, south-central British Columbia, Canada; *in* Porphyry systems of central and southern British Columbia: tour of central British Columbia porphyry deposits from Prince George to Princeton, (ed.) J.M. Logan and T.G. Schroeter; Society of Economic Geologists, Field Trip Guidebook, Series 44, p. 55–66.

Wilkinson, J.J., Baker, M.J., Cooke, D.R., Wilkinson, C.C., and Inglis, S., 2017a. Exploration targeting in porphyry Cu systems using propylitic mineral chemistry: a case study of the El Teniente deposit, Chile; *in* Mineral resources to discover, volume 3, proceedings of the 14th Biennial Society of Geology Applied to Mineral Deposits meeting, (ed.) P. Mercier-Langevin; Society of Geology Applied to Mineral Deposits, p. 1111–1115.

Wilkinson, J.J., Cooke, D.R., Baker, M.J., Chang, Z., Wilkinson, C.C., Chen, H., Fox, N., Hollings, P., White, N.C., Gemmell, J.B., Loader, M.A., Pacey, A., Sievwright, R.H., Hart, L.A., and Brugge, E.R., 2017b. Porphyry indicator minerals and their mineral chemistry as vectoring and fertility tools; *in* Application of indicator mineral methods to bedrock and sediments, (ed.) M.B. McClengaghan and D. Layton-Matthews; Geological Survey of Canada, Open File 8345, p. 67–77. https://doi.org/10.4095/306317

APPENDIX A

Laser-ablation inductively coupled plasma mass spectrometry analytical results of epidote

The complete list of laser-ablation inductively coupled plasma mass spectrometry analytical results of major, minor, and trace-element concentrations in epidote are found in the file:POR-08_Appendix A.xlsx. Values are in parts per million (ppm). Analytical results of standard samples are included on separate worksheets. The table contains basic information on sample type and location. *See* text for analytical details. This Appendix has not been edited to Geological Survey of Canada specifications.

Heavy mineral and geochemical signatures of porphyry copper mineralization: examples from the Casino porphyry Cu-Au-Mo deposit, Yukon

M.B. McClenaghan[1], M.W. McCurdy[1], R.G. Garrett[2], C.E. Beckett-Brown[3], M.I. Leybourne[4, 5], S.G. Casselman[6], and P. Pelchat[1]

McClenaghan, M.B., McCurdy, M.W., Garrett, R.G., Beckett-Brown, C.E., Leybourne, M.I., Casselman, S.G., and Pelchat, P., 2021. Heavy mineral and geochemical signatures of porphyry copper mineralization: examples from the Casino porphyry Cu-Au-Mo deposit, Yukon; in *Targeted Geoscience Initiative 5: contributions to the understanding and exploration of porphyry deposits, (ed.) A. Plouffe and E. Schetselaar; Geological Survey of Canada, Bulletin 616, p. 159–202. https://doi.org/10.4095/327987*

Abstract: We report results of a detailed indicator mineral and geochemical study of the Casino calc-alkaline porphyry Cu-Au-Mo deposit in the unglaciated terrain of west-central Yukon. It is one of the largest and highest-grade porphyry Cu-Au-Mo deposits in Canada and is hosted by Late Cretaceous quartz monzonite and associated breccias. At 22 sites, a large (10–14 kg) stream-sediment sample, streamwater and stream silt samples were collected to compare geochemical and heavy mineral signatures. The Casino deposit has an obvious indicator mineral signature in the less than 2 mm heavy (>3.2 specific gravity (SG)) and mid-density (2.8–3.2 SG) fractions of stream sediments that is detectable at least 14 km downstream and consists of, in order of effectiveness, gold>chalcopyrite>molybdenite>sphalerite >jarosite>goethite>pyrite. Similar indicator mineral patterns occur in creeks downstream of other local porphyry occurrences (i.e. Cockfield, Zappa). The geochemical signature of the deposit is best defined by Ag, As, Au, Bi, Cd, Cu, Fe, Mn, Mo, Pb, U, and Zn in the less than 0.177 mm fraction of stream sediment and Cd, Co, Cu, Mo, Pb, Re, and Zn in stream water. Governments and exploration companies will benefit from adding indicator mineral sampling to routine stream-sediment sampling protocols during geochemical surveys in which detailed follow up during the same season is impossible.

Résumé : Dans le présent article, nous rendons compte des résultats d'une étude détaillée de la géochimie et des minéraux indicateurs du gisement porphyrique calco-alcalin à Cu-Au-Mo de Casino, situé dans le terrain ayant échappé à l'englaciation du centre ouest du Yukon. Il s'agit de l'un des gisements porphyriques à Cu-Au-Mo des plus grands et des plus riches au Canada. Il est encaissé dans une monzonite quartzique du Crétacé tardif et les brèches associées. À 22 sites, nous avons prélevé un gros échantillon (de 10 à 14 kg) de sédiments de ruisseau ainsi que des échantillons d'eau et de silt de ruisseau pour comparer leurs signatures géochimiques et en minéraux lourds. Le gisement de Casino présente une signature manifeste en minéraux indicateurs dans les composantes lourde (densité >3,2) et de densité moyenne (densité de 2,8 à 3,2) de la fraction <2 mm des sédiments de ruisseau. Cette signature peut être relevée jusqu'à au moins 14 km en aval et se manifeste par les minéraux suivants, par ordre d'efficacité : or>chalcopyrite>molybdénite>sphalérite>jarosite>goethite>pyrite. Des configurations de minéraux indicateurs semblables se retrouvent dans des ruisseaux en aval d'autres indices locaux de minéralisations porphyriques (c.-à-d. Cockfield, Zappa). La signature géochimique du gisement est mieux définie par les éléments Ag, As, Au, Bi, Cd, Cu, Fe, Mn, Mo, Pb, U et Zn dans la fraction <0,177 mm des sédiments de ruisseau et par les éléments Cd, Co, Cu, Mo, Pb, Re et Zn dans l'eau de ruisseau. Les gouvernements et les sociétés d'exploration minérale gagneraient à ajouter l'échantillonnage des minéraux indicateurs à leurs protocoles d'échantillonnage régulier de sédiments de ruisseau lors des levés géochimiques qui ne permettent pas de faire des suivis détaillés au cours de la même saison.

[1]Geological Survey of Canada, 601 Booth Street, Ottawa, Ontario K1A 0E8
[2]Emeritus Scientist, Geological Survey of Canada, 601 Booth Street, Ottawa, Ontario K1A 0E8
[3]Harquail School of Earth Sciences, Laurentian University, 935 Ramsey Lake Road, Sudbury, Ontario P3E 2C6
[4]Department of Geological Sciences and Engineering, Queen's University, 36 Union Street, Kingston, Ontario K7L 3N6
[5]McDonald Institute, Canadian Particle Astrophysics Research Centre, Stirling Hall, Department of Physics, Engineering Physics & Astronomy, Queen's University, Kingston, Ontario K7L 3N6
[6]Yukon Geological Survey, 300 Main Street, Whitehorse, Yukon Y1A 2B5
*Corresponding author: M.B. McClenaghan (email: beth.mcclenaghan@canada.ca)

INTRODUCTION

The recovery of indicator minerals from surficial sediments is a well established exploration method for gold (e.g. Averill, 2001; McClenaghan and Cabri, 2011) and diamonds (e.g. McClenaghan and Kjarsgaard, 2007) in glaciated terrain. Recently, indicator mineral methods for porphyry copper exploration have been tested in glaciated (e.g. Kelley et al., 2011; Chapman et al., 2015, 2018; Hashmi et al., 2015; Canil et al., 2016; Plouffe et al., 2016; Pisiak et al., 2017; Plouffe and Ferbey, 2017, 2019) and unglaciated terrain (Averill, 2011). The objective of the Geological Survey of Canada's (GSC) Targeted Geoscience Initiative (TGI) porphyry indicator mineral research is to further develop a porphyry copper indicator mineral suite that can be used for surficial sediment sampling in both the glaciated and unglaciated regions of Canada (McClenaghan et al., 2018, 2019, 2020). This new research includes the detailed examination and chemical characterization of tourmaline (Beckett-Brown et al., 2019, this volume), magnetite (McClenaghan et al., 2019), epidote, rutile, and zircon (Kobylinksi et al., 2017, 2018; Plouffe et al., 2018, 2019, this volume).

One component of the TGI porphyry copper indicator mineral research is a study carried out at the Casino porphyry Cu-Au-Mo deposit (McClenaghan et al., 2018, 2019), one of Canada's largest and highest grade undeveloped porphyry Cu-Au-Mo deposits (Casselman and Brown, 2017). The Casino deposit was used as a test site because it has been minimally disturbed by exploration drilling, has not yet been mined, and is known to contain tourmaline, and because metal-rich sediments and waters are known to occur in local creeks draining the deposit (Archer and Main, 1971). Here we report the results of mineralogical and geochemical studies of the Casino deposit, including indicator minerals in stream sediments and the geochemistry of stream silt and water.

Location and access

The Casino study area is located in west-central Yukon, 300 km north of Whitehorse (Fig. 1), within the Klondike Plateau ecoregion (Smith et al., 2004) and NTS map areas 115J/10 and 115J/15. The deposit is at latitude 62°44′N and longitude 138°50′W, and is accessed by fixed-wing aircraft or helicopter. Creeks draining the northwest side of the deposit flow north and eventually drain into the Yukon River. Creeks draining the south side of the deposit eventually drain into the White River. Most of the terrain lies at elevations of 1000 to 1500 m a.s.l. The climate of the study area is cold and semiarid (Bond and Lipovsky, 2011) with a mean annual temperature of approximately –5.5°C (mean annual summer temperature: 10.5°C, mean annual winter temperature: –23°C), and the mean annual precipitation ranges from 300 to 450 mm (Smith et al., 2004).

GEOLOGY

Deposit discovery history

The earliest exploration in the Casino area was for placer gold in the lower reaches of Canadian Creek in 1911 (Bostock, 1959; Fig. 2). Further upstream on Canadian Creek, on the northwest flank of what is now the Casino deposit, a gold-tungsten placer occurrence was first worked to mine tungsten in 1916. When the upper gold-tungsten placer occurrence was worked again in 1940s, the following minerals were recovered from the black sand: ferberite, gold, magnetite, hematite, scheelite, molybdenite, zircon, cassiterite, tourmaline, and titanite (Bostock, 1959; Archer and Main, 1971). Over the years, placer gold mining also took place on Rude Creek (Fig. 2), 10 km southeast of the Casino deposit (Chapman et al., 2014). Other early exploration work in the Casino area focused on the silver-lead-zinc veins at the Bomber occurrence (Yukon Geological Survey, 2018a) on the southern periphery of what is now known as the Casino deposit (Fig. 2).

Prior to the initial diamond drilling that resulted in the discovery of Cu-Au-Mo mineralization, surface indications of the presence of the Casino deposit included the prominent (730 m long) limonite gossan along a small creek that drains into upper Casino Creek (Fig. 2) on the southeast side of the deposit; the presence of the local gold-tungsten placer occurrence; intense hydrothermal alteration; the presence of limonite, jarosite, and weak malachite staining in leached rocks at the surface; the peripheral silver-zinc-lead veins; and anomalous Cu concentrations in –80 mesh (<0.177 mm) stream silt samples in Casino Creek compared to values for the Dawson Range compiled over several years by Archer and Main (1971). Anomalous Cu and Mo in –80 mesh soil samples collected in 1968 were used to guide initial drilling in 1969 that revealed significant mineralization (Archer and Main, 1971). Current total measured, indicated, and inferred resources of the deposit are 101 000 000 t of 0.39 g/t Au in the oxide gold zone; 87 000 000 t grading 0.25% Cu, 0.29 g/t Au, 0.02% Mo, and 1.7 g/t Ag in the supergene oxide–enriched zone; and 2 700 000 000 t of sulfide ore grading 0.16% Cu, 0.19 g/t Au, 0.02% Mo, and 1.5 g/t Ag in the supergene sulfide and hypogene zones (Huss et al., 2013; Casselman and Brown, 2017).

Bedrock geology

The Casino deposit area is underlain by metamorphosed and deformed basement rocks of the Yukon-Tanana terrane, an allochthonous, tectonic terrane that extends more than 2000 km from Alaska, U.S.A., through Yukon, and south into British Columbia. The terrane consists of rocks formed in a mid- to late Paleozoic continental arc system that separated the Yukon-Tanana arc from the western margin of Laurentia (Nelson et al., 2006, 2013). The terrane consists

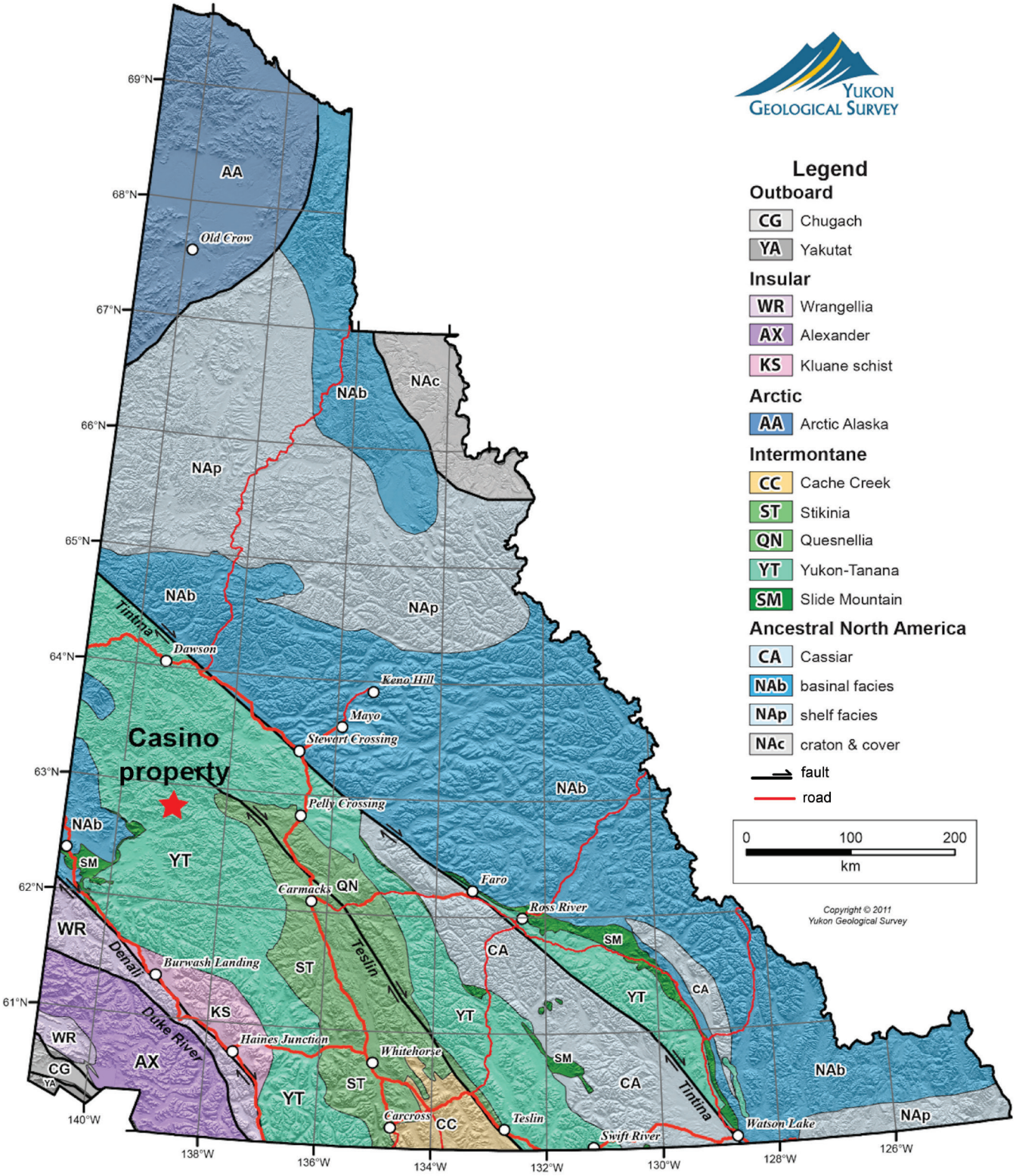

Figure 1. Location of the Casino porphyry copper deposit in west-central Yukon (*modified from* Relf et al., 2020).

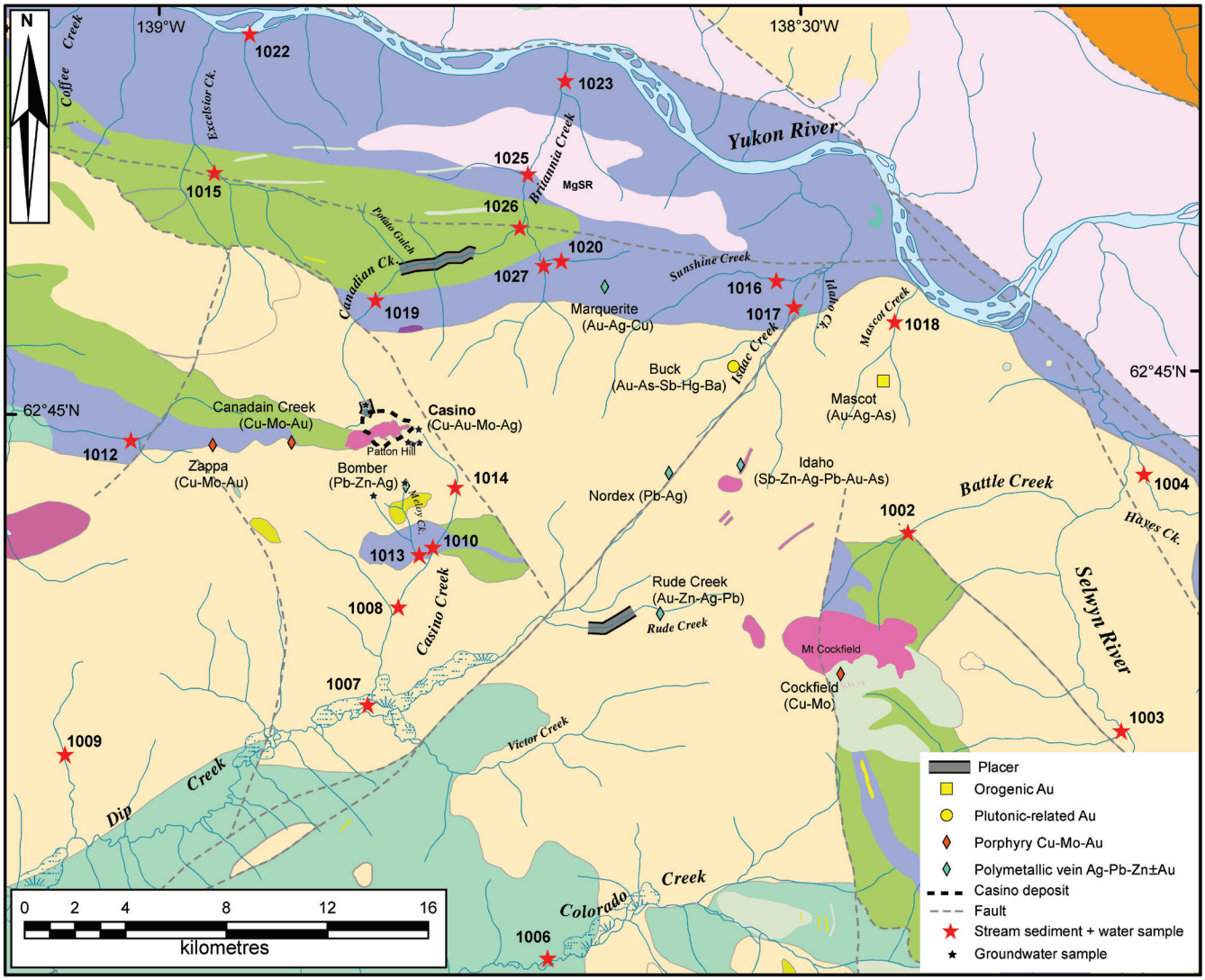

Bedrock Geology

PALEOCENE TO LOWER EOCENE
- RHYOLITE CREEK: rhyolite and dacite
- RHYOLITE CREEK: andesite

LATE CRETACEOUS
- PROSPECTOR MOUNTAIN SUITE: syenite
- CASINO SUITE: quartz-feldspar porphyry

MID-CRETACEOUS
- WHITEHORSE SUITE: granodiorite, diorite
- WHITEHORSE SUITE: quartz monzonite, granite, leucogranite
- MOUNT NANSEN: andesite to dacite flows

UPPER CRETACEOUS
- CARMACKS: augite-olivine basalt and breccia
- CARMACKS: andesite, porphyry
- CARMACKS: sandstone, pebble conglomerate, shale, tuff, coal

LATE TRIASSIC TO EARLY JURASSIC
- MINTO SUITE: granodiorite, gneissic schlieren

LATE TRIASSIC
- STIKINE SUITE: gabbroic Hbl orthogneiss

MIDDLE TO LATE PERMIAN
- SULPHUR CREEK SUITE: granite, metaporphyry
- KLONDIKE SCHIST: qtz-ms-chl schist

MISSISSIPPIAN
- SIMPSON RANGE SUITE: metagranodiorite, metadiorite, metatonalite

DEVONIAN, MISSISSIPPIAN, AND(?) OLDER
- FINLAYSON: intermediate to mafic volcanic and volcaniclastic rocks
- FINLAYSON: carbonaceous metasedimentary rocks, metachert
- FINLAYSON: ultramafic rocks, serpentinite; metagabbro

LATE DEVONIAN TO MISSISSIPPIAN
- MT BAKER SUITE: gneissic granodiorite, diorite, monzogranite, gabbro, minor pyroxenite

ORDOVICIAN TO LOWER DEVONIAN
- SCOTTIE CREEK: quartzite, Qtz-Ms-Bt±Grt schist

NEOPROTEROZOIC AND PALEOZOIC
- SNOWCAP: quartzite, psammite, pelite, marble; minor greenstone and amphibolite
- SNOWCAP: marble

Figure 2. Map of the Casino deposit area showing local bedrock geology (Yukon Geological Survey, 2015b), locations of mineral occurrences (Yukon Geological Survey, 2011a, b, c, 2013a, b, 2015a, 2017, 2018a, b, c, d, e), stream sediment and water sample sites (red stars), and groundwater sample sites (black stars). Sample numbers are listed in black beside each site.

of the Snowcap assemblage of metamorphosed sedimentary and minor volcanic rocks, which is unconformably overlain by the Finlayson, Klinkit, and Klondike assemblages that are predominantly composed of arc metavolcanic rocks and associated metasedimentary rocks (Colpron et al., 2006, 2016; Ryan et al., 2013).

The bedrock geology of the deposit and surrounding area is briefly summarized in this paper based on detailed descriptions by Archer and Main (1971), Godwin (1975, 1976), Bower et al. (1995), Ryan et al. (2013), Casselman and Brown (2017), and Yukon Geological Survey (2015b, 2018c). The Casino deposit is classified as a calc-alkaline porphyry deposit and is centred on the Patton porphyry, a Late Cretaceous (74–72 Ma) stock that intrudes the Mesozoic Dawson Range batholith and Paleozoic Yukon Crystalline Complex schist and gneiss. The intrusion of the small porphyry into these older rocks caused brecciation along its contacts. The porphyry is locally mineralized and is surrounded by a potassic-altered intrusion breccia at its outer contacts. Elsewhere, the porphyry consists of discontinuous dykes (up to tens of metres wide) that cut the porphyry and Dawson Range batholith. The overall composition of the porphyry is rhyodacite, with dacite phenocrysts and a quartz latite matrix.

Primary copper, gold, and molybdenum mineralization was deposited from hydrothermal fluids in the contact breccias and fractured wall rocks and consists of pyrite, chalcopyrite, molybdenite, and minor hübnerite (manganese-tungsten oxide). The primary mineralization is concentrated in the phyllic zone and surrounded by weakly developed argillic and propylitic alteration zones. Grades decrease away from the contact zone toward the centre of the stock and outward into the wall rocks.

Godwin (1975, 1976) suggested that the warm and wet climate of the Paleogene (Zachos et al., 2001; Moran et al., 2006; Vavrek et al., 2012) is the likely timeframe for supergene enrichment of the deposit. The deep weathering profile is largely intact because minimal to no glacial erosion of the region occurred during the last 2 000 000 y (Bond and Lipovsky, 2011, 2012a, b). Thus, the deposit has well-formed zonation consisting of a leached cap, supergene oxide mineralization, supergene sulfide mineralization, and hypogene (primary) mineralization. The leached cap averages 70 m thick, is enriched in gold and depleted in copper, and consists primarily of boxwork textures filled with jarosite, limonite, goethite, and hematite. The deep weathering has obliterated bedrock textures and replaced most minerals with clay. The supergene oxide zone consists of a few isolated lenses within the leached cap and is thought to have formed by more recent fluctuations in the water table. It is rich in copper and contains chalcanthite, malachite, and brocanthite along with minor cuprite, azurite, tenorite, neotocite, and trace molybdenite as coatings on fractures and in vugs. The supergene sulfide zone underlies the leached cap, averages 60 m thick, and outcrops at surface in places. It has Cu grades commonly almost double those in the hypogene zone and contains pyrite, chalcopyrite, bornite, and tetrahedrite that may be altered along grain boundaries to chalcocite, digenite, or covellite, as well as molybdenite that is locally altered to ferrimolybdite. Hypogene mineralization underlies the supergene sulfide zone and consists of pyrite, chalcopyrite, molybdenite, sphalerite, bornite, and tetrahedrite. In the hypogene zone, gold occurs as discrete grains (50–70 µm) in quartz and as inclusions (1–15 µm) in pyrite and chalcopyrite. On the eastern and northern flanks of the deposit, the supergene oxide zone is absent, the other zones are thinner, and the hypogene zone is closest to the surface (<25 m). Potential indicator minerals of the deposit are listed in Table 1.

Mineral occurrences near the Casino deposit are shown in Figure 2. They include porphyry Cu-Mo-Au occurrences 20 km to the southeast on Mount Cockfield (e.g. Cockfield; Yukon Geological Survey, 2018d) and 3 to 6 km west of the Casino deposit (Canadian Creek, Zappa; Yukon Geological Survey, 2018b, e). Additional polymetallic vein occurrences are located 10 km to the northeast (Marquerite; Yukon Geological Survey, 2013b), 10 km to the east (Nordex and Idaho; Yukon Geological Survey, 2011a, b), and 12 km to the southeast (Rude Creek; Yukon Geological Survey, 2011c) of Casino. Two gold occurrences have been reported 13 to 16 km east-northeast of the deposit (Buck and Mascot; Yukon Geological Survey, 2013a, 2015a).

Surficial geology

The surficial geology of the Casino area is summarized below from maps and reports by Duk-Rodkin (2001), Huscroft (2002a, b, c), Duk-Rodkin et al. (2002, 2004), Bond and Sanborn (2006), Jackson et al. (2009), Bond and Lipovsky (2011, 2012a, b), Lipovsky and Bond (2012), and McKillop et al. (2013). The deposit is in the northern Dawson Range, a series of broad ridges and summits that vary in elevation from approximately 1000 to 1800 m a.s.l. and comprise the south part of the Klondike Plateau physiographic region (Bostock, 1970; Mathews, 1986). The highest peaks in the study area are an unnamed peak (1672 m a.s.l.), 3 km to the northwest of Patton Hill (the highest point of the Patton porphyry intrusion, approximately 1432 m a.s.l.), and Mount Cockfield (1856 m a.s.l.), 20 km to the southeast (Fig. 2). The landscape is largely unglaciated. Bedrock outcrop and tors (rocky peaks) are common along the ridges and summits and have disintegrated in situ through mechanical (freeze-and-thaw) and/or chemical weathering. Surficial material in upland areas flanking ridges and summits consists of colluvium and weathered bedrock intermixed with variable amounts of loess. Material moves downslope by gravity-driven processes — creep, solifluction, landslides, and snow avalanches — and eventually into local creeks. Lower lying areas are covered with loess.

Table 1. Potential indicator minerals of the Casino porphyry Cu-Au-Mo deposit, summarized from deposit descriptions by Bostock (1959), Archer and Main (1971), Godwin (1975), Bower et al. (1995), Casselman and Brown (2017), and Huss et al. (2013), and indicator minerals found in stream-sediment samples in this study.

Mineral	Interpretation	Formula	Specific gravity	Hardness	In bedrock HMC in this study	In stream HMC in this study	First reported presence in deposit
Hematite	Potassic alteration	Fe_2O_3	5.3	6.5	No	Yes	Godwin (1975)
Magnetite	Potassic alteration	Fe_3O_4	5.1–5.2	5.5–6	Yes	Yes	Godwin (1975)
Anhydrite	Potassic alteration	$CaSO_4$	2.96–2.98	3.5	No	No	Godwin (1975)
Tourmaline	Potassic alteration	$NaMg_3Al_6(BO_3)_3Si_6O_{18}(OH)_4$	2.98–3.2	7–7.5	Yes	Yes	Godwin (1975)
Ankerite	Potassic alteration	$Ca(Fe,Mg,Mn)(CO_3)_2$	3–3.1	3.5–4	No	No	Godwin (1975)
Pyrite	Potassic alteration	FeS_2	5–5.0	6.5	Yes	Yes	Godwin (1975)
Chalcopyrite	Potassic alteration	$CuFeS_2$	4.1–4.3	3.5	Yes	Yes	Godwin (1975)
Molybdenite	Potassic alteration	MoS_2	5.5	1.0	Yes	Yes	Godwin (1975)
Sphalerite	Potassic alteration	(Zn,Fe)S	3.9–4.2	3.5–4	No	Yes	Godwin (1975)
Bornite	Potassic alteration	Cu_5FeS_4	4.9–5.3	3	No	No	Godwin (1975)
Jarosite	Potassic alteration	$KFe_3(SO_4)_2(OH)_6$	2.9–3.3	2.5–3.5	No	Yes	Godwin (1975)
Tourmaline	Phyllic alteration	$NaMg_3Al_6(BO_3)_3Si_6O_{18}(OH)_4$	2.98–3.2	7–7.5	Yes	Yes	Archer and Main (1971)
Titanite	Phyllic alteration	$CaTiSiO_5$	3.4–3.56	5–5.5	No	Yes	Huss et al. (2013)
Pyrite	Phyllic alteration	FeS_2	5–5.0	6.5	Yes	Yes	Archer and Main (1971)
Chalcopyrite	Phyllic alteration	$CuFeS_2$	4.1–4.3	3.5	Yes	Yes	Archer and Main (1971)
Molybdenite	Phyllic alteration	MoS_2	5.5	1.0	Yes	Yes	Archer and Main (1971)
Hematite	Phyllic alteration	Fe_2O_3	5.3	6.5	No	Yes	Archer and Main (1971)
Magnetite	Phyllic alteration	Fe_3O_4	5.1–5.2	5.5–6	Yes	Yes	Godwin (1975)
Jarosite	Phyllic alteration	$KFe_3(SO_4)_2(OH)_6$	2.9–3.3	2.5–3.5	No	Yes	Archer and Main (1971)
Epidote	Propylitic alteration	$Ca_2(FeAl)_3(SiO_4)_3(OH)$	3.3–3.6	7	Yes	Yes	Godwin (1975)
Pyrite	Propylitic alteration	FeS_2	5–5.0	6.5	Yes	Yes	Godwin (1975)
Limonite	Leached cap	$FeO(OH)•nH_2O$	2.7–4.3	4–5.5	No	No	Archer and Main (1971)
Jarosite	Leached cap	$KFe_3(SO_4)_2(OH)_6$	2.9–3.3	2.5–3.5	No	Yes	Archer and Main (1971)
Plumbojarosite	Leached cap	$PbFe_6(SO_4)_4(OH)_{12}$	3.6–3.67	1.5–2	No	Yes	Huss et al. (2013)
Beudantite	Leached cap	$PbFe_3(AsO_4)(SO_4)(OH)_6$	4.1–4.3	4	No	Yes	Huss et al. (2013)
Pyrolusite	Leached cap	MnO_2	4.4–5.06	6–6.5	No	Yes	Huss et al. (2013)
Goethite	Leached cap	$FeO(OH)$	3.3–4.3	5–5.5	Yes	Yes	Godwin (1975)
Hematite	Leached cap	Fe_2O_3	5.3	6.5	No	Yes	Archer and Main (1971)

Table 1 (cont.). Potential indicator minerals of the Casino porphyry Cu-Au-Mo deposit, summarized from deposit descriptions by Bostock (1959), Godwin (1975), Bower et al. (1995), Casselman and Brown (2017), and Huss et al. (2013), and indicator minerals found in stream-sediment samples in this study.

Mineral	Interpretation	Formula	Specific gravity	Hardness	In bedrock HMC in this study	In stream HMC in this study	First reported presence in deposit
Ferrimolybdite	Leached cap	$Fe_2(MoO_4)_3•8(H_2O)$	4–4.5	2.5–3	No	No	Godwin (1975)
Chalcanthite	Supergene oxide	$Cu(SO_4)•5(H_2O)$	2.12–2.3	2.5	No	No	Godwin (1975)
Brochantite	Supergene oxide	$Cu_4(SO_4)(OH)_6$	3.97	3.5–4	No	No	Godwin (1975)
Malachite	Supergene oxide	$Cu_2(CO_3)(OH)_2$	3.6–4	3.5–4	No	No	Godwin (1975)
Azurite	Supergene oxide	$Cu_3(CO_3)_2(OH)_2$	3.77–3.89	3.5–4	No	No	Godwin (1975)
Tenorite	Supergene oxide	CuO	6.5	3.5–4	No	No	Godwin (1975)
Cuprite	Supergene oxide	Cu_2O	6.1	3.5–4	No	No	Bower et al. (1995)
Neotocite	Supergene oxide	$(MnFe)SiO_3•(H_2O)$	2.8	3–4	No	No	Godwin (1975)
Native copper	Supergene oxide	Cu	8.94–8.95	2.5–3	No	No	Godwin (1975)
Digenite	Supergene sulfide	Cu_9S_5	5.6	2.5–3	No	No	Archer and Main (1971)
Chalcocite	Supergene sulfide	Cu_2S	5.5–5.8	2.5–3	No	No	Archer and Main (1971)
Covellite	Supergene sulfide	CuS	4.6–4.76	1.5–2	No	No	Archer and Main (1971)
Enargite	Supergene sulfide	Cu_3AsS_4	4.4–4.5	3	No	No	Casselman and Brown (2017)
Bornite	Supergene sulfide	Cu_5FeS_4	4.9–5.3	3	No	No	Huss et al. (2013)
Pyrite	Hypogene mineralization	FeS_2	5–5.0	6.5	Yes	Yes	Archer and Main (1971)
Chalcopyrite	Hypogene mineralization	$CuFeS_2$	4.1–4.3	3.5	Yes	Yes	Archer and Main (1971)
Molybdenite	Hypogene mineralization	MoS_2	5.5	1.0	Yes	Yes	Archer and Main (1971)
Sphalerite	Hypogene mineralization	(Zn,Fe)S	3.9–4.2	3.5–4	No	Yes	Godwin (1975)
Bornite	Hypogene mineralization	Cu_5FeS_4	4.9–5.3	3	No	No	Godwin (1975)
Gold	Hypogene mineralization	Au	16–19.3	2.5–3	Yes	Yes	Archer and Main (1971)
Galena	Hypogene mineralization	PbS	7.2–7.6	2.5	No	No	Archer and Main (1971)
Tetrahedrite	Hypogene mineralization	$Cu_9Fe_3Sb_4S_{13}$	4.6–5.2	3.5–4	No	No	Bower et al. (1995)
Bismuthinite	Hypogene mineralization	Bi_2S_3	6.8–7.2	2.0	No	Yes	Huss et al. (2013)
Ankerite	Hypogene mineralization	$Ca(Fe,Mg,Mn)(CO_3)_2$	3–3.1	3.5–4	No	No	Bower et al. (1995)
Barite	Polymetallic veins	$BaSO_4$	4.5	3–3.5	Yes	Yes	Archer and Main (1971)
Sphalerite	Polymetallic veins	(Zn,Fe)S	3.9–4.2	3.5–4	No	Yes	Archer and Main (1971)
Ag-rich galena	Polymetallic veins	PbS	7.2–7.6	2.5	No	No	Archer and Main (1971)
Scheelite	Polymetallic veins	$CaWO_4$	5.9–6.1	4–5	No	Yes	Archer and Main (1971)

Table 1 (cont.). Potential indicator minerals of the Casino porphyry Cu-Au-Mo deposit, summarized from deposit descriptions by Bostock (1959), Godwin (1975), Bower et al. (1995), Casselman and Brown (2017), and Huss et al. (2013), and indicator minerals found in stream-sediment samples in this study.

Mineral	Interpretation	Formula	Specific gravity	Hardness	In bedrock HMC in this study	In stream HMC in this study	First reported presence in deposit
Chalcopyrite	Polymetallic veins	$CuFeS_2$	4.1–4.3	3.5	Yes	Yes	Archer and Main (1971)
Pyrite	Polymetallic veins	FeS_2	5–5.0	6.5	Yes	Yes	Archer and Main (1971)
Gold	Placer: upper Canadian Creek	Au	16–19.3	2.5–3	Yes	Yes	Bostock (1959)
Ferberite	Placer: upper Canadian Creek	$Fe(WO_4)$	7.5	4.5	No	No	Bostock (1959)
Scheelite	Placer: upper Canadian Creek	$CaWO_4$	5.9–6.1	4–5	No	Yes	Bostock (1959)
Molybdenite	Placer: upper Canadian Creek	MoS_2	5.5	1.0	Yes	Yes	Bostock (1959)
Cassiterite	Placer: upper Canadian Creek	SnO_2	6.8–7	6–7	No	No	Bostock (1959)
Tourmaline	Placer: upper Canadian Creek	$NaMg_3Al_6(BO_3)_3Si_6O_{18}(OH)_4$	2.98–3.2	7–7.5	Yes	Yes	Bostock (1959)
Titanite	Placer: upper Canadian Creek	$CaTiSiO_5$	3.4–3.56	5–5.5	No	Yes	Bostock (1959)
Hematite	Placer: upper Canadian Creek	Fe_2O_3	5.3	6.5	No	Yes	Bostock (1959)
Magnetite	Placer: upper Canadian Creek	Fe_3O_4	5.1–5.2	5.5–6	Yes	Yes	Bostock (1959)

HMC: heavy mineral concentrate

Isolated alpine glaciers existed on Mount Cockfield during the middle Pleistocene Reid glaciation, extending west into the headwaters and a tributary valley of Victor and Colorado creeks and east into an unnamed tributary that drains into the Selwyn River (Bond and Lipovsky, 2012a). Glacial sediments (end moraines) and cirques are present on the east flank of Mount Cockfield; stream sediments in the creeks draining this east flank will be derived, in part, from the glacial sediments. Evidence of past glaciation also exists in the headwaters of Canadian Creek, immediately northwest of Patton Hill, where cirques formed during early Pleistocene (pre-Reid) glaciation (Duk-Rodkin et al., 2002; Bond and Lipovsky, 2012a).

Permafrost is discontinuous and is most common on north-facing slopes and valley bottoms that are covered by thick, fine-grained colluvium and organic veneers (Smith et al., 2009; Bond and Lipovsky, 2011). The presence of permafrost is indicated by features such as solifluction lobes, pingos, and thermokarst features.

First- and second-order streams (e.g. Casino Creek) occur in narrow V-shaped valleys and contain subangular to subrounded gravel to boulders composed of locally derived bedrock. Higher order streams occur in broader valleys and are filled with more distally derived colluvium, loess, and rounded gravel (e.g. Dip Creek, Colorado Creek). Bond and Lipovsky (2012a) reported that understanding the relationship between valley morphology and the variable texture and sources of fluvial sediments is important when sampling for and interpreting stream silt geochemical surveys. Because loess content in fluvial sediments is variable, Bond and Lipovsky (2012a) recommended that stream samples ideally be collected from high-energy streams in narrow valleys where the loess content is lowest.

Previous stream-sediment geochemical surveys

Archer and Main (1971) reported that, at the time of discovery, the Casino deposit had an obvious geochemical signature in stream silts (Cu, Mo, Au, and Ag) and waters (Cu) overlying the deposit. Subsequent reconnaissance-scale stream silt and water sampling in Yukon by the GSC (Geological Survey of Canada, 1987; 19 elements in <0.177 mm silt using 3:1 HNO_3:HCl, pH, 2 elements in water) and subsequent reanalysis of these GSC stream-sediment samples (53 elements in <0.177 mm silt using 1:3 HNO_3:HCl; Jackaman, 2011; Yukon Geological Survey, 2016; Mackie et al., 2017; Arne et al., 2018) show an obvious multi-element geochemical anomaly (Ag, Cu, Mo, Pb, Sb, W) in the local creeks draining the Casino deposit.

The Yukon Geological Survey collected a few isolated heavy mineral samples from local creeks while mapping the surficial geology of the Casino area. They reported the presence of gold grains in two of their nine samples: one sample from upper Casino Creek and one sample from Rude Creek (Bond and Lipovsky, 2012a, b; Lipovsky and Bond, 2012).

Chapman et al. (2014, 2018) compared lode gold signatures in the Casino deposit and large (100 kg) bulk gravel samples from known placer occurrences along Casino, Canadian, and Rude creeks (Fig. 2). They reported that gold grains in the Casino deposit bedrock samples were between 50 to 1000 µm (long axis of grains) and in gravel samples between 500 to 2000 µm. Using gold grain trace-element chemistry and inclusion compositions, they concluded that the large gold placer occurrence in the middle reaches of Canadian Creek contained a mixture of gold derived from two sources: the Casino porphyry deposit and unknown epithermal mineralization. Barkov et al. (2008) reported the presence of several indicator minerals in a heavy mineral concentrate (HMC) sample from the same large placer occurrence on Canadian Creek, below the confluence with Potato Gulch (Fig. 2). In addition to tin-rich hematite, they recovered ferberite, hübnerite, bismuthinite, daubréeite, tetradymite, and goethite in the sample. In the same placer sample, Fedortchouk and LeBarge (2008) reported the presence of one grain of platinum-iron alloy.

METHODS

Sample collection

A total of 24 stream-silt and water samples and 22 heavy mineral samples were collected at 22 sites (Fig. 2) around the Casino deposit in September 2017 using GSC protocols established by Friske and Hornbrook (1991) and described in detail by Day et al. (2013) and Plouffe et al. (2013). Field observations were digitally recorded on a tablet using a standard form developed jointly by the GSC and the Northwest Territories Geological Survey. Field data and photographs of all stream-sediment sample sites are included in McCurdy et al. (2019).

At each site, two 60 mL water samples were collected in the mid-channel of local creeks: i) a filtered, acidified sample ('FA') and ii) a filtered, unacidified sample ('FU'). On site, each 60 mL water sample was filtered through a 0.45 µm disposable filter into a triple-rinsed 60 mL Nalgene® bottle. In situ stream water measurements included temperature, pH, conductivity, dissolved oxygen (DO), and oxidation-reduction potential (ORP) with automatic temperature compensation for pH and DO. After the water samples were collected, approximately 1 to 2 kg of silt and fine sand was collected by hand from various points in the active channel while moving upstream, over a distance of 5 to 15 m. A third bulk heavy mineral stream-sediment sample of between 8 and 16 kg was collected from large gravel bars, boulder traps, or tiny pools of sediment in rocky narrow streams. Samples were wet sieved onsite to remove the fragments greater than 2 mm.

Nine groundwater samples were collected by Western Copper and Gold Corporation during the same time period from monitoring wells in eight locations (Fig. 2). Samples for total metals analyses were collected in 120 mL acid-washed plastic bottles and preserved in the field with laboratory-supplied, ultrapure HNO_3. Samples for dissolved metal analyses were filtered through a 0.45 µm disposable filter in the field and preserved with ultrapure HNO_3 immediately after filtration. Western Copper and Gold Corporation shared these water samples with the GSC after splits were analyzed at a commercial laboratory.

Heavy mineral sample processing

The stream-sediment heavy mineral samples were weighed and processed at Overburden Drilling Management Ltd. (ODM), Ottawa, Ontario, for recovery of HMCs using methods outlined by Plouffe et al. (2013). There were 22 stream-sediment samples plus 3 blank quality control (QC) samples (for a total of 25 samples) processed. Samples were first passed across a shaking table to prepare a less than 2.0 mm preconcentrate. The preconcentrate was micropanned to recover and count fine-grained gold, sulfide minerals, and other indicator minerals. Gold grain size and shape characteristics were classified using DiLabio's (1990) scheme (pristine-modified-reshaped) adapted for fluvial transport distance (Averill, pers. comm., 2020) and then all panned grains were returned to the concentrate. Gold grain counts reported in this paper reflect this stage of the sample processing procedure. The preconcentrate was then subjected to two heavy-liquid separations to produce 2.8 to 3.2 specific gravity (SG) and greater than 3.2 SG non-ferromagnetic HMCs for visual identification of indicator minerals. Before examination, the grains were subjected to an oxalic acid wash to facilitate mineral identification. The 0.25 to 0.5, 0.5 to 1.0, and 1.0 to 2.0 mm non-ferromagnetic greater than 3.2 SG fractions and the 0.25 to 0.5 mm non-ferromagnetic 2.8 to 3.2 SG fraction of bedrock and stream-sediment samples were examined by ODM, potential indicator minerals were counted, and selected grains were removed for chemical analysis. The mass of all fractions produced and abundance of indicator minerals in the 22 stream-sediment and 3 QC samples, along with sample processing flow charts, are reported by McClenaghan et al. (2020).

Geochemical analysis

Stream-silt samples were air dried at less than 40°C, disaggregated, and sieved to recover the less than 0.177 mm fraction for geochemical analysis. Geochemical analytical data quality was monitored by inserting CANMET Certified Reference Material (CRM) Stream Sediment-1

(STSD-1) and Stream Sediment-4 (STSD-4; Lynch, 1990, 1999; CANMET, 2020) and analytical duplicate samples into each block of 20 samples. A 30 g aliquot of each sample was tested for 35 elements by instrumental neutron activation analysis (INAA) at Maxxam Analytics (formerly Becquerel Labs), Mississauga, Ontario. A separate 0.5 g aliquot was analyzed for 65 elements at Bureau Veritas Commodities Canada (BVCC), Vancouver, British Columbia, using a modified aqua regia solution (1:1 HCl:HNO_3) and detection by inductively coupled plasma mass spectrometry (ICP-MS). Lead collection fire assay was used to concentrate Au, Pt, and Pd from a separate 30 g aliquot into a silver doré bead that was then digested in HNO_3, and the solution was analyzed by ICP-MS. Stream silt geochemical data for all methods and the evaluation of quality-control data were reported by McCurdy et al. (2019). A separate split of dried, unsieved stream silt was analyzed in a 4 dram (approximately 15 mL) plastic vial covered with 4 µm Prolene® film using a hand-held portable X-ray fluorescence (pXRF) unit at the GSC's Inorganic Geochemistry Research Laboratory (IGRL), Ottawa, Ontario. Samples were analyzed twice and the mean values for each sample were used for data interpretations (McCurdy et al., 2019).

Streamwater samples collected by the GSC were kept cool and in the dark until shipment to the IGRL, where they were acidified within 48 h of arrival with 0.5 mL 8M ultrapure HNO_3. Anion analysis (FU series) was completed using a Dionex™ ICS 2100 ion chromatograph fitted with an AS-AP autosampler. Acidified and filtered (FA series) streamwater samples were analyzed for trace metals and major elements using a quadrupole inductively coupled plasma–mass spectrometer (ICP-MS). Major element analysis was performed using an inductively coupled plasma–optical emission spectrometer (ICP-OES). The groundwater samples from Western Copper and Gold were also analyzed at the IGRL using the same methods. In addition to analyses performed at the GSC, water samples were subsequently analyzed for $\delta^{18}O$, $\delta^{2}H$, $\delta^{34}S_{SO_4}$, and $\delta^{18}O_{SO_4}$ (for samples with sufficient SO_4), $\delta^{65}Cu$, and $^{87}Sr/^{86}Sr$ at the Queen's University Facility for Isotope Research (QFIR).

RESULTS

Stream sediment mineralogy

Grain counts for selected indicator minerals are reported in Table 2 and described below as values normalized to 10 kg of material of less than 2 mm to allow comparison between samples of different mass. Individual mineral distribution maps are included in McClenaghan et al. (2020) and are summarized below. Unless otherwise stated, the results are for the 0.25 to 0.5 mm size HMC fraction.

Stream sediments contain between 0 and 44 gold grains (Fig. 3a) in the pan concentrate fraction. Abundances are highest in samples from Casino Creek on the south side of the deposit and Canadian and Britannia creeks draining the north side of the deposit (Fig. 4). Gold grains in these three creeks range in size from 25 to 1500 µm, with most grains being between 25 and 200 µm in size and modified to reshaped in appearance (Table 3).

Chalcopyrite (Fig. 3b) was recovered from most stream-sediment samples, with the largest number of grains being recovered from sample 1003 (26 grains), downstream of the Cockfield occurrence; sample 1012 (13 grains), downstream of the Zappa occurrence; and sample 1019 (7 grains), downstream of the Casino deposit. Most other stream-sediment samples contained between 0 and 4 grains (Fig. 5). The presence of chalcopyrite is somewhat unexpected because the terrain, except for east of Mount Cockfield, is unglaciated and the deep weathering of bedrock was expected to have destroyed chalcopyrite in rocks exposed at surface.

Pyrite (Fig. 3c) was recovered from all but two stream-sediment samples. It is most abundant in sample 1012 (2113 grains) from the creek draining the Zappa occurrence; sample 1003 (397 grains), downstream of the Cockfield occurrence, sample 1004 (194 grains) on Hayes Creek, and sample 1015 (168 grains) on Excelsior Creek, 12 km northwest of the Casino deposit. The highest count in Casino Creek samples is 79 grains (sample 1015).

Molybdenite (Fig. 3d) was recovered from four stream-sediment samples (Table 2): sample 1014 from Casino Creek; sample 1003, downstream of the Cockfield occurrence; sample 1013, approximately 20 km downstream of the deposit in Britannia Creek; and sample 1012, downstream of the Zappa occurrence (Fig. 6).

Low-Fe sphalerite grains were identified in three stream-sediment samples by their honey brown colour (Fig. 3e). Some of the grains appear to be corroded, indicating that they underwent chemical weathering. The grains were recovered from sample 1013 from Meloy Creek, sample 1014 from Casino Creek, and sample 1019 from Canadian Creek (Table 2). In addition to chalcopyrite, pyrite, and sphalerite, a few grains of bismuthinite (Fig. 3f) and arsenopyrite (Fig. 3g) were recovered from samples collected downstream of the Cockfield occurrence.

A few tourmaline grains (Fig. 3h) were recovered from the 2.8 to 3.2 SG fraction of samples from Casino Creek, but the greatest number of grains were recovered farther downstream in Canadian (sample 1026) and Britannia creeks (sample 1025), in creeks downstream of the Cockfield occurrence (samples 1002, 1003), and in Sunshine Creek (sample 1016; *see* Fig. 1 in Beckett-Brown et al., this volume). The presence of tourmaline is obvious throughout the Casino deposit as disseminations, in veins, and in breccias (Beckett-Brown et al., 2019, this volume), thus the recovery of tourmaline from local stream sediments is not surprising.

Scheelite (Fig. 7a, b) is most abundant in stream sediments from Casino and Canadian creeks, downstream of the Cockfield and Zappa occurrences, and on Sunshine Creek.

Table 2. Abundance (grain count) of select indicator minerals in the >3.2 specific gravity (SG) and 2.8 to 3.2 SG 0.25 to 0.5 mm non-ferromagnetic fractions and pan concentrate gold fraction of stream-sediment samples. Counts have been normalized to 10 kg of less than 2 mm (table feed) material.

Sample number	Creek	Gold (pan conc.)	Pyrite	Chalco	Moly	Sphal	Plumb	Beaudan	Pyro	Goethite	Barite	Green epidote	Tur	Scheel	Fluorite	Jarosite SG 2.8–3.2	Tur SG 2.8–3.2
1002	Battle Creek	1	1	2	0	0	1	0	0	407	41	472	0	11	0	163	24
1003	Unnamed creek near Cockfield occurrence	1	397	26	3	0	0	0	0	3311	993	4967	0	26	0	331	26
1004	Hayes Creek	5	194	1	0	0	0	0	0	4651	9302	0	0	2	0	78	0
1006	Colorado Creek	2	0	0	0	0	0	0	0	379	1	0	0	1	0	45	30
1007	Casino Creek	44	13	0	0	0	0	0	0	1007	805	16 308	0	40	0	0	0
1008	Casino Creek	21	4	2	0	0	0	0	0	5825	777	3223	0	4	0	291	4
1009	Unnamed tributary of Dip Creek	1	0	0	0	0	0	0	0	28	0	0	0	0	0	0	0
1010	Casino Creek	8	0	0	0	0	0	1	0	18 349	459	5725	0	37	0	183	11
1012	Unnamed creek near Zappa occurrence	1	2113	13	3	0	0	0	0	141	423	14 085	0	35	0	423	0
1013	Meloy Creek	0	11	4	0	11	86	0	2518	17 986	719	1324	0	2	0	36	0
1014	Casino Creek	1	79	0	1	9	0	0	0	9868	526	3816	0	0	0	132	0
1015	Excelsior Creek	0	168	3	0	0	0	0	0	168	25	65 546	0	1	0	50	2
1016	Sunshine Creek	0	22	1	0	0	0	0	0	1079	7194	45 324	6	36	0	144	360
1017	Isaac Creek	6	3	0	0	0	0	0	0	840	126	7143	0	8	0	0	0
1018	Mascot Creek	3	28	1	0	0	0	0	0	1724	103	4828	0	4	0	0	0
1019	Upper Canadian Creek	28	115	7	0	1	0	0	0	4615	115	19 615	0	23	0	31	0
1020	Unnamed creek near Marquerite occurrence	14	26	0	0	0	0	0	0	34 783	1043	126 086	0	11	0	0	0
1022	Unnamed creek draining into Yukon River	0	63	3	0	0	0	0	0	794	31746	126 984	24	10	2	40	317
1023	Britannia Creek	2	122	1	1	0	0	0	0	3659	366	207 317	0	0	1	183	0
1025	Britannia Creek	19	35	0	0	0	0	0	0	13 274	44	145 133	2	2	0	1327	88
1026	Lower Canadian Creek	6	15	2	0	0	0	0	0	7692	0	153 846	7	2	0	1231	62
1027	Unnamed creek near Marquerite occurrence	0	2	0	0	0	0	0	0	4110	1712	22 603	0	3	0	27	0

Abbreviations: Chalco: chalcopyrite; Moly: molybdenite; Sphal: sphalerite; Plumb: plumbojarosite; Beudan: beaudantite; Pyro: pyrolusite; Scheel: scheelite; Tur: tourmaline
SG: specific gravity; HMC: heavy mineral concentrate

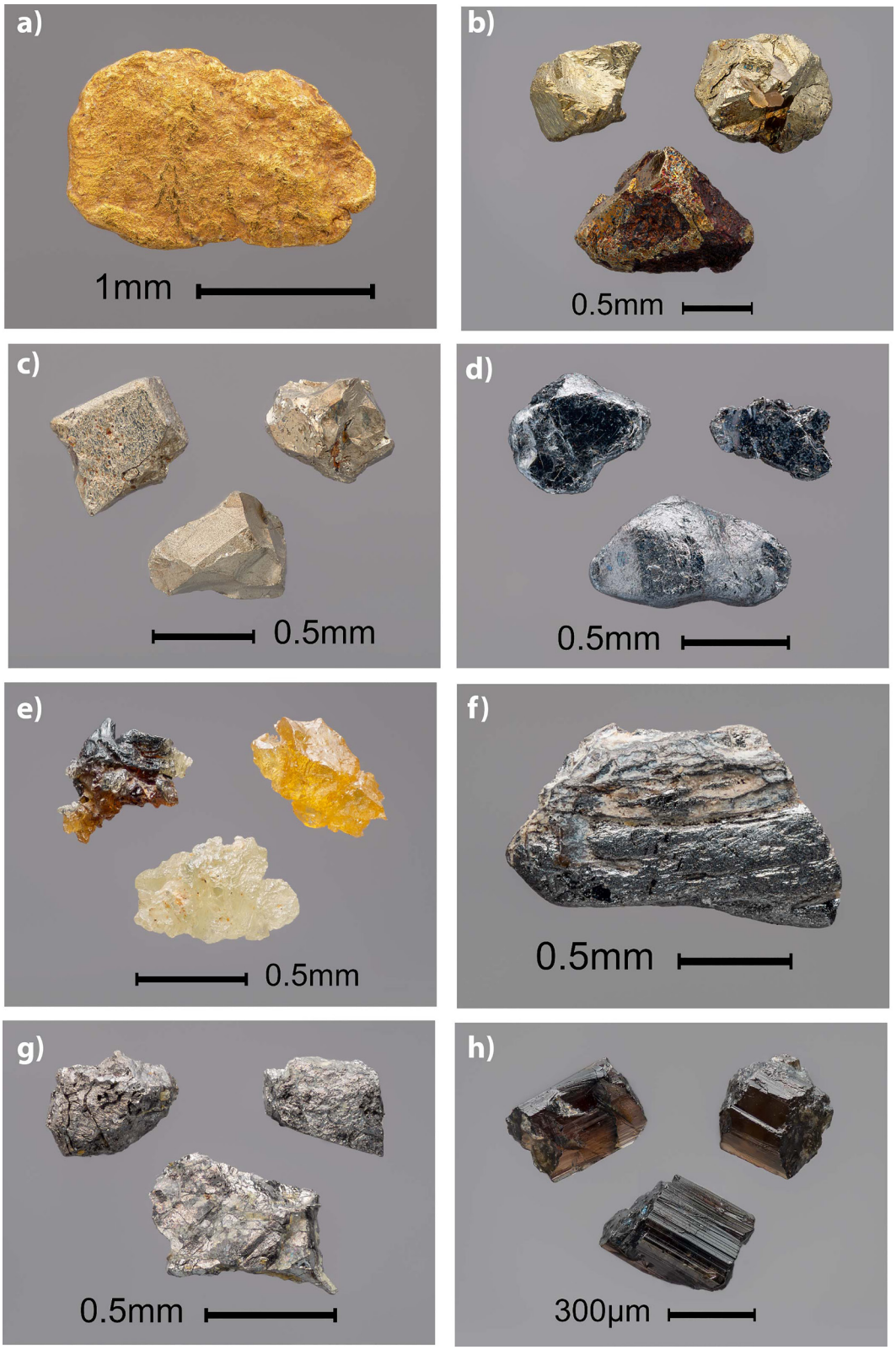

Figure 3. Colour photographs of indicator minerals recovered from the heavy mineral fraction of stream sediments collected around the Casino deposit: **a)** gold; **b)** chalcopyrite; **c)** pyrite; **d)** molybdenite; **e)** sphalerite; **f)** bismuthinite; **g)** arsenopyrite; and **h**) tourmaline (mid-density fraction). Photographs courtesy of Michael J. Bainbridge Photography.

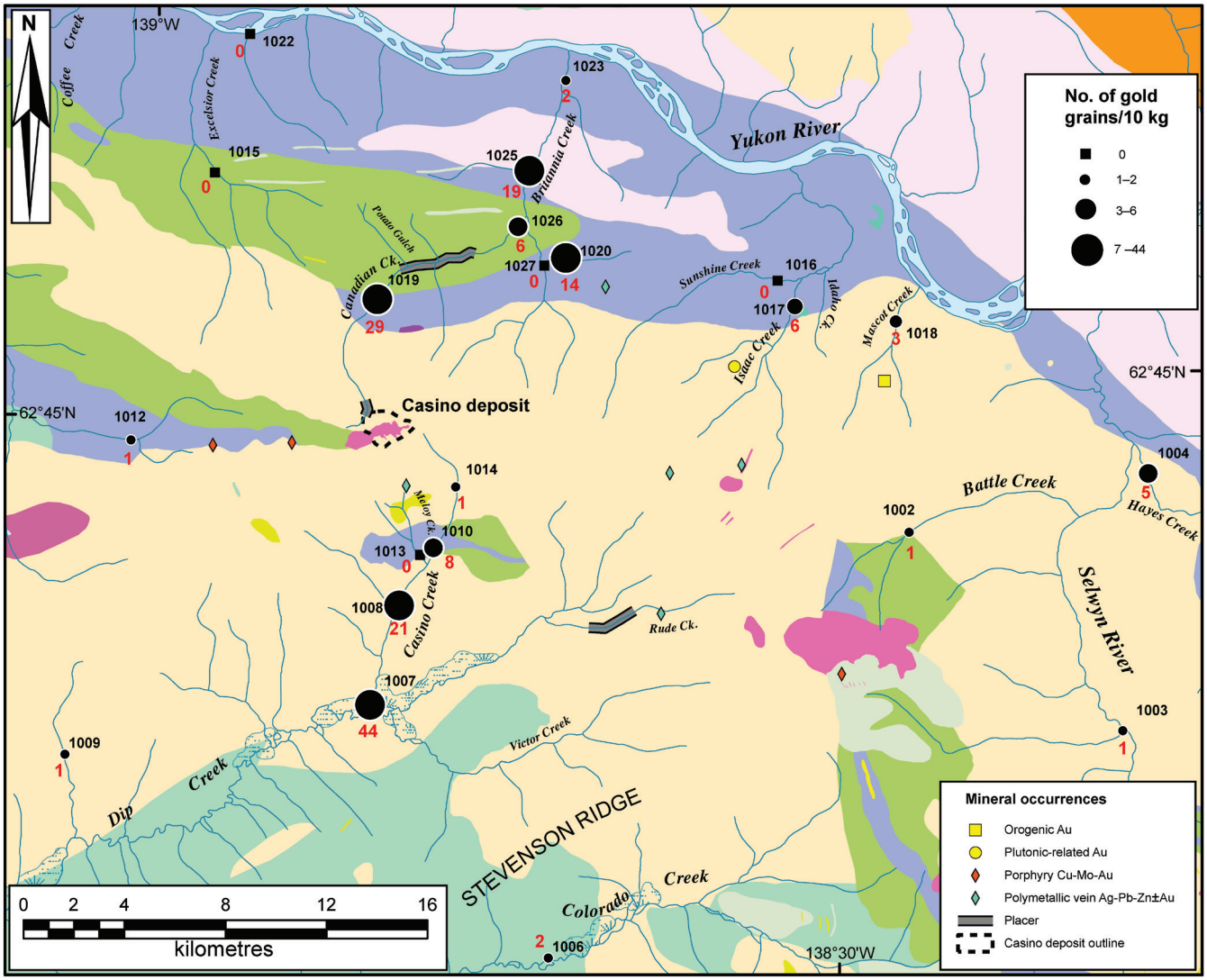

Figure 4. Gold grain abundance in the pan concentrate fraction of heavy mineral stream-sediment samples collected in 2017 (n = 22) in the Casino deposit area. Samples numbers are labeled in black and abundance values are in red. *See* Figure 2 for bedrock geology legend.

Table 3. Abundance (count), size, and shape of gold grains in stream-sediment samples collected from creeks draining the Casino deposit.

Sample	Creek	Mass of <2 mm fraction (kg)	Grain dimensions		Grain shape			Total no. of grains
			Width (µm)	Length (µm)	Reshaped	Modified	Pristine	
1007	Casino	14.9	25	25		1		65
			25	50	1	1	1	
			25	75	1	1		
			50	50	3	1		
			50	75			1	
			50	100	2	1		
			50	150	2			
			75	75	1	2		
			75	100	4	1		
			75	125	3	2		
			75	150	2	2		
			100	100	4			
			100	125	2			
			100	150	3	1		
			100	200	2	1		
			125	125	2	1		
			125	175	3	2		
			150	150	1	1		
			150	200	2			
			150	300	2			
			150	400	3			
			200	200	1			
			250	250	1			
1008	Casino	10.3	25	25	1	2		22
			25	50		1	1	
			50	50		1		
			50	75	1	1		
			50	100		1		
			75	75	1	2		
			75	100	1	1		
			75	125	1			
			100	150		1		
			100	200	2			

Table 3 (cont.). Abundance (count), size, and shape of gold grains in stream-sediment samples collected from creeks draining the Casino deposit.

Sample	Creek	Mass of <2 mm fraction (kg)	Grain dimensions		Grain shape			Total no. of grains
			Width (µm)	Length (µm)	Reshaped	Modified	Pristine	
			100	150	1			
			125	175	1			
			150	250	1			
			150	300	1			
1010	Casino	10.9	75	100	1			9
			75	200		1		
			100	125	1			
			100	150	1			
			200	300	1			
			200	350	1			
			250	250	1			
			250	750	1			
			300	900	1			
1013	Meloy	13.9			0			0
1014	Casino	15.2	200	300	1			2
			250	400	1			
1023	Britannia	16.4	75	125		1		3
			75	150		1		
			125	125	1			
1025	Britannia	11.3	25	50		1		21
			50	75	1			
			50	100	1			
			75	125	1			
			100	125	2			
			100	250	1			
			125	125	1			
			125	175	1			
			125	250	1			
			150	175	1			
			175	200	1			
			200	350	1			
			250	250	3			

Table 3 (cont.). Abundance (count), size, and shape of gold grains in stream-sediment samples collected from creeks draining the Casino deposit.

Sample	Creek	Mass of <2 mm fraction (kg)	Grain dimensions		Grain shape			Total no. of grains
			Width (µm)	Length (µm)	Reshaped	Modified	Pristine	
			250	300	1			
			250	350	1			
			250	500	1			
			300	350	1			
			1000	1500	1			
1026	Canadian	13.0	50	100			1	8
			75	125	2	1		
			100	175		1		
			125	125	1			
			125	150	1			
			250	650	1			
1019	Canadian	13.0	25	50		2	2	37
			25	75			1	
			50	50	1	1	1	
			50	75		2		
			50	125		1		
			75	75	1	1		
			75	100	2			
			75	125	4	1		
			75	150		2		
			75	200		1		
			100	100	1			
			100	150	1	1		
			100	200		1		
			125	150	1			
			125	200	1			
			150	300	1			
			150	350	1			
			175	350	1			
			175	400	1			
			200	300	1			
			300	400	1			
			300	500	1			
			500	750	1			

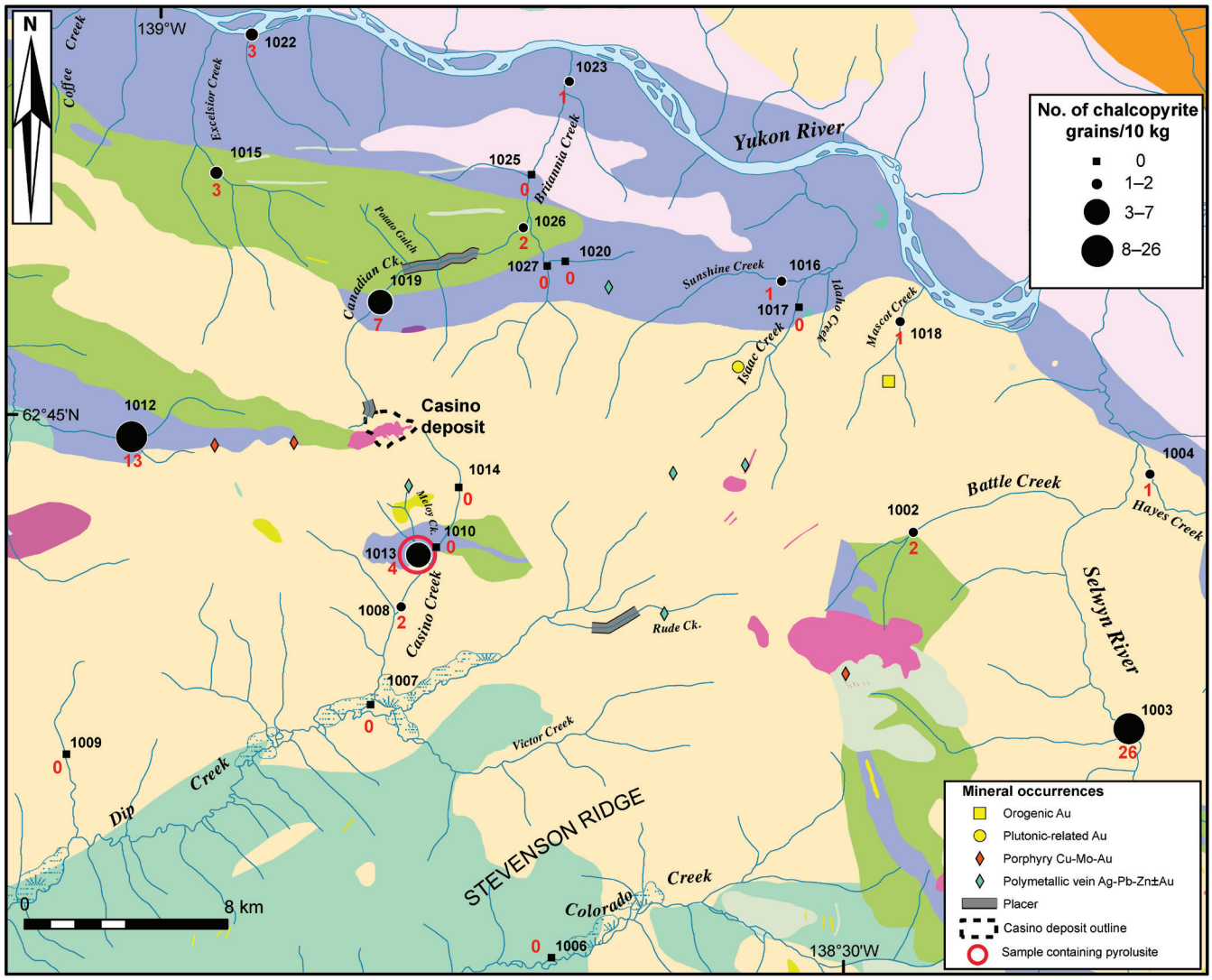

Figure 5. Chalcopyrite abundance in the 0.25 to 0.5 mm heavy mineral fraction of stream-sediment samples collected in 2017 (n = 22) in the Casino deposit area. Location of the sample containing pyrolusite and plumbojarosite grains is indicated by the red circle. Samples numbers are labelled in black and abundance values in red. *See* Figure 2 for bedrock geology legend.

The presence of scheelite was noted in the upper Canadian Creek placer occurrence by Bostock (1959), thus its presence was not unexpected in local stream-sediment samples.

Jarosite was visually identified in the 2.8 to 3.2 SG fraction of stream sediments and is yellowish to light brown (Fig. 7c). Stream-sediment samples 1025 and 1026 from Britannia Creek and lower Canadian Creek contained the most jarosite (1200–1300 grains; Table 2). Samples that contained hundreds of jarosite grains include those from Casino Creek and samples downstream of the Cockfield and Zappa occurrences.

Pyrolusite was visually identified in stream-sediment HMC by its dull, black, amorphous appearance (Fig. 7d) and was confirmed by scanning electron microscopy (SEM). Approximately 2500 grains were recovered from Meloy Creek (sample 1013; Fig. 5). In addition to pyrolusite, approximately 86 grains of plumbojarosite (Fig. 7e) were recovered from the same sample. One plumbojarosite grain was also recovered from sample 1002, downstream of the Cockfield occurrence. Beudantite, a secondary Pb-As sulfate mineral, was identified in sample 1010 from Casino Creek (Table 2). Goethite (Fig. 7f) and hematite were recovered from all but two stream-sediment samples (Table 2). Potential porphyry indicator minerals green epidote (Fig. 7g), barite,

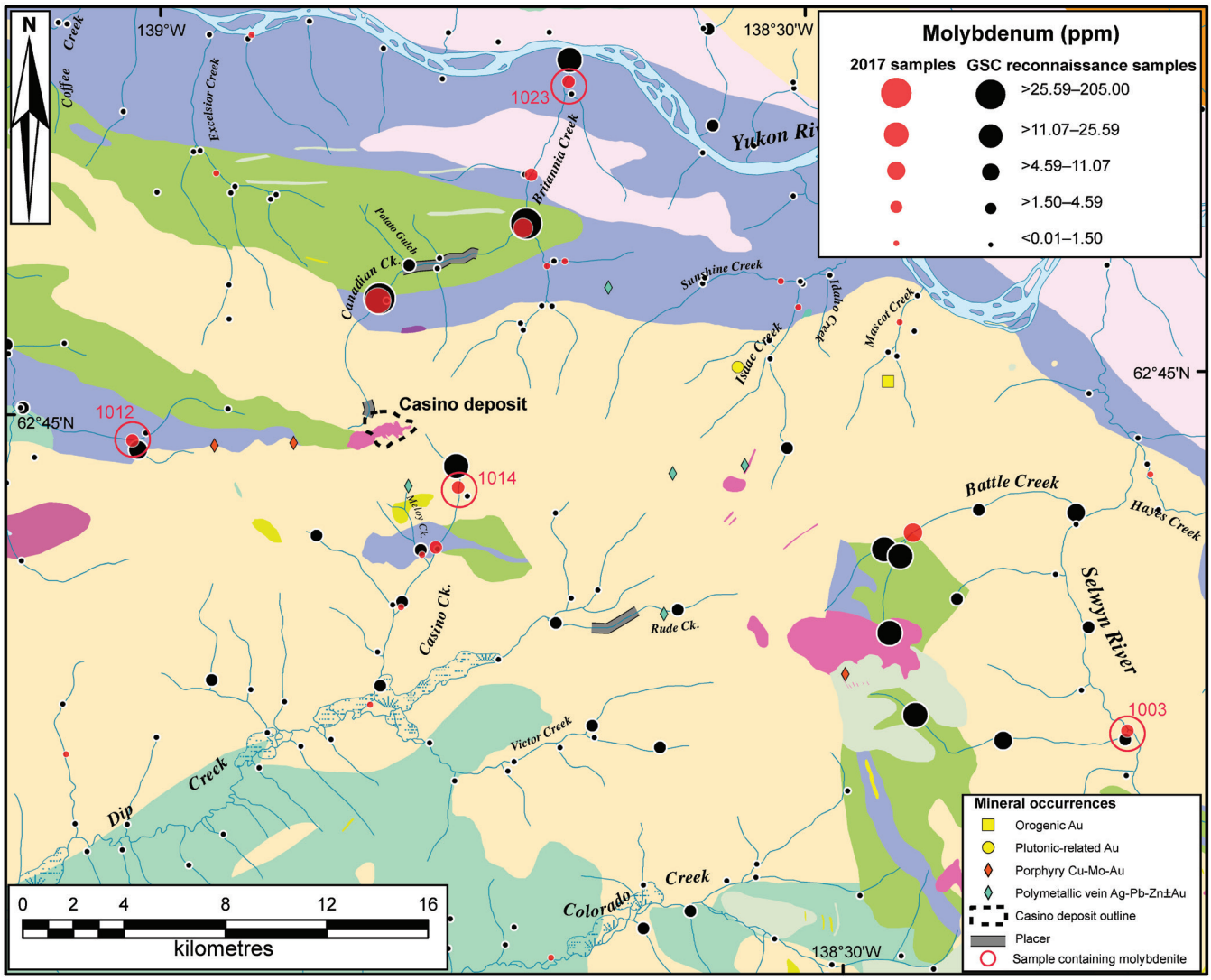

Figure 6. Location of stream-sediment samples containing molybdenite grains in heavy mineral concentrates (red circles and red sample numbers) and molybdenum concentrations, for the less than 0.177 mm fraction of stream-sediment samples collected during 2017 (this study, red dots, n = 22) and reconnaissance samples reanalyzed in 2011 (black dots, n = 1301; Jackaman, 2011). *See* Figure 2 for bedrock geology legend.

and zircon were recovered from stream sediments (Table 2) but their distribution patterns do not reflect the presence of the Casino deposit.

Stream-sediment geochemistry

Comparison of Au analytical methods

The range of Au values determined by all three analytical methods in 2017 are compared in scatterplots in Figure 8a–c. Note that one extremely high fire assay Au value (4056 ppb in sample 1010) was not included in Figure 8 so that similar scales could be used on all three plots, making visual comparisons easier for readers. Gold concentrations determined by INAA (<2–211 ppb) and fire assay (6–4056 ppb) are higher than those by aqua regia followed by ICP-MS (0.8–23.7 ppb). Fire assay and INAA values are most similar, with the fire assay values being slightly higher.

Spatial patterns

Correlation coefficients for the 2017 data are summarized in Figure 9. Copper displays strong positive correlations with Au, Ag, Bi, Cd, Mn, Mo, Pb, W, and Zn, thus all these elements should be considered as pathfinder elements for porphyry copper mineralization in the area. The 2017 data for Cu, Mo, Au by aqua regia, and Au by fire assay were each plotted with data from the GSC reconnaissance samples

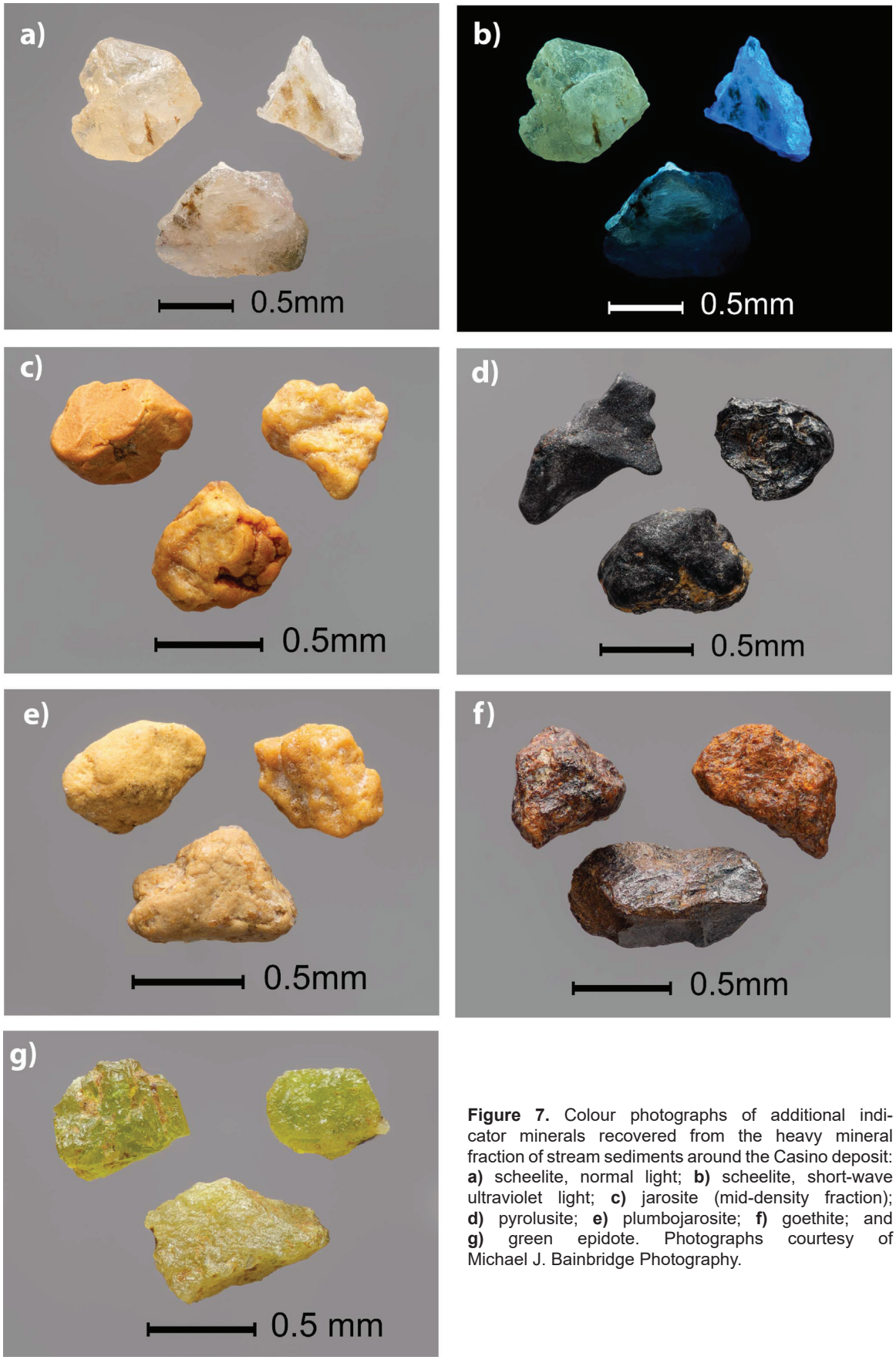

Figure 7. Colour photographs of additional indicator minerals recovered from the heavy mineral fraction of stream sediments around the Casino deposit: **a)** scheelite, normal light; **b)** scheelite, short-wave ultraviolet light; **c)** jarosite (mid-density fraction); **d)** pyrolusite; **e)** plumbojarosite; **f)** goethite; and **g)** green epidote. Photographs courtesy of Michael J. Bainbridge Photography.

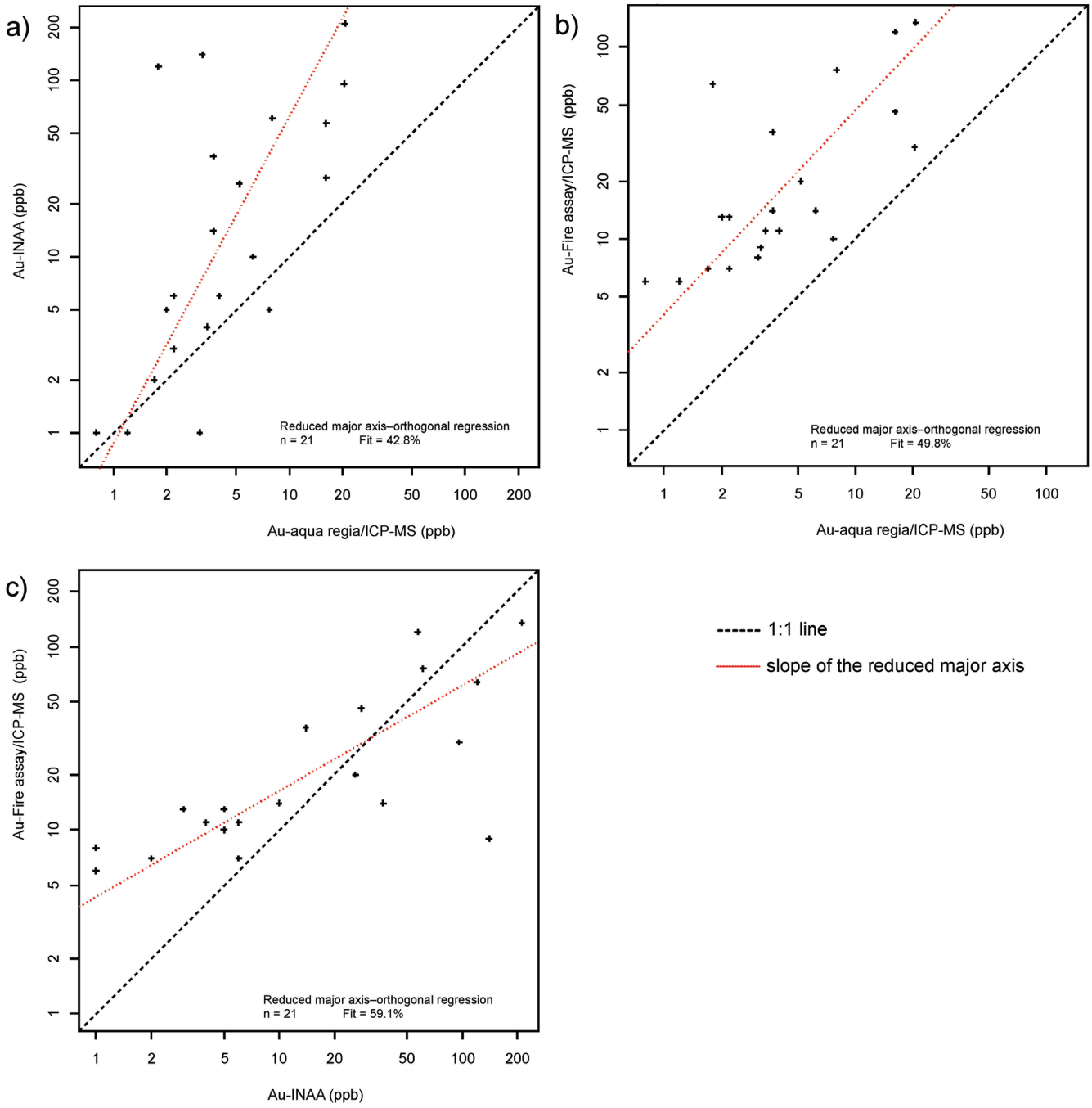

Figure 8. Reduced major-axis plots of Au concentrations in the less than 0.177 mm fraction of 21 stream silt samples determined by three analytical methods in 2017: **a)** instrumental neutron activation analysis (INAA; 30 g sample) versus aqua regia (AR) and inductively coupled plasma mass spectrometry (ICP-MS; 0.5 g sample); **b)** fire assay and ICP-MS (30 g sample) versus AR and ICP-MS (0.5 g sample); and **c)** INAA (30 g sample) versus fire assay and ICP-MS (30 g sample). Data are log transformed.

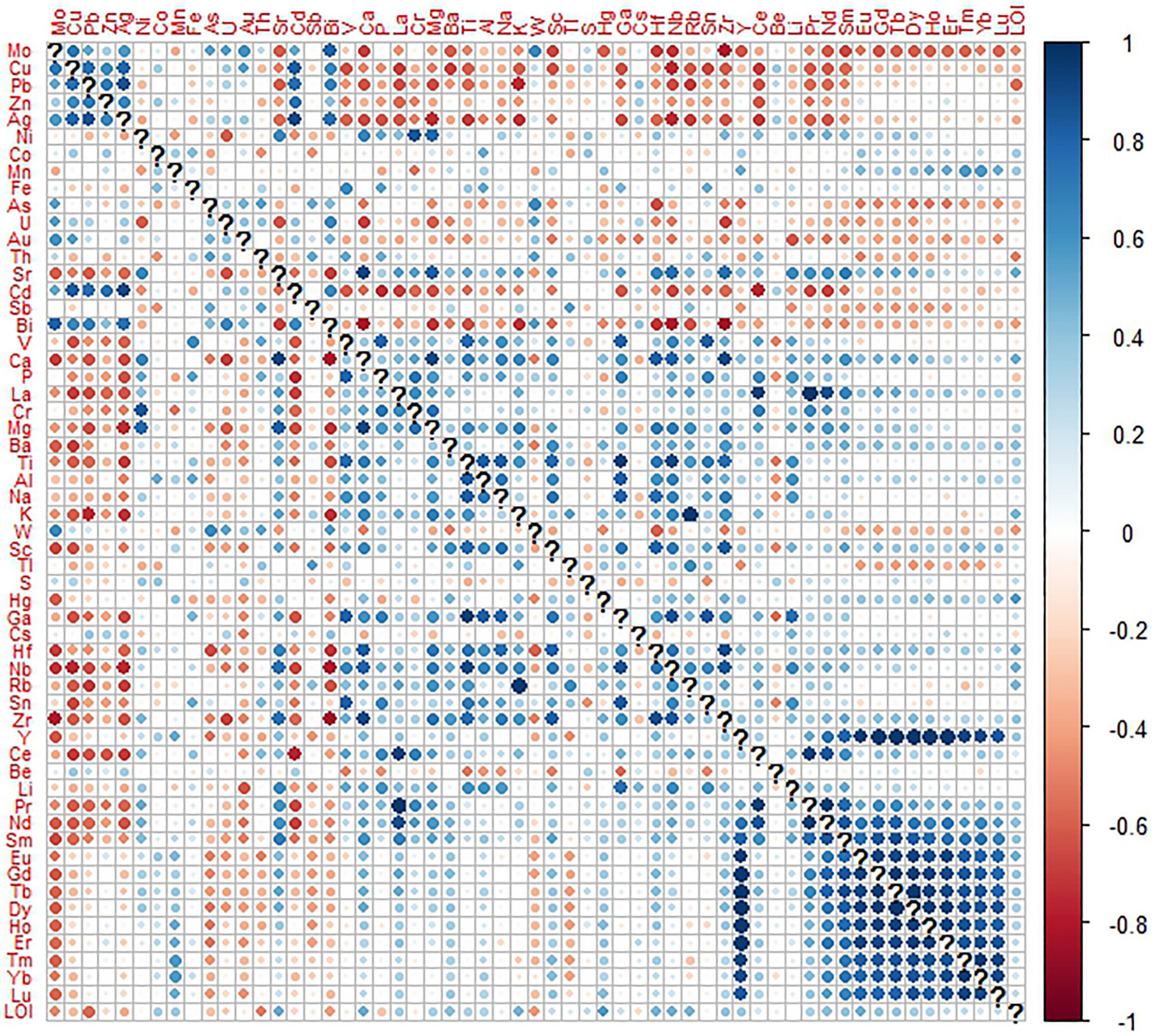

Figure 9. Graphic display using symmetric coordinates to calculate Spearman correlation coefficients between the abundances of elements in 22 stream-silt samples determined by aqua regia and inductively coupled plasma mass spectrometry (ICP-MS) and loss-on-ignition (LOI). The symmetric coordinate procedure is uninfluenced by the closure inherent to geochemical data, that is they are relative and sum to a constant (Garrett et al., 2017; Reimann et al., 2017). Small dots reflect weak correlation and large dots reflect strong correlation. The colour scale indicates the strength of the correlation.

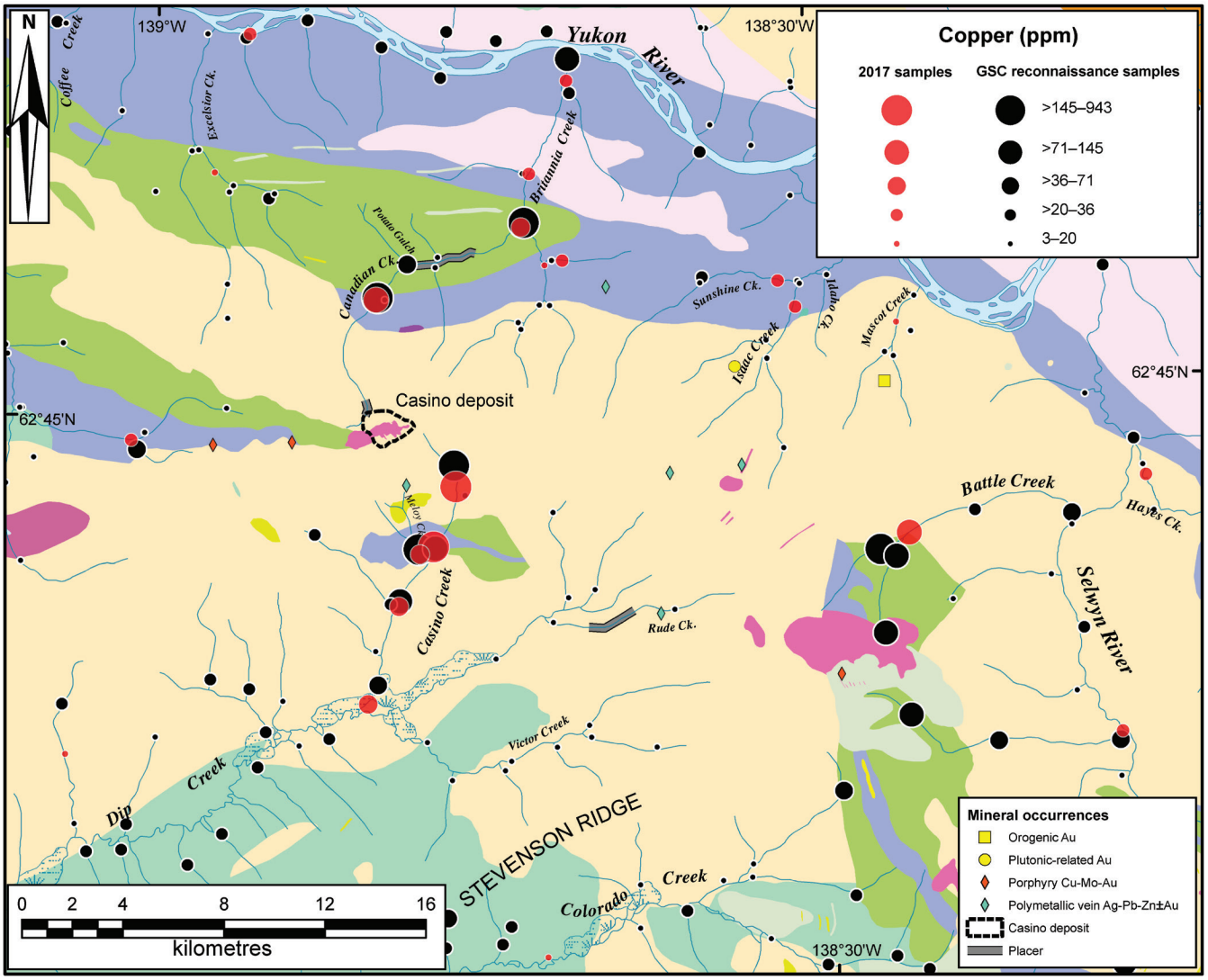

Figure 10. Comparison of copper abundance data for the less than 0.177 mm fraction of stream-sediment samples determined by aqua regia/inductively coupled plasma mass spectrometry in 2017 (this study; red dots, n = 22) and reconnaissance samples reanalyzed in 2011 (black dots, n = 1301; Jackaman, 2011). *See* Figure 2 for bedrock geology legend.

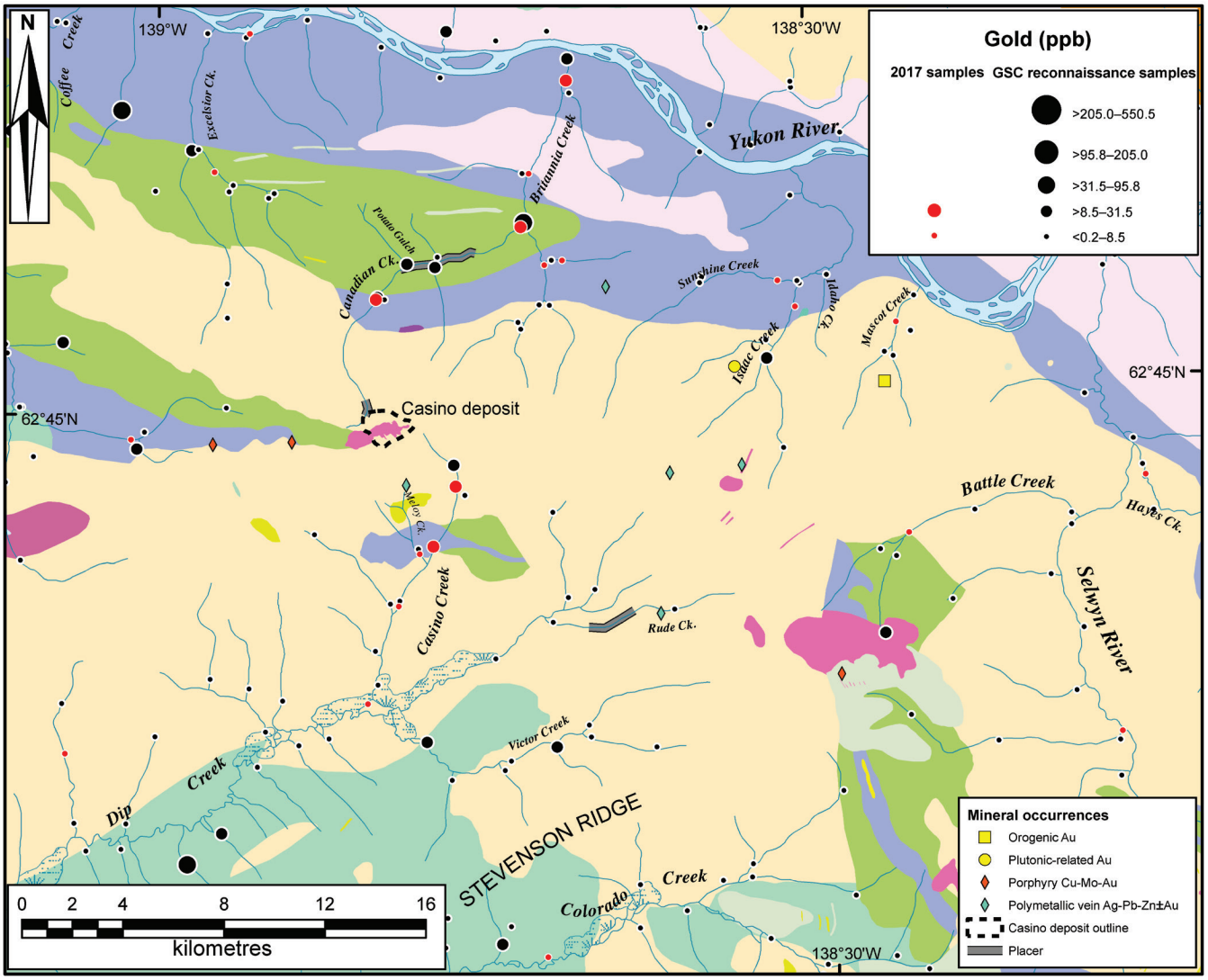

Figure 11. Comparison of gold abundance data for the less than 0.177 mm fraction of stream-sediment samples determined by aqua regia and inductively coupled plasma mass spectrometry (ICP-MS) in 2017 (this study; red dots, n = 22) and reconnaissance samples re-analyzed in 2011 (black dots, n = 1301; Jackaman, 2011). *See* Figure 2 for bedrock geology legend.

collected in NTS map areas 115J and 115K in 1986. Figures 6, 10, and 11 plot aqua regia and ICP-MS data for the 2017 samples (red dots) and the earlier, reanalyzed reconnaissance samples (black dots; Jackaman, 2011). Figure 12 is a plot of Au determined by fire assay and ICP-MS during this study (red dots) and fire assay preconcentration followed by INAA of the doré bead in 1986 (black dots; Geological Survey of Canada, 1987). Proportional dot sizes for both data sets were determined using a subset of the reconnaissance data set for the NTS map areas, not just the samples that plot in the study area, using the Jenks natural breaks method (Howard et al., 2008) in ArcGIS.

Copper concentrations in stream silt samples (Fig. 10) are highest in the two creeks draining the Casino deposit (Casino and Canadian) and in Battle Creek, which drains the Cockfield occurrence. The 2017 values are similar to the 1986 reconnaissance samples at nearby locations even though these older samples were collected 30 years earlier.

Gold (aqua regia) concentrations in 2017 stream silts are moderate (8–31 ppb) in the Casino, Canadian, and Britannia creeks and low (<8 ppb) elsewhere (Fig. 11). Gold (aqua regia) concentrations in the 1986 reconnaissance samples are similar to the 2017 values in Casino Creek but are slightly higher than the 2017 samples in Canadian Creek (maximum 69 ppb). Figure 12 shows that Au (fire assay) values are similar between the 1986 and 2017 samples, except for at sites 1010 (Casino Creek), and 1025 and 1026 (Canadian Creek), where Au values in 2017 samples are considerably higher.

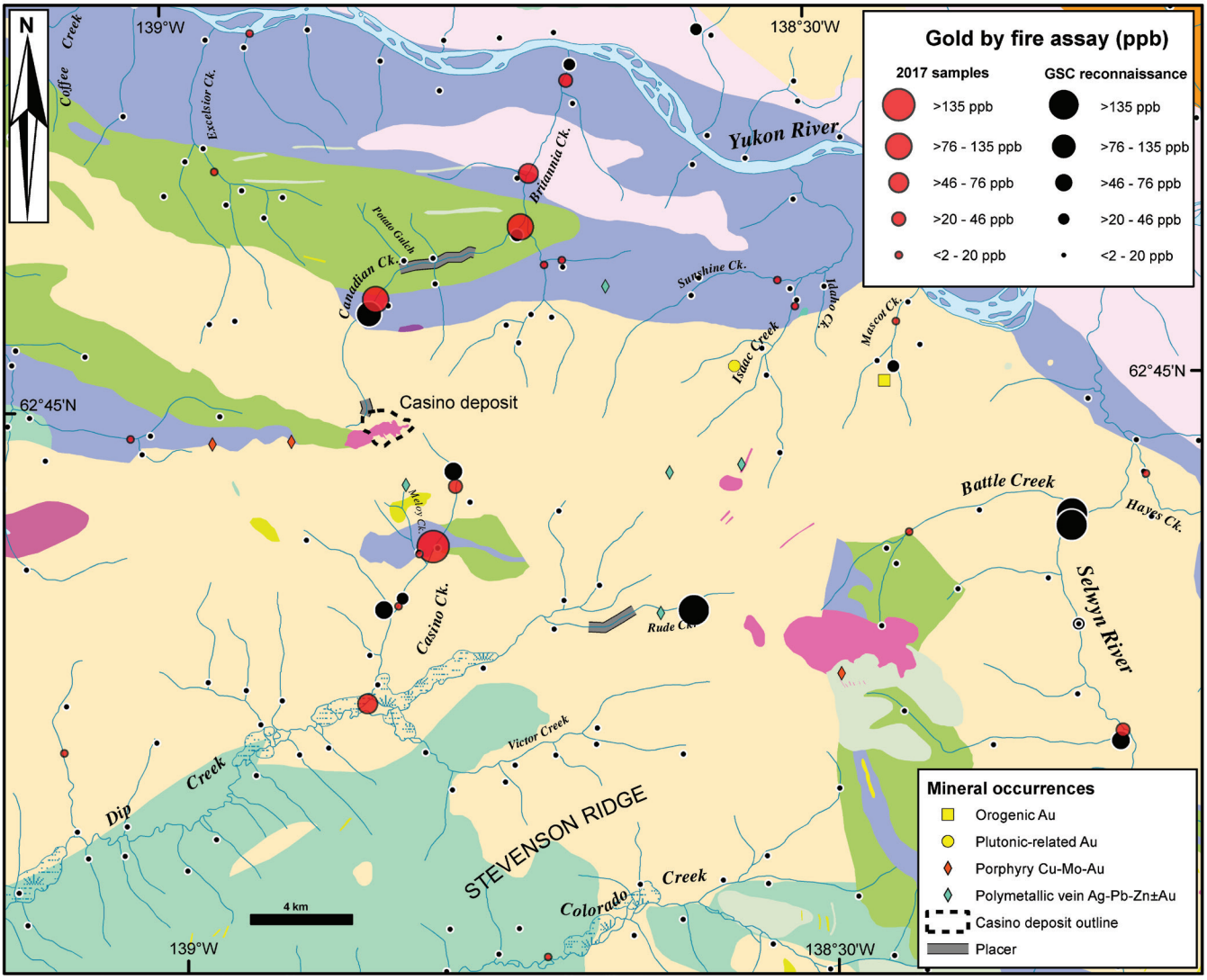

Figure 12. Comparison of gold abundance data for the less than 0.177 mm fraction of stream-sediment samples determined by fire assay in 2017 (this study; red dots, n = 22) and reconnaissance samples (black dots, n = 1301; Geological Survey of Canada (1987)). *See* Figure 2 for bedrock geology legend.

Molybdenum values (Fig. 6) are highest downstream of the Casino deposit in Canadian Creek and downstream of the Cockfield occurrence in Battle Creek. In all cases, the 2017 values are lower than the 1986 reconnaissance samples but show the same general trends in concentration. The lower values in 2017 may be related to differences in the digestion protocols used in 1986 (3:1 HNO_3:HCl) and 2017 (1:1 HNO_3:HCl).

Although not shown on maps, the highest concentrations of Ag, Bi, Te, and W (aqua regia) occur in similar locations to the highest Au (fire assay, INAA) values, that is in Casino and Canadian creeks, and downstream from the Cockfield occurrence. Similar to Cu, the highest concentrations of Cd, Pb, and Zn in stream sediments are on the south side of the Casino deposit in Casino and Meloy creeks. Antimony content is greatest in samples from Meloy, Canadian, and Sunshine creeks.

Portable XRF

The concentrations of elements determined using pXRF on dried, unsieved splits of the stream-sediment samples display similar trends to the less than 0.177 mm aqua regia and ICP-MS data for As, Cu, Mn, Mo, Zn (Fig. 13), and S, and less than 0.177 mm INAA data for Fe. Concentrations for other elements determined by pXRF were too low to be detected, not readily detected by pXRF, or much lower than the values determined by aqua regia and ICP-MS.

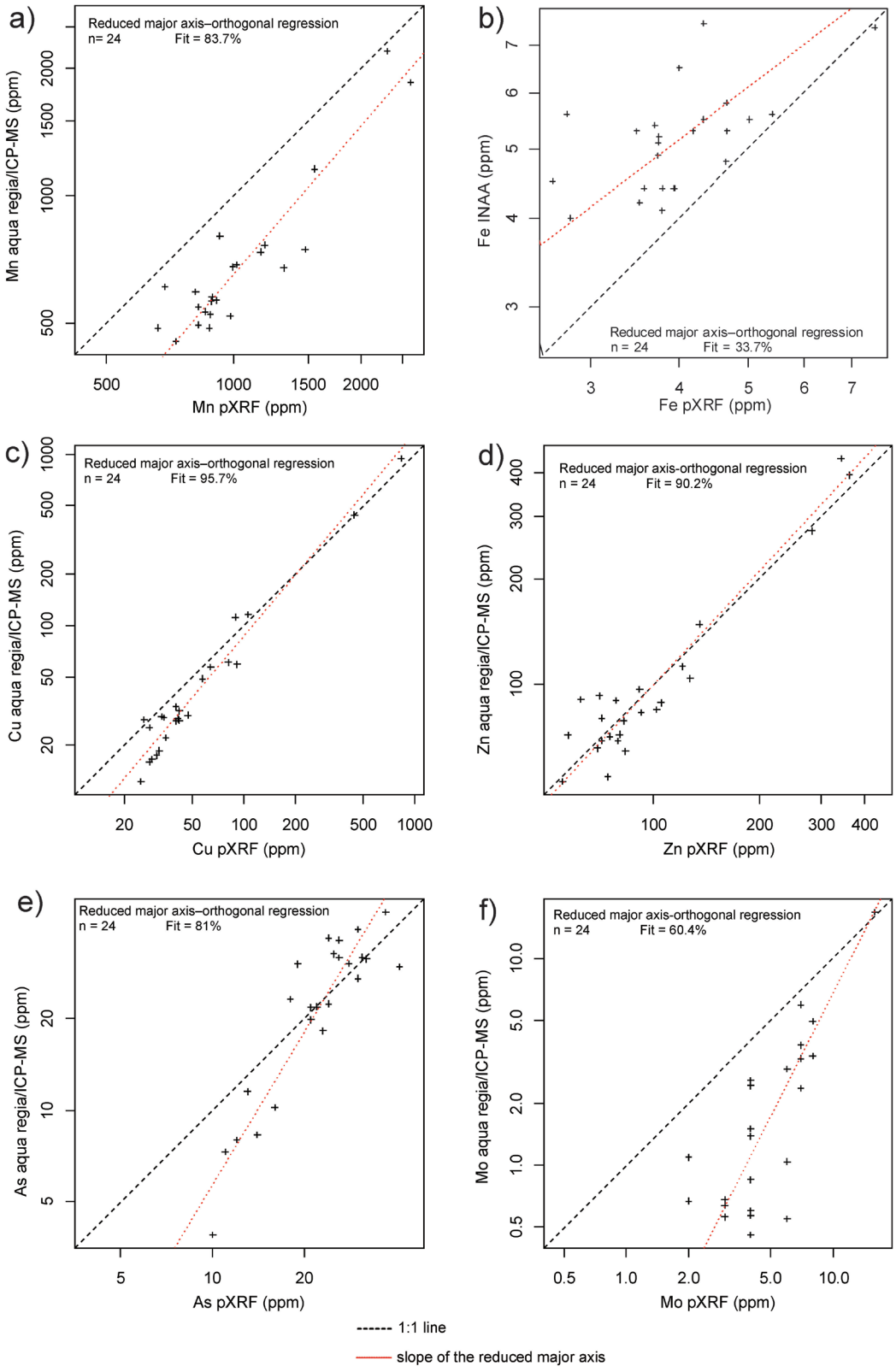

Figure 13. Reduced major-axis plots comparing log-transformed element concentrations in stream-sediment samples determined by aqua regia and inductively coupled plasma–mass spectrometry (ICP-MS) or instrumental neutron activation analysis (INAA) of the less than 0.177 mm fraction and portable X-ray fluorescence (pXRF) of dry, unsieved stream silt: **a)** Mn; **b)** Fe; **c)** Cu; **d)** Zn; **e)** As; and **f)** Mo.

Water geochemistry

Comparison of surface and groundwater

Ground- and streamwater pH values for samples collected in the area around the Casino deposit range from 6.7 to 8.3, values that are typical to slightly alkaline for groundwater and stream water in crystalline rock systems (Leybourne et al., 2006). Groundwater and stream water from the Casino study area are dominantly $CaHCO_3$ to $CaSO_4$ type (Fig. 14).

The Casino groundwater samples typically have higher salinities, with total dissolved solids (TDS) ranging from 74 to 1320 mg/L, whereas TDS in streamwater samples range from 98 to 654 mg/L (Fig. 15). Groundwater salinities are highest proximal to the Casino deposit, whereas streamwater salinities are highest in creeks draining to the north of the deposit. Stream water and groundwater are dominated by Ca (and Mg) as the major cations, with only four samples showing slightly elevated Na concentrations (14–20 mg/L; Fig. 15). All waters have low Cl (<1 mg/L) and F (<1 mg/L) concentrations, and anions are dominated by HCO_3 and, particularly in the groundwater samples close to the Casino deposit, by SO_4 (up to 800 mg/L SO_4; Fig. 15). Thus, Ca, Mg, HCO_3, and SO_4 show relatively strong correlations with TDS (r = 0.985, 0.893, 0.502, and 0.963, respectively).

Selected trace-element concentrations in groundwater and surface water samples have been plotted against dissolved SO_4 (Fig. 16) because oxidation of sulfide minerals is a primary mechanism for increasing SO_4 in shallow waters in crystalline terranes; there are no chemical (evaporite) sediments in the catchment. Stream waters around the Casino deposit have low sulfate concentrations (55 to 84 mg/L) except for sample 1014, which is adjacent to the deposit (105 mg/L). The highest sulfate concentrations (>100 mg/L) in the stream water in the study area occur in Britannia and other creeks to the north of the Casino deposit. Generally, samples with the highest sulfate concentrations have the highest metal and metalloid concentrations. Iron concentrations in most waters in the study area are low (<0.1 mg/L), typical of stream water exposed to atmospheric oxygen. In contrast, the more saline, higher sulfate groundwater has elevated Fe and Mn concentrations (<100 and 10 000 mg/L, respectively; Fig. 16). Groundwater with elevated Fe and Mn also has elevated Cu, Mo, As, Re, B, U, and Zn concentrations (Fig. 16), with values up to greater than 1000, 25.2, 17, 0.71, 11.7, 39.6, and 354 µg/L, respectively.

Spatial patterns

Values for pH change only slightly between samples closest to mineralization (pH = 7.21) and samples farther downstream in Casino Creek (pH = 7.9). Water samples from Casino Creek collected up to 14 km downstream of the Casino deposit have elevated concentrations of Mo, Cu (Fig. 17, 18, respectively), Zn, Pb, Cd, Co, and Re compared to other samples in the study area. Site 1002, downstream from the Cockfield occurrence, has moderately elevated Cd and Cu concentrations and the highest Mo concentration (2.9 ppb) of all the streamwater samples in this study.

DISCUSSION

Indicator minerals

Studies of porphyry copper indicator minerals in glaciated terrain have reported two groups of indicator minerals (Plouffe and Ferbey, 2017). The first group includes minerals that can be directly linked to porphyry mineralization based on their spatial distribution and abundance in bedrock or surficial sediments; the second group includes minerals for which mineral chemistry must be used to establish the link to porphyry copper mineralization. Group 1 indicator minerals recovered from stream-sediment samples around the Casino deposit (Casino, Meloy, Canadian creeks) include chalcopyrite, pyrite, gold, molybdenite, sphalerite, jarosite, and goethite. The distribution of these minerals in local stream sediments in this study is a direct indication of the presence of porphyry Cu mineralization or peripheral Pb-Zn-Ag veins.

Well rounded molybdenite grains (not flakes; Fig. 3d) were recovered from stream sediments downstream of the Casino deposit as well as two porphyry copper occurrences in the area. Molybdenite was observed by Bostock (1959) in the upper Canadian Creek placer occurrence on the west flank of the deposit. Its presence in local creeks is unexpected because molybdenite is soft (hardness = 1) and thus is not expected to survive fluvial transport. In the glaciated terrain of eastern Canada, molybdenite was only recovered from till and stream sediment samples that directly overlie (i.e. <1 km of transport) the intrusion-hosted Sisson W-Mo deposit (McClenaghan et al., 2017) and not in samples down-ice or downstream.

Local stream sediments also contain potential Group 2 minerals: epidote, tourmaline, scheelite, zircon, barite, and magnetite. Studies of tourmaline chemistry are ongoing (Beckett-Brown, 2019, this volume) and results to date indicate that a combination of physical characteristics (lack of inclusions, dark brown–black colour) and chemical characteristics (oxy-dravite to povondraite trend, high concentrations of Sr, low concentrations of Zn and Pb) of the tourmaline grains can distinguish between porphyry-derived and background tourmaline in stream sediments. Future studies comparing mineral chemistry of tourmaline, magnetite, epidote, zircon, and scheelite in the Casino deposit to those recovered from local stream sediments may provide additional insights into the bedrock source(s) of these mineral grains (e.g. Baksheev et al., 2012; Cooke et al., 2014, 2017; Bouzari et al., 2016; Kobylinski et al., 2017, 2018; Wilkinson et al., 2017; Poulin et al., 2018; Plouffe et al., 2019, this volume).

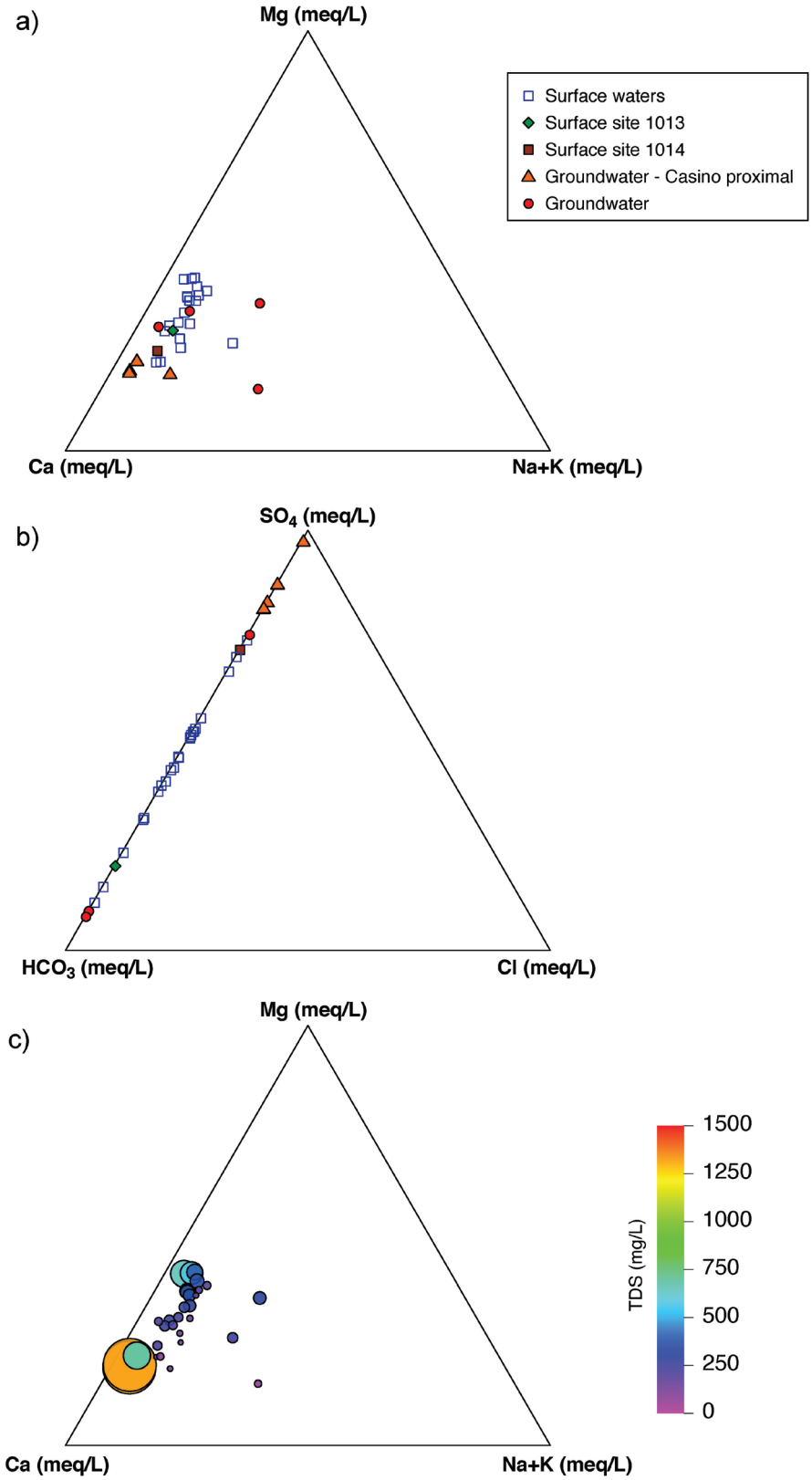

Figure 14. Modified piper plots of surface and groundwaters in the Casino deposit area: **a)** cations; **b)** anions; **c)** total dissolved solids (TDS). Waters closest to the Casino deposit have proportionally higher SO_4 and Ca concentrations and the highest TDS values (n = 31 surface water plus groundwater). Streamwater samples that are closest to the Casino deposit (1013 and 1014) are plotted as unique symbols.

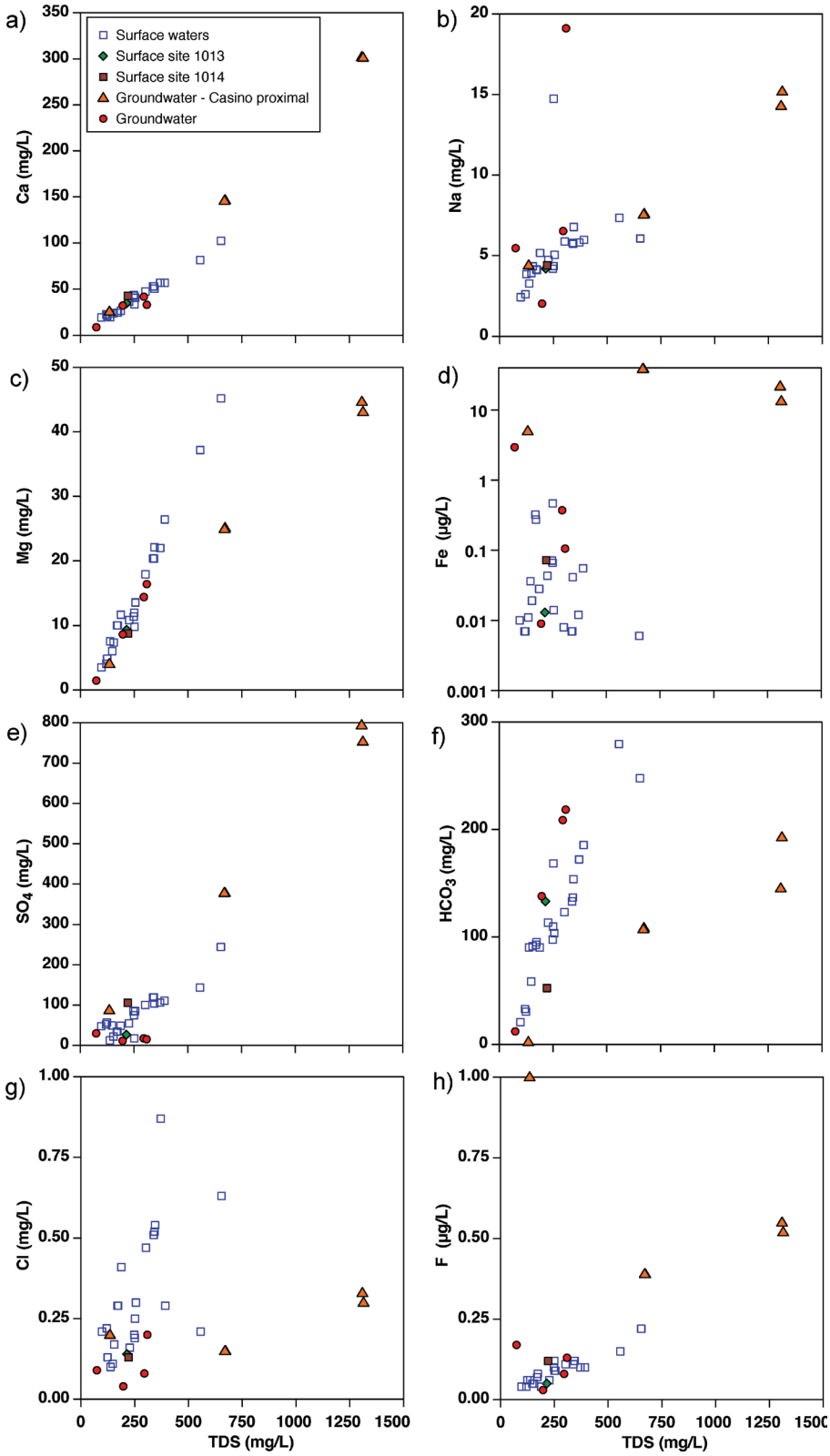

Figure 15. Plots of major ion, Fe and F concentrations versus total dissolved solids (TDS) for surface and groundwaters in the Casino deposit area (n = 31 surface water plus groundwater): **a)** Ca; **b)** Na; **c)** Mg; **d)** Fe; **e)** SO_4; **f)** HCO_3; **g)** Cl; and **h)** F. Streamwater samples that are closest to the Casino deposit (1013 and 1014) are plotted as unique symbols.

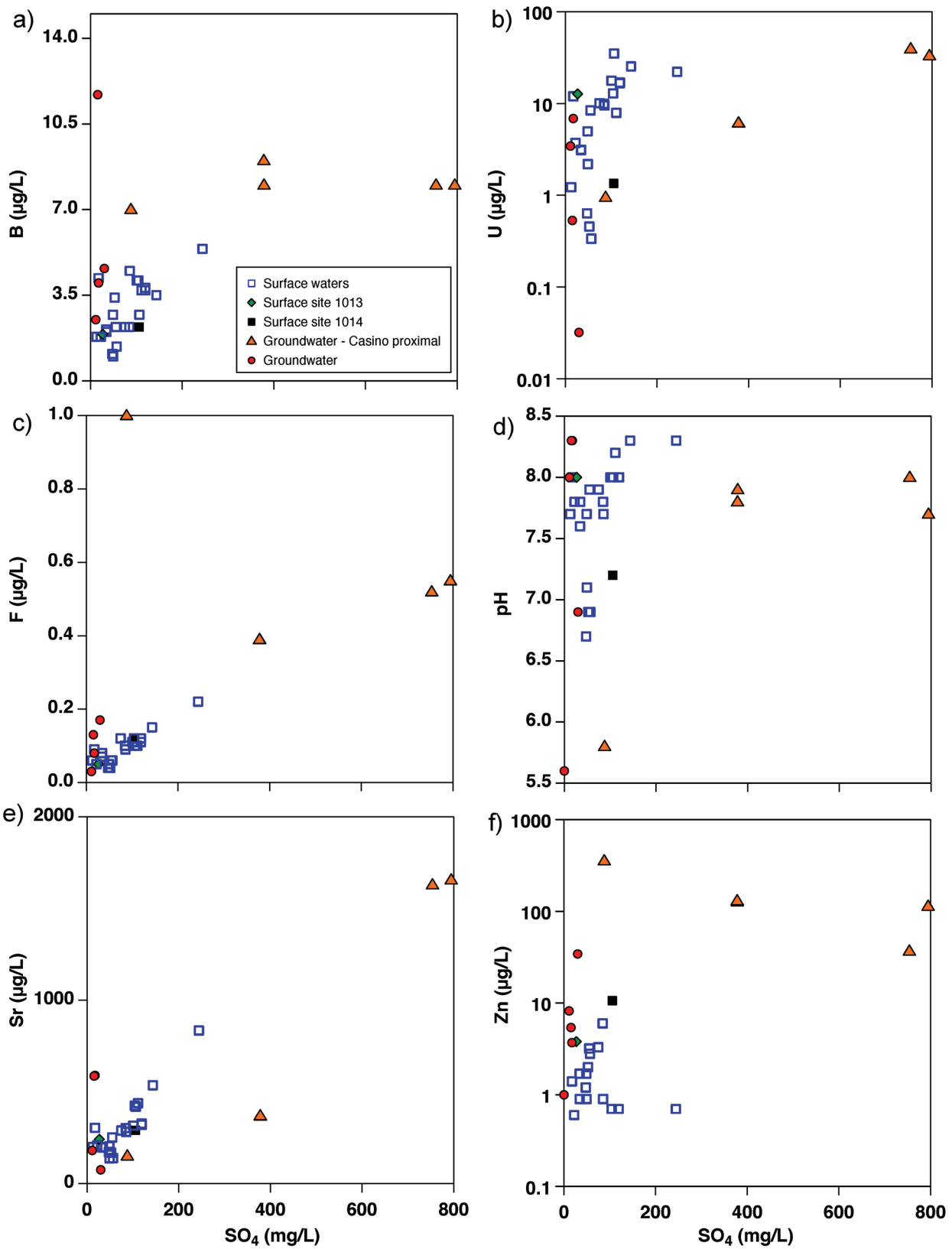

Figure 16. Plots of trace-element concentrations and pH versus SO_4 concentration for surface and groundwaters in the Casino deposit area (n = 31 surface water plus groundwater): **a)** B; **b)** U; **c)** F; **d)** pH; **e)** Sr; and **f)** Zn. Streamwater samples that are closest to the Casino deposit (1013 and 1014) are plotted as unique symbols.

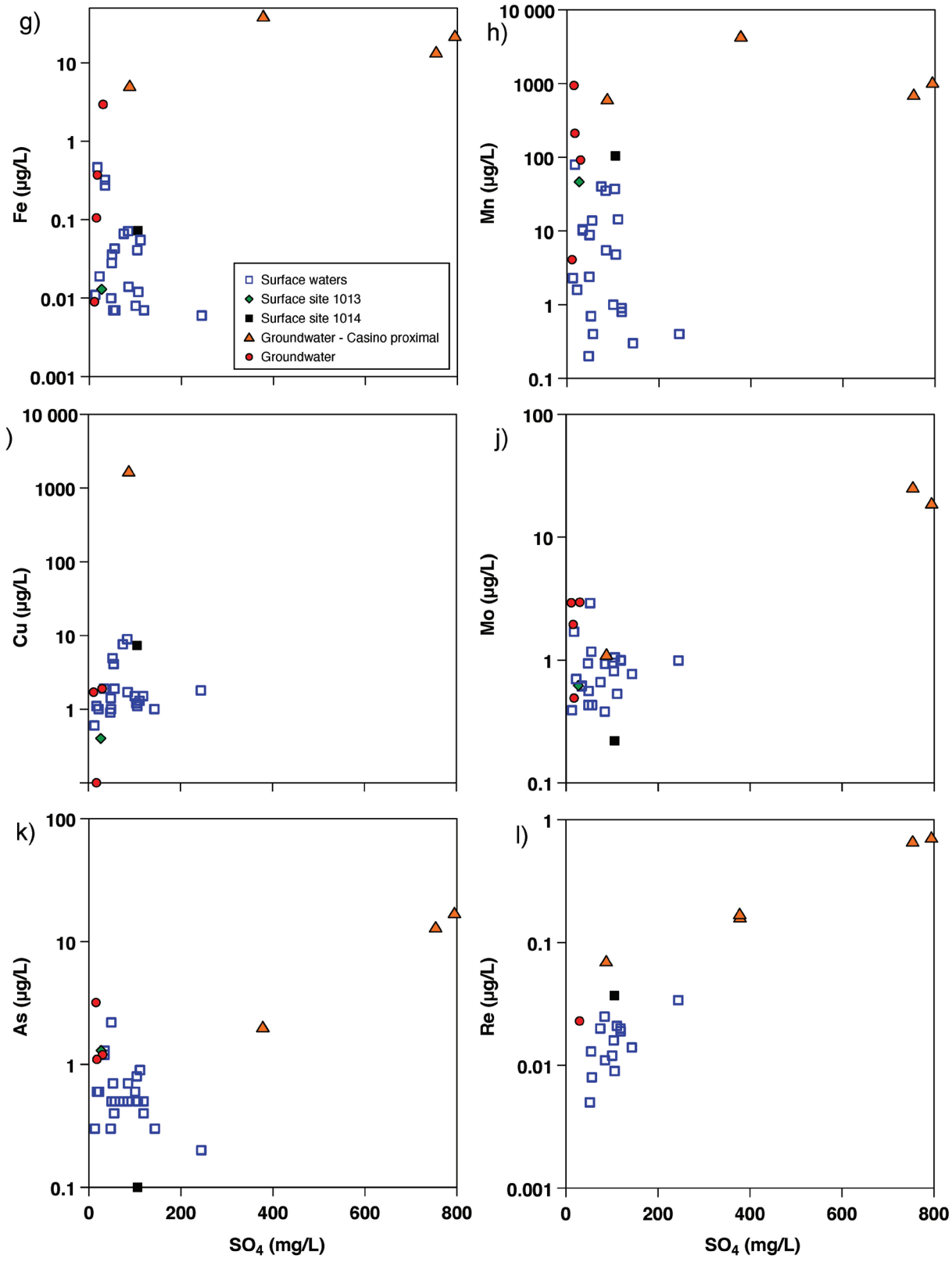

Figure 16 (cont.). Plots of trace-element concentrations and pH versus SO_4 concentration for surface and groundwaters in the Casino deposit area (n = 31 surface water plus groundwater): **g)** Fe; **h)** Mn; **i)** Cu; **j)** Mo; **k)** As; and **l)** Re. Streamwater samples that are closest to the Casino deposit (1013 and 1014) are plotted as unique symbols.

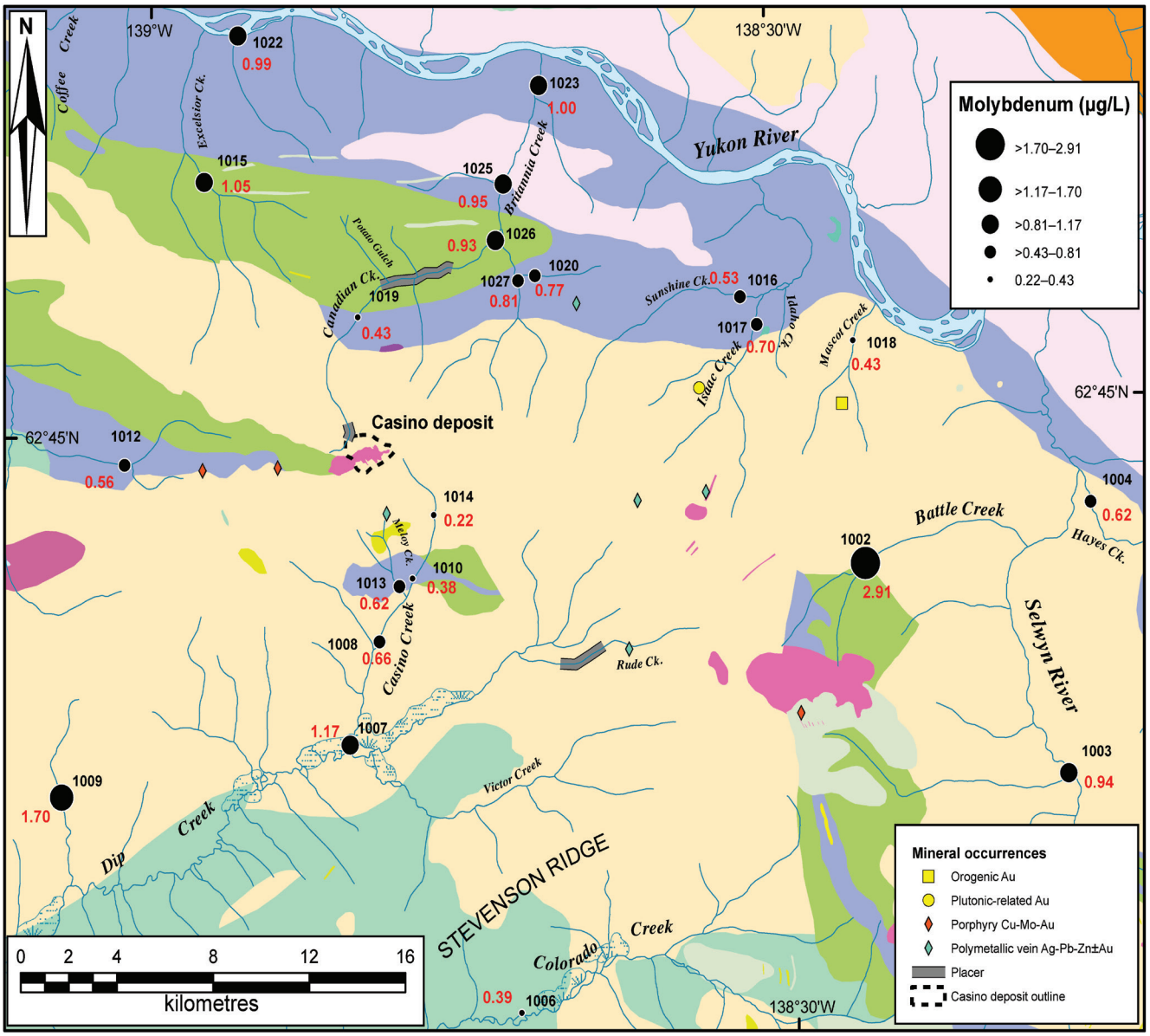

Figure 17. Concentrations of Mo in streamwater samples (n = 22) collected in 2017 in the Casino deposit area. Sample numbers are labelled in black; values are reported in red. *See* Figure 2 for bedrock geology legend.

Gold grains

Numerous 25 to 100 µm gold grains were recovered from bedrock samples examined in this study; this is similar to the gold grain-size range (50–70 µm) reported by Huss et al. (2013) for the hypogene zone, but Chapman et al. (2014) reported a broader range (5–1000 µm). The largest dimension of approximately 80% of the gold grains in stream-sediment samples from creeks immediately draining the Casino deposit (Table 3) is similar (25–200 µm) to that for bedrock samples. Not surprisingly, gold grain shapes in local creeks around Casino are a combination of modified and reshaped, reflecting fluvial transport.

Based on gold grain alloy compositions and mineral inclusion assemblages, Chapman et al. (2014, 2018) concluded that gold in the Canadian Creek placer occurrence downstream of Potato Gulch was a mixture of grains derived from the Casino deposit and from shallow epithermal mineralization. The chemistry and inclusion compositions of gold grains in GSC samples are under investigation and will be compared to the results of Chapman et al. (2014, 2018) in future work.

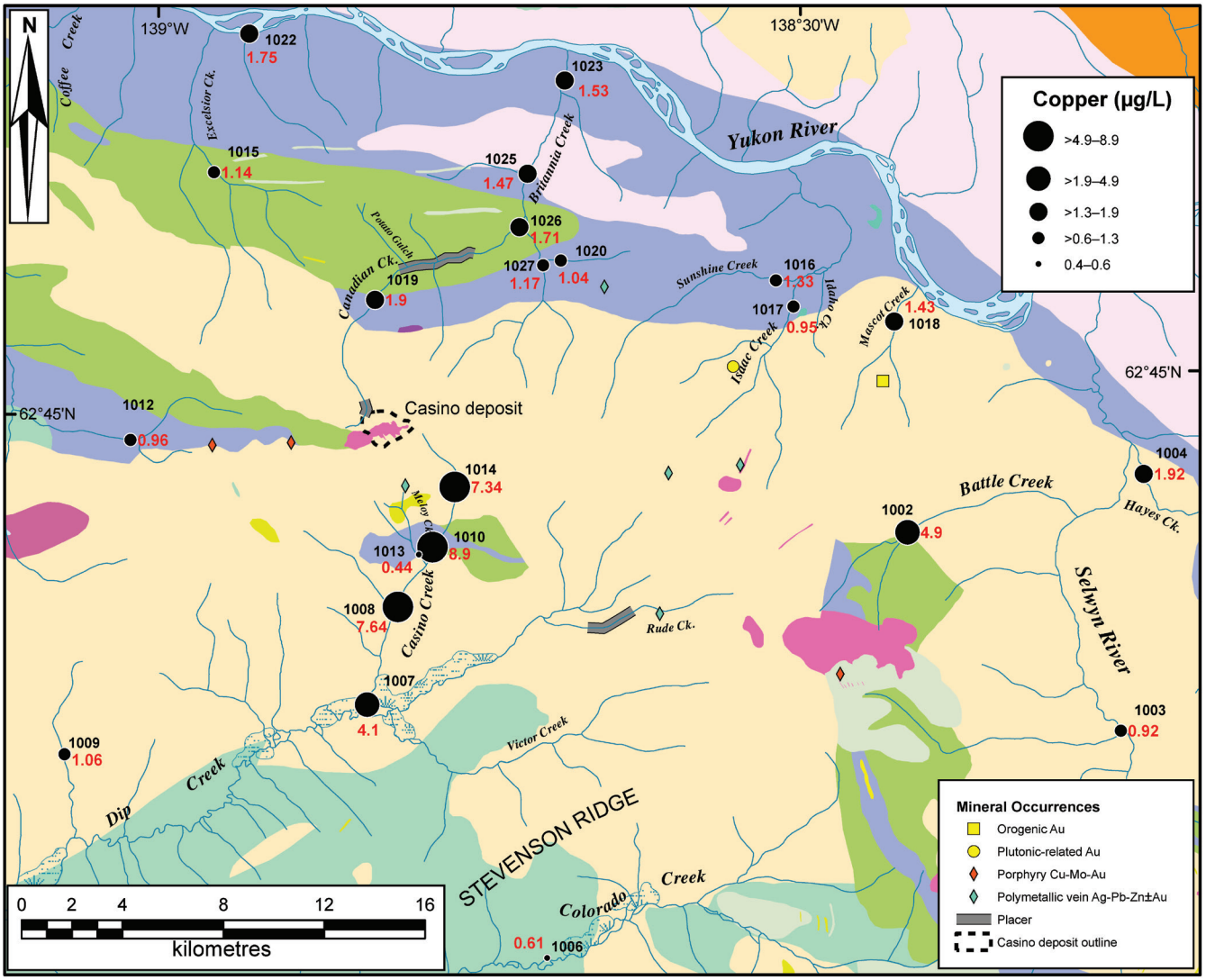

Figure 18. Concentrations of Cu in streamwater samples collected in 2017 in the Casino deposit area. Samples numbers are labelled in black; values are reported in red. *See* Figure 2 for bedrock geology legend.

Comparison of local creeks draining the deposit

Abundances for selected indicator minerals in samples from the creeks that drain the Casino deposit (Casino, Meloy, Canadian, Britannia) are listed in Table 4. Thresholds between background and anomalous indicator mineral abundances were estimated using distal samples 1006 and 1009, which contain very few indicator minerals and have low metals values in stream sediments. This estimation of background based on just two samples is not optimal and could be improved if additional heavy-mineral sampling was conducted in the area.

Abundances of gold, chalcopyrite, pyrite, molybdenite, sphalerite, jarosite, goethite, and scheelite are greater than the values reported for samples 1006 and 1009. Meloy Creek, which drains the Bomber Pb-Zn-Ag vein area, displays a similar suite of indicator minerals without gold and with the addition pyrolusite and plumbojarosite. The presence of pyrolusite in this sample was not unexpected because black manganese coatings were observed on stream cobbles and pebbles at this site. Pyrolusite and plumbojarosite likely formed from the weathering of the Pb-Zn-Ag veins. A pipe discharging water from the Bomber vein adit into the headwaters of Meloy Creek may have contributed to the formation of pyrolusite grains or pyrolusite coatings on other mineral grains in the stream bed at this location.

Table 4. Abundances of selected indicator minerals and trace elements in stream sediments and stream water in samples from the four creeks draining the Casino deposit: Casino, Meloy, Canadian, and Britannia. Samples are listed in order of increasing distance downstream from the deposit. Thresholds for elements in stream sediments are the upper bounds of background variability and were calculated following log transformation of the Yukon-Tanana subset of the 1986 Geological Survey of Canada reconnaissance data (n = 1301; *see* McCurdy et al. (2019) for additional explanation). Background abundances of indicator minerals in stream sediment and elements in water were defined using samples 1006 and 1009. Values greater than the background threshold are highlighted in a colour unique for those minerals that have a direct relationship to an element(s) (e.g. gold grains and Au in ppb). Mineral counts are normalized to 10 kg sample mass and reported for the 0.25 to 0.5 mm >3.2 specific gravity fraction unless otherwise indicated.

Heavy minerals in stream sediment (0.25–05 mm, >3.2 SG)

Sample site	Creek	Distance down stream from deposit (km)	Gold grains	Chalco	Moly	Sphal	Plumbo	Scheel	Jaro SG 2.8–3.2	Pyrol	Tur SG 2.8–3.2			
threshold**			1	0	0	0	0	1	45	0	30			
1014	Casino	2.5	1	0	1	9	0	0	132	0	0			
1013	Meloy	3*	0	4	0	11	86	2	36	2518	0			
1019	Canadian	3	28	7	0	1	0	23	31	0	0			
1010	Casino	6	8	0	0	0	0	37	183	0	11			
1008	Casino	9	21	2	0	0	0	4	291	0	4			
1026	Canadian	10	6	2	0	0	0	2	1231	0	62			
1025	Britannia	12.5	19	0	0	0	0	2	1327	0	88			
1007	Casino	13.5	44	0	0	0	0	40	0	0	0			
1023	Britannia	16.5	2	1	1	0	0	0	183	0	0			

Chalco: chalcopyrite; Moly: molybdenite; Sphal: sphalerite; Plumbo: plumbojarosite; Scheel: scheelite; Jaro: jarosite; Pyrol: pyrolusite; Tur: tourmaline; SG: specific gravity

Stream sediment (<0.177 mm)

Sample site	Creek	Distance down stream from deposit (km)	Au Fire (ppb)	Au AR (ppb)	Au INAA (ppb)	Cu AR (ppm)	Mo AR (ppm)	Ag AR (ppb)	Pb AR (ppm)	Zn AR (ppm)	Cd AR (ppm)	Sb AR (ppm)	W INAA (ppm)	Mn AR (ppm)
threshold**			134	12	2**	57	3.8	309	18	123	0.5	0.9	2**	746**
1014	Casino	2.5	46	16	28	943	3.8	441	50	394	3.1	1.3	4	1850
1013	Meloy	3*	11	4	6	57	1.1	1917	568	439	4.8	5.7	2	2194
1019	Canadian	3	120	16	57	115	16.8	412	20	148	1.6	1.4	13	686
1010	Casino	6	4056	24	17	441	3.3	383	37	274	2.0	1.1	6	1154
1008	Casino	9	8	3	<2	59	0.6	139	17	89	0.5	0.5	1	565
1026	Canadian	10	135	21	211	49	5.0	173	15	97	0.7	1.7	11	576
1025	Britannia	12.5	76	8	61	29	2.4	120	12	80	0.4	1.4	4	562
1007	Casino	13.5	64	2	120	61	1.0	201	40	104	0.6	0.9	9	485
1023	Britannia	16.5	30	21	96	32	2.9	116	12	71	0.3	1.2	5	531

Fire: fire assay/inductively coupled plasma mass spectrometry; AR: aqua regia/inductively coupled plasma mass spectrometry
INAA: instrumental neutron activation analysis

Table 4 (cont.). Abundances of selected indicator minerals and trace elements in stream sediments and stream water in samples from the four creeks draining the Casino deposit: Casino, Meloy, Canadian, and Britannia. Samples are listed in order of increasing distance downstream from the deposit. Thresholds for elements in stream sediments are the upper bounds of background variability and were calculated following log transformation of the Yukon-Tanana subset of the 1986 Geological Survey of Canada reconnaissance data (n = 1301; *see* McCurdy et al. (2019) for additional explanation). Background abundances of indicator minerals in stream sediment and elements in water were defined using samples 1006 and 1009. Values greater than the background threshold are highlighted in a colour unique for those minerals that have a direct relationship to an element(s) (e.g. gold grains and Au in ppb). Mineral counts are normalized to 10 kg sample mass and reported for 0.25 to 0.5 mm >3.2 specific gravity fraction unless otherwise indicated.

Stream water

Sample site	Creek	Distance down stream from deposit (km)	Cu (µg/L)	Mo (µg/L)	Ag (µg/L)	Pb (µg/L)	Zn (µg/L)	Cd (µg/L)	Sb (µg/L)	Co (µg/L)	W (µg/L)	Mn (µg/L)	Re (µg/L)	SO_4 (mg/L)
threshold **			1.1	1.70	0.01	0.02	1.4	0.02	0.05	0.15	0.02	79.3	0.005	17.3
1014	Casino	2.5	7.3	0.22	<0.005	0.01	10.6	0.18	0.07	3.86	<0.02	104.1	0.037	105.5
1013	Meloy	3*	0.4	0.62	<0.005	0.15	3.8	0.07	0.19	<0.05	<0.02	46.4	<0.005	26.7
1019	Canadian	3	1.9	0.43	<0.005	<0.01	2.8	0.03	0.21	<0.05	<0.02	0.4	0.008	56.7
1010	Casino	6	8.9	0.38	<0.005	0.01	6.0	0.10	0.11	1.19	<0.02	35.1	0.025	84.3
1008	Casino	9	7.6	0.66	<0.005	0.02	3.3	0.06	0.13	0.48	<0.02	40.1	0.020	74.7
1026	Canadian	10	1.7	0.93	<0.005	0.01	0.9	<0.02	0.32	<0.05	<0.02	5.5	0.011	85.2
1025	Britannia	12.5	1.5	0.95	<0.005	<0.01	<0.5	<0.02	0.24	<0.05	<0.02	1.0	0.012	100.5
1007	Casino	13.5	4.1	1.17	<0.005	0.02	3.2	0.03	0.14	0.07	<0.02	13.8	0.013	54.8
1023	Britannia	16.5	1.5	1.00	<0.005	0.01	0.7	<0.02	0.23	<0.05	<0.02	0.9	0.020	118.9

* Distance downstream from Bomber Pb-Zn-Ag veins
** refer to table caption for an explanation of calculation of thresholds for each sample medium

Comparison with other creeks in the study area

We compare the highest indicator mineral abundances for Casino, Meloy, and Canadian creeks to the highest values reported in stream sediments from other creeks in the study area and to background samples 1006 and 1009 in Table 5. Values greater than the background samples are highlighted using a different colour for each creek. Sediments downstream of the Cockfield (purple) and Zappa (pink) porphyry occurrences display similar suites of anomalous indicator minerals to the those from the creeks draining the Casino deposit (grey) with the exception of gold grains, which are much more abundant in the creeks draining the Casino deposit (Casino and Canadian). The other creeks listed in Table 5 contain noteworthy combinations of gold, sulfide minerals, secondary minerals, scheelite, and tourmaline that could indicate the presence of other types of mineralization.

Sources of minerals in streams

The presence of fresh sulfide minerals in stream sediments from Casino Creek may indicate that the creek is directly eroding less-oxidized parent material related to the Casino deposit and/or peripheral mineralization. Ongoing cryoturbation and downslope gravity movement also contributes weathered and less oxidized material to local creeks. Older gravel deposits along creeks may also be the source of some sulfide minerals.

The minor disturbance from surface exploration activity has likely had minimal impact on the mineralogical and geochemical signatures of the deposit in local creeks, except for at site 1013 on Meloy Creek, where water draining from an old adit into the headwaters of the creek 4 km upstream of the sample site has likely affected the geochemistry of the stream sediment and the water. Former placer mining operations on Canadian Creek may have contributed indicator minerals to Canadian and Britannia creeks.

Stream silt geochemistry

Comparison of local creeks draining the deposit

Abundances for selected trace elements in stream silt samples from the creeks that drain the Casino deposit (Casino, Meloy, Canadian, Britannia) are listed in Table 4. A subset of GSC reconnaissance stream-sediment data (n = 1301) from sites underlain by similar bedrock geology was used to provide a regional context in which to evaluate

Table 5. Comparison of the indicator minerals and elements in stream sediments, silt, and water from the creeks that drain the Casino deposit and other known occurrences in the area. Background thresholds for elements in stream silt are the upper bounds of background variability and were calculated following a log transformation of the Yukon-Tanana subset of the 1986 Geological Survey of Canada reconnaissance data (n = 1301; *see* McCurdy et al. (2019) for additional explanation). Thresholds for indicator minerals and elements in stream water and heavy mineral stream-sediment analyses were defined using samples 1006 and 1009. Anomalous values (greater than the corresponding threshold) are highlighted in a colour unique to each deposit/occurrence.

Sample medium	Mineral/element	Background threshold*	Casino (Casino Creek)	Casino (Canadian Creek)	Bomber veins (Meloy Creek)	Cockfield (Battle + unnamed creek)	Mascot (Mascot Creek)	Buck (Isaac Creek)	Buck (Sunshine Creek)	Marquerite (unnamed Creek)	Zappa (unnamed creek)
Stream HMC	Gold	1	44	29	0	1	3	6	0	14	1
Stream HMC	Chalcopyrite	0	4	7	4	27	1	0	1	0	13
Stream HMC	Molybdenite	0	1	0	0	3	0	0	0	0	3
Stream HMC	Pyrite	0	79	115	11	397	28	3	22	26	2113
Stream HMC	Sphalerite	0	9	1	11	0	0	0	0	0	0
Stream HMC	Bismuthinite	0	0	0	0	1	1	0	0	0	0
Stream HMC	Arsenopyrite	0	0	2	0	3	2	0	0	0	0
Stream HMC	Jarosite	45	291	1231	36	331	0	0	144	0	423
Stream HMC	Plumbojarosite	0	0	0	86	1	0	0	0	0	0
Stream HMC	Pyrolusite	0	0	0	2518	0	0	0	0	0	0
Stream HMC	Goethite	379	18 000	7700	18 000	3311	1724	840	1079	35 000	141
Stream HMC	Hematite	7576	6711	2308	1439	5298	1035	1261	7194	87 000	352
Stream HMC	Scheelite	1	40	23	2	27	4	8	36	11	35
Stream HMC	Tourmaline	30	11	62	0	27	0	0	360	0	0
Stream silt	Au AR (ppb)	12	24	21	4	8	2	4	6	3	5
Stream silt	Au INAA (ppb)		120	211	6	14	5	37	10	4	26
Stream silt	Au Fire (ppb)	134	4056	135	11	36	13	14	14	11	20
Stream silt	Cu (ppm)	57	943	115	57	111	16	22	28	28	29
Stream silt	Mo (ppm)	3.8	3.8	16.8	1.1	6	0.6	0.7	0.6	0.6	2.4
Stream silt	Ag (ppb)	309	441	412	1917	376	121	159	153	123	148
Stream silt	Pb (ppm)	18	50	20	578	25	13	10	13	9	12

Contents

Table 5 (cont.). Comparison of the indicator minerals and elements in stream sediments, silt, and water from the creeks that drain the Casino deposit and other known occurrences in the area. Background thresholds for elements in stream silt are the upper bounds of background variability and were calculated following a log transformation of the Yukon-Tanana subset of the 1986 Geological Survey of Canada reconnaissance data (n = 1301; *see* McCurdy et al. (2019) for additional explanation). Thresholds for indicator minerals and elements in stream water and heavy mineral stream-sediment analyses were defined using samples 1006 and 1009. Anomalous values (greater than the corresponding threshold) are highlighted in a colour unique to each deposit/occurrence.

Sample medium	Mineral/element	Background threshold*	Casino (Casino Creek)	Casino (Canadian Creek)	Bomber veins (Meloy Creek)	Cockfield (Battle + unnamed creek)	Mascot (Mascot Creek)	Buck (Isaac Creek)	Buck (Sunshine Creek)	Marquerite (unnamed Creek)	Zappa (unnamed creek)
Stream silt	Zn (ppm)	123	393	148	439	90	83	85	72	69	72
Stream silt	Cd (ppm)	0.5	3.1	4.8	1.6	0.9	0.4	0.6	0.4	0.4	0.5
Stream silt	Bi (ppm)	0.6	0.8	1.2	0.6	1.8	0.2	0.2	0.2	0.2	0.4
Stream silt	As (ppm)	32	31	32	30	45	27	22	32	8	30
Stream silt	Sb (ppm)	0.89	1.25	1.73	5.74	1.02	1.55	1.36	1.96	0.51	1.08
Stream silt	Te (ppm)	0.05	0.08	0.13	<0.02	0.09	0.03	0.03	0.03	<0.02	0.08
Stream silt	W (ppm)	0.6	1.8	2.5	0.2	36.3	0.2	0.2	0.2	0.2	0.7
Stream water	Cu (µg/L)	1.10	7.64	1.90	0.44	4.90	1.43	0.95	1.33	1.04	0.96
Stream water	Mo (pbb)	1.70	1.17	0.93	0.62	2.91	0.43	0.70	0.53	0.77	0.56
Stream water	Pb (µg/L)	0.02	0.02	<0.01	0.15	<0.01	<0.01	<0.01	<0.01	<0.01	<0.01
Stream water	Zn (µg/L)	1.40	10.60	2.80	3.80	2.00	1.70	0.60	<0.05	<0.05	0.90
Stream water	Cd (µg/L)	<0.02	0.18	0.03	0.07	0.06	<0.02	<0.02	<0.02	<0.02	<0.02
Stream water	Co (µg/L)	0.15	3.86	<0.05	<0.05	<0.05	<0.05	<0.05	<0.05	<0.05	<0.05
Stream water	Re (µg/L)	<0.005	0.037	0.71	<0.005	0.005	<0.005	<0.005	<0.005	0.014	<0.005
Stream water	Sb (µg/L)	0.05	0.14	0.32	0.19	0.09	0.27	0.27	0.24	0.06	0.26
Stream water	W (µg/L)	<0.02	<0.02	<0.02	<0.02	<0.02	<0.02	<0.02	<0.02	<0.02	<0.02
Stream water	Bi (µg/L)	<0.02	<0.02	<0.02	<0.02	<0.02	<0.02	<0.02	<0.02	<0.02	<0.02
Stream water	Te (µg/L)	<0.02	<0.02	<0.02	<0.02	<0.02	<0.02	<0.02	<0.02	<0.02	<0.02
Stream water	Mn (µg/L)	79.3	104.1	5.5	46.4	0.7	2.4	1.6	14.3	0.3	8.8
Stream water	SO_4 (mg/L)	17.33	105.54	85.21	26.7	52.59	48.62	22.1	111.05	143.49	49.3

HMC: heavy mineral concentrate; Fire: fire assay/inductively coupled plasma mass spectrometry; AR: aqua regia/inductively coupled plasma mass spectrometry; INAA: instrumental neutron activation analysis
* refer to table caption for an explanation of calculation of thresholds for each sample medium

the 2017 data from the Casino deposit. The fences routine in the R package rgr (Garrett, 2018) was used to estimate the upper and lower bounds of background variability for selected elements in the reconnaissance data, following log transformation of the data. Tukey fences were calculated based on the median and quartiles (25th and 75th percentiles) to obtain the interquartile range of the selected elements. The upper limit of background variability was used as the threshold between background and anomalous populations in the reconnaissance subset (*after* McCurdy et al., 2019) and compared to the highest values reported for each creek sampled in 2017 (Table 4). The elements well above the threshold values are Au, Ag, Bi, Cd, Cu, Mn, Mo, Pb, Sb, Te, W, and Zn and are highlighted with coloured cells in Table 4. The Meloy Creek sample exceeds the threshold for Ag, Cd, Mn, Pb, Sb, and Zn, reflecting its proximity to the Bomber Pb-Zn-Ag veins and water drainage from the old adit into the headwaters.

The pathfinder elements in stream sediments downstream from the Casino deposit are similar to the elements (Cu, Mo, Au) reported in previous stream-sediment surveys around porphyry copper deposits (e.g. Coope, 1973; Huff, 1976; Learned et al., 1985; Britten and Marr, 1995; Richardson, 1995). In our study, Ag, Bi, Cd, Mn, Pb, Sb, Te, W, and Zn are also potential porphyry copper pathfinders in stream silt samples.

Comparison with other creeks in study area

We compare the threshold values to the most abundant indicator minerals and elements reported in other creeks in the study area in Table 5. Anomalous values are highlighted with colours corresponding to each creek. Sediments downstream of the Cockfield occurrence (purple) display similar anomalous element concentrations to those from the creeks draining the Casino deposit (grey) with the exception of Au, which is higher in the creeks draining the Casino deposit. The stream silt geochemical values for the other creeks listed in Table 5 are unremarkable.

Gold in stream sediments

Gold concentrations in 2017 stream-sediment samples are considerably higher in the 30 g aliquots analyzed by fire assay and INAA than in the 0.5 g aliquots analyzed using an aqua regia digestion. The 30 g total (INAA and fire assay) methods show greater contrast between background and anomalous Au concentrations and the Au-rich signature of the Casino deposit (Fig. 12). Aqua regia (0.5 g) values for the 2017 samples may be significantly lower than those of the fire assay and INAA methods because some gold is tied up in undigested minerals such as quartz and/or by the nugget effect because of the smaller aliquot mass (0.5 g versus 30 g). Comparisons of aqua regia Au values to those determined by INAA and fire assay provide indications of amount of Au that might be present as inclusions in mineral phases not dissolved in aqua regia and also not visible in HMCs. This information is useful to the exploration geologist/geochemist. Additional analyses for Au using aqua regia and ICP-MS on 30 g aliquots of the 2017 samples would provide insight into the reasons for the observed differences.

Usefulness of pXRF analysis

A few studies have reported the use of pXRF to characterize the chemical composition of dried, sieved stream-sediment samples in glaciated (Luck and Simandl, 2014; Mackay et al., 2016) and unglaciated (De Almeida et al., 2019) terrains. This study is the first to report data for unsieved stream silt samples and to compare pXRF analyses to aqua regia and ICP-MS as well as INAA analyses of the same samples. The pXRF data display similar trends to commercial laboratory data for Mn, Fe, Cu, Zn, As, Mo (Fig. 13a–f), and S. Greater similarity between element concentrations measured by pXRF and aqua regia or INAA methods would be expected if the samples were dried and sieved prior to pXRF analysis. This study demonstrates that pXRF analyses on unsieved samples can quickly define reasonable differences in concentrations of some elements and can be used to identify geochemical anomalies and guide follow-up sampling while still in the field, saving the project time and money.

Water geochemical patterns

Comparison of creeks

The abundances of selected trace elements in streamwater samples from the creeks that directly drain the Casino deposit are listed in Table 4. Thresholds between background and anomalous streamwater samples were defined using estimated background samples 1006 and 1009. Elements with abundances well above the threshold include Cd, Co, Cu, Zn, and SO_4. The Meloy Creek sample (sample 1013) exceeds the threshold for Cd, Pb, Sb, and SO_4, reflecting its proximity to the Bomber Pb-Zn-Ag veins and the effect of water drainage from the old adit into the headwaters.

We compare the elements with the highest concentrations in the local creeks to those with the highest concentrations in other creeks in the study area in Table 5. Casino and Canadian creek waters (grey) have some of the highest Cu, Mo, Zn, Cd, and Re values for streamwater samples in this study. These high metal values are not unexpected because Archer and Main (1971) reported values of up to 2030 µg/L Cu in stream water from a small creek that drains into upper Casino Creek. Streamwater sample 1013 from Meloy Creek (blue) contains the highest concentration of Pb (0.15 µg/L) reported in this study, as well as high concentrations of

Zn and Cd. This sample is downstream from the Bomber Pb-Zn-Ag veins, and water draining from the old adit into the headwaters of Meloy Creek may have contributed to these high values (Casino Mining Corporation, 2014). Samples 1002 and 1003, from downstream of the Cockfield occurrence (purple), also have high values of Cu, Mo, Zn, and Cd in stream water. Mascot Creek (green) displays elevated concentrations of Cu, Zn, Sb, and SO_4.

Pathfinders in streamwater samples downstream from the Casino deposit reported in this study are similar to those reported in previous streamwater studies of porphyry copper deposits (Cu, Mo, Au, SO_4; e.g. Coope, 1973; Learned et al., 1985; Rebagliati et al., 1995; Taufen, 1997; Eppinger et al., 2012; Mathur et al., 2013). In our study, Cd, Co, Mn, Pb, Re, and Zn are also potential pathfinders for porphyry Cu-Mo-Au deposits in stream water.

Comparison of three sample media

Table 4 compares indicator mineral abundances to selected trace-element concentrations in stream sediments and streamwater in samples from the creeks draining the Casino deposit. Coloured cells are assigned so that a colour is unique to a mineral and its related element(s) (e.g. chalcopyrite and Cu concentrations, sphalerite and Zn concentrations). In general, samples that contain indicator minerals also have elevated concentrations of corresponding elements. This is most obvious between Au concentration and the number of gold grains. All stream-sediment samples in Table 4 contain gold grains, except that from Meloy Creek. Stream sediments contain corresponding anomalous contents of Au (INAA), with very low Au values in samples 1013 and 1008. Trace-element measurements of stream sediment samples will reflect the presence of detrital grains that contain these elements as well as material adsorbed onto the surface of mineral grains on the stream bed.

The Zn content in five stream silt samples is anomalous, but sphalerite was only recovered from three of these samples. In contrast, W content is elevated in three samples, but noteworthy numbers of scheelite grains were detected in seven samples. High Pb content is apparent only in silt sample 1013, which also contains plumbojarosite. Samples 1008, 1023, and 1025 have unremarkable stream silt and water chemistry that would not normally generate further interest, yet the presence of gold grains, chalcopyrite, scheelite, and jarosite in these three samples is worthy of further investigation.

Indicator minerals recovered from local creeks are physical evidence of the presence of mineralization (gold grains, chalcopyrite, molybdenite, sphalerite) or the weathering of the mineralization (jarosite, goethite, plumbojarosite, beudantite). They can be examined with a binocular or scanning electron microscope and chemically analyzed to provide detailed information about the nature of the mineralizing system. They may be present in very low abundances (e.g. 1–2 grains of molybdenite in a 10 kg sample) at sites that do not have a coincident anomalous geochemical signature in stream silt samples.

Indicator mineral information can be especially important for reconnaissance and regional-scale surveys, where the presence of a few indicator grains in broadly spaced samples may indicate that a region is worthy of more detailed sampling. Government and exploration surveys in which detailed follow up is not possible during the same field season would benefit the most from the addition of indicator mineral sampling to stream-sediment sampling programs.

CONCLUSIONS AND IMPLICATIONS FOR EXPLORATION

The purpose of this study is not to redefine the already well-known geochemical signature of the Casino deposit or prove that stream silt geochemistry is well suited to porphyry copper exploration. Instead, the focus is testing the use of indicator minerals as an additional porphyry copper exploration tool for unglaciated terrain. The Casino test site is well suited to this type of study because its geochemical signature in local stream sediments and water is already well known and because the deposit has not yet been mined. The abundances of indicator minerals in stream sediments reported in this paper offer a guide to what might be expected downstream of porphyry Cu-Au deposits in the unglaciated terrain of the Yukon. Indicator minerals provide additional information that silt geochemistry alone cannot.

This study is the first detailed indicator mineral study around a major porphyry copper deposit in unglaciated terrain in Canada. The deposit and/or peripheral mineralization has an obvious indicator mineral signature in stream sediments that consists of, in order of effectiveness, gold>chalcopyrite >molybdenite>sphalerite>jarosite>goethite>pyrite, and is detectable at least 14 km downstream from the deposit in Casino Creek. Similar indicator mineral patterns were detected in creeks downstream of other local porphyry occurrences (i.e. Cockfield and Zappa).

Estimates of threshold values for indicator minerals and streamwater based on only two samples were used to evaluate the data. As more stream sediment heavy mineral sampling is conducted in this region, these thresholds will be refined and improved. Readers are encouraged to read the individual open files that report the raw data for indicator minerals, stream sediments, and stream water and to examine the individual mineral and element distribution maps to fully interpret and compare the data sets.

Stream-sediment sampling is a highly successful geochemical method for porphyry copper exploration globally. Our limited sampling around the Casino deposit confirms this fact. Thirty years after the GSC's reconnaissance-scale survey of the Casino region, the Cu signature in stream sediments around the Casino deposit is almost the same. Few,

if any, stream-sediment studies have ever been repeated 30 years later to demonstrate the similarities or differences in geochemical signatures over time.

FUTURE WORK

Indicator mineral methods are now widely used for precious- and base-metal exploration in the glaciated terrain of Canada. Regional indicator mineral surveys have not been conducted across the unglaciated part of the Yukon and have the potential to provide further insights into the effectiveness of heavy minerals as indicators during porphyry copper and gold exploration in this part of Canada.

Automated SEM-based methods (MLA, QEMSCAN) are useful for detecting indicator minerals in the fine fraction of HMCs (Lehtonen et al., 2015; Layton-Matthews et al., 2017; Lougheed et al., in press). Grain mounts are expensive to prepare and analyze, thus automated SEM-based methods are not yet routinely applied to every heavy mineral sample in government surveys. Future research will include MLA analysis of the less than 0.25 mm heavy and mid-density fractions of bedrock and stream sediments from the Casino deposit to determine the indicator minerals present and how their distribution in creeks is influenced by grain size. Mineral chemistry characterization of gold, tourmaline, scheelite, and magnetite from bedrock and stream sediments is ongoing and will be reported in future publications.

The Cu isotopic compositions of stream water (2017 GSC samples) and groundwater samples collected from drillholes by Western Copper and Gold are being analyzed to investigate the fractionation of copper as a function of sulfide weathering and aqueous transport. Additionally, the isotopic signatures of water will be compared to those of oxidized and fresh mineralized bedrock, and stream sediments. These combined data will provide valuable information regarding the utility of Cu isotopes in aqueous samples as exploration vectors to sulfide mineralization. The Cu isotopic composition of waters may also be useful for indicating if isolated Cu anomalies, such as that measured in water sample 1002 from Battle Creek (Cockfield occurrence; Fig. 18), are related to porphyry copper mineralization. Future investigations of stream silt geochemistry will include aqua regia and ICP-MS analysis of 30 g aliquots to compare the Au content to that determined on 30 g aliquots by INAA and fire assay.

ACKNOWLEDGMENTS

This paper is a contribution to Geological Survey of Canada's Targeted Geoscience Initiative program, through the Porphyry-style Mineral Systems project, Activity P-3.3: Mineralogical markers of fertility porphyry-style systems. We gratefully acknowledge Western Copper and Gold Corporation and the Casino Mining Corporation, and in particular M. Mioska and H. Brown, for providing access, assistance, and knowledge of the deposit. We thank K. Spalding (expediting services), B. Younker (Casino camp manager), A. Turcotte, and L. Turcotte (Casino water sampling) for facilitating GSC fieldwork, and J. Bond, Yukon Geological Survey, for sharing geological information and advice for the Casino area. This paper benefited from thoughtful reviews by D. Arne (Telemark Geosciences), P. Gammon (GSC), and A. Plouffe (GSC), and comments by L. Jackson (GSC–retired).

REFERENCES

Archer, A.R. and Main, C.A., 1971. Casino, Yukon – A geochemical discovery of an unglaciated Arizona-type porphyry; *in* Geochemical Exploration, Proceedings of the 3rd international geochemical exploration symposium, (ed.) R.W. Boyle; Canadian Institute of Mining and Metallurgy, Special Volume 11, p. 67–77.

Arne, D., Mackie, R., and Pennimpede, C., 2018. Catchment analysis of re-analyzed regional stream sediment geochemical data from the Yukon; EXPLORE, Association of Applied Geochemists no. 179, p. 1–13.

Averill, S.A., 2001. The application of heavy indicator mineralogy in mineral exploration with emphasis on base metal indicators in glaciated metamorphic and plutonic terrains; *in* Drift exploration in glaciated terrain, (ed.) M.B. McClenaghan, P.T. Bobrowsky, G.E.M. Hall, and S.J. Cook; Geological Society, London, Special Publication 185, p. 69–81. https://doi.org/10.1144/GSL.SP.2001.185.01.04

Averill, S.A., 2011. Viable indicators in surficial sediments for two major base metal deposit types: Ni-Cu-PGE and porphyry Cu; Geochemistry: Exploration, Environment, Analysis, v. 11, p. 279–291. https://doi.org/10.1144/1467-7873/10-IM-022

Baksheev, I.A., Prokof'ev, V.Y., Zaraisky, G.P., Chitalin, A.F., Yapaskurt, V.O., Nikolaev, Y.N., Tikhomirov, P.L., Nagornaya, E.V., Rogacheva, L.I., Gorelikova, N.V., Kononov, O.V., 2012. Tourmaline as a prospecting guide for the porphyry-style deposits; European Journal of Mineralogy, v. 24, no. 6, p. 957–979. https://doi.org/10.1127/0935-1221/2012/0024-2241

Barkov, A.Y., Martin, R.F., Shi, L., LeBarge, W., and Fedortchouk, Y., 2008. Oscillatory zoning in stanniferous hematite and associated W-and Bi-rich minerals from Canadian Creek, Yukon, Canada; The Canadian Mineralogist, v. 46, no. 1, p. 59–72. https://doi.org/10.3749/canmin.46.1.59

Beckett-Brown, C.E., McDonald, A.M., and McClenaghan, M.B., 2019. Unravelling tourmaline in mineralized porphyry systems: assessment as a valid indicator mineral; *in* Targeted Geoscience Initiative: 2018 report of activities, (ed.) N. Rogers; Geological Survey of Canada, Open File 8549, p. 345–351. https://doi.org/10.4095/313669

Bond, J.D. and Lipovsky, P.S., 2011. Surficial geology, soils and permafrost of the northern Dawson Range; *in* Yukon Exploration and Geology 2010, (ed.) K.E. MacFarlane, L.H. Weston, and C. Relf; Yukon Geological Survey, p. 19–32.

Bond, J.D. and Lipovsky, P.S., 2012a. Surficial geology of Colorado Creek (NTS 115 J/10) Yukon; Yukon Geological Survey, Open File 2012-2, scale 1:50 000.

Bond, J.D. and Lipovsky, P.S., 2012b. Surficial geology Selwyn River (NTS 115 J/09) Yukon; Yukon Geological Survey, Open File 2012-1, scale 1:50 000.

Bond, J.D. and Sanborn, P.T., 2006. Morphology and geochemistry of soils formed on colluviated weathered bedrock: case studies from unglaciated upland slopes in west-central Yukon; Yukon Geological Survey, Open File 2006-19, 70 p.

Bostock, H.S., 1959. Yukon Territory; *in* Tungsten deposits of Canada; Geological Survey of Canada, Economic Geology Series, no. 17, p. 14–37.

Bostock, H.S., 1970. Physiographic regions of Canada; Geological Survey of Canada, Canadian Geoscience Map 1254A, scale 1:5 000 000. https://doi.org/10.4095/108980

Bouzari, F., Hart, C.J.R., Bissig, T., and Barker, S., 2016. Hydrothermal alteration revealed by apatite luminescence and chemistry: a potential indicator mineral for exploring covered porphyry copper deposits; Economic Geology, v. 111, p. 1397–1410. https://doi.org/10.2113/econgeo.111.6.1397

Bower, B., Payne, J., DeLong, C., and Rebagliati, C.M., 1995. The oxide-gold, supergene and hypogene zones at the Casino gold-copper-molybdenum deposit, west central Yukon; *in* Porphyry deposits of the northwestern Cordillera of North America, (ed.) T.G. Schroeter; Canadian Institute of Mining, Metallurgy and Petroleum, Special Volume 46, p. 352–366.

Britten, R.M. and Marr, J.M., 1995. The Eaglehead porphyry copper prospect system, northern British Columbia; *in* Porphyry deposits of the northwestern Cordillera of North America, (ed.) T.G. Schroeter; Canadian Institute of Mining and Metallurgy, Special Volume 46, p. 530–533.

Canil, D., Grondahl, C., Laourse, T., and Pisiak, L.K., 2016. Trace elements in magnetite from porphyry Cu-Mo-Au deposits in British Columbia, Canada; Ore Geology Reviews, v. 72, p. 1116–1128. https://doi.org/10.1016/j.oregeorev.2015.10.007

CANMET, 2020. STSD-1 to STSD-4 certificate of analysis. <https://www.nrcan.gc.ca/our-natural-resources/mining-resources/certified-reference-materials/discontinued-certified-reference-materials/stsd-1-stsd-4-certificate-analysis/8023> [accessed January 24, 2020]

Casino Mining Corporation, 2014. Water quality; Chapter 7 *in* Project proposal Yukon Environmental Socio-economic Assessment Board (YESAB) submission, Volume 3. <https://casinomining.com/project/yesab-proposal/> [accessed November 5, 2019]

Casselman, S. and Brown, H., 2017. Casino porphyry copper-gold-molybdenum deposit, central Yukon (Yukon MINFILE 115J 028); *in* Yukon exploration and geology overview 2016, (ed.) K.E. MacFarlane; Yukon Geological Survey, p. 61–74.

Chapman, R.J., Grimshaw, M.R., Allan, M.M., Mortensen, J.K., Wrighton, T.M., and Casselman, S., 2014. Pathfinder signatures in placer gold derived from Au-bearing porphyries; *in* Yukon exploration and geology 2014, (ed.) K.E. MacFarlane, M.G. Nordling, and P.J. Sack; Yukon Geological Survey, p. 21–31.

Chapman, J.B., Plouffe, A., and Ferbey, T., 2015. Tourmaline: the universal indicator?; *in* Short course No. 2, Application of indicator mineral methods to exploration, 27th international applied geochemistry symposium, Tucson; Association of Applied Geochemists, p. 25–31.

Chapman, R.J., Allan, M.M., Mortensen, J.K., Wrighton, T.M., and Grimshaw, M.R., 2018. A new indicator mineral methodology based on generic Bi-Pb-Te-S mineral inclusion signature in detrital gold from porphyry and low/intermediate sulfidation epithermal environments in Yukon Territory, Canada; Mineralium Deposita, v. 53, p. 815–834. https://doi.org/10.1007/s00126-017-0782-0

Colpron, M., Nelson, J.L., and Murphy, D. C., 2006. A tectonostratigraphic framework for the pericratonic terranes of the northern Cordillera; *in* Paleozoic evolution and metallogeny of pericratonic terranes at the Ancient Pacific Margin of North America, Canadian and Alaskan Cordillera, (ed.) M. Colpron and J.L. Nelson; Geological Association of Canada, Special Paper 45, p. 1–23.

Colpron, M., Israel, S., Murphy, D., Pigage, L., and Moynihan, D., 2016. Yukon bedrock geology map; Yukon Geological Survey, Open File 2016-1, scale 1:1 000 000.

Cooke, D.R., Baker, M., Hollings, P., Sweet, G., Chang, Z., Danyushevsky, L.D., Gilbert, S., Zhou, T., White, N.C., Gemmell, J.B., and Inglis, S.I., 2014. New advances in detecting the distal geochemical footprints of porphyry systems – epidote mineral chemistry as a tool for vectoring and fertility assessments; Paper 7 *in* Building exploration capability for the 21st century; Society of Economic Geologists, Special Publication 18, p. 127–152.

Cooke, D.R., Agnew, P., Hollings, P., Baker, M., Chang, Z., Wilkinson, J.J., White, N.C., Zhang, L., Thompson, J., Gemmell, J.B., Fox, N., Chen, H., and Wilkinson, C.C., 2017. Porphyry indicator minerals (PIMS) and porphyry vectoring and fertility tools (PVFTS) – indicators of mineralization styles and recorders of hypogene geochemical dispersion haloes; *in* Proceedings of Exploration 17: Sixth Decennial International Conference on Mineral Exploration, (ed.) V. Tschirhart and M.D. Thomas; p. 457–470.

Coope, J.A., 1973. Geochemical prospecting for porphyry copper-type mineralization – a review; Journal of Geochemical Exploration, v. 2, no. 2, p. 81–102. https://doi.org/10.1016/0375-6742(73)90008-3

Day, S.J.A., Wodicka, N., and McMartin, I., 2013. Preliminary geochemical, mineralogical and indicator mineral data for stream silts, heavy mineral concentrates and waters, Lorillard River area, Nunavut (parts of NTS 56-A, -B, and -G); Geological Survey of Canada, Open File 7428, 11 p. https://doi.org/10.4095/293113

De Almeida, G.S., Marques, E.D., da Silva, F.J., Pinto, C.P., and Silva-Filho, E.V., 2019. Application of pXRF (field portable X-ray fluorescence) technique in fluvial sediments geochemical analysis – Bule Stream, Minas Gerais State, Brazil; Journal of Sedimentary Environments, v. 4, p. 143–158. https://doi.org/10.12957/jse.2019.43279

DiLabio, R.N.W., 1990. Classification and interpretation of the shapes and surface textures of gold grains from till on the Canadian Shield; *in* Current Research, Part C, Geological Survey of Canada, Paper 90-1C, p. 323–329. https://doi.org/10.4095/131269

Duk-Rodkin, A., 2001. Glacial limits, Stevenson Ridge, west of sixth meridian, Yukon Territory; Geological Survey of Canada, Open File 3804, scale l:250 000. https://doi.org/10.4095/212275

Duk-Rodkin, A., Weber, F., and Barendregt, R.W., 2002. Glacial limits map of upper Yukon River; Geological Survey of Canada, Open File 4275, scale 1:1 000 000. https://doi.org/10.4095/213393

Duk-Rodkin, A., Barendregt, R.W., Froese, D.G., Weber, F., Enkin, R., Smith, I.R., Zazula, G.D., Waters, P., and Klassen, R., 2004. Timing and extent of Plio-Pleistocene glaciations in northwestern Canada and east-central Alaska; *in* Quaternary glaciation – extent and chronology, Part II: North America, (ed.) J. Ehlers and P.L. Gibbard; Developments in Quaternary Science, v. 2, part b, p. 313–345. https://doi.org/10.1016/s1571-0866(04)80206-9

Eppinger, R.G., Fey, D.L., Giles, S.A., Kelley, K.D., and Smith, S.M., 2012. An exploration hydrogeochemical study at the giant Pebble porphyry Cu-Au-Mo deposit, Alaska, USA using high resolution ICP-MS; Geochemistry: Exploration, Environment, Analysis, v. 12, p. 211–226. https://doi.org/10.1144/1467-7873/11-RA-070

Fedortchouk, Y. and LeBarge, W., 2008. Sources of placer platinum in Yukon: provenance study from detrital minerals; Canadian Journal of Earth Sciences, v. 45, no. 8, p. 879–896. https://doi.org/10.1139/E08-032

Friske, P.W.B. and Hornbrook, E.H.W., 1991. Canada's National Geochemical Reconnaissance programme; Institution of Mining and Metallurgy, Transactions, Section B: Applied Earth Sciences, v. 100, p. B47–B56.

Garrett, R.G., Reimann, C., Hron, K., Kynčlová, P., and Filzmoser, P., 2017. Finally, a correlation coefficient that tells the geochemical truth; EXPLORE, Association of Applied Geochemists, no. 176, p. 1–10.

Garrett, R.G., 2018. The GSC applied geochemistry EDA package. <http://cran.r-project.org/web/packages/rgr/index.html> [accessed February 22, 2019]

Geological Survey of Canada, 1987. Regional stream sediment and water geochemical reconnaissance data, Yukon (NTS 115J, 115K (E1/2)); Geological Survey of Canada, Open File 1363, 142 pages (25 sheets); 1 diskette. https://doi.org/10.4095/130284

Godwin, C.I., 1975. Geology of the Casino porphyry copper-molybdenum deposit, Dawson Range, Yukon Territory; Ph.D. thesis, The University of British Columbia, Vancouver, British Columbia.

Godwin, C.I., 1976. Casino; *in* Porphyry deposits of the Canadian Cordillera, (ed.) A.S. Brown; Canadian Institute of Mining and Metallurgy, Special Volume 15, p. 344–358.

Hashmi, S, Ward, B.C., Plouffe, A., Leybourne, M.I., and Ferbey, T., 2015. Geochemical and mineralogical dispersal in till from the Mount Polley Cu-Au porphyry deposit, central British Columbia, Canada; Geochemistry: Exploration, Environment, Analysis, v. 15, no. 2, p. 234–249. https://doi.org/10.1144/geochem2014-310

Howard, H.H., McMaster, R.B., Slocum, T.A., and Kessler, F.C., 2008. Thematic cartography and geovisualization; Upper Saddle River, NJ: Pearson Prentice Hall.

Huff, L.C., 1976. A comparison of alluvial exploration techniques for porphyry copper deposits; *in* Geochemical Exploration, Proceedings of the 3rd international geochemical exploration symposium, (ed.) R.W. Boyle; Canadian Institute of Mining and Metallurgy, Special Volume 11, p. 190–194.

Huscroft, C.A., 2002a. Surficial geology, Britannia Creek, Yukon Territory (115J/15); Geological Survey of Canada, Open File 4345, 1 sheet. https://doi.org/10.4095/213868

Huscroft, C.A., 2002b. Surficial geology, Coffee Creek, Yukon Territory (115J/14); Geological Survey of Canada, Open File 4344, 1 sheet. https://doi.org/10.4095/213867

Huscroft, C.A., 2002c. Surficial geology, Cripple Creek, Yukon Territory (115J/16); Geological Survey of Canada, Open File 4346, 1 sheet, https://doi.org/10.4095/213869.

Huss, C., Drielick, T., Austin, J., Giroux, G., Casselman, S., Greenaway, G., Hester, M., and Duke, J., 2013. Casino project: Form 43-101F1 technical report, feasibility study, Yukon, Canada; Internal report, M3 Engineering and Technology Corp., 248 p. <https://www.westerncopperandgold.com/_resources/CasinoNI43-101-Jan2013.pdf> [accessed May 8, 2020].

Jackaman, W., 2011. Regional stream sediment geochemical data Stevenson Ridge, Yukon (NTS 115J & K); Yukon Geological Survey, Open File 2011-28.

Jackson, L.E. Jr., Froese, D.G., Huscroft, C.A., Nelson, F.E., Westgate, J.A., Telka, A.M., Shimamura, K., and Rotheisler, P.N., 2009. Surficial geology and Late Cenozoic history of the Stewart River and northern Stevenson Ridge map areas, west-central Yukon Territory; Geological Survey of Canada, Open File 6059, 414 p., 1 CD-ROM. https://doi.org/10.4095/248232

Kelley, K.D., Eppinger, R.G., Lang, J., Smith, S.M., and Fey, D.L., 2011. Porphyry Cu indicator minerals in glacial till samples as an exploration tool: example from the giant Pebble porphyry Cu-Au-Mo deposit, Alaska, USA; Geochemistry: Exploration, Environment, Analysis, v. 11, no. 4, p. 321–334. https://doi.org/10.1144/1467-7873/10-IM-041

Kobylinski, C.H., Hattori, K., Plouffe, A., and Smith, S.W., 2017. Epidote associated with the porphyry Cu-Mo mineralization at the Gibraltar deposit, south-central British Columbia; Geological Survey of Canada, Open File 8279, 19 p. https://doi.org/10.4095/305912

Kobylinski, C.H., Hattori, K., Smith, S.W., and Plouffe, A., 2018. High cerium anomalies in zircon from intrusions associated with porphyry copper mineralization in the Gibraltar deposit, south central British Columbia; Geological Survey of Canada, Open File 8430, 19 p. https://doi.org/10.4095/311194

Layton-Matthews, D., Hamilton, C., and McClenaghan, M.B., 2017. Modern techniques and applications to exploration; in Application of indicator mineral methods to bedrock sediments, (ed.) M.B. McClenaghan and D. Layton-Matthews; Geological Survey of Canada, Open File 8345, p. 10–24. https://doi.org/10.4095/306308

Learned, R.E., Chao, T.T., and Sanzolone, R.F., 1985. A comparative study of stream water and stream sediment as geochemical exploration media in the Rio Tanama porphyry copper district, Puerto Rico; Journal of Geochemical Exploration, v. 24, no. 2, p. 175–195. https://doi.org/10.1016/0375-6742(85)90044-5

Lehtonen, M., Lahaye, Y., O'Brien, H., Lukkari, S., Marmo, J., and Sarala, P., 2015. Novel Technologies for indicator mineral-based exploration; *in* Novel technologies for greenfield exploration, (ed.) P. Sarala; Geological Survey of Finland, Special Paper 57, p. 23–62.

Leybourne, M.I., Clark, I.D., and Goodfellow, W.D., 2006. Stable isotope geochemistry of ground and surface waters associated with undisturbed massive sulfide deposits; constraints on origin and water-rock reactions; Chemical Geology, v. 231, p. 300–325. https://doi.org/10.1016/j.chemgeo.2006.02.004

Lipovsky, P.S. and Bond, J.D., 2012. Surficial geology of Doyle Creek (115J/11), Yukon (1:50 000 scale); Yukon Geological Survey, Open File 2012-3.

Lougheed, D., McClenaghan, M.B., Layton-Matthews, D., and Leybourne, M.I., in press. Indicator minerals in till fine-fraction heavy mineral concentrates: examples from two Canadian polymetallic base metal deposits; in Targeted Geoscience Initiative 5: Volcanic- and sediment-hosted massive sulfide deposit genesis and exploration methods, (ed.) J.M. Peter and M.G. Gadd; Geological Survey of Canada, Bulletin 617.

Luck, P. and Simandl, G.J., 2014. Portable X-ray fluorescence in stream sediment chemistry and indicator mineral surveys, Lonnie carbonatite complex, British Columbia; *in* Geological Fieldwork 2013; British Columbia Ministry of Energy and Mines, British Columbia Geological Survey, Paper 2014-1, p. 169–182.

Lynch, J.J., 1990. Provisional elemental values for eight new geochemical lake sediment and stream sediment reference materials LKSD-1, LKSD-2, LKSD-3, LKSD-4, STSD-1, STDS-2, STSD-3 and STSD-4; Geostandards Newsletter, v. 14, no. 1, p. 153–167. https://doi.org/10.1111/j.1751-908X.1990.tb00070.x

Lynch, J.J., 1999. Additional provisional elemental values for LKSD-1, LKSD-2, LKSD-3, LKSD-4, STSD-1, STDS-2, STSD-3 and STSD-4; Geostandards Newsletter, v. 23, no. 2, p. 251–260. https://doi.org/10.1111/j.1751-908X.1999.tb00577.x

Mackay, D.A.R., Simandl, G.J., Ma, W., Redfearn, M., and Gravel, J., 2016. Indicator mineral-based exploration for carbonatites and related specialty metal deposits – a QEMSCAN® orientation survey, British Columbia, Canada; Journal of Geochemical Exploration, v. 165, p. 159–173. https://doi.org/10.1016/j.gexplo.2016.03.005

Mackie, R.A., Arne, D.C., and Pennimpede, C., 2017. Assessment of Yukon regional stream sediment catchment basin and geochemical data quality; Yukon Geological Survey, Open File 2017-4.

Mathur, R., Munk, L., Nguyen, M., Gregory, M., Annell, H., and Lang, J., 2013. Modern and paleofluid pathways revealed by Cu isotope compositions in surface waters and ores of the Pebble porphyry Cu-Au-Mo deposit, Alaska; Economic Geology, v. 108, no. 3, p. 529–541. https://doi.org/10.2113/econgeo.108.3.529

Mathews, W.H., 1986. Physiography of the Canadian Cordillera; Geological Survey of Canada, Map 1701A, scale 1:5 000 000.

McClenaghan, M.B. and Cabri, L.J., 2011. Gold and platinum group element indicator minerals in surficial sediments; Geochemistry: Exploration, Environment, Analysis, v. 11, no. 4, p. 251–263. https://doi.org/10.1144/1467-7873/10-IM-026

McClenaghan, M.B., and Kjarsgaard, B.A., 2007. Indicator mineral and surficial geochemical exploration methods for kimberlite in glaciated terrain: examples from Canada; *in* Mineral deposits of Canada: a synthesis of major deposit types, district metallogeny, the evolution of geological provinces, and exploration methods, (ed.) W.D. Goodfellow; Geological Association of Canada, Mineral Deposits Division, Special Publication No. 5, p. 983–1006.

McClenaghan, M.B., Parkhill, M.A., Pronk, A.G., Seaman, A.A., McCurdy, M., and Leybourne, M.I., 2017. Indicator mineral and geochemical signatures associated with the Sisson W-Mo deposit, New Brunswick, Canada; Geochemistry: Exploration, Environment, Analysis, v. 17, no. 4, p. 297–313. https://doi.org/10.1144/geochem2015-396

McClenaghan, M.B., Beckett-Brown, C.E., McCurdy, M.W., McDonald, A.M., Leybourne, M.I., Chapman, J.B., Plouffe, A., and Ferbey, T., 2018. Mineral markers of porphyry Cu mineralization: progress report on the evaluation of tourmaline as an indicator mineral; *in* Targeted Geoscience Initiative: 2017 report of activities, volume 1, (ed.) N. Rogers; Geological Survey of Canada, Open File 8358, p. 69–77. https://doi.org/10.4095/306427

McClenaghan, M.B., McCurdy, M.W., Garrett, R.G., Beckett-Brown, C.E., Leybourne, M.I., Casselman, S.G., and Pelchat, P., 2019. Mineral and geochemical signatures of porphyry copper mineralization: work in progress at the Casino Cu-Au-Mo-Ag porphyry deposit; *in* Targeted Geoscience Initiative: 2018 report of activities, (ed.) N. Rogers; Geological Survey of Canada, Open File 8549, p. 333–344. https://doi.org/10.4095/313667

McClenaghan, M.B., McCurdy, M.W., Garrett, R.G., Beckett-Brown, C.E., and Casselman, S.G., 2020. Indicator mineral signatures of the Casino porphyry Cu-Au-Mo deposit, Yukon; Geological Survey of Canada, Open File 8711, 42 p. (11 sheets). https://doi.org/10.4095/322191

McCurdy, M.W., McClenaghan, M.B., Garrett, R.G., and Pelchat, P., 2019. Geochemical signatures of the silt fraction from streams near the Casino porphyry Cu-Au-Mo deposit, Yukon Territory; Geological Survey of Canada, Open File 8632, 39 p. (41 sheets). https://doi.org/10.4095/321381

McKillop, R., Turner, D., Johnston, K., and Bond, J., 2013. Property-scale classification of surficial geology for soil geochemical sampling in the unglaciated Klondike Plateau, west-central Yukon; Yukon Geological Survey, Open File 2013-15.

Moran, K., Backman, J., Brinkhuis, H., Clemens, S.C., Cronin, T., Dickens, G.R., Eynaud, F., Gattacceca, J., Jakobsson, M., Jordan, R.W., Kaminski, M., King, J., Koc, N., Krylov, A., Martinez, N., Matthiessen, J., McInroy, D. Moore, T.C., Onodera, J., O'Regan, M., Pälike, H., Rea, B., Rio, D., Sakamoto, T., Smith, D.C., Stein, R., St John, K., Suto, I., Suzuki, N., Takahashi, K., Watanabe, M., Yamamoto, M., Farrell, J., Frank, M., Kubik, P., Jokat, W., and Kristoffersen, Y., 2006. The Cenozoic paleoenvironment of the Arctic Ocean; Nature, v. 441, p. 601–605. https://doi.org/10.1038/nature04800

Nelson, J.L., Colpron, M., Piercey, S. J., Dusel-Bacon, C., Murphy, D. C., and Roots, C. F., 2006. Paleozoic tectonic and metallogenic evolution of the pericratonic terranes in Yukon, northern British Columbia and eastern Alaska; *in* Paleozoic evolution and metallogeny of pericratonic terranes at the Ancient Pacific Margin of North America, Canadian and Alaskan Cordillera, (ed.) M. Colpron and J.L. Nelson; Geological Association of Canada, Special Paper 45, p. 323–360.

Nelson, J.L., Colpron, M., and Israel, S., 2013. The Cordillera of British Columbia, Yukon, and Alaska: tectonics and metallogeny; *in* Tectonics, metallogeny, and discovery: the North American Cordillera and similar accretionary settings, (ed.) M. Colpron, T. Bissing, B.G. Rusk, and J.F.H. Thompson; Society of Economic Geologists, Special Publication 17, p. 53–109.

Pisiak, L.K., Canil, D., Plouffe, A., Ferbey, T., and Lacourse, T., 2017. Magnetite as an indicator mineral in the exploration of porphyry deposits; a case study in till near the Mount Polley Cu-Au deposit, British Columbia, Canada; Economic Geology, v. 112, p. 919–940. https://doi.org/10.2113/econgeo.112.4.919

Plouffe, A. and Ferbey, T., 2017. Porphyry Cu indicator minerals in till: a method to discover buried mineralization; *in* Indicator minerals in till and stream sediments of the Canadian Cordillera, (ed.) T. Ferbey, A. Plouffe, and A. Hickin; Mineral Association of Canada, Topics in Mineral Sciences, Volume 47, Geological Association of Canada, Special Paper 50, p. 129–159.

Plouffe, A. and Ferbey, T., 2019. Indicator mineral content of bedrock and till at the Gibraltar porphyry Cu-Mo deposit and the Woodjam porphry Cu-Au-Mo prospect, south-central British Columbia; Geological Survey of Canada, Open File 8580, 33 p. https://doi.org/10.4095/315647

Plouffe, A., McClenaghan, M.B., Paulen, R.C., McMartin, I., Campbell, J.E., and Spirito, W.A., 2013. Processing of unconsolidated glacial sediments for the recovery of indicator minerals: protocols used at the Geological Survey of Canada; Geochemistry: Exploration, Environment, Analysis, v. 13, no. 4, p. 303–316. https://doi.org/10.1144/geochem2011-109

Plouffe, A., Ferbey, T., Hashmi, S., and Ward, B.C., 2016. Till geochemistry and mineralogy: vectoring towards Cu porphyry deposits in British Columbia, Canada; Geochemistry: Exploration, Environment, Analysis, v. 16, no. 3, p. 213–232. https://doi.org/10.1144/geochem2015-398

Plouffe, A., Kobylinksi, C.H., Hattori, K., Wolfe, L., and Ferbey, T., 2018. Mineral markers of porphyry copper mineralization: work in progress at the Gibraltar deposit, British Columbia; *in* Targeted Geoscience Initiative: 2017 report of activities, volume 1, (ed.) N. Rogers; Geological Survey of Canada, Open File 8358, p. 57–67. https://doi.org/10.4095/306423

Plouffe, A., Kjarsgaard, I., Kobylinski, C., Hattori, K., Petts, D., Venance, K., and Ferbey, T., 2019. Discovering the next generation of Cu porphyry deposits using mineral markers; *in* Targeted Geoscience Initiative: 2018 report of activities, (ed.) N. Rogers; Geological Survey of Canada, Open File 8549, p. 321–331. https://doi.org/10.4095/313666

Poulin, R.S., McDonald, A., Kontak, D.J., and McClenaghan, M.B., 2018. Assessing scheelite as an ore-deposit discriminator using its trace-element and REE chemistry; The Canadian Mineralogist, v. 56, no. 3, p. 265–302. https://doi.org/10.3749/canmin.1800005

Rebagliati, C.M., Bowen, B.K., Copeland, D.J., and Nioso, D.W.A., 1995. Kemess South and Kemess North porphyry gold-copper deposits, northern British Columbia; *in* Porphyry deposits of the northwestern Cordillera of North America, (ed.) T.G. Schroeter; The Canadian Institute of Mining and Metallurgy, Special Volume 46, p. 377–396.

Reimann, C., Filzmoser, P., Hron, K., Kynčlová, P., and Garrett, R.G., 2017. A new method for correlation analysis of compositional (environmental) data – a worked example; Science of the Total Environment, v. 607–608, p. 965–971. https://doi.org/10.1016/j.scitotenv.2017.06.063

Relf, C., 2020. Yukon Geological Survey: planning for the future; in Yukon Exploration and Geology Overview 2019, (ed.) K.E. MacFarlane; Yukon Geological Survey, p. 1–22.

Richardson, P.W., 1995. The Whipsaw porphyry system, Similkameen district, British Columbia; in Porphyry deposits of the northwestern Cordillera of North America, (ed.) T.G. Schroeter; The Canadian Institute of Mining and Metallurgy, Special Volume 46, p. 530–533.

Ryan, J.J., Zagorevski, A., Williams, S.P., Roots, C., Ciolkiewicz, W., Hayward, N., and Chapman, J.B., 2013. Geology, Stevenson Ridge (northeast part), Yukon; Geological Survey of Canada, Canadian Geoscience Map 116 (preliminary edition), scale 1:100 000. https://doi.org/10.4095/292371

Smith, C.A.S., Meikle, J.C., and Roots, C.F. (ed.), 2004. Ecoregions of the Yukon Territory: Biophysical properties of Yukon landscapes; Agriculture and Agri-Food Canada, PARC Technical Bulletin No. 04-01, Summerland, British Columbia, 313 p.

Smith, C.A.S., Sanborn, P.T., Bond, J.D., and Frank, G., 2009. Genesis of turbic cryosols on north-facing slopes in a dissected, unglaciated landscape, west-central Yukon Territory; Canadian Journal of Soil Science, v. 89, p. 611-622. https://doi.org/10.4141/CJSS09001

Taufen, P.M., 1997. Ground waters and surface waters in exploration geochemical surveys; *in* Proceedings of Exploration 97: fourth decennial international conference on mineral exploration, (ed.) A.G. Gubbins; p. 271–284.

Vavrek, M.J., Evans, D.C., Braman, D.R., Campione, N.E., and Zazula, G.D., 2012. A Paleogene flora from the upper Bonnet Plume Formation of northeast Yukon Territory, Canada; Canadian Journal of Earth Sciences, v. 49, no. 3, p. 547–558. https://doi.org/10.1139/e11-073

Wilkinson, J.J., Cooke, D.R., Baker, M.J., Chang, Z., Wilkinson, C.C., Chen, H., Fox, N., Hollings, P., White, N.C., Gemmell, J.B., Loader, M.A., Pacey, A., Sievwright, R.H., Hart, L.A., and Brugge, E.R., 2017. Porphyry indicator minerals and their mineral chemistry as vectoring and fertility tools; in Application of indicator mineral methods to bedrock and sediments, (ed.) M.B. McClenaghan and D. Layton-Matthews; Geological Survey of Canada, Open File 8345, p. 67–77. https://doi.org/10.4095/306317

Yukon Geological Survey, 2011a. Idaho occurrence (115J 099) record summary, Yukon mineral occurrence database; Government of Yukon, Yukon Geological Survey. <http://data.geology.gov.yk.ca/Occurrence/15100> [accessed January 24, 2020]

Yukon Geological Survey, 2011b. Nordex occurrence (115J 023) record summary, Yukon mineral occurrence database; Government of Yukon, Yukon Geological Survey. <http://data.geology.gov.yk.ca/Occurrence/14372> [accessed January 24, 2020].

Yukon Geological Survey, 2011c. Rude Creek occurrence (115J 022) record summary, Yukon mineral occurrence database; Government of Yukon, Yukon Geological Survey. <http://data.geology.gov.yk.ca/Occurrence/14371> [accessed January 24, 2020]

Yukon Geological Survey, 2013a. Buck occurrence (115J 071) record summary, Yukon mineral occurrence database; Government of Yukon, Yukon Geological Survey. <http://data.geology.gov.yk.ca/Occurrence/14418> [accessed January 24, 2020]

Yukon Geological Survey, 2013b. Marquerite occurrence (115J 070) record summary, Yukon mineral occurrence database; Government of Yukon, Yukon Geological Survey. <http://data.geology.gov.yk.ca/Occurrence/14417> [accessed January 24, 2020]

Yukon Geological Survey, 2015a. Mascot occurrence (115J 074) record summary, Yukon mineral occurrence database; Government of Yukon, Yukon Geological Survey. <http://data.geology.gov.yk.ca/Occurrence/14421> [accessed January 24, 2020]

Yukon Geological Survey, 2015b. Yukon digital bedrock geology. <http://www/arcgis.com/home/webmap/viewer.html?webmap=c1544758b4ff4d24ab6638e32b8465114&extent=-167.8739,55.535,-102.9666,72.0503> [accessed January 24, 2020]

Yukon Geological Survey, 2016. RGS Re-analysis. Yukon Geological Survey, point GIS layer. <http://data.geology.gov.yk.ca/Compilation/21> [accessed January 24, 2020]

Yukon Geological Survey, 2017. Zappa occurrence (115J 036) record summary, Yukon mineral occurrence database; Government of Yukon, Yukon Geological Survey. <http://data.geology.gov.yk.ca/Occurrence/14384> [accessed January 24, 2020]

Yukon Geological Survey, 2018a. Bomber occurrence (115J 027) record summary, Yukon mineral occurrence database; Government of Yukon, Yukon Geological Survey. <http://data.geology.gov.yk.ca/Occurrence/14376> [accessed January 24, 2020]

Yukon Geological Survey, 2018b. Canadian Creek occurrence (115J 101) record summary, Yukon mineral occurrence database; Government of Yukon, Yukon Geological Survey. <http://data.geology.gov.yk.ca/Occurrence/14431> [accessed January 24, 2020]

Yukon Geological Survey, 2018c. Casino occurrence (115J 028) record summary, Yukon mineral occurrence database; Government of Yukon, Yukon Geological Survey. <http://data.geology.gov.yk.ca/Occurrence/15019> [accessed January 24, 2020]

Yukon Geological Survey, 2018d. Cockfield occurrence (115J 017) record summary, Yukon mineral occurrence database; Government of Yukon, Yukon Geological Survey. <http://data.geology.gov.yk.ca/Occurrence/14367> [accessed January 24, 2020]

Yukon Geological Survey, 2018e. Zappa occurrence (115J 036) record summary, Yukon mineral occurrence database; Government of Yukon, Yukon Geological Survey. <http://data.geology.gov.yk.ca/Occurrence/14384> [accessed January 24, 2020]

Zachos, J.C., Pagani, M., Sloan, L., Thomas, E., and Billups, K., 2001. Trends, rhythms, and aberrations in global climate 65 Ma to present; Science, v. 292, p. 686–693. https://doi.org/10.1126/science.1059412

Automated indicator-mineral analysis of the fine-sand, heavy-mineral concentrate fraction of till: a promising exploration tool for porphyry copper mineralization

A. Plouffe[1]*, D.H.C. Wilton[2], R. McNeil[1], and T. Ferbey[3]

Plouffe, A., Wilton, D.H.C., McNeil, R., and Ferbey, T., 2021. Automated indicator-mineral analysis of the fine-sand, heavy-mineral concentrate fraction of till: a promising exploration tool for porphyry copper mineralization; in *Targeted Geoscience Initiative 5: contributions to the understanding and exploration of porphyry deposits, (ed.) A. Plouffe and E. Schetselaar; Geological Survey of Canada, Bulletin 616, p. 203–223. https://doi.org/10.4095/327991*

Abstract: Previous studies indicated that heavy mineralogy (specific gravity (SG) = 2.8–3.2 and >3.2) of the medium-sand fraction (0.25–0.50 mm) of till contains porphyry copper indicator minerals (PCIM) derived from mineralization or alteration zones. To improve the PCIM method for mineral exploration, we analyzed the heavy mineralogy (>3.2 SG) of the fine-sand fraction (0.125–0.180 mm) of till using an automated method that combines scanning electron microscopy (SEM) and mineral-liberation analysis (MLA). The MLA-SEM method identifies mineralogy based on grain composition determined by SEM–energy dispersive spectroscopy. The distributions of epidote and chalcopyrite in till at four porphyry copper deposits in British Columbia show similarities between the fine-sand fraction analyzed by MLA-SEM and the medium-sand fraction analyzed by optical mineralogy: both show dispersal parallel to ice-flow movements. Analyzing the fine-sand, heavy-mineral concentrate (HMC) fraction of till by MLA-SEM can be used in exploration for porphyry copper mineralization. We estimate 5 to 8 kg of bulk till is sufficient to prepare 0.3 g aliquots of fine-sand HMC for MLA-SEM; this is smaller than the 9 to 15 kg required for optical mineral analysis of the medium-sand HMC fraction. Smaller field samples can lower costs for reconnaissance mineral exploration.

Résumé : Des études antérieures ont indiqué que les minéraux lourds (densité = 2,8–3,2 et >3,2) dans la fraction du sable moyen (0,25–0,50 mm) du till renferment des minéraux indicateurs de minéralisation de cuivre porphyrique (MIMCP) qui proviennent des zones minéralisées ou des zones d'altération de ce type de minéralisation. Afin d'améliorer la méthode des MIMCP pour l'exploration minérale, nous avons analysé les minéraux lourds (densité >3,2) dans la fraction du sable fin (0,125–0,180 mm) du till en utilisant une méthode automatisée qui combine la microscopie électronique à balayage (MEB) et l'analyse de libération minérale (ALM). La méthode ALM-MEB permet d'identifier les minéraux d'après la composition des grains déterminée par la spectroscopie à dispersion d'énergie du microscope électronique à balayage. Les distributions de l'épidote et de la chalcopyrite dans le till aux environs de quatre gisements de cuivre porphyriques en Colombie-Britannique montrent des similitudes entre la fraction du sable fin analysée par ALM-MEB et la fraction du sable moyen analysée par minéralogie optique. Les deux méthodes montrent une dispersion parallèle aux directions de l'écoulement glaciaire. L'analyse de la fraction du sable fin des concentrés de minéraux lourds (CML) du till par ALM-MEB peut être utilisée pour la recherche de minéralisations de cuivre porphyriques. Nous estimons que 5 à 8 kg de till en vrac sont suffisants pour préparer 0,3 g d'aliquotes de sable fin des CML pour la méthode ALM-MEB, ce qui est beaucoup moins que les 9 à 15 kg nécessaires pour l'analyse des minéraux par microscopie optique de la fraction du sable moyen des CML. Le prélèvement d'échantillons plus petits sur le terrain peut entraîner une réduction des coûts pour l'exploration minérale de reconnaissance.

[1]Geological Survey of Canada, 601 Booth Street, Ottawa, Ontario K1A 0E8
[2]Department of Earth Sciences, Memorial University, St. John's, 9 Arctic Avenue, Newfoundland A1B 3X5
[3]British Columbia Geological Survey, British Columbia Ministry of Energy, Mines and Petroleum Resources, 1810 Blanshard Street, Victoria, British Columbia V8T 4J1
*Corresponding author: A. Plouffe (email: alain.plouffe@canada.ca)

INTRODUCTION

Porphyry copper deposits to be discovered in the Canadian Cordillera are unlikely to be 'easy finds', well exposed at surface. They will most likely be at depth, below the exposed bedrock or covered by glacial or other surficial sediments. Innovative and cost-effective mineral exploration methods will be required to find these buried deposits. As part of the Targeted Geoscience Initiative of the Geological Survey of Canada (GSC), researchers are developing mineral exploration methods based on the detection of minerals indicative of porphyry copper mineralization (termed porphyry copper indicator minerals (PCIMs)) in till and stream sediments (Hashmi et al., 2015; Plouffe and Ferbey, 2015, 2017; Plouffe et al., 2016; McClenaghan et al., 2018, 2019b, this volume; Beckett-Brown et al., 2019, this volume). This method relies on the optical identification of PCIM in the medium-sand, heavy-mineral concentrate (MSHMC) fraction of till (0.25–0.50 mm; 2.8–3.2 and >3.2 specific gravity (SG)). Certain ore (e.g. chalcopyrite, gold grains) and alteration (e.g. epidote, garnet) minerals define mineralogical anomalies in till dispersed by ice-flow movements and extending, in some cases, more than 10 km (Plouffe and Ferbey, 2017). Identifying PCIM in the MSHMC fraction of till is now considered an efficient approach to detect porphyry copper mineralization buried by glacial sediments.

To improve the PCIM method, we have investigated the mineralogy of the fine-sand, heavy-mineral concentrate (FSHMC) fraction (0.125–0.180 mm; >3.2 SG) of till using an automated method that combines a scanning electron microscope (SEM) and a mineral-liberation analysis (MLA) database with the energy dispersive fingerprints of minerals. We compare the abundance of two PCIMs in till (epidote and chalcopyrite) identified in the FSHMC fraction with the MLA-SEM, to the mineralogy of the MSHMC fraction determined by optical methods. We compare samples from four porphyry copper study sites in south-central British Columbia: Gibraltar, Highland Valley Copper, Mount Polley, and Woodjam. We show that the heavy minerals identified are similar in both size fractions and, as such, the fine-sand fraction of till provides valuable information in a mineral exploration program targeted at porphyry copper mineralization.

GEOLOGICAL SETTING AND PREVIOUS STUDIES

Our investigation of till mineralogy has benefited from archived samples collected as part of reconnaissance till-sampling surveys in the region of three porphyry copper deposits and one prospect in south-central British Columbia (Fig. 1): the Gibraltar porphyry Cu-Mo deposit (1 220 000 000 t of ore grading 0.3% Cu and 0.01% Mo; van Straaten et al., 2013; Taseko Mines Ltd., 2020); the Mount Polley porphyry Cu-Au±Ag deposit (150 000 000 t of ore grading 0.2 to 0.3% Cu and 0.2 to 0.3 g/t Au; Rees, 2013); the Highland Valley Copper porphyry Cu-Mo deposit (1 600 000 000 t of ore grading 0.4% Cu and 0.01% Mo; Byrne et al., 2013); and the Woodjam porphyry Cu-Au prospect (221 000 000 tonnes of ore grading 0.2 to 0.3% Cu and 0.3 to 0.5 g/t Au; Sherlock et al., 2013; Sherlock and Trueman, 2013). These deposits are hosted in felsic to intermediate Late Triassic to Early Jurassic intrusions of the Quesnel terrane, which is dominantly composed of the Nicola Group mafic volcanic and associated sedimentary rocks (Schiarizza, 2017). Field and laboratory methods along with till mineralogical and geochemical data produced as part of these surveys are presented in Ferbey et al. (2016) and Plouffe and Ferbey (2016).

Hashmi et al. (2015), Plouffe et al. (2016), and Plouffe and Ferbey (2017) interpreted the till composition data, taking into account ice-flow movements of the last glaciation. In short, three ice-movement events occurred at Gibraltar (in chronological order): 1) glaciers from local mountainous regions moved to the southeast, 2) coalescing valley glaciers derived from the Cariboo Mountains advanced to the southwest, and 3) a regional ice-flow movement to the northwest was derived from an ice divide located at approximately lat. 52°. Only the last two ice movements have affected the Woodjam and Mount Polley regions. The Highland Valley Copper deposits were only covered by south- to southeast-flowing ice derived from the ice divide at lat. 52°.

METHODS

Field methods for the regional till-sampling surveys completed at the four study sites are detailed in Ferbey et al. (2016) and Plouffe and Ferbey (2016). Till samples (9–15 kg) were processed for the optical identification of heavy minerals in the non-magnetic, 0.25 to 0.50 mm, 2.8 to 3.2, and greater than 3.2 SG fractions. The sample processing methodology is summarized in Figure 2a and in Plouffe and Ferbey (2015, 2016) and Ferbey et al. (2016). In these previous studies, the abundance of chalcopyrite is reported in the 0.25 to 0.50 mm, greater than 3.2 SG, and greater than 1.0 A and epidote is reported in the 0.25 to 0.50 mm, greater than 3.2 SG, and 0.8 to 1.0 A paramagnetic fraction (Fig. 2a). Here, we report the total abundance of epidote in the greater than 3.2 SG and 0.25 to 0.50 mm fraction prior to paramagnetic separation (Fig. 2a). Only a select number of samples at each study site were processed for total epidote abundance (Table 1; Appendix A); in other words, fewer 0.25 to 0.50 mm, greater than 3.2 SG samples were analyzed for total epidote abundance compared to chalcopyrite abundance. In the context of our study, the non-magnetic 0.25 to 0.50 mm and greater than 3.2 SG fraction is referred to as the MSHMC.

For our MLA-SEM study, we selected a limited number of samples from each study site that had been previously processed for PCIM in the MSHMC (Table 1) based on their location within and outside the PCIM dispersal trains

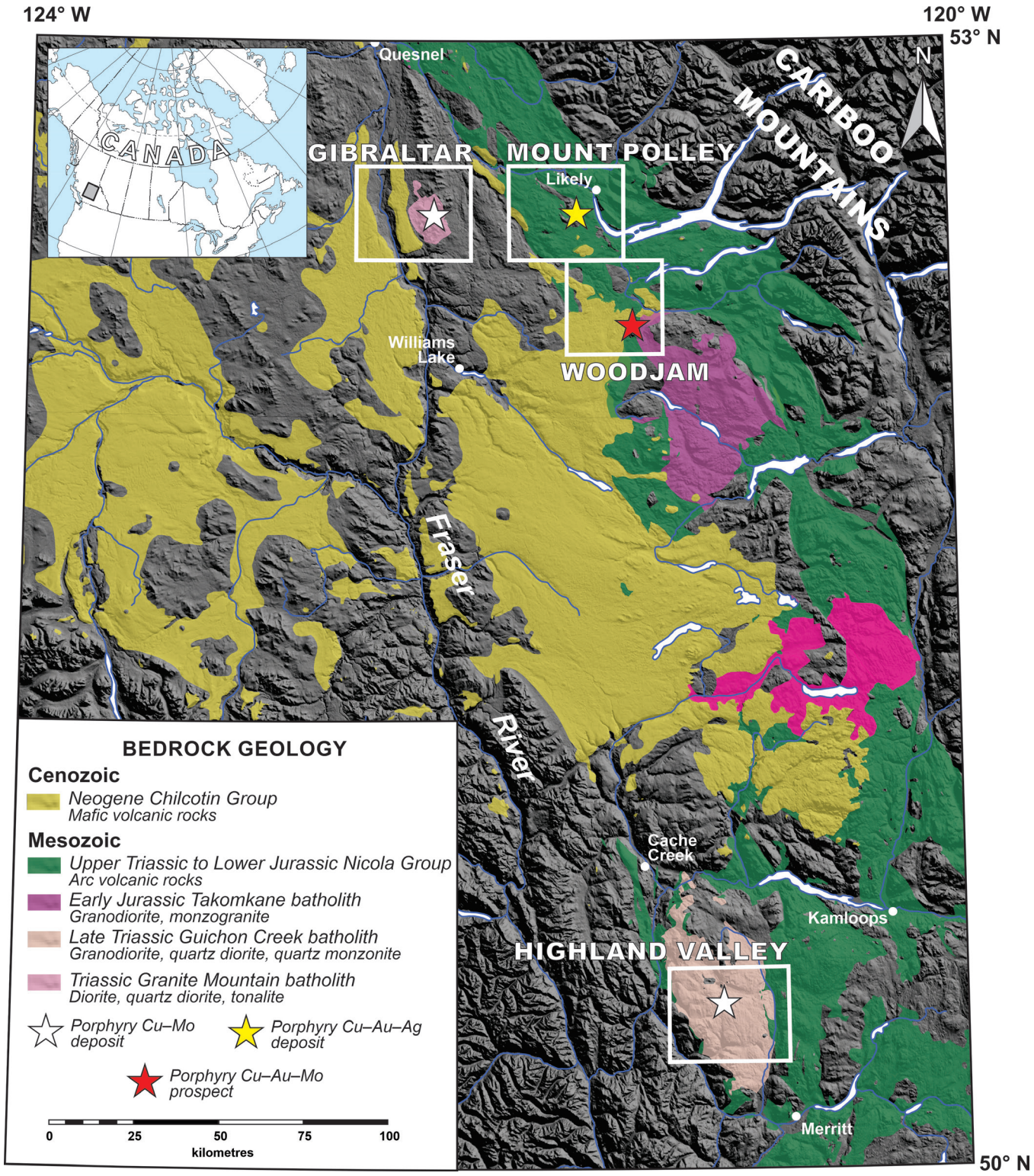

Figure 1. Location of the four porphyry copper study sites in British Columbia.

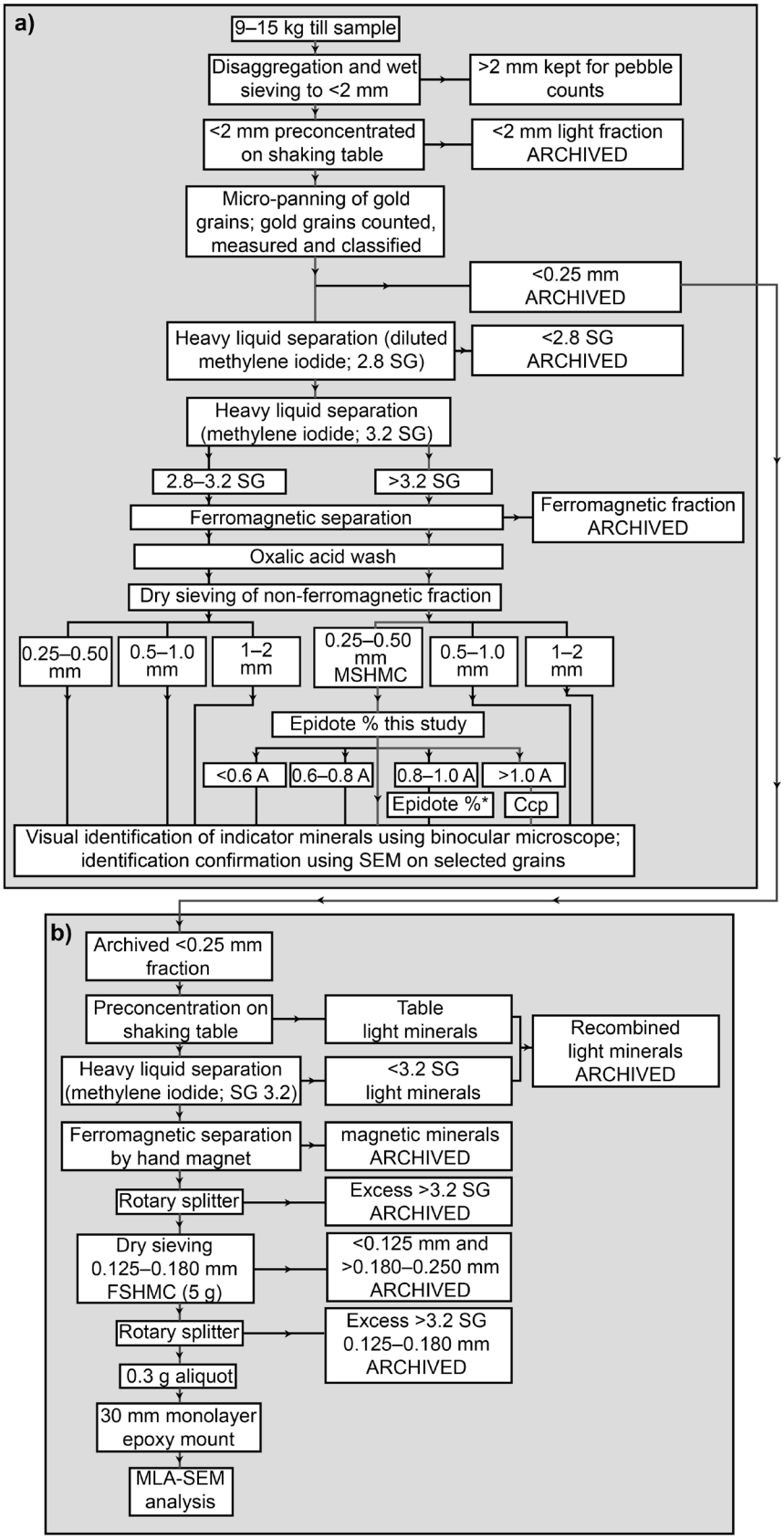

FSHMC: Non-magnetic, fine-sand, heavy-mineral concentrate
MSHMC: Non-magnetic, medium-sand, heavy-mineral concentrate
Ccp: Chalcopyrite

Path for the proccessing of:
MSMHC ——
FSHMC ——

Figure 2. Flow charts representing: **a)** processing till samples for indicator minerals in the 0.25 to 2.00 mm size fraction (*modified from* Plouffe and Ferbey, 2016). Hashmi et al. (2015), Plouffe et al. (2016), and Plouffe and Ferbey (2017) reported the percentage of epidote in the 0.25 to 0.50 mm, greater than 3.2 specific gravity (SG), 0.8 to 1 A fraction, labelled 'Epidote %*'; we report epidote % in the 0.25 to 0.50 mm, greater than 3.2 SG fraction prior to paramagnetic separation, labelled 'Epidote % this study'; **b)** processing the less than 0.250 mm fraction to obtain a 0.125 to 0.180 mm fraction for mineral liberation analysis (MLA)–scanning electron microscopy (SEM).

Table 1. Number of till samples processed for heavy mineral analysis in the 0.25 to 0.50 mm (Ferbey et al., 2016; Plouffe and Ferbey, 2016) and 0.125 to 0.180 mm size fractions (this study) of samples from four porphyry copper study sites in British Columbia.

Study site	0.25–0.50 mm Optical mineralogy (MSHMC)		0.125–0.180 mm MLA-SEM (FSHMC)
	Chalcopyrite	Epidote	Epidote and chalcopyrite
Highland Valley Copper	109	70	29
Gibraltar	96	50	20
Mount Polley	87	48	20
Woodjam	91	53	21
FSHMC: fine-sand, heavy-mineral concentrate; MLA-SEM: mineral-liberation analysis and scanning electron microscopy; MSHMC: medium-sand, heavy-mineral concentrate			

outlined in Plouffe and Ferbey (2017); therefore, there are fewer MLA-SEM samples than MSHMC samples. The archived less than 0.250 mm fraction of these selected samples was repassed on the shaking table, concentrated in a heavy liquid (methylene iodide; 3.2 SG) and separated with a hand magnet to remove magnetic minerals at Overburden Drilling Management Ltd. (Ottawa, Ontario). The resulting less than 0.250 mm non-magnetic heavy mineral samples were passed through a rotary splitter to provide a representative split, which was dry sieved in the Sedimentology Laboratory at the GSC (Ottawa, Ontario) to obtain approximately 5 g of non-magnetic 0.125 to 0.180 mm, greater than 3.2 SG material (Fig. 2b), referred to in this paper as a fine sand heavy mineral concentrate (FSHMC). The sieves were cleaned between samples with Alconox® laboratory detergent in a sonic bath and rinsed with tap and distilled water. Grenier et al. (2015) did not find evidence of sample cross-contamination while using this sieve cleaning method. Sample loss during dry sieving is negligible, having been evaluated at 1.2% by Lougheed et al. (2019) after dry sieving heavy mineral concentrates (HMCs; <0.250 mm) of till.

Aliquots weighing approximately 0.3 g were obtained from each FSHMC sample using a rotary splitter, which produces homogeneous subsamples. These aliquots were mounted as a monolayer in a 30 mm diameter epoxy (Epofix resin) puck as described by Wilton and Winter (2012) and Wilton et al. (2017). Each mount contains up to 20 000 particles (Wilton et al., 2017). The monolayer mounting procedure eliminates preferential settling of heavy mineral grains in epoxy, which can result in over-representation of heavier minerals on the analyzed grain-mount surface (cf. Lougheed et al., 2018, 2020, this volume). The samples were polished using a Struers polishing system with a protocol for silicate minerals developed internally at Memorial University (MUN). All grain mounts were carbon-coated prior to MLA-SEM analyses. One grain mount was made per sample.

Following our method, only a portion of the FSHMC obtained from the original 9 to 15 kg samples was processed for MLA-SEM. In contrast, 100% of the MSHMC was analyzed, as reported in Ferbey et al. (2016) and Plouffe and Ferbey (2016). As part of our research we evaluated if the 0.3 g aliquots used for MLA-SEM are representative of PCIM present in till as identified in the MSHMC.

The MLA-SEM system

The MLA-SEM facility in the Core Research Equipment and Instrument Training Network laboratories at MUN consists of a FEI Quanta 400 environmental SEM equipped with a dual Bruker energy dispersive spectroscopy (EDS) detector controlled by MLA software developed at the University of Queensland Julius Kruttschnitt Mineral Research Centre (JKTech) in Australia. The SEM was operated at a voltage of 25 kV and a beam current of 13 nA. The working distance between sample and detector was 12 mm and spot size was approximately 5 µm, representing the minimum detectable particle diameter. The imaging dwell time (i.e. time spent acquiring data) was 16 µs, with frame resolution of 800 pixels, and X-ray collection at 12 ms.

Mineral-liberation analysis software maps mineral particles based on their backscattered-electron (BSE) profiles; individual particles are defined based on subtle variations in the brightness of the BSE greyscale image, wherein minerals containing elements with greater atomic number are brighter (Fig. 3a). The MLA software controls full X-ray spectrum (EDS) analysis of each particle based on the distinct mapped brightness. The mineralogy of each particle is finally identified by the MLA software based on matching the energy dispersive X-ray signal from each particle in the grain mount to a database. False colour images of the grain mounts can be created to provide a visual overview of the distribution of the most abundant minerals (Fig. 3b).

For each analysis, the greyscale threshold was set with the epoxy as black (very low greyscale) and metallic copper as white (very high greyscale). The dwell time for each X-ray analysis of a particle was 60 µs. The MLA-SEM

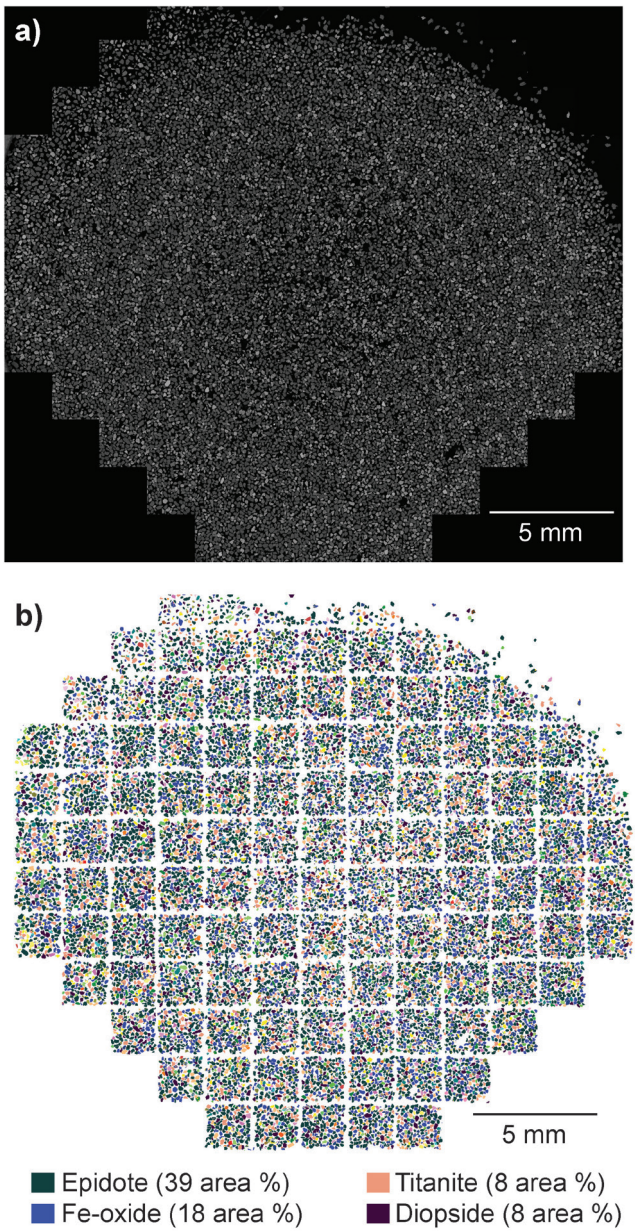

Figure 3. Example of **a)** a backscattered-electron image and **b)** a composite false colour image of a complete grain mount from sample 15PMA113A01 from the Highland Valley Copper study site, British Columbia. Only the most abundant minerals (≥ 8 area per cent) are shown in the legend.

analytical time was 45 to 60 min per sample and the post-processing time ranged from 10 to 30 min depending on the complexity of the sample.

The confidence level for matching individual spectra with the database was set at 90% during the initial analysis, where 100% is a perfect match and 50% is an average match. Following post-processing and identification of unknowns, the confidence level was reset to 70% for final calculation.

Following MLA-SEM analysis, each sample was post-processed on live SEM to evaluate any detected unknowns to ascertain whether each was truly an unidentified mineral or a defect in the polished surface (i.e. crack or hole). In rare cases, the analysis was obtained on the boundary between two minerals in a particle containing more than one mineral species and was, therefore, a mix of two mineral spectra. Higher resolution BSE images were obtained for a limited number of specific particles to better evaluate their mineralogy.

Non-mineral objects such as holes and parts of the grain mount were removed from the MLA-SEM maps. The final results include a list of the minerals in each sample reported as an area per cent of the total area of all minerals mapped in the sample. Through the MLA data processing, all minerals greater than 5 µm in size present in polymineral grains are identified as their respective mineral.

The SEM-EDS spot size of 5 µm corresponds to a circular particle with an area of 20 µm^2 (0.00002 mm^2). The 30 mm pucks used in our study were covered with FSHMC within a 25 mm diameter, corresponding to a total area of 491 mm^2. Assuming 85% mineral grain coverage of this area, a 0.00002 mm^2 particle corresponds to 5 x 10^{-6}% or 0.000005% of the total area analyzed; consequently, we conservatively report the area per cent of chalcopyrite to five decimal places. Lougheed et al. (2020) calculated the analytical precision of mineral identification by MLA-SEM at less than ±1 area per cent based on replicate analytical runs of identical sections with proper calibration measures between runs.

RESULTS

The full list of minerals obtained from the MLA-SEM analyses included a number of light minerals (e.g. albite, quartz, biotite) present in small percentages varying from 1.6 to 10.6 area per cent with an average of 4.8 area per cent (Table 2). These light minerals were present as part of polymineral grains with SG greater than 3.2. Light monomineral grains were detected in a few samples. We suspect that these grains were entrained with the heavy minerals during heavy mineral separation and attest to the technical difficulty of perfectly separating dense minerals from the fine-sand fraction. The Fe-oxide/hydroxide category includes the potential combination of hematite, goethite, limonite, and magnetite, which could only be differentiated with a longer analytical time than we applied. If magnetite was present, it occurred as a small percentage of polymineral grains, too small to have been removed during the magnetic separation. A small amount of contamination (average of 0.04%) in the form of brass and steel was detected in the samples (Fig. 4a). This contamination is most likely derived from field sampling tools (Plouffe et al., 2014; Lehtonen et al., 2015).

Table 2. Minimum, maximum, and average abundance of minerals identified by mineral-liberation analysis–scanning electron microscopy in the 0.125 to 0.180 mm heavy-mineral concentrate of samples of four porphyry copper study sites in British Columbia, presented as area per cent of the total area of all minerals mapped.

Minerals	Abundance (area %)			Minerals	Abundance (area %)		
	minimum	maximum	average		minimum	maximum	average
Aenigmatite	0.00	0.48	0.04	Ilmenite	0.01	13.28	3.34
Albite	***0.16***	***2.12***	***0.82***	Jagowerite	0.00	0.01	0.00
Allanite	0.00	0.64	0.00	Jarosite	0.00	0.02	0.00
Almandine	0.06	31.36	8.07	Leucoxene	0.00	0.69	0.18
Al-Si oxides	0.00	2.47	0.44	Mn-oxides	0.00	0.25	0.01
Fine-grained alteration minerals (typically clay)	0.78	6.52	2.95	Monazite	0.00	0.06	0.01
Andradite	0.15	21.60	1.66	***Muscovite***	***0.08***	***0.88***	***0.26***
Anhydrite	***0.00***	***0.01***	***0.00***	Olivine	0.02	18.15	2.80
Apatite	0.01	4.47	0.65	***Orthoclase***	***0.06***	***1.87***	***0.45***
Astrophyllite	0.00	0.22	0.04	Orthopyroxene	0.00	27.26	2.11
Augite	0.20	4.25	0.77	Pentlandite	0.00	0.03	0.00
Barite	0.00	5.11	0.07	Perovskite	*0.00*	0.02	0.00
Biotite	***0.03***	***0.55***	***0.15***	***Perthite***	***0.10***	***2.20***	***0.49***
Bornite	0.00	0.43	0.00	***Phlogopite***	***0.00***	***0.08***	***0.01***
Brass and steel	0.00	0.27	0.04	Piemontite	*0.00*	0.29	0.02
Calcite	***0.00***	***0.59***	***0.05***	***Plagioclase***	***0.09***	***3.72***	***1.01***
Cassiterite	***0.0000***	***0.0001***	***0.0000***	Polymignyte	0.00	0.01	0.00
Chalcocite	0.00	0.80	0.01	Pyrite	0.00	7.10	0.16
Chalcopyrite	0.00	2.29	0.06	Pyrolusite	0.00	0.001	0.00
Chlorapatite	0.01	3.37	0.52	Pyrope	0.00	0.52	0.06
Chlorite	0.11	3.07	0.48	Pyrrhotite	0.00	6.78	0.64
Chromite	0.00	0.49	0.07	***Quartz***	***0.00***	***4.89***	***1.36***
Copper, native	0.00	0.01	0.00	Rutile	0.02	4.05	1.24
Cordierite	***0.00***	***0.05***	***0.01***	***Scapolite***	***0.01***	***0.55***	***0.12***
Coronadite	0.00	0.05	0.00	Scheelite	*0.00*	0.02	0.00
Corundum	0.00	0.03	0.01	***Serpentine***	***0.00***	***0.12***	***0.01***
Covellite	0.00	0.004	0.00	Siderite	0.00	0.43	0.04
Diopside	0.88	93.41	25.35	Spessartine	0.00	1.78	0.11
Dolomite	***0.00***	***0.06***	***0.00***	Sphalerite	0.00	0.01	0.00
Epidote	0.07	49.42	17.78	Spinel	0.00	0.50	0.05
Fe-oxide/hydroxide	0.23	41.47	11.37	Staurolite	0.00	5.83	1.41
Florencite-(Ce)	0.00	0.02	0.00	Sulfide-oxide	0.00	3.24	0.64
Fluorite	0.00	0.003	0.00	Thorite	0.00	0.10	0.00
Fuchsite	0.00	0.89	0.12	Titanite	0.02	21.39	3.88
Gahnite	0.00	0.50	0.00	Topaz	0.00	0.14	0.04
Galena	0.000	0.001	0.000	Tourmaline	0.01	1.09	0.22
Grossular	0.00	7.56	0.36	Wollastonite	0.00	0.06	0.01
Hedenbergite	0.00	0.20	0.02	Xenotime	0.00	0.02	0.00
Hercynite	0.00	0.09	0.01	Zircon	0.00	3.52	0.58
Hornblende	0.47	14.93	5.58	Zoisite	0.00	3.31	1.09
Minerals in bold italic are light minerals (<3.2 specific gravity)							

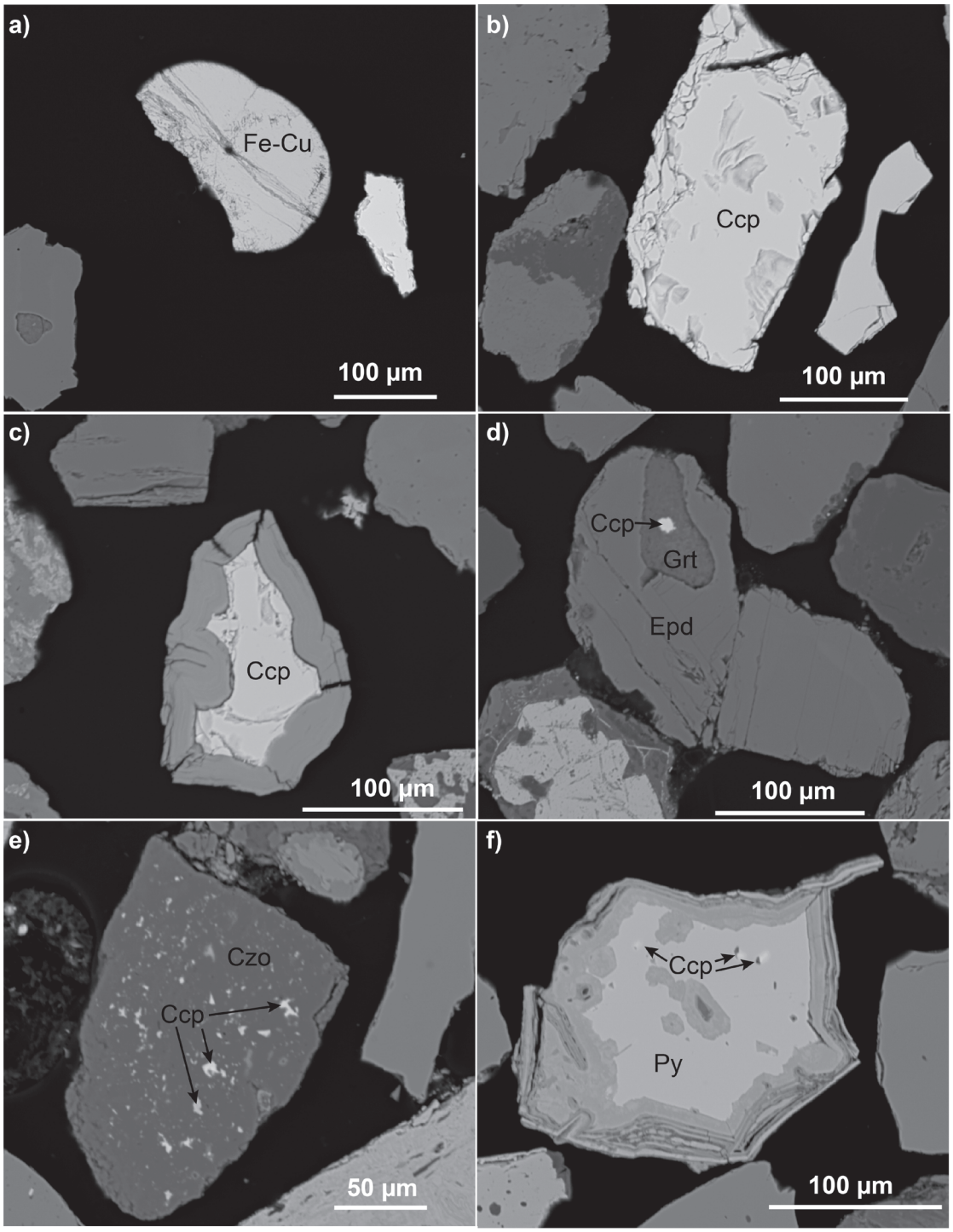

Ccp: chalcopyrite; Czo: clinozoisite; Epd: epidote; Fe-Cu: iron-copper contaminant; Grt: garnet; Py: pyrite

Figure 4. Backscattered-electron images of the fine-sand, heavy-mineral concentrate of till samples from porphyry copper study sites in British Columbia: **a)** Fe-Cu contaminant in sample 11PMA024A01 from Gibraltar; **b)** discrete unoxidized chalcopyrite grain in sample 11PMA024A01 from Gibraltar; **c)** partly oxidized chalcopyrite grain in sample 15PMA112A01 from Highland Valley Copper; **d)** chalcopyrite in garnet in epidote in sample 12PMA585A01 from Mount Polley; **e)** abundant chalcopyrite inclusions in clinozoisite (aluminium-rich epidote) in sample 12TFE047A01 from Gibraltar; and **f)** chalcopyrite inclusions in partly oxidized pyrite in sample 12TFE126A01 from Woodjam.

The most abundant minerals identified by MLA-SEM include clinopyroxene (diopside), epidote, and Fe-oxide/hydroxide. Titanite was found in large percentages (>15%) in a limited number of samples. These minerals were also the main constituents of the till MSHMC (Ferbey et al., 2016; Plouffe and Ferbey, 2016). We interpret the clinopyroxene to be derived from the mafic volcanic rocks of the Quesnel terrane, including Nicola Group and Chilcotin Group basalts (Schiarizza, 2016). Titanite is interpreted to be derived from intrusive rocks, including the batholiths that host the porphyry mineralization (Bouzari et al., 2011; Celis, 2015; Kobylinski et al., 2020). Epidote is derived dominantly from two sources: the hydrothermal alteration zones related to porphyry mineralization and the metamorphosed Nicola Group rocks (Plouffe et al., this volume).

We present the distribution patterns of two PCIMs identified in till: 1) chalcopyrite, an ore mineral, and 2) epidote, a mineral present in the alteration zones associated with porphyry mineralization. The distributions of chalcopyrite in the MSHMCs were previously described by Hashmi et al. (2015), Plouffe et al. (2016), and Plouffe and Ferbey (2017) and are only summarized here. At the four study sites, chalcopyrite, the main copper-ore mineral, is more abundant in till MSHMC near and down-ice of economic and subeconomic mineralization than it is regionally (Fig. 5a, 6a, 7a, and 8a). At Gibraltar, chalcopyrite in till follows an amoeboid dispersal pattern controlled by the three phases of ice-flow movement, which eroded a cluster of economic and subeconomic porphyry copper mineralized zones (Fig. 5a). At Mount Polley and Highland Valley Copper, glacial dispersal of chalcopyrite extends more than 10 km parallel to the dominant ice-flow movement: to the northwest at Mount Polley and south-southeast at Highland Valley Copper (Fig. 6a, 7a). At Woodjam, chalcopyrite dispersal in till extends approximately 2 km southwest and northwest from the mineralized zones, that is, parallel to both ice movements (Fig. 8a).

Regional glacial dispersal based on FSHMC of till cannot be assessed with the same level of detail as was determined using MSHMC given the smaller number of FSHMC samples (Table 1); however, chalcopyrite distribution in the FSHMC of till shows greater abundance near mineralization compared to its regional distribution at Gibraltar, Highland Valley Copper, and Woodjam (Fig. 5b, 7b, and 8b), which we interpret as being derived from porphyry copper occurrences. Chalcopyrite occurs as discrete grains and as inclusions in other minerals (Fig. 4). At Mount Polley, chalcopyrite in the MSHMC is most abundant near and down-ice of mineralization; this is not the case in the FSHMC (Fig. 6a, b). This could result from chalcopyrite being less abundant in the fine sand fraction compared to the medium sand fraction of till at that site. Also, the aliquot weight (0.3 g), despite containing approximately 20 000 grains, might be insufficient to represent the abundance of chalcopyrite in the FSHMC at that site. We estimate that the chalcopyrite area per cent in the FSHMC linked to mineralization is equivalent to greater than 0.02459 area per cent at Gibraltar, greater than 0.00922 area per cent at Woodjam, and greater than 0.07984 area per cent at Highland Valley (Fig. 5b, 7b, and 8b). In other words, the chalcopyrite area per cent threshold value in the FSHMC varies between the four study sites, which is likely related to the extent and grade of mineralization exposed to glacial erosion, as was suggested by Plouffe et al. (2016) in their interpretation of the chalcopyrite abundance in the MSHMC.

At the four study sites, pale green to pistachio green epidote in the MSHMC of till is more abundant in samples near and down-ice from porphyry mineralization and associated alteration zones compared to samples from surrounding areas barren of mineralization (Fig. 5c, 6c, 7c, and 8c). The dispersal patterns of total epidote abundances in the MSHMC reported here are similar to those presented by Hashmi et al. (2015), Plouffe et al. (2016), and Plouffe and Ferbey (2017) based on the abundance of epidote in the 0.8 to 1.0 A fraction of the MSHMC. At Gibraltar, till samples with greater than 45% epidote in the MSHMC occur across a minimum distance of 26 km north to south and 9 km east to west, centred on the Granite Mountain batholith, which is known to contain hydrothermal alteration epidote as far as 10 km from the ore zones (Fig. 5c; Ash and Riveros, 2001; van Straaten et al., 2013; Kobylinski et al., 2017, 2020). Epidote abundance greater than 45% in till north of the Granite Mountain batholith likely results from glacial dispersal; however, greater than 45% epidote in till south of the Granite Mountain batholith is likely derived from a combination of southeastward glacial transport in the early phase of glaciation and the underlying Early Cretaceous intrusive bedrock (Sheridan stock), which is known to contain hydrothermal alteration epidote (Ash and Riveros, 2001). At Mount Polley, greater than 7% epidote in the MSHMC of till defines a dispersal train extending 3 km southwest of the intrusion parallel to the first phase of ice flow and down-ice from the alteration zones with epidote (Fig. 6c; Rees, 2013). At Highland Valley, till samples with greater than 39% epidote are heterogeneously distributed along and down ice of the Highland Valley fault, where sodic-calcic and propylitic alteration characterized by epidote veins was mapped over a 34 km^2 area centred on mineralization (Fig. 7c; Casselman et al., 1995; Lesage et al., 2016; Byrne et al., 2020a, b). The source of 70% epidote in the MSHMC of one till sample collected in the northwest of the Guichon Creek batholith, is uncertain; it is most likely derived from propylitic alteration associated with subeconomic porphyry copper mineralization in that region (British Columbia Geological Survey, 2020). Similarly, the source of epidote (60% of the MSHMC) in one till sample at the southern limit of sampling is uncertain; it is most likely derived from alteration zones associated with porphyry copper mineral occurrences, potentially along the Lornex fault, up-ice from the sampling site. Lastly, at Woodjam, till samples with greater than 25% epidote are all located within 1.5 km of the mineralized zones where propylitic alteration with epidote is reported (Fig. 8c; Sherlock and Trueman, 2013; Sherlock et al., 2013).

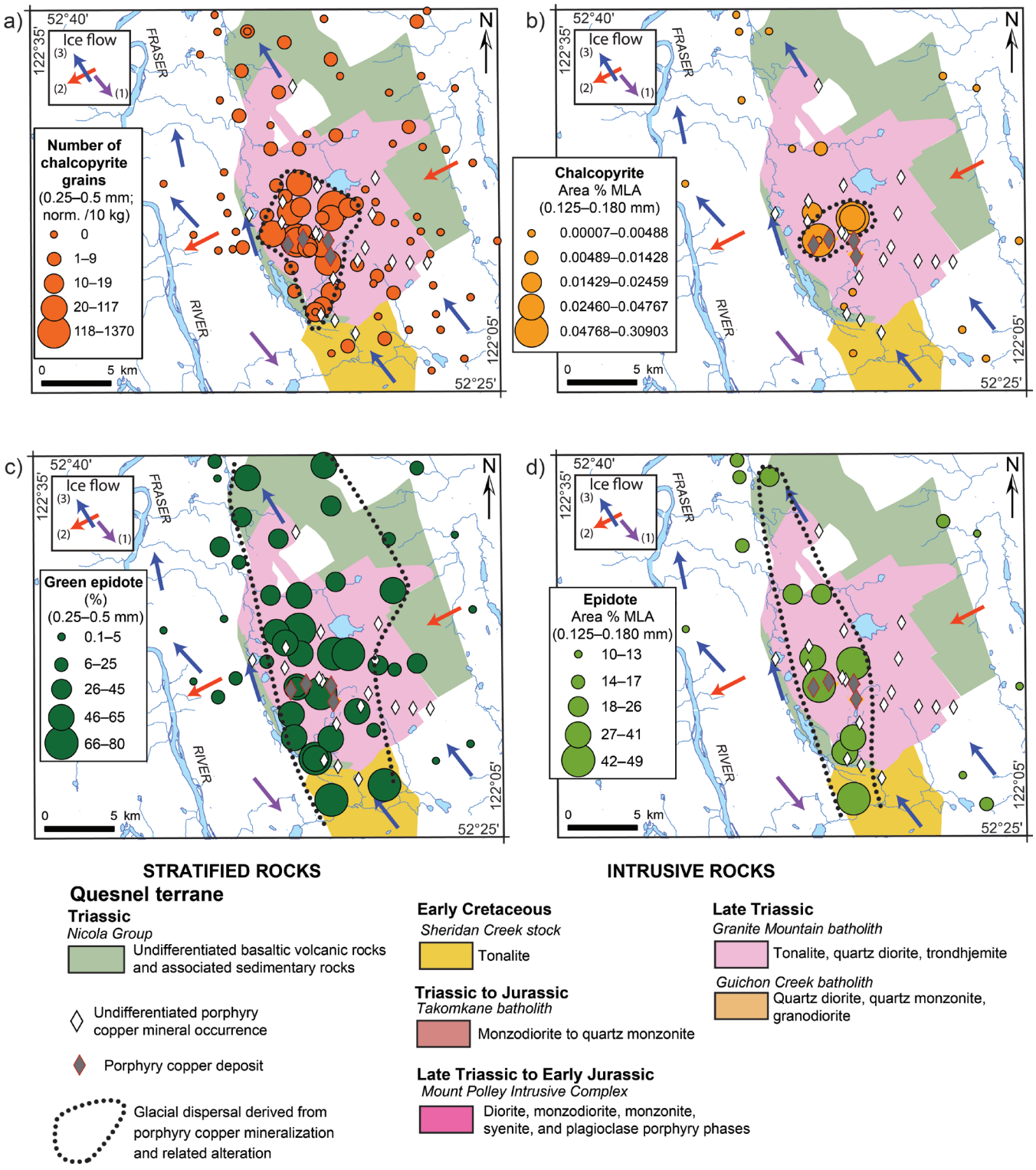

Figure 5. Till mineralogy in the region of the Gibraltar porphyry copper-molybdenum deposit, British Columbia: **a)** chalcopyrite grain counts in the medium-sand, heavy-mineral concentrate (MSHMC) normalized to a 10 kg bulk sample (*modified from* Plouffe et al., 2016 and Plouffe and Ferbey, 2017); **b)** chalcopyrite area per cent in the fine-sand, heavy-mineral concentrate (FSHMC) as determined by mineral-liberation analysis (MLA)–scanning electron microscopy (SEM); **c)** epidote percentages in the MSHMC, and **d)** epidote area per cent in the FSHMC as determined by MLA-SEM. Simplified bedrock geology *after* Massey et al. (2005) and Schiarizza (2015).

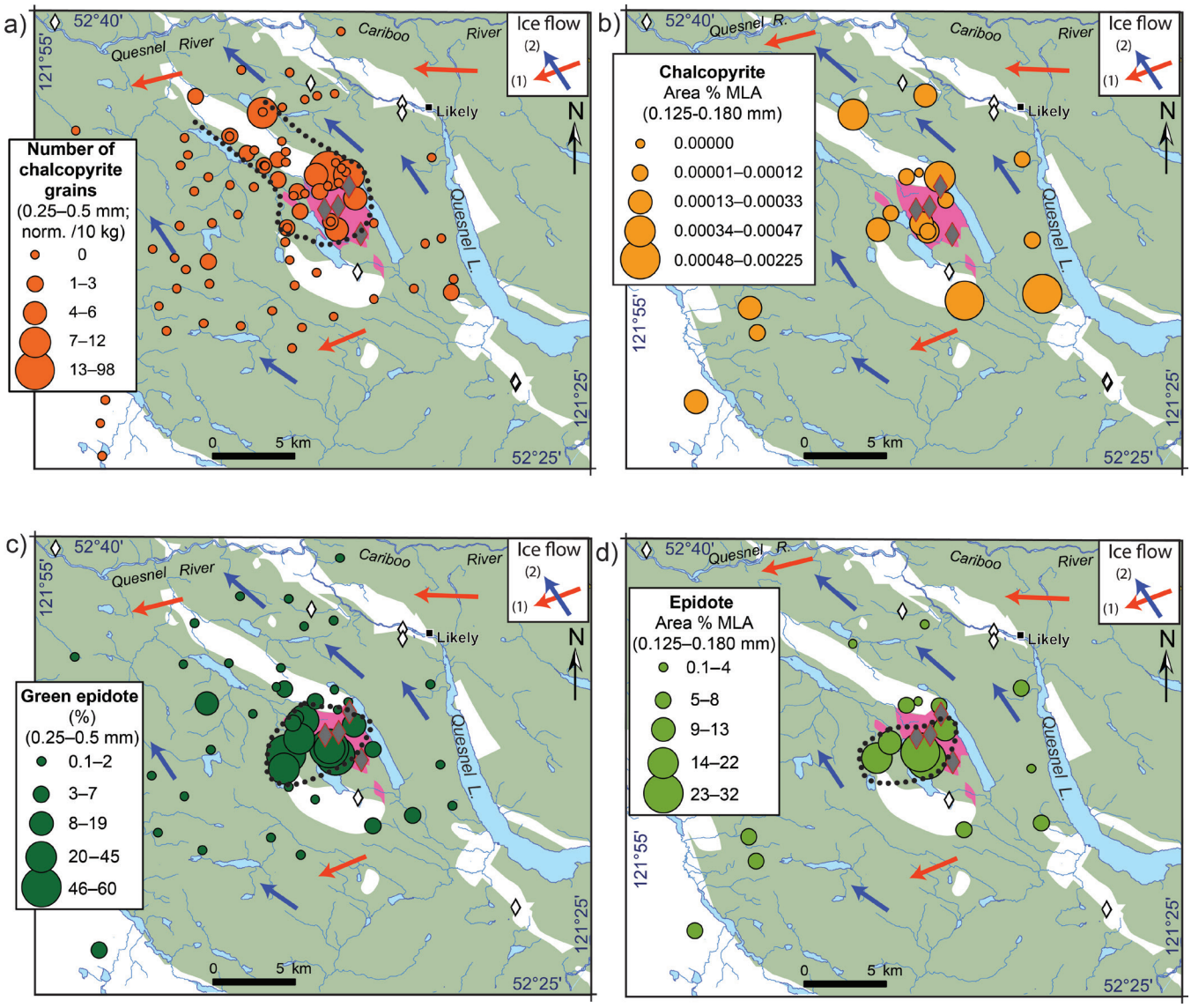

Figure 6. Till mineralogy in the region of the Mount Polley porphyry copper-gold deposit, British Columbia: **a)** chalcopyrite grain counts in the medium-sand, heavy-mineral concentrate (MSHMC) normalized to 10 kg bulk sample (*modified from* Hashmi et al., 2015; Plouffe et al., 2016; and Plouffe and Ferbey, 2017); **b)** chalcopyrite area per cent in the fine-sand, heavy-mineral concentrate (FSHMC) as determined by mineral-liberation analysis (MLA)–scanning electron microscopy (SEM); **c)** epidote percentages in the MSHMC, and **d)** epidote area per cent in the FSHMC as determined by MLA-SEM. *See* Figure 5 for bedrock geology legend. Simplified bedrock geology *after* Massey et al. (2005) and Rees (2013).

Although the number of FSHMC samples processed by MLA-SEM is less than the number of MSHMC samples, epidote distribution patterns in both size fractions show similarities (Fig. 5d, 6d, 7d, and 8d). At Gibraltar, samples with greater than 17 area per cent epidote in the FSHMC follow a north-south extent over a minimum distance of 26 km, similar to the distribution of greater than 45% epidote in the MSHMC (Fig. 5d). Samples with greater than 17 area per cent epidote in the FSHMC to the north-northwest of mineralization result from glacial transport. At Mount Polley, samples with greater than 8 area per cent epidote are located above the Mount Polley Intrusive Complex or 3 km to the southwest, parallel to the first phase of ice flow (Fig. 6d). At Highland Valley, samples with greater than 10 area per cent epidote are located close to or down-ice (south) from the Highland Valley fault, except for one sample in the northwest, which contains 19 area per cent epidote in the FSHMC and 70% epidote in the MSHMC (Fig. 7d). At Woodjam, samples with greater than 16 area per cent epidote are located within 1.5 km of the main mineralized zones (Fig. 8d). Just as Hashmi et al. (2015), Plouffe et al. (2016), and Plouffe and Ferbey (2017) concluded, we interpret the greater abundance of epidote in till near porphyry copper mineralization as being derived from the associated propylitic alteration

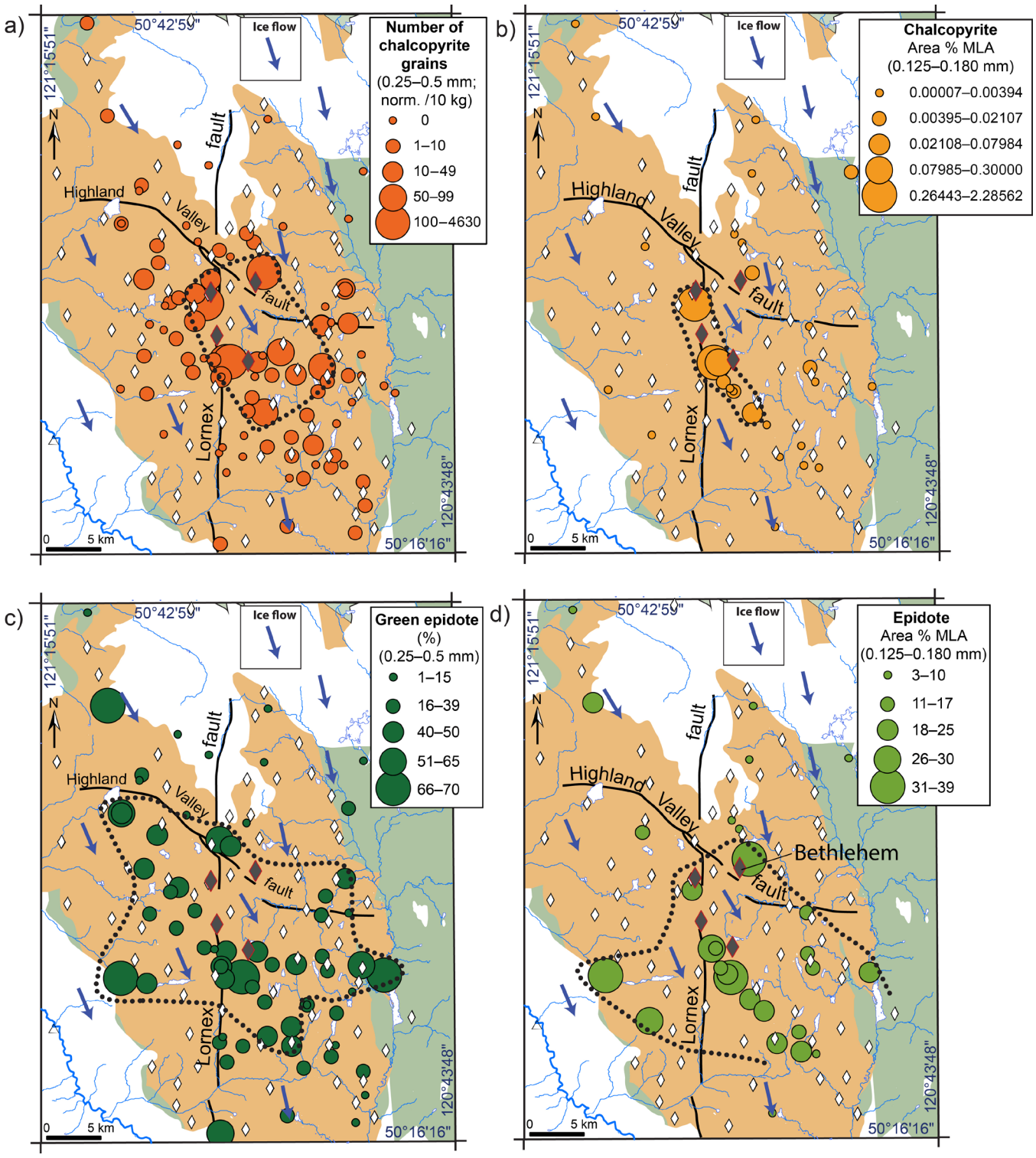

Figure 7. Till mineralogy in the region of the Highland Valley Copper porphyry copper-molybdenum deposit, British Columbia: **a)** chalcopyrite grain counts in the medium-sand, heavy-mineral concentrate (MSHMC) normalized to a 10 kg bulk sample (*modified from* Plouffe and Ferbey, 2017); **b)** chalcopyrite area per cent in the fine-sand, heavy-mineral concentrate (FSHMC) as determined by mineral-liberation analysis (MLA)–scanning electron microscopy (SEM); **c)** epidote percentages in the MSHMC, and **d)** epidote area per cent in the FSHMC as determined by MLA-SEM. *See* Figure 5 for bedrock geology legend. Simplified bedrock geology *after* McMillan et al. (2009).

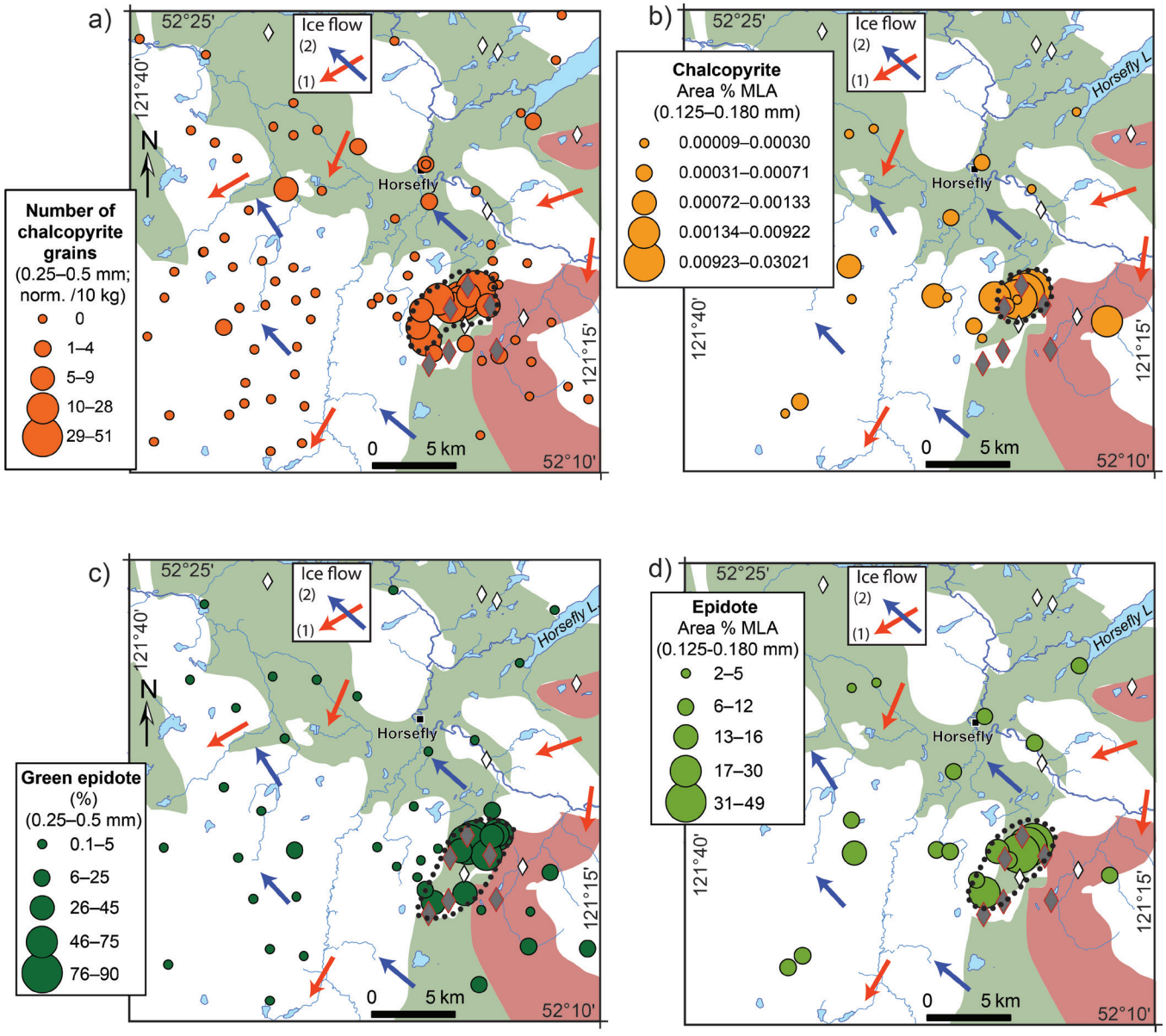

Figure 8. Till mineralogy in the region of the Woodjam porphyry copper-gold prospect, British Columbia: **a)** chalcopyrite grain counts in the medium-sand, heavy-mineral concentrate (MSHMC) normalized to a 10 kg bulk sample (*modified from* Plouffe et al., 2016; Plouffe and Ferbey, 2017); **b)** chalcopyrite area per cent in the fine-sand, heavy-mineral concentrate (FSHMC) as determined by mineral liberation analysis (MLA)–scanning electron microscopy (SEM); **c)** epidote percentages in the MSHMC, and **d)** epidote area per cent in the FSHMC as determined by MLA-SEM. *See* Figure 5 for bedrock geology legend. Simplified bedrock geology *after* Massey et al. (2005) and Logan et al. (2010).

zones. This interpretation is also supported by Plouffe et al. (this volume), who conclude based on epidote chemistry that a large amount of epidote in till at Gibraltar, Mount Polley, and Woodjam was derived from hydrothermal alteration associated with porphyry copper mineralization.

DISCUSSION

Previous studies report the successful application of MLA-SEM or other SEM-based automated mineral identification methods to mineral exploration in the Canadian Cordillera and elsewhere in Canada. Mackay et al. (2016) and Simandl et al. (2017) presented a two-step approach combining portable XRF and a quantitative evaluation of minerals by scanning electron microscopy (QEMSCAN®) from a commercial laboratory to detect carbonatite indicator minerals in stream sediments. They reported the detection of minerals of the pyrochlore supergroup and the columbite-tantalite series, and rare-earth element (REE)–fluorocarbonates and monazite in the 0.125 to 0.250 mm fraction of stream sediments draining carbonatites at three study sites: Alley, Lonnie, and Wicheeda. They identified these minerals in the 0.125 to 0.250 mm fraction of heavy concentrates produced with a Mozley C800 table and the non-concentrate of the same size fraction.

In another study based on MLA-SEM analysis of the less than 0.250 mm and greater than 3.2 SG fraction of four till samples at each of the Izok Lake volcanogenic massive sulfide deposit in the Northwest Territories and the Sisson granite-hosted W-Mo deposit in New Brunswick, Lougheed et al. (2020, this volume) conclude that ore (e.g. chalcopyrite, galena, sphalerite, scheelite, wolframite, Bi minerals) and alteration minerals (e.g. gahnite, corundum, epidote) can be identified in till up to 8 km down-ice from mineralization at Izok Lake and 10 km down-ice at Sisson, in both cases further extending the glacial dispersal identified from the 0.25 to 0.50 mm, greater than 3.2 SG mineralogy. They show that the greater than 3.2 SG, 0.125 to 0.250 mm fraction is optimal for MLA-SEM analysis.

In a research project testing the use of MLA-SEM for the mineral exploration of nickel deposits associated with serpentinized ophiolites, Wilton and Winter (2012) and Wilton et al. (2017) identified awaruite, a Ni-Fe alloy, and asbolane and pecoraite (two hydrated nickel-bearing minerals) in stream sediments and till from Newfoundland. These minerals were detected in the 0.125 to 0.180 mm fraction of till and stream sediments concentrated with a Wilfley shaking table (Wilton and Winter, 2012).

Lastly, McClenaghan et al. (2019a) presented the results from the MLA-SEM examination of one gossan and one till sample from the Cu–Ni–platinum-group elements–Au Broken Hammer deposit in the North Range of the Sudbury structure, Ontario. Analyses of five size fractions (0.180 to 0.250, 0.125 to 0.180, 0.075 to 0.125, 0.045 to 0.075, and <0.045 mm) concentrated with a hydroseparator are reported. In both the gossan and till samples, MLA-SEM reveals the presence of the same ore minerals identified by optical mineralogy (e.g. sperrylite, gold, and chalcopyrite) and additional minerals unrecognized optically (e.g. cassiterite, arsenopyrite, pentlandite, pyrrhotite, and galena). Chalcopyrite and pyrite in the till sample are dominantly present in the 0.125 to 0.250 mm heavy fraction.

Together, these results indicate the effectiveness of MLA-SEM at identifying minerals in the fine (<0.250 mm) fraction of detrital sediments and thus its direct application to mineral exploration.

Our study is the first to describe and compare the regional distributions of minerals identified by MLA-SEM in the FSHMC of till to the mineralogy identified optically in the MSHMC of samples from regions of porphyry mineralization. Even with a limited number of samples, the abundance of ore (chalcopyrite) and alteration (epidote) minerals identified in the FSHMC by MLA-SEM reflects the presence of porphyry copper mineralization with a greater abundance of these minerals in till near mineralization and associated alteration zones compared to regions barren of mineralization (Fig. 5b, 5d, 6d, 7b, 7d, 8b, and 8d), with the exception of chalcopyrite abundances at Mount Polley (Fig. 6b). Correlations in the abundance of chalcopyrite and epidote in the FSHMC and MSHMC can be illustrated geographically (Fig. 5–8), but also graphically (Fig. 9, 10). Chalcopyrite abundance generally correlates well between both size fractions at Gibraltar and Highland Valley Copper (Fig. 9a, c). The strong correlation is confirmed with Pearson correlation coefficients of 0.9 in both cases. We selected the Pearson method to calculate the correlation coefficients because it applies to data sets that include a number of observations with a value of zero (Huson, 2007). There is no obvious correlation between chalcopyrite in the FSHMC and the MSHMCs at Mount Polley and Woodjam (Fig. 9b, d). In this case, the Pearson correlation coefficient is –0.1 for Mount Polley and 0.4 for Woodjam. As mentioned above, the poor correlation between chalcopyrite abundance in the FSHMC and the MSHMC at Mount Polley could be related to the low abundance of this mineral in the FSHMC of till at the site. At Woodjam, although samples with the greatest abundance of chalcopyrite in the FSHMC and the MSHMC are all located near porphyry copper mineralization (Fig. 7b), the low correlation between the chalcopyrite content of both size fractions ($r = 0.4$) is likely related to the heterogeneous distribution of this mineral in till. At all sites, there are samples for which chalcopyrite was identified in the FSHMC and not in the MSHMC, probably because it is only present as discrete particles less than 0.250 mm in size or as inclusions within other minerals (Fig. 4d, e, f). The abundance of epidote in the FSHMC and MSHMC generally correlates better than for chalcopyrite at all study sites, with Pearson correlation coefficients of 0.8 at Gibraltar, 0.9 at Mount Polley, 0.8 at Highland Valley Copper, and 0.9 at Woodjam (Fig. 10). At Mount Polley and Woodjam, a few samples only contain epidote in the FSHMC (Fig. 10b, d). Based on

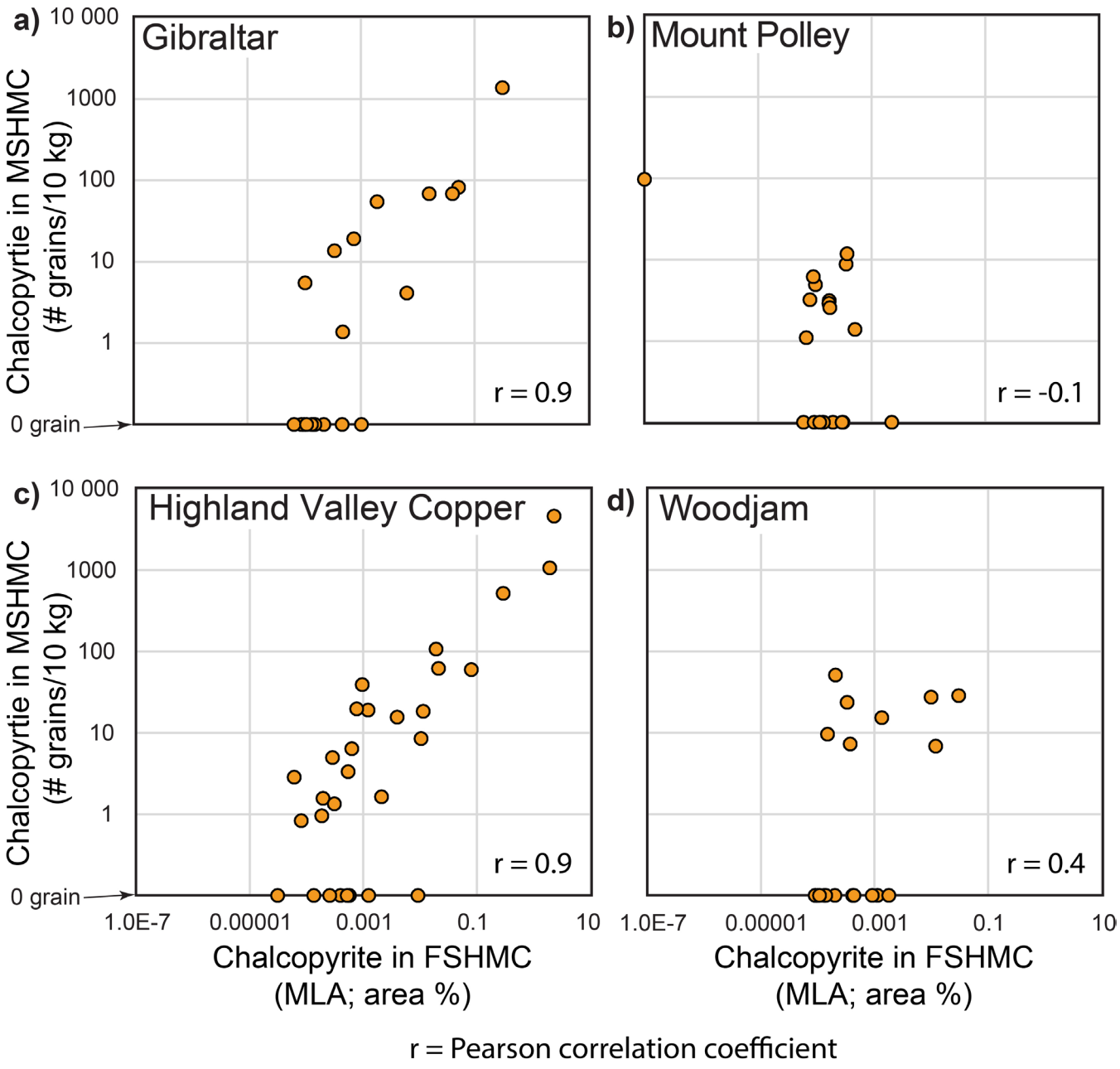

Figure 9. Correlation graph between the numbers of chalcopyrite grains normalized to a 10 kg bulk sample in the medium-sand, heavy-mineral concentrate (MSHMC) and the area per cent of chalcopyrite determined by mineral-liberation analysis (MLA)–scanning electron microscopy (SEM) in the fine-sand, heavy-mineral concentrate (FSHMC) of till at: **a)** Gibraltar, **b)** Mount Polley, **c)** Highland Valley Copper, and **d)** Woodjam porphyry study sites.

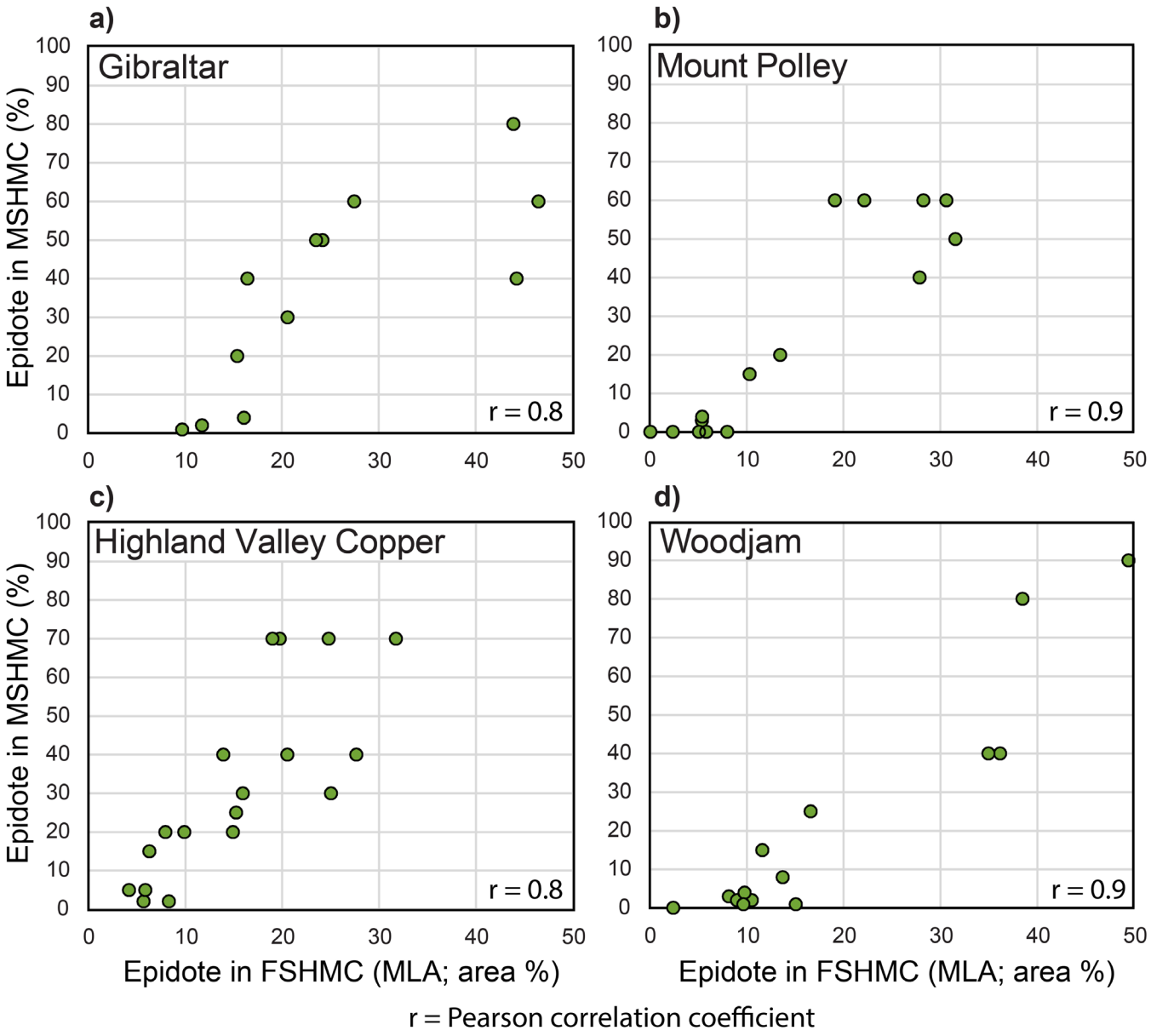

Figure 10. Correlation graph between the percentage of epidote in the medium-sand, heavy-mineral concentrate (MSHMC) and the area per cent of epidote determined by mineral-liberation analysis (MLA)–scanning electron microscopy (SEM) in the fine-sand, heavy-mineral concentrate (FSHMC) of till at: **a)** Gibraltar, **b)** Mount Polley, **c)** Highland Valley Copper, and **d)** Woodjam porphyry study sites.

the comparison of the mineralogy between the MSHMC and the FSHMC and the greater abundance of ore and alteration minerals near mineralization compared to the background region with no mineralization, we conclude that the mineralogy of the FSHMC of till determined by MLA-SEM provides an indication of porphyry copper mineralization.

The aliquot weight (0.3 g) used for MLA-SEM was sufficient to identify in till evidence of copper mineralization and/or associated alteration at the four study sites. The requirement of small aliquots (0.3 g) for MLA-SEM is an advantage because it only requires a small bulk-till sample. Based on the abundance of less than 0.250 mm material from till samples (Ferbey et al., 2016; Plouffe and Ferbey, 2016), we estimate that 5 to 8 kg of bulk till is sufficient to prepare 0.3 g aliquots for MLA-SEM of the FSHMC. This is smaller than the typical 9 to 15 kg bulk-till sample weight required for optical mineralogy analysis of the MSHMC. The required bulk-till sample weight for MLA-SEM will vary depending on till texture, but smaller sample sizes are faster to collect in the field and are less expensive to ship and process for heavy mineral separation, as Lehtonen et al. (2015) also pointed out. Smaller samples (5–8 kg instead of 9–15 kg) could be collected as part of a reconnaissance till-sampling survey. Follow-up till sampling with larger

samples (9–15 kg) could be pursued in regions with anomalous results and processing them for the geochemistry of the till matrix (<0.063 mm or <0.002 mm) and identification of PCIM in the FSHMC and MSHMC. Using such an approach, even the porphyry copper mineralization would have been detected in a reconnaissance phase at Mount Polley because there was a copper anomaly defined from the till geochemistry at that site (Plouffe et al., 2016).

In their study of epidote in the alteration zones associated with porphyry copper mineralization and in the metamorphosed Nicola Group mafic volcanic rocks, Plouffe et al. (2019, this volume) show that metamorphic epidote is generally fine grained and less than 0.250 mm in size, suggesting that the FSHMC could potentially include more metamorphic epidote unrelated to porphyry copper mineralization compared to MSHMC; however, our results indicate that even with the potential 'contamination' with metamorphic epidote, the abundance of this mineral in the FSHMC can be correlated with the presence of alteration associated with porphyry copper mineralization (Fig. 5d, 6d, 7d, and 8d).

Previous research has shown that, MLA-SEM and other SEM-based mineral identification techniques (e.g. QEMSCAN®; cf. Layton-Matthews et al., 2017) can provide benefits over the traditional optical identification of minerals in detrital sediments (Wilton and Winter, 2012; Mackay et al., 2016; Layton-Matthews et al., 2017; Simandl et al., 2017; Wilton et al., 2017; Lougheed et al., 2020, this volume), including

- once a mineral library is developed or obtained from services offered at a commercial laboratory, mineral identification is not operator dependent and is based on mineral composition (i.e. no inherent bias from human observation);
- minerals present as discrete grains less than 0.250 mm, as inclusions greater than 0.000020 mm^2 (2 μm^2), or as constituents of polymineral grains are identified;
- SEM images generated during MLA provide details of internal mineral zonation and texture;
- the abundance of major mineral constituents are precisely determined based on mineral composition as opposed to being estimated from the optical evaluation in a greater than 0.250 mm HMC; and
- specific mineral grains identified in the FSHMC can easily be revisited for more detailed analysis (e.g. laser-ablation inductively coupled plasma mass spectrometry (LA-ICP-MS)) because they are already mounted and polished.

This last point could be of importance for certain minerals that need to be characterized geochemically to be related to a porphyry copper source (cf. group 2 PCIM described in Plouffe and Ferbey, 2017). For example, the study of zircon REE composition as related to porphyry fertility (Ballard et al., 2002; Dilles et al., 2015; Bouzari et al., 2016; Lu et al., 2016; Lee et al., 2017; Loader et al., 2017; Plouffe et al., 2019) could be applied to this mineral in the FSHMC; zircon grains large enough for LA-ICP-MS analysis were identified in our samples (Fig. 11).

In our study, the MLA-SEM results are based on the area per cent of two PCIM in 30 mm grain mounts of the FSHMC of till samples. These MLA-SEM results could be further processed to provide additional information. For example, Lougheed et al. (this volume) processed the MLA-SEM results to determine the number of mineral grains, which, combined with the area per cent, can provide valuable information about the dominant form of a mineral and,

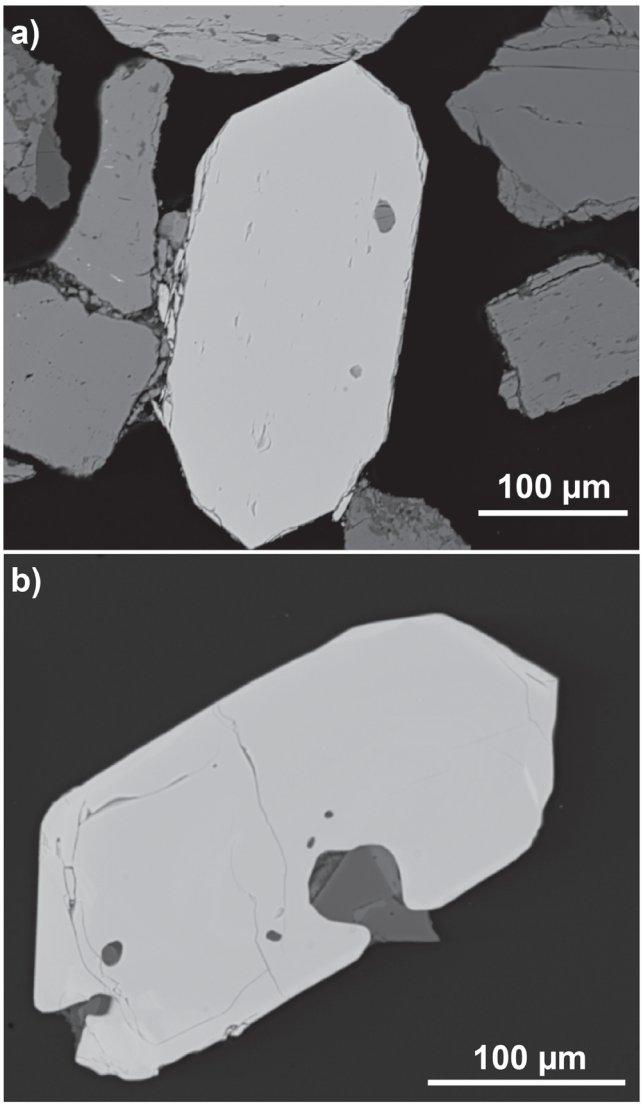

Figure 11. Backscattered-electron images of zircon from the fine-sand, heavy-mineral concentrate of till samples from porphyry copper study sites in British Columbia: **a)** sample 11PMA033A01 from Gibraltar and **b)** sample 15PMA005A01 from Highland Valley Copper.

potentially, the anomalous nature of a sample. Large grain counts combined with small area per cent values likely reflect the dominant presence of inclusions or small mineral particles on polymineral grains; conversely, small grain counts combined with large area per cent values suggest the presence of discrete mineral particles. For example, in the 0.185 to 0.250 mm HMC fraction of one till sample at the Izok Lake volcanogenic massive-sulfide deposit, galena abundance reported as area per cent is low and non-anomalous; however, the large number of small galena particles in this same sample makes it anomalous (Lougheed et al., this volume).

CONCLUSION

Using mineralogy determined by MLA-SEM of the FSHMC of 91 till samples from four porphyry copper study sites, we show that chalcopyrite is more abundant in till near mineralization at three out of four sites and that epidote, dominantly derived from hydrothermal alteration zones, is more abundant near porphyry mineralization at the four sites. These results corroborate previous mineralogical investigations of the MSHMC determined by optical methods, demonstrating that till mineralogy is an effective method to detect porphyry copper mineralization and associated alteration zones that were exposed to glacial erosion. The spatial distribution of these minerals in till follows the patterns of established ice-flow movements. In mineral exploration, till mineralogical anomalies could be traced to their potential bedrock source using reconstructed ice-flow vectors. Smaller (5–8 kg) bulk-till samples are required to obtain a sufficient FSHMC for MLA-SEM, which is an advantage over the 9 to 15 kg samples typically required to process the MSHMC for PCIMs. A reconnaissance till-sampling program aimed at determining the potential of porphyry copper mineralization in greenfield regions would benefit from smaller samples treated for MLA-SEM and geochemical analysis. Detailed follow-up could be pursued in targeted anomalous areas with a combination of PCIMs identified in the FSHMC and the MSHMC. Future research should test the identification of PCIMs by MLA-SEM in stream sediments of glaciated and unglaciated areas.

ACKNOWLEDGMENTS

This project was completed as part of the Porphyry-style Mineral Systems project, Activity P-3.3: Mineralogical markers of fertility porphyry-style systems, part of the GSC's Targeted Geoscience Initiative program. Laboratory support at Memorial University was provided by David Grant and Dylan Goudie of the Micro Analysis Facility (MAF), Core Research Equipment & Instrument Training Network (CREAIT). The manuscript benefited from reviews by Matthew Polivchuck, Ernst Schetselaar, and Gary Thompson.

REFERENCES

Ash, C.H. and Riveros, C.P., 2001. Geology of the Gibraltar copper-molybdenite deposit, east-central British Columbia (93B/9); *in* Geological Fieldwork 2000, British Columbia Geological Survey, British Columbia Ministry of Energy and Mines, Paper 2001-1, p. 119–134.

Ballard, J.R., Palin, J.M., and Campbell, I.H., 2002. Relative oxidation states of magmas inferred from Ce(IV)/Ce(III) in zircon: application to porphyry copper deposits of northern Chile; Contributions to Mineralogy and Petrology, v. 144, p. 347–364. https://doi.org/10.1007/s00410-002-0402-5

Beckett-Brown, C.E., McDonald, A.M., and McClenaghan, M.B., 2019. Unravelling tourmaline in mineralized porphyry systems: assessment as a valid indicator mineral; *in* Targeted Geoscience Initiative: 2018 report of activities, (ed.) N. Rogers; Geological Survey of Canada, Open File 8549, p. 345–351. https://doi.org/10.4095/313669

Bouzari, F., Hart, C.J.R., Barker, S., and Bissig, T., 2011. Porphyry indicator minerals (PIMS): a new exploration tool for concealed deposits in south-central British Columbia; Geoscience BC Report 2011-17, 31 p.

Bouzari, F., Hart, C.J.R., Bissig, T., and Barker, S., 2016. Hydrothermal alteration revealed by apatite luminescence and chemistry: a potential indicator mineral for exploring covered porphyry copper deposits; Economic Geology, v. 111, p. 1397–1410. https://doi.org/10.2113/econgeo.111.6.1397

British Columbia Geological Survey, 2020. MINFILE 092INW013 record summary; MINFILE BC mineral deposits database; British Columbia Ministry of Energy, Mines and Petroleum Resources, British Columbia Geological Survey. <https://minfile.gov.bc.ca/> [accessed February 2020].

Byrne, K., Stock, E., Ryan, J., Johnson, C., Nisenson, J., Alva Jimenez, T., Lapointe, M., Stewart, H., Grubisa, G., and Syroka, S., 2013. Porphyry Cu-(Mo) deposits in the Highland Valley district, south-central British Columbia; *in* Porphyry systems of central and southern British Columbia: tour of central British Columbia porphyry deposits from Prince George to Princeton, Guidebook series of the Society of Economic Geologists, (comp.) J.M. Logan and T.G. Schroeter; Society of Economic Geologists, Guidebook 44, p. 99–116.

Byrne, K., Lesage, G., Gleeson, S.A., Piercey, S.J., Lypaczewski, P., and Kyser, K., 2020a. Linking mineralogy to lithogeochemistry in the Highland Valley Copper district: implications for porphyry copper footprints; Economic Geology, v. 115, p. 871–901. https://doi.org/10.5382/econgeo.4733

Byrne, K., Trumbull, R.B., Lesage, G., Gleeson, S.A., Ryan, J., Kyser, K., and Lee, R.G., 2020b. Mineralogical and isotopic characteristics of sodic-calcic alteration in the Highland Valley Copper district, British Columbia, Canada: implications for fluid sources in porphyry Cu systems; Economic Geology, v. 115, p. 841–870. https://doi.org/10.5382/econgeo.4740

Casselman, M.J., McMillan, W.J., and Newman, K.M., 1995. Highland Valley porphyry copper deposits near Kamloops, British Columbia: a review and update with emphasis on the Valley deposit; *in* Porphyry deposits of the northwestern Cordillera of North America, (ed.) T.G. Schroeter; Canadian Institute of Mining, Metallurgy and Petroleum, Special Volume 46, p. 161–191.

Celis, A., 2015. Titanite as an indicator mineral for alkalic porphyry Cu-Au deposits in south-central British Columbia; M.Sc. thesis, The University of British Columbia, Vancouver, British Columbia, 247 p.

Dilles, J.H., Kent, A.J.R., Wooden, J.L., Tosdal, R.M., Koleszar, A., Lee, R.G., and Farmer, L.P., 2015. Zircon compositional evidence for sulphur-degassing from ore-forming arc magmas; Economic Geology, v. 110, p. 241–251. https://doi.org/10.2113/econgeo.110.1.241

Ferbey, T., Plouffe, A., and Bustard, A.L., 2016. Geochemical, mineralogical, and textural data from tills in the Highland Valley Copper mine area, south-central British Columbia; British Columbia Ministry of Energy and Mines, British Columbia Geological Survey, GeoFile 2016-11, and Geological Survey of Canada, Open File 8119, 1 .zip file. https://doi.org/10.4095/299242

Grenier, A., Connell-Madore, S., McClenaghan, M.B., Wygergangs, M., and Moore, C.S., 2015. Study of cleaning methods for electro-welded sieves to reduce/eliminate carry over contamination between till samples; Geological Survey of Canada, Open File 7769, 1 zip file. https://doi.org/10.4095/296314

Hashmi, S., Ward, B.C., Plouffe, A., Leybourne, M.I., and Ferbey, T., 2015. Geochemical and mineralogical dispersal in till from the Mount Polley Cu-Au porphyry deposit, central British Columbia, Canada; Geochemistry: Exploration, Environment, Analysis, v. 15, p. 234–249. https://doi.org/10.1144/geochem2014-310

Huson, L.W., 2007. Performance of some correlation coefficients when applied to zero-clustered data; Journal of Modern Applied Statistical Methods, v. 6, p. 530–536. https://doi.org/10.22237/jmasm/1193890560

Kobylinski, C., Hattori, K., Plouffe, A., and Smith, S., 2017. Epidote associated with the porphyry Cu-Mo mineralization at the Gibraltar deposit, south central British Columbia; Geological Survey of Canada, Open File 8279, 1 .zip file. https://doi.org/10.4095/305912

Kobylinski, C., Hattori, K., Smith, S., and Plouffe, A., 2020. Protracted magmatism and mineralized hydrothermal activity at the Gibraltar porphyry copper-molybdenum deposit, British Columbia; Economic Geology, 18 p. https://doi.org/10.5382/econgeo.4724

Layton-Matthews, D., Hamilton, C., and McClenaghan, M.B., 2017. Modern techniques and applications of mineral chemistry to exploration; *in* Application of indicator mineral methods to bedrock and sediments, (ed.) M.B. McClenaghan and D. Layton-Matthews; Geological Survey of Canada, Open File 8345, p. 10–24. https://doi.org/10.4095/306308

Lee, R.G., Dilles, J.H., Tosdal, R.M., Wooden, J.L., and Mazdab, F.K., 2017. Magmatic evolution of granodiorite intrusions at the El Salvador porphyry copper deposit, Chile, based on trace element composition and U/Pb age of zircons; Economic Geology, v. 112, p. 245–273. https://doi.org/10.2113/econgeo.112.2.245

Lehtonen, M., Lahaye, Y., O'Brien, H., Lukkari, S., Marmo, J., and Sarala, P., 2015. Novel technologies for indicator mineral-based exploration; *in* Novel technologies for greenfield exploration, (ed.) P. Sarala; Geological Survey of Finland, Special Paper 57, p. 23–62.

Lesage, G., Byrne, K., and Lypaczewski, P., 2016. Characterizing the district-scale alteration surrounding a large porphyry Cu system: the footprint of Highland Valley Copper, British Columbia; Geological Association of Canada–Mineralogical Association of Canada, Whitehorse, Yukon, June, 2016, Abstracts Volume 39, p. 52.

Loader, M.A., Wilkinson, J.J., and Armstrong, R.N., 2017. The effect of titanite crystallisation on Eu and Ce anomalies in zircon and its implications for the assessment of porphyry Cu deposit fertility; Earth and Planetary Science Letters, v. 472, p. 107–119. https://doi.org/10.1016/j.epsl.2017.05.010

Logan, J.M., Schiarizza, P., Struik, L.C., Barnett, C., Nelson, J.L., Kowalczyk, P., Ferri, F., Mihalynuk, M.G., Thomas, M.D., Gammon, P., Lett, R., Jackaman, W., and Ferbey, T. (comp.), 2010. Bedrock geology of the QUEST map area, central British Columbia; Geoscience BC Report 2010-5, British Columbia Geological Survey Geoscience Map 2010-1, and Geological Survey of Canada Open File 6476, scale 1:500 000. https://doi.org/10.4095/261517

Lougheed, H.D., McClenaghan, M.B., and Layton-Matthews, D., 2018. Mineral markers of base metal mineralization: progress report on the identification of indicator minerals in the fine heavy mineral fraction; *in* Targeted Geoscience Initiative: 2017 report of activities, volume 2, (ed.) N. Rogers; Geological Survey of Canada, Open File 8373, p. 101–108. https://doi.org/10.4095/306605

Lougheed, H.D., McClenaghan, M.B., Layton-Matthews, D., and Leybourne, M.I., 2019. Evaluation of single-use nylon screened sieves for use with fine-grained sediment samples; Geological Survey of Canada, Open File 8613, 13 p. https://doi.org/10.4095/315138

Lougheed, H.D., McClenaghan, M.B., Layton-Matthews, D., and Leybourne, M.E., 2020. Exploration potential of fine-fraction heavy mineral concentrates from till using automated mineralogy: a case study from the Izok Lake Cu–Zn–Pb–Ag VMS deposit, Nunavut, Canada; Minerals, v. 10, no. 4, 310. https://doi.org/10.3390/min10040310

Lu, Y.-J., Loucks, R.R., Fiorentini, M., McCuaig, T.C., Evans, N.J., Yang, Z.-M., Hou, Z.-Q., Kirkland, C.L., Parra-Avila, L.A., and Kobussen, A., 2016. Zircon composition as a pathfinder for porphyry Cu ± Mo ± Au deposits; *in* Tectonics and metallogeny of the Thetyan Orogenic Belt, (ed.) J. Richard; Society of Economic Geologists, Special Publication 19, p. 329–347.

Mackay, D.A.R., Simandl, G.J., Ma, W., Redfearn, M., and Gravel, J., 2016. Indicator mineral-based exploration for carbonatites and related specialty metal deposits — a QEMSCAN® orientation survey, British Columbia, Canada; Journal of Geochemical Exploration, v. 165, p. 159–173. https://doi.org/10.1016/j.gexplo.2016.03.005

Massey, N.W.D., MacIntyre, D.G., Desjardins, P.J., and Cooney, R.T., 2005. Geology of British Columbia; British Columbia Ministry of Energy, Mines and Petroleum Resources, British Columbia Geological Survey, Geoscience map 2005-3, scale 1:1 000 000.

McClenaghan, M.B., Beckett-Brown, C.E., McCurdy, M.W., McDonald, A.M., Leybourne, M.I., Chapman, J.B., Plouffe, A., and Ferbey, T., 2018. Mineral markers of porphyry copper mineralization: progress report on the evaluation of tourmaline as an indicator mineral; *in* Targeted Geoscience Initiative: 2017 report of activities, volume 1, (ed.) N. Rogers; Geological Survey of Canada, Open File 8358, p. 69–77. https://doi.org/10.4095/306427

McClenaghan, M.B., Ames, D.E., and Cabri, L.J., 2019a. Indicator mineral and till geochemical signatures of the Broken Hammer Cu–Ni–PGE–Au deposit, North Range, Sudbury Structure, Ontario, Canada; Geochemistry: Exploration, Environment, Analysis. https://doi.org/10.1144/geochem2019-058

McClenaghan, M.B., McCurdy, M.W., Garrett, R.G., Beckett-Brown, C.E., Leybourne, M.I., Casselman, S.G., and Pelchat, P., 2019b. Mineral and geochemical signatures of porphyry copper mineralization: work in progress at the Casino Cu-Au-Mo-Ag porphyry deposit; *in* Targeted Geoscience Initiative: 2018 report of activities, (ed.) N. Rogers; Geological Survey of Canada, Open File 8549, p. 333–344. https://doi.org/10.4095/313667

McMillan, W.J., Anderson, R.G., Chan, R., and Chow, W., 2009. Geology and mineral occurrences (MINFILE), Guichon Creek Batholith and Highland Valley porphyry copper district, British Columbia; Geological Survey of Canada, Open File 6079, scale 1:100 000 and 1:150 000, 2 sheets. https://doi.org/10.4095/248060

Plouffe, A. and Ferbey, T., 2015. Till composition near Cu-porphyry deposits in British Columbia: highlights for mineral exploration; *in* TGI 4 – Intrusion Related Mineralisation Project: new vectors to buried porphyry-style mineralisation, (ed.) N. Rogers; Geological Survey of Canada, Open File 7843, p. 15–37. https://doi.org/10.4095/296464

Plouffe, A. and Ferbey, T., 2016. Till geochemistry, mineralogy and textural data near four Cu porphyry deposits in British Columbia; British Columbia Ministry of Energy and Mines, British Columbia Geological Survey, Geofile 2016-10, and Geological Survey of Canada, Open File 8038, 1 .zip file. https://doi.org/10.4095/298805

Plouffe, A. and Ferbey, T., 2017. Porphyry Cu indicator minerals in till: a method to discover buried mineralization; *in* Indicator minerals in till and stream sediments of the Canadian Cordillera, (ed.) T. Ferbey, A. Plouffe, and A. Hickin; Geological Association of Canada, Special Paper, v. 50 and Mineral Association of Canada, Topics in Mineral Sciences, v. 47, p. 129–159.

Plouffe, A., McClenaghan, M.B., Paulen, R.C., McMartin, I., Campbell, J.E., and Spirito, W., 2014. Quality assurance and quality control measures applied to indicator mineral studies of glacial sediments at the Geological Survey of Canada; *in* Application of indicator mineral methods to mineral exploration, (ed.) M.B. McClenaghan, A. Plouffe, and D. Layton-Matthews; Geological Survey of Canada, Open File 7553, p. 19–25. https://doi.org/10.4095/293858

Plouffe, A., Ferbey, T., Hashmi, S., and Ward, B.C., 2016. Till geochemistry and mineralogy: vectoring towards Cu porphyry deposits in British Columbia, Canada; Geochemistry: Exploration, Environment, Analysis, v. 16, p. 213–232. https://doi.org/10.1144/geochem2015-398

Plouffe, A., Kjarsgaard, I.M., Kobylinski, C., Hattori, K., Petts, D.C., Venance, K.E., and Ferbey, T., 2019. Discovering the next generation of copper porphyry deposits using mineral markers; *in* Targeted Geoscience Initiative: 2018 report of activities, (ed.) N. Rogers; Geological Survey of Canada, Open File 8549, p. 321–331. https://doi.org/10.4095/313666

Rees, C., 2013. The Mount Polley Cu-Au deposit, south-central British Columbia, Canada; *in* Porphyry systems of central and southern British Columbia: tour of central British Columbia porphyry deposits from Prince George to Princeton, Guidebook series of the Society of Economic Geologists, (comp.) J.M. Logan and T.G. Schroeter; Society of Economic Geologists, Guidebook 44, p. 67–98.

Schiarizza, P., 2015. Geological setting of the Granite Mountain batholith, south-central British Columbia; *in* Geological Fieldwork 2014, British Columbia Ministry of Energy and Mines, British Columbia Geological Survey, Paper 2015-1, p. 19–39.

Schiarizza, P., 2016. Toward a regional stratigraphic framework for the Nicola Group: Preliminary results from the Bridge Lake – Quesnel River area; *in* Geological Fieldwork 2015, British Columbia Ministry of Energy, Mines and Petroleum Resources, British Columbia Geological Survey, Paper 2016-1, p. 13–30.

Schiarizza, P., 2017. Ongoing stratigraphic studies in the Nicola Group: Stump Lake - Salmon River area, south-central British Columbia; *in* Geological Fieldwork 2016, British Columbia Ministry of Energy, Mines and Petroleum Resources, British Columbia Geological Survey, Paper 2017-1, p. 17–33.

Sherlock, R. and Trueman, A., 2013. NI 43-101 technical report for 2012 activities on the Woodjam south property; Gold Fields Horsefly Exploration Group and Consolidated Woodjam Copper Corporation, Cariboo Mining Division, British Columbia, 158 p.

Sherlock, R., Blackwell, J., and Skinner, T., 2013. NI 43-101 technical report for 2012 activities on the Woodjam North property; Gold Fields Horsefly Exploration Group, Consolidated Woodjam Copper Corporation, Cariboo Mining Division, British Columbia, 275 p.

Simandl, G.J., Mackay, D.A.R., Ma, X., Luck, P., Gravel, J., and Akam, C., 2017. The direct indicator mineral concept and QEMSCAN® applied to exploration for carbonatite and carbonatite-related ore deposits; *in* Indicator minerals in till and stream sediments of the Canadian Cordillera, (ed.) T. Ferbey, A. Plouffe, and A. Hickin; Geological Association of Canada, Special Paper, v. 50 and Mineral Association of Canada, Topics in Mineral Sciences, v. 47, p. 175–190.

Taseko Mines Ltd., 2020. Taseko Mines Ltd. <tasekomines.com> [accessed July 2020]

van Straaten, B.I., Oliver, J., Crozier, J., and Goodhue, L., 2013. A summary of the Gibraltar porphyry copper-molybdenum deposit, south-central British Columbia, Canada; *in* Porphyry systems of central and southern British Columbia: tour of central British Columbia porphyry deposits from Prince George to Princeton, Guidebook series of the Society of Economic Geologists, (comp.) J.M. Logan and T.G. Schroeter; Society of Economic Geologists, Guidebook 44, p. 55–66.

Wilton, D.H.C. and Winter, L.S., 2012. SEM-MLA (Scanning electron microscope - Mineral Liberation analyzer) research on indicator minerals in till and stream sediments - an example from the exploration for awaruite in Newfoundland and Labrador; *in* Quantitative mineralogy and microanalysis of sediments and sedimentary rocks, (ed.) P. Sylvester; Mineralogical Association of Canada, Short Course Series, v. 42, p. 265–283.

Wilton, D.H.C., Thompson, G.M., and Grant, D.C., 2017. The use of automated indicator mineral analysis in the search for mineralization – a next generation drift prospecting tool; Explore, v. 174, p. 1–18.

APPENDIX A

Results of mineral liberation analysis by scanning electron microscopy (MLA-SEM) of the heavy fine sand fraction of till

This file POR-11_Plouffe et al_Appendix A.xlsx contains the heavy mineralogy of the fine sand fraction (>3.2 SG; 0.125–0.180 mm) as determined by MLA-SEM and the chalcopyrite and epidote content of the heavy medium sand fraction (>3.2 SG; 0.25–0.50 mm) of till as determined by optical mineralogy (Ferbey et al., 2016; Plouffe and Ferbey, 2016). The file includes sample locations and a short legend. This Appendix has not been edited to Geological Survey of Canada specifications.